NIFS-PROC-95

Proceedings of the Third Meeting for A3 Foresight Program Workshop on Critical Physics Issues Specific to Steady State Sustainment of High-Performance Plasmas 9-24 May,, 2013, Beijing, China

(Eds.) L. Hu, S. Morita and Y.-K. Oh

Dec. 05, 2013

Proceeding of A3 Foresight Program Seminar on Critical Physics Issues Specific to Steady State Sustainment of High-Performance Plasmas

19-24 May, 2013, Beijing, China

Edited by

Liqun HU, Shigeru MORITA and Yeong-Kook OH

Abstract

To enhance close collaborations among scientists in three Asian countries (China, Japan and Korea), A3 foresight program on Plasma Physics was newly started from August 2012 under the auspice of JSPS (Japan), NRF (Korea) and NSFC (China). The main purpose of this project is to solve several key physics issues through joint experiments on three Asian advanced fully superconducting fusion devices (EAST in China, LHD in Japan and KSTAR in Korea) and other magnetic confinement devices to carry out multi-faceted and complementary physics researches. To summarize the progress and achievement in the first academic year under this A3 foresight program, this workshop was hosted by Institute of Plasma Physics, Chinese Academy of Sciences and held in Beijing during 19-24 May, 2013. Collaborated research and communication with other A3 programs and bilateral programs, as well as participation of young scientists were encouraged in this workshop. The topics include steady state sustainment of magnetic configurations, edge and divertor plasma control and confinement of alpha particles.

Key words: magnetically confined devices, toroidal plasmas, high performance plasmas, steady state operation, edge plasma, divertor plasma and alpha particle.

Organization Committee

Liqun HU (Institute of Plasma Physics, Chinese Academy of Sciences, China)
Shigeru MORITA (National Institute for Fusion Science, Japan)
Yeong-KooK OH (National Fusion Research Institute, Korea)

Program Committee

Liqun HU (Institute of Plasma Physics, Chinese Academy of Sciences, China)
Shigeru MORITA (National Institute for Fusion Science, Japan)
Yeong-Kook OH (National Fusion Research Institute, Korea)
Ge ZHUANG (Huazhong University of Science and Technology, China)
Hong QIN (University of Science and Technology of China, China)
Yi LIU (Southwestern Insitute of Physics, China)
Ze GAO (Tsinghua University, China)
Houyang GUO (Institute of Plasma Physics, Chinese Academy of Sciences, China)
Guangnan LUO (Institute of Plasma Physics, Chinese Academy of Sciences, China)

Conference Secretariats

Yong LIU (Institute of Plasma Physics, Chinese Academy of Sciences, China)
Shaohua DONG (Institute of Plasma Physics, Chinese Academy of Sciences, China)
Masanori KAKIAGE (National Institute for Fusion Science, Japan)
Jun-hie HAN (National Fusion Research Institute, Korea)

Preface

Steady-state sustainment of high-performance plasmas is one of the crucial issues needed to be addressed for fusion reactor development. To enhance close collaborations among scientists in three Asian countries (China, Japan and Korea), A3 foresight program on Plasma Physics was newly started from August 2012 under the auspice of JSPS (Japan), NRF (Korea) and NSFC (China). The main purpose of this project is to solve several key physics issues through joint experiments on three Asian advanced fully superconducting fusion devices (EAST in China, LHD in Japan and KSTAR in Korea) and other magnetic confinement devices to carry out multi-faceted and complementary physics researches. The topics include steady state sustainment of magnetic configurations, edge and divertor plasma control and confinement of alpha particles.

The 1st coordinator meeting hosted by NFRI (Korea) was held in Jeju Island, Korea on 22nd August, 2012. The 2nd meeting of A3 foresight program on Plasma Physics, i.e. the first seminar hosted by NIFS (Japan) was held in Kushiro, Japan from January 22 to 25, 2013. To summarize the progress and achievement in the first academic year under this A3 foresight program, this workshop, as the third meeting of A3 program, was hosted by Institute of Plasma Physics, Chinese Academy of Sciences and held in Beijing during 19-24 May, 2013. Collaborated research and communication with other A3 programs and bilateral programs, as well as participation of young scientists were encouraged in this workshop. In total 95 participants attended this meeting, among whom 18 were from Japan, 18 from Korea, and the remaining from China. 69 reports were presented, particularly 33 of them were by young scientists and occupied a whole day for oral presentation. Results of the collaboration based on A3 program are published as the proceeding which can ensure better communication among the A3 community. In the proceeding, 41 papers are collected in the end. Officials from all the 3 parties attended the meeting, and they are: Shigeyuki KATOH (Deputy director), Akiko TAKEUCHI (International Program Associate), and An JIANG (Assistant), from JSPS; Mei JIN (Researcher) from NRF; Yinglan ZHANG (Director), and Yongtao ZHANG (Deputy director) from NSFC. Director Yinglan ZHANG addressed a keynote speech in the opening.

The presentations focus on the following topics which are important issues in the present A3 foresight program, regardless of the differences among magnetic configurations such as tokamaks and helical devices. The result is covered with 5 topics:

(i) Current drive and profile control, (ii) Transport of edge and divertor plasmas, (iii) Stability of edge plasma, (iv) Interaction between energetic particle and bulk plasma, and (v) Experimental and theoretical study in other magnetically confined fusion devices.

The workshop was closed with great success, clarifying remarkable progress obtained through A3 collaboration in the researches concerning the above important topics and also contributing to the fostering of younger scientists in related field. The organizing and program committees are deeply grateful to all participants and to strong and continuous support from foundation of three countries, with whose support and corporation the seminar was smoothly and successfully concluded.

Liqun HU, Shigeru MORITA and Yeong-KooK OH

Chairpersons of the Organizing Committee

3rd A3 Foresight Program Seminar on Critical Physics Issues Specific to Steady State Sustainment of High-Performance Plasma 20-23 May, 2013, Beijing, China

Contents

Category I: Steady state sustainment of magnetic configurations

Category II: Edge and divertor plasma control

Category III: Confinement of alpha particles

Progress in the development of JT-60SA toward steady-state high-beta plasma research

A. Isayama and the JT-60SA team

Japan Atomic Energy Agency, Naka, Ibaraki 311-0193, Japan

Abstract : This paper describes recent progress in the development of JT-60SA. The disassembly of JT-60U was completed in October 2012, and the assembly of JT-60SA was started in January 2013 by installing a 280 t cryostat base fabricated in Spain. The fabrication of device components is steadily progressed both in EU and Japan toward the first plasma in 2019. In addition, JT-60SA research plan is extensively discussed by researchers in EU and Japan.

1. Introduction

Steady-state high-performance plasmas are essential for realizing an economical fusion reactor. Here, 'high-performance' stands for simultaneous achievement of key values characterizing the plasma, which are the confinement enhancement factor (so-called *H*-factor), beta value (the ratio of the plasma pressure to the magnetic pressure) and non-inductive current drive fraction and so on. Septangle plots as shown in Fig. 1 have been used to evaluate the degree of high performance since evaluations were made for the performance of JT-60U plasmas [1].

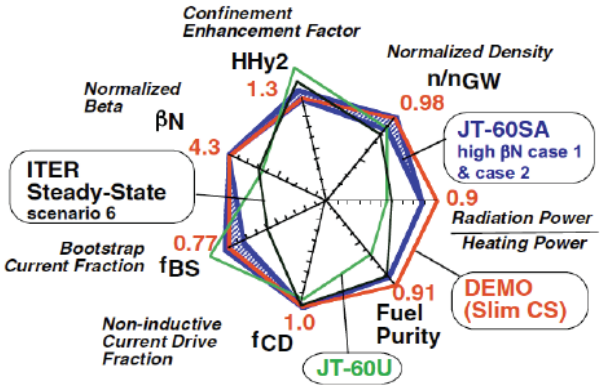

Fig. 1. A septangle plot representing the degree of simultaneous achievement of key values [1].

With regard to steady state, different types of time scales governing the plasma behavior need to be kept in mind, especially for controlling the plasma actively; they are the energy confinement time (typically 10^{-1} to 1 s in JT-60U), current diffusion time (several to 10 s) and wall recycling time (10 s or longer). Furthermore, it must be recognized that in such a high-performance plasma, linkage between plasma parameters tends to be stronger. Such linkage is graphically shown in Fig. 2 [1].

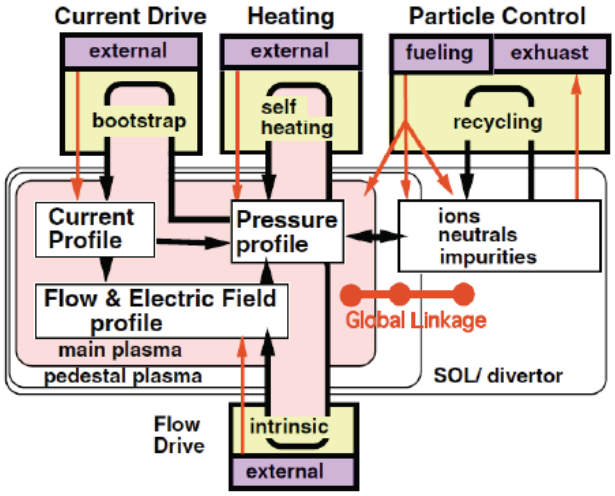

Fig. 2. Linkage between plasma parameters and relationship with external actuators [1].

In view of plasma control in DEMO, the knob for plasma control is very limited. Thus, for controlling a

high-performance plasma in steady state, it is important to understand the above linkage and develop a system to control it with limited detectors and actuators. Experiences obtained in developing real-time control systems for JT-60U are to be succeeded to establishing those for JT-60SA.

The JT-60SA project is a combined project of JAEA's program for national use and JA-EU Satellite Tokamak Program collaborating with EU and Japan fusion community. The main mission of the JT-60SA project is to contribute to early realization of fusion energy by supporting the exploitation of ITER and by complementing ITER in resolving key physics and engineering issues for DEMO reactors.

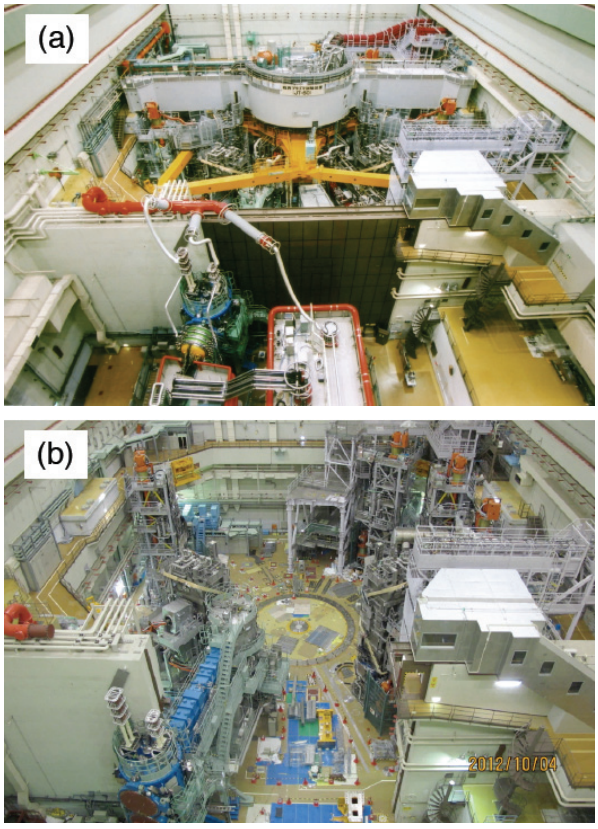

Fig. 3. Torus hall (a) before disassembly and (b) after disassembly.

Device construction of JT-60SA is in progress toward the first plasma in 2019. The disassembly of JT-60 device was started in 2010, and completed in October 2012 (Fig. 3). And in January 2013, the construction of the JT-60SA device was started by installing a 280 t cryostat base, which was fabricated in Spain and transported via Hitachi port.

2. Status of the Development of JT-60SA [2]

2.1 Target and Device

The target regime of the JT-60SA plasma is shown in Fig. 4, with regimes of JT-60U, ITER and DEMO. The value of the normalized beta, β_N, in JT-60SA ranges from 3.5 to 5.5, which is above the ideal-MHD limit without conducting walls (so-called 'no-wall' limit). The discharge duration is typically 100 s, which enables physics studies with long time-scale such as wall recycling. With the use of long-duration high-power heating/current drive systems described later, a high-β_N fully non-inductive discharge reaching the high-beta regime in DEMO, is possible. The cross section of the JT-60SA plasma, shown in Fig. 5, is characterized by a high shape parameter $S = q_{95}I_p/(aB_t)$, with which β_N is known to increase. Here, q_{95}, I_p, a, and B_t are the safety factor at 95% flux surface, plasma current, plasma minor radius and toroidal magnetic field at the plasma center, respectively. Compared with the JT-60U plasma (shown in Fig. 5), a plasma with higher triangularity ($\delta_x \sim 0.5$) and high elongation ($\kappa \sim 1.9$) is simultaneously achieved in JT-60SA. Typical parameters of JT-60SA are listed in Table 1.

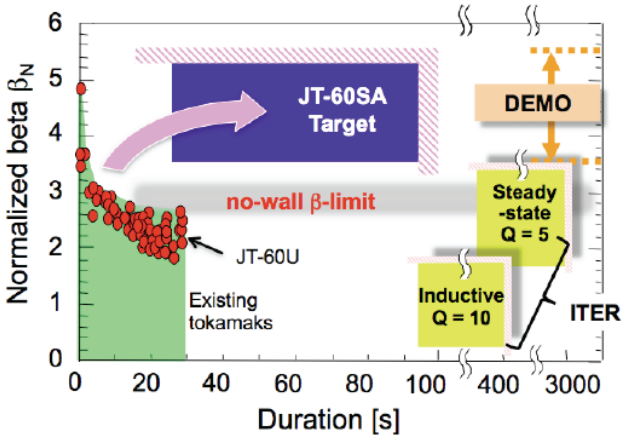

Fig. 4. Target regime of JT-60SA in the space of the normalized beta versus duration. Also shown are results in JT-60U and typical operational regimes in ITER and DEMO.

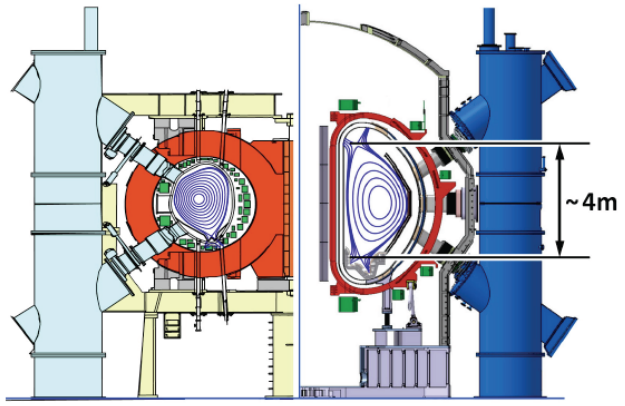

Fig. 5. Plasma cross-section of JT-60U (left) and JT-60SA (right).

Table 1: Typical parameters of JT-60SA.

Plasma Current	5.5 MA
Toroidal Field, B_t	2.25 T
Major Radius, R_p	2.96
Minor Radius, a	1.18
Elongation, κ_X	1.95
Triangularity, δ_X	0.53
Aspect Ratio, A	2.5
Shape Parameter, S	6.7
Safety Factor, q_{95}	~3
Flattop Duration	100 s
Heating & CD Power	41 MW
N-NBI P-NBI ECRF	10 MW 24 MW 7 MW
Divertor wall load	15 MW/m^2

The region of JT-60SA is located close to that of ITER and DEMO with respect to the normalized plasma parameter. For example, the values of the normalized collisionality and the normalized poloidal gyroradius are on the same order as those in ITER and DEMO, as shown in Fig. 6. In addition, strong electron heating by negative-ion-based neutral beams (N-NBs) and electron cyclotron (EC) waves can simulate reactorrelevant conditions where electron heating by alpha particles dominates. Furthermore, the N-NBs can address physics issues related to high-energy particles: fast-ion beta of 0.1-1 is possible for fast-ion velocity normalized to the Alfvén velocity of ~2, which is in the same range as that of alpha particles in ITER and DEMO.

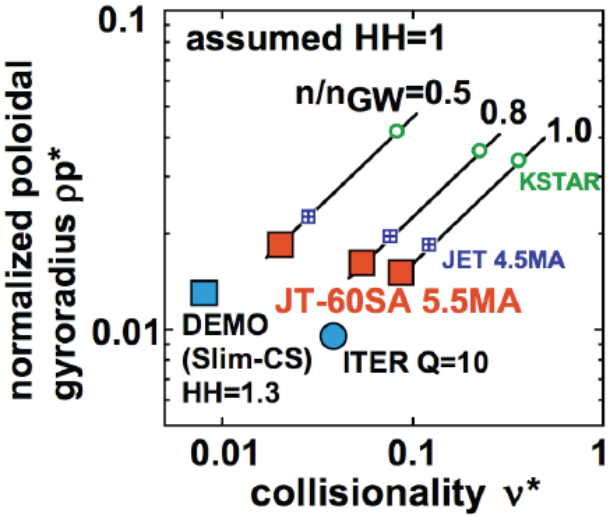

Fig. 6. Plasma regime of JT-60SA in the space of the normalized collisionality ν* and the normalized poloidal gyroradius ρ_p*

To achieve the above missions, JT-60SA has a variety of heating and current drive systems with the total injection power of 41 MW. The layout of these systems is shown in Fig. 7. The systems are composed

of 24 MW of 85 keV positive-ion-based neutral beams (P-NBs), 10 MW of 500 keV N-NB and 7 MW of EC range of frequency (ECRF) waves (110 GHz and 138 GHz). Two out of four tangential P-NBs are in the co-direction (the same direction as that of the plasma current), and the others are in the counter-direction. The direction of the other eight beams is in the nearly perpendicular direction. The direction of NNB is in the co-tangential direction. The height of the NNB beams is lowered by 55 cm compared with the case in JT-60U to enable strong off-axis current drive. The combination of these NBs enables variable momentum input profile. The ECRF system is composed of 9 transmission lines and 4 launchers. The EC waves are injected from upper oblique direction, and their directions can be changed independently using linearmotion launchers. In addition, fast power modulation, typical above 5 kHz, is possible for neoclassical tearing mode stabilization.

2.2 Fabrication of Tokamak Component

Fabrication of tokamak components is procured both by EU and Japan. The status of the fabrication is briefly described below [2].

2.2.1 Poloidal field coils (procured by Japan)

The poloidal field (PF) coils are composed of four modules of central solenoid (CS) coils made of Nb_3Sn and six equilibrium field (EF) coils made of NbTi. Manufacture of the conductors is in progress at a 680 m length jacketing facility in the Naka site. Some of the tests for the conductors were performed in collaboration with NIFS. The fabrication of the first EF coil, EF4 with the radius of 1.9 m, was completed in March 2012. The fabrication of EF5 and EF6, whose radius is 3.9 m and 5.0 m, respectively, is in progress at Naka site. In addition, the first production of a pancake for the CS coils was also successfully completed.

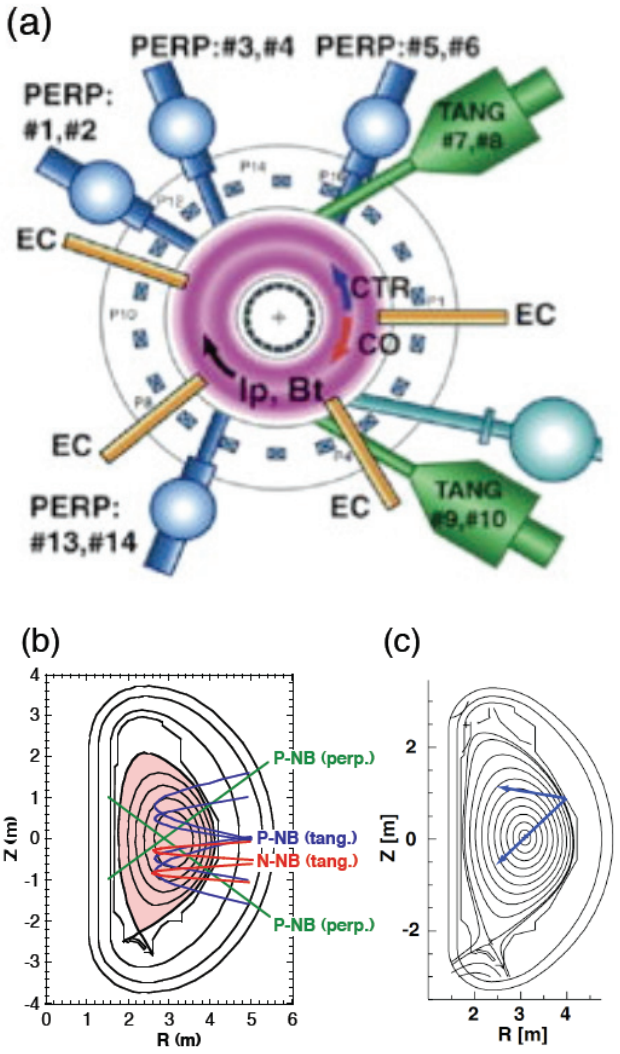

Figure 7: Layout of heating systems: (a) top view, (b) side view of NB beam lines and (c) side view of EC wave injection range.

2.2.2 Toroidal field coils (procured by EU)

The toroidal field (TF) coils of JT-60SA are composed

of 18 coils made of NbTi. The conductor is fabricated in progress in EU. The winding of the TF coils are done in ENEA in Italy and CEA in France. Fabrication of TF coils in these institutes is being started. A facility to test CS coils, where tests under the full operational condition with respect to cooling and energization are done, is ready in CEA.

2.2.3 Vacuum vessel (procured by JAEA)

The vacuum vessel (VV) for JT-60SA has a double wall structure to withstand a large electromagnetic force applied especially at a disruption and to keep a high one-turn voltage in the toroidal direction. The most critical issue in fabricating the VV with high accuracy is to reduce deformation during welding. To minimize the deformation, several welding methods were compared using a mockup (upper half, 20º in the toroidal direction). After the R&D activities, manufacture of the first three 40º sectors were completed in March 2012. At present, five 40º sectors were completed. The key dimension was controlled within the tolerance of ±5 mm successfully.

2.2.4 Divertor (procured by JAEA)

JT-60SA has a water-cooled W-shaped divertor, which is designed to allow the maximum heat flux of 15 MW/m^2. In addition, cryopanels installed behind the divertor enable divertor pumping at variable pumping speeds ranging 0-100 m^3/s. The divertor cassettes are designed so that they can be replaced using a remote handling system to be used in the high radioactive phase. After R&D to establish high manufacture accuracy, the fabrication of all 36 divertor cassettes was finished. In addition, the fabrication of all 100 carbon monoblock targets was also finished.

2.3 Development of Heating Systems [3,4]

Operations of heating systems have been continued to meet the requirement in JT-60SA; the most critical issue is to achieve 100 s duration to cover the full discharge duration of JT-60SA.

With regard to the P-NBs, it was found that the capability required in JT-60SA can be reached without large modifications. The development of the N-NB system has been continued by transferring it from the JT-60 torus hall to another building. The issue was to clarify the voltage-holing characteristics of a large area multi-aperture grid. By clarifying the characteristics through operations, the voltage-holding capability of 200 kV for 100 s without breakdown was demonstrated in a single gap. This suggests stable beam acceleration up to 500 keV is feasible using a 3-gap accelerator to be used in JT-60SA, and also 1 MeV using a 5-gap accelerator in ITER

The development of the ECRF system using 110 GHz gyrotrons used for JT-60U has been continued with improvements of gyrotron components such as a mode convertor. In 2012, the transmission line was replaced from a 31.75 mm diameter one to a 60.3 mm diameter one to reduce the power density in the transmission line and the mode conversion loss at miter bends. As a result, the oscillation duration at 1 MW output reached

70 s. Also, operations to achieve output power above 1 MW were continued, and 1.4 MW output was sustained for 9 s. In addition to the development of 110 GHz gyrotrons, the development of a new dualfrequency, which can output 110 GHz and 138 GHz, was started in order to enable heating and current drive at the plasma core region at Bt = 2.25 T. As a result of operations, oscillations at both frequencies were confirmed. Operations for high-power long-duration are in progress.

2.4 Progress in Research Activities

The capability of the JT-60SA such as heating power will be upgraded during the operational phase; the research phases are categorized into the Initial Research Phase, Integrated Research Phase and Extended Research Phase. To achieve the missions of the JT-60SA project along with the research phases, the schedule of JT-60SA experiments was defined in the JT-60SA Research Plan. The present version of the Research Plan is 3.0, to which more than 330 researchers from EU and Japan contributed. Results and plans of research activities in EU and Japan are reported in the Research Coordination Meeting (RCM). The second RCM was held in May 2013 in Naka, and the Research Plan is being updated to 3.1 by the end of 2013.

3. Summary

Device fabrications, heating system developments, and research activities have been extensively continued both in EU and Japan toward the first plasma of JT-60SA. Fabrication of components is progressing on schedule, and the construction of the JT-60SA device was started in January 2013. Assembly in the JT-60 torus hall is to be in full swing in 2013. This work was partly supported by the JSPS-NRFNSFC A3 Foresight Program in the field of Plasma Physics (NSFC: No.11261140328). This work was also partly supported by a Grant-in-Aid for Young Scientists (B) #22760662 from MEXT Japan.

4. References

[1] Y. Kamada et al., Nucl Fusion **51**, 073011(2011).

[2] Y. Kamada et al., Proc. 24th IAEA Fusion Energy Conf. (San Diego, USA, 2012), OV/4-1.

[3] M. Hanada et al., Proc. 24th IAEA Fusion Energy Conf. (San Diego, USA, 2012), FTP/P1-18.

[4] A. Isayama et al., Proc. 24th IAEA Fusion Energy Conf. (San Diego, USA, 2012), FTP/P1-16.

Plan for the sawtooth control by the ECH in KSTAR

J. H. Jeong[1], Y. S. Bae[1], M. Joung[1], B. B. Sahu[1], M. H. Woo[1], S. H. Hahn[1], K. D. Lee[1], J. H. Kim[1], H. H. Lee[1], H. L. Yang[1], J. G. Kwak[1], M. Kwon[1], W. Namkung[2], H. Park[2] and M. H. Cho[2]

[1] Steady-state operation division, National Fusion Research Institute, 305-333 Daejeon, Korea

[2] Department of Physics, POSTECH, 790-784 Pohang, Korea

Abstract: The sawtooth control in tokamak is very important because the long period sawtooth is able to trigger TM/NTMs which are significantly reducing the operational performance of plasma and even lead disruptions. The different sawtooth period behaviors by ECH and NBI with different injection conditions are observed in KSTAR during the 2012 campaign. The period of sawtooth is shortened by on-axis X2 110 GHz ECCD in NB-heated plasmas, and the stabilization of the sawtooth is also observed by off-axis X2 110 GHz ECCD. This means that the sawtooth period can be controlled in an accurate way by various EC beam injection conditions in KSTAR and to lengthen it as well. Two new recent sawtooth control methods are of interest and under the plan in KSTAR experiments: sawtooth locking and sawtooth pacing which is a well-known technique to control the sawtooth period behavior by periodic forcing by electron cyclotron waves nearby $q=1$ surface. The locking range can be investigated with a variable deposition location and the modulated RF power with a certain period and duty cycle in an open-loop control. And then, using the best parameters to lengthen in a controlled-way the sawtooth period, the relations between the sawtooth period and triggering of TM/NTM will be obtained at different beta values. For these experiments, the real-time control development of EC beam power modulation is under plan to control the sawtooth periods to a desired value. This requires the arbitrary power modulation of EC beam synchronized with external waveform generator which can be set the various modulation frequencies. This paper presents the sawtooth characteristics in present KSTAR operation scenario and the plan of the real-time sawtooth control. Also, the upgrade plan of the fast EC power modulation is presented including the present status of KSTAR ECH systems.

Keywords: sawtooth control, ECH, ECCD, on-/off-axis, co-/counter-current drive, KSTAR.

PACS: 52.50.Qt

1. Introduction

The sawtooth oscillation is a periodic relaxations of the core plasma density and temperature [1, 2] which is able to trigger neoclassical tearing modes (NTMs) well below the ideal β-limits [3, 4], especially when the sawtooth period is long [5] due to stabilization effects. As a results, developing techniques to control the sawtooth period as a way of controlling the onset of NTMs has been an important area of research in recent.

The sawtooth crash is associated with both the magnetic shear on the $q = 1$ surface [6] and the orbits of energetic ions with respect to the same surface [7-9] (Here, the safety factor is $q = d\psi_\varphi/d\psi_\theta$ and the magnetic shear is $s = r/q\ dq/dr$ with ψ_θ and ψ_φ the poloidal and toroidal magnetic fluxes respectively.). It has been shown experimentally that the sawtooth period can be manipulated by either neutral beam injection (NBI) [10, 11] and/or ion cyclotron (IC) waves [12, 13] or electron cyclotron (EC) waves [14, 15]. The particularly effective method for the control of sawtooth period is electron cyclotron current drive (ECCD), which can modify the magnetic shear evolution near the *q=1* surface effectively due to its highly localized deposition ability. One of the greatest potential advantage of ECH is that the absorption location can be easily adjusted by changing external parameters (launcher mirrors) only.

The fundamental trigger of the sawtooth crash remains the onset of an $m = n = 1$ mode, although the dynamics of this instability are constrained by many factors including not only the macroscopic drive from ideal MHD, but collisionless kinetic effects related to high energy particles [16-18] and thermal particles [19], as well as non-ideal effects localized in the narrow layer around $q = 1$. It is found that in auxiliary heated plasmas, the most relevant criterion for determining the onset of the sawtooth crash can be written as [20]

$$s_1 > s_{1,\mathrm{crit}}, \text{ where, } s_1 = r_1 \cdot q'(r_1) \qquad (1)$$

For controlling sawteeth the main consideration is when the plasma conditions have been met in order for a sawtooth crash to occur. From equation (1), it is evident that sawteeth can be destabilized (i.e. a crash can be triggered) by enhancing s_1 through localized current drive and also it means that the sawtooth can be stabilized by decreasing s_1. When the ECH is applied to the $q = 1$ surface, this has the consequence of moving the radius of the $q = 1$ surface, r_1, and changing the magnetic shear at $q = 1$, s_1, thus affecting the sawtooth crash. Benefits of a long period sawteeth by the sawtooth control provide the improved performance with gradients build-up and the increase of stored energy. However, the long sawtooth period can create a seed island on magnetic flux surfaces triggering secondary long-lasting MHD activity, so called neo-classical tearing mode (NTM) which causes confinement degradation or disruption [20]. It means that the sawtooth control in ITER is very important because the very long sawtooth periods is expected due to large fusion-born alpha particle population in the core [21]. Therefore, the sawtooth control by the ECRH will be needed to avoid NTMs in ITER and it is well demonstrated in many tokamak devices that ECH system can stabilize and destabilize sawtooth depending power deposition position.

In this paper, the sawtooth stabilization and destabilization is summarized by the different injection conditions of ECH, such as co-/counter-ECCD and on-/off-axis ECCD on KSTAR in section 2. The plan for the real-time sawtooth control for the KSTAR is summarized with the conceptual design in section 3.

Then, the plan with the preliminary results of the real-time antenna mirror also has been shown in section 3. Finally it will be summarized in section 4.

2. Sawtooth experiments using ECH/ECCD in KSTAR

2.1 Experimental set-up

For the sawtooth control experiments in KSTAR, 110 GHz ECH system is used with a maximum power of 0.4 MW. For the second harmonic X-mode with the frequency of 110 GHz, the cold resonance lies at B_T = 2.0 T in the plasma centre which is R=1.8 m in KSTAR. The plasma current is I_p = 0.4 MA and the line-averaged electron densities are about n_e = 1~2 × 10^{19} m^{-2}. KSTAR ECH launcher has two-mirror front steering launcher without actively water cooling. The first mirror is fixed focusing mirror which is located after the corrugated waveguide end and the second mirror is a steerable mirror in both poloidal and toroidal directions. The steering mirror has a toroidal range of +/- 30 degrees to produce controllable amounts of CD in both the co- and counter-directions and a poloidal range of 50 to 90 degrees from the vertical axis to allow on/off injection of EC beam. The scan of steering is possible during the pulse with accuracy of +/- 1 degree at the speed of 10 degrees/s. The pivot position of steerable mirror is not located at the center but is located at 279 mm to the left and 300 mm down from the center [22]. **Figure 1** shows the poloidal cross section of 110 GHz ECH beam trajectories from 0 degrees injection (parallel beam injection) to 17 (or 19) degrees injection for on-axis EC beam injection at the toroidal magnetic field of 2.0 Tesla which is nominal operation conditions for X2 mode of 110 GHz.

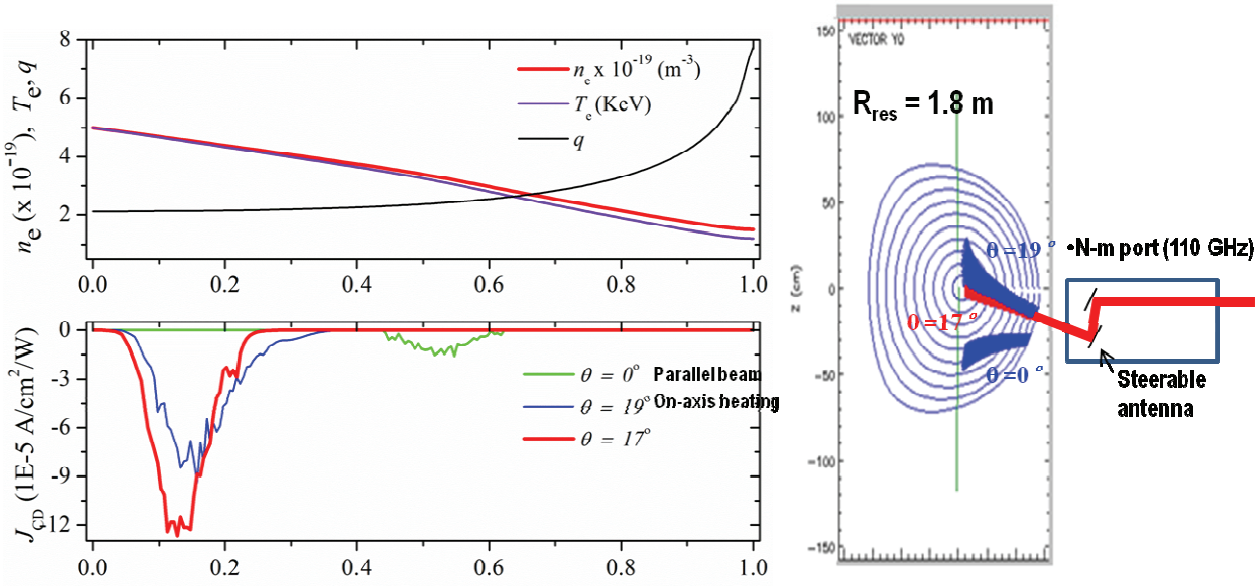

Fig. 1. Poloidal cross section of EC beam trajectory from the 0 degrees (parallel beam injection angle) to 17 (or 19) degrees (for the off-axis injection) in poloidal at the toroidal magnetic field of 2.0 Tesla, which is nominal operation conditions for 110 GHz second harmonic. The pivot position of steerable mirror is located

300 mm down from the mid-plane. The parameters of Te(0)=5.0 keV and ne(0) =5.0 × 1019m-3 is considered for the calculation of ray tracing (Toray-GA code).

2.2 Sawtooth behavior by on/off-axis ECH/ECCD

The first ECCD stabilization/destabilization experiments in KSTAR which is performed by the different deposition location across the q=1 surface shows that the sawtooth period is highly sensitive to the location of the deposition with respect to the sawtooth inversion radius [23-25]. In accordance with equation (1), increasing the co-current just inside q=1 increases s_1 and so destabilizes the sawteeth, whilst co-ECCD localized just outside q=1 decreases s_1 and so stabilizes the sawteeth. Conversely, counter-ECCD just inside q = 1 results in stabilization and just outside q = 1 gives rise to destabilization [14, 15, 25, 27].

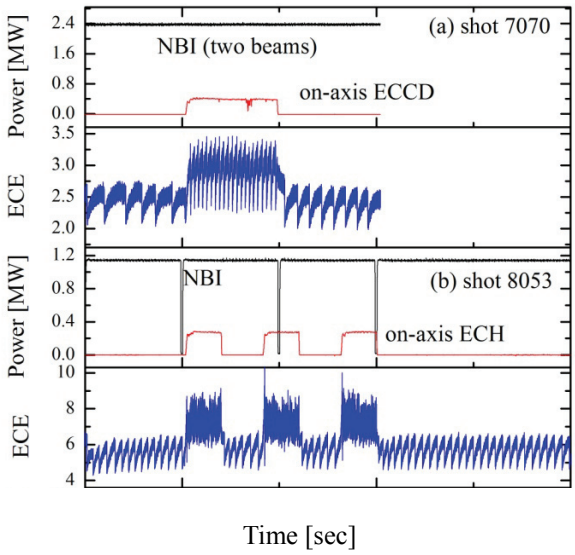

Fig. 2 Sawtooth destabilization by on-axis ECH (inside the q=1 surface) in NBI-heated plasma in KSTAR [28].

Figure 2(a) shows that the period of sawtooth destabilized (shortened) from 100 ms to 20 ms in NB-heated plasmas by on-axis X2 co-ECCD of ~0.4 MW. The grassy sawtooth is also obtained with on-axis ECRH in NBI (1.2 MW)-heated plasma as shown in **Fig. 2(b)**. Since the heating acts like co-ECCD, the efficient destabilization occurs with on-axis ECH (or co-ECCD) just inside the q=1 surface.

On the other hand, the sawtooth period stabilized (lengthen) with almost same amplitude is observed by off-axis co-ECCD as shown in **Fig. 3(a)**. The deposition position of the off-axis co-ECCD is about ρ=0.4 which is just outside the inversion radius of ρ=0.2 as shown in **Fig. 3(b)**. The beam deposition is calculated using Toray-GA ray tracing code and the inversion radius is calculated from the ECE channels. As a result, the sawtooth period increased from 110 ms to ~200 ms by the co-ECCD injection just outside the q=1 surface. Such behavior is demonstrated in many other machines as well, for example [14, 15, 22, 23, 25].

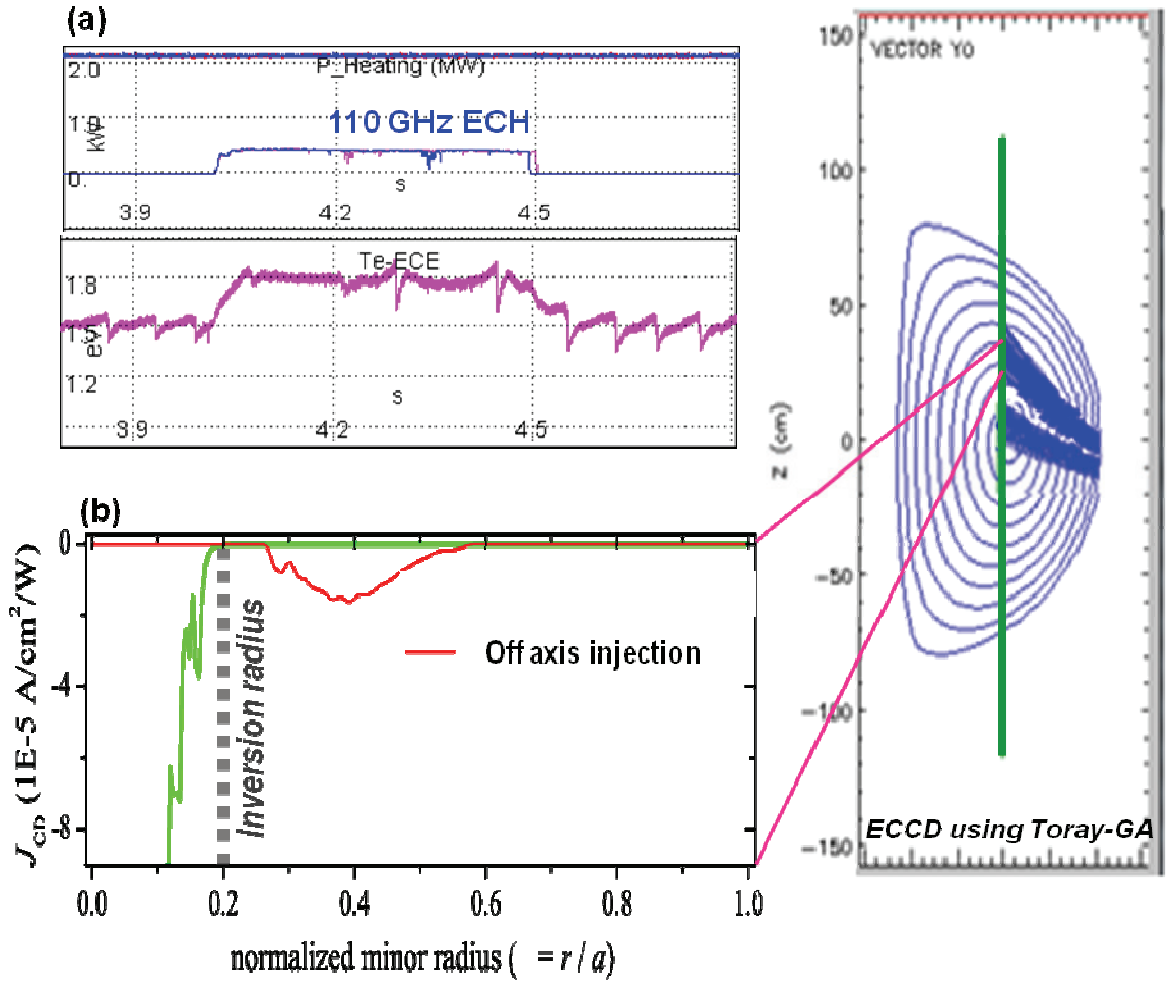

Fig. 3. (a) Sawtooth stabilization by off-axis co-ECCD (outside the q=1 surface) in NBI-heated plasma in KSTAR. (b) The EC beam deposition position of off-axis co-ECCD, which is calculated using Toray-GA code at the toroidal magnetic field of 2.0 Tesla with the parameters of $T_e(0)$=5.0 keV and $n_e(0) = 5.0 \times 10^{19} m^{-3}$.

To be able to compare the variation in the sawtooth period with co- and counter-ECCD current drive with pure heating (perpendicular injection) without current drive, the different angles of the ECH mirrors are set to +/- 20° in toroidal direction with respect to the plasma current. The vertical position at the resonance layer is fixed with z=10 cm to deposit close to q=1 surface but just inside the inversion radius. The sawtooth period is normalized with the sawtooth period of discharges without ECH: $\tau_{norm} = \tau_{sawtooth} / \tau_o = \tau_{ECH,\ ECCD} / \tau_{ohmic}$. In this experiment the sawtooth period without ECH is usually 9 ms depending on the just ohmic heating. In **Fig. 4**, a maximum in the sawtooth period with τ_{norm}=2, equivalent with $\tau_{sawtooth}$=17 ms, is observed by the counter-CD injection at ρ_{pol}=0.2 which is the just inside the sawtooth inversion radius of ρ=0.37 marked with a dashed line. And a decrease in sawtooth period by the co-CD injection at the same position is observed with τ_{norm}=0.75 (τ=6 ms). It means that the efficient stabilization of sawtooth occurs counter-CD just inside

the q=1 surface, while the efficient destabilization occurs with co-CD and ECH inside the q=1 surface. The sawtooth inversion radius in **Fig. 4** is determined from the ECE channel positions and the inversion radius was almost same for the three different shots. The deposition position of EC beam is calculated with the TORAY-GA beam tracing code.

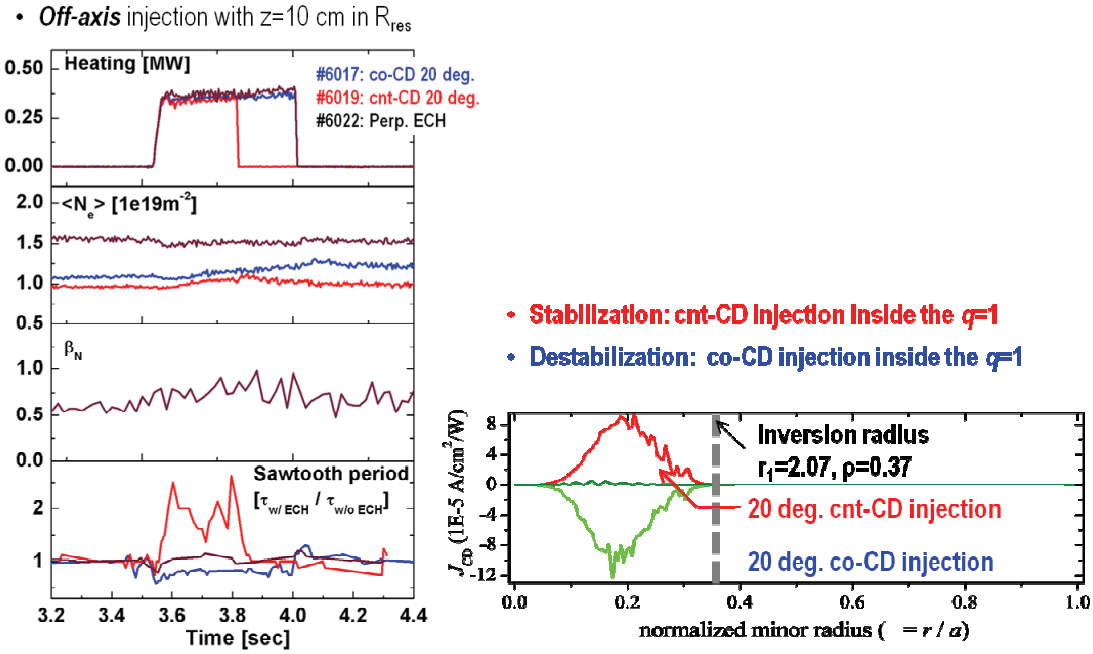

Fig. 4. Sawtooth behavior in KSTAR as the counter-CD increased just inside the inversion radius. The EC beam deposition position is calculated using Toray-GA code at the toroidal magnetic field of 2.0 Tesla with the parameters of $T_e(0)$=5.0 keV and $n_e(0) = 5.0 \times 10^{19} m^{-3}$.

3. Conceptual design and requirements for the real-time sawtooth control

In order to build a real-time sawtooth control system on KSTAR, it is essential to understand the sawtooth response according to movements in the EC launcher injection angle. In section 2, the sawtooth behaviors in KSTAR were well-corresponded with earlier experiments in response to EC deposition across the q = 1 surface. Controller designs for the sawtooth instability are necessary to achieve and maintain any desired sawtooth period, even in the presence of disturbances or uncertainties. The performance of such controllers is expressed in terms of how fast and accurate it achieves this goal. A high-performance sawtooth controller should force the period from an initial value to a desired one as fast as possible, with the minimum steady-state error and very little overshoot. Considering all of these conditions, the first conceptual design for the real-time sawtooth control system in KSTAR is shown in **Fig. 5** and detailed requirements are followed in section 3.1.

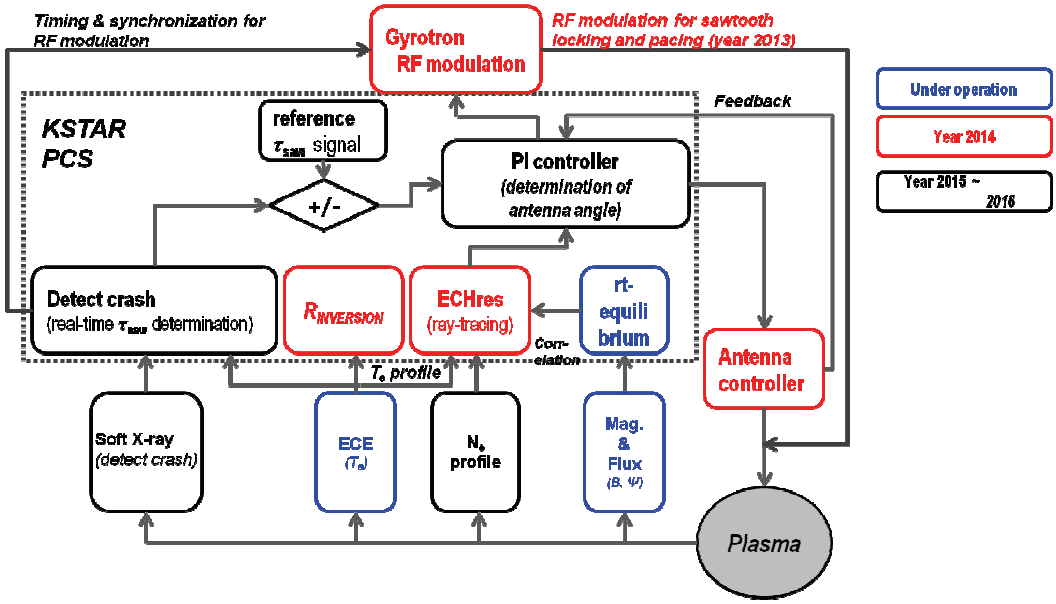

Fig. 5. Block diagram for the first conceptual design of real-time sawtooth control in KSTAR.

3.1. Requirements for the real-time sawtooth control

The first requirements for the real-time sawtooth control system should undertake is to find the observed sawtooth period by detecting each sawtooth crash. This must be reliably detected over a wide range of sawtooth periods, crash sizes and sawtooth shapes [29]. This is especially critical if the sawteeth become very small as several missed detections will result in the calculating the desired sawtooth periods an unrealistic large sawtooth period and subsequently the system could become unreliable or even unstable. For the realistic sawtooth periodic detection, finding large negative derivatives in the ECE diagnostics will be based and the negative derivate of soft x-ray intensity is also under consideration.

The real-time sawtooth control algorithm in the main control system also should know the position of the q = 1 surface together with the launcher injection angle required to deposit EC at and around this location. This would require a real-time data acquisition of ECE channels and equilibrium reconstruction to find the q = 1 surface as well as real-time ray tracing using electron temperature and density profile data would be required to calculate the required injection angle. Although the real-time equilibrium reconstruction is under operation by rt-EFIT using magnetic probe systems for KSTAR, real time ray tracing is not yet possible. In the 2014 year, the construction of *ECHres* code is under planning for the calculation of EC beam ray tracing, and the real-time measurement of electron density profile is under consideration.

New recent sawtooth control method of sawtooth locking is under the design in KSTAR experiments. The locking range can be investigated with a variable deposition location and the modulated RF power with a certain period and duty cycle in an open-loop control. For this experiment, the real-time control development

of EC beam power modulation is considered by the up gradation of anode power supply for the beam current modulation to control the sawtooth periods to a desired value. Also, the arbitrary power modulation of EC beam synchronized with external waveform generator which can be set the various modulation frequencies are under development.

4. Preliminary results of real-time antenna mirror control (feed-forward mirror control)

Table 1 shows the master plan of the real-time antenna mirror control in KSTAR upto year 2016. The final destination of this plan is the real-time feed-back control of the antenna mirror to apply the sawtooth control and NTMs suppression in KSTAR. At the first step, for the validation in 2013 KSTAR campaign, the feed-forward mirror control by the KSTAR PCS is constructed and the preliminary test was successfully carried out as shown in **Fig. 6**. The antenna mirror angle is changed (red line) with the desired value (black line) which comes from KSTAR PCS controller. Since the limited data-transmission-performance of the antenna controller, time-delays between the requested-position and the measure-position is about 0.5 sec. However, this kind of slow response performance will be improved within 0.1 sec through the upgrades of hardware systems such as antenna controller and antenna actuators.

Table. 1. Master plan of the real-time antenna mirror control in KSTAR

2013 Campaign	2014 Campaign	2015 Campaign	2016 Campaign
Feed forward control of the ECCD mirror (Setting-up network system**)**	**Upgrade** of antenna controller for **fast movements and feed- back control**	Real-time heating deposition detection (**network system for diagnostics**)	Validation of the real- time feedback sawtooth control in KSTAR (PCS)

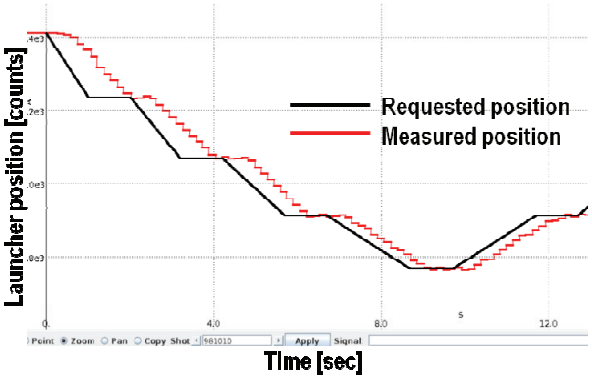

Fig. 6. Schematic of the feed-forward control of antenna mirror by the KSTAR PCS; the antenna was successfully able to track the target value with a time of 0.5 sec. However, the time-delay may be improved through the hardware upgrades of antenna controller system.

4. Summary

In burning plasmas such as ITER case, the significant energetic ion population is likely to result in long sawtooth periods, which in turn are predicted to

increase the likelihood of the sawtooth crash triggering other confinement-degrading instabilities. Consequently, recent experiments have purposefully identified various methods to control sawtooth oscillations in an attempt to avoid seeding NTMs whilst retaining the benefits of small, frequent sawteeth, such as the prevention of core impurity accumulation. Follow the same purpose of sawtooth control, the ability to control sawteeth using EC heating has been demonstrated on KSTAR. The change in the plasma current density can be useful to control sawteeth. Increase in the current just inside q = 1 surface causing the value of s_1 to increase and which in turn help in destabilizing the mode, whilst localized co-CD just outside q = 1 decreases s_1, and so stabilizes the sawteeth. Conversely, driving counter-current just inside q = 1 results in stabilization. These results exhibiting the sawtooth behaviors in KSTAR were well-corresponded with earlier experiments in many tokamaks, and it means that the sawtooth period can be also controlled in an accurate way by various EC beam injection conditions to stabilize/destabilize it, as well. Using the preliminary result, real-time sawtooth control in KSTAR is under development. The first conceptual design for the real-time sawtooth control is introduced, and the detailed plan is on advancement. As a first step of the real-time antenna mirror control, the feed-forward antenna mirror control is successfully demonstrated by the KSTAR PCS control. The validation of real-time feed-back antenna mirror control will be in year 2016 to apply the real-time sawtooth control using the control of EC beam deposition position.

Acknowledgments

This work was partly supported by the JSPS-NRF-NSFC A3 Foresight Program in the field of Plasma Physics (NSFC No.11261140328) and by the National Research Foundation of Korea (NRF) under contract No. NRF-2012-0005919.

REFERENCES

[1] Hastie R J, 1998, Astrophys. Space Sci., 256: 177

[2] Wesson J, 1997, TOKAMAKS (Oxford: Oxford Science Publications, Clarendon Press)

[3] Gude A., Günter S., Sesnic S. et al. 1999, Nuclear Fusion, 39**:** 127

[4] Chapman I. et al. 2010, Nuclear Fusion, 50: 102001

[5] Sauter O. et al. 2002, Physical Review Letters, 88: 105001

[6] Porcelli F., Boucher D., Rosenbluth M.N., 1996, Plasma Physics and Controlled Fusion, 38: 2163–86

[7] Campbell D.J. et al. 1988, Physical Review Letters, 60: 2148

[8] Chapman I.T. et al. 2007, Plasma Physics and Controlled Fusion, 49: B385

[9] Graves J.P., Chapman I., Coda S. et al. 2009, Physical Review Letters, 102: 065005

[10] Chapman I.T., Jenkins I., Budny R.V. et al. 2008, Plasma Physics and Controlled Fusion, 50: 045006

[11] Chapman I.T., Pinches S.D., Koslowski H.R. et al. 2008, Nuclear Fusion 48: 035004

[12] Eriksson L.G. et al. 2006, Nuclear Fusion, 46: S951

[13] Lennholm M. et al. 2011, Nuclear Fusion, 51: 073032

[14] Mück A., Goodman T.P., Maraschek M. et al. 2005, Plasma Physics and Controlled Fusion 47: 1633

[15] Angioni C., Goodman T.P., Henderson M.A. et al. 2003, Nuclear Fusion, 43: 455

[16] Porcelli F, 1991, Plasma Physics and Controlled Fusion, **33:** 1601

[17] Graves J.P., Sauter O. and Gorelenkov N., 2003, Physics of Plasmas, **10:** 1034

[18] Graves J.P., 2004, Physical Review Letters, **92:** 185003

[19] Kruskal M. and Oberman C., 1958, Physics of Fluids, **1:** 275

[20] Chapman I.T. Plasma Physics and Controlled Fusion, 2011, 53: 013001

[21] Nave M. et al. 2003, Nuclear Fusion, **43:** 1204

[22] Y. S. Bae et al., 2007, Fusion Science and Technology, 52: 321

[23] Hanada K et al. 1991, Physical Review Letters, **66:** 1974

[24] Snider R T et al. 1989, Physics of Fluids B, **1:** 404

[25] Pietrzyk Z A et al. 1999, Nuclear Fusion, **39:** 587

[26] Henderson M A et al. 2001 Fusion Engineering and Design, **53:** 241

[27] Zohm H et al. 2003, Nuclear Fusion, **43:** 1570

[28] Y. S. Bae et al. 2013, Fusion Sience and Technology, submitted

[29] J I Paley, F Felici, S coda et al., 2009, Plasma Physics and Controlled Fusion, 51: 055010

Threshold of mode penetration in helical plasmas

S. Sakakibara[1], Y. Narushima[1], Y. Suzuki[1], K.Y. Watanabe[1], K. Ida[1], K. Tanaka[1], I. Yamada[1], H. Yamada[1] and LHD Experiment Group

[1] National Institute for Fusion Science, Gifu 509-5292, Japan

Abstract

Magnetic configuration dependence of mode penetration has been investigated in the Large Helical Device. Resonant magnetic perturbation (RMP) field was ramped up in various magnetic configurations so as to estimate the threshold of the penetration. The threshold linearly increases with the increase in the magnetic shear, and mitigation of magnetic hill is also effective for the increase in the threshold. The configurational effects on the threshold are much stronger than that on the plasma flow. The RMP ramp-up experiments in high beta regime indicate that the threshold in high beta and high collisionality regime was much higher than that in the low-beta and low collisionality regime. The RMP field gradually decreased the core and edge pressure even before the penetration in the high beta regime.

1. Introduction

Generally, an error field caused by the misalignment of confinement coils and/or magnetic materials is one of problems for productions of high performance and high beta plasmas in magnetic confinement systems because formed magnetic island degrades plasma confinement and triggers MHD instabilities. In tokamaks and RFPs, rotation of tearing mode is slowed down by the flow damping due to the error field, and the mode rapidly grows and leads to major disruption after the stop of the rotation. Also, even when the tearing mode is stable, the error field grows and degrades the plasma performance if the amplitude is more than the threshold. Therefore, the threshold of the perturbation field triggering the MHD instability, so-called mode penetration, has been energetically investigated through the joint experiments in tokamaks in order to construct the empirical scaling [1], which is required to clarify the tolerance to the error field in ITER.

In the Large Helical Device (LHD), the spontaneous growth and healing of the magnetic island were observed and reported [2], and dependences of beta, collisionality and poloidal flow on it were found out [3-5] in the experiments with resonant magnetic perturbation (RMP). The results can be interpreted by applying the theoretical models [6,7], whereas they are obtained in a specific configuration.

Here we focus on the configuration dependence of the mode penetration. Although the magnetic island physics have been theoretically investigated in not only tokamaks, but also helical devices, effects of magnetic

configurations on the mode penetration have not been treated so far. To clarify this experimentally, we changed the magnetic shear and/or magnetic hill by controlling poloidal and helical coils. Also, the effect of RMP field on the high beta plasmas is important from a viewpoint of the interaction between change of magnetic topology due to finite-beta effects and the RMP field. The threshold of the penetration was studied in the high-beta plasmas with about 4 % and compared to the low-beta case.

2. Experimental Set-up

LHD is a heliotron device with a pair of helical coil and three pairs of poloidal coils. All coils are superconductive. The major and minor radii in standard configuration are 3.6 m and 0.65 m, respectively. In the experiments for investigating the magnetic shear dependence, the pitch parameter of helical coil, γ_c, was changed from 1.13 to 1.20. The γ_c is 1.25 in the standard configuration. The γ_c can be changed by controlling the center of helical coil current, which can change plasma aspect ratio with keeping the magnetic axis, R_{ax}. The plasma aspect ratio is increased with central rotational transform, and the magnetic shear is decreased as well. The R_{ax} was set at 3.6 m in the experiments. In the experiments for investigating the effect of magnetic hill on the mode penetration, the configuration with R_{ax}= 3.75 m and γ_c = 1.13 was applied and compared to the 3.6 m case. When the R_{ax} is shifted from 3.6 m to 3.75 m, the magnetic hill is mitigated with keeping the same magnetic shear. The volume averaged beta value, $<\beta_{dia}>$, of 1~2 % were produced in the experiments described above. Finally, we applied the RMP to the high beta plasmas of the configuration with R_{ax} = 3.6 m and γ_c = 1.20, and compared with results in the low-beta plasma in the same configuration.

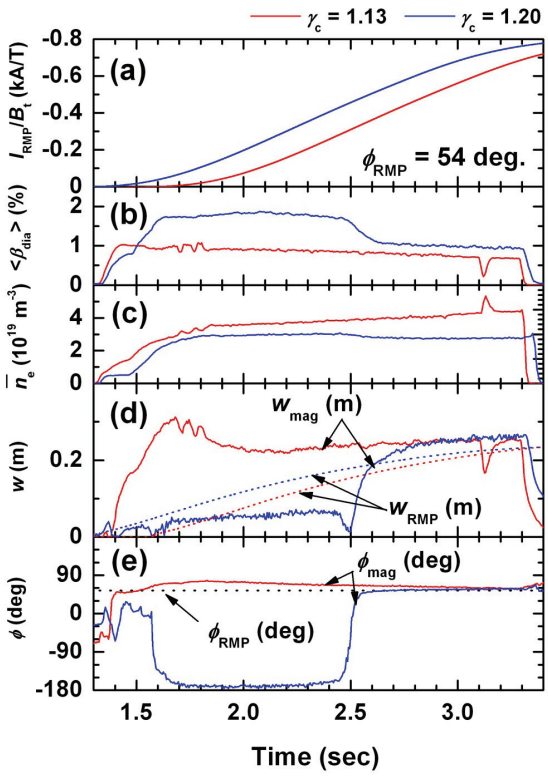

Fig. 1. Time development of (a) I_{RMP}/B_t, (b) $<\beta_{dia}>$, (c) line averaged electron density, (d) m/n = 1/1 island width and (e) toroidal angle where the O-point exists on the midplane of low field side in γ_c = 1.13 (red) and 1.20 (blue) configurations [10].

Ten pairs of RMP coils are equipped with LHD and major Fourier mode is m/n = 1/1, where m and n are poloidal and toroidal mode numbers, respectively. In the experiments for studying configurational effects on the penetration, the RMP current, I_{RMP}, was ramped up

during a discharge, and ramp-up rate is 0.38 kA/s. After two co- and counter neutral beams (NBs) were applied for production of target plasma, balanced NBs were injected for maintaining the plasma because of avoidance of the net plasma current. The decrease in the magnetic shear due to the plasma current destabilizes the ideal interchange instability [8], which complicates the study of the mode penetration. The total port-through power of NBs is about 15MW, which was the same as the high-beta RMP experiments.

The formation of the magnetic island was identified by saddle loop arrays [9] and by detecting the local flattening of plasma profile measured with Thomson scattering system.

3. Experimental Results

3.1 Magnetic Shear Dependence

The experiments were done in the γ_c = 1.13, 1.15, 1.18 and 1.20 configurations to clarify the magnetic shear effect on the penetration. The magnetic shear, $1/\iota(d\iota/d\rho)$, was increased from 1.02 to 1.99 when the γ_c was changed from 1.13 to 1.20. The toroidal field at R_{ax}, B_t, was set at 0.9 T. The toroidal angle where the O-point exists on the midplane of low field side, ϕ_{RMP}, was set at 54 or -126 degree, which was realized by changing the polarity of the RMP current. Figure 1 shows the time developments of plasma parameters in γ_c = 1.13 and 1.20 configurations with ϕ_{RMP} = 54 degree. The three NBs were applied at 1.3-1.8s and plasma was maintained by balanced injection to 3.3 s. In the γ_c = 1.13 configuration with weak magnetic shear, the large magnetic island appeared before the RMP current was applied as shown in Fig.1 (d). The formed island was in phase with that produced by RMP field, and the island width was always larger than the prediction. The flattening of the electron temperature profile was observed around the $\iota/2\pi$ = 1 resonance during a discharge [10]. In the γ_c = 1.20 configuration with strong shear, the RMP field was penetrated when the RMP current exceeded a threshold at 2.5 s. before that, m/n = 1/1 magnetic field out of phase with RMP field was observed, which suggests that the m/n = 1/1 perturbation current out of phase with RMP field flows on the resonance for shielding the RMP field. After the penetration, the width of the island is almost the same as the weak magnetic shear case.

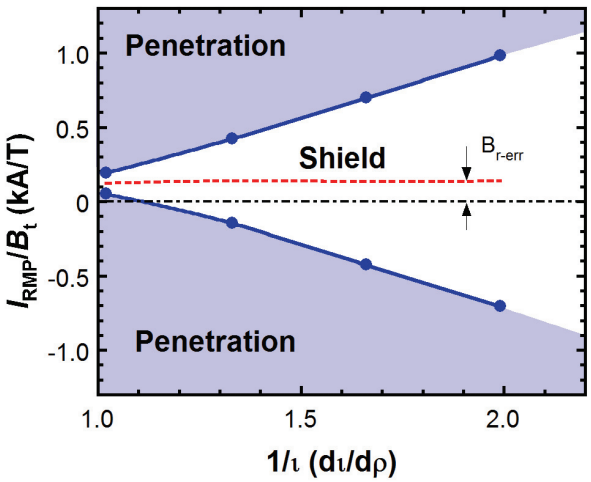

Fig. 2. Changes of threshold of mode penetration as a function of magnetic shear on the m/n = 1/1 resonance [10].

Figure 2 shows the summary of RMP ramp-up experiments in different magnetic shear configurations. The threshold linearly increases with the increase in the magnetic shear. The thresholds obtained in both positive and negative RMP ramp-up experiments have an offset (red dotted line), which corresponds to the natural error field. The error filed was previously identified by magnetic surface mapping[11], and the results are consistent with the experiments shown in Fig.2. This is the reason why the magnetic island appeared even before RMP field was applied in the γ_c = 1.13 configuration in Fig.1.

3.2 Magnetic Hill Dependence

In order to investigate another configurational effect, magnetic well/hill, on the mode penetration, the R_{ax} was shifted from 3.6 m to 3.75 m in the γ_c = 1.13 configuration with the weakest magnetic shear. The magnetic shear is almost the same in both configurations. In the weakest shear configuration with R_{ax} = 3.6 m, the magnetic island due to the error field appeared even without additional RMP field as shown in Figs.1 and 2. Figure 3 shows comparison of island formation between the R_{ax} = 3.6 m and 3.75 m cases. The perpendicular NB was intermittently applied for the plasma flow measurement in addition to the co- and counter NBs in both discharges. In the R_{ax} = 3.6 m discharge, m/n = 1/1 magnetic island due to the error field appeared at the beginning of discharge. Then the increment of $<\beta_{dia}>$ was clearly suppressed. When the R_{ax} was shifted to 3.75 m, the error field was shielded to the end of discharge, and higher beta was realized compared to the R_{ax} = 3.6 m case.

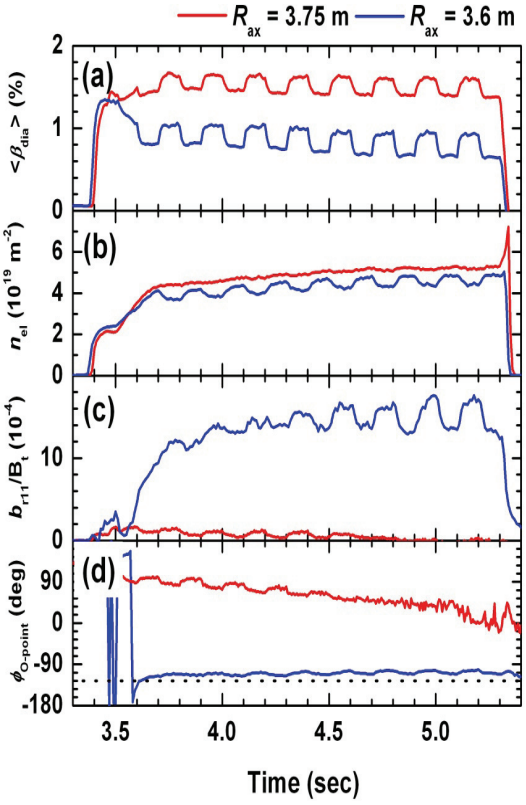

Fig. 3. Time evolutions of (a) $<\beta_{dia}>$, (b) line-integrated electron density, (c) radial magnetic field normalized to toroidal field and (d) toroidal angle where O-point exists on the midplane of the low field side in R_{ax} = 3.6 m (blue) and 3.75 m (red) configurations with γ_c = 1.13 [10].

In addition, two kinds of experiments were done to confirm that the threshold of the penetration in the outward-shifted configuration is higher than that in the inward-shifted one. One is the real time swing of R_{ax} from 3.75 m to 3.6 m during a discharge. As a result, the magnetic island appeared when the R_{ax} < 3.61 m. The other is RMP ramp-up in the configuration with R_{ax} = 3.75 m and γ_c = 1.13. The experiments show that

the threshold of the penetration, I_{RMP}/B_t is, at least, more than 0.6 kA/T. Thus, an enhancement of magnetic shear and/or mitigation of the magnetic hill are effective for increasing the threshold of the mode penetration.

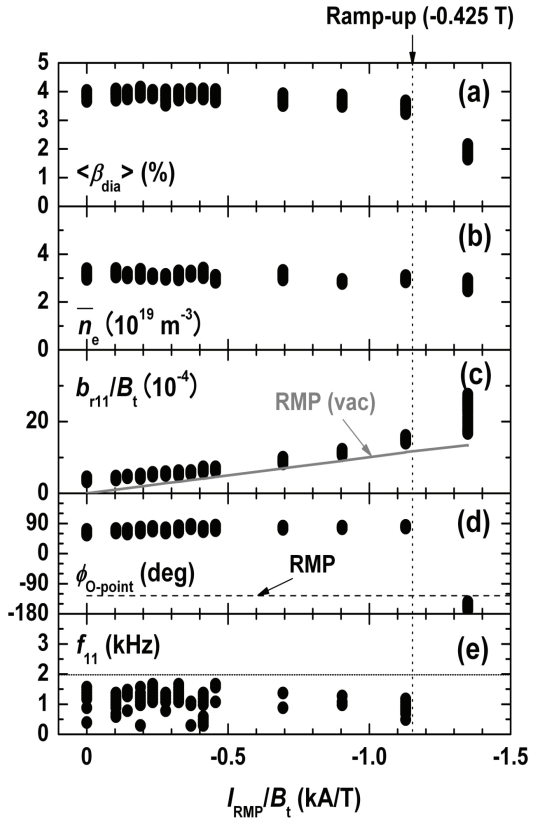

Fig. 4. Changes of (a) <β_{dia}>, (b) line-averaged electron density, (c) radial magnetic field normalized to toroidal field, (d) toroidal angle where O-point exists on the midplane of the low field side and (e) frequencies of rotating m/n = 1/1 mode in the configuration with R_{ax} = 3.6 m and γ_c = 1.20 [5].

3.3 Mode penetration in high-beta plasma

In LHD, <β_{dia}> of 5 % was achieved in the configuration with R_{ax} = 3.6 m and γ_c = 1.20, and characteristics of the stability and equilibrium are summalized in Ref. 12. Here we applied static RMP field in <β_{dia}> ~ 4% plasmas as shown in Fig.4. The B_t was set at 0.425 T. The negative I_{RMP}/B_t corresponds to ϕ_{RMP} = -126 degree. The <β_{dia}> gradually decreased when I_{RMP}/B_t increased to 1.15 kA/T and the <β_{dia}> was lost by 50 % after the penetration. This threshold is slightly higher than the low beta case [5]. Previous study indicates that the island formation depends on the beta and collisionality [3]. Since the high (low) beta plasma has high (low) collisionality in the experiments, further experiments in the extended beta and collisionality ranges are required. As shown in Figs.4 (c) and (d), the m/n = 1/1 perturbation field is out of phase with RMP field at I_{RMP}/B_t < -1.15 kA/T. However, the plasma regime was gradually shrunk and also core pressure decreased with the increase in I_{RMP}/B_t (see Fig.5). There are two possibilities for this tendency. One is due to shortening of the connection length of magnetic field structure in the edge plasma caused by RMP field. The LHD has the stochastic magnetic structure in the edge even in vacuum, and the stochastic regime penetrates to the core regime and the connection length of the magnetic field line becomes shorter when the beta increases, which is predicted by 3D MHD equilibrium code HINT2 [5]. If it is true, the plasma confinement regime is limited and core pressure is also decreased. The other possibility for reduction of core pressure is due to the coupling between core resonant surfaces and other Fourier components of the RMP field, although m/n = 1/1 component is shielded. The HINT2 predicts that the

RMP field produces ι/2π = 1/2 and 2/3 magnetic islands. The flattening structures of the pressure profile inside ι/2π = 1 are shown in Fig.5, which is consistent with the theoretical prediction.

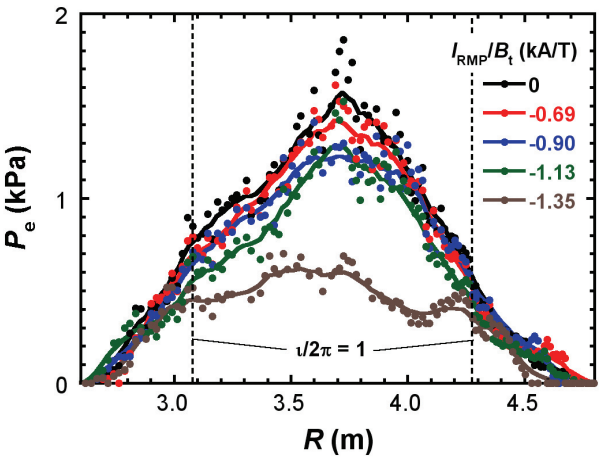

Figure 5 Electron pressure profiles at I_{RMP}/B_t = 0, -0.69, -0.90, -1.13 and -1.35 kA/T in Fig.6 discharges [5].

4. Discussion and Summary

The RMP ramp-up experiments were done in order to investigate configurational effects on the threshold of the mode penetration in helical plasmas. The threshold linearly increases with the increase in the magnetic shear under the condition that the electron density and heating power are constant. The mitigation of the magnetic hill is also effective for the increment of the threshold. Since the strong magnetic shear and mitigation of the magnetic hill contributes stability of the interchange mode, the relationship between the threshold and stability parameters, e.g., Mercier criteria, D_I, should be clarified in the experiments. Because such configuration effects are not included in the empirical scaling of the mode penetration in tokamaks, further experiments are expected to find new knowledge on the mode penetration. In high beta plasmas, plasma confinement was degraded with the increase in RMP field even before the penetration. The relationship between the change of the magnetic topology due to finite beta effects and RMP field should be clarified, which is important for estimating the tolerance of high-beta fusion reactor.

This work was partly supported by the JSPS-NRF-NSFC A3 Foresight Program in the field of Plasma Physics (NSFC: No.11261140328).

5. References

[1] R.J. Buttery et al., The impact of 3D fields on tearing mode stability of H-modes, Nucl. Fusion **51**, 073016, (2011).

[2] N. Ohyabu et al., Island Dynamics in the Large-Helical-Device Plasmas, Phys. Rev. Lett. **88**, 055005, (2002).

[3] Y. Narushima et al., Dependence of spontaneous growth and suppression of the magnetic island on beta and collisionality in the LHD, Nucl. Fusion **48**, 075010, (2008).

[4] Y. Narushima et al., Experimental study of the poloidal flow effect on magnetic island dynamics in LHD and TJ-II, Nucl. Fusion **51**, 083030, (2011).

[5] S. Sakakibara et al, Modification of the magnetic field structure of high-beta plasmas with a perturbation field in the Large Helical Device, Plasma Phys. Control. Fusion **55**, 014014, (2013).

[6] C.C. Hegna, Healing of magnetic islands in

stellarators by plasma flow, Nucl. Fusion **51** 113017 (2011).

[7] S. Nishimura et al, Influence of resonant magnetic perturbation on a rotating helical plasma, Plasma Phys. Control. Fusion **55**, 014013, (2013).

[8] S. Sakakibara et al., Recent Progress of MHD Study in High-Beta Plasmas of LHD, Fusion Sci. Technol. **50**, 177, (2006).

[9] S. Sakakibara, H. Yamada, LHD Experiment Group, Magnetic Measurements in LHD, Fusion Sci. Technol. **58**, 471, (2010).

[10] S. Sakakibara et al., Response of MHD stability to resonant magnetic perturbation in the Large Helical Device, Nucl. Fusion **53**, 043010, (2013).

[11] T. Morisaki et al., Flux Surface Mapping in LHD, Fusion Sci. Technol. **58**, 465, (2010).

[12] S. Sakakibara S. et al., MHD study of the reactor-relevant high-beta regime in the Large Helical Device, Plasma Phys. Control. Fusion **50**, 124014, (2008).

Power balance estimation in long duration discharges on QUEST

K.Hanada[1], H.Zushi[1], H.Idei[1], K.Nakamura[1], M.Ishiguro[2], S.Tashima[2], E.I.Kalinnikova[2], Y.Nagashima[1], M.Hasegawa[1], A.Fujisawa[1], A.Higashijima[1], S.Kawasaki[1], H.Nakashima[1], O.Mitarai[3], T.Maekawa[4], A.Fukuyama[5], Y.Takase[6], X. Gao[7], H.Liu[7], J.Qian[7], M.Ono[8], R.Raman[9], M. Peng[10]

[1] RIAM, Kyushu University, Japan,

[2] Interdisciplinary Graduate School of Engineering Science, Kyushu University, Japan,

[3] School of Industrial Engineering, Tokai University, Japan

[4] Graduate School of Energy Science, Kyoto University, Japan,

[5] Graduate School of Technology, Kyoto University, Japan

[6] Graduate School of Frontier Science, University of Tokyo, Japan

[7] IPP, Chinese Academy of Sciences, China

[8] PPPL, USA

[9] University of Washington, USA

[10] ORNL, USA

Abstract: Fully non-inductive plasma start-up was successfully achieved by using a well-controlled microwave on the spherical tokamak, QUEST. Non inductive plasmas could be maintained for approximately 3~5 min, where power balance could be achieved in the view of monitoring of wall and cooling water temperature. Approximately 80% of the injected power could be detected by a calorimetric measurement and the residual power may be lost in two antenna systems to inject the well-controlled microwave. Almost more than 50% of injected power is deposited on the vacuum wall, not depending on the magnetic configuration. The power distribution to PFCs significantly depends on the magnetic configuration, however some of them is providing from energetic electrons, which have large poloidal orbits and are likely to deposit on the vessel in the low field side.

Keywords: steady state operation, spherical tokamak, plasma wall interaction, power balance

1. Introduction

Steady state operation (SSO) of magnetic fusion devices is one of the goals for fusion research. Issues related to plasma wall interaction (PWI) is highly addressed to get SSO. Especially, power and particle balances during plasma discharges are indispensable subjects to develop SSO. In a future steady-state fusion power, huge heat load must be delivered from main plasmas to plasma facing components (PFCs) and it should be handled in steady-state. Divertor plates and limiters, which are directly connected to plasmas depending on plasma magnetic configurations, may play an essential role in its heat handling. Few knobs remain to avoid such huge heat load to PFCs in the steady-state fusion power plant, and modification of magnetic configuration is one of a few candidates to control the heat load. Actually, control of contact point of PFCs to plasma has been applied in many long duration discharge devices such as TRIAM-1M [1], TS [2], EAST [3], LHD [4] and they could successfully

obtain longer duration discharges. The world record of plasma duration on tokamaks for more than 5 h was achieved in TRIAM-1M [1], where an accurate power balance of the discharge was investigated [5] and a particle balance was also studied [6]. The power balance of the discharge seems to be complete, because every monitor of temperature on plasma facing components (PFCs) kept constant. However, the longest plasma was spontaneously terminated and the reason is still unclear.

In a low aspect ratio spherical torus (ST) magnetic geometry, an inherently large divertor figure of merit P /R, where P is the input power and R is the major radius, and a number of ST scrape-off layer (SOL) and divertor geometry features lead to higher divertor heat fluxes, raising concerns over divertor operation in the proposed ST-based fusion power plant concepts [7]. Substantial experimental work has been carried out on partial detached divertor [8] and improved divertor geometry [9, 10]. Therefore, power balance estimation on STs gives an important information on conceptional design of ST-based future fusion power plants.

QUEST, which is a medium size of spherical tokamak (R=0.68m, a=0.4m, Bt<0.25T at R=0.64m) [11], can be operated in various types of magnetic configurations up to 3-5 min using 8.2GHz RF of approximately 100kW injected as a well-controlled microwaves [12]. Main part of PFCs, which are covered by 19 tungsten blocks (W) tightly attached with cupper (Cu) blocks, has been actively cooled down by water, and the heat load to the PFCs can be measured with increment of water temperature and water flux. The power balance during long duration discharges has been studied for various types of magnetic configurations such as limiter, upper and lower single-null divertor, and inboard null. In this paper, experimental apparatus will be introduced in the next section and experimental results will be described in section 3, and in section 4 the contents of the paper will be summarized.

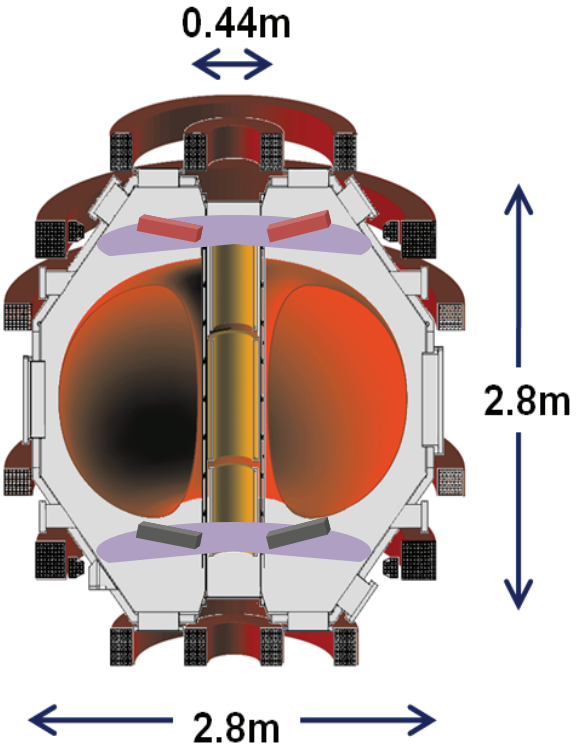

Fig. 1. Schematic view of QUEST is illustrated. Six pairs of PF coils are installed for forming various types of plasma configurations such as limiter, double and single null divertor, and inboard null. Each coil can operate individually to form various configurations. Flat divertor plates coated by tungsten plasma spray are installed in upper and lower side of the vacuum vessel. Four divertor limiters made of tungsten block tightly connected with cupper block was installed on the top and bottom divertor plate, respectively since 2011 S/S campaign. Tungsten side was faced to plasma and cupper side was used to connect with inlet and outlet of water cooling channel. They on the top side were started to cool down since 2012 S/S campaign.

2. Experimental Apparatus and historical review for SSO on QUEST

The schematic view of QUEST [11,13] is shown in Fig. 1. QUEST has four pairs of poloidal field (PF) coils and three separated center solenoid (CS) coils and combination of currents on these coils can make various magnetic configurations. Two kinds of microwaves of 2.45GHz, 50kW and 8.2GHz, 400kW are available to drive plasma current and heat plasmas and they have the capability to operate in steady state. A system of 8.2GHz has the well-designed antenna to adjust injection mode, polarization, injection angle [12].

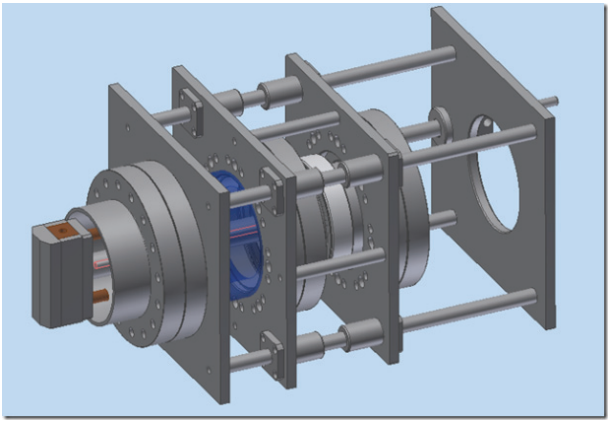

Fig. 2. Schematic view of the movable limiter installed on the vessel in the low field side is illustrated. A water cooled head is movable by 5 cm in radial direction. The head of the limiter is made of W tightly attached with a Cu block and is electrically isolated. Since 2012 S/S campaign, the movable limiter has been installed on QUEST.

The inner part of the vacuum vessel is completely covered by stainless steel of 3mm in thickness coated by W plasma spray. Moreover four fixed water-cooled limiters made of W are installed around only mid-plane on the inner part of the vessel. Lower and upper flat-divertors are composed of W-coated 16 panels made of stainless steel. Four water-cooled limiters made of W block on projects out top divertor plates and four W blocks also project out bottom divertor plate by 5cm. Therefore approximately 17 m^2 of the plasma facing components are covered by stainless steel and the residual surface (4 m^2) is covered by tungsten. Four fixed water-cooled protectors and a movable water-cooled limiter made of W block as shown Fig. 2 are installed in the low filed side of the vessel. The water cooled movable limiter has been installed since 2012 S/S campaign and the fixed outer protectors have been cooled-down actively since 2012 A/W campaign.

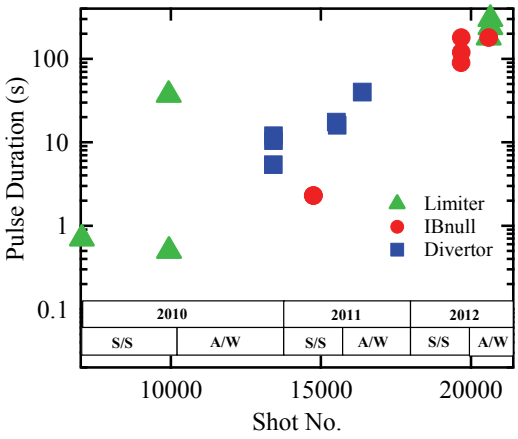

Fig. 3 Historical progress on SSO on the various types of magnetic configurations is summarized. Triangles, circles, and rectangles show the data set of limiter, inboard null, and divertor configurations. In 2012 S/S campaign, the tungsten limiters on the divertor plates was cooled down and the outer fixed protectors were replaced to the limiter made of tungsten. Moreover the water cooled movable limiter was installed. In 2012 A/W campaign, outer protectors made of tungsten was cooled down.

Historical progress for SSO on QUEST is summarized in Fig. 3 and typical magnetic configurations are also illustrated in Fig. 4. In the first phase of experiments (before 2010S/S), plasma start-up was a significant

issue and a 0.7 s full non-inductive current driven discharge could be obtained [6]. In 2010 S/S campaign, a 37 s discharge on the limiter configuration was achieved and it was found that much of heat load was delivered by energetic electrons to the vessel in the low field side (We will call "outer vessel".). The plasma in the limiter configuration sheared big volume in the vessel and sometimes directly attached to the outer vessel. Several hot spots appeared on the outer vessel and provided significant out-gas in the vessel, which prevented from maintaining long duration discharges. It can recognize as local power unbalance between heat load and cooling capability. In 2010 A/W campaign, we made efforts to form plasmas on a divertor configuration and a 10 s discharge was obtained [13]. To do a further extension of plasma duration, eight divertor limiters were installed on the top and bottom side of the divertor plates to effectively remove heat load from the divertor region. In 2010 A/W campaign, a 40 s discharge on the divertor configuration was achieved. Although the strong modification of plasma configuration was executed, much of heat load to the outer vessel still remained. Therefore, the movable limiter shown in Fig. 2 was installed to remove the heat load. Finally we could obtain a 3 min discharge on the board null configuration in 2012 S/S campaign. In 2012 A/W campaign, four water-cooled outer protectors made of tungsten installed and a 5 min discharge in a limiter configuration was successfully achieved. Before 2012 S/S campaign, power balance was the main issue to get long duration discharges and we must make an effort to remove the heat load. Since 2012 S/S campaign, tentative power balance could be achieved in this power level and main issue is shifting to particle balance.

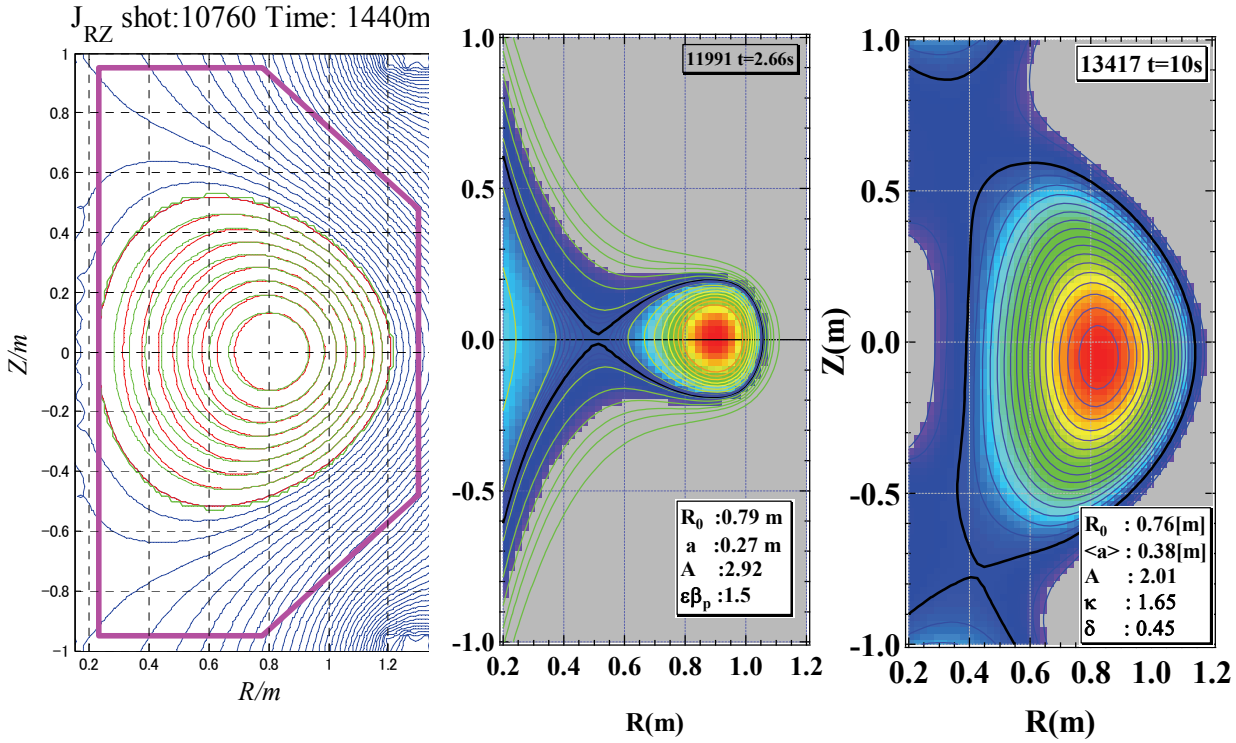

Fig. 4. Typical magnetic configurations on QUEST are illustrated. Left, middle, and right figures show limiter, inboard null, and divertor configurations, respectively.

3. Experimental results on power balance.

Non-inductive plasma start-up [14] and long duration maintenance has been successfully demonstrated. The discharge forms a limiter configuration and shifts to inboard null configuration in higher βp region. The peak electron temperature measured with Thomson scattering is approximately 100 eV and density is 1-2 x 10^{17} m^{-3}. Clear formation of a closed flux surface was

observed with magnetic reconstruction.

Power balance in fully non-inductive plasma has been investigated using a calorimetric method using water cooling channels. The same technique in TRIAM-1M has been applied to the QUEST experiment. In TRIAM-1M, the vacuum vessel was water-cooled and the deposited power to the vacuum vessel was easily measured [5], however, the vacuum vessel of QUEST does not install any water-cooling channels because of keeping relatively higher temperature than room temperature (RT) and a different technique to measure the deposited power is required.

Normally, the temperature of the vacuum vessel is kept constant to 373K by a baking system and it is difficult to estimate a little modification of heated power due to heat load from plasma and injected microwave. Therefore we try to make a plasma operation without the baking system during several experimental days and monitoring of the vessel temperature was executed. The results are shown in Fig. 5. Clear increment of the vessel temperature caused by plasma operation was observed. Thermal isolation capability of the vessel could be demonstrated in the temperature flatness during lunch time from around 8000-12000 sec. Here no spike is observed. As the spike is originally driven by shot noise, therefore no spike means no plasma operation. Four temperature monitor are illustrated and the thermocouples located on the upper vessel is likely to heat-up compared with those on the lower vessel. This difference may be mainly caused by the position of thermocouples, because thermocouples on the upper vessel were located on the plasma facing vessel and those on the lower vessel were set behind the lower divertor plate. Therefore the difference of temperature increment may be arising from plasma radiation and charge exchange neutral. Averaged temperature increment and thermal capacity give a deposited energy during each discharge. The relation between pulse length and the deposited energy provide a deposited power which corresponds to more than 60% of the injected power as shown in Fig. 5.

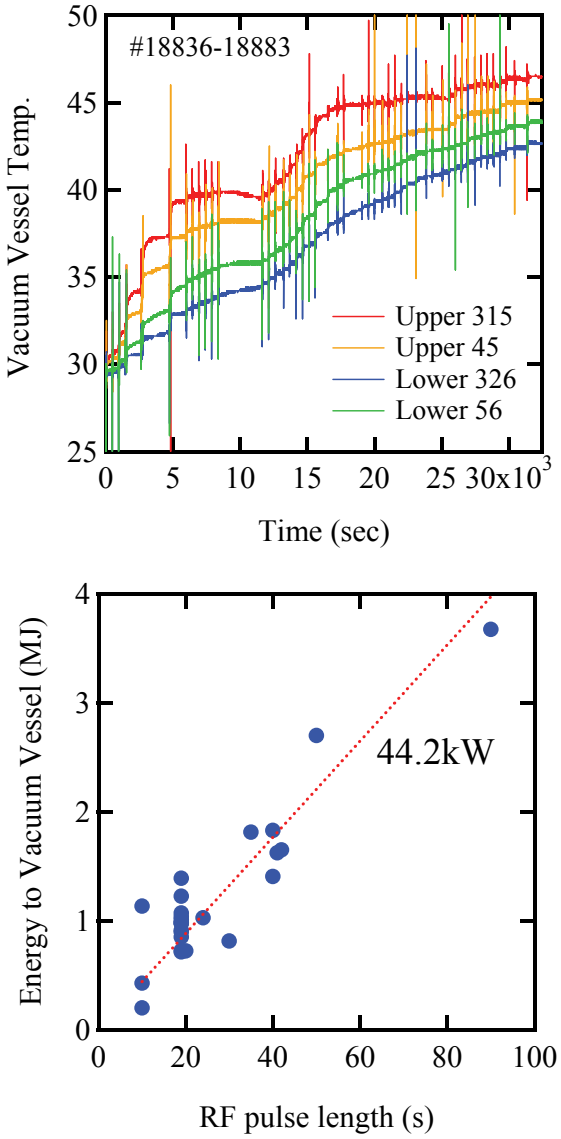

Fig. 5. Top: Time evolution of vessel temperature during one-day plasma operation without vessel baking system. It shoud be noted that two thermocouples on upper vessel (red and orange lines) were located on plasma facing vessel and those on lower one (green and blue lines) were set behind the lower divertor plate. Bottom: The estimated deposited energy as the function of pulse length are shown and a dotted line corresponds to 63% of the injected power.

The other parts of PFCs has been cooled down by

water and deposited energy could be monitored by same calorimetric technique applied to TRIAM-1M [5]. Measured deposited energy was plotted as the function of pulse length and then the gradient of the plot shows the deposited power in the magnetic configuration. The power distribution of PFCs on various magnetic configurations is plotted as shown in Fig. 6. Approximately 80-90 % of injected power in every case can be detected by the calorimetric measurement. Residual power may be lost in a microwave antenna, because the monitor of injected power was located just before the antenna.

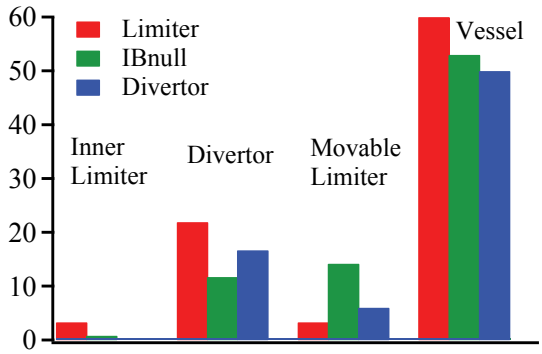

Fig. 6 Power distribution to PFCs in various magnetic configurations is plotted. Red, Green, and Blue show heat load in limiter, inboard null, and divertor configurations, respectively. Approximately 80% of injected power can be detected.

Significant portion of heat loaded to the divertor limiter even in a limiter configuration and it was natural. Magnetic surface just outside of last closed flux surface in low field side was directly connected to the divertor limiter via magnetic surface and the heat load was likely to be delivered from core plasma. While the heat load to divertor limiters on a single null divertor configurations has strong top-down asymmetry. For example, on upper single null divertor configuration, almost of heat load was delivered to top side of divertor region, and only one-tenth of the heat load reached on down side. On all the magnetic configuration, significant heat load is deposited on the movable limiter, therefore the heat load is delivered by significant large orbit in its poloidal projection and is likely to reach the movable limiter. In fact, floating potential of the movable limiter sometimes reaches to minus several keV. It clearly indicated the heat load was delivered by energetic electrons accelerated by injected microwave. As the results of making efforts to remove local heat load, power balance was tentatively achieved in 3-5 min discharges, because temperature on all the PFCs is almost constant during the discharge.

4. Summary

Present status of the QUEST experiments towards steady state operation is introduced. Power balance in the long duration discharges are investigated. Calorimetric measurement is applied to wall-cooled PFCs with increment of water temperature. The deposited energy on the vacuum vessel was investigated by the increment of the vessel temperature, when the wall baking system purposely stopped. It found that approximately more than 50% of injected power delivered to the vessel and power deposition of PFCs have significant variation depending on magnetic configurations. As the results on making efforts to avoid excess heat-up, finally the power seems to be balanced in long duration discharges.

5. Acknowledgements

This work was supported by Grant-in-Aid for JSPS Fellows (KAKENHI) and performed with the support and under the auspices of the NIFS Collaboration Research Program (NIFS05KUTRO14, NIFS11KUTR061). This work was supported in part by the Collaborative Research Program of Research Institute for Applied Mechanics, Kyushu University.

6. References

[1] H.Zushi, *et al.*, Nuclear Fusion, Vol. 45, No. 10

(2005) S142-S156.

[2] D. van Houtte *et al*., *Nuclear fusion*, Vol.**44**, No.5, L11-L15 (2004).

[3] Baonian Wan, *et al.*, Special issue: FEC2012 Expected online publication: June 2013

[4] T.Mutoh *et al*., J. Plasma and Fusion research, 81 (2005) 229-230.

[5] K.Hanada, *et al.*, Fusion Engineering and Design, Volume 81, Issue 19, September 2006, Pages 2257-2265

[6] M.Sakamoto, *et al.*, Nuclear Fusion, Vol. 44, (2004), P693-698.

[7] Maingi R. *et al.,* Nucl. Fusion 43 (2003) 969.

[8] R. Maingi, *et al.*, J. Nucl. Mater. 363–365 (2007) 196–200.

[9] V.A. Soukhanovskii et al., J. Nucl. Mater. 415 (2011) S365–S368.

[10] M. Kotschenreuther, *et al.*, Nucl. Fusion **50** (2010) 035003.

[11] K.Hanada, *et al.*, Plasma Science and Technology, Vol. 13, No.3, pp. 307.

[12] H.Idei, H.Idei *et al.*, Proc. 32nd International Conf. on Infrared and Millimetre Waves, Cardiff, UK, 789-790 (2007).

[13] K.Hanada, *et al.* IEEJ, Vol. 132 / No. 7 / Sec. A, pp.490-498.

[14] M. Ishiguro, *et al.*, Phys. Plasmas 19, (2012), 062508

Fuelling efficiency studies by particle balance in KSTAR

Yaowei Yu[1], Jiansheng Hu[1], Suk-Ho Hong[2], Si-Woo Yoon[2], Kwang-Pyo Kim[2], and Woong-Chae Kim[2]

[1] Institute of Plasma Physics, Chinese Academy of Sciences, Hefei, 230031, P.R. China

[2] National Fusion Research Institute, Daejeon, 305-806, Korea

yuyaowei@ipp.ac.cn

Abstract: Fuelling efficiency in a tokamak strongly affects plasma density control, further it affects the fuel recycling and particle confinement. In KSTAR fuelling efficiency of gas puffing and SMBI are studied by particle balance. A new method for calculation of fuelling efficiency of gas puffing is proposed from particle balance. The results show that gas puffing efficiency is 20-75%, which is higher than the effective efficiency due to different definition. The effect of plasma parameters on the fuelling efficiency is studied, including plasma density, and the gap between plasma boundary and outer limiter. The results are important for fuel recycling and retention studies. The effective Supersonic Molecular Beam Injection (SMBI) is investigated in KSTAR, it's in the range of 9-60%, and plasam density, plasma shape and Neutral Beam Injection (NBI) has strong effect on the SMBI efficiency.

Keywords: Gas puffing, SMBI, fuelling efficiency, KSTAR

PACS: 52.55.Fa, 28.52.Cx

1. Introduction

Fuelling efficiency in a tokamak strongly affects plasma density control, further it affects the fuel recycling and particle confinement [1]. Fig. 1 shows different particle flux between outside, plasma, and first wall in a tokamak discharge. Where *Ne* is the plasma inventory, *R* is global recycling coefficient, τ_p particle confinement time, $Q_{injection}$ the particle injection rate in D/s, and $f_{injection}$ the fuelling efficiency. $N_{neutral}$ is the neutral particles around the plasma, usually $N_{neutral}$ is much smaller than other particle contents, therefore in the calculation $N_{neutral}$ is always omittd [2].

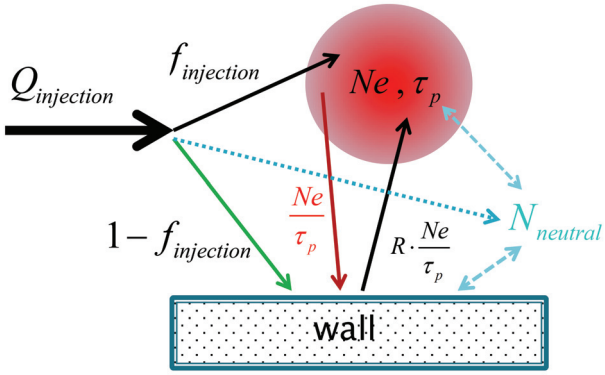

Fig. 1. Different particle flux during a plasma discharge

Particle balance is a basic method to study plasma inventory variation according to plasma confinement, particle injection, fuelling efficiency, and fuel recycling from first wall. Particle balance is described

by equation (1) [3]:

$$\frac{dNe}{dt} = (R-1)\cdot\frac{Ne}{\tau_p} + f_{injection}\cdot Q_{injection} \quad (1)$$

Equation (1) shows clearly that fuelling efficiency affects plasma inventory, i.e. plasma density control. Moreover, fuelling efficiency could also affect the recycling and particle confinement, which is an improtant issue for tokamak operation. Wall retention is also an improtant issue for tokamak operation, especially for steady state opeartion in future tokamaks, such as ITER. Wall retention from global particle balance can be cauculated by equation (2) [2]:

$$Q_{wall} = Q_{injection} - \left[\frac{dNe}{dt} + \frac{dN_{neutral}}{dt} + Q_{pump}\right] \quad (2)$$

where Q_{wall} is the wall retention rate in D/s, Q_{pump} the pumped particle, and $N_{neutral}$ the neutral particles around the plasma. However, if the particle balance is focused on the wall from Fig. 1, wall retention can be described by equation (3):

$$Q_{wall} \approx (1-R)\cdot\frac{Ne}{\tau_p} + (1-f_{injection})\cdot Q_{injection} \quad (3)$$

Here $N_{neutral}$ is omitted because it's much smaller than other particle content. The equation (3) indicates that low fuelling efficiency could increase the real-time wall retention, which would further impact the recycling and particle confinement time.

2. Calculation of fuelling efficiency of gas puffing

The fuelling efficiency of gas puffing was studied for a long time [4,5,6,7], and its definition is different for various study purposes. The effective fuelling efficiency is defined by [4]:

$$\alpha_{puff} = \frac{dNe/dt}{Q_{puff}} \quad (4)$$

where Q_{puff} is the puffing rate in D/s. This definition shows the reaction of plasma density on the gas puffing, here "effective" means the controllablity of gas puffing on the plasma density, the influence of recycling is not considered. Another method is so-called standard method of fuelling efficiency of gas puffing [4,5],

$$f_{puff} \approx \frac{(dNe/dt)_{before} - (dNe/dt)_{after}}{Q_{puff}} \quad (5)$$

where "before" and "after" means before and after the stopping of gas puffing. This method assumes that (1) wall recycling and particle confinement time is same and constant before and after the gas puffing, and (2) the increment of *Ne* is very small compared to *Ne* itself. This assumption is reasonable during a short gas puffing pulse (~100 ms, smaller than or similar with particle confinement time).

However, for the long gas puffing pulse case (>200 ms, which is longer than particle confinement time), both R and τ_p are changed by gas puffing, therefore the above assumption is not proper any more. Actually, it we only assume a constant effective particle confinement time τ_p^* during gas puffing phase:

$$\tau_p^* = \frac{\tau_p}{1-R} \quad (6)$$

then an analytical solution of *Ne* could be obtained from the particle balance equation (1),

$$Ne(t) = \left(Ne_{t=t_0} - f_{puff} Q_{puff} \tau_p^*\right) \cdot \exp(-\frac{t-t_0}{\tau_p^*}) + f_{puff} Q_{puff} \tau_p^* \quad (7)$$

This assumption is more reasonable because it's just during gas puffing phase rather than before and after gas puffing. Moreover, *Ne(t)* in equation (7) coincides with the experimental data.

Fig. 2 shows an example of f_{puff} calculation by using the above new method. It could be seen that before gas puffing, τ_p^* is almost infinite, during gas puffing, τ_p^* decreases to 0.22 s, and after that it increased again to 0.33 s. It indicates that the global recycling coefficient R is 1 before gas puffing, and decreased to <1 by gas puffing, and then after gas puffing, it recovers again gradually. In Fig. 2, the fuelling efficiency obtained by the new method is 0.68, which is much higher than the value of 0.11 from standard method. The difference between the new method and standard method is due to the recycling. In the standard method, R is considered as constant during and after gas puffing, while in the new method *R* is lower during gas puffing than that after gas puffing.

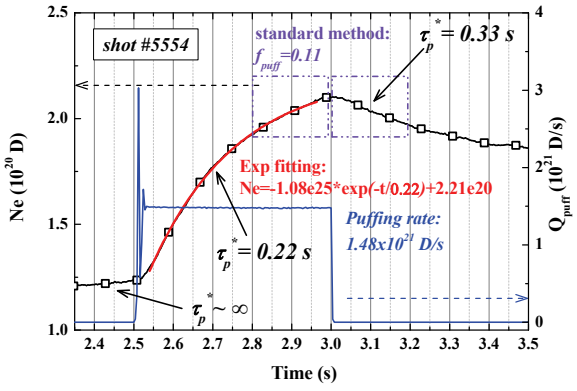

Fig. 2 An example of f_{puff} calculation in KSTAR shot #5554

3. Result of f_{puff} by the new method

By using the new method, f_{puff} is calculated and the result is shown in Fig. 3 under different puffing rate. It shows that f_{puff} is in the range of 10-75%, which is higher than the typical known efficiency of 10-20%. The gap means the distance between the plasma boundary and the outer limiter. Fig. 3 shows that fuelling efficiency is largely discrete with the gap, and the gap effect on the fuelling efficiency is very weak under the puffing rate of (3-30) $\times 10^{20}$ D/s.

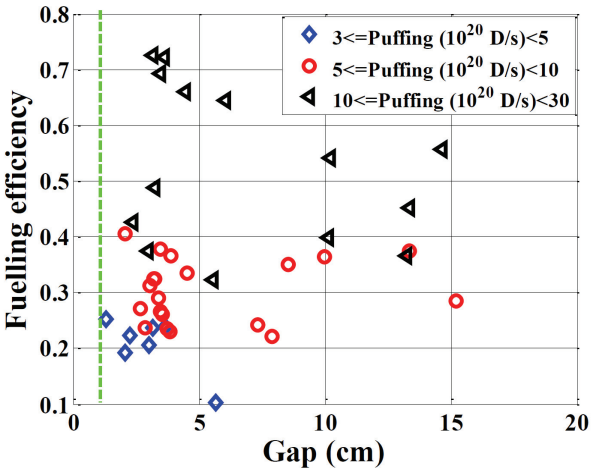

Fig. 3 f_{puff} and gap with different gas puffing rate

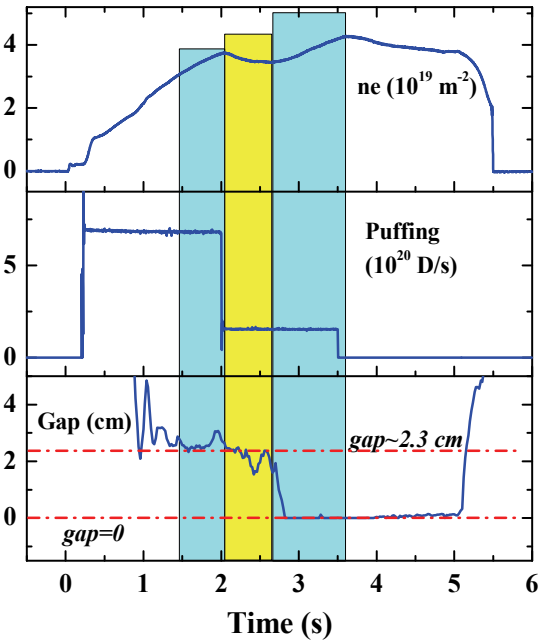

Fig.4 Gap effect on f_{puff} under low puffing rate

However, in the low puffing rate (~1.6×10^{20} D/s) case, the gap effect on the f_{puff} is different. Fig. 4 shows an example of low puffing rate shot. In the yellow range, the puffing rate is low, and the gap is ~ 2.3 cm, in this case the plasma density is decreasing, and the f_{puff} ~ 0. But when the plasma moves to outside, and the gap decreases to almost 0 as shown in the right blue range, plasma density starts to increase, and the calculated f_{puff} by the new method is ~76%, which is much higher than the case with gap ~2.3 cm. After gas puffing, it's observed that plasma density is decreasing even through the gap is still 0, which indicates that the plasma density increase in the right blue range is really due to the small gap rather than the wall outgassing.

Fig. 3 also shows that the puffing rate has a positive effect on the fuelling efficiency, it's observed that higher puffing rate induces higher fuelling efficiency. However, the analysis also shows that τ_p^* is decreased with the increase of puffing rate, therefore the effective fuelling efficiency is not affected by the puffing rate.

4. Fuelling efficiency of SMBI

SMBI uses short pulse of 1-10 ms, and on KSTAR it's typically 2-5 ms. Because of the short pulse, the method for f_{puff} calculation is nor proper. Here the fuelling efficiency of SMBI (α_{smbi}) is calculated by the increment of plasma inventory (ΔNe) by SMBI normalized by the total injection ($\Delta SMBI$) of one SMBI pulse, it reflects the effective fuelling efficiency,

$$\alpha_{smbi} \approx \Delta Ne / \Delta SMBI \qquad (8)$$

where $\Delta SMBI$ is obtained from the SMBI pulse length and corresponding injection value of SMBI from SMBI calibration. ΔNe is calculated by the peak value of Ne (usually ~ 50 ms after SMBI) subtracted by the initial Ne, as shown in Fig. 5. Here the symbol α is used instead of f because this definition is an effective fuelling efficiency, which is different from f_{puff}.

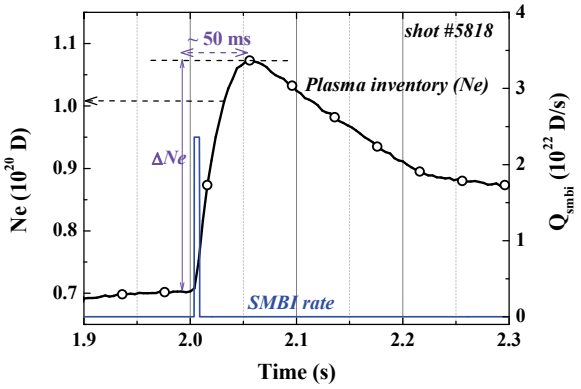

Fig. 5 SMBI calculation: ΔNe/ΔSMBI

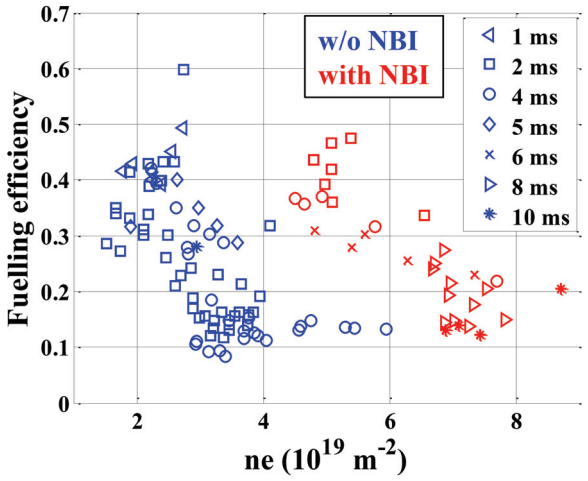

Fig. 6 Fuelling efficiency of SMBI with plasma density under different pulse length

Fig. 6 shows fuelling efficiency of SMBI with different SMBI pulse length under different plasma density. The shots without NBI are most circular L-mode discharges, while the shots with NBI are divertor H-mode discharges. It shows that α_{smbi} is 9-60%, and there is a

clear trend that f_{smbi} is decreased with the increase of plasma density both with and without NBI injection. The SMBI pulse length does not have any effect on f_{smbi}. The interesting phenomenon is that both shots with and without NBI are in the same range. At the same level of f_{smbi}, the shots with NBI have ~ 2 times higher plasma density than that without NBI.

It should be noted that α_{smbi} is 9-60%, which seems lower than f_{puff} ~ 20-75%. However, the definition of α_{smbi} is effective fuelling efficiency, while f_{puff} is not. The effective fuelling efficiency of gas puffing is ~10-20% as mentioned in section. 3. It indicates that the fuelling efficiency of SMBI is much higher than gas puffing.

5. Conclusion

Fuelling efficiency of gas puffing and SMBI are studied by particle balance in KSTAR. A new method for the calculation of the fuelling efficiency of gas puffing (f_{puff}) in long puffing pulse is proposed directly from the basic particle balance equation, which shows f_{puff} ~ 20-75%, the value is much higher than effective fuelling efficiency (10-20%) and standard efficiency. The plasma density and gap has little strong effect on f_{puff}. But at the low puffing rate (~1.6x10^{20} D/s), f_{puff} is obviously increased by reducing the gap from ~2.3 cm to 0. These results are important for fuel recycling and retention studies. The effective fuelling efficiency of SMBI (α_{smbi}) is 9 - 60%, it decreases with the increase of ne, α_{smbi} are in the same range both in circular L-mode discharges and divertor H-mode discharges. SMBI has higher effective fuelling efficiency than gas puffing, it's a promising method for tokamak fuelling.

Acknowledgement

The authors would like to thank the KSTAR team who made valuable efforts on the fuelling experiments. This work was partly supported by the JSPS-NRF-NSFC A3 Foresight Program in the field of Plasma Physics (NSFC: No.11261140328).

REFERENCES

[1] Wesson J, "Tokamaks", 4th edition, Oxford University press

[2] Yu Y W, et al., 2012 Plasma Physics and Controlled Fusion 54: 105006

[3] Loarer T, et al., 2007 Nuclear Fusion 47: 1112

[4] Miyazawa J, et al., 2004 Nuclear Fusion 44: 154

[5] Miyazawa J, et al., 2003 Journal of Nuclear Materials 313–316: 534

[6] Bucalossi J, et al., 2002 Proc. 19th International Conference on Fusion Energy (Lyon, France, 2002)

[7] Baylor L R, et al., 2003 Journal of Nuclear Materials 313–316: 530

Development of a real-time control system for NTMs suppression with ECRH/ECCD on EAST tokamak

Yang Zhang, Xiaoguang Wang, Xiaojie Wang, Xiaodong Zhang, and EAST Team

Institute of Plasma Physics, Chinese Academy of Sciences, Hefei 230031, China

Abstract: Neoclassical tearing modes (NTMs) in tokamaks limit the achievable β and induce a major disruption in some cases. They should be stabilized to overcome the limit and therefore improve the efficiency of magnetic confinement. On EAST tokamak, ECRH/ECCD will be used as a main tool for NTMs suppression. In order to achieve more effective application of ECRH/ECCD, a real-time control system for NTM suppression is needed. In this paper, a feasible design of the control system is proposed. The real time algorithms of mode localization and phase tracking are developed. The allowed latency of the control system is evaluated based on the modeling of magnetic island dynamics. Control scheme, hardware, some technical parameters are discussed as well. Mode localization is a key problem for NTMs suppression with ECRH/ECCD due to its quite narrow power deposition. Depending on the character of the temperature perturbation associate with the island, ECE measurements are used to make a correlation analysis (Te fluctuation correlated with magnetic signals) to determine the mode radial location. Island phase tracking is necessary for NTMs suppression with modulated ECRH/ECCD power. The O and X point of the island is identified based on the features of magnetic perturbation associate with the island. Due to absence of magnetic measurements close to the gyrotron, a reference signal for controller is derived from the coil located at the midplane in the low field side. The real-time control system will be implemented in FPGA environment. Its maximum allowed latency is required to match the growth times of NTMs, which is predicted to be in order of 100 ms on EAST.

1. Introduction

Neoclassical tearing modes (NTMs) in tokamaks limit the achievable β and may lead to major disruption. They should be stabilized and therefore improve the plasma performance and the efficiency of magnetic confinement. The NTMs can be suppressed by replacement of the "missing" bootstrap current [1, 2] using an externally driven current localized in the island structure. Electron cyclotron heating and current drive (ECRH/ECCD) is a particularly promising approach due to its highly local deposition [3]. For NTMs suppression using ECRH/ECCD, it is required to maintain a good alignment of the ECCD deposition with the magnetic island. More effective application of ECCD/ECRH can be achieved through the design of active control system. Several tokamaks such as

DIII-D [4, 5], JT-60U [6], ASDEX-U [7, 8], FTU [9] and TEXTOR [10] have made efforts on real time NTMs control using their EC systems.

EAST is a superconducting tokamak with a non-circular plasma cross-section in major radius R = 1.75m and minor radius a = 0.45 m. NTMs has been observed on EAST [11] and will be inevitable in future high confinement plasma. A 140 GHz, 4MW, 100 s Electron Cyclotron Resonance Heating (ECRH) system is being developed in present and will be used as a dominant tool in the future for the NTMs suppression and avoidance on EAST. A real-time control system is required to be capable of put exactly the ECRH/ECCD power into the magnetic island. In this paper, the design of the real time control system is presented. The ECRH and ECE installations on EAST are introduced generally in the in the session 2. The characters of temperature fluctuation associated with tearing mode are identified in session 3, and the algorithms of mode localization and phase tracking are developed based on these characters. The structure of the control system is figured out in session 4 and its hardware and requirements are discussed.

2. ECRH installation and ECE diagnostics on EAST

The 140GHz, 4MW, 100s ECRH installation on EAST tokamak consists of four gyrotrons with steerable launcher, operating at second harmonic X-mode EC wave. The launcher is installed at M-port of EAST machine. The steerable mirrors locate at Z = +-30 cm in the vertical plane and actuate from -30° to +30° in the toroidal direction and from +-35° to -+15° in poroidal direction. Through the wide range of achievable poloidal and toroidal angles, it is possible to heat and/or drive current in a wide range of plasma configurations (0.1 a ~ 0.8 a). As the suppression of NTMs requires, the accuracy of the mirror rotation is desired to 1°.

EAST has been equipped with two heterodyne radiometer systems (HRS) for electron cyclotron emission (ECE) measurements [12]. The first 16-channel HRS covers frequency range from 98.5 to 126 GHz with radial resolution of about 2 cm, and the second 32-channel HRS covers from 104 to 168 GHz with a better resolution of around 1 cm. Their RF frequencies are equally spaced every 2 GHz, providing the possibility of measuring the electron temperature perturbation associated with tearing mode. Furthermore, a new 16-channel HRS system with the frequency range from 90 to 110 GHz is being installed specially for the measurements of NTMs at q=1.5 and q=2 near the low-field-side. For this purpose, the space of RF frequencies between channels is improved to 1 GHz, allowing further determination of magnetic island width in experiments.

3. Mode localization and phase tracking

3.1 Characters of temperature perturbation associated with magnetic island

The relationship between the magnetic structure of a saturated tearing mode and the associated helical

perturbation of the electron temperature profile has been demonstrated in [13, 14]. Here some important characters are reviewed. Tearing mode is described by the perturbed flux $\psi_{mn}=\psi_{mn}(r)\cos\zeta$, where ζ is helical phase angle of the mode $\zeta=m\theta-n\phi+\omega(t)$, and m and n are the poloidal and toroidal mode numbers, respectively. The perturbed flux surfaces are periodic in the helical phase angle ζ, repeating every 2π rads. There is a π phase difference between the X-point and O-point of the magnetic island. In the outer region of the magnetic island, the temperature perturbation measured with ECE is sinusoidal as a function of time with the same period of perturbed magnetic flux. The ECE signal is characterized by a 180^o phase jump between signals on either side of island. In the inner region of the magnetic island, there is no flattening of the temperature profile for the small size island ($W<<W_c$), whereas for the larger size island ($W>>W_c$), the temperature is flattened within the island, corresponding to flux surface inside the separatrix, while the principal harmonic profile is antisymmetric about the rational surface, reaching local extreme of amplitude on flux outside the separatrix. These characters are not only used, in conjunction with experimental ECE data, to determine the structure of tearing mode, but also the physics basis for the development of real-time algorithms of mode localization and phase tracking.

An ohmic discharge #39781 (I_p=256 kA, $n_e=2.0\times10^{19}m^{-3}$, B_t =1.8 T) is selected to analyze the ECE temperature fluctuations caused by an m/n = 2/1 tearing mode. Although NTMs have been observed during H-mode discharge on EAST, their magnetic structure cannot be revealed with ECE measurement due to the usage of low hybrid wave (LHW) as an auxiliary heating. The experimental data of the existing 16-channel HRS are used here due to the signals with good SNR. In the following, the off-line mode localization is performed also based on this system, whereas the final implementation of the real time control system will adopt the new 16-channel system.

Figure 1 shows time traces of ECE channel measurements at five positions in the vicinity of the high-field-side q=2 surface. Only the temperature perturbation for each channel is plotted and the averaged electron temperature has been subtracted by filtering the signal with a band pass filter. It shows that there is a clearly phase jump between ECE channel 11 and 13, indicating the existence of a tearing mode. The perturbation is invisible in channel 12 because it measures the temperature within the magnetic island. Therefore, the mode location is determined approximately at the position of ECE channel 12. It also shows that a clipping of the oscillation happens on the channel 11, which reveals that the separatrix of magnetic island is very close to this channel. The island width can be estimated depending on the spatial space between channel 11 and 12 (about 5 cm in high field side). Furthermore, the heat is transported along a boundary layer located on the island separatrix, and flows across the rational surface in the vicinity of the X points. In other words, heat flows towards the X

points in $r<r_s$ region and backwards the X points in $r>r_s$, where r_s is the radius of the resonant surface where the island is located. This results in that the ECE signal from $r<r_s$ has a minimum at the O-point and a maximum at the X-point, and vice versa for the signal from $r>r_s$. The X-and O-points pass the toroidal position of the ECE diagnostic in two periods have also been indicated in figure 1. The ECE temperature perturbations are also analyzed with a Fast Fourier Transform. The perturbation amplitude and phase of the first fourier component is plotted along the radial position as shown in figure 2. The radial positions viewed by the ECE channels depend on the magnetic field and are easily computed. It shows that the amplitude profile has a local minimum in at channel 12, which is enclosed by two local maxima, and meanwhile a π phase jump occurs around this channel. It further confirms that the mode locates approximately at the position of channel 12, corresponding to R = 1.575 m.

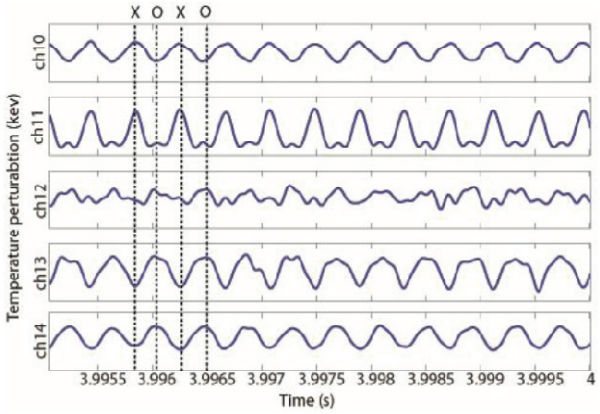

Fig. 1. Time traces of ECE temperature perturbations caused by 2/1 tearing mode. Channel 10 to 14 measures at five positions in the vicinity of the high-field-side q=2 surface

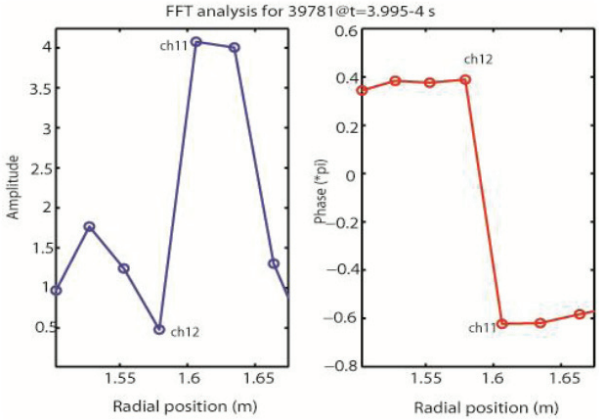

Fig. 2. Fast Fourier Transform analysis for the discharge #39781@3.995-4.000 s. Amplitude and phase profiles of the first fourier component (f=2.8kHz) is plotted.

3.2 Real-time mode localization

The mode localization is prerequisite for the real-time NTMs control using ECRH/ECCD. Several algorithms have been mentioned in Ref [5, 10, 15]. All of them are developed based on the characters of ECE temperature fluctuations associated with the magnetic island. In this paper, an algorithm similar to suggestions made by Reich et al. [15] is developed due to its higher reliability.

The toroidal number (n=1 or n=2) signal of a tearing mode is firstly obtained by linear combinations of Mirnov signals. Through the correlation between each ECE signal with the toroidal mode signal and its Hilbert transform, the amplitude and phase with respect to the magnetic reference is then obtained. The phase changes along the radial position can be built, which is much higher reliability than by cross correlation of ECE channels alone. Moreover, the way

to determine the mode position by identifying phase change as well as the local minimum of amplitude profile could make the localization more reliable.

In this work, the algorithm of mode localization is adopted and modified to suit to the EAST application. It is implemented and simulated with MATLAB programming. An off-line analysis for discharge 39781 during the time interval from 2.5 s to 4.5s is shown in figure 3. The top plot gives the spectrum of a tearing mode, which indicates a 2/1 tearing mode rotating at frequency of 2.8 kHz. The second curve shows that the toroidal mode number of the island is n=1 (assuming m=n+1). The third plot indicates the mode position in normalized radius (r/a) and the bottom one is the island width, which reveals that the resonant q=2 surface where 2/1 mode locates moves gradually towards the plasma edge as the island width increases. The off-line analysis has already successfully demonstrated island localization, but only for selected examples. The algorithm needs to be further validated with much more available experimental data or by comparing with the flux reconstruction of MSE-EIFT. Moreover, the precision of the determination can be improved by high spatial resolution of the ECE system.

3.3 Island phase tracking

It has been proved experimentally that modulating ECCD to deposit solely in the O-point enhances the stabilization efficiency of a NTM [16]. In this case, besides the mode radial location should be determined, it is required to further track the X-point and O-point of a magnetic island. The X-point and O-point can identified either by temperature perturbation signals, seeing figure 1, or by Mirnov signals, seeing figure 4. It is found that on EAST the X point of a magnetic island always corresponds to $d(dB/dt)/dt>0$ in the Mirnov signal and while the O point corresponds to $d(dB/dt)/dt<0$. Depending on this character, an algorithm that tracks the change in the time derivative of a Mirnov signal is developed to identify the X-point and O-point of a NTM island in real time.

Due to the lack of Mirnov coils at the position of ECCD deposition on EAST, a reference signal is constructed to simulate the magnetic perturbation close to a ECCD deposition. FFT analysis is performed on an existing Mirnov signal to obtain the frequency and phase information of a NTM, and then a phase correction is shifted to derive the phase of the reference signal. The phase correction is calculated with the relationship between mode helical angle and the coils installation angle. Assuming that the signal phase measured with a existing coil is $\zeta 1$, then the phase of reference signal should be $\zeta 1+(m\Delta\theta-n\Delta\varphi)$, in which the $\Delta\theta$ and $\Delta\varphi$ are angle differences between the coils installation in the the poloidal and toroidal direction, and m and n are the poloidal and toroidal mode number, respectively. The bottom plot of figure 4 shows an example of a reference signal (dashed line), and depending on this a modulated wave for ECCD/ECRH power is generated (red solid line).

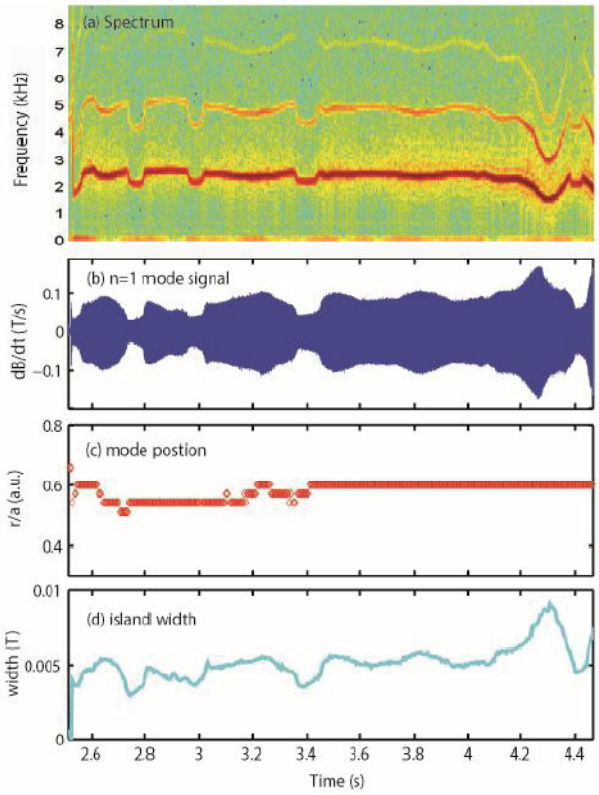

Fig. 3. Simulation results for off-line test of the real-time mode localization: (a) frequency spectrum of the magnetic perturbation, (b) n=1 mode signal, (c) island location in normalized radius and (d) the island width.

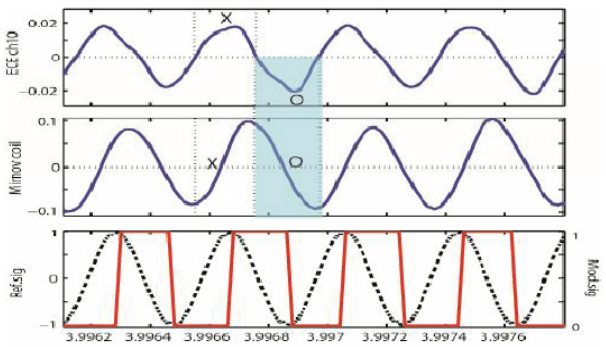

Fig. 4. Simulation results for mode phase tracking. ECE10 monitors the temperature perturbation in *r<rs*, and Mirnov coil is chosen for the same toroidal position with ECE measurement. The reference signal (dashed line) simulates the magnetic perturbation close to ECCD deposition, and a modulated wave is generated (red solid line) based on the reference signal.

4. Real-time control system

The real time control system is designed mainly for the suppression of 3/2 and 2/1 NTMs due to their serious effects on plasma confinement. Its structure and detailed flow is shown in figure 5. The ECE and magnetic signals are acquired from the diagnostic measurements. The toroidal number (n=1 or n=2) signal of a tearing mode is firstly obtained by linear combinations of two Mirnov coils signals (dB_θ/dt) at opposite (180^o) toroidal position on the low field side of the tours. Secondly, taking the toroidal mode number signal as a reference, each ECE measurement is correlated with the reference and its Hilbert transform respectively, and therefore the correlated amplitude (A_i) and phase profile (Φ_i) are constructed along the radial position. The mode radial position is determined in geometry coordinate and then is translate to radial flux surface coordinates ($\rho_{NTM,ECE}$)by using the available real-time equilibrium reconstruction (rt-EFIT). With Mirnov signals, the NTM frequency (f_{mode}), phase (θ_{mode}) and island width (W_{island}) can be obtained, in which the width of island estimated with $W \sim \sqrt{\dot{B}_\theta f_{mode}^{-1}}$ is used to monitor the occurrence of NTMs and evaluate the NTMs stabilization efficiency. Since NTMs can be stabilized with either continual or modulated ECCD/ECRH power injection, two control strategies are considered.

In the first one, the NTM controller is designed to steer the ECRH mirrors to deposit power at the mode location (PID), and furthermore a necessary correction is applied to the mirror tilt to move the EC-beam pointing into the island's center based on changes in the island width of a NTM (manual). A nominal value for the ECCD position is computed off-line using the TORAY ray tracing code. A feedback control on the mirrors by the aid of a real time TORAY calculation is not considered here, but will be part of future work. In the second one, the mode phase and frequency information are used to construct a reference signal to simulate the magnetic perturbation close to the ECCD deposition, with which the X –point and O-point of the island can be identified further. After a good alignment of ECRH power deposition with mode radial location is achieved, a modulation signal (S_{modu}) is generated and then used to control the ECCD/ECRH power solely in the island's O-point.

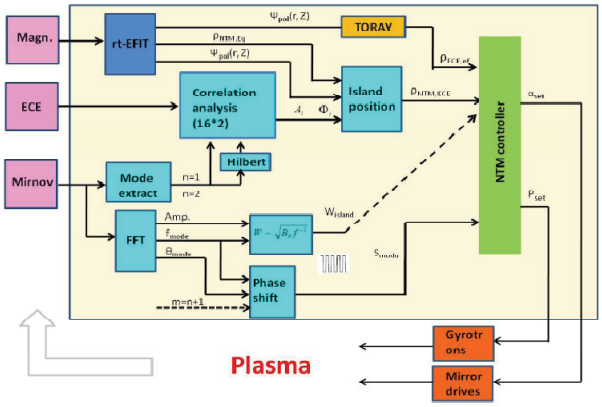

Fig. 5 Structure and detailed flow of the real time control system

The NTM real time control system present in this paper works as a subsystem of the present EAST control system (PCS) communicating to the other parts of the system. It will be implemented in a FPGA environment based on a PXI architecture composed by 1 PXIe-8135 RT , 3 FPGA Virtex-5 and 1 GE cPCI-5565PIORC. Three FPGAs Virtex-5 are used to acquire the 21 fast analog channels (16 ECE and 5 Mirnov signals) at the sample frequency of 100 kHz and perform filtering for all signals using band-pass filters and FFT analysis for one of Mirnov signal. On the PXIe-8135RT, the algorithms of mode localization and phase tracing are implemented. The real plasma equilibrium is received with the GE cPCI-5565PIORC from PCS and used for the mode location and ray tracing codes. The control strategies may be written into the PXIe-8135 RT but it has not been decided ultimately. A feedback control requires acquiring the ECRH/ECCD deposition position either by ray tracing predictions or by ECE measurement in real time. The system can be update in the further due to its FPGA modules connected by PXI bus.

The latency of the control system is estimated. The real-time equilibrium performs in about 1~2 ms, and the algorithms are capable of detecting the mode position by correlation in about 5 ms and identifying the island's O point with FFT analysis in about 2 ms. Since the allowed latency of control system is required to match the growth times of NTMs on EAST, which is predicted to be about 100 ms, the control cycle period including the TORAY calculation is expected to perform sufficiently fast (20~40 ms), which further needs a desired angular mirror rotation in the poloidal plane of 100 in 100 ms, with a desired

position accuracy of 10.

References

[1] A.W. Morris et al., in Proceedings of the 19th EPS Conference on Controlled Fusion and Plasma Physics, Innsbruck, 1992 (Pergamon, New York, 1992).

[2] C. C. Hegna and J. D. Callen, Phys. Plasmas 4, 2940 (1997).

[3] R. Prater, Nucl. Fusion, 43 (2003) 1128–1134

[4] D.A. Humphreys, et al., Phys. Plasmas 13 (2006).

[5] Y S Park, A S Welander, Plasma Phys. Control. Fusion 48 (2006) 1447–1454

[6] A. Isayama, Nucl. Fusion 43 (2003) 1272–1278

[7] M. Reich, 37th EPS Conference on Plasma Physics, P2.189

[8] N. K. Hicks, FUSION SCIENCE AND TECHNOLOGY VOL. 57(2010), 1-9

[9] J. Berrino, E. Lazzaro, et al, Nucl. Fusion 45 (2005) 1350–1361

[10] B A Hennen, Plasma Phys. Control. Fusion 52 (2010) 104006 (20pp)

[11] Tonghui Shi et al 2013 Plasma Phys. Control. Fusion 55 055007

[12] Y. Liu, et al., Plasma Science and Technology 13 (2011), 352-355

[13] R. Fitzpatrick, Phys. Plasmas 2, 825 (1995);

[14] J P Meskat, et al., Plasma Phys. Control. Fusion 43 (2001) 1325–1332

[15] M. Reich, FUSION SCIENCE AND TECHNOLOGY 61 (2012), 309-313.

[16] M. Maraschek, PRL 98, 025005 (2007)

Short interval measurement of the Thomson scattering system at the pellet injection by using the event triggering system in LHD

R. Yasuhara, R. Sakamoto, G. Motojima, I. Yamada, H. Hayashi

National Institute for Fusion Science, Toki, Gifu 509-5292, Japan

Abstract: We have demonstrated Thomson scattering measurements of a short interval less than 1 ms by using the event triggering system with a multi-laser configuration. We have tried to measure this system at the pellet injection and obtained electron temperature and density profiles before and just after the pellet injection. Obtained profiles were dramatically changed after pellet injection with shot-by-shot measurements. This measurement technique will contribute understanding the physics of the pellet deposition.

Keywords: Thomson scattering, pellet injection, event trigger.

PACS: 52.50.Qt

1. Introduction

Thomson scattering (TS) measurements of a short interval less than 1 ms are strongly desired for a research on transient plasma events such as a pellet injection [1]. The time interval of electron temperature (Te) and electron density (ne) profiles is limited by the laser system. A joule class commercially based Nd:YAG lasers is pumped by flush lamp. A high repetition rate laser operation cannot be carried out by this pumping scheme. By researches in recent year the solid-state laser has demonstrated the Joule class output energy and over 10 Hz repetition rate with good beam quality by using laser diode [2-4] which can decrease the heat load dramatically from flush lamp scheme. However, high energy diode pumped laser system is not available commercially and is high cost now.

One of the practical solutions to realize a short time interval measurement is the burst mode operation with a multi laser configuration. Each laser in a multi-laser configuration can adjust the laser output timing independently. It allows a short interval burst mode measurement within the number of laser systems. MAST TS system has demonstrated such burst mode measurement of TS system [5] by using 8 probe lasers with the FPGA triggering system. They have obtained the Te and ne values from the transient plasma phenomena [6]. In LHD, we have three lasers for the probe laser of the TS [7]. Three burst pulses can use for a short time interval measurement. In addition, we have developed the coaxial beam combining technique to improve the spatial uncertainty of Te and ne values measured by each probe lasers [8]. By using multi-laser system with the coaxial beam combining

shot by shot TS measurement is available at the transient plasma phenomena in LHD.

In the paper, we report the detail of this burst mode measurement system and the result of the demonstration of this system at the pellet injection. This diagnostics method will contribute for cross-validation of the simulation and the experiment in transient plasma events.

2. Burst mode triggering system at the transient event

Figure 1 show the triggering system for the burst mode operation of the multi-laser TS system. TTL triggers from the tangent event such as the pellet injector or LHD timing system are used as master triggers of this system. Logic OR of this 2 line is the master trigger of the triggering system. Triggers for the three laser outputs are distributed by the DG645 which is the commercial pulse generator based on the FPGA system. The accuracy of trigger timing is less than 1 ns. It can generate the arbitrary timing trigger for the flash lamp and the Q-switch of three lasers. Then, the trigger timing duration between the Q-switch and the flash lamp should be fixed due to maintain the laser extraction efficiency. The shortest time interval of the multi-laser output for TS measurement is about a few micro second. This is depending on the data acquisition system of the LHD TS system.

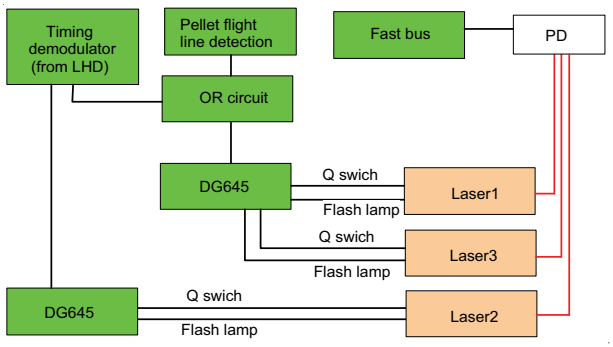

Fig. 1A schematic diagram of the event trigger system.

At first the multi-laser system is operated by the triggers from the LHD timing system for the stable laser operation. Before the some plasma event, the multi-system is stopped by stopping the LHD timing system and waited for the trigger from the events. In the case of the pellet injection, triggers from LHD timing system is stopped at 3.7 s of the LHD plasma shot for the waiting the pellet injection at 3.75 s. Finally, when the event provides the trigger, multiple laser light pulses are fired with the short time interval which is set by the DG645.

3. Multi-laser system

A partially high-reflectance coated mirror or the polarization beam combining technique [8] is adapted to form the bundle beam emitted from multiple lasers. By using the polarization beam combining, the laser beam axis is perfectly same. We can compare the ne profiles in time series of multi-laser. However, by using a partially high reflectance coated mirror laser beam axis is different between the multi-lasers. The laser beams are packed along a common beam axis at a regular interval of 1 cm by the packing mirror and a

partial overlap in the far field where they are focused on a common point inside the LHD vessel at the major radius of 3.65 m.

For the comparing the ne profiles in time series, we use the one laser for the standard laser. ne profiles measured by another lasers are normalized by the ne profiles measured by the standard laser. By adding this procedure, we can compare ne profiles by shot to shot of the multi-laser system. In near future, we planned to install the method of combining three or more laser beams by using a Pockels cell.

4.Synchronized measurement at the pellet injection

By using this short time interval measurement, we tried to measure at the pellet injection. Triggers from the pellet injector were used for the master trigger of the burst mode operation of the TS system. We have tested this synchronized measurement system for LHD TS system from 15th experiment campaign and confirmed the synchronized measurement of the TS system and the pellet injection. Figure 2 shows the Timings of the lasers for the Thomson scattering system relative to Hα emission light signal from the pellet ablation at the #113431 (16th experiment campaign). In this measurement, a pellet light gate signal with about 3.5 ms delay was used for the trigger of laser triggering sequences. A duration of two laser pulses after pellet injection was 200 μs. We have demonstrated the burst mode TS measurements within 1 ms after pellet ablation. Figure 3 shows Te and ne profiles from Thomson scattering measurements before and after pellet injection. Laser 2 put into the plasma before pellet injection (3.73358 s, red plots). After that, Laser 1 was injected after pellet injection (3.751974 s, green plots). After 200 μs of Laser 1, Laser 3 was worked for the measurement of Te and ne profiles (3.752175 s, blue plots). Finally, Laser 2 put into the plasma again (3.766912 s, orange plots). From the Fig. 3, we can see Te and ne profiles were dramatically changed after pellet injection with shot-by-shot TS measurements. This measurement technique will contribute understanding the physics of the pellet deposition.

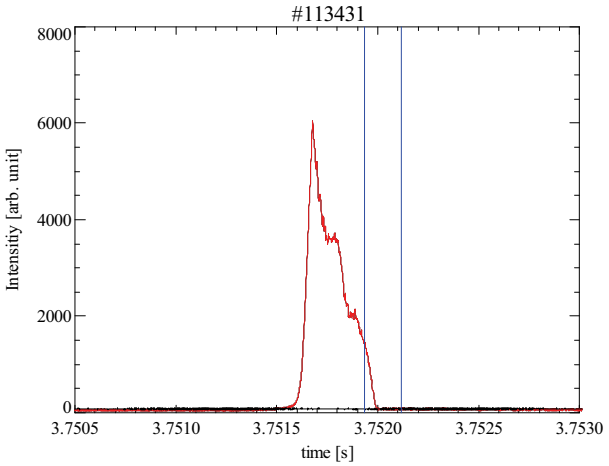

Fig. 2Timings of the lasers (blue lines) for the Thomson scattering system relative to Hα emission light signal (red line)from the pellet ablation.

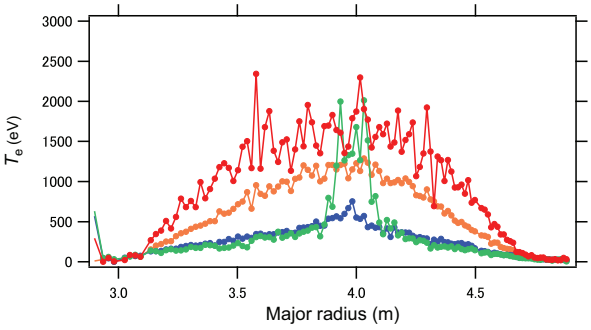

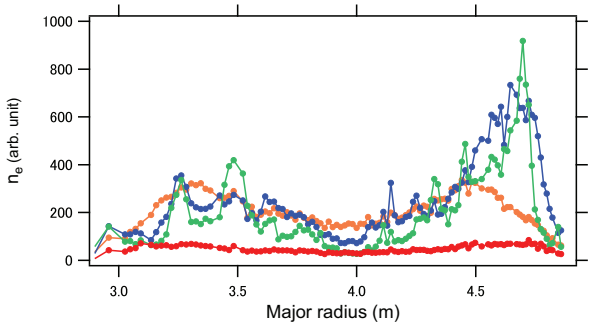

Fig. 3Te and Ne profiles from Thomson scattering measurements before and after pellet ablation.

5. Summary

We have demonstrated TS measurements of a short interval less than 1 ms by using the event triggering system with a multi-laser configuration. We have tried to measure this system at the pellet injection and obtained Te and ne profiles before and just after pellet injection. This measurement technique will contribute understanding the mechanism of the pellet deposition and the transient phenomena of the LHD plasmas.

Acknowledgments

This work was supported by a Grant-in-Aid for Young Scientists (B), Grant No. 23760813 from MEXT and is partially carried out under the LHD project financial support (Grant No. NIFS11ULHH005).This work was partly supported by the JSPS-NRF-NSFC A3 Foresight Program in the field of Plasma Physics (NSFC: No.11261140328).

REFERENCES

[1]. M. Valoviˇc, K. Axon, L. Garzotti, S. Saarelma, A. Thyagaraja, R. Akers, C. Gurl, A. Kirk, B. Lloyd, G.P. Maddison, A.W. Morris, A. Patel, S. Shibaev, R. Scannell, D. Taylor, M.Walsh and the MAST team, Nucl. Fusion 48 (2008) 075006

[2]. A. Bayramian, J. Armstrong, G. Beer, R. Campbell, B. Chai, R. Cross, A. Erlandson, Y. Fei, B. Freitas, R. Kent, J. Menapace, W. Molander, K. Schaffers, C. Siders, S. Sutton, J. Tassano, S. Telford, C. Ebbers, J. Caird, and C. Barty, J. Opt. Soc. Am. B 25(7), B57–B61 (2008).

[3]. R. Yasuhara, T. Kawashima, T. Sekine, T. Kurita, T. Ikegawa, O. Matsumoto, M. Miyamoto, H. Kan, H. Yoshida, J. Kawanaka, M. Nakatsuka, N. Miyanaga, Y. Izawa, and T. Kanabe, Opt. Lett. 33(15), 1711–1713 (2008).

[4]. S. Banerjee, K. Ertel, P. D. Mason, P. J. Phillips, M. Siebold, M. Loeser, C. Hernandez-Gomez, and J. L. Collier, Opt. Lett. 37(12), 2175–2177 (2012).

[5]. G. Naylor, Rev. Sci. Instrum. 81, 10E110 (2010).

[6]. K J Gibson, N Barratt, I Chapman, N Conway, M R Dunstan, A R Field, L Garzotti, A Kirk, B Lloyd, H Meyer, G Naylor, T O'Gorman, R Scannell, S Shibaev, J Snape, G J Tallents, D Temple, A Thornton, S Pinches, M Valovic, M J Walsh, H R Wilson and the MAST team, Plasma Phys. Control. Fusion 52 (2010) 124041

[7]. K. Narihara, I. Yamada, H. Hayashi, K. Yamauchi. Rev. Sci. Instrum. 72 (2001) 1122.

[8]. R. Yasuhara, I. Yamada, K. Narihara, H. Funaba, and H. Hayashi, Plasma and Fusion Research 7, 2402030 (2012).

Shape reconstruction of steady state divertor plasma on QUEST

K. Nakamura[1], H. Fujita[2], X.L. Liu[3], E.B. Xue[4], F. Xia[3], O. Mitarai[5], K. Kurihara[6], Y. Kawamata[6], M. Sueoka[6], M. Hasegawa[1], K. Tokunaga[1], H. Zushi[1], K. Hanada[1], A. Fujisawa[1], K. Matsuoka[1], H. Idei[1], Y. Nagashima[1], S. Kawasaki[1], H. Nakashima[1], A. Higashijima[1], K. Araki[1], and A. Fukuyama[7]

[1] RIAM, Kyushu Univ., Kasuga, 816-8580 Japan

[2] IGSES, Kyushu Univ., Kasuga, 816-8580 Japan

[3] CFS, SWIP, P.O.Box 432, 610041 Chengdu, P.R.China

[4] Donghua Univ., Songjiang, Shanghai, 201620 P.R.China

[5] Kumamoto Campus, Tokai Univ., Kumamoto, 862-8652 Japan

[6] JAEA, Naka, Ibaraki, 311-0193Japan

[7] Kyoto Univ., Kyoto, 606-8502 Japan

Abstract: In the present RF-driven plasma with a lot of high-energy electrons, there may be anisotropic plasma pressure, which makes difficult a usual equilibrium analysis, but the CCS method can reconstruct the plasma shape precisely regardless of the anisotropy. And the plasma current effect in the open magnetic surfaces outside of the closed magnetic surfaces is considered in the RF-driven plasma. In the reconstruction process, SVD (Singular Value Decomposition) is used and optimal criterion function for GCV (Generalized Cross Validation) is estimated concerning truncation or reduction of the small-SV components.

1. Introduction

In the spherical tokamak QUEST (B_t = 0.25T, R = 0.68m, a = 0.40m), as the methods to obtain a steady-state divertor plasma, we have two methods: First, a high-density divertor plasma is made by OH (ohmic heating) and the plasma current is planned to be sustained by EBW current drive. Second, a low-density plasma is made by ECRH, the plasma current is ramped up by ECCD (Electron Cyclotron Current Drive) and sustained by ECCD.

OH divertor plasma of lower triangularity (Candy-shape) was produced with PF35-12 inner and outer divertor coils connected in series. And OH divertor plasma of higher triangularity (D-shape) was produced with PF35-1 inner divertor coil [1]. The divertor plasma was designed by TASK/EQU code and the plasma boundary shape was reconstructed by CCS (Cauchy Condition Surface) method according to data from two kinds of magnetic sensors (flux loops and magnetic probes including partial Rogowski). The reproduced result showed a double-null divertor configuration and was compared with that by EFIT code.

The CCS method is an exact numerical method which

is based on the boundary integral equation. The CCS is defined as a hypothetical plasma surface, where both the Dirichlet (poloidal flux function) and Neumann (poloidal magnetic field tangent to the CCS) conditions are unknown [2]. Though eddy current is also unknown, poloidal field coil current is known including connecting and returning windings of toroidal field coils.

In the present RF-driven plasma with a lot of high-energy electrons, plasma current flows in the open magnetic surfaces outside of the closed magnetic surfaces according to PCF (Plasma Current Fitting) method [3]. And there may be anisotropic plasma pressure due to the above open-magnetic-surface current by trapped particles [4], which makes difficult a usual equilibrium analysis.

The CCS method can reconstruct the plasma shape precisely regardless of the anisotropy [5]. In the reconstruction process, SVD (Singular Value Decomposition) is used and optimal criterion function for GCV (Generalized Cross Validation) is estimated concerning truncation or reduction of the small-SV components.

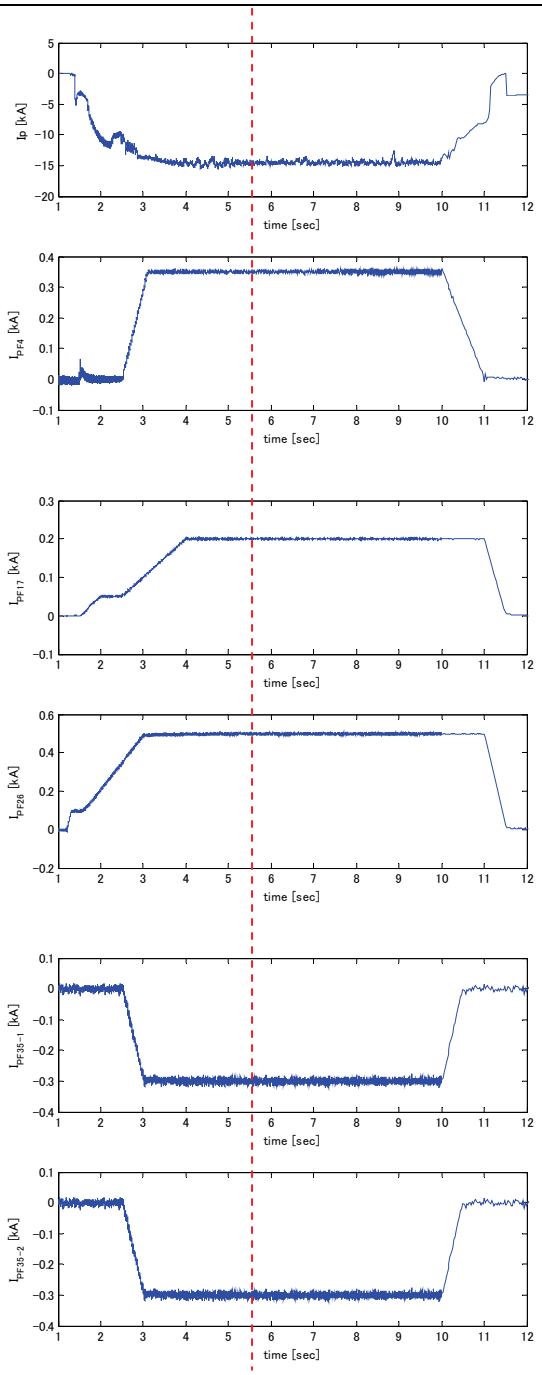

Figure 1: RF-startup, ramp-up and sustained divertor plasma on QUEST. Ip: plasma current, PF4: center solenoid coil, PF17: vertical field coil with negative n-index, PF26: vertical field coil with positive n-index and PF35-1: inner divertor coil, PF35-2: outer divertor coil.

2. RF-Driven Plasma on QUEST

In RF-startup, ramp-up and sustained divertor plasma on QUEST (Fig. 1), plasma current is driven even in the outside of the LCFS (Large Closed Flux Surface) on the low-field side. The current is interpreted t be carried by trapped particles in the open magnetic surfaces. The magnetic surfaces are reconstructed by assuming multi-filament current in the vacuum chamber [3] or assuming truncated current profile,

which is a function of poloidal magnetic flux even in the outside of the closed magnetic surfaces [6]. In both cases, the current density profile is shifted to the low-field side from the LCFS. The trapped particles carry current also in the inside of the closed magnetic surfaces, and the equilibrium can be reconstructed by taking into account the anisotropic pressure profile all over the plasma [4]. In this reconstruction, the perpendicular pressure profile is shifted outward reflecting the perpendicular velocity component of the trapped particles.

3. Isotropic Pressure Profile

Plasma equilibrium solution is fitted assuming all plasma current is flowing in the inside of the LCFS. It is solved within the isotropic pressure profile by EFIT code (Fig. 2). The overall current density profile is shifted to the low-field side from the LCFS and apparent poloidal beta becomes larger than unity. Opposite-polarity current density region appeared in the high-field region (negative n-index), where $R <$ 0.56 m. The fraction of the opposite-polarity current is small to be about 2 %. The elongation ratio of the LCFS (separatrix) is about unity and the aspect ratio is lower than two. The elongation ratio of the same-polarity region is about 1.4 though the aspect ratio becomes larger than two.

Plasma equilibrium solution is fitted assuming open-field plasma current flows discretely in in-vessel poloidal field coils in the outside of the LCFS. Anisotropic pressure component is expressed by the in-vessel poloidal field coils and isotropic pressure component is fitted by EFIT code (Fig. 3). From the result, where the opposite polarity current disappears, the amount of the open field current fraction is estimated to be about 30 % of the total current.

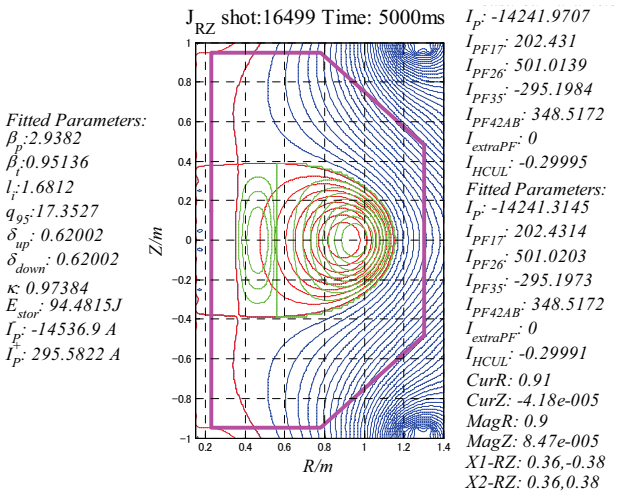

Figure 2: Plasma equilibrium solution fitted assuming all plasma current is flowing in the inside of the LCFS within the isotropic pressure profile by EFIT code. Red and blue contours: poloidal flux function, green contours: current density.

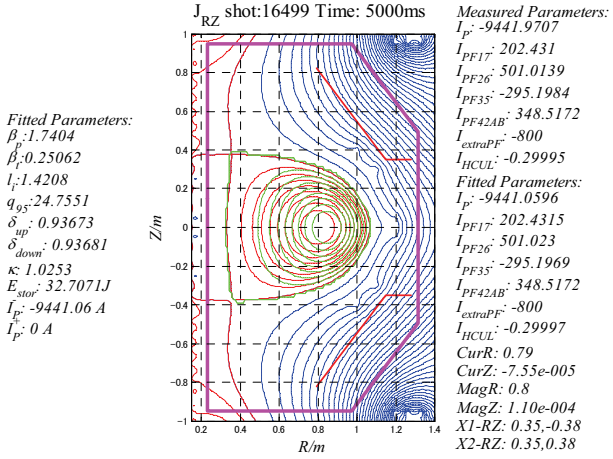

Figure 3: Plasma equilibrium solution fitted assuming open-field plasma current is expressed by current in in-vessel poloidal field coils in the outside of the LCFS. Red and blue contours: poloidal flux function, green contours: current density.

4. Anisotropic Pressure Profile

Plasma shape is reproduced assuming all plasma current is flowing in the inside of the LCFS. It is reproduced even for anisotropic pressure profile by CCS method [5]. In this CCS method, we consider only vacuum magnetic field region by setting CCS in the inside of the plasma boundary. All the information about the plasma is represented by the unknown boundary conditions on the CCS. The unknowns are obtained by fitting to measured data at magnetic sensors of flux loops and magnetic probes.

4.1 Least Square Method

When the above observation equation is solved by LSM (Least Square Method), Ill-posedness appears as shown in Fig. 4. The ill posedness could not be prevented by reducing the number of fitting parameters or increasing it. Namely, even if the number of CCS points is reduced to 4 (poor fitting) or increased to 8 (over fitting), the ill-posedness is not erased.

Regularization of LSM is applied. First, it is regularized so that the summation of the squares of each flux values on CCS (Fig. 5). The ill-posedness disappears for relative epsilon (with respect to diagonal element of coefficient matrix in the normal equation) larger than 0.005. Second, it is regularized so that the summation of the square of difference between adjacent flux values on the CCS (Fig. 6). The ill-posedness disappears for relative epsilon larger than 0.002. When the above mentioned Tikhonov regularization is applied to the LSM, it is a problem, how to select Tikhonov matrix and how to determine the regularization parameter.

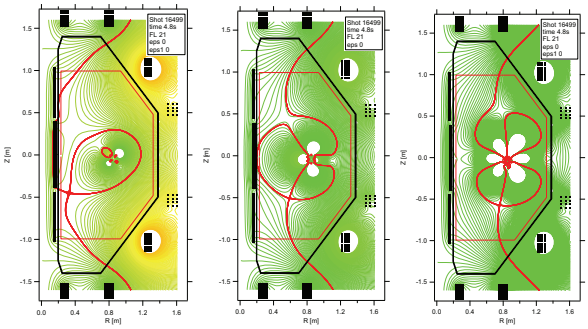

Figure 4: Ill-posedness for various number of CCS points (4, 6 and 8). Poor fitting for 4 (left) and over fitting for 8 (right).

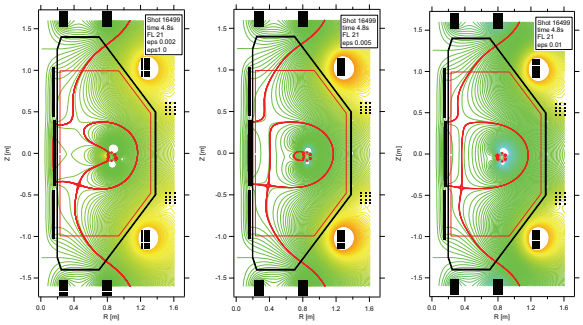

Figure 5: LSM is regularized so that the summation of the squares of each flux values on CCS. The ill-posedness disappears for relative epsilon larger than 0.005 (center).

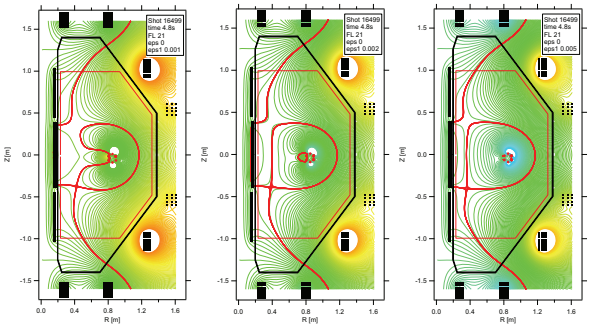

Figure 6: LSM is regularized so that the summation of the squares of difference between adjacent flux values on the CCS. The ill-posedness disappears for relative epsilon larger than 0.002.

4.2 Singular Value Decomposition

Singular values of coefficient matrix in the observation equation are shown in Fig. 7. The 0th SV (Singular Value) is much larger than the other singular values. Cumulative contribution ratio of the 0th SV is over 95 %, where it is defined by the following equation.

$$\sigma_0^2 / \left(\sigma_0^2 + \sigma_1^2 + \ldots + \sigma_5^2\right)$$

Normalized singular vectors are shown in Fig. 8. The 0th, 2nd and 4th singular vectors are even with respect to the equatorial plane.

Regularization of SVD is applied. First, truncation of small SV's is adopted. Reconstruction results are shown for various *N*sv (Fig. 9). Here the *N*sv is defined as the number of largest singular values. The ill-posedness disappears for *N*sv smaller than 3.

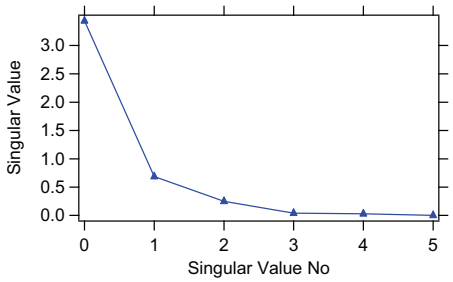

Figure 7: Singular values of coefficient matrix in the observation equation. The 0th singular value is much larger than the other singular values.

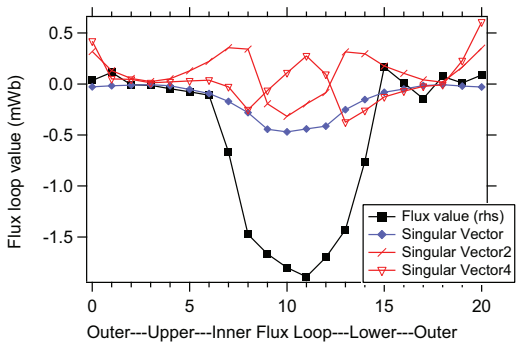

Figure 8: Normalized singular vectors. The 0th, 2nd and 4th singular vectors are even with respect to the equatorial plane.

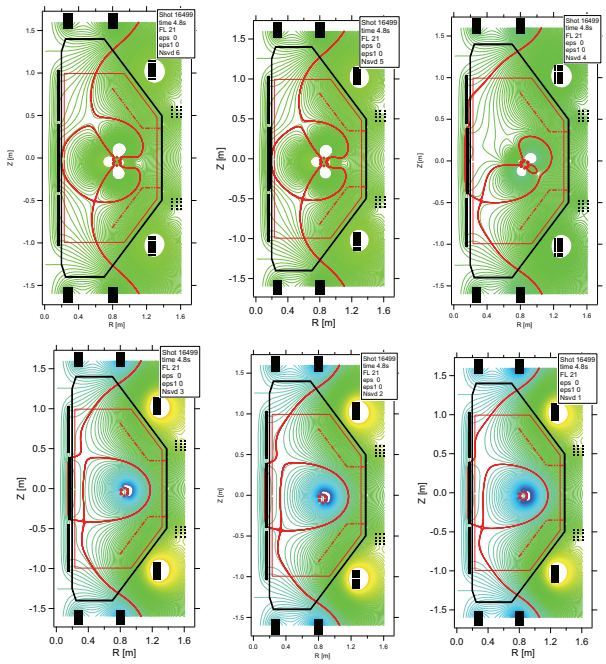

Figure 9: Reconstruction results for various *N*sv. Truncation of small SV's is adopted. The ill-posedness disappears for *N*sv smaller than 3 (lower left).

4.3 Generalized Cross Validation

In GCV (Generalized Cross Validation), we estimate the error by leaving one out and fitting. And we minimize the weighted average of the squared error with respect to regularization parameter λ.

$$GCV = \frac{1}{n}\sum_{\alpha=1}^{n} w_\alpha \left(b_\alpha - A^{(-\alpha)} x_\alpha\right)^2 = \frac{\sum\left(\frac{\lambda^2}{\sigma^2+\lambda^2}c\right)^2 + \|\Delta b\|^2}{\left(\sum\frac{\lambda^2}{\sigma^2+\lambda^2} + (n-m)\right)^2}$$

$$Ax = b, \quad A = U\Sigma V^T, \quad \Delta b = b - UU^T b, \quad c = U^T b$$

Optimal Criterion Function for the GCV is shown in Fig. 10. From the minimum of the values at discrete

points, it is concluded that optimum number *N*sv is 2 (SV0 and SV1). This conclusion does not contradict with the above results in the previous subsection.

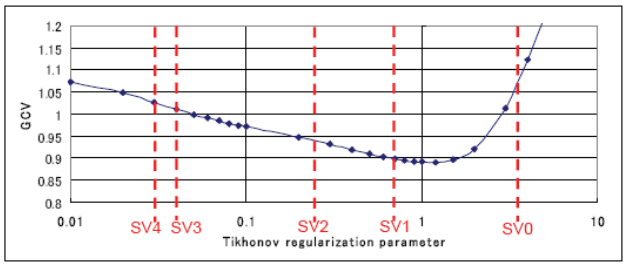

Figure 10: Optimal criterion function for generalized cross validation.

4.4 Filtering of small SV's

Second, filtering of small SV's is adopted (Fig. 11). When the regularization parameter is set to the minimum value of 1, the largest SV0 (100 %) and the second SV1 (30 %) are included, and smaller SV's are filtered out to lower than 10 %. The reconstruction results for various regularization parameters are shown in Fig. 12. The ill-posedness disappears when the regularization parameter is larger than 0.1, which does not contradict with the results in subsection 4.2.

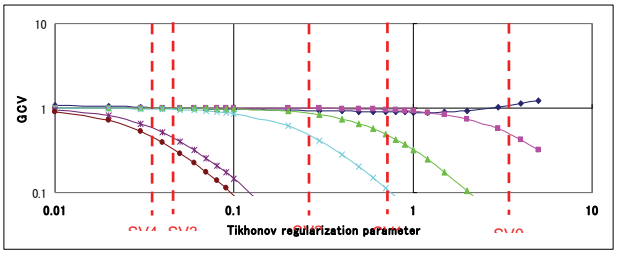

Figure 11: Wiener filter functions and optimal criterion function for generalized cross validation.

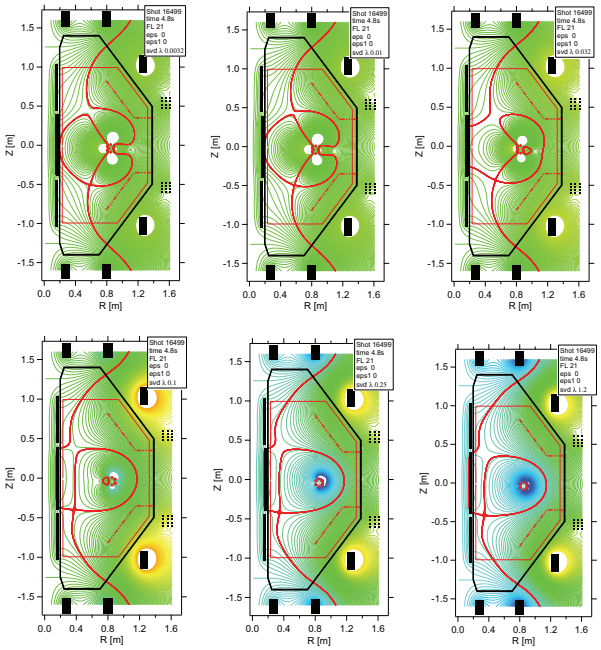

Figure 12: Reconstruction results for various regularization parameters. Filtering of small SV's is adopted. The ill-posedness disappears for the regularization parameter larger than 0.1 (lower left).

5. Summary

Plasma equilibrium solution was fitted assuming all plasma current is flowing in the inside of the LCFS. It was solved within the isotropic pressure profile by EFIT code. Opposite-polarity current density region appeared in the high-field region (negative n-index). The elongation ratio of the LCFS (separatrix) is about unity and the aspect ratio is lower than two. The elongation ratio of the same-polarity region is about 1.4 though the aspect ratio becomes larger than two.

Plasma shape was reproduced by CCS method assuming all plasma current is flowing in the inside of the LCFS. The ill posedness could not be prevented by reducing the number of fitting parameters. It is

reproduced preventing ill-posedness by Tikhonov regularization. When Tikhonov regularization is applied to LSM, it is a problem, how to select the Tikhonov matrix and how to determine the regularization parameter. When the Tikhonov regularization is applied to SVD method, the regularization parameter may be determined according to the optimal criterion function for GCV.

In preparation for high-temperature wall in QUEST in near future, we'd like to shift inward the current density by shifting inward the region with positive n-index. We'd like to increase the elongation ratio. Such a divertor plasma configuration may be produced using only inner divertor coil (PF35-1).

Concerning high-precision CCS method, CCS method can reproduce even for anisotropic pressure profile. Introducing magnetic probes including partial Rogowski may increase the precision further.

After the magnetic probes are installed in addition to flux loops inside the vacuum chamber, CCS can be set also on the measuring (magnetic sensor) surface. Vacuum vessel and the outer space are also outside of the CCS. Boundary integral equation is applied also on this CCS. Eddy current and PFC do not have to be considered in this case, since they are located in the outside of the CCS. And the plasma current effect in the open magnetic surfaces outside of the closed magnetic surfaces can be considered in the RF-driven steady-state plasma.

Acknowledgements

This work was partly supported by the JSPS-NRF-NSFC A3 Foresight Program in the field of Plasma Physics (NSFC No.11261140328), was partly supported by JSPS A3 Foresight Program "Innovative Tokamak Plasma Startup and Current Drive in Spherical Torus", and was performed partly with the support and under the auspices of the NIFS Collaboration Research program (NIFS11KUTR066).

References

[1] K. Nakamura, X.L. Liu, O. Mitarai, K. Kurihara, Y. Kawamata, M. Sueoka, M. Hasegawa, K. Tokunaga, H. Zushi, K. Hanada, A. Fujisawa, H. Idei, Y. Nagashima, S. Kawasaki, H. Nakashima, A. Higashijima and K. Araki. Reconstruction Method of the MHD Equilibrium Taking Eddy Current Effects into Account. 2012 Joint Meeting of US-Japan MHD Workshop and ITPA MHD Stability / Energetic Topical Group, NIFS, March 5-9, 2012.

[2] K. Kurihara. A New Shape Reproduction Method Based on the Cauchy-Condition Surface for Real-Time Tokamak Reactor Control. Fusion Eng. Design, **51-52**, 1049-1057, (2000).

[3] M. Ishiguro, K. Hanada, H.Q. Liu, H. Zushi, K. Nakamura, A. Fujisawa, H. Idei, Y. Nagashima, M. Hasegawa, S. Tashima, Y. Takase, Y. Kishimoto, O. Mitarai, S. Kawasaki, H. Nakashima, and A. Higashijima. Non-Inductive Current Start-Up Assisted by Energetic Electrons

in Q-shu University Experiment with Steady-State Spherical Tokamak. Physics of Plasmas, **19**, 062508-1 to 062508-11, (2012).

[4] T. Maekawa, T. Yoshinaga, M. Uchida, F. Watanabe and H. Tanaka. Open Field Equilibrium Current and Cross-Field Passing Electrons as an Initiator of a Closed Flux Surface in EC-Heated Toroidal Plasmas. Nuclear Fusion, **52**, 083008 (19pp), (2012).

[5] K. Nakamura, Y. Jiang, X.L. Liu, O. Mitarai, K. Kurihara, Y. Kawamata, M. Sueoka, M. Hasegawa, K. Tokunaga, H. Zushi, K. Hanada, A. Fujisawa, M. Sakamoto, H. Idei, S. Kawasaki, H. Nakashima, A. Higashijima, K. Araki. Eddy Current-Adjusted Plasma Shape Reconstruction by Cauchy Condition Surface Method on QUEST. Fusion Eng. Design, **86**, 1080-1084, (2011).

[6] A. Ejiri, Y. Takase, T. Oosako, T. Yamaguchi, Y. Adachi, O. Watanabe, Y. Nagashima, B.I. An, H. Kobayashi, H. Kurashina, H. Hayashi, H. Matsuzawa, K. Yamada, H. Tojo, T. Masuda, M. Sasaki, R. Kumazawa, H. Kasahara and F. Shimpo. Non-Inductive Plasma Current Start-up by EC and RF Power in the TST-2 Spherical Tokamak. Nucl. Fusion, 49, 065010 (12pp), (2009).

Recent LHCD experiments in EAST

B J Ding, EAST Team and Collaboration Team

Institute of Plasma Physics, Chinese Academy of Sciences, Hefei, 230031, China

Abstract: LHCD system of 2.45 GHz in EAST has been updated to 4MW in last campaign. Aimed at high confinement (H-mode) plasma in EAST, the LHW-plasma coupling and current drive experiments were continued. Experiments of local gas puffing near LHW antenna shows that gas puffing from electron side is better to improve LHW-plasma coupling than that from ion side. LHCD experiments at high density are also performed, demonstrating that the decrease of current efficiency at high density may be related to the parametric decay instability (PDI) effect. Lithiation and local gas puffing near LHW antenna are utilized so as to sustain H-mode plasma. H-mode plasma is obtained by LHCD with a wide range of parameters: Ip=0.4~0.8MA, B_t=1.35~1.81T, n_e=1.5~2.5x10^{19} m^{-3}, P_{LHW}>=0.5MW. LHW power deposition and driven current profile with C3PO/LUKE are calculated with the experimental parameters, showing that central and large driven current seems not a necessary condition for the H-mode plasma. H-mode is reproduced with CRONOS. Long pulse plasmas, >400s L mode fully driven by LHCD and >30s H-mode with LHCD and ICRF, have been achieved and demonstrated in EAST.

Key words: coupling, LHCD, PDI, H-mode

1. Introduction

Lower hybrid current drive (LHCD) [1–3] plays a key role in controlling current profile in tokamak experiments aimed at achieving important goals relevant to fusion plasma. Good lower hybrid wave (LHW)-plasma coupling is the first necessary condition for LHCD experiment and high current drive (CD) efficiency is important for driving plasma current and controlling current profile, especially for sustaining long pulse high confinement (H-mode). Aimed at H-mode plasma in EAST, LHW-plasma coupling and current drive experiments were continued, especially, local gas puffing from electron (GIM_e) and ion side (GIM_i) of LHW antenna and high density experiments with LHCD.

Reactor relevant steady state regimes have faced lower hybrid (LH) with the challenge of effectively penetrating the main plasma without excessive power dissipation in the relatively high density plasma edge. The efficiency of LHCD is predicted to scale with the inverse of the electron density [4]. However, LHCD experiments on many tokamaks [5–8] have observed a decrease in non-thermal tails and a drop in bremsstrahlung emission much steeper than $1/n_e$ at high density, which is stronger than expected based on current models. Some possible mechanisms, individually or simultaneously, have been identified to preclude the penetration of lower hybrid (LH) waves,

dissipating the power in the plasma periphery and degrade LH efficiency: Collisional Absorption (CA) [9], Parametric Decay Instabilities (PDI) [10], Scattering from Density Fluctuations (SDF) [11], and so on.

H-mode has been obtained by means of heating and current drive, including neutral beam injection (NBI), ion cyclotron resonance heating (ICRH), electron cyclotron resonance heating (ECRH) and LHCD [12-15]. Among of them, the mechanism of H-mode generated by LHCD is not clear yet and the related study is not enough compared to others.

Since high density is an inevitable issue in further LHCD, in order to pursue the high performance in EAST, it is necessary to further investigate LHW-plasma coupling, LHCD experiments at high density, and H-mode experiments with LHCD, so as to further understand the physical mechanism.

2. Experimental set-up

EAST is a first full superconducting tokamak with an advanced configuration in the world [16-20]. The superconducting coils can create and maintain a toroidal magnetic field, B_t, of up to 3.5 T in steady state [20]. In EAST, a LHW is launched into the tokamak plasma by a multi-junction grill [21] type of antenna with 5 modules arranged by 5 rows in the poloidal direction.

In order to improve LHW-plasma coupling, two gas pipes covering the total grill in the poloidal direction are installed near the LHW antenna in EAST. One is in the electron side (GIM_e), and the other is in the ion side (GIM_i). The toroidal angle between antenna and pipe is about 33 degree. The layout of top view is shown in Fig .1, in which the positions in radial direction are also shown. The major radius of the pipe location is about 2400mm.

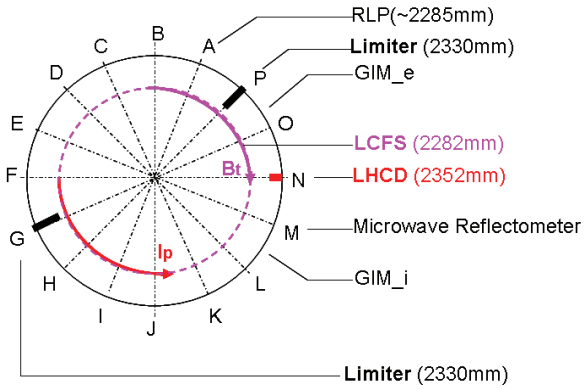

Fig.1 Top view of local gas puffing

3. LHW-plasma coupling experiments

A typical waveform of multi-L-H transitions without local gas puffing is shown in Fig.2. The H-mode phase is characterized by a low D_a with ELM free accompanying high radiation (Prad). It is seen that plasma-wave coupling deteriorates as the transition of L-H occurs, due to the steep gradient density profile in H-mode. The density is then recovered slowly until the H-L transition occurs. This can be seen from the measured density profile in SOL shown in Fig. 3 during L and H mode plasma in another similar discharge. The plasma radiation has a correspondingly periodic characteristic behavior during L-H and H-L transition. Such changes of radiated power and coupled LHW power may lead to the multiple L-H-L transitions, suggesting that the net power for H-mode plasma is marginal. Therefore, it is necessary to reduce

impurity radiation and improve LHW-plasma coupling to sustain H-mode plasma, eg., by means of lithium coating and local gas puffing.

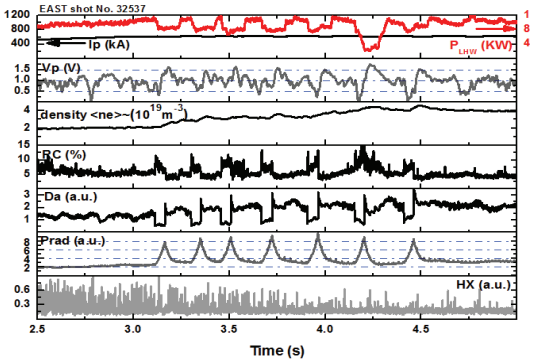

Fig. 2 Typical L-H-L waveform

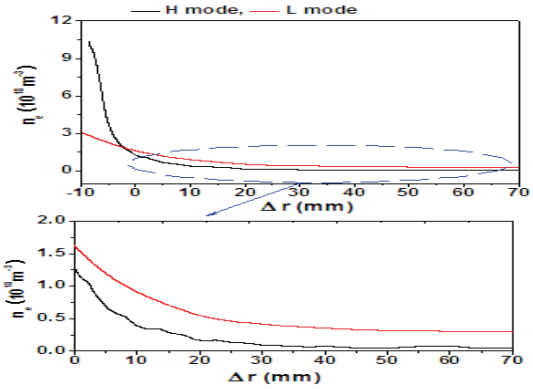

Fig.3 Density profile in SOL

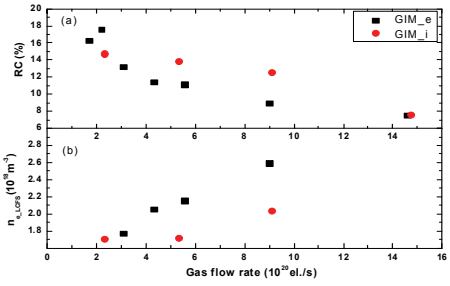

Fig.4 RC and ne_LCFS vs gas flow rate

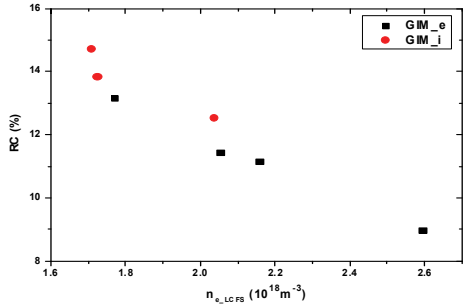

Fig.5 RC vs ne_LCFS first performed in EAST.

In order to investigate the effect of gas puffing LHW-plasma coupling, experiments of gas puffing from electron-side and ion-side on LHW-plasma are the plasma and LHW parameters are Ip = 400kA, Bt= 2T, and the launched spectrum of $N_{//}^{peak}$=2.1. It is performed with varying gas flow rate by investigating reflection coefficients and density measured by reciprocating probes. The electron density at the last closed flux surface (LCFS) and the RCs with different gas flow rate are plotted in Fig. 4 (a) and (b). It is shown that the density is higher and the RC is lower in the case of gas puffing from GIM_e, meaning that it is more efficient to improve density with GIM_e puffing. Further comparison (see Fig. 5) shows that for a same density at the LCFS, the RC in the case of GIM_e puffing is a little smaller than that in the case of GIM_i puffing, implying a higher density at the grill mouth when gas puffing from electron-side. This could be explained by the different movement direction of the electron after ionization. When puffing from GIM_e, the ionized electron moves toward to LHW antenna, whereas the one moves away from antenna when puffing from GIM_i. The electron moving to antenna will be useful to increase the grill density compared to the opposite direction, since the later is not magnetically connected to the grill due to some first components (e.g., limiter). Therefore, the density at the grill will be different even if with a same density at the LCFS, hence, leading to different RC.

4. High density experiments with LHCD

In order to improve CD efficiency at high density, experiments were performed by increasing density in one discharge with different operation conditions, i.e., poor and strong lithiation, density feedback with gas puffing and supersonic molecular beam injection (SMBI). For comparison, the launched LHW spectrum is $N_{//}^{peak}$ =2.1, the configuration is fixed double configuration, and local gas puffing from GIM_e is utilized in the experiments. The effect of driven current is estimated by the count of hard X-ray rate (60keV~200keV) normalized by the injected LHW power, which is proportional to current driven efficiency. The relationship between normalized bremsstrahlung emission and line averaged density (n_e) is shown in Fig. 6, indicating that with strong lithiation, the effect of current drive is much better than that poor one in the case of gas puffing. It is seen that in the strong lithized discharge, there is no sudden decrease of driven current, which deviates from the curve of $1/n_e$, until density up to $3.0\times10^{19}m^{-3}$, which is much larger the value of $2.0\times10^{19}m^{-3}$ in the poor lithiation. This is consistent with the previous studies [10] that lithium coating is beneficial to increase CD efficiency at high density, due to the low cycling and high temperature in the lithium condition. It is also seen that for a similar lithiation, the current drive effect with SMBI is worse than that with gas puffing. The reason for this is not clear. The possible reason for this is the SDF due to the larger density fluctuation with the SMBI experiments in the edge region (Fig. 7). In addition, in the SMBI case, a relative high neutral deuterium radiation is observed. This may result in high density in the edge (Fig.8), leading to the low CD effect possibly due to PDI or CA.

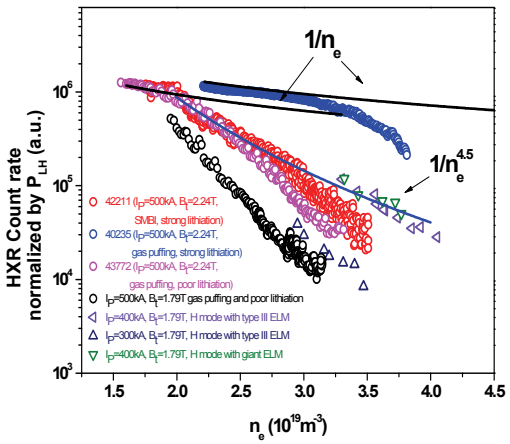

Fig.6 HXR vs density

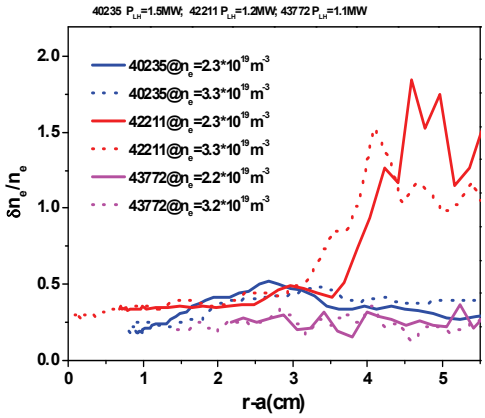

Fig.7Density fluctuation in SOL

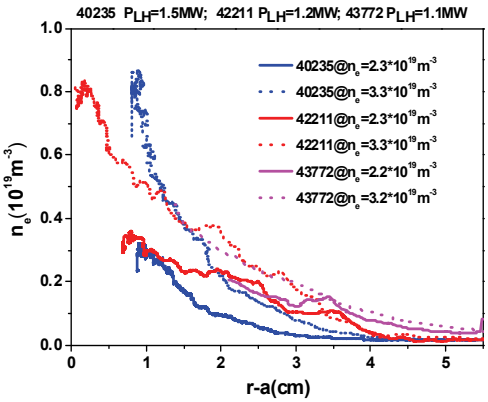

Fig.8 Density profile in SOL

Wave accessibility and PDI [22,23] have been suggested as possible explanations for the density limits observed on previous LHCD experiments. Since the same magnetic toroidal field and the LHW spectrum are fixed in the experiments, the discrepancy in sharp decay of bremsstrahlung emission is not due to wave accessibility. In addition, the dependences of CD effect on density are nearly consistent with the frequency of ion-cyclotron (IC) sideband (Fig. 9), measured by a RF loop antenna located outside the machine, implying the sharp decay of HXR counts is correlated with PDI [10].

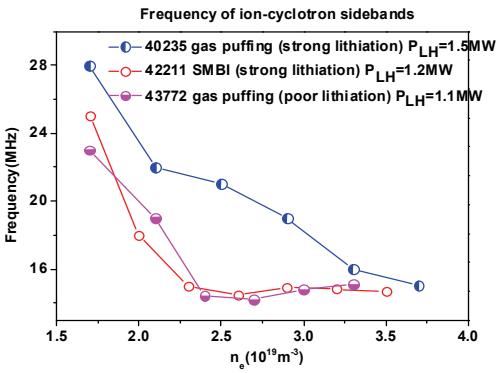

Fig.9 Frequency of IC sidebands

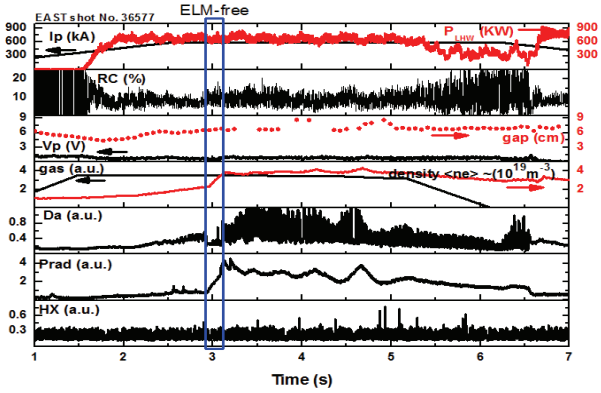

Fig.10 H-mode with gas puffing

Comparing the experimental data for different current and magnetic field, experiments also show that CD effect is better in higher plasma current or higher toroidal magnetic field, being in agreement with studies in Tore-Supra [24]. This is because high plasma current is favorable to increase temperature, hence improving CD efficiency. The effect of magnetic field on efficiency is mainly ascribed to wave accessibility condition. By further comparing the counts in L- and H-mode, it is seen that CD efficiency in H-mode is larger than that in L-mode for a same density. This means that efficiency at high density could be improved in H-mode plasma. As studied in FTU [7], this is mainly due to high temperature near edge region in H-mode associated with lithiation.

5. Investigation of H-mode experiments

Based on the above experiments, H-mode plasmas in EAST have been obtained by LHCD by means of using lithium coating and gas-puffing near LHW antenna in a wide range of parameters: Ip=0.4~0.8MA, B_t=1.35~1.81T, n_e=1.5~2.5x10^{19} m^{-3}, P_{LHW}>=0.5MW. An example of H-mode plasma sustained by LHCD alone is shown in Fig.10. Comparing L mode and ELM-free H-mode phases in Figs. 2 and 10, it is seen that there is no obvious change in RC(8%→10%) when L-H transition occurs in Fig. 10. The coupling deteriorates after switching off the gas puffing, thus leading to H-L transition. The strong variation of RC in H-mode can be explained by the ELMs, whereas the reason for variations in L-mode is not clear, possible due to density fluctuations. Unfortunately, no measurement is available in this discharge. Also, the radiation in Fig. 10 is much smaller than that in Fig. 2.

This indicates that lithiation and local gas puffing are effective to reduce radiation and improve LHW-plasma coupling, so as to obtain repeatable H-mode plasma.

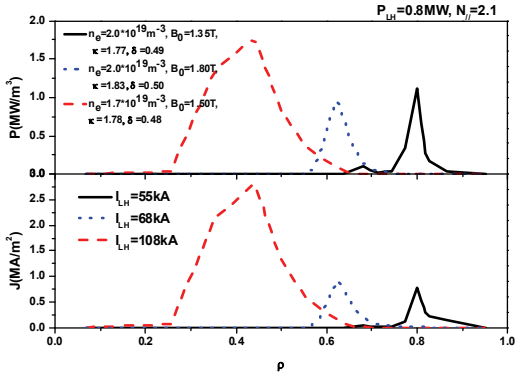

Fig.11 Simulation with C3PO/LUKE

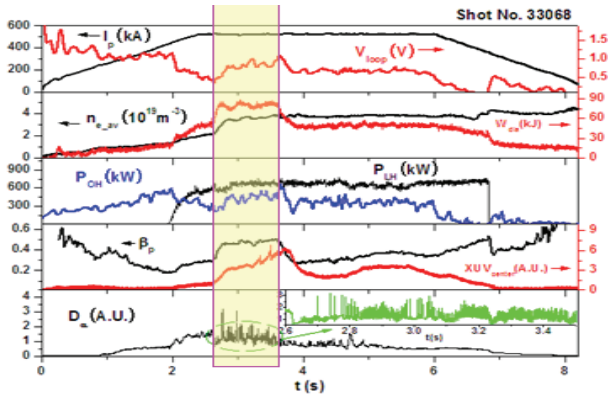

Fig.12 Typical H-mode waveform

Next, we would like to investigate dependence of H-mode on power deposition and driven current profile, which is calculated with a ray tracing and Fokker-Planck code of C3PO/LUKE [24]. Since magnetic field, plasma density and plasma configurations play important roles in determining LHW power deposition and current profile, three cases (1.n_e=2.0×10^{19}m^{-3}, B_t=1.35T, κ =1.77, δ =0.49; 2. n_e=2.0×10^{19}m^{-3}, B_0=1.8T, κ =1.83, δ =0.5; 3. n_e=1.7×10^{19}m^{-3}, B_t=1.5T, κ =1.78, δ =0.48) before L-H transition are selected from experiments for the calculation, where κ is the elongation and is δ the triangularity. Calculation results (Fig. 11) show the well known high dependency of the LH current drive calculations on plasma parameters(n_e, B_t, κ,δ) in the weak damping regime. The normalized peak power deposition ρ varies from 0.45 to 0.8, leading to different driven current profiles and total driven current, suggesting that L-H transition seems not so sensitive on current profile.

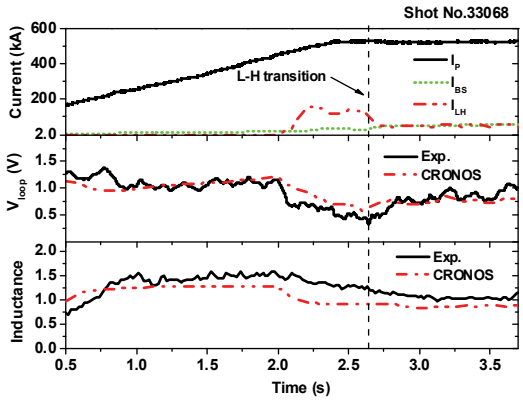

Fig.13 Simulations with CRONOS

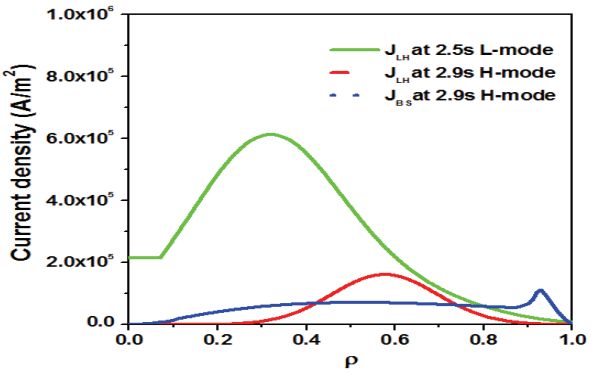

Fig.14 Simulation with CRONOS and LUKE

A typical H-mode discharge, characterized by the decrease of deuterium emission and ELM generation, and pedestal formation for the temperature and density profiles, is shown in Fig. 12. After L-H transition, plasma density increases quickly and stored energy is

up to 85kJ. The electron temperature decreases during the H phase, due to increasing density, leading to a little increase in loop voltage. Such change in loop voltage may be explained by the decrease of LH driven current due to decreasing Te and wave accessibility condition at high density during the H-mode phase. This can be also seen from I_{LH} (100kA in L and 50kA in H phase) (Fig. 13) and driven current profile (Fig. 14) predicted by the LUKE/C3PO and CRONOS [25,26], from which H-mode is reproduced with the initial equilibrium from EFIT and density from experiments. It is seen that Vp and inductance are qualitatively consistent between experiment and CRONOS (Fig.13). Though CRONOS results are preliminary, it offers an effective tool to investigate the experiment.

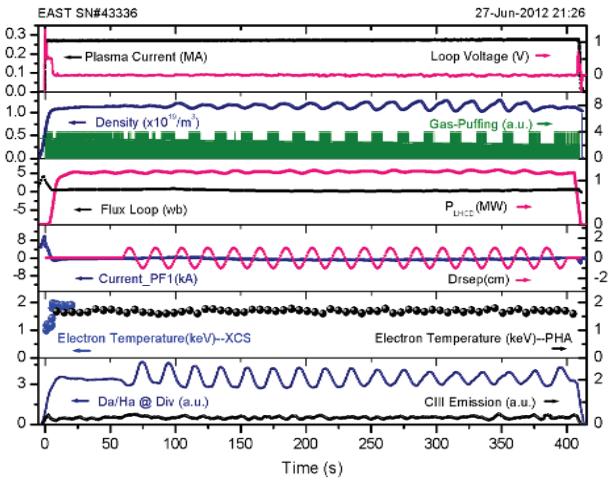

Fig.15 Long pulse over 400s in EAST

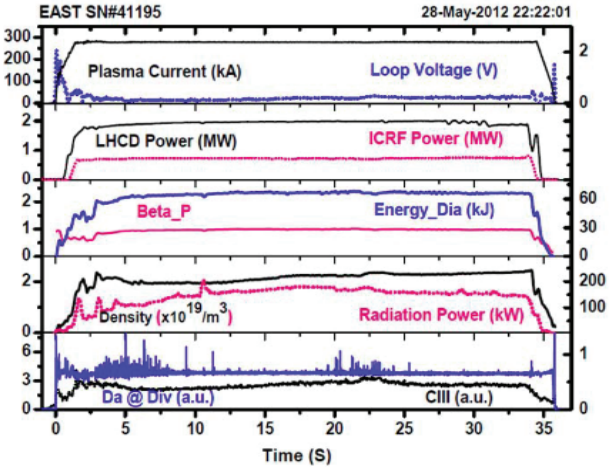

Fig.16 Long H-mode discharge (32s)

6. Demonstration of high performance, long pulse operation [27,28]

Long pulse plasma fully drive by LHW over 400s has been achieved in EAST (see Fig. 15) by carefully controlling heat exhaust and neutral recycling. Considering the present steady-state power handling capability (2MW/m^2), plasma configuration was varied from USN via DN to LSN during the discharge with sweeping strike point, thus minimizing divertor heat load, impurity influxex and plasma wall interaction. Plasma shape was real-time controlled so as to keep effective LHW coupling. LHW power is feedback controlled by flux. For a safe operation, all PF coil currents keep at a minimum level (<2kA), well below the critical current limit (14.5kA).

H-mode has now been extended with combination of LHCD and ICRH in EAST. Fig. 16 shows a typical long pulse H-mode (32s) discharge under the DN divertor configuration with the following parameters: Bt~1.9T, Ip=0.28MA, ne~2.2×10^{19}m^{-3}, q_{95}~6.8, triangularity δ ~ 0.48 and elongation κ ~ 1.7. It is dominated by small ELMS, with $H_{98,y2}$ ~0.8±0.1 and total injection of ~ 2.5MW. LHW and ICRF were applied during current ramp phase to reduce loop voltage and L-H transition occurred during the current flattop, accompanied with dithering phase. The plasma density and total radiation power in H-mode were

comparable to that in L-mode, suggesting possible high particle transport, especially no impurity accumulation in core plasma, which is beneficial for the sustainment of the long pulse H-mode.

7. Conclusion

Effect of local gas puffing from GIM_e and GIM_i of LHW antenna on LHW-plasma coupling is firstly investigated in EAST. Experimental results show that gas puffing from GIM_e is more favorable to improve coupling. Due to decreased coupled power together with the increasing radiation power in H-mode, H-L transition occurs. High density experiments with LHCD show that strong lithiation is useful for improve the density limit for LHCD. Studies indicate that the sharp decrease of current drive efficiency is correlated with PDI.

Using lithum coating and gas puffing from GIM_e of LHW antenna, H-mode plasma is obtained by LHCD in a wide range of parameters: Ip=0.4~0.8MA, B_t=1.35~1.81T, n_e=1.5~2.5x10^{19} m^{-3}, P_{LHW}>=0.5MW. Simulation shows that central and large driven current seems not a necessary condition for H-mode plasma. H-mode is reproduced by CRONOS, suggesting it can offer a tool to explain experiments. Long pulse plasmas (>400s L mode and >30s H-mode) have been achieved.

Acknowledgements: This work is supported by the National Magnetic Confinement Fusion Science Program of China (Grant No 2010GB105000), the National Natural Science Foundation of China under Grant No. 11175206, 10875149 and 10928509.

References:

[1] Fisch N.J. 1978 *Phys. Rev. Lett.* **41** 873.

[2] Bernabei S. *et al* 1982 *Phys. Rev. Lett.* **49** 1255.

[3] Fisch N.J. 1987 *Rev. Mod. Phys.* **59** 175.

[4]N. J. Fisch and A. H. Boozer 1980 *Phys. Rev. Lett.* **45** 720.

[5]Pericoli-Ridolfini V., et al 1994 *Nucl. Fusion* **34** 469.

[6]Cesario R., *et al* 2011 *Plasma Phys. Control. Fusion* **53** 085011.

[7]Cedario R., et al 2010 *Nature Commun.* http://dx.doi.org/10.1038/ncomms1052

[8]Wallace, G.M., *et al* 2010 *Phys. Plasmas* **17** 082508.

[9]Bonoli P.T., and Englade, R.C. 1986 *Phys. Fluids* **29** 2937.

[10] Liu C.S., and TRIPATHI, V.K. 1986 Phys. Rep. 130 143.

[11] Peysson Y., Decker J., Morini L., et al 2011 *Plasma Phys. Contr. Fusion* **53** 124028.

[12] Wagner F. *et al* 1982 *Phys. Rev. Lett.* **49** 1408.

[13]Steinmetz K. *et al* 1987 *Phys. Rev. Lett.* **58** 124.

[14] Lohr J.M., *et al* 1988 *Phys. Rev. Lett.* **60** 2630.

[15] Tsuji S., *et al* 1990 *Phys. Rev. Lett.* **64** 1023.

[16] Wan Y.X. *et al* 2000 *Nucl. Fusion* **40** 1057.

[17] Weng P.D. *et al* 2005 *Fusion Eng. Des.* **75–79** 143.

[18] Fu P. *et al* 2006 *Nucl. Fusion* **46** S85.

[19] Liu X.N. *et al* 2006 *Nucl. Fusion* **46** S90.

[20] Wan Y.X. *et al* 2006 *Plasma Sci. Technol.* **8** 253.

[21] Brambilla M. 1976 *Nucl. Fusion* **16** 47.

[22]Takase Y., Porkolab M., Schuss J. J., *et al* 1985 *Phys. Fluids* **28** 983.

[23] Hooke W. 1984 *Plasma Phys. Contr. Fusion* **26** 133.

[24] Peysson Y. and the Tore Supra Team 2001 *Nucl. Fusion* **41** 1703.

[25]Peysson Y. and Decker J. 2008 *AIP Conf. Proc.* **1069** 176.

[26] Artaud J. F., *et al* 2010, *Nucl. Fusion* **50** 043001.

[27] Wan B N et al, 2012 Fusion energy conference OV/2-5.

[28] Guo H Y et al, 2012 Fusion energy conference EX/P5-15.

Radiated power measurement with AXUV photodiodes in EAST tokamak

DUAN Yanmin, HU liqun, DU Wei, MAO Songtao, CHEN Kaiyun, ZHANG Jizhong

Institute of Plasma Physics, Chinese Academy of Sciences, Hefei 230031, China

Abstract: The fast bolometer diagnostic system for absolute radiated power measurement on EAST tokamak is introduced, which is based on the absolute extreme ultraviolet (AXUV) photodiodes. The relative calibration of AXUV detectors is carried out using X-ray tube and standard luminance source in order to evaluate the sensitivity degradation caused by cumulative radiation damage during experiments. The calibration result shows a 23% sensitivity decrease in the X-ray range for the detector suffering ~27000 discharges, but the sensitivity for the visible light changes little. The radiated power measured by AXUV photodiodes is compared with that measured by resistive bolometer. The total radiated power in main plasma deduced from AXUV detector is lower a factor of 1~4 than that deduced from resistive bolometer. Some typical measurement results are also shown in this article.

Keywords：Radiated power, AXUV photodiodes, relative calibration, ELMy H-mode

PACS: 52.55.Rk, 52.55.Fa, *52.70.Kz,*

1. Introduction

In fusion plasma, part of the input power can be dissipated by radiation [1]. Bolometer diagnostic has been used to determine the total radiated power and the radiation profile in magnetically confined plasma for the study of power balance, particle transport, transient radiative activities, and so on. At present, two types of detectors, metal foil resistive bolometer and absolute extreme ultraviolet（AXUV） photodiodes, are widely utilized for radiated power measurement in many fusion devices [2-5]. The resistive bolometer is a common tool on most tokamaks as it has a fairly linear response to radiation power up to 200nm. But, its low temporal resolution of ~ms is the most restriction. Additionally, it is also sensitive to neutral particles. The AXUV photodiodes based on silicon *p-n* junctions are developed in last decade, which are characterized by a flat spectral sensitivity from vacuum ultraviolet to x-ray energies and a fast response of ~μs .Its compact structure and high time resolution allow them to be used to study fast processes as they are used on DIII-D and Alcator C-Mod for disruption analysis and on TCV for fast radiation dynamics studies [6-8]. The deficiency of the use of AXUV photodiodes as absolute bolometer is that its spectral sensitivity is dependent on photon energy, as shown in Fig.1.The very low sensitivity for photo energy below 30eV will lead to an underestimate of the radiation loss due to the strong line emission of low-charge impurities at plasma edge. Research on Alcator C-mode and LHD have shown that in some operation condition the total radiated power deduced from AXUV photodiodes is

about half of that from the resistive bolometer after excluding the contribution of neutral particles [3,6].

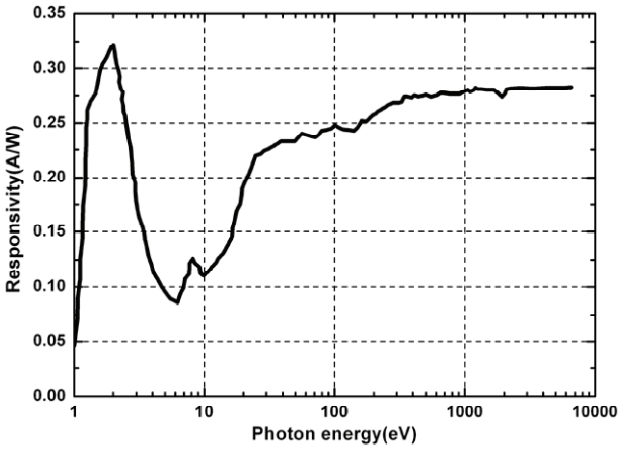

Fig. 1 The responsivity of AXUV photodiodes.

Both the AXUV photodiodes and metal foil resistive bolometer are used for absolute radiated power measurement in EAST (Experimental Advanced Superconducting Tokamak) device [9]. The AXUV photodiodes measurement system and the relative calibration are introduced in the section 2. Some measurement results of AXUV photodiodes are presented and are compared with that of foil resistive bolometer in section 3. A brief summary and upgrade plan for next experimental campaign are given in the final section 4.

2. Experimental setup

2.1 Arrangement of the AXUV arrays

The AXUV photodiodes are the type of AXUV-16ELG linear array produced by IRD Corp. [9]. Five pinhole cameras with total of 80 channels have been successfully developed presently, as shown in Fig.2. Each camera is one 16-channel array with a spatial resolution δr of ~ 3 cm. Four cameras are installed in the horizontal port to fully cover the poloidal cross section .The upper two cameras and the lower two cameras are symmetrical on the equatorial plane. Another vertical camera is installed in the upper port to view the lower divertor through bulk plasma. All the detectors are placed in the vacuum vessel. The current outputs of the detectors are directly led to the outside of the vacuum vessel through feedthrough and then to the amplifiers. The output voltages signals of amplifiers are transmitted to the data acquisition system (DAQ) through long twist cable. The sample frequency of DAQ is 100 kHz.

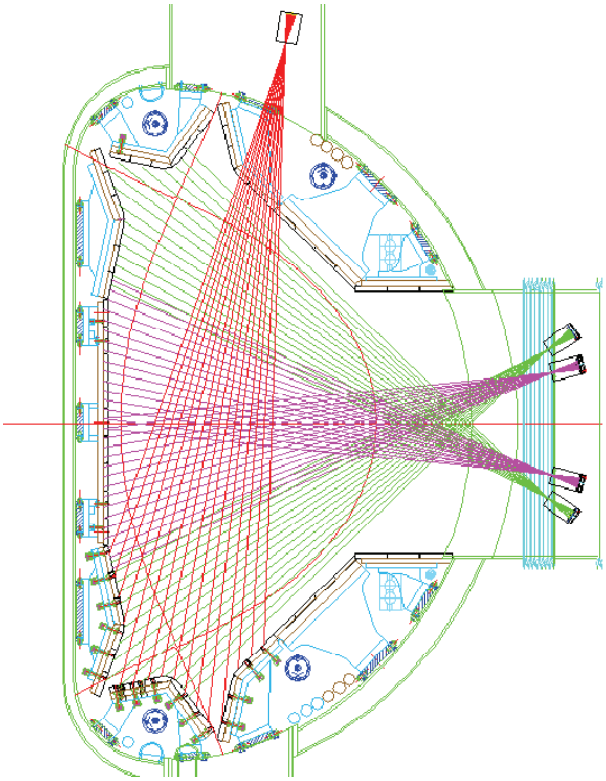

Fig. 2 Geometry of Viewing chords of AXUV arrays installed on EAST

2.2 The relative calibration of AXUV photodiodes

It is found that the sensitive of AXUV photodiodes

have the trend of decrease caused by cumulative radiation exposure during plasmas discharges. Thus, four detectors which have ever been used on EAST and HT-7 are selected and are calibrated relatively. The relative calibrations are carried out by the Mini X-ray tube and standard luminance source separately. The photon energy of the X-ray tube is controlled in the range of 1-10keV. The output light of the standard luminance source is from 380(3.26eV) nm to 780 nm (1.59eV). Fig.3 shows the schematic of calibration. The light source is fixed and the detector can move by adjusting manually the support so that the light can aim at the detector unit one by one. The output current of the detector is amplified and then the output voltage is shown in the oscilloscope. A collimator with 2mm diameter is used for the X-ray tube while not for the standard luminance source. So, a new detector is also tested as reference. The output signals of each detector are normalized to the reference signals. Fig.4 gives the calibration results. It's found that the degree of the sensitive degradation depends on the plasma discharges number for photon energy in X-ray range. The sensitivity of the detector suffering ~27000 EAST discharges decreases about 23% for X-ray and changes little for visible light. However, sensitivity of the detector only suffering ~1000 HT-7 discharges increases on the contrary for visible light. The sensitive surfaces of this detector have a strong mark compared with the new detector which may be caused by bombing of glowing arc. The changes of the sensitivity are related with the front silicon dioxide window [10]. The passivating SiO_2 layer will create surface recombination after receiving large dose of radiation (>Grads) resulting in loss of quantum efficiency and damage of the thin oxide layer probably causes the sensitivity increase for low energy photon.

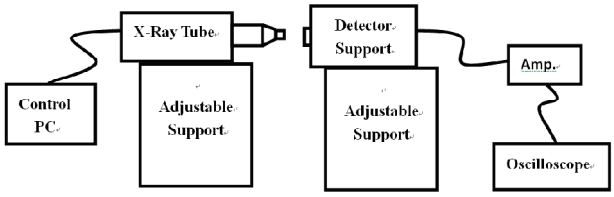

Fig. 3 The relative calibration schematic of AXUV photodiodes

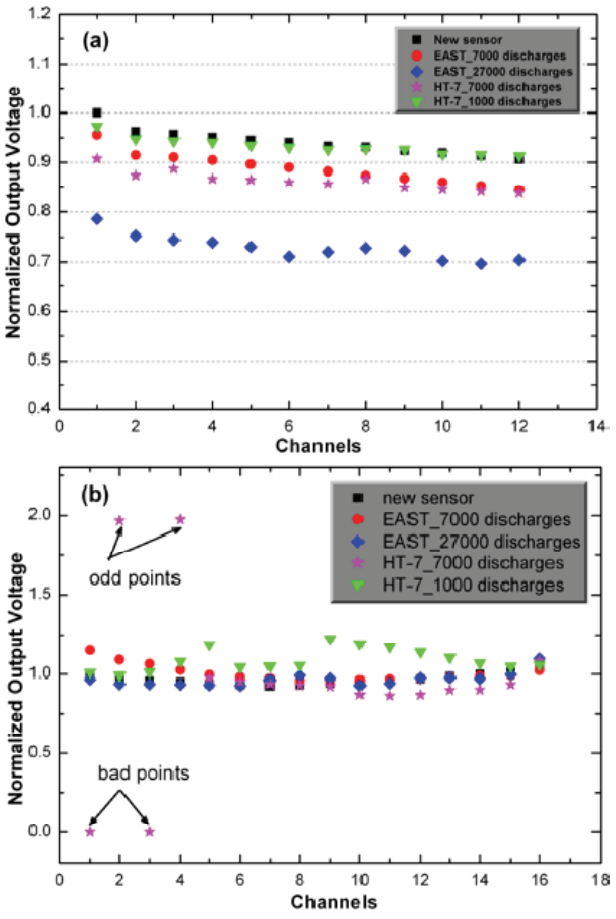

Fig.4 The relative calibration result (a) by Mini X-ray tube; (b) by standard luminance source

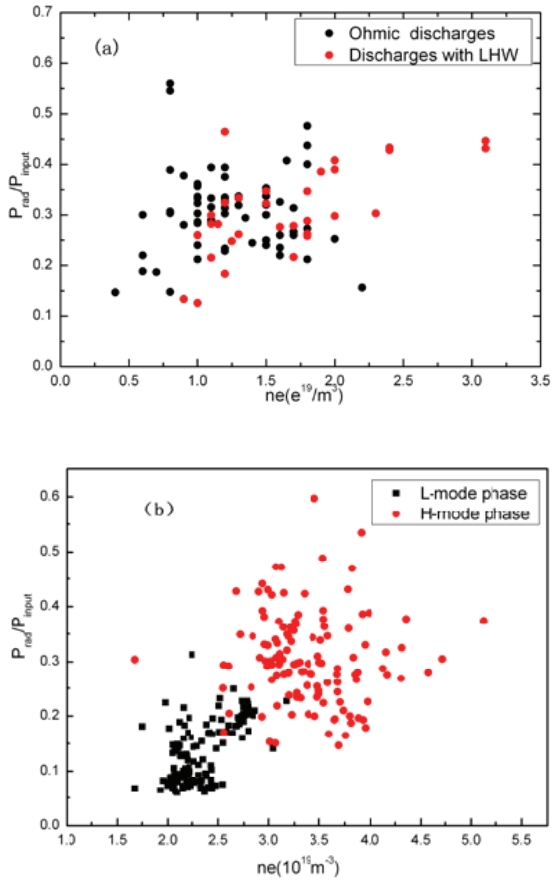

Fig.5 Dependence of the radiated power fraction (P_{rad} to P_{input}) on the line-averaged electron density (a) for L-mode discharges;(b) for H-mode discharges

3. Measurement results

The total radiated power in main plasma can be calculated by integrating the measured chord-integrated signals of the horizontal arrays [11]. Here, a flat spectral response 0.26 A/W is used for AXUV photodiodes when calculating the radiated power. The statistic results of radiated power loss fraction (the ratio of radiated power to input power) in different electron density conditions are shown separately in Fig.5a for L-mode discharges and Fig 5b for H-mode discharges. The radiated power loss fraction is in the range of 10%~60% and no strong dependence on the electron density is found due to data dispersion. The total radiated power deduced from AXUV photodiodes are compared with that deduced from resistive foil bolometer. Generally, the time evolution trend of the radiated power deduced from the two type detectors can agree well, but the absolute value given by AXUV photodiodes is lower a factor of 1~4 than that given by resistive bolometer.

The high temporal resolution of AXUV photodiodes enables it to observe fast plasma process, such as ELM radiation process. An example is given in Fig.6 showing a comparison of the AXUV signal with the foil resistive bolometer signal during ELM. The ELMs can produce modulation in the radiated power signals at the edge plasma. Thus, the radiated energy loss caused by one ELM can be obtained by time integrating the total radiated power. The background intensity need be subtracted during integration. The results show that the radiated energy loss caused by one type-III ELM is lower than 10% of the ELM-induced energy loss.

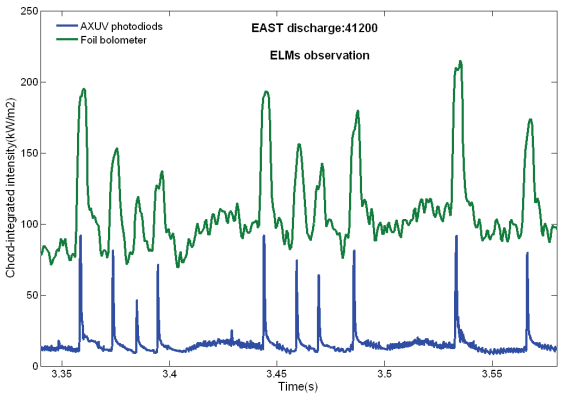

Fig.6 Comparison of the AXUV signal with the foil resistive bolometer signal during ELM

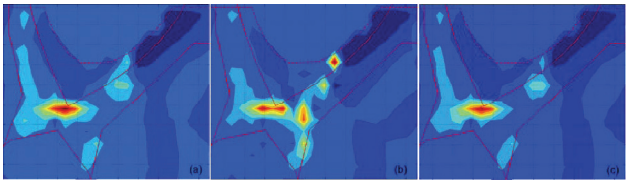

Fig.7 Tomographic reconstruction of radiated power density in the divertor region for EAST discharge #38300. (a) pre-ELM at 3.540 s; (b) during-ELM at 3.545 s; (c) after-ELM at 3.555 s.

The relative changes of radiation distribution during one ELM period can be analyzed by two dimensional tomography reconstructions techniques. The hybrid inversion algorithm is adopted due to the poor coverage of the vertical array at the present time. The whole rectangular poloidal cross section is divided into 20×40 pixels. The divertor region is separated from the main plasma by adopting the similar method used on JT-60U [12]. Analytic method based on Bessel expansion with the symmetrical hypothesis is used for bulk plasma and the finite element method is used for divertor region. Fig.7 presents the radiation patterns in the divertor region at three different time of one ELM cycle. It can be found that the radiation is focused on X point region between ELMs. The radiation region moves toward the targets and the radiation near outer target region shows clear increase during ELMs. The radiation from released particles due to the ELM-wall interaction, such as C impurity, would contribute partly to the increase of the radiated power near the outer target region.

4. Conclusion

The AXUV photodiodes are successfully applied on EAST as fast bolometer. The relative calibrations are carried out in order to evaluate the sensitive degradation of AXUV photodiodes after several experimental campaigns on EAST. About 23% sensitivity decrease is found for the detector exposed to 27000 discharges. The photon energy depended sensitivity of AXUV photodiodes will lead to an underestimate of the radiation loss as absolute bolometer. Compared with resistive bolometer, the total radiated power in main plasma deduced from AXUV detector is lower a factor of 1~4. The fast response time (~ μs) make it possible to study radiated pattern in one ELM cycle. So, the viewing region of vertical array need to be expanded to improve the precision of the tomography reconstructions and one tangential array will be added for next experimental campaign.

Acknowledgments

This work was partly supported by the JSPS-NRF-NSFC A3 Foresight Program in the fieldof Plasma Physics (NSFC No.11261140328)

REFERENCES

[1] E.R. Müller, K.Behringer and H.Niedermeyer, Nucl. Fusion 22, 1651(1982)

[2] R.L.Boivin, J.A.Goetz,E.S.Marmar, J. E. Rice, and J. L. Terry, Rev. Sci.Instrum,70, 260(1999)

[3]B.J.Peterson, A.Yu Kostrioukov, et al., Plasma Phys.

Control. Fusion, 45, 1167(2003)

[4] K..McCormick, A. Huber, C. Ingesson, et al. , Fusion Engineering and Design 74, 679 (2005)

[5]S. Konoshima, A. W. Leonard, T. Ishijima, et al , Plasma Phys. Control. Fusion 43, 959(2001)

[6]M.L. Reinke and I. H. Hutchinson, Rev. Sci.Instrum,79, 10F306(2008)

[7] I. Furno, H. Weisen, J. Mlynar, et al., Rev. Sci.Instrum,70, 4552(1999).

[8] G. Veres , R.A. Pitts , A. Bencze,et al. Journal of Nuclear Materials 390–391, 835(2009).

[9] http://www.ird-inc.com

[10] R. Korde and J. Geist, Applied Optics, 26, 5284-5290(1987).

[11] Y.M.Duan, L.Q.Hu, et al., Plasma Science and Technology, 13,546(2011).

[12] S. Konoshima, A. W. Leonard, et al., Plasma Phys. Control. Fusion 43 (2001) 959.

Introduction to the wide-angle visible observation diagnostic on EAST using catadioptric optics

J H Yang[1] , X F Yang[2], L Q Hu[1], Q Zang[1], X F Han[1], C Q Shao[1], T F Sun[1], H Chen[1], T F Wang[1], F J Li[1], A L Hu[1]

[1] Institute of Plasma Physics，Chinese Academy of Sciences, P.O. Box 1126，Hefei，Anhui 230031，People's Republic of China

[2] Jiangsu Province Key Laboratory of Modern Optical Technology, Soochow University, Suzhou, Jiangsu 215006, People's Republic of China

Author to whom correspondence should be addressed. Electronic mail: yangjh@ipp.ac.cn

Abstract: A new wide-angle endoscope for visible light observation on EAST tokamak has been developed recently. The head part of the optical system is based on a mirror reflection which is borrowed from the ITER-like wide-angle observation diagnostic on JET. However, the design of the optical system has been simplified and improved. As a result, the global transmittance of the system is as high as 79.6% from 380nm to 780nm and the spatial resolution is <5mm for the full depth of field (4000mm). Further, the optical system also owns a large relative aperture (1:2.4) and can be applied in high-speed camera diagnostic. As an important diagnostic, the optical system has been installed on HT-7 in the final experiment campaign and confirmed it can be applied to investigate the transient process in plasma such as ELMy eruption in H-mode on EAST.

Keyword: plasma wall interaction; wide-angle visible observation diagnostic; high speed camera; EAST tokamak

1. INTRODUCTION

Visible camera is an important diagnostic to monitor the plasma position and shape on tokamaks. The visible light observation is also an indispensable diagnostic to monitor the plasma wall/antenna interaction, especially for the process of ELMy eruption in H-mode discharges. A lot of particles and energy can be pushed out from the edge region of the confined plasma in such an event (Ref.1). It is especially serious in ITER where the heat loading is too large to cause the plasma facing component materials erosion or melting (Ref.2).

Kinds of visible imaging systems for plasma devices have been discussed during the last two decades (Ref.2-6). The earlier imaging systems on EAST were mainly composed of two tangential stainless tubes and installed on D window nearby the mid-plane. The diameter of each tube was 200mm. Two industrial cameras were fixed at the end of the tubes separately around the first wall of EAST. An industrial lens was mounted on each camera to image the plasma. The problem was that the cameras had to sustain intensive electromagnetic interference and high level of radiations from energetic particles and x-rays, especially at the moment of the discharge disruption. It often made the cameras broken down, or even

damaged. Further, the limited space of the tube made it impossible to develop a high-speed camera diagnostic on EAST since the body of the camera was too large to install in the tube.

So it is strongly required to transmit the light from the vacuum chamber to the outside on EAST. For this reason a new visible wide-angle optical system has been developed recently. The technology of ITER-like wide-angle observation diagnostic on JET (J-WOD, Ref.2) is mainly adopts and improved for the optical design. Ultimately, the f/# of the system is enhanced from 10 to 2.4. On the other hand, the maximum diameter of the optical tube is as small as 140mm and the global transmittance of the optical system is nearly 80% for the full visible light. The large f/# and high transmittance make it possible to develop a high-speed visible camera system on EAST (section II and III). In fact, in September 2012, the endoscope was successfully installed on HT-7 in order to test the performance of the optical system. The experiment indicated that this endoscope combined with the high-speed camera pco.dimax could meet the needs of studying the ELMy eruption event in H-mode discharges on EAST (section IV). Since the first H-mode was achieved in 2009 on EAST (Ref.7-8), it has become an urgent issue to control the ELMy behavior. This high-speed camera plays an important role to provide timely information for the related physics research.

2. OPTICAL DESIGN

EAST tokamak is the first fully superconducting tokamak with modern divertor configurations in the world (Ref.8-9). It has a major radius of 1.7m and minor radius of 0.4m. The corresponding imaging distance, from the first intersection of the optic axis and the last closed flux surface to the farthest viewing position on the first wall, covers an area from about 1m to 5m with respect to the entrance aperture.

The analysis shows that the optical system should meet a field of view (FOV) of $\pm 25°$ as well as a depth of filed (DOF) of 4m in order to observe the full cross-section of the EAST vacuum chamber. It also should be compact because some other diagnostics will be integrated on EAST in the future. Taking into account the above reasons, the optical principle of the ITER-like wide-angle observation diagnostic on JET (J-WOD, Ref.2) was adopted to design the optical system. In order to make the system more compact, cassegrain telescope at the end of the optical path was abandoned and the stainless steel mirrors (flat mirror and concave aspheric mirror) were replaced with zerodur mirrors, as shown in Fig.1.

The FOV of the optical system is designed as $47°$ in horizontal direction and $50°$ in vertical direction. As a result, the FOV is large enough to image the cross section of the device, including the upper and lower divertors, the inner and outer wall as well as the existing RF antennas.

The principle of the optical system is shown in Fig.1. The light beam firstly hits on a concave ellipsoidal mirror through a small hole which is located in a flat

mirror, as shown in the upper figure of Fig.1. Then the beam is reflected by the flat mirror and transmitted into an about 1300mm stainless tube, in which the light beams will be collimated by a lens made of silica. Through the collimator lens there is a vacuum-sealed glass, as shown in the lower figure of Fig 1. After the vacuum-sealed glass, the light beam is transmitted successively through an achromatic doublet, the replaceable optical filter and neutral optical attenuator, the second achromatic doublet and two single lenses.

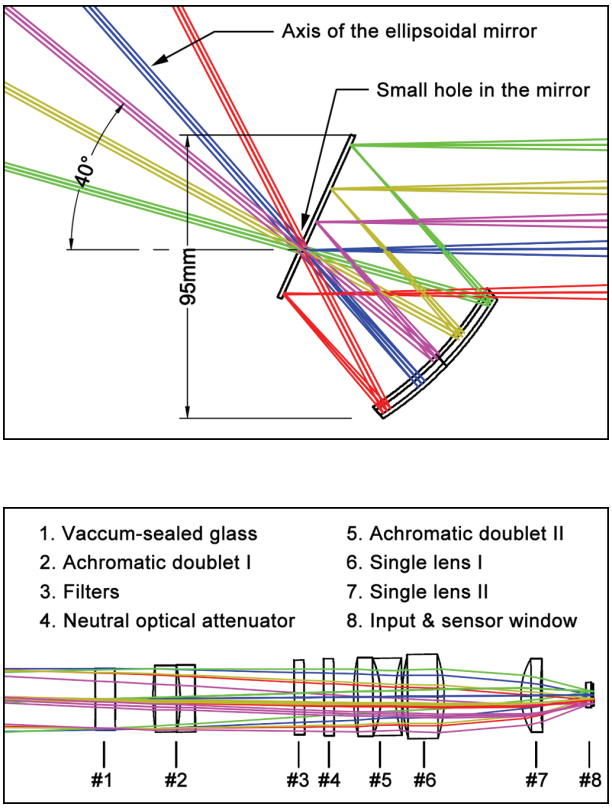

Figure 1 Optical design of the front mirrors is shown in the upper figure and the aberrations correction system is shown in the lower figure.

In order to meet the requirements of transmittance, the last single lens is made of SF4. The filters can be used to observe all kinks of impurities spectral lines, such as MoI, CIII, LiI, etc. The neutral optical attenuator is set in the optical path to prevent the CCD/CMOS from saturation when the emission intensity of plasma is too high.

Comparing with the upper figure in Fig.2, Ref.2, the most difference is that the mirrors (both flat mirror and aspheric mirror) are made of zerodur and coated with aluminum while in J-WOD they are made of stainless steel and coated with gold. Also the primary mirror has a diameter of about 65mm compare with the diameter of 120mm for the condition of J-WOD, which makes the optical system only have a maximum diameter of 140mm at last.

The front mirrors are the key components of the endoscope, which are made of zerodur and coated with aluminum. The zerodur, as its name noted, owns nearly zero thermal expansion for a wide temperature range. The high application temperature of $600°C$ insures the safety of the front mirrors located around the first wall, where the working temperature may reach above $250°C$. In fact the thermal stress analysis shows that the image is nearly not needed to refocus from 0 to $300°C$. The hole in the flat mirror is designed as small as 2.5mm to protect the mirrors from damage by high energy particles and this is especially important for EAST because of lithium coating experiments. Considering the above reasons, the optimized focus is 6mm and the corresponding f/# is 2.4.

The upper figure in Fig.2 shows the designed modulation transition function (MTF) curve. As shown, the MTF of the optical system is higher than 0.4 at 45lp/mm in the wavelength range from 380nm to

780nm and the full FOV. It is good match to the sensor of the pco.dimax whose MTF is 45.5lp/mm in theory. The corresponding spatial resolution is about 10mm for the object located at 5000mm away from the entrance aperture. The spatial resolution is in the order of the width of the filament which presents during the ELMy eruption in H-mode discharge (Ref.9).

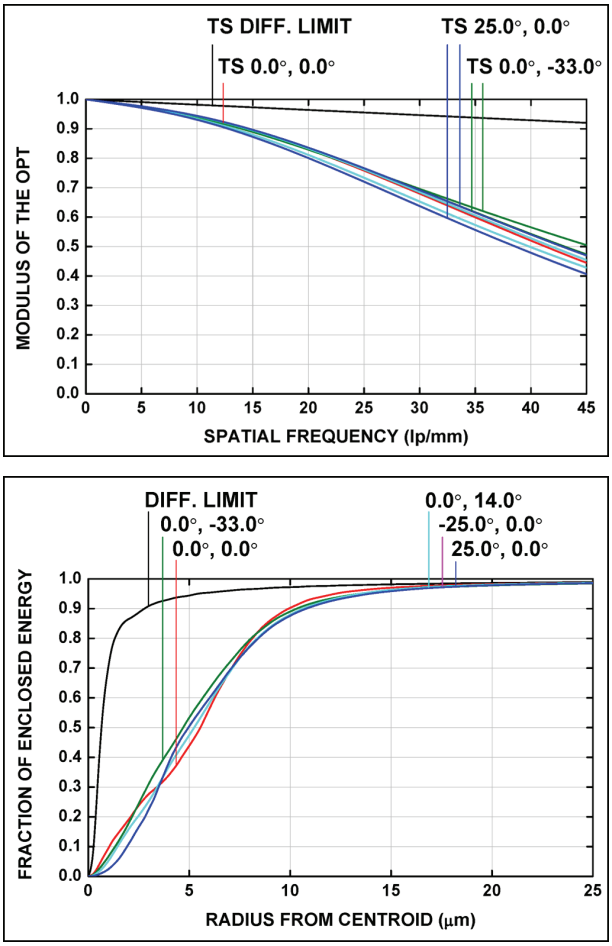

Figure 2 The MTF (upper) and encircled energy (lower) designed for the optical system

The encircled energy (ENC) of the optical system indicates that 80% energy from a point object shall fall within a diameter of 16μm, as shown in the lower figure of Fig.2. This result is corresponding to a Rayleigh resolution limit of 8μm and so the optical system is match to the sensor of the pco.dimax from the standard point of the Rayleigh criterion (Ref.10) view perfectly. Some margin for manufacturing and adjustment tolerances is also leaved.

3. PERFORMANCE PARAMETERS TESTING

As the last section pointed out, some important technical parameters determinating the application requirement and the image quality of the optical system should be satisfied: the FOV at least in 47° and 50° for the horizontal and vertical directions respectively, the DOF better than 4000mm, and the spatial resolution better than 10mm in the full DOF. These parameters are measured carefully using different methods. In this article one method and the corresponding results will be presented in the following.

The FOV has been simply measured with a reading microscope and the testing result is consistent with the optical design. The reading microscope can also be used to test the spatial resolution of the optical system. However, as the MTF is believed to be the most comprehensive of all optical system performance criteria (Ref.11), it has been tested carefully for the EAST wide-angle optical system. For this reason eight MTF targets are manufactured specially in stainless steel. The widths of the bars are 1-6mm, 8mm and 10mm.

The spatial frequency of the MTF target can be interpreted as the image spatial frequency determined by the following equation,

$$\nu = \frac{D}{2f}\frac{1}{d} \quad (1)$$

where D is the distance between the MTF target and the entrance aperture, f is the focus length of the optical system, and d is the width of the MTF target bar in millimeters. Accordingly, it may be more reasonable to use the image modulation depth (IMD) instead of the MTF to evaluate the performance of the optical system for finite square-wave targets such as the ones used in this testing (Ref.12),

$$IMD(\nu) = \frac{M_{\text{output}}(\nu)}{M_{\text{input-bar-target}}(\nu)} \quad (2)$$

where M is the modulation depth of the target, which is generally defined as

$$M = \frac{I_{\max} - I_{\min}}{I_{\max} + I_{\min}} \quad (3)$$

here $I_{\min}$ and $I_{\max}$ are the minimum and maximum values describing either the input-object exitance or output-image irradiance. When the bars of the target tend to infinite the IMD is identical with the contrast transfer function (CTF), which is written as,

$$CTF(\nu) = \frac{M_{\text{output}}(\nu)}{M_{\text{input-square-wave}}(\nu)} \quad (4)$$

Therefore the CTF can be approximated by the IMD in some case.

In practice $M_{\text{input-bar-target}}$ for the MTF target can be simply set as 1. So the IMD is only determined by the M_{output}, which can be calculated with the image acquired by a CCD mounted at the end of the optical system. In this testing the Stingray F504B is adopted and focused onto the target located at a distance of 5000mm. The equation (1) shows that these MTF targets have different measuring ranges for different target locations. The cutoff is mainly determined by the Nyquist frequency of F504B, which is about 145lp/mm in theory, since the MTF in theory of optical system is approximate 758lp/mm at 550nm. The testing result is shown in Fig. 3. In these tests, the targets were located at 1000mm, 2000mm, 4000mm and 5000mm respectively in order to simulate the conditions of the plasma in EAST. One designed CTF is presented in the top-left figure in Fig.3 in order to compare with the measurement.

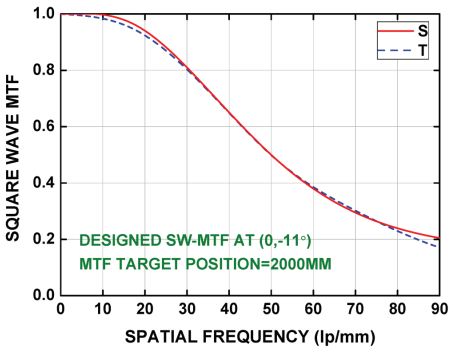

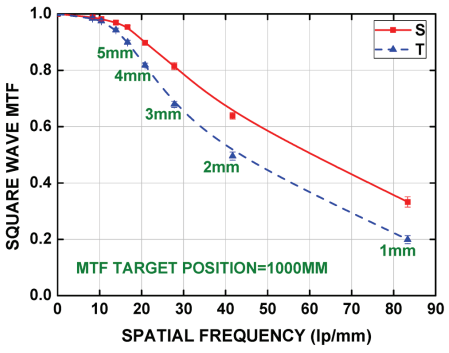

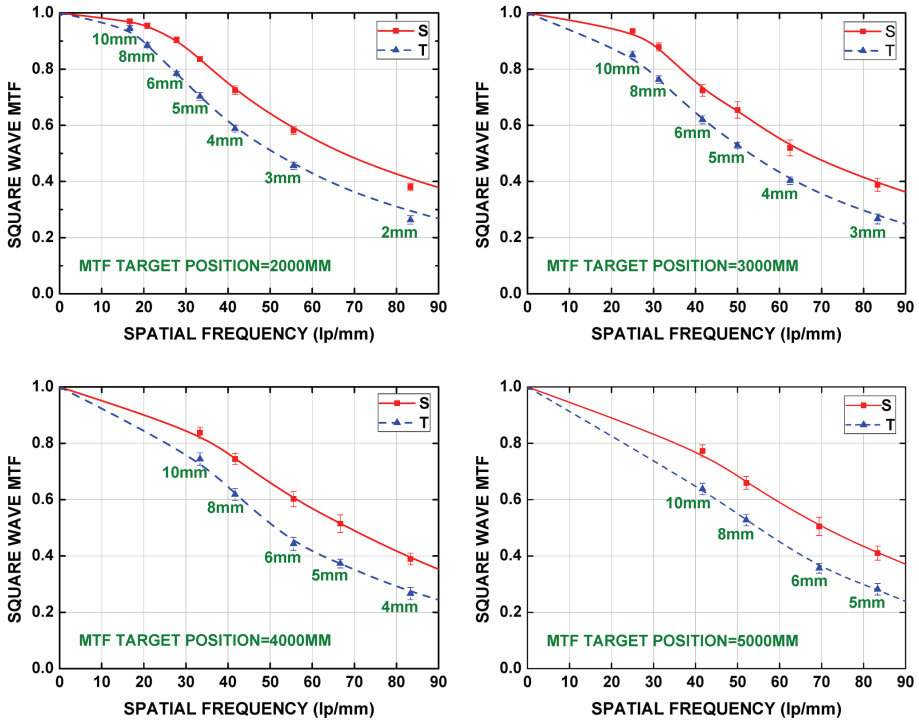

Figure 3 The designed contrast transfer function (CTF, top left) versus the measured image modulation depth (IMD) showing the contrast at various spatial frequency at different position

Fig.3 indicates the spatial resolution is better than 5mm for the full DOF, which completely fulfils the requirement of application. However it should also be pointed out that the differences of the IMD between the sagittal and tangential directions are much larger than the designed ones. Usually the IMD is also higher than the CTF as indicated by the theory (Ref.12).

Another important performance parameter is the total visible light transmittance of the optical system, which determines the minimum illumination required for the final image system. Though it is not measured directly, the optical transmittance is believed better than 79%. In fact every lens and mirror of the optical system owns an optical transmittance of 99.5% and reflectance of 90% for the spectral range from 380nm to 780nm, respectively. The global optical transmittance is as high as 79.6% which is calculated with those parameters and the thickness of the lenses.

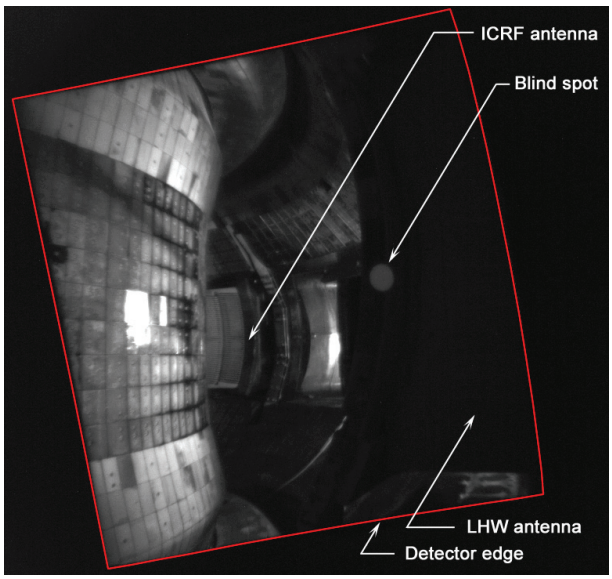

Figure 4 The FOV of the optical system in EAST measured by v710

4. TEST IN HT-7 AND EAST MACHINE

Fig.4 shows the image grabbed by Phantom v710 on EAST. Because the pixel size of this camera is $20\mu m$, nearly twice larger than the pco.dimax, a lens M1614-MP2 of computar is placed back-to-front between the optical system and the v710 in order to magnify the image 2 times. So the system owns the same spatial resolution as the pco.dimax, though it is not measured in this test.

The image in Fig.4 shows that the FOV of this endoscopy surely covers the upper and lower divertor as well as the inside and outside wall of the EAST chamber, which satisfies the application requirement.

It should be indicated that there is a rotation for the image since the optical system has been rotated $4.2°$ on its optical axis. The purpose of this rotation is to compensate the change of the FOV caused by a vertical displacement of the endoscope installation on the EAST window. However, Fig.4 indicates that the rotation is not necessary due to the large FOV and the optical system can be installed normally on the EAST window.

The optical system was tested on HT-7 tokamak during the September 2012 campaign. The pco.dimax was mounted at the rear of the optical system for the testing. This high-speed camera has an excellent light sensitivity for its high ISO speed of 50000 and high peak quantum efficiency of 50%. The optical system with this camera can be applied to monitor the plasma even though the electron density is lower than $1\times10^{17}m^{-3}$, such as the process of the plasma breakdown.

The image size of the optical system is $5.03\times5.32mm^2$ in theory. It is determinated by the focal length and FOV. Considering the range of interest (ROI) step of 48×4, the ROI for the pco.dimax can be set as 432×476 in order to avoid the darkness edge and improve the frame rate. The corresponding frame rate can reach nearly 16kfps. In HT-7 experiment the pco.dimax was test in various ROI to achieve the different frame rates.

Figure 5 Visible image of the plasma-wall interaction in HT-7 in a disruption event on shot 117750#

Fig.5 shows the visible image of a transient event of discharge interruption on shot 117750#. The ROI for the image acquisition was 672×504 with an exposure time of $20\mu s$ and a frame rate of 11.6kfps. In Fig.5 the raw image has been clipped and removed

the unexposed pixels as well as the low interest area. As shown, the plasma was interacting intensively with the wall in such an event, especially for the bulged components such as the guarded limiter of the LHW antenna, the upper, lower and inner toroidal limiters and so on.

The test on HT-7 confirmed that the optical system with the high-speed camera can be used to observe the ~100μs transient event of the ELMy crush during EAST H-mode. In fact, various kind of interesting and complex phenomena have been observed using this high-speed camera system, for example, the plasma edge localized rotation (ELR).

5. CONCLUSION

An endoscopy of high-speed and wide-angle visible light diagnostic for EAST has been completed recently. It adopts the reflective optics of the ITER-like observation diagnostic on JET to design the front end of the optical system (OPT). However the back end of the OPT is simplified and optimized into total 9 lens, including the window protected glass, the optical filters and one neutral optical attenuator. The field of view of the OPT can cover the upper and lower divertors, inner and outside wall, etc. Experimental results show that the OPT with the pco.dimax can be used to monitor the transient event such as ELMy crush.

ACKNOWLEDGEMENT

This work was supported by the National Nature Science Foundation of China No. 10935004, and by the JSPS-NRF-NSFC A3 Foresight Program in the field of "Plasma Physics" (NSFC No.11261140328).

REFERANCE

[1]D. N. Hill, Journal of Nuclear Materials **241-243**, 182 (1997).

[2]E. Gauthier, H. Roche, E. Thomas, S. Droineau, B. Bertrand, J. B. Migozzi, W. Vliegenthart, L. Dague, P. Andrew, T. Tiscornia *et al*., Fusion Engineering and Design **82**, 1335 (2007).

[3]M Z Zhu, G Zhuang, Z J Wang, Y H Ding, L Gao, X W Hu and Y Pan, Plasma Science and Technology, **12**, 641 (2010).

[4]Jinil Chung, Deok Kyo Lee, Dongcheol Seo, and Myoung Choul Choi, Rev. Sci. Instrum. **79**, 10F510 (2008).

[5]J. Cantarini, D. Hildebrandt, R. König, F. Klinkhamer, K. Moddemeijer, W. Vliegenthart, and R. Wolf, Rev. Sci. Instrum. **79**, 10F513 (2008).

[6]A. Huber, S. Brezinsek, Ph. Mertens, B. Schweer, G. Sergienko, A. Terra, G. Arnoux, N. Balshaw, M. Clever, T. Edlingdon, *et al*., Rev. Sci. Instrum. **83**, 10D511 (2012).

[7]G. S. Xu, B. N. Wan, J. G. Li, X. Z. Gong, J. S. Hu, J. F. Shan, H. Li, D. K. Mansfield, D. A. Humphreys and V. Naulinfor, Nucl. Fusion **51**, 072001 (2011).

[8]L Wang, G. S. Xu, H. Y Guo, R. Chen, S. Ding, K. F. Gan, X. Gao, X. Z. Gong, M. Jiang, P. Liu, *et al*., Nucl.

Fusion **52**,063024 (2012).

[9]A. Kirk, B. Koch, R. Scannell, H. R. Wilson, G. Counsell, J. Dowling, A. Herrmann, R. Martin, M. Walsh and the MAST team, PRL **96**, 185001 (2006).

[10]Robert E. Fischer, Biljana Tadic-Galeb and Paul R. Yoder, *Optical System Design* (SPIE, Washington, 2004) p.183.

[11]Robert E. Fischer, Biljana Tadic-Galeb and Paul R. Yoder, *Optical System Design* (SPIE, Washington, 2004) p.193.

[12]Glenn D. Boreman and Sidney Yang, Supplement to Applied Optics **1** December, 8050 (1995).

The simultaneous measurements of core and outer core density fluctuations in L-H transition using CO_2 laser collective scattering diagnostic in the EAST superconducting tokamak

G. M. Cao[1], Y. D. Li[1], X. D. Zhang[1], P. J. Sun[1], L. Q. Hu[1], J. G. Li[1], G. J. Wu[1] and the EAST Team

[1] Institute of Plasma Physics, Chinese Academy of Sciences, Hefei 230031, China

Abstract: The H-mode is the projected basic operation scenario for the ITER tokamak. The turbulence de-correlation by the synergistic effect of zonal flow and equilibrium E×B flow shear is believed to be the reason for L-H transition, however, the detailed physical mechanism has not been identified so far. Tangential multi-channel CO_2 laser collective scattering diagnostic system (mainly k_r measurement) was first installed to investigate electron density fluctuations on EAST tokamak. The measurements in a spontaneous dithering L-H transition show that in core plasma($0 < r/a < 0.5$) the low-frequency fluctuations strengthen greatly before L-H transition; meanwhile in outer core plasma($0.2 < r/a < 1$) the low-frequency fluctuations strengthen slightly. Bispectral analysis reveals that the coupling strength between low- and high- frequency fluctuations in both core and outer core plasma strengthens greatly before the transition, but the latter is greater than the former. The results indicate that the low-frequency fluctuations of the core and outer core plasma play active, but different, roles in the spontaneous L-H transition.

Keywords: L-H transition, core and outer core density fluctuations, CO2 laser collective scattering, low-frequency fluctuations.

1.Introduction

The high confinement mode (H mode) with edge transport barrier(ETB) is the projected basic operation scenario for the ITER tokamak, and it is important to understand the mechanism of the Low to High confinement mode transition (L-H transition) [1]. The drift wave turbulence has been revealed as the major cause of enhancing plasma transport and degrading plasma confinement in the confinement study of toroidal plasmas in the past decades. Recently Substantial evidence provided by theoretical and experimental investigations shows that turbulence de-correlation by sheared flows is responsible for the formation of edge transport barriers and transition dynamics. The sheared flows contains the large-scale mean equilibrium E×B flows and fine-scale zonal flows: the former is caused by the pressure gradient ∇ P or external momentum driven; the latter is caused by turbulent Reynolds stress driven [8]. The predator-prey model, which is based on the complex interaction between turbulence, zonal flows and equilibrium E×B flows, is believed to be one of the most convincing

explanations for L-H transition mechanism. In this model, the zonal flows and equilibrium sheared flows are two competing predators interacting with the drift wave turbulence (prey): before and during the edge transport barrier formation and the L-H transition, the mean equilibrium flow shear is generally weak, therefore the zonal flows provide the dominant shearing effect and even trigger the transition by regulating the turbulence; as the H mode forms, due to the steepening edge pressure gradient the mean equilibrium flow shear grows gradually and eventually become high enough to suppress turbulence effectively and impede the zonal flows generation [2,3,6]. According to this model, the L-H transition will pass through an intermediate transient stage, which is marked by an oscillatory behavior because of the self-regulation between turbulence and flows [23]. Many experimental observations are consistent with this model, for example, the increased Reynolds stress thought to generate zonal flows has been measured directly in the HT-6M tokamak [22]; there is enhanced low frequency edge turbulence coupling prior to and during L-H transition in the DIII-D tokamak [4]; in the ASDEX-U tokamak, a limit-cycle oscillation with competition between the turbulence level and the edge geodesic acoustic mode (GAM) flow shearing, has been observed preceding the L-H transition in low density plasmas [5]; Periodic turbulence suppression in a narrow layer at and just inside the separatrix, with characteristic signatures of a low zonal flows frequency (much below the GAM frequency), has been observed preceding the L-H transition in the DIII-D tokamak [6]. Due to the coincidence between the spatial extent of the edge transport barrier and that of the E×B shear layer [7], most experimental investigations for the dynamics of the turbulence-flow interaction are focused on the edge plasma region.

However, some experimental results were interpreted to imply a clear coupling between core turbulence and edge turbulence [8], for example, the core plasma turbulence amplitude is rapidly reduced corresponding to the L–H transition that occurs in the edge region in JET tokamak [9]; the turbulence well inside the last closed flux surface (LCFS) shows a significant suppression within 10ms of the L–H transition in DIII-D tokamak [10]. These observations might imply that the dynamics of edge turbulence in the L–H transition has effect on the more core localized plasma turbulence. In order to get a comprehensive understanding of the transition mechanism, more attention should be paid to the dynamics of more core localized turbulence in the L-H transition.

Tangential multi-channel CO2 laser collective scattering diagnostic system was first installed to investigate the core localized electron density fluctuations in a so-called dithering L-H transition with input power near the L-H transition threshold on EAST tokamak. From the turbulence scale point of view, the system can measure density fluctuation with the wave-number $k_{\perp}$(mainly k_r) ranging from 10cm^{-1} to 26cm^{-1} simultaneously by changing the angle between the local oscillator beam and main beam; from the

turbulence location point of view, it also can measure density fluctuations in both the core region($0 < r/a < 0.5$) and the outer core region ($0.2 < r/a < 1$) simultaneously by choosing different scattering plane.

In this paper, the density fluctuations in core and outer core region are contrasted, and is found to evolve differently in dithering L-H transition：In the whole LCO phase, the high-frequency portion of the core fluctuations is not suppressed significantly until the end of phase, however the low-frequency portion has a significant increase nearly at the beginning of this phase; the high-frequency portion of outer core fluctuations is suppressed gradually from high frequency to low frequency, and the low-frequency portion begins to increase almost in the middle of this phase. Bispectral analysis reveals that the coupling strength between low-frequency and high-frequency fluctuations in both core and outer core region increases greatly before the transition, but the coupling intensity of high wave-number fluctuations is larger than that of low wave-number fluctuations. The results indicate that the self-regulation of core and outer core fluctuations may have active, but different, effect on the spontaneous L-H transition.

2. Experimental setup

EAST is a superconducting tokamak with a noncircular cross-section, major radius R=1.88 m, minor radius a=0.45 m, toroidal magnetic field $B_T < 3$ T, inverse aspect ratio $\varepsilon = 0.24$, plasma current Ip~1 MA and elongation ratio κ=1.2– 2. It is a modern divertor tokamak designed for steady-state divertor operation for a duration of 1000 s [4] and recently has achieved 400 s. EAST can be operated in various configurations, for example, single-null divertor configuration, double-null divertor configuration or circular limiter configuration [25]. The plasma density is feedback controlled through gas puffing with deuterium as the working gas.

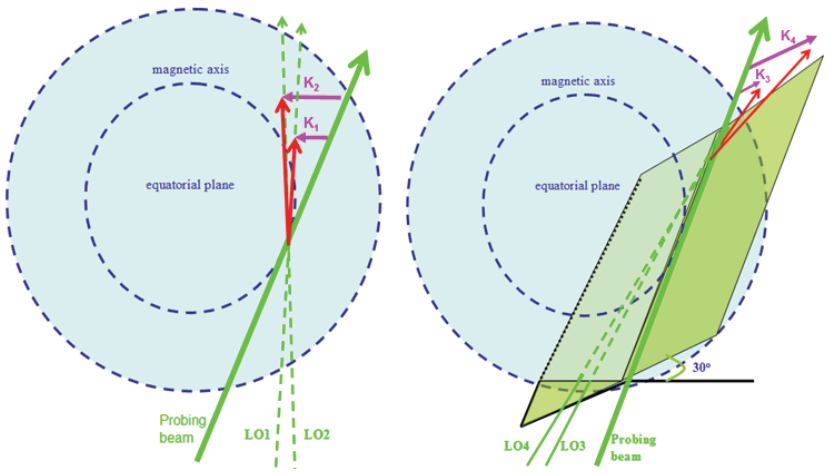

FIG.1. Schematic diagram of CO_2 collective scattering system on EAST tokamak. LO1, LO2, LO3 and LO4 are 'local oscillator' beams; k_1 and k_2 are on the equatorial plane, k_1=10cm^{-1}, k_2=18cm^{-1}; k_3 and k_4 are on the plane which has a angle of 30^0 with the equatorial plane. k_3=10cm^{-1}, k_4=18cm^{-1}

Tangential multi-channel CO_2 laser collective scattering diagnostic system was first installed to measure the density fluctuations in the core plasma on EAST tokamak. It is a powerful technique capable of providing a direct measure of the spectral power of electron density fluctuations, and could be useful to detect short-scale fluctuations in the next generation of burning plasma experiments [11]. The scattering wave vector k of the measured density fluctuations is the difference between the scattered beam wave vector k_s and the incident beam wave vectors k_i, i.e. $k = k_s - k_i$. Since in this paper $\omega_s \approx \omega_0$ and $k_s \approx k_0$, the scattering angle θ should satisfy the Bragg condition, $k = 2k_i \sin(\theta/2)$ [12]. This system employs a probing wave with a wavelength of 10.6μm, together with a four-channel homodyne receiver capable of providing full information on the frequency spectrum of measured signals. As shown in Fig.1, its incident beam is almost tangential with the magnetic axis, and considering the strong anisotropy of short-scale turbulence in tokamak [11] ($k_\parallel << k_\perp$, with $k_\parallel$ and $k_\perp$ the wave vector components parallel and perpendicular to the magnetic field, respectively), though changing the angle between the local oscillator beams and main beam, it can detect density fluctuations of different wave vectors ($k_{1,\,2,\,3,\,4}$) simultaneously (in the range 10–26cm^{-1}), which are mainly perpendicular to the magnetic axis. The beam width is about 2cm, so the wave-number resolution Δk is about 1cm^{-1}. Besides, though the spatial resolution of such measurements is generally defective, by changing the angle between the scattering plane and equatorial plane, the approximate estimation of the scattering region is the core region($k_{1,\,2}$: $0 < r/a < 0.5$) and the outer core region($k_{3,\,4}$: $0.2 < r/a < 1$).

3.Experimental results

3.1 H-mode access in EAST

Figure.2 shows the time evolution of basic parameters in a spontaneous dithering L-H transition, induced by the available total heating power limited to about 1 MW, a value just above the H-mode transition power threshold (at a toroidal magnetic field B_T=2T and plasma current I_p~0.5MA).

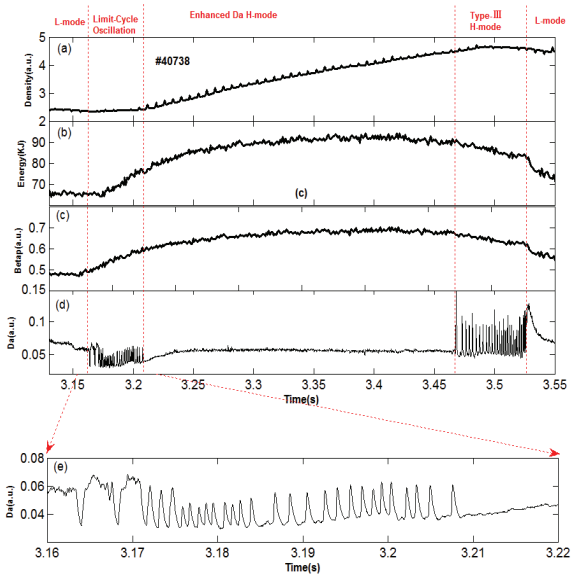

FIG.2. Time evolution of a H-mode shot(#40738) on EAST: (a)Central-chord-average density, (b)the plasma diamagnetic energy, (c)poloidal beta, (d) D_α emission near the inner target of the lower divertor, (e)zoom of the D_α signal.

A lot of cycle state in L-H transition have been discovered upon the L–H transition after type-III ELMy H-mode plasmas was achieved for the first time in EAST [15]. The limit-cycle oscillation (LCO) state is characterized by quasi-periodic oscillations of the divertor D_α signals and the oscillating amplitude smaller than that of Type-III H-mode by more than one order of magnitude, as shown in Fig.2 and the zoom-in plot in Fig.2(f), where typical Type-III ELMs appear over 3.46–3.53 s. The frequency of the oscillations ranges from 0.4 to 2 kHz centered near 1 kHz, and the frequency or amplitude does not have a clear relationship with the input heating power and configuration parameters [16]. The plasma confinement mode evolves from L-mode to enhanced D_α(EDA) H-mode though a limit-cycle oscillations; after the stabilization of EDA H-mode, Type-III ELMs appear.

3.2 Density fluctuations in the L-H transition

As a dithering L-H transition allows the investigation of the transition dynamics on an expanded time scale, it is a suitable phase to study the evolution of density fluctuations. The density fluctuations of different regions can be measured simultaneously using CO_2 laser collective scattering diagnostic system.

3.2.1 Time-frequency spectrum of fluctuations in L-H transition

Fig.3 shows the time-frequency spectrum of the same wave-number density fluctuations in the core region and outer core region from L-mode to H-mode though the LCO phase. As the cycle oscillations go on, the core fluctuations, which seems to be not affected greatly by the oscillation, has not been suppressed dramatically until the end of the LCO phase; however, the outer core fluctuations, which responds actively to the cycle oscillations, are suppressed gradually from high frequency to low frequency. After a final D_α transient, the transition to sustained H-mode takes place, characterized by that both core and outer core fluctuations begin to increase gradually from low frequency to high frequency.

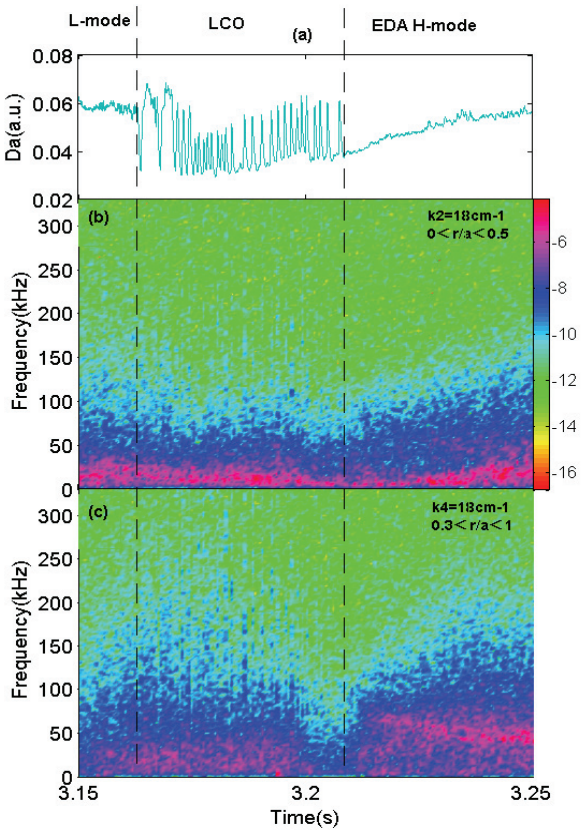

FIG.3. (a) D_α emission near the inner target of the lower divertor, time-frequency spectrum of fluctuations(spectrum power in logarithmic scale) (b) k_2 =18cm^{-1}, core region: $0 < r/a < 0.5$, (c) k_4 =18cm^{-1}, outer core region: $0.2 < r/a < 1$.

In the overall LCO phase, though the outer core fluctuations are enhanced and suppressed periodically with the oscillations, finally the high-frequency portion are suppressed gradually from high frequency to low frequency; the core fluctuations are not suppressed greatly until the end of LCO phase. The results might imply that the suppression of turbulence in L-H transition has order of precedence in both frequency-domain and spatial-domain.

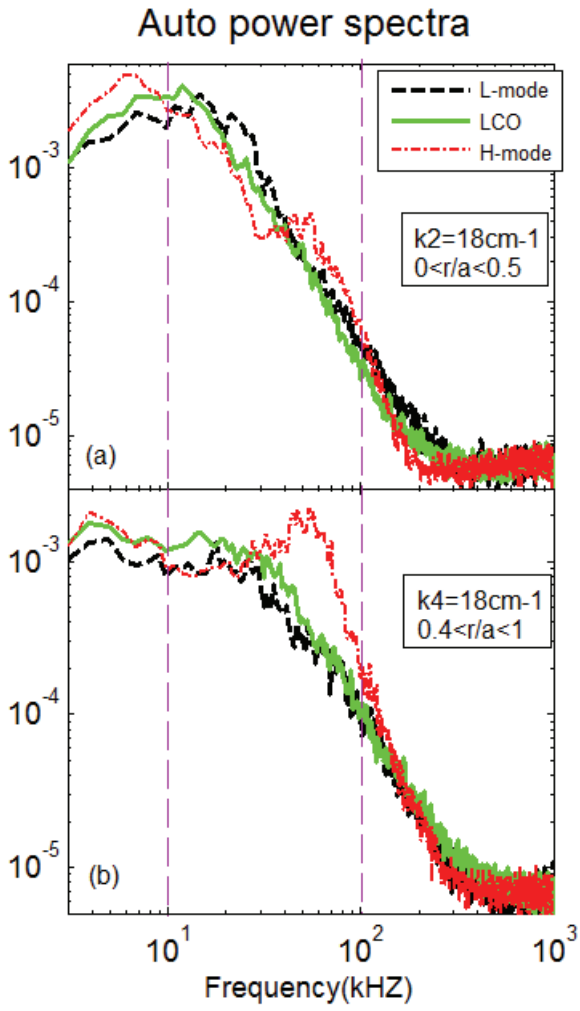

FIG.4. Frequency spectrum for density fluctuations of (a) k_2 =18cm^{-1}, core region: 0 < *r*/*a* < 0.5, (b) k_4 =18cm^{-1}, outer core region: 0.2 < *r*/*a* < 1 in L-mode(black), LCO phase(green) and H-mode(red).

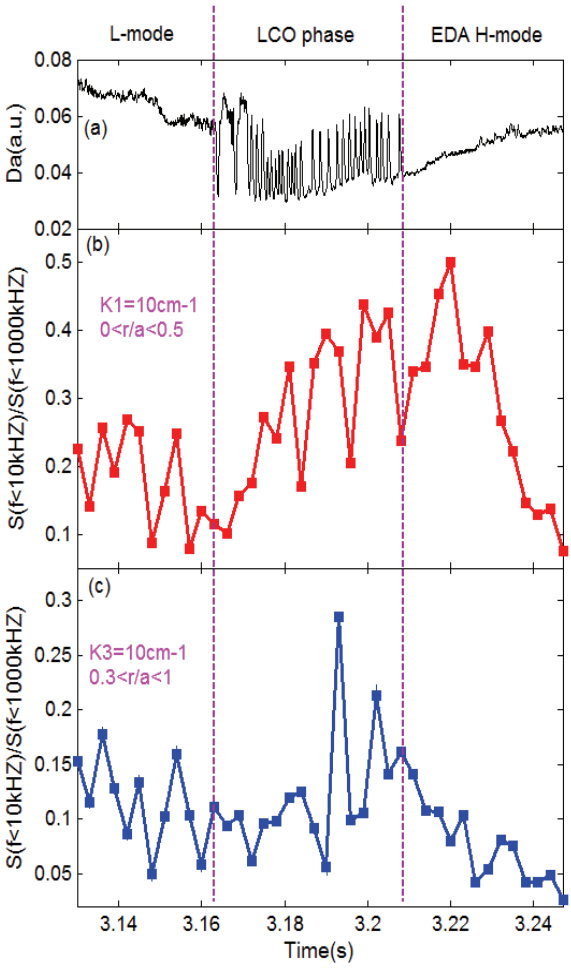

FIG.5. (a) D_α emission near the inner target of the lower divertor, time evolution of the low-frequency proportion of the fluctuations (< 15kHZ) (b) k_2 =18cm^{-1}, core region: 0 < *r*/*a* < 0.5, (c) k_4 =18cm^{-1}, outer core region: 0.2 < *r*/*a* < 1.

3.2.2 Increase of the low-frequency fluctuations in L-H transition

Fig.4 shows the power spectrum density analysis of the core and outer core density fluctuations in L-mode, LCO phase and H-mode, respectively. It is found that the low-frequency portion of both core and outer core

fluctuations increase greatly in the L-H transition, however the increase of the former is much larger than that of the latter in LCO phase. In order to give an detail illustration, the low-frequency region is valued as less than 15kHZ, the time evolution of the low-frequency proportion of the fluctuations can be shown in Fig.5, the low-frequency proportion of the core fluctuations increases greatly nearly at the beginning of LCO phase, until about 15ms after that, the low-frequency proportion of the outer core fluctuations does not have a significant increase.

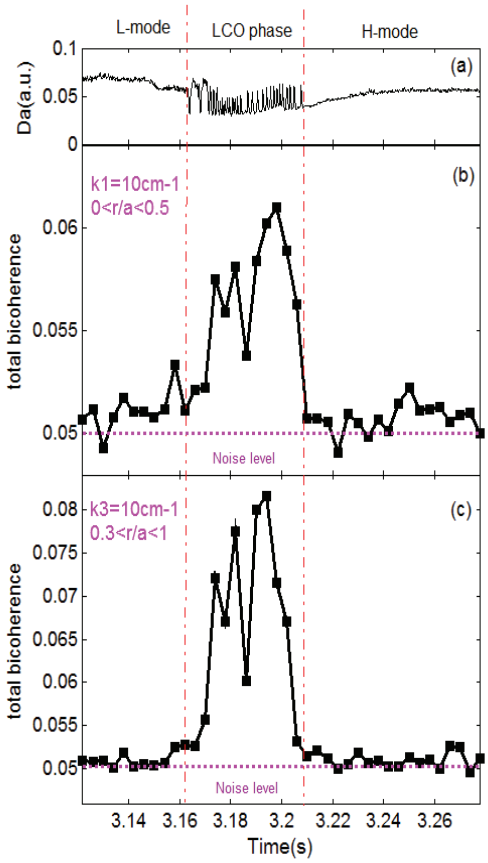

FIG.6.Time evolution of (a) D_α emission near the inner target of the lower divertor, total bicoherence $b^2(t)$ for the fluctuations (b) K_1 =10cm^{-1}, core region: 0 〈*r/a* 〈0.5 and (c) K_3 =10cm^{-1},outer core region: 0.3 〈*r/a* 〈1. Note: the noise level~1/M, M is the number of records in the averaging processing.

3.3 Coupling analysis between the high- and low-frequency portion of fluctuations in the L-H transition

Bispectral analysis is a higher order statistical technique, which is useful for study a quadratic nonlinearity [15]. This paper will present autobicoherence calculated using only the FFT method. The total bicoherence is used as a measure of total coupling intensity, which is the ensemble average of $b^2(f_1, f_2)$. It represents the temporal evolvement of the coupling intensity among different frequency bands in a fluctuations spectra. The total bicoherence of the fluctuations evolves with time as showed in FIG.6, it shows that in LCO phase both core and outer core fluctuations have a great increase in the coupling between the high- and low-frequency portion. This increasing coupling of both core and outer core fluctuations might have an impact on L-H transition.

4.Summary

In this paper, the core and outer core density fluctuations are measured in dithering L-H transition. The time-frequency spectrum of fluctuations shows that the fluctuations in outer core plasma is suppressed gradually from high frequency to low frequency, but that in core plasma is not suppressed significantly until the end of phase. In flourier-domain analysis, in core

plasma the low-frequency fluctuations strengthen greatly before L-H transition; meanwhile in outer core plasma the low-frequency fluctuations do not increase significantly until the end of the transition. Bispectral analysis reveals that the coupling intensity between low-frequency and high-frequency fluctuations in both core and outer core plasma increases greatly before the transition. The results indicate that the low-frequency fluctuations in both core and outer core plasma have impact on the L-H transition.

Acknowledgments

The author thanks Prof. C. X. Yu, Q. Q. Yu, L. Chen, V. Igochine, X. G. Wang, X. T. Ding, Z. X. Wang, J. Q. Dong, and Y. Liu for their useful discussion. This work was supported by the National Nature Science Foundation of China with Contracts Nos. 10975159, 11275232. Besides, this work was partly supported by the JSPS-NRF-NSFC A3 Foresight Program in the field of Plasma Physics (NSFC No.11261140328)

REFERENCES

[1] ITER Physics Expert Groups on Confinement and Transport et al, Nuclear Fusion 39, 2175(1999).

[2] E.-J. Kim and P.H. Diamond, Phys. Plasmas 10, 1698(2003).

[3] M.A. Malkov and P.H. Diamond, Phys. Plasmas 16, 012504 (2009).

[4] R.A. Moyer et al., Phys. Rev. Lett.87, 135001 (2001).

[5] G.D. Conway et al., Phys. Rev. Lett.106, 065001(2011).

[6] L. Schmitz *et al*, Phys. Rev. Lett.108,155002 (2012).

[7] Burrell K H et al., Phys. Plasmas.1, 1536(1994).

[8] G R Tynan et al., Plasma Physics and Controlled Fusion 51, 113001 (2009).

[9] Cordey J G et al., Nucl. Fusion.35, 505 (1995).

[10] McKee G, Plasma Fusion Res.2, S1025(2007).

[11] E Mazzucato, Plasma Physics and Controlled Fusion 48, 1749 (2006).

[12] Rosenbluth M N and Rostoker N, Phys. Fluids.5, 776(1962).

[13] Mazzucato E, Phys. Plasmas.10, 753(2003).

[14] W Y Zhang et al., Plasma Physics and Controlled Fusion 54, 035005 (2012).

[15] G. S. Xu et al., Nucl. Fusion.51, 072001 (2011).

[16] G. S. Xu et al., Phys. Plasmas.19, 122502(2012).

[17] Andre L. Rogister et al., Nucl. Fusion.44, 869 (2004).

[18] P.H. Diamond et al., Nucl. Fusion.41, 1067 (2001).

[19] Hasegawa A, Maclennan C G and Kodama Y Phys. Fluids.22,2122(1979)

[20] Nagashima Y et al., Plasma Physics and Controlled Fusion 49, 161125 (2007).

[21] Akihide Fujisawa et al., Nucl. Fusion.49, 013001 (2009).

[22] Y. H. Xu et al., Phys. Rev. Lett.84, 3867 (2000).

[23] T. Estrada *et al*, Phys. Rev. Lett.107, 245004 (2011).

[24] Wan Y.X., HT-7 Team and HT-7U Team Nucl. Fusion40, 1057(2000)

[25] Petrie T.W. et al J. Nucl. Mater. 290, 935(2001)

Performance and analysis of the TVTS diagnostic system on HT-7 tokamak

Xiaofeng Han, Chunqiang Shao, Xiaoqi Xi, Junyu Zhao, Zang Qing,

Jianhua Yang and Xingxing Dai

Institute of Plasma Physics, Chinese Academy of Sciences, Hefei,230031, China

Author to whom correspondence should be addressed. Electronic mail: hxf@ipp.ac.cn

Abstract: A high spatial resolution imaging Thomson scattering diagnostic system was developed in ASIPP. After about one month trial running on the superconducting HT-7 tokamak, the system was proved to be capable of measuring plasma electron temperature. The system setup and data calibration are described in this paper and then the instrument function is studied in detail, as well as the measurement capability, an electron temperature of 50eV to 2keV and density beyond $1*10^{19}$ m^{-3}. Finally, the data processing method and experimental results are presented.

Keywords: Imaging Thomson scattering, electron temperature, instrument broadening

PACS numbers: 42.62.Fi, 52.38.Kd

1. Introduction

A Thomson Scattering (TS) diagnostic is recognized as the most accurate method to measure plasma electron temperature and density[1, 2], which are two of the basic parameters of tokamak plasma. TS diagnostic is also one of the most technically difficult diagnostics on tokamak devices. In order to observe and understand the physical processes such as L-H transitions, ELMS, and disruptions, multi-pulse laser systems are required[3-5]. At the same time, the high spatial resolution imaging Thomson scattering, also known as TVTS, is designed to enhance spatial resolution[6].

TVTS gains name from the television-like detectors placed after a spectrometer for receiving a two-dimensional image. TVTS was originally developed in 1967 on PLT as a relatively simple setup. The system performs the spatial-resolution-oriented electron temperature and density measurements for the observation of confinement-related structures[7-10], while the evolution of such structures is also measurable on TEXTOR due to the high temporal resolution[11, 12].

An imaging Thomson scattering diagnostic system was developed in ASIPP. After about one month commissioning and trial running on HT-7 tokamak, the system was proved to be capable of measuring plasma electron temperature.

This paper is organized as follows: after introduction, the system set-up is described in section 2. Section 3 presents the wavelength calibration and relative sensitivity calibration, followed by analysis of instrument broadening and measuring range in section 4. The data processing method and experimental results are presented in section 5. Finally, conclusion is drawn in section 6.

2. Description of the system

2.1. Operating conditions

The HT-7 superconducting tokamak[13] is a medium size fusion research device. It has a major radius of R=1.22 m, minor radius of a=0.27 m with a circular geometry cross section. The experimental conditions in which TVTS operation was carried out were as follows: plasma current I_p=100–250kA, toroidal magnetic field B_t=2 T, central line-averaged plasma density n_{el}= 1-3×$10^{19}$$m^{-3}$, central electron temperature T_{e0}=0.5-2.0keV, and central ion temperature T_{i0}=0.2-1.0keV. The plasma current, position and central line-averaged density was feedback controlled during discharges. It was a great advancement in the study to sustain discharge under quasi-steady state operation.

2.2. System set-up and discussion

TVTS diagnostic system on HT-7 tokamak was composed of high-energy laser, transfer optics, grating spectrometer, image intensifier, EMCCD system and data acquisition system, as shown in Fig. 1. There were three dielectric mirrors with highly reflectivity and one convex lens to guide the laser beam into the vacuum chamber and focused into the plasma. Then, the scattering signal passed orderly through the collection optics system for imaging scattering signal onto the fibers, delivery fiber bundle, slit and grating spectrometer, coupling optics for image intensifier and CCD[14].

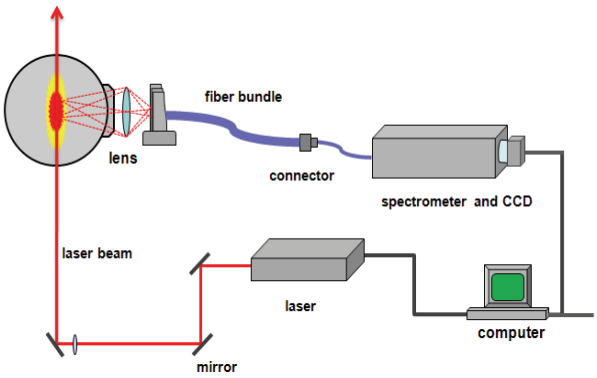

FIG. 1. Sketch of the TV Thomson scattering system on HT-7 tokamak. This system is composed of high-energy laser, mirrors, grating spectrometer, image intensifier, EMCCD and data acquisition system.

The configuration of fiber bundle was designed to change conveniently the measuring position for different experimental requirements. Two independent parts were connected with the SMA connectors. For the input side, there were 100 fibers (10 collimation fibers) with a length of 15 meters. For the output side, there were 30 fibers with a length of 3 meters corresponding to the spectrometer. The NA of the fiber was 0.39 and the core/clad ratio was 0.8/0.83mm, which matched the collection lens. The fiber bundle allowed the spatial resolution down to one fiber of scattering length about 4mm. It should be noted that the fibers could be binned in the software of the detector to get more signals at the cost of decreasing the spatial resolution.

TVTS diagnostic can not only provide fine profiles of temperature and density, but also directly measure the shape of scattering spectrum, while the scattering

signal is much weaker and the diagnostic system is more difficult. In order to reduce the disadvantage, the system employed a high-energy Nd:YAG laser with a pulse energy of 5J working at the fundamental wavelength of 1064 nm. Due to the relatively low quantum efficiency of CCD detectors in near infrared region, a frequency multiplier was designed to transfer the wavelength from 1064nm to 532nm for the TVTS system. Due to this change, the single laser energy reduced fifty percents to about 2.5 joule. The gate time of the Image intensifier was about 15ns which was only long enough to capture the laser pulse. In order to obtain much more signal from the image intensifier, the gate time of the CCD was synchronization with the image intensifier and the gate width was set about 1ms, taking the screen relaxation time into account.

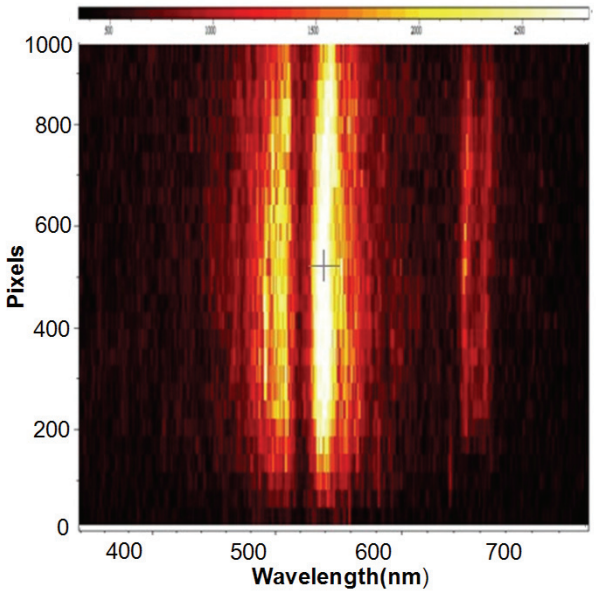

FIG. 2. The three-dimensional scattering signal of TVTS system. The effective pixels of EMCCD are 1004×1002 and the reciprocal of line dispersion is 0.38 nm/pix, approximately.

With these parameters setting, the three-dimensional scattering signal was obtained. As shown in Fig. 2, the abscissa, ordinate and brightness represent the wavelength, pixels number and signal intensity, respectively. As a result of the notch filter, the region near 532nm is relatively aphotic, corresponding to a black bar in Fig. 2. It should be noted that the characteristic of weak scattering signal is the most important feature of Thomson scattering[14, 15]. In order to improve signal-to-noise ratio, a polarizer was installed on the receiving end of the fiber bundle. Because the scattering signal was polarized and the background radiation was approximately natural light, the background signal, especially strong line radiation, was reduced to about half of the original but the scattering signal remained almost constant with the same polarization direction as the polarizer.

3. Wavelength and sensitivity calibrations

The spectrometer was designed to cover a spectral range of about 380-720nm and so a grating covering an appropriate temperature range was selected. The groove frequency of the transmission grating was 720gr/mm for 50eV < T_e < 2keV. Finally, the spectral image at the image intensifier of 25mm diameter was imaged onto the cathode of the detector (image size 8*8 mm^2) by a camera objective.

The line radiations were used to calibrate the corresponding relationship between wavelength and pixel on the cathode of the detector. It should be emphasized that the entrance slit should be set as

narrow as possible in order to reduce the line broadening and improve the calibration accuracy. The calibration results were described by the following formula:

$$\lambda = c_0 + c_1 p + c_2 p^2 \quad (1)$$

where $[c_0, c_1, c_2] = [751.11, -0.38744, -3.0771*10^{-6}]$, p is the pixel number of EMCCD. Then, the experimental reciprocal of line dispersion is $|d\lambda/dp| = c_1 + 2c_2 p \approx 0.387$ nm/pix.

By applying a calibrated lamp (deuterium and halogen lamp), the relative efficiency curve was verified. It should be noted that the system must be set up with the working parameters. In other words, before the calibration we prepared the stable operation parameters of the system, including the gain adjustment, signal synchronization, pulse width and so on.

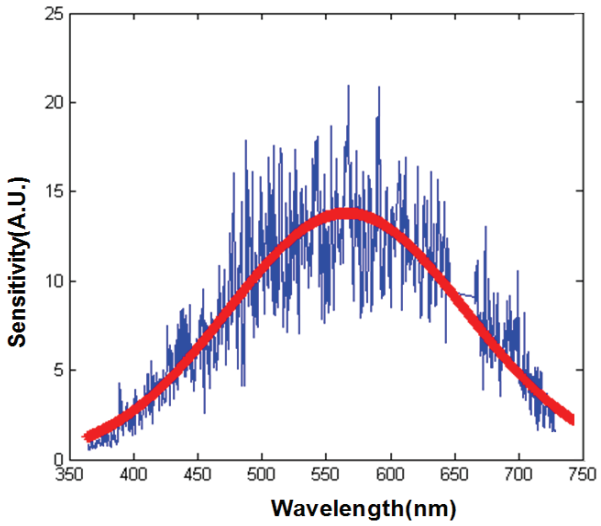

FIG. 3. Relative efficiency curve obtained with the working parameters. This sensitivity factor includes the effect of lens, fiber bundle, optical spectrometer, image intensifier, coupling lens and EMCCD. The relative efficiency is higher between 500nm and 650nm.

The sensitivity curve obtained from the relative calibration system is shown in Fig. 3. The relative calibration presented the sensitivity of the system as a function of wavelength and the sensitivity factor included the effect of lens, fiber bundle, optical spectrometer, image intensifier, coupling lens and EMCCD. As shown in Fig. 3, the relative efficiency is higher between 500nm and 650nm.

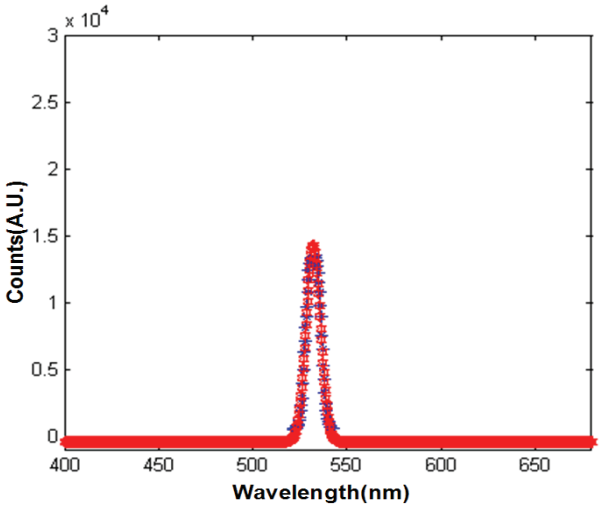

FIG. 4. Instrument broadening in blue and Gaussian fitting function in red. The full width at half maximum (FWHM) of instrument function is about 10 nm which corresponds to the Doppler broadening of scattering electron at 16eV.

4. Discussion on instrument broadening and measuring range

4.1. Instrument broadening

Using the same experimental setup of magnification and stray light (532nm) as the incident signal, the instrument function was obtained as shown in Fig. 4 in blue. The instrument broadening was fitted with a Gaussian function and they were in good agreement

with each other. The full width at half maximum (FWHM) of instrument function was about 10 nm which corresponded to the Doppler broadening of scattering electron at 16eV. This broadening was mainly due to the larger slit. In order to get more scattering signal, the slit was set as large as the diameter of the fiber, about 0.8mm.

For Gaussian function s(x) and f(x), their convolution $g(x)=s(x)*f(x)=\int s(m)f(x-m)dm$ is still a Gaussian function and in addition, their broadenings satisfy the following formula

$$\Delta s=\sqrt{\Delta g^2-\Delta f^2} \quad (2)$$

As we know, the signal of Thomson scattering is Gaussian function approximatively and the electron temperature is proportional to the square of FWHM of the scattering signal. Taking the impact of the instrument broadening into account, the experimental electron temperature is on the high side, about 16eV which should be deducted from the experimental results by data processing.

4.2. Measuring range

The measuring range of TVTS system in electron temperature was determined by the bandwidth of notch filter and effective wavelength range of system covering. In addition, the instrument broadening also influenced on the measuring range. The notch filter was designed to eliminate the stray light and the bandwidth of the notch filter was about 17 nm typically (Tavg<90%:37nm). The detailed parameters are provided in Table1. As shown schematically in Fig.5, considering the notch bandwidth and instrument broadening of 10 nm, the measurable minimum electron temperature is about 50eV. Spectrometer covering wavelength range is from 380nm to 720nm effectively which implies that the relevant electron temperature is less than 2keV approximatively. In order to get a better signal-to-noise ratio, the electron density is preferably larger than $1.0*10^{19}m^{-3}$. These parameters fulfill the requirements of the HT-7 tokamak operation.

TABLE 1. Parameters table of the notch filter.

Transmission Band 1	Tavg > 90% 399 – 513 nm
Transmission Band 2	Tavg > 90% 550 – 709 nm
Notch Bandwidth	17 nm (typically)

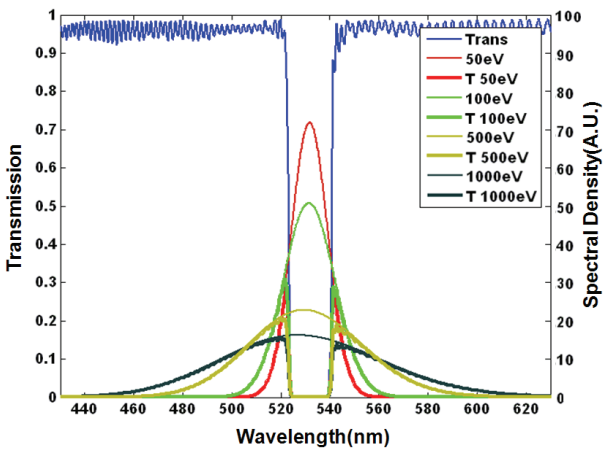

FIG.5. Transmissivity of the notch filter in blue and scattering spectral density of different temperatures in other colors. The thick lines of scattering spectrum include calculation of the transmissivity and the thin lines do not include the transmissivity, respectively. The measurable minimum electron temperature is about 50eV.

5. Experimental results and data analysis

The signal of Thomson scattering is close to Gaussian function and the electron temperature is proportional to the square of FWHM of the function, as shown in the following formula

$$T_e = k\Delta s^2 = k(\Delta g^2 - \Delta f^2) \quad (3)$$

Where k is a proportionality constant. Δg and Δf are the FWHMs of scattering signal and instrument function.

In principle, Gaussian function with four parameters was selected to fit the scattering signal spectrum and then the FWHM Δg was determined, as shown in Fig. 6. It should be noted that the blue shift of relativistic effect has been taken into account here. The influence of relativistic effect on the broadening is much weak when the electron temperature is less than 1keV. Due to the lack of absolute calibration, the signal intensity, corresponding to the electron density, was temporarily ignored.

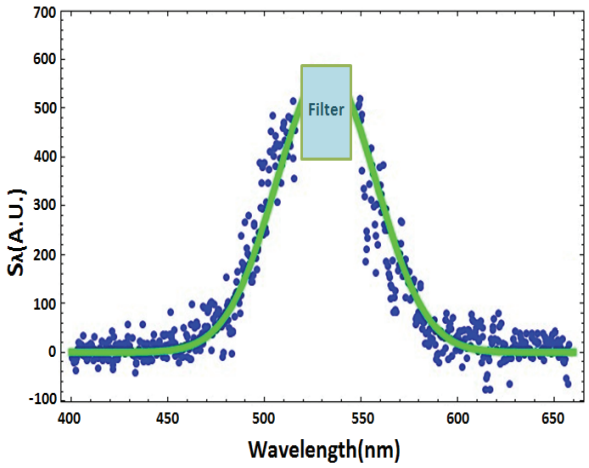

FIG.6. Thomson scattering signal in blue and corresponding fitting function curve in green.

The experimental results are shown in Fig.7. As seen from the figure, the electron temperature is about 900eV near the core with spatial resolution 8mm. In order to obtain a larger signal, three optical fibers were integrated to correspond to a measurement point.

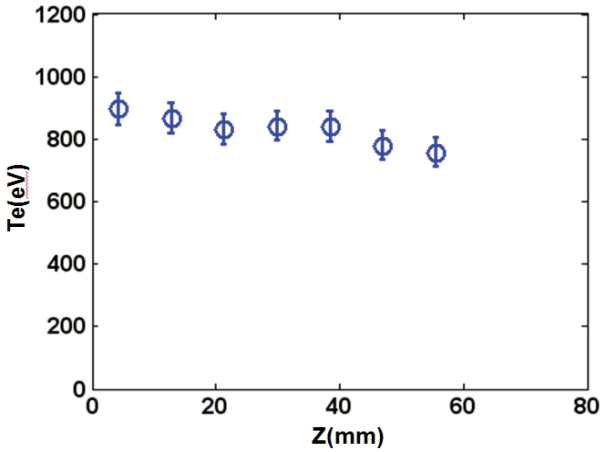

FIG.7. The profile of electron temperature measured by TVTS system. The plasma current is in the region of 150 kA and the central line-averaged plasma density is about 2.6×10^{19} m^{-3}.

In the case of no auxiliary heating, the electron temperature measured by TVTS and the ECE system were agree well with each other. On the other hand with LHW current driven, it was difficult to find any other method to verify the electron temperature profile. However, the electron temperature values and time-dependence trends were the same with each other when the experimental conditions were repeated for several times.

The noise of the image intensifier was EBI (Equivalent Background Illumination), which was thermal emission of the cathode. This noise was almost negligible in our situation with small gate time. On the

other hand, the noise of the EMCCD came from several sources: readout noise, shot noise, dark current noise and CIC (Clock Induced Charge) noise which was caused by the impact ionization when charges were shifted pixels to pixels. In addition, both in intensifying and EM process there was a multiplicative noise effect called noise factor. The value of the statistical observational errors was limited to below 10% in T_e (for 50eV < T_e < 2keV, $n_e > 1.0\times10^{19}$ m^{-3}) during many successful measurements of core profiles. Considering the stabilities of collection, calibrations and data processing, the error of the resultant electron temperature was estimated to be about 12%.

6. Conclusion

A high resolution Thomson scattering system was installed on HT-7 tokamak and successfully obtained scattering signal for the first measurement of electron temperature profiles. A high-energy Nd:YAG laser and a frequency multiplier were employed to work for this system. The method of wavelength calibration and relative efficiency curve are presented. In addition, the influence of instrumental broadening and measuring range, minimum to 50eV, are analyzed in detail. Finally, data processing method considering the instrumental function and the experimental results are presented.

Acknowledgments

The authors would like to thank the HT-7 team for the help of experimental operation. This work was funded jointly by National Nature Science Foundation of China with Contracts No.11075187 and 11275233 and 11261140328.

References

[1] T. N. Carlstrom, G. L. Campbell, J. C. Deboo, R. Evanko, J. Evans, C. M. Greenfield, J. Haskovec, C. L. Hsieh, E. Mckee, R. T. Snider, R. Stockdale, P. K. Trost and M. P. Thomas, Review of Scientific Instruments 63 (10), 4901-4906 (1992).

[2] A. Alfier and R. Pasqualotto, Review of Scientific Instruments 78 (1) (2007).

[3] P. K. Trost, T. N. Carlstrom, J. C. Deboo, C. M. Greenfield, C. L. Hsieh and R. T. Snider, Review of Scientific Instruments 61 (10), 2864-2866 (1990).

[4] K. Narihara, I. Yamada, H. Hayashi and K. Yamauchi, Review of Scientific Instruments 72 (1), 1122-1125 (2001).

[5] Q. Zang, J. Y. Zhao, L. Yang, Q. S. Hu, X. Q. Xi, X. X. Dai, J. H. Yang, X. F. Han, M. T. Li and C. L. Hsieh, Review of Scientific Instruments 82 (6) (2011).

[6] H. J. Van der Meiden, S. K. Varshney, C. J. Barth, T. Oyevaar, R. Jaspers, A. J. H. Donne, M. Y. Kantor, D. V. Kouprienko, E. Uzgel, W. Biel, A. Pospieszczyk and T. Team, Review of Scientific Instruments 77 (10) (2006).

[7] N. Bretz, D. Dimock, V. Foote, D. Johnson, D. Long and E. Tolnas, Appl Optics 17 (2), 192-202 (1978).

[8] D. Johnson, D. Dimock, B. Grek, D. Long, D. Mcneill, R. Palladino, J. Robinson and E. Tolnas,

Review of Scientific Instruments 56 (5), 1015-1017 (1985).

[9] C. J. Barth, M. L. P. Dirkx, B. J. J. Grobben, G. C. H. M. Verhaag, A. T. M. Wilbers and A. J. H. Donne, Review of Scientific Instruments 63 (10), 4947-4949 (1992).

[10] M. N. A. Beurskens, C. J. Barth, N. J. L. Cardozo and H. J. van der Meiden, Plasma Phys Contr F 41 (11), 1321-1348 (1999).

[11] H. J. van der Meiden, C. J. Barth, T. Oyevaar, S. K. Varshney, A. J. H. Donne, M. Y. Kantor, D. V. Kouprienko, A. Alexeev, W. Biel and A. Pospieszczyk, Review of Scientific Instruments 75 (10), 3849-3851 (2004).

[12] A. J. H. Donne, C. J. Barth and H. Weisen, Fusion Sci Technol 53 (2), 397-430 (2008).

[13] X. Gao, Y. X. Jie, Y. Yang, C. Y. Xia, M. S. Wei, S. Y. Zhang, Y. F. Cheng, L. Q. Hu, J. S. Mao, X. D. Tong, B. N. Wan, G. L. Kuang, J. G. Li, Y. P. Zhao, J. R. Luo, N. Qiu, K. Yang, G. Li, J. K. Xie and Y. X. Wan, Phys Plasmas 7 (7), 2933-2938 (2000).

[14] X. Q. Xi, J. Y. Zhao, K. Shinichiro, Q. Zang, X. F. Han, X. X. Dai, J. H. Yang, M. T. Li and C. Q. Shao, Proc Spie 8194 (2011).

[15] L. Yang, B. N. Wan, J. Y. Zhao, Q. S. Hu, Y. Q. Jia, X. Q. Xi, X. F. Han and Q. Zang, Plasma Sci Technol 12 (3), 284-288 (2010).

Pellet injector of EAST tokamak and its first experimental results

LI Changzheng[1*], HU Jiansheng[1**], CHEN Yue[1], LIANG Yunfeng [1,2], LI Jiangang[1], LI Jiahong[1], WU Jinghua[1] , HAN Xiang[1]

[1] Institute of Plasma Physics, Chinese Academy of Sciences, Hefei 230031, China

[2] Institute for Energy and Climate Research-Plasma Physics, Forschungszentrum Jülich, Association EURATOM-FZJ,Trilateral Euregio Cluster, 52425 Jülich, Germany

Abstract: A new pellet injection system designed for fuelling was installed at EAST tokamak and has been successfully tested on 2012 campaign. Typical phenomena of pellet-plasma interaction include: a sudden increase of the electron density and H_α/D_α emission; a significant decrease of plasma electron temperature, etc. Some profiles have been investigated to check out the influence of pellet fuelling on plasma. The comparison of fuelling efficiency has been examined with different pellet injected velocities and locations (HFS and LFS). Using pellet to trigger ELMs has also been tried, and it is found that pellets with speed of 170m/s sometimes triggered a high frequency (up to~ 300 Hz) ELM-like events during ELMs free phase in a short time.

Keywords： Pellet injector, fuelling efficiency, ELMs trigger, EAST

PACS: 28.52.Cx，52.35.Py, 52.55.Fa

1. Introduction

Pellet fuelling for fusion plasmas has been under development for fuelling and density profile control for many years since 1977. It provides not only a fuelling source but also induce changes in plasma transport [1]. Pellet fuelling experiments on DIII-D have demonstrated that HFS pellet injection has much higher fuelling efficiency than LFS injection due to deeper mass penetration and a reduced ELM perturbation [2]. Pellet injection has also been proven to be a valid approach to ELMs control. The feasibility of ELM control by continuous injection of small frozen deuterium pellet into H-mode discharges has been demonstrated on ASDEX Upgrade. Starting from H-mode target discharges with large intrinsic ELMs at 3 Hz and injecting small pellets at 19 Hz, the large compound ELMs have been completely replaced by regular, pellet induced type-I ELMs at the pellet frequency [3]. Further results on ASDEX Upgrade showed that injection of small size cryogenic deuterium pellets (~$(1.4\ mm)^2 \times 0.2\ mm \approx 2.5 \times 10^{19}$ D) at rates up to 83 Hz imposed persisting ELM control without significant fuelling, enabling for investigations well inside the type-I ELM regime [4].

The pellet pacing ELM control concept developed at the mid-sized tokamak ASDEX Upgrade was also considered for the larger machines JET [5] and ITER as well. And recent investigations were clear steps forward to validate the pellet pacing approach for ITER [6].

The Experimental Advanced Superconducting Tokamak (EAST) is a non-circular advanced steady-state experimental device. The scientific mission is to study the physical issues involved in steady-state advanced tokamak devices. The engineering mission is to establish the technology basis of fully superconducting tokamaks in support of future magnetic fusion reactors [7]. Significant technical improvements have been made since the first plasma achieved in October 2006 which enhance EAST operation capabilities. Long pulse plasmas up to 400 seconds and stationary H-mode plasmas up to 32 seconds have been achieved in 2012 campaign. In the near years, EAST tokamak is expected to obtain steady-state operation with plasma current up to 1MA, and total auxiliary heating power up to 20~30 MW (including LHCD, NBI, ECRH, ICRF). The goal of long pulse discharge is to achieve 1000 seconds for L-mode discharge and 400 seconds for H-mode discharge. And also advanced plasma-facing components will be designed, such as actively-cooled ITER W/Cu divertor. Meanwhile, extensive advanced diagnostics will be developed. It also requires new fuelling techniques, such as SMBI and pellet injection (PI). With the purpose of achieving plasma core fuelling with a higher fueling efficiency, we have successfully designed a set of pellet injection system for EAST recently. We expect that the core fueling by pellet injector would improve plasma confinement and promote H-mode plasma parameters. Additionally, ELMs control becomes very important since stationary H-Mode plasma with giant ELMs has been obtained on EAST. New methods, such as pellet injection, resonance magnetic perturbation (RMP), has developed for ELMs control. Encouraged by the experiment on other machines such as DIII-D, ASDEX-U and JET, we would also like to try to use the present pellet injector for the ELMs control.

The pellet injection system has been firstly and successfully tested in the latest campaign of EAST. The test showed that the new fuelling system could be used not only for advanced fueling, but also for ELMs control. In this paper, we will show the design of pellet system and its first results obtained in the 2012 campaign of EAST. The influences of pellet injection on various plasmas from both HFS and LFS side will be introduced. And the fuelling efficiency of pellet injection with various injected speed from both HFS and LFS side will be studied and compared with that of GP and SMBI. In the last, the first attempt of ELMs trigger experiments using pellet will be also shown. Section 2 will describe experimental setup with introduction of EAST pellet injector and indispensable diagnostics. Experimental observations and results are presented in the section 3. A summary and outlook is given in section 4.

2. Experimental setup

Experiments were performed on EAST(R=1.75 m, a=0.4 m, $V_{plasma} = 12\ m^3$), a non-circular superconducting advanced divertor tokamak with a strong auxiliary heating power (4 WM ICRF and 4 MW LHCD) in 2012 . With the cooperation of PELIN Laboratory in St Petersburg, a new pellet injection system has been successfully installed on EAST in 2011. The scheme of pellet injector was shown in Fig.1. The pellet injector which based on a screw extruder was developed by PELIN Laboratory [8]. It cooled by liquid helium and can produce a continuous hydrogen and deuterium rod of ice of rectangular cross section. An electromagnetic cutter provides repetitive pellet production from solid hydrogen rod at different frequencies, which are accelerated by a small gas puff （high purity helium） from a fast valve. The injector is capable of manufacturing and injecting numbers of pellets at a long time up to 100 s with reliability better than 99.6% during one round of tests. The main pellet parameters are as follow: pellet diameter and length are both 2 mm, and the pellet content is 3.78×10^{20} D atoms; the maximum injected frequency is 10 Hz, and pellet velocity is adjustable from 150 to 300 m /s. The flight tubes which in place to convey the pellets toward the plasma either from low field side or from high field side. And the length of LFS flight tube is nearly 4.5 m while the HFS flight tube is 9.5 m with minimum bend radius of the HFS guide tube up to 300 mm. An injection line was designed to connect the injector to the flight tubes. The injection line is able to pump the propellant gas effectively to make sure no influence to the vacuum of the plasma vessel during the long steady pellet injection.

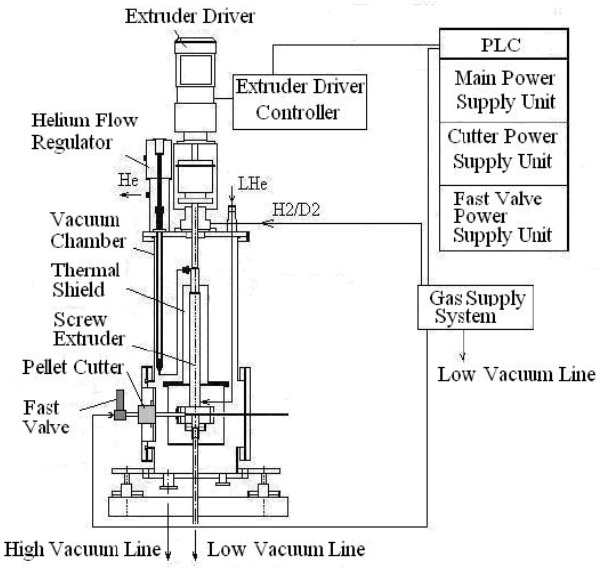

Fig.1 Schematic diagram of EAST pellet injector

Diagnostics in the pellet injection line helped measure pellet velocity and monitor completeness for each pellet. The pellet velocity was measured by two photodiodes in a distance and a CCD camera with high resolution was used for completeness checking of flying pellet. The process of producing hydrogen and deuterium rod was recorded and displayed by another set of CCD camera. Helpful diagnostics on EAST were needed during the experiments. A vertical 3-channel far-infrared (FIR) 337-μm hydrogen cyanide (HCN) laser interferometer to measure the line-averaged electron density. A 16-channel heterodyne electron cyclotron emission (ECE) to measure the profile of electron temperature, multi-channel soft X-ray arrays for intensity measurement, two sets of absolutely

extreme ultraviolet (AXUV) arrays to measure plasma radiation losses. Three thirty-five-channel Photo-diode (PDA) H_α/D_α cameras to measure distributions of H_α/D_α line radiation, and the PDA diagnostic refers to an array of discrete photodiodes. Layout of H_α/D_α arrays was shown in Fig.2. EAST soft x-ray imaging system can provide information on soft x-ray intensity which is determined by electron temperature, electron density and impurity content. Also two tangential visible couple charged device (CCD) cameras together with one tangential Infra Red CCD camera provide the opportunity to capture images of flying pellet in plasma [9].

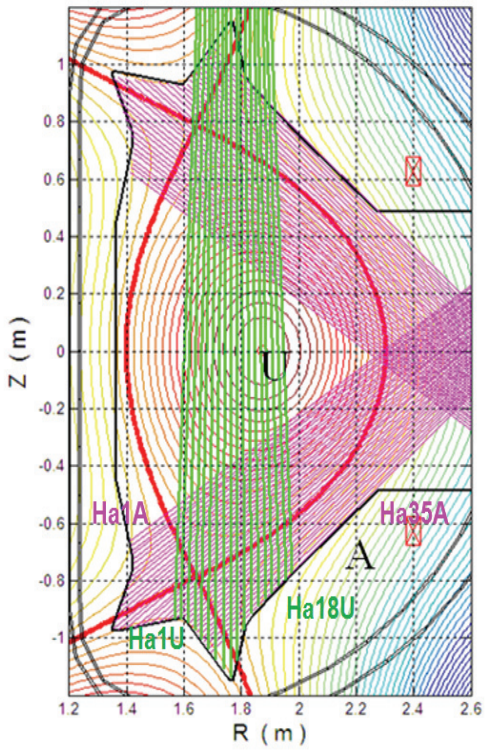

Fig.2 Layout of H_α/D_α arrays on East

3. Results

3.1 Influence of pellet fuelling on plasma

Generally, cold pellet could cause perturbation in hot plasmas after entering the plasma region from different injecting locations. While pellet flying in the plasma, the high temperature plasma forced pellet to be ablated and so called ablation cloud could be found. Accompanying the process of ablating, the plasma density increases, and in some cases, pellet injection can make the plasma density reach or even beyond Greenwald limit [10, 11]. On EAST, we could find that after pellet injection, obvious changes occurred in plasma include a sudden increase of the electron density, loop voltage and H_α/D_α emission; a significant decrease of plasma electron temperature and soft X-ray intensity. And also other impurity radiation such as CIII, OII become stronger. The typical phenomenon after pellet injecting into plasma on EAST was demonstrated in Fig.3. Pellet was injected at 3.0 s (inject time refers to the triggering signal controlled by PCS system to launch pellets) from HFS with a speed of 250 m/s. For this discharge, the plasma current(I_P)~400 KA, plasma electron density(n_e)~2.2×19 m^{-3}, the toroidal magnetic field (B_t)~2 T. Shortly after pellet injection, the n_e suddenly rose to ~3.4×19 m^{-3} own to pellet fuelling effect; the central electron temperature nearly decreased by one half and recovered more than 200 milliseconds later.

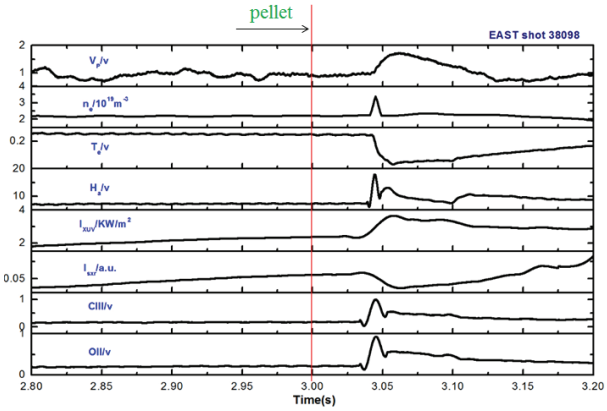

Fig.3 Typical change of plasma discharge (I_p~400 KA, n_e~2.2×19 m^{-3}, B_t~2 T) after pellet injected from HFS at 3.0 s on EAST.

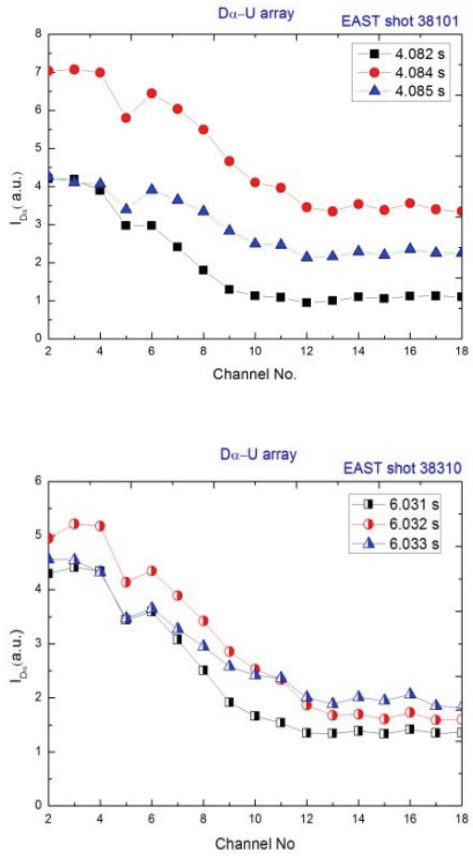

Fig.4 (a) EAST shot 38101with auxiliary heating power（P_{LHCD}~1.0 MW），I_p~400 KA ，B_t~2 T，n_e~2.3×19 m^{-3}; Pellet velocity was 257 m/s and injected at 4.0s from HFS; (b)EAST shot 38310 with auxiliary heating power（P_{LHCD}~1.1 MW），I_p~400 KA ，B_t~2 T，n_e~3.0×19 m^{-3}; Pellet velocity is 257 m/s and injected at 6.0s from LFS

The D_α profiles have been investigated to check out influences brought by injected pellets. D_α profiles derived from D_α-U arrays were shown in Fig.4. Pellets injected into plasma both from LFS and HFS, and the discharge condition was similar for each comparison. The I_P were both 400 KA and B_t were both 2 T for those two shots; the n_e was 2.3×19 m^{-3} for shot 38101and n_e was 3.0×19 m^{-3} for shot 38310. The initial pellet velocity was about 257 m/s for both pellet from HFS and LFS, and with auxiliary heating power (LHCD heating) 1.0 MW and 1.2 MW, respectively. Profiles of D_α-U showed that pellet from HFS caused a more significant D_α increase than that of LFS. For HFS pellet injection, the intensity of arrays which close to high field side have been nearly double increased, and for those arrays close to low field side, the intensity have been increased by several times. On the contrary, only the intensity of arrays close to low field side have been increased roughly by double for LFS pellet injection, the intensity of arrays which close to high field side had no significant increase. Inference can be made that pellet from HFS has injected into core plasma according to the layout of H_α/D_α arrays, while pellet from LFS cannot penetrate so deep to cause far-reaching perturbation to core plasma. From

Fig.4 (a), we found that pellet from HFS can penetrate into core plasma, and then it would spread to LFS in a short time. This might be caused by ∇B-induced drift effect, which has been investigated in other machines [11].

Investigation of plasma electron temperature influenced by pellet has also been done. The results were shown in Fig.5. For those four plasma, I_P~400 KA, B_t~2 T. And shot 38301，38308， 38097 with auxiliary heating power（P_{LHCD}~1.0 MW，P_{LHCD}~1.2 MW and P_{ICRF}~0.8 MW, respectively）. The last shot was ohmic discharges. Comparisons have been made between pellet from HFS (Fig.5(a) and (c)) and LFS (Fig.5(b) and (d)). Pellet injected from HFS caused larger reduction of plasma electron temperature and had a longer influenced time. This also might be explained by the core fuelling from HFS injection and the ∇B-induced drift effect [11]. And from shot 38097, core plasma electron temperature dropped even greater. It also provides evidence that pellet injected from HFS can achieve core fuelling. On the contrary, pellets from LFS cannot lead a significant plasma electron temperature decrease when compared to HFS injection.

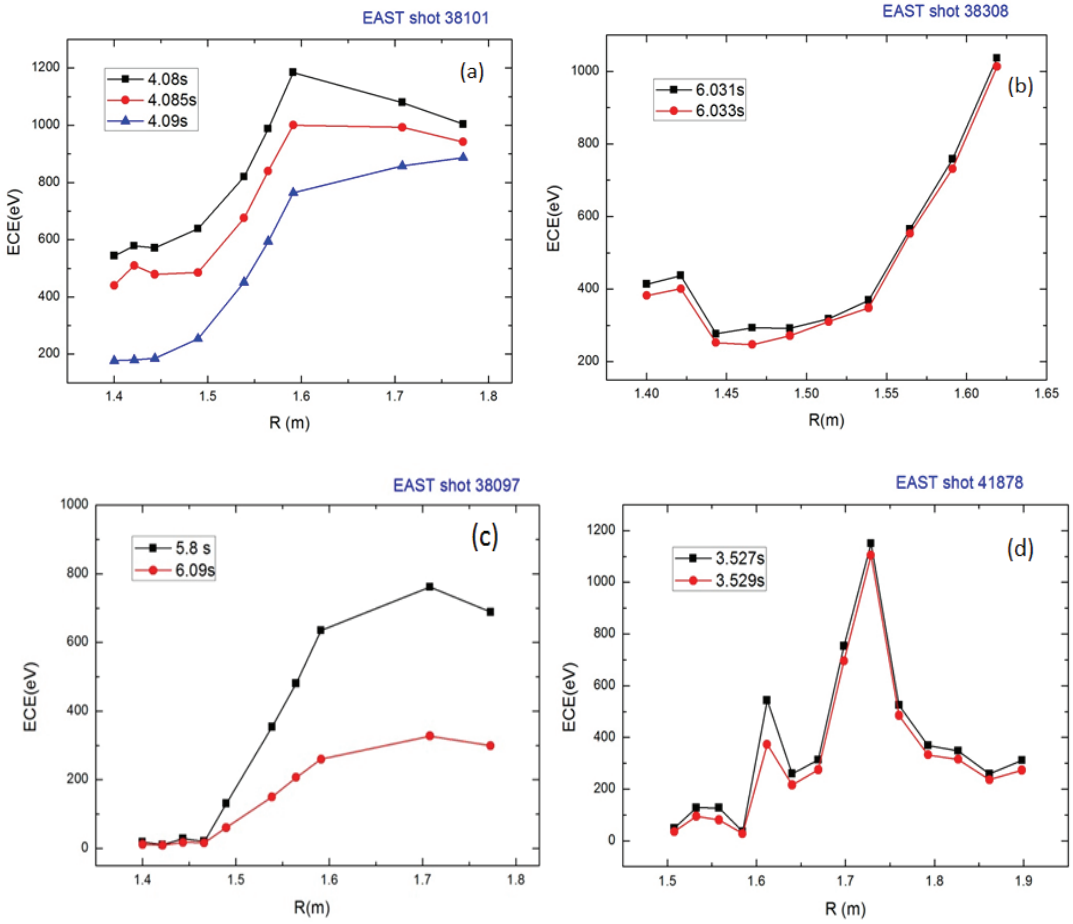

Fig.5 Results of ECE profiles. (a)EAST shot 38101with auxiliary heating power（P_{LHCD}~1.0 MW），I_p~400 KA ， B_t~2 T，n_e~2.3X19 m^{-3}; Pellet velocity was 257 m/s and injected at 4.0s from HFS; (b)EAST shot 38308 with auxiliary heating power（P_{LHCD}~1.2 MW），I_p~400 KA，n_e~3.0X19 m^{-3} ，B_t~2 T; pellet velocity was

215 m/s and injected at 6.0s from LFS; (c)EAST shot 38097 with auxiliary heating power (P_{ICRF}~800 KW), I_p~400 KA，B_t~2 T ,n_e~2.3×19 m^{-3}; pellet velocity was 257 m/s and injected at 6.0s from HFS; (d)EAST shot 41878 without auxiliary heating power, I_p~400 KA，B_t~2 T ,n_e~2.0×19 m^{-3}; pellet velocity was 257 m/s and injected at 3.5s from LFS

3.2 Pellet fuelling efficiency

Fuelling systems for EAST include gas puffing injection system, supersonic molecules beam injection system and pellet injection system. The latter two systems were newly developed and successfully tested on EAST last campaign. The gas puffing system has thirteen puffing ports, which distribute at LFS, HFS and divertor region (outer, inner and dome) [12]. The supersonic molecules beam injection system is based on a Laval nozzle, which will be reported later. Injected gas cooled at 80 K by liquid N_2. And maximum gas flux is 2.47× 1022 per second.

The fuelling efficiency η, is defined as $\eta=\Delta N_e/N_p$ [1], where N_p is the pellet particle content decided by the difference value between nominal particles of each pellet and the ablative pellet mass in the convey line while ΔN_e is the increase in plasma electron content determined by density increase measured with HCN laser interferometer. In our experiment and η calculation process, we presupposed the ablative rate in the convey line for each pellet was 5% for LFS injection while 15% for HFS injection. This calculated method was not so accurate because there was no implement such as microwave cavity to measure the pellet mass. However, rough results of fuelling efficiency can be obtained in this condition.

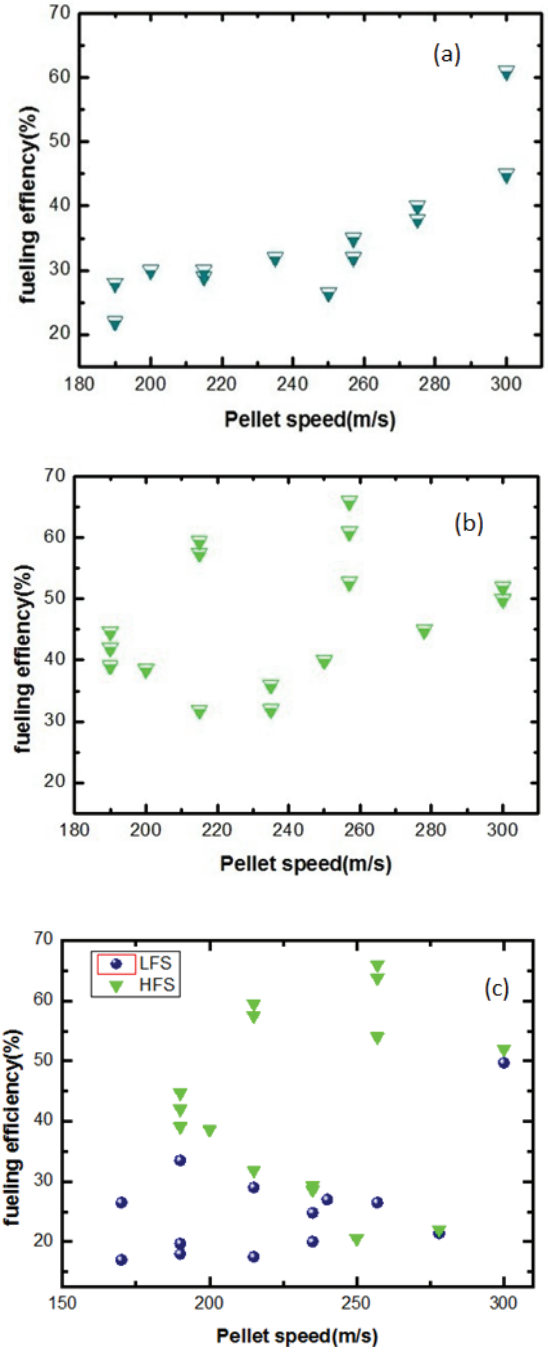

Fig. 6 (a) fuelling efficiency as a function of pellet

speed for LFS injection (b) fuelling efficiency as a function of pellet speed for HFS injection (c) comparison of fuelling efficiency between LFS and HFS injection due to different pellet speed

The calculated fuelling efficiency η as a function of the injection speed from different injection locations on EAST is presented in Fig.6. As shown in Fig.6, fuelling efficiency is a function of pellet injected speed both for HFS and LFS injection. The η for LFS injection was about 20%~40% while 30%~60% for HFS injection. The error limit might little high,~30%. The data given are all L-mode plasma fuelling.

Generally, in the same plasma discharge conditions, the higher the injected speed, the higher the efficiency obtained. That's because the higher speed caused higher penetration of injected pellet into plasma. And pellet injected from HFS lead to a higher efficiency than that from LFS during the almost same discharge conditions with the same injected speed. The main reason was properly pellet injected from LFS had a relative shallow penetration when compared with the pellet injected from HFS. Our results are similar with the previous experiments carried out at other machines. For example, on ASDEX Upgrade, compared to LFS injection, pellets injected from the HFS had a higher fuelling efficiency; the efficiency was enhanced by a factor of 4 and the depth of pellet penetration more than 2 times. Magnetic force pushed a diamagnetic plasma cloud towards LFS, caused rapid particle loss for shallow LFS injection, but enhanced fuelling efficiency and pellet penetration for HFS injection [13].

Comparison between PI , SMBI and GP demonstrated that higher fuelling efficiency can be achieved by PI. The efficiency of SMBI is about 15%~25%, while 18% for the GP (from HFS). However, it was found that fuelling efficiency of pellet injection on EAST is lower than that on other machines. Normally, in reference [14], three possible effects have been discussed for reduced fuelling efficiency. First, pellet is partially ablated in the scrape off layer (SOL) before it reaches the last closed flux surface or separatrix of the plasma. Another effect is that the expulsion of pellet ablatant from the plasma by outward drift effects on the ablatant as it propagates along the field lines. Such drift effects may be caused by an **E×B** drift that arises from a polarization of the ablatant cloud or from a pressure gradient-driven effect. The third effect that reduces the ideal fuelling efficiency is that of pellets triggering ELMs in H-mode plasmas, which then eject particles and energy from the edge barrier plasma. Those would help explain that on EAST, the fueling efficiency of pellet injection was relative lower. The first effect occurred because energetic particles in the SOL that impinges on the pellet [14]. And this effect was small for most pellet discharges on EAST as measured by D_α light emitted by the ablating pellet. However, for some pellet discharges, this effect reduced the fuelling efficiency. The second effect might also account for the low η for LFS injection on

EAST. The third effect seems not the dominated reason for low η because ELM-like event induced by pellet only occurred in very few discharges during last campaign, and would be described later. On the other hand, for both LFS and HFS injection, the ablative rate for each pellet might much higher than our assumption (5% for LFS and 15% for HFS). Especially for HFS injection, pellet would lose quite part of the mass when flying through the curved convey tube, the ablative rate might much higher than 15%. However, all these possible reasons should be verified with more and helpful diagnostics dedicated for PI on the convey line and also on the EAST.

3.3 ELM trigger attempts

Edge localized modes (ELMs) are instabilities typical for H-mode scenarios that result in large quasi-periodic heat and particle flows to the first wall and divertor target plates. The corresponding heat load is high enough to lead potentially to an important erosion of these plasma facing components (PFCs), this negative effect has become a significant consideration for ITER operation [11]. Pellet injection is a representative technique to mitigate type-I ELM energy loss along with ELM suppression techniques such as RMP [15]. According to the empirical formula $W_{ELM} \times f_{ELM}$=constant, the ELM energy W_{ELM} is reduced by raising the ELM frequency f_{ELM} [16]. Successful ELM pacing and mitigation by the injection of cryogenic deuterium pellets was demonstrated first at ASDEX Upgrade and also achieved on JET, etc [3-6]. Those experimental results indicated that pellet injection as a promising technique for ELM control is feasible, not only for mid-sized machines but also for larger ones such like JET and ITER.

On one hand, H-mode operation had been achieved for the first time on EAST during 2010 campaign, and stationary H-mode up to 32 seconds has been obtained during last campaign. Now, H-mode operation can be achieved flexibly driven by lower hybrid current drive or ion cyclotron heating on EAST. Giant type-I ELM and typical type-III ELMs were found and caused considerable power loads and heat flux on divertor targets. On the other hand, EAST tokamak has the similar structure and first wall condition with ITER (ITER will operate with a full tungsten first wall and it is also the second phrase for EAST PFCs strategy); it is believed that the ELM control experiments on EAST will definitely provide some useful and meaningful data and experience for ITER H-mode operation in future. In this case, even though the present pellet injection system was not designed for ELM control due to little big pellet size and relative small injection frequency, it was also worthy to test and find appropriate parameters of pellet for ELMs control. And it would be beneficial for the design of a pellet injector dedicated for ELMs control. The test on EAST showed that the present pellet can trigger ELMs if appropriate parameters (injected speed and location) were chosen.

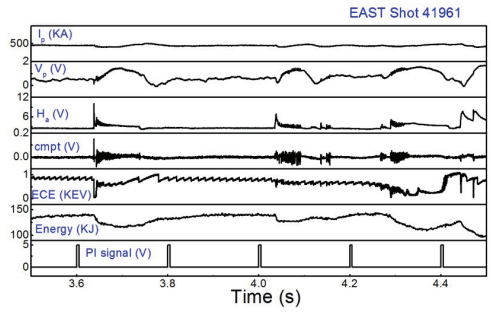

Fig. 7 ELMs triggered by pellets injected at 5 Hz from LFS; B_t~2 T，I_p ~500 KA；auxiliary heating power（LHCD~1.2 MW; ICRF~1.1 MW）

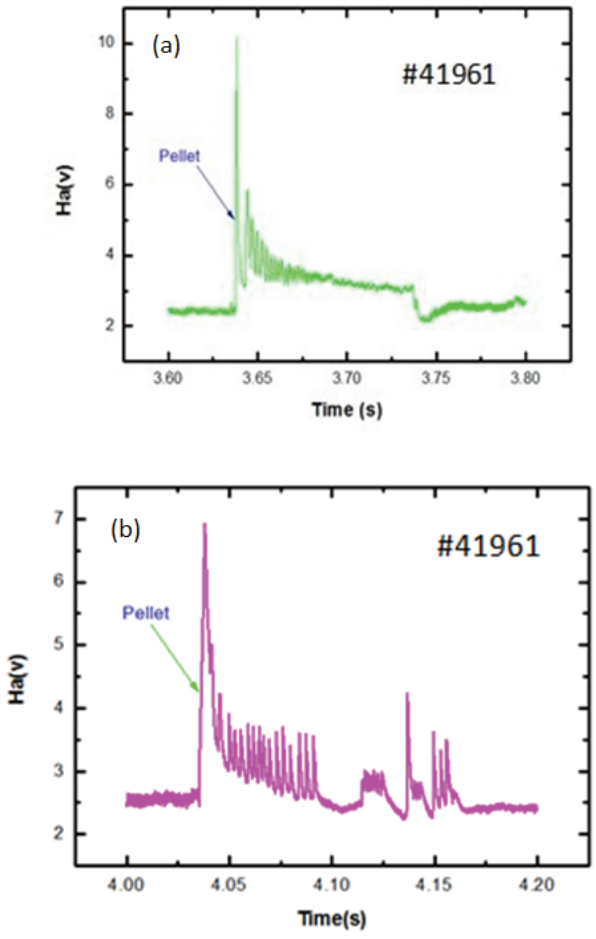

Fig. 8 Enlarged view of triggered ELMS. (a) Pellet injected at 3.6 s, V_p=170 m/s; f_{ELMs}~300Hz, (b) Pellet injected at 4.0 s, V_p=170 m/s; f_{ELMs}~300Hz

During ELM trigger experiments, the initial plasma density before PI was ne~3.2X19 m-3 with Bt~2 T, Ip~500 KA, and plasma heating power was P_{LHCD}~1.2 MW, P_{ICRF}~1.1 MW. Two groups of experiments have been carried out, one for LFS injection and another for HFS injection. To get suitable injection speed for ELMs control, for each group, pellet launch speed was changed for each shot. Injected speed was scanned from 150 m/s and gradually increased to 300 m/s, and the interval for the scans was 20 m/s. Fortunately, triggered ELMs have been observed during pellet injected from LFS with a speed of 170 m/s and an injecting frequency of 5 Hz, as shown in Fig.7 and in Fig. 8. The density given in Fig.7 refers to core plasma density. The pellets fired at a low speed from LFS might penetrate not so deep, and cause no significant density increase in the core plasma.

In this shot, pellet was launched from 3.6 s. Before pellet arriving, it was an ELM-free H-mode discharge. After the first pellet injected into the targeted plasma, ELMs with a high frequency were successfully triggered. In this plasma，two of the five pellets (pellets fired at 3.6s and 4.0s) have successfully triggered ELMs, and frequency of the two triggered ELMs were both nearly to 300 Hz.

Compelling results were obtained in this set of triggering experiments. However, as mentioned at the beginning，the primary purpose of present injection system was fuelling. The ELMs trigger only obtained while injected at a low speed. Actually, the physics of

ELM triggering mechanism has not been completely understood so far due to technical restrictions and the complexity of ELM generation processes [17]. Investigations on present tokamaks revealed that pellets used for triggering ELM should be small to avoid fuelling effect. Meanwhile, minimum pellet size and penetration were required to establish a sufficient perturbation for the triggering [6]. The ELMs cannot be triggered at any time as we want. The main reason may be the present pellet is oversized. So fuelling effect was unavoidable for most of the shots, except the pellet was broken to smaller fragment during convey process. Another possible explanation for the results presented above is that large pellets with lower launch speed cannot penetrate deep and sometimes affect the pedestal parameters such that a small rapid ELM regime is entered for a brief time. Pellets injected from high field side cannot trigger ELMs during experiments may because of present pellets penetrate far beyond the ELMing region because of pellet size and speed on EAST. A new pellet injection system with high frequency and small pellet size should be developed dedicated for ELMs control.

4. Summary and outlook

A repetitive pellet injection system has been successfully installed on EAST. And some primary results were obtained during 2012 campaign. Typical phenomena of pellet injected into plasma discharge were observed, and influences for D_α, plasma electron temperature were also been investigated. A comparison of fuelling efficiency has been done with different pellet injecting speeds, and a comparison with injecting from different locations also has been made. It was found that the higher injecting speed, the higher fuelling efficiency was obtained. And the result also showed that pellet injected from high filed side caused a higher efficiency than that from low field side with the approximate same discharge conditions at the same injected speed. And we also found that the fuelling efficiency was much higher than GP and SMBI. ELMs trigger experiments have also been tested on EAST last campaign. And high frequency ELMs has been triggered at particular situation while pellets injected from low field side. The reason why pellet injected from high field side failed to trigger ELMs may be the penetration far beyond ELMing region but further investigations are needed.

One future plan for pellet injection on EAST is to improve diagnostics of our system. For example, a resonant microwave cavity to measure pellet mass is needed in order to gain a more precise fuelling efficiency. Another plan is to install curved tubes from vertical direction on EAST, to examine vertical injection and to compare with results from other devices. Results on DIII-D showed that vertical injection of pellets inside the magnetic axis had an increased penetration and fuelling efficiency when compare that for LFS injection. And pellets from vertical HFS injection have high speed which can be injected deep into large plasma while inner wall

injection will always limit the pellet speed [2]. On the other hand, development of another set of pellet injection system with smaller pellet size and higher inject frequency which aims for ELMs control is under consideration.

Acknowledgements

This research is funded by National Magnetic confinement Fusion Science Programs under Contracts No.2013GB114004, 2011GB107000 and the National Nature Science Foundation of China under Contract No. 11075185. We gratefully acknowledge the support and assistance from the EAST operation group and diagnostic group.

REFERENCES

[1] L.R. Baylor, T.C. Jernigan, P.B. Parks et al. 2007, Nucl. Fusion, 47: 1598

[2]L.R. Baylor, T.C. Jernigan, R.J Colchin et al. 2001, J. Nucl. Mater., 290~293: 398

[3]P.T. Lang, J. Neuhauser, L.D. Horton et al. 2003, Nucl. Fusion, 43: 1110

[4]P.T. Lang, G.D. Conway, T. Eich et al. 2004, Nucl. Fusion, 44: 665

[5]P.T. Lang, B. Alper, R. Buttery et al. 2007, Nucl. Fusion, 47: 754

[6]P.T. Lang, A. Alonso, B. Alper et al. 2011, Nucl. Fusion, 51 033010

[7] J. S. Hu, J. G. Li, Y.P. Zhao et al. 2008, J. Nucl. Mater., 376:207

[8]I. Vinyar. Hydrogen/Deuterium Ice Pellet Injector PI-20 for EAST Tokamak [M]. Saint Petersburg Russia: PELIN LLC, 2011

[9]L. Q. Hu , et al. 2011, Plasma Sci. and Technol., 13:1

[10 P.T. Lang, J. Gafert, O. Gruber et al. 2000, Nucl. Fusion, 40: 2

[11]B Pégourié. 2007, Plasma Phys. Control. Fusion., 49:R87

[12]J. S. Hu, X. M. Wang, J.H. Li et al. 2009, Fusion Eng. Des., 84:2167

[13] P.T. Lang, K. Büchl, M. Kaufmann, et al. 1997, Phys Rev Lett., 79: 1487

[14] L.R. Baylor, T.C. Jernigan, C.J. Lasnier et al. 1999, J. Nucl. Mater., 266~269: 457

[15] Ki Min Kim, Yong-Su Na, Sumin Yi, et al. 2011, Nucl. Fusion, 51/063003

[16] A Herrmann. 2002, Plasma Phys. Control. Fusion., 44:883

[17] L.R. Baylor, P. B. Parks, T.C. Jernigan et al. 2007, Nucl. Fusion, 47:443

A problem to be solved for tungsten diagnostics through EUV spectroscopy in fusion devices

S.Morita[1, 2], I.Murakami[1, 2], H.A.Sakaue[1], C.F.Dong[1], M.Goto[1, 2], D.Kato[1], T.Oishi[1, 2], X.L.Huang[2] and E.H.Wang[2]

[1] National Institute for Fusion Science, Toki 509-5292, Gifu, Japan

[2] Department of Fusion Science, Graduate University for Advanced Studies, Toki 509-5292, Gifu, Japan

Abstract: Tungsten spectra have been observed from Large Helical Device (LHD) in extreme ultraviolet (EUV) wavelength ranges of 10-650Å. When the electron temperature is less than 2keV, the EUV spectra from plasma core are dominated by unresolved transition array (UTA) composing of a lot of spectral lines, e.g., 6g-4f, 5g-4f, 5f-4d and 5p-4d transitions for $W^{+24-+33}$ in 15-35Å. In order to understand the UTA spectrum, the EUV spectra measured from LHD plasmas are compared to those measured from Compact electron Beam Ion Trap (CoBIT), in which the electron beam is operated with monoenergetic energy of $E_e \leq 2$keV. The tungsten spectra from LHD are well analyzed based on the knowledge from CoBIT tungsten spectra. The collisional-radiative (C-R) model has been developed to explain the UTA spectra from LHD in details. Radial profiles of EUV spectra from highly ionized tungsten ions have been measured and analyzed by impurity transport simulation code with ADPAK atomic database to examine the ionization balance determined by ionization and recombination rate coefficients. If the electron temperature is higher than 2keV, Zn-like WXLV (W^{44+}) and Cu-like WXLVI (W^{45+}) spectra can be observed in LHD. Such ions of W^{44+} and W^{45+} can exhibit much simpler atomic configuration compared to other ionization stages of tungsten. Quantitative analysis of the tungsten density is attempted for the first time on the radial profile of Zn-like WXLV (W^{44+}) 4p-4s transition measured at 60.9Å, based on the emission rate coefficient calculated with HULLAC code. As a result, a total tungsten ion density of $3.5 \times 10^{10} cm^{-3}$ at the plasma center of LHD is reasonably obtained. Finally, the present problem for tungsten diagnostics in fusion plasmas is summarized.

1. Introduction

Recently, tungsten spectra have been widely studied in fusion research because the tungsten was adopted as divertor material of ITER instead of carbon which has been used for most of fusion devices [1-3]. At present, however, atomic data on the tungsten necessary for the impurity transport study are entirely insufficient [4-6]. The tungsten spectroscopy has been also started in Large Helical Device (LHD) by injecting carbon pellet included a small amount of tungsten [7].

Many tungsten line emissions have been measured so far from high-temperature tokamak plasmas in different wavelength ranges of EUV to visible light. At least, however, the spectral line which has been used for the plasma diagnostics is basically only one neutral tungsten line emitted at 4009Å [7]. Since the

tungsten line at 4009Å is well isolated from other lines and the line intensity is not so weak, it has been frequently used for studying the plasma wall interaction [8]. However, any quantitative analysis has not been done on the tungsten diagnostics in the plasma edge in addition to the plasma core. Then, a problem in studying the tungsten transport of fusion plasmas is summarized in the present paper.

2. Ionization energy of tungsten ions

Figure 1 shows the ionization energy of tungsten ions as a function of the charge state [9]. The electron temperature range in NBI discharges of LHD is indicated with gray hatched region. The highest charge state of tungsten ions which can be observed from LHD plasmas is probably Ni-like W^{46+}. Since the central temperature of ITER is very high as indicated with gray striped region, the atomic configuration of partially L-shell-ionized tungsten ions in the plasma core is simple and the impurity diagnostics using such ions is relatively easier. However, the partially N- and O-shell-ionized tungsten ions existing in the edge plasma of ITER still have many electrons in the bound orbit forming complicated atomic structure. The spectroscopic study of tungsten ions in LHD can give the information on such ions for the edge plasma diagnostics of ITER.

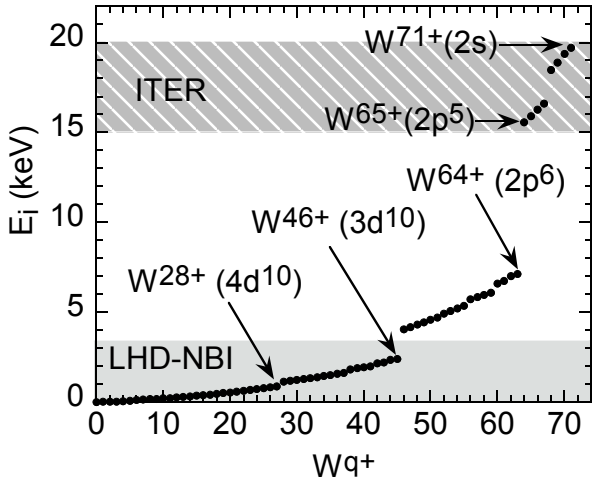

Fig.1 Ionization energy of W ions with charge state of q^+. Hatched and striped areas indicate electron temperature ranges at $T_e=E_i$ for NBI discharges in LHD and typical discharges in ITER, respectively.

The energy level among sublevels is illustrated in Fig.2 (a). In the impurity diagnostics the electric dipole transition as the resonance transition is usually measured for the impurity diagnostics of fusion plasmas due to the simple configuration. Then, the ionic sequence with one or two electrons in the outside bound orbit has been used for the diagnostics, i.e., H- or He-like, Li- or Be-like, Na- or Mg-like and so on. Looking at Fig. 2 (a) Pr- (W^{15+}) or Ce-like (W^{16+}) ions are also the good candidate for tungsten diagnostics. However, the ionization energies in such ions of W^{15+} and W^{16+} are entirely overlapped with those in partially 4f-subshell-ionized ions of W^{12+} and W^{27+}. The spectra from Pr- and Ce-like ions are not therefore simple due to the presence of several electrons in the outside bound orbit. The possible candidate for measuring the resonance transition in simpler ionic sequences is to use Zn- (W^{44+}) or Cu-like (W^{45+}) ions

for tungsten diagnostics. The 4p-4s resonance transition for such two ions illustrated in Fig.2 (b) becomes quite simpler compared to transitions for other ionization stages. Here, it should be noticed that the production of the W^{44+} and W^{45+} ions needs a relatively high electron temperature discharge as estimated from Fig.1.

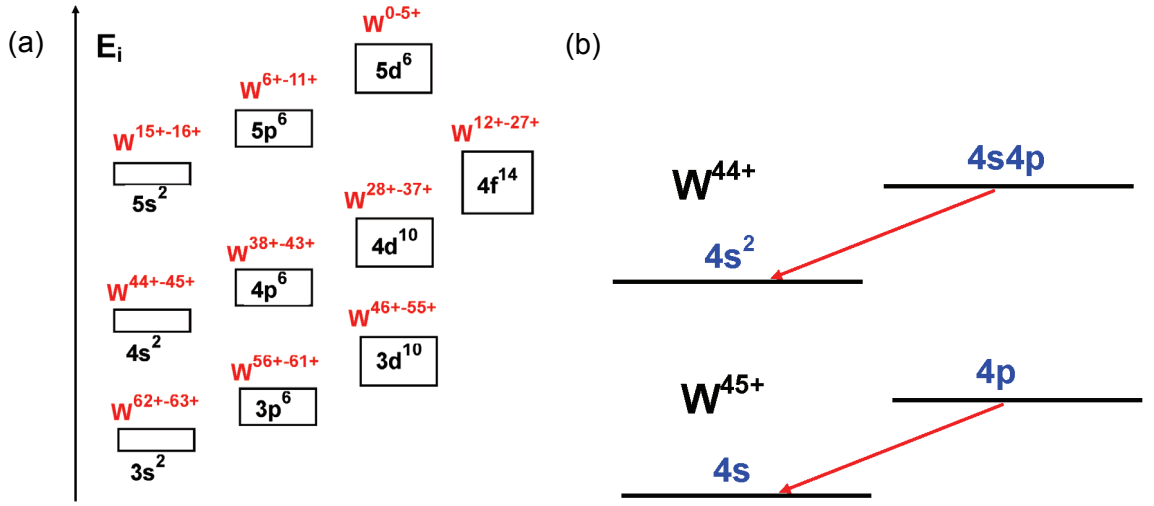

Fig.2 (a) Ionization levels of tungsten among sublevels and (b) 4p-4s resonance transitions for Zn-like W^{44+} and Cu-like W^{45+} ions. The ionization level of '4f' sublevel is overlapped with that of '5s' sublevel.

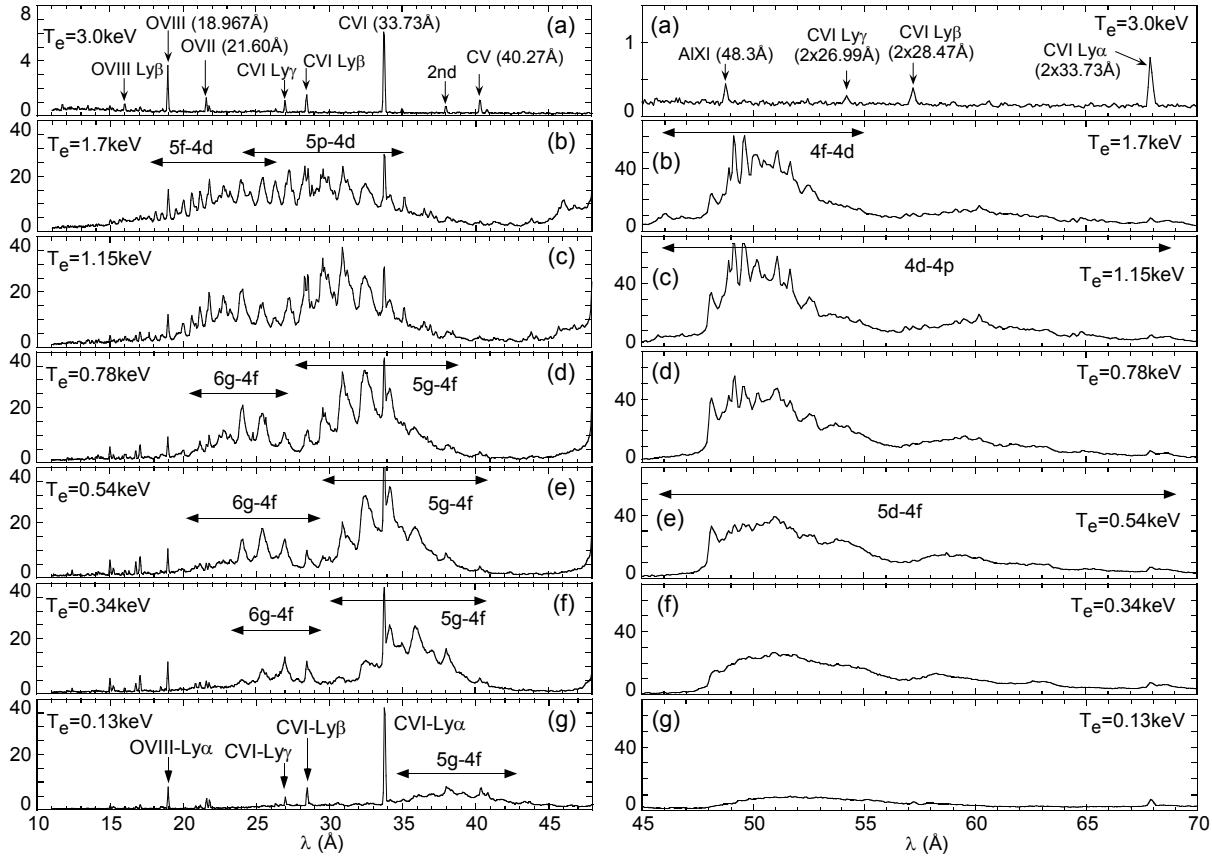

Fig.3 (a) LHD tungsten EUV spectra at 10-45Å (left) with 6g-4f, 5g-4f, 5f-4d and 5g-4f transitions in different electron temperatures of (b) 1.7keV, (c) 1.15keV, (d) 0.78keV, (e) 0.54keV, (f) 0.34keV and (g) 0.13keV and at 45-70Å (right) with 4f-4d, 4d-4p and 5d-4f transitions in different electron temperatures of (b)

1.7keV, (c) 1.15keV, (d) 0.78keV, (e) 0.54keV, (f) 0.34keV and (g) 0.13keV observed after carbon pellet injection with tungsten. Reference spectrum at T_e=3.0keV before pellet injection is plotted in (a). The 5d-4f transitions from W^{17+}-W^{27+} ions in 45-70Å interval are appeared at relatively low temperature range.

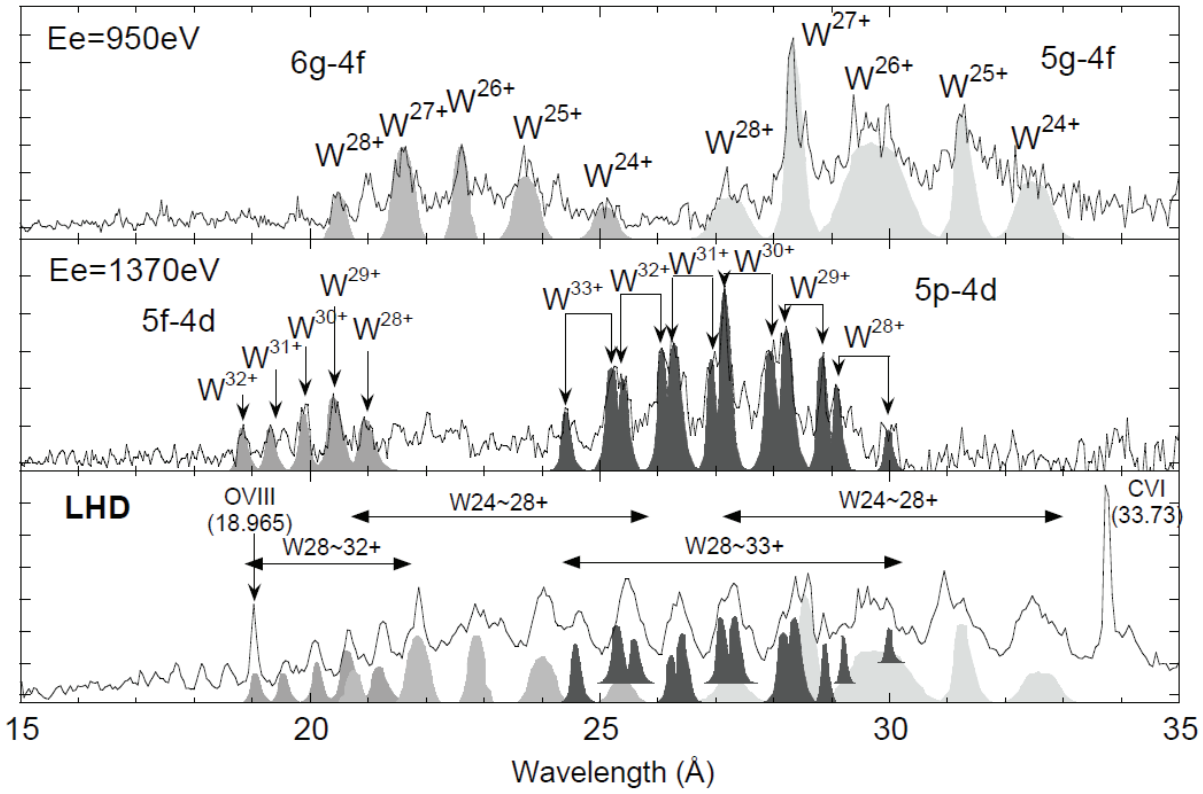

Fig.4 CoBIT tungsten EUV spectra with electron beam energies of (a) 950eV and (b) 1370eV, and (c) comparison between LHD EUV spectrum and composed spectrum of 6g-4f, 5g-4f, 5f-4d, 5p-4d transitions analyzed by HULLAC code against CoBIT spectra of (a) and (b).

3. EUV spectra from tungsten ions with lower ionization stages in LHD

A cylindrical carbon pellet ($1.2mm^{\phi}\times1.2mm^{L}$) with a small amount of tungsten enclosed in a narrow hole [10] is injected in NBI discharges to observe the tungsten spectra. The tungsten spectra measured from LHD using EUV spectrometers [11,12] are plotted in Fig.3 as a parameter of central electron temperature at two different wavelength ranges of 10-45Å (left) and 45-70Å (right). The EUV spectrum is recorded with sampling time of 5ms and a few frames are summed up for the plots. Several tungsten lines in such wavelength ranges have been already identified as earlier works [13]. The spectra observed before the pellet injection shown in Fig.3 (a) indicate He- and H-like emissions from intrinsic impurities of carbon and oxygen. The wavelength of tungsten emissions is determined using these lines. Since the Al pellet is injected in previous discharges, AlXI line is seen at 48.3Å.

The unresolved transition array (UTA) seen in Fig.3 (left) consists of the following transitions at various ionization stages of tungsten ions;

(1) 6g-4f (20-40Å) and 5g-4f (20-45Å)

transitions for $4s^24p^64d^{10}4f^q$ configurations

(2) 5f-4d (18-30Å) and 5p-4d (20-45Å) transitions for $4s^24p^64d^q$ configurations.

The shape of UTA changes with electron temperature because the radial location of tungsten ions also changes as a function of electron temperature. The transition array moves to longer wavelength side with decreasing electron temperature. It means that the tungsten emission from lower ionization stages exists in longer wavelength side, while the identification of each spectral line is entirely difficult due to the formation of UTA.

Similar UTA is also seen in Fig.3 (right), which consists of the following transitions;

(1) 4f-4d (45-55Å) and 4d-4p (45-70Å) transitions for $4s^24p^q4d^r4f^s$ configurations in W^{17+}-W^{43+} ions.

(2) 5d-4f (45-70Å) transitions for $4s^24p^64d^q4f^r$ configurations in W^{17+}-W^{27+} ions.

In order to analyze the UTA in 15-35Å the tungsten spectra are observed from CoBIT [14] working in NIFS. The EUV spectra from tungsten ions are shown in Figs.4 (a) and (b), which are observed at electron beam energies of 950 and 1370eV, respectively. The UTA are analyzed using HULLAC code with the presence of monoenergetic electrons. The results are also plotted in the same figures for the comparison. The EUV spectra observed from CoBIT are well explained by the present analysis with four transitions of 6g-4f, 5f-4d, 5f-4d and 5p-4d. The four transitions obtained from HULLAC code are compared with the LHD spectrum, as shown in Fig.4 (c). The contribution of each transition to the LHD spectrum is distinct, when the CoBIT spectra are used for the analysis on the LHD spectrum. We thus understand that the EBIT/CoBIT data are very useful for spectral analysis of high-Z elements in the fusion plasma.

The modeling of EUV spectra from highly ionized tungsten has been also developed in NIFS [15]. At present, the collisional-radiative (CR) model is constructed for tungsten ions (W^{q+}) with ionization stages of q=20 to 45, considering parameter range of LHD. Atomic data are calculated by HULLAC code under Maxwellian electron velocity distribution. In the present modeling the excited fine structure levels up to n=6 ($l \leq 5$) are considered, while the recombination process is not included. Therefore, the level population of 2,000-26,000 sublevels is examined for one ion.

4. Quantitative analysis of Zn-like (W^{44+}) tungsten

The Zn-like (W^{44+}) tungsten spectrum can be observed at 60.9Å if the electron temperature is higher than 2.3 keV, as shown in Figs.5 (a) - (e). The Zn-like tungsten is emitted with strong intensity in the range of $2.3 \leq T_e \leq 3.2$keV, but it begins to disappear when the electron temperature increases above 3.2keV, since the W^{44+} ion moves to outer side of the LHD plasma. The Zn-like tungsten at 60.9Å is a little blended with other lines at the shorter and longer wavelength sides. Ga-like tungsten (W^{43+}) exists at 60.5Å in shorter wavelength side of Zn-like tungsten. In the longer

wavelength side Ge-like (W^{42+}) and Ga-like (W^{43+}) tungsten also exist at 61.3Å. The detailed spectral structure near Zn-like tungsten [16] observed at T_e=2.90keV is shown in Fig.5 (f).

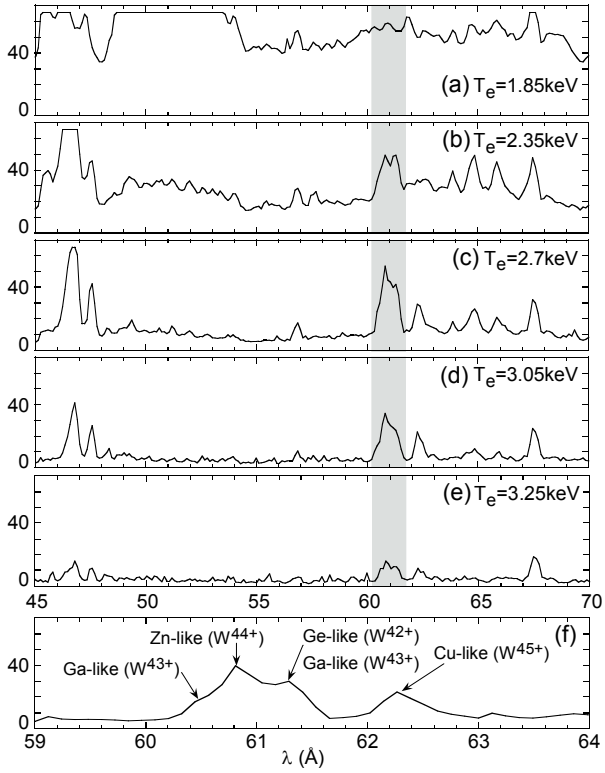

Fig.5 EUV spectra from Zn-like (W^{44+}: 60.9Å) tungsten ions at different electron temperatures of (a) 1.85keV, (b) 2.35keV, (c) 2.7keV, (d) 3.05keV and (e) 3.25keV. Hatched area indicates the vicinity of the Zn-like tungsten. Enlarged spectrum at T_e=2.90keV near Zn-like tungsten is plotted in (f).

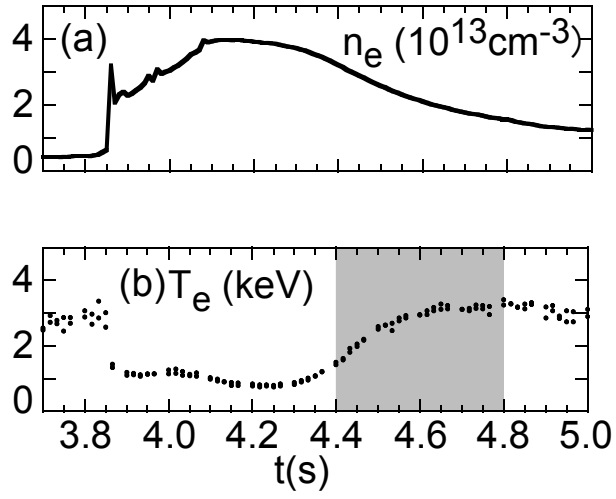

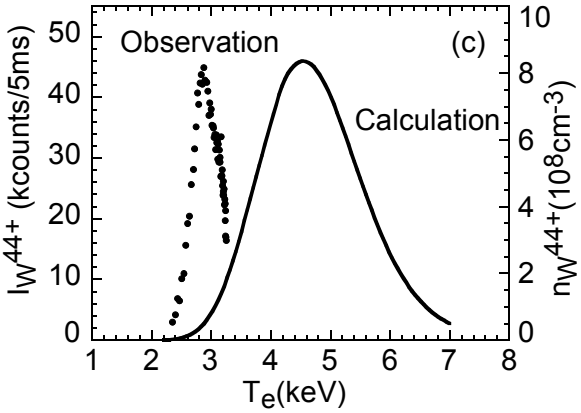

Fig.6 Waveforms of (a) electron density and (b) temperature after injection of cylindrical carbon pellet (1.2mm$^{\phi}$×1.2mm^{L}) with tungsten in LHD and (c) temperature dependence of Zn-like (W^{44+}) 4p-4s transition at 60.9Å (observation: solid circles and impurity transport calculation: solid line). The pellet is injected at 3.85s in NBI discharge and Zn-like tungsten is analyzed for 4.4-4.8s indicated with hatched area.

In order to examine the accuracy of the rate coefficients used in the impurity transport code the intensity of Zn-like tungsten is analyzed against the electron temperature using the temperature recovery phase after injection of the carbon pellet with tungsten. Electron density and temperature behavior after the impurity pellet injection is shown in Figs.6 (a) and (b), respectively. The density rise, Δn_e, after injection of tungsten-enclosed carbon pellet with size of 12.mm$^{\phi}$×1.2mm^{L} is Δn_e=2x10^{13}cm^{-3}, whereas the density rise is expected to be Δn_e=3x10^{13}cm^{-3} if all the particles of the pellet are fully confined in the plasma. The gradual increase in the density after the pellet injection from 3.87s to 4.07s is due to the change in the edge particle transport. When the edge temperature decreases in LHD, the edge particle confinement

increases because of the reduced particle screening in the edge stochastic magnetic field layer [17, 18]. After 0.45s from the pellet injection the electron temperature begins to recover since the electron density decreases. Although the density of tungsten ions after the pellet injection is not exactly known, at least, it gradually decreases as a function of time because the impurity confinement time roughly ranges in 0.2-1.0s at the plasma center.

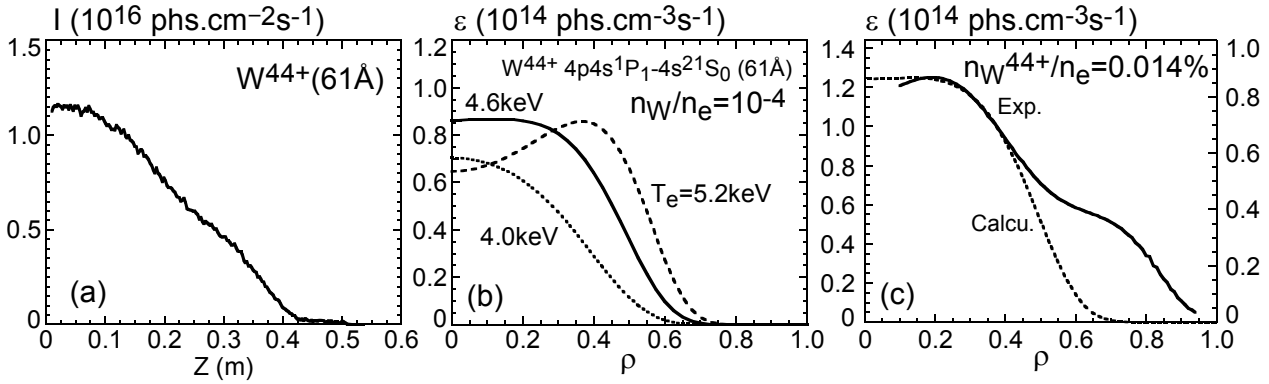

Fig.7 Observed vertical intensity profile and (b) calculated local emissivity profile of Zn-like (W^{44+}: 60.9Å) 4p-4s transition and (c) determination of W^{44+} ion density. The calculated local emissivity profile at T_e=4.6keV is used for the fitting to observed local emissivity profile.

The intensity of Zn-like tungsten is analyzed for the electron temperature recovery phase indicated with hatched area in Fig.6 (b). The result is plotted with solid circles in Fig.6 (c) as a function of central electron temperature. The Zn-like tungsten intensity evaluated from the present discharge takes the maximum value at T_e=2.8keV as a sharp function of electron temperature. The density of Zn-like tungsten calculated at the plasma center is also plotted in Fig.6 (c) with solid line. The electron temperature at which the n_W^{44+} takes the maximum is 4.5keV in the present impurity transport code. A large difference is clearly seen between the observation and the calculation. The reason definitely originates in a discrepancy in the ionization and recombination rate coefficients. The discrepancy of the rate coefficients from ADPAK code is studied for several ionization stages of tungsten [5]. The present result shows a similar tendency to the previous result, that is, the recombination rate of ADPAK is small compared to the experiment for Zn-like tungsten. However, several data from other ionization stages of tungsten are necessary to improve the impurity transport code by comparing the data between the present and previous results quantitatively.

Radial intensity profile of Zn-like tungsten with 4p-4s transition at 60.9Å has been measured using a space-resolved EUV spectrometer in LHD [19]. The absolute sensitivity of the spectrometer is accurately determined using bremsstrahlung continuum from LHD [20]. A typical result is shown in Fig.7 (a). The centrally peaked profile indicates the Zn-like tungsten ion exists in the plasma center. In order to compare

with the impurity transport calculation, the chord-integrated vertical profile of Zn-like tungsten in Fig.7 (a) is reconstructed to the local emissivity profile using Abel inversion technique. The resultant profile plotted in Fig.7 (c) with solid line seems to have two components. It is probably an effect of the line blending with tungsten emission from ions in lower ionization stage. We need further examination on the Zn-like tungsten spectrum to conclude the true reason.

We calculate the emission coefficient of 4p-4s transition for the Zn-like tungsten based on HULLAC code. The radial emissivity profile of Zn-like tungsten is also calculated with different electron temperatures, as seen in Fig.7 (b). The emission location moves from the central region to the outside of plasma when the central electron temperature increases. In this calculation the tungsten ion density integrated along the whole plasma volume is assumed to be 10^{-4} to the electron density. In order to determine the tungsten density the measured local emissivity profile in Fig.7 (c) is compared with the transport calculation. The best fitting to the measured profile is obtained at T_e=4.6keV, as shown in Fig.7 (c) with dotted line. Of course, the temperature used in the present analysis is much different from the real temperature (T_e=2.8keV) because of the uncertainty of recombination rate. From this analysis the n_W^{44+} is estimated to be 1.4×10^{-4} to the electron density of 4×10^{13}cm^{-3} at the plasma center. The total tungsten density in the plasma center can be then evaluated from n_W^{44+} to be 3.5×10^{10}cm^{-3} ($n_W/n_e=8.8\times10^{-4}$). The total radiation loss, P_{rad}, is calculated with average ion model [21, 22] using the present tungsten density. We roughly estimate the value as P_{rad}=4MW. Since the measured P_{rad} in the present discharge ranges in 3-4MW after the tungsten pellet injection, the estimated P_{rad} from the present analysis seems to be reasonable.

5. Summary

Tungsten spectra in EUV wavelength range have been studied in LHD with radial distribution. Several problems are pointed out through the present study in addition to the previous works carried out in tokamaks if we study the impurity transport of tungsten ions. The subjects to be solved for the tungsten diagnostics are summarized in the following.

1. In relatively low-temperature range ($T_e\leq$2keV) the EUV spectrum from tungsten is very complicated due to the appearance of UTA, which is not easy to analyze.

2. Collisional-radiative model has to be constructed to analyze the UTA structure.

3. A quantitative analysis of tungsten is possible in high-temperature range (T_e>2keV) when Zn-like (W^{44+}) or Cu-like (W^{45+}) ions are measured.

4. At present the tungsten transport study is entirely difficult due to a large uncertainty of the recombination rate.

5. Accuracy of the recombination rate has to be increased in addition to the wavelength.

6. The use of magnetic dipole transition (M1) is

alternative method to diagnose the tungsten ions by finding the good M1 line in visible or VUV range [23].

Acknowledgments

The authors wish to thank the LHD experiment team for their cooperation. This work was partially carried out under the LHD project financial support (NIFS12ULPP010). This work was partly supported by JSPS KAKENHI Grant Number 23340183 and the JSPS-NRF-NSFC A3 Foresight Program in the field of Plasma Physics (NSFC: No.11261140328).

References

[1] R.Stambaugh et al., Nucl. Fusion **39** (1999) 2391.

[2] R.Neu, R.Dux, A.Kallenbach, et al., Nucl. Fusion **45** (2005) 209.

[3] J.Roth, E.Tsitrone, T.Loarer et al., Plasma Phys. Control. Fusion **50** (2008) 103001.

[4] K.Asmussen, K.B.Fournier, J.M.Laming et al., Nucl. Fusion **38** (1998) 967.

[5] T.Putterich, R.Neu, R.Dux et al., Plasma Phys. Control. Fusion **50** (2008) 085016.

[6] J.Yanagibayashi, T.Nakano, A.Iwamae et al., J.Phys.B **43** (2010) 144013.

[7] S.Morita, C.F.Dong, M.Goto et al., to be published in AIP Conference Proceedings on 8th ICAMDATA, Gaithersburg (USA), 30 Sep. - 4 Oct. 2012.

[8] A.Thoma, K.Asmussen, R.Dux, et al., Phys. Control. Fusion **39** (1977) 1487.

[9] A.E.Kramida and T.Shirai Atomic Data Nucl. Data Tables **95** (2009) 305.

[10] R.Katai, S.Morita, M.Goto et al., Jpn. Soc. Appl. Phys. **46** (2007) 3667.

[11] M.B.Chowdhuri, S.Morita, M.Goto, et al., Rev.Sci.Instrum. **78** (2007) 023501.

[12] M.B.Chowdhuri, S.Morita and M.Goto Appl.Optics **47** (2008) 135.

[13] M.B.Chowdhuri, S.Morita and M.Goto Plasma Fusion Res. **2** (2007) S1060.

[14] H.A.Sakaue, N.Yamamoto, S.Morita, et al., J. Appl. Phys. **109** (2011) 073304.

[15] I.Murakami, N.Yamamoto, D.Kato, F.Koike, H.A.Sakaue and C.Suzuki, submitted to Plasma Fusion Res.

[16] T.Putterich, R.Neu, C.biedermann et al., J.Phys.B **38** (2005) 3071.

[17] M.B.Chowdhuri, S.Morita, M.Kobayashi et al., Phys.Plasmas **16** (2009) 062502.

[18] M.Kobayashi, S.Morita, C.F.Dong, et al., Nucl. Fusion **53** (2013) 033011

[19] C.F.Dong, S.Morita, M.Goto et al., Rev. Sci. Instrum. **81** (2010) 033107.

[20] C.F.Dong, S.Morita, M.Goto et al., Rev. Sci. Instrum. **82** (2011) 113102.

[21] D.E.Post and R.V.Jensen Atomic Data Nucl. Data Tables **20** (1977) 397.

[22] T.Putterich, R.Neu, R.Dux et al., Nucl. Fusion **50** (2010) 025012.

[23] D.Kato, M.Goto, S.Morita et al., to be published in Physica Scripta (2013).

Measurements of visible forbidden lines and ion distributions of tungsten highly charged ions at the LHD

D. Kato[1], H.A. Sakaue[1], I. Murakami[1], M. Goto[1], S. Morita[1], N. Nakamura[2], F. Koike[3], A. Sasaki[4], X.-B. Ding[5], C.-Z. Dong[5]

[1] National Institute for Fusion Science, Toki, Gifu 509-5292, Japan

[2] ILS, The University of Electro-Communications, Tokyo 182-8585, Japan

[3] Faculty of Science and Technology, Sophia University, Tokyo 102-8554, Japan

[4] Japan Atomic Energy Agency, Kyoto 619-0215, Japan

[5] Northwest Normal University, Lanzhou 730070, China

Abstract: Visible lines, which are presumably associated with forbidden lines from tungsten highly charged ions, were clearly observed in a spectrum of 370 – 410 nm recorded shortly after a tungsten pellet injection at the LHD. One of the measured lines has been assigned to a magnetic-dipole (M1) line of the ground-term fine-structure transition of W^{26+}. Photon emission was observed at 44 lines of sight divided along the vertical direction of a horizontally elongated poloidal cross section of the LHD plasma. The line-integrated intensity of the lines along each line of sight indicates peaked profiles near the plasma center, while visible line emissions of neutral hydrogen and helium recoded in the same sampling time have a maximum located in the peripheral region of the poloidal cross section.

1. Introduction

One of important issues concerning steady state sustainment of magnetically confined plasmas (MCPs) is distribution of impurity ions in the MCPs and radiation powers by the impurity ions. Since tungsten divertors will be used in ITER, the primary element of heavy impurity ions would be tungsten. Thus, strong emission lines of highly ionized tungsten ions in core plasmas have intensively been measured in short wavelength regions, e.g. extreme-ultra-violet (EUV) [1-3].

Visible forbidden lines from highly charged ions (HCIs) of heavy elements provide new diagnostics means to study behaviors of heavy impurity ions in the fusion plasmas. High-resolution spectroscopy and fiber optics are available in the visible region, which enable precise plasma diagnostics and advantageous for preventing detection systems from neutron damage. Since fine-structure splitting of heavy ions such as tungsten increases rapidly with ionization degrees, forbidden lines of highly ionized ions could be observed in visible ranges. Spectral data for the visible forbidden-lines of highly charged tungsten ions, however, are very limited [4]. An M1 transition of

Ti-like W^{52+} ($3d^4$) $^5D_3$ - $^5D_2$ has been known by numbers of studies by means of Electron-Beam-Ion-Traps (EBITs) ([5] and references therein). Recently, Komatsu [6] and Watanabe [7] found a strong visible M1 line of Cd-like W^{26+} in the EBITs. The line has been identified as the ground-term fine-structure transition of $4f^2$ $^3H_5$ - $^3H_4$ [8]. In the present work, we conducted measurements of visible lines from the tungsten HCIs in the Large Helical Device (LHD) using solid pellet injection techniques [9].

2. LHD Experiment

Discharges for present measurements were started with electron cyclotron heating followed by hydrogen neutral beam injection (NBI) heating. In steady state, the maximum electron temperature is 2 - 3 keV at the plasma center. Then, a solid pellet containing tungsten was injected into background hydrogen plasmas. Two kinds of pellets were used in the present experiments. One is so called as Tracer-Encapsulated Solid Pellet (TESPEL) [10]. The TESPEL is a double-layered impurity pellet, which consists of polystyrene polymer as an outer shell (diameters of 400 - 900 μmφ) and tracer particles as an inner core. We used another impurity pellet [11] also (henceforth, we denote this pellet as the impurity pellet), which has a cylindrical carbon shell (diameter of 1.2 μmφ) with tin coating. Tungsten powders are contained inside a hole at the center of the carbon shell. The TESPEL and the impurity pellet are injected at speeds of 200 - 500 m/s and 30 - 300 m/s by specially designed pellet injectors, respectively.

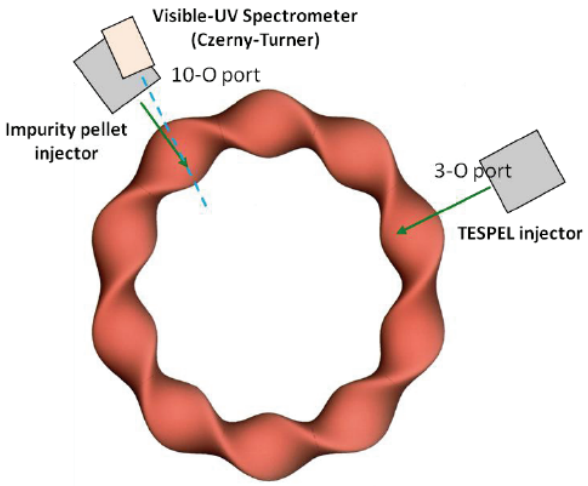

Figure 1: A top view of helical plasmas, pellet injectors and a visible-UV spectrometer.

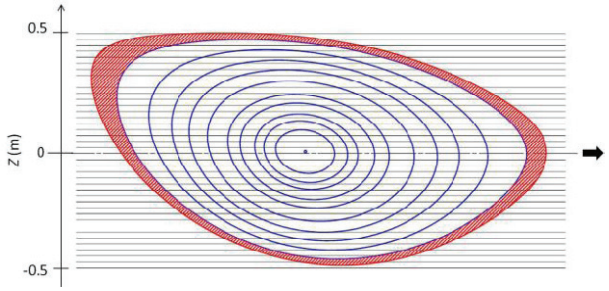

Figure 2: Horizontally elongated poloidal cross section and lines of sight. Shaded area represents the peripheral region. The black allow indicates the viewing direction.

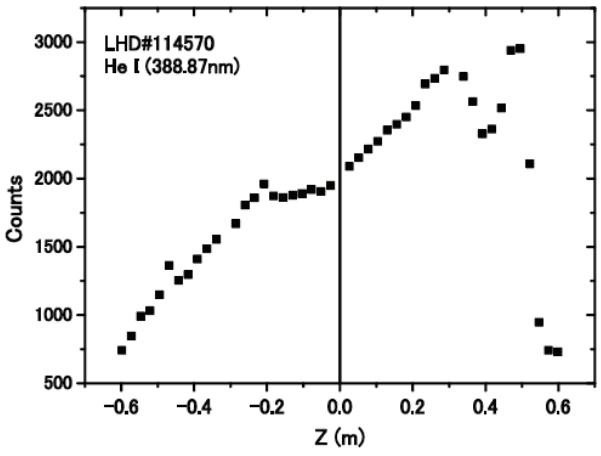

Figure 3: Vertical distribution of line-integrated intensity for a He I line.

Time-resolved (sampling times for 38 and 140 ms at every 100 and 250 ms, respectively) measurements were conducted using Czerny-Turner visible-UV spectrometers equipped with CCD detectors. Figure 1 shows a viewing port as well as two pellet injection ports. Using an optical fiber array, photon emission was observed at 44 lines of sight divided along the vertical direction (Z) of a horizontally elongated poloidal cross section of a helical plasma, as shown in Fig. 2. It is noted that the poloidal cross section is asymmetric with respect to Z = 0, because the cross section is tilted a little from the normal direction. This asymmetry manifests itself in vertical distributions of line-integrated intensities (along each line of sight) of emission lines in peripheral regions of the poloidal cross section [12]. Figure 3 illustrates a typical example with the He I line (388.87 nm) emitted in the peripheral region.

3. Results and Discussion

3.1 Observation of visible M1 lines of W HCIs at the LHD

Figure 4 shows a series of CCD images of line emissions obtained in three successive sampling time frames before (f14: 3550 - 3690 ms) and after (f15: 3800 - 3940 ms and f16: 4050 – 4190 ms) the TESPEL injection (3800 ms). 3.32×1017 tungsten atoms were contained in this TESPEL core. After the TESPEL injection, central electron temperatures decrease due to power exhaust by pellet ablation and ionization and line emission of tungsten ions, while the NBI heating is kept turned on. The line emissions from highly charged tungsten ions are anticipated only for the instant before the electron temperature decreases to so low that the ions cannot be created appreciably. In the present measurement, before the TESPEL injection, i.e. f14, the maximum electron temperature exceeds 2 keV at the plasma center. Then, the electron temperatures decreased down to 350 eV or lower at the beginning of f16. Strong line emissions peaked at vertical positions around Z = 0.5 and 0.25 are from peripheral regions of the poloidal cross sections (see Fig. 3). However, a distinct emission profile is found for the time frame just after the TESPEL injection, i.e. f15; there is another peak centered around Z = 0. To see this emission component separately, the CCD image of f14 is subtracted from that of f15 as shown in the upper panel of Fig. 5.

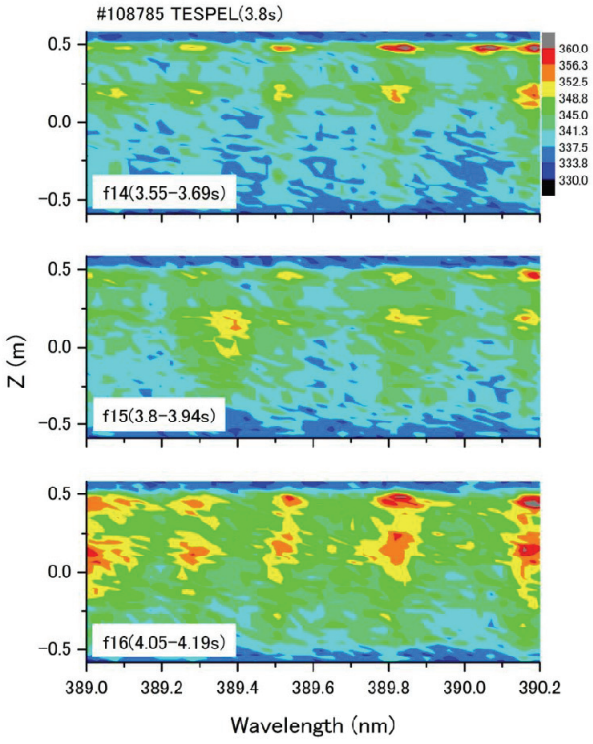

Figure 4: CCD images of line emissions in a visible

range obtained in three successive sampling time frames before (f14: 3550 - 3690 ms) and after (f15: 3800 - 3940 ms and f16: 4050 – 4190 ms) the TESPEL injection.

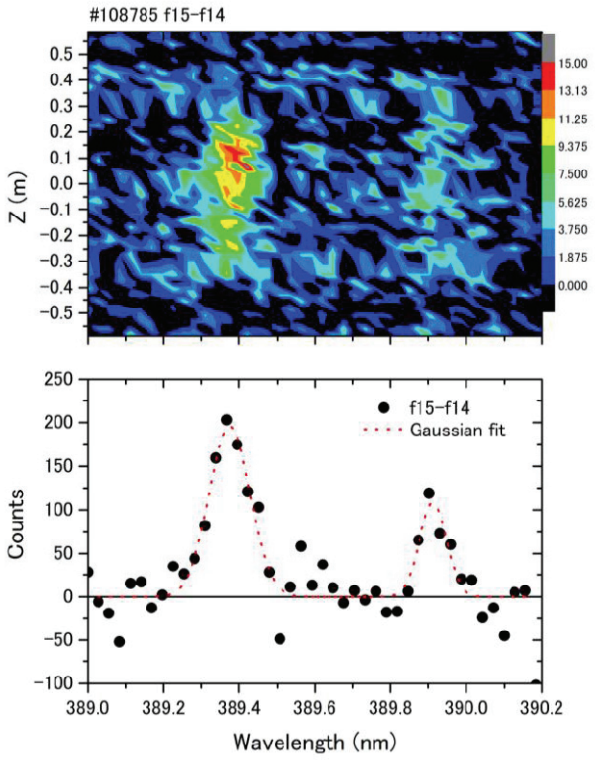

Figure 5: A spectrum of emission lines from highly charged tungsten ions observed at LHD (shot #108785). The scale on the right hand side of the top panel shows photon counts per pixel of the CCD detector. See text for details.

Table 1: Measured wavelengths (nm) and references. Numbers in parentheses are uncertainties.

Peak	Present	EBIT	Theory
A	389.37(4)	389.41(6) [6] 389.35(3) [7]	388.43 [8]
B	389.91(4)	389.89(6)[13]	-

In the lower panel, two peaks, which are absent in the spectrum measured during the former sampling time frame, i.e. f14, are apparent. Gaussian fitting of the two peaks gives central wavelengths of 389.37 nm (Peak A) and 389.91 nm (Peak B), respectively. The results are compared with available references in Table 1. Uncertainties of the central wavelengths are totally about 0.04 nm. Although standard deviations of the central wavelengths (the confidence level is 63.8 %) are less than 0.01 nm, the dominant uncertainty is due to errors in wavelength calibration which has been done with the hydrogen Balmer series of lines emitted in the last phase of the same discharge. The present wavelength for Peak A is identical to within the uncertainty a tungsten line measured in various EBITs [6, 7]. That line has been identified due to a ground-term M1 transition of W^{26+} ($4f^2$) $^3H_5$ - $^3H_4$ by large-scale multi-configuration Dirac-Fock calculations [8]. Peak B is presumably due to a line emission from W^{24+}, because an emission line with the almost identical wavelength has been observed recently with a compact EBIT (CoBIT) [13]. Both of the lines are absent in spectra of sampling times of f16 where the electron temperatures are lower than 350 eV.

3.2 Ionization equilibrium and radial distribution of W^{26+}

Figure 6 shows fractional abundances of tungsten ions of different charge states as a function of electron temperature calculated by using a collisional-radiative (CR) model [14] for an electron density of 1020 /m3. The fractional abundance of W^{26+} ions is peaked around 400 - 500 eV according to this calculation. It is

noted that different models give significantly different fractional abundances especially at electron temperatures lower than 1 keV, mainly because of uncertainties in rate coefficients of atomic processes involved in the models. Using an electron temperature profile measured by the Thomson scattering system at the LHD, a radial distribution of W^{26+} ions is calculated as shown in Fig. 7. The radial distribution has a peak at radial positions apart from the plasma center (major radius R = 3.6 m) in a case that the electron temperature profile measured at t = 3933 ms (the end of the time frame f15) is used. This seems inconsistent with the M1 intensity profile of W^{26+} ions which is peaked around the plasma center. It is noted that an electron temperature profile at an earlier time has a higher central value, the peak position of the W^{26+} fractional abundance would be even far apart from the plasma center with such the temperature profile.

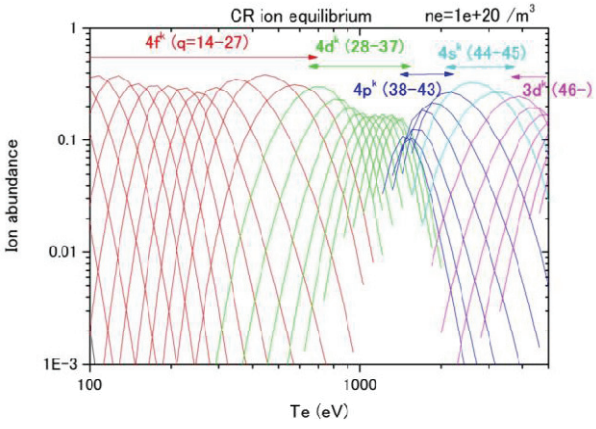

Figure 6: Fractional abundance of tungsten ions as a function of electron temperature calculated by using a collisional-radiative (CR) model [14] for an electron density of 10^{20} /m^3.

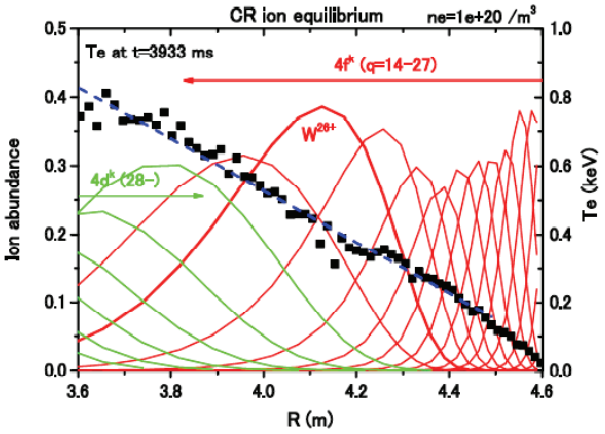

Figure 7: Radial distribution of W^{26+} ions in the LHD plasmas and an electron temperature profile measured by the Thomson scattering system.

Ion transports give significant effects in the ion fractional abundance. Suppose that a high-temperature core plasma acquires a significant in-flux of lower charged ions in a time scale shorter than that required to achieve an ionization-equilibrium, the factional abundance of the lower charged ions in the core plasma would be enhanced. This has been known as a non-equilibrium ionization effect, since Post investigated this effect in terms of a scaled ion transport time [15], which is given by a product of electron densities and ion transport times limited by diffusion or convection. Apparent inconsistence found in this work between the measured M1 intensity profile and the calculated ion distribution may be ascribed to the ion transport effect, which will be addressed in our future studies.

3.3 New visible lines of W HCIs and comparison with EBIT spectra

We have conducted further measurements to seek other forbidden lines of tungsten HCIs in the visible range using another spectrometer which has a shorter focal length (30 cm) and a smaller F-number. In this measurement, tungsten was injected with the impurity pellet. Figure 8 shows electron temperature profiles measured before and after the pellet injection (about 4060 ms), central electron temperatures decrease rapidly, while two NBIs (#4 and #5) are turned on.

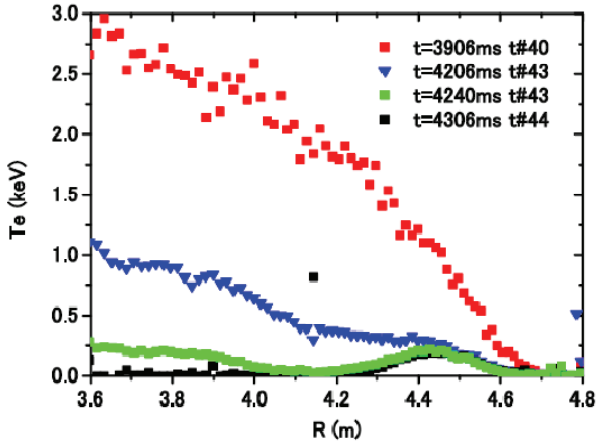

Figure 8: Variation of electron temperature profiles before and after a tungsten pellet injection (LHD#114570).

Figure 9 shows line-integrated spectra along a line of sight (Z = 2.6 cm) which passes through about the plasma center. These spectra were measured in three sampling time frames (t#40: 3900 – 3938 ms, t#43: 4200 – 4238 ms, and #t44: 4300 - 4338 ms), respectively. In the figure assignments of emission lines are also indicated. Most of prominent lines in the spectra of t#40 and t#44 can be assigned to those of the impurities inherent in the LHD, neutral hydrogen and helium atoms. Fe I lines appears in the spectrum of t#40 but not that of t#44. Fe contamination may be ascribed to sputtering from the first-wall of the main chamber made of stainless steels by bombardments of high-energy charge-exchange neutrals anticipated only for t#40. The hydrogen Balmer series is clearly seen in the spectrum of t#44, because of the lower central electron temperature as well as better statistics in photon counting (higher electron densities).

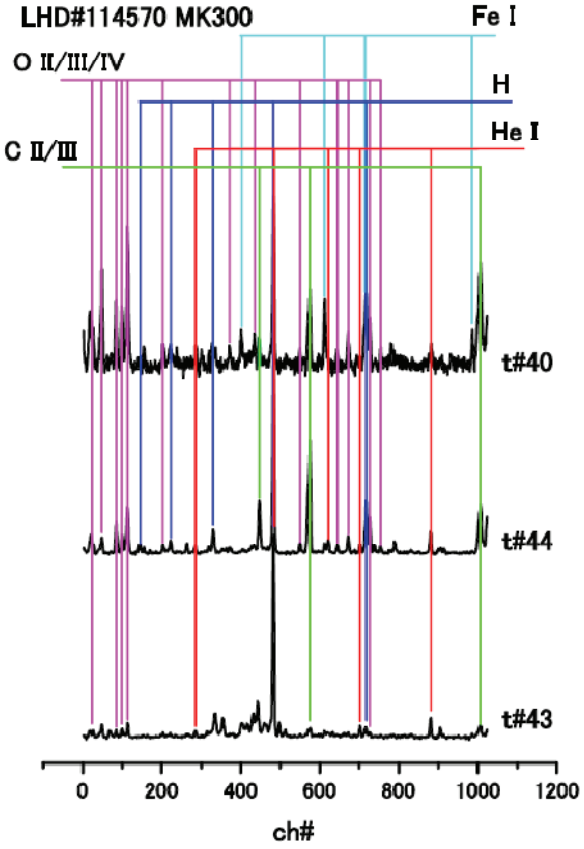

Figure 9: Line-integrated spectra along a line of sight (Z = 2.6 cm) through about the plasma center. The spectra are obtained in three sampling time frames (t#40: 3900 – 3938 ms, t#43: 4200 – 4238 ms, and #t44: 4300 - 4338 ms). The horizontal axis is channel number of a CCD detector.

There are still many unassigned lines remained in the

spectrum of t#43. In Fig. 10, the line-integrated spectra along two lines of sight are compared. One is the same as in Fig. 9, i.e. the line of sight which passes through about the plasma center, the other is that along a line of sight at a large vertical position (Z = 49.5 cm) of the horizontally elongated poloidal cross section. The later line of sight passes through a peripheral region of the poloidal cross section only (see Fig. 2). By comparing the two spectra, emission lines from the core plasma can be identified, which are indicated by arrows in the figure. Two of them (indicated by red arrows) are assigned to the previously identified M1 line of W^{26+} ($4f^2\ {}^3H_5$ – ${}^3H_4$) and a visible line of W^{24+} ions, respectively. Other unassigned lines are presumably also visible lines of tungsten HCIs.

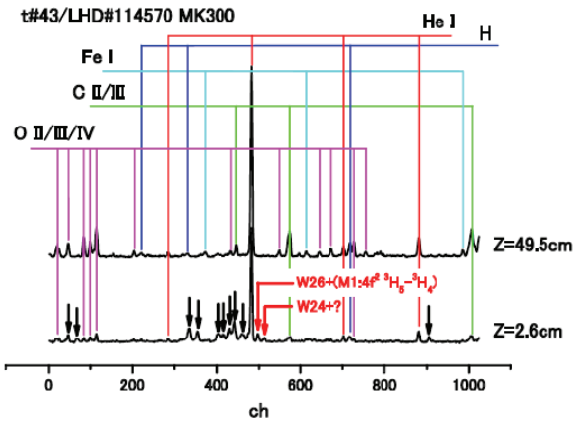

Figure 10: Line-integrated spectra along different lines of sight. Lower spectrum is the same as in Fig. 9, i.e. the line-integrated spectrum along the line of sight through about the plasma center, upper is that along the line at a large vertical position of the horizontally elongated poloidal cross section (Z = 49.5 cm, see Fig. 2).

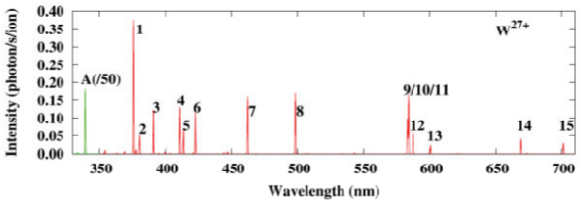

Figure 11: A synthetic spectrum of W^{27+} ions in an EBIT calculated by a collisional-radiative model [16]. Electron density of 10^{16} /m^3 and monochromatic electron beam energy of 830 eV are assumed for the EBIT. Intensity of line A is divided by 50.

Recently, quite a bit of spectral data for visible lines of the tungsten HCIs have been obtained by means of the CoBIT [13] which is very useful for analysis of the LHD spectra. However, it is not always straightforward to deduce the tungsten lines in LHD spectra by simply comparing with the CoBIT spectra. In the EBIT, trapped ions are excited by collisions with a quasi-monochromatic and unidirectional electron beam confined with a parallel magnetic field. A typical electron density obtained in the CoBIT is about 10^{16} /m^3, which is three or four orders of magnitude smaller than those in the LHD plasmas. Such large discrepancies in the electron density may give different population kinetics of fine-structure levels, which results in different emission line spectra. For instant, visible forbidden lines due to transitions in a fine-structure of an electronic excited level are hardly anticipated at low electron densities, unless the excited level is highly meta-stable. On the other hand, larger electron collision frequencies at higher electron

densities may quench the line emissions of longer life times, like the forbidden lines. Collisional-radiative (CR) models for detailed multiplet levels of the tungsten HCIs are required to address this issue. By collaboration with Chinese researchers, such a CR model for W^{27+} ions has been developed and electron density dependent variation of relative intensities of visible forbidden lines was investigated [16]. Figure 11 shows an example of calculated line spectra for W^{27+} ions in an EBIT assuming an electron density of 10^{16} /m^3 and a monochromatic electron beam energy of 830 eV. The strongest line A around 340 nm is identified as an M1 line due to the ground-term fine-structure transition ($4f\ ^2F_{7/2} - {}^2F_{5/2}$), which has recently been confirmed experimentally by collaborators in Fudan University using an EBIT [17].

4. Summary

As a concluding remark, the present work demonstrates that observation of faint forbidden-lines from highly ionized heavy elements such as tungsten is feasible at the LHD by using pellet injection techniques. The forbidden lines of the highly ionized heavy elements may provide a new diagnostics mean of core plasmas in visible ranges. Given a spatial distribution of the forbidden-line emission and a corresponding electron temperature profile, it is possible to investigate ion transport effects on the charge state distribution of highly ionized species in the LHD.

EBIT measurements are used to analyze the LHD spectra. Electron density dependence of relative line intensities is an important issue for more precise comparison of the EBIT spectra with those of the LHD plasmas. To this end, collisional-radiative models with detail atomic processes of the tungsten HCIs are being developed.

Acknowledgements

The authors acknowledge all members of the LHD experiment group for their technical supports and fruitful discussions. This work is performed with the support and under the auspices of the NIFS Collaboration Research program (NIFS10KLPF009) and JSPS-NRF-NSFC A3 Foresight Program in the field of Plasma Physics (NSFC: No.11261140328). DK is grateful for a financial support by KAKENHI (23246165).

References

[1] M. B. Chowdhuri et al. Plasma Fusion Res. **2**, S1060, (2007).

[2] T. Putterich et al. Plasma Phys. Control. Fusion **50**, 085016 (2008).

[3] C. S. Harte et al. J. Phys. B: At. Mol. Opt. Phys. **43**, 205004 (2010).

[4] A. E. Kramida and T. Shirai. At. Data Nucl. Data Tables **95**, 305 (2009).

[5] H. Watanabe et al. Phys. Rev. A **63**, 042513 (2001).

[6] A. Komatsu et al. Phys. Scr. T144, 014012 (2011).

[7] H. Watanabe et al. Can. J. Phys. **90**, 497 (2012).

[8] X.-B. Ding et al. J. Phys. B: At. Mol. Opt. Phys. **44**, 145004 (2011).

[9] D. Kato et al. to be published in a topical issue of Phys. Scr. as proceedings of the 16th Int. Conf. on the Phys. of Highly Charged Ions (HCI2012), Heidelberg. Germany, 2 – 7 Sept. 2012.

[10] S. Sudo. J. Plasma Fusion Res. **69**, 1349 (1993).

[11] H. Nihei et al. Rev. Sci. Instrum. **71**, 3747 (2000).

[12] E. Wang et al. Plasma Sci. Tech. **15**, 106 (2013).

[13] A. Komatsu et al. Plasma Fusion Res. **7**, 1201158 (2012).

[14] A. Sasaki. High Energy Density Phys. **9**, 325 (2013).

[15] D. E. Post. J. Nucl. Mater. **220-222**, 143 (1995).

[16] X.-B. Ding et al. Plasma Fusion Res. **7**, 2403128 (2012).

[17] Z. Fei et al. Phys. Rev. A **86**, 062501 (2012).

Development of impurity profile diagnostics in the ergodic layer of LHD using space-resolved 3 m normal incidence VUV spectrometer

T. Oishi[1,2], S. Morita[1,2], C. F. Dong[1], E. H. Wang[2], X. L. Huang[2], M. Goto[1,2], and LHD Experiment group

[1] National Institute for Fusion Science, Toki 509-5292, Japan

[2] Department of Fusion Science, Graduate University for Advanced Studies, Toki 509-5292, Japan

Abstract: Space-resolved vacuum ultraviolet (VUV) spectroscopy using a 3 m normal incidence spectrometer has been developed in the large helical device (LHD) to study the plasma transport in the ergodic layer by measuring the spatial profile of VUV lines from impurities emitted in wavelength range of 300-3200 Å. The sightline is basically adjusted to measure the edge plasma profile with high-spatial resolution, while it can be expanded to measure the full plasma profile with wider viewing angle if a mirror unit installed between the spectrometer and the torus is used. Measurements of intensity profiles of CIV 1548.20×2 Å, ArVII 585.75 Å, HeI 584.33 Å, and HeII 303.8 Å line emissions are demonstrated as preliminary results. Intensity and ion temperature profiles were obtained simultaneously using the CIV emissions in high-density discharges.

1. Introduction

Control of the impurity transport in the edge region of magnetically-confined plasmas has attracted an attention in the fusion research to sustain highperformance plasma and mitigation of the divertor heat flux [1,2]. For the purpose the edge impurity transport and its effect on the plasma performance have been investigated in the large helical device (LHD) [3]. In particular, effects of thick stochastic magnetic field layer located outside the core plasma called “ergodic layer” on the impurity transport have recently attracted [4]. Therefore, a precise measurement on the spatial profile of impurity line emissions in the ergodic layer is necessarily required to investigate the characteristics of the impurity transport in such stochastic magnetic field layer in detailed. The vacuum ultraviolet (VUV) lines from impurity ions are significantly emitted in the ergodic layer because the electron temperature around LCFS ranges from 10 to 500 eV [5]. Space-resolved spectroscopy has been applied to measure the intensity profiles of line emission from impurities in the ergodic layer. A 3 m normal incidence spectrometer has favorable characteristics to measure the VUV emission in wavelength range of 300-3200 Å [6-8]. In this paper, details of the diagnostic system for impurity profile measurement in the ergodic layer of LHD are presented with preliminary experimental results.

2. Development of Diagnostics Systems

Figure 1 shows a schematic drawing of the impurity diagnostics system in LHD. LHD is a large-sized superconducting heliotron device having major radius

of 3.6 m, averaged minor radius of 0.64 m, toroidal magnetic field of 3 T, toroidal period number of 10 and poloidal mode number of 2. A 3 m normal incidence VUV spectrometer (McPherson model 2253) was installed on a horizontal diagnostic port (#10-O). This spectrometer has been used for observation of intrinsic impurity lines [9] or identification of forbidden magnetic dipole emission lines [10-12] in LHD. In this study, the optical axis was arranged perpendicular to the toroidal magnetic field in the bottom edge at holizontally-elongated plasma cross section to adjust the observable region to the ergodic layer. The wavelength resolution is 0.15 Å when an entrance slit is set to 20・m in width and a 1200 g/mm grating is used. A back-illuminated CCD detector (Andor model DO435-BN: 1024×1024 ch) is placed at the position of exit slit. The size of the CCD is 13.3 × 13.3 mm2 and the pixel size is 13 × 13・m^2. The line dispersion of the spectrometer changes almost linearly from 0.0362 to 0.0370 Å/pix, while the wavelength changes from 300 to 3200 Å. Then, the wavelength interval which can be measured in a single discharge is about 37 Å.

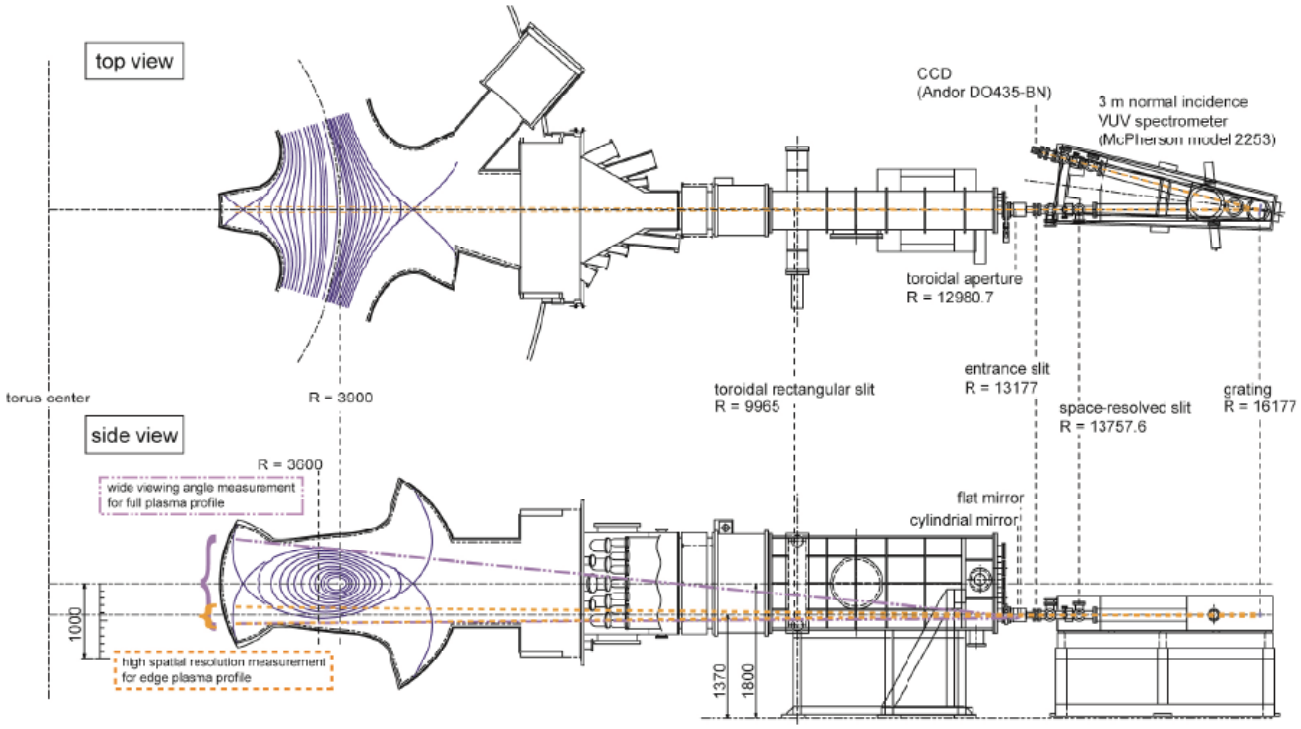

Figure 1: Top and side views of LHD and impurity diagnostics system for study of ergodic layer using space-resolved 3 m VUV spectrometer.

The vertical profile of VUV emissions as a wavelength-dispersed image is projected on the CCD detector by a slit for spatial resolution called “space-resolved slit” mounted between the entrance slit and the grating in the spectrometer. Vertical width of the space-resolved slit can be controlled from 50 to 14000・m and it determines the spatial resolution. We can optimize the slit width which is appropriate for the compatibility of the measured line intensity and the

spatial resolution by the method measuring the profiles of CIV 1548.20 × 2 Å emission intensity with scanning width of the slit [13].

A mirror unit which consists of a flat mirror and a cylindrical mirror was designed and installed between the spectrometer and the torus to switch the view angle. The sightline is basically adjusted to measure the edge plasma profile with high-spatial resolution, while it can be expanded to measure the full plasma profile with wider viewing angle if the mirror unit is used. To limit the observable region in toroidal direction, a rectangular aperture called "toroidal aperture" is mounted in the housing of mirror unit. For the edge profile measurement, the toroidal aperture width can be selected among 0.4, 1.0, and 2.0 mm, of which the width corresponds to the toroidal interval in the observable region of 19.5, 48.8, and 97.6 mm at the major radius R = 3600 mm, respectively. For the full profile measurement, a toroidal aperture of the 1.6 mm width is used and it corresponds 98.9 mm toroidal interval of the observable region at R = 3600 mm.

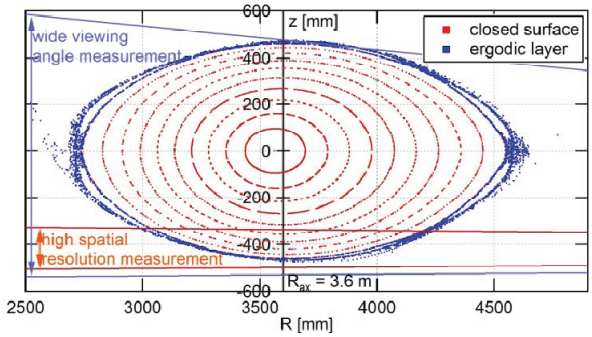

Figure 2: Enlarged view of the observable region for measurements of CIV line emission having the wavelength of 1548.2×2 Å on the Poincare plot of vacuum magnetic fields with the magnetic axis R_{ax} = 3.6 m

Precise calibration of the observable region for different wavelength is required because the distance between the grating and the entrance slit automatically changes with the wavelength to be adjusted to the wavelength-dependent focal length, which causes a change of view angle against the wavelength. To determine the vertical position of the observable region absolutely, a toroidally-movable slit with rectangular-corrugated edge located at R = 9965 mm is utilized [14]. The vertical width with opened space of the rectangular corrugated edge changes monotonically in the vertical direction. Therefore, we can determine the vertical position of the observable region by measuring the image of line emissions from LHD plasmas through the rectangularcorrugated slits. This calibration was applied to both cases in the edge profile measurement without the mirror unit and the full profile measurement with the mirror unit. Figure 2 shows an enlarged view of the observable region for measurements of CIV 1548.2 × 2 Å emission on the Poincare plot of vacuum magnetic fields with the magnetic axis R_{ax} = 3.6 m. The z-coordinate of sightlines at R = 3600 mm is used for the horizontal axis of measured spatial profiles. In the edge profile measurement, the observable region of roughly 20cm in the vertical direction can cover the whole range of the ergodic layer with the thickness of several centimeters on the bottom edge of the plasma. However, in the full profile measurement, the upper edge of the

ergodic layer is slightly out of the observable region at present. Therefore, we are planning to expand the observable region in the full profile measurement by rearrangement of the mirror unit.

3. Result of Measurements

3.1 High spatial resolution measurement for edge plasma profile

In this section, results obtained using sightlines with high spatial resolution measurement for the edge plasma profile are reported. Conditions of the diagnostics are as follows: time resolution of 100 milliseconds, entrance slit width of 20 μm, space-resolved slit width of 600 μm, toroidal aperture width of 1.0 mm, number of sightlines of 51 ch (20 pixels binning is applied for 1 ch). Preliminary VUV spectroscopy data were measured in high-density discharges of LHD using the system developed in the present study. Helium plasma was initiated by electron cyclotron heating and further heated by hydrogen neutral beams with negative ion sources (NBI #2, 3) and positive ion sources (NBI#4, 5). The line averaged density is about 1.4×10^{20} m^{-3}.

Figure 3 (a) shows a wavelength spectrum in the full wavelength range covered in a single discharge including CIV lines with wavelength of 1548.20 × 2 Å together with the Gaussian profile as a fitting function. The line shape of the wavelength spectrum I(λ) has a Gaussian profile if it is assumed that the ions have a Maxwellian velocity distribution as follows:

$$I(\lambda) = \frac{1}{\sqrt{\pi}\Delta_D} exp\left(-\frac{(\lambda-\lambda_0)^2}{\Delta_D^2}\right) \quad (1)$$

where λ_0 is the center wavelength and ΔD is the Doppler width. The Doppler width at full width at half maximum (FWHM), Δ_{FWHM}, is given by $\Delta_{FWHM} = 2(\ln 2)^{1/2}\Delta D$. The ion temperature T_i in eV is thus given by $T_i = 1.68 \times 10^8 M (\Delta^{FWHM}/\lambda_0)^2$, where M is the atomic mass number. Deconvoluting the instrumental function of 0.15 Å in FWHM measured using a Mercury lamp from the Δ_{FWHM} of the fitted profile, Δ_{FWHM} = 0.364 Å and T_i = 22.2 eV are obtained. Figure 3 (b) and (c) shows the vertical profiles of CIV line intensity and T_i, respectively. LCFS of the vacuum magnetic field is indicated with arrow. It is known that the spatial profile of the CIV intensity has a steep peak in the ergodic layer [14-17]. CIV emission is released only in the outermost region of the ergodic layer in LHD plasmas because the low ionization energy of 65eV for C^{3+} ions causes less fractional abundance in the core plasma. Therefore, the peak of the intensity profile outside LCFS shown in Fig. 4 (b) is a result of line integration in a long path along the sightline through the ergodic layer at the bottom edge of the holizontally-elongated elliptical plasma. The T_i profile also indicates the edge T_i in the ergodic layer at corresponding vertical position.

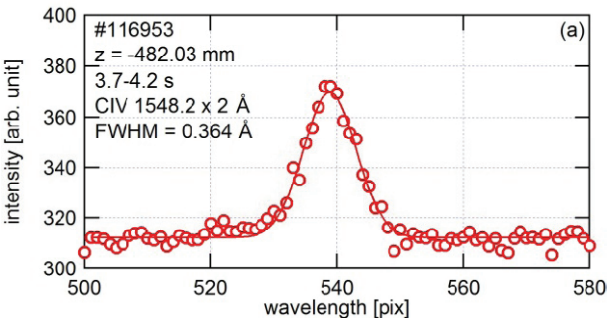

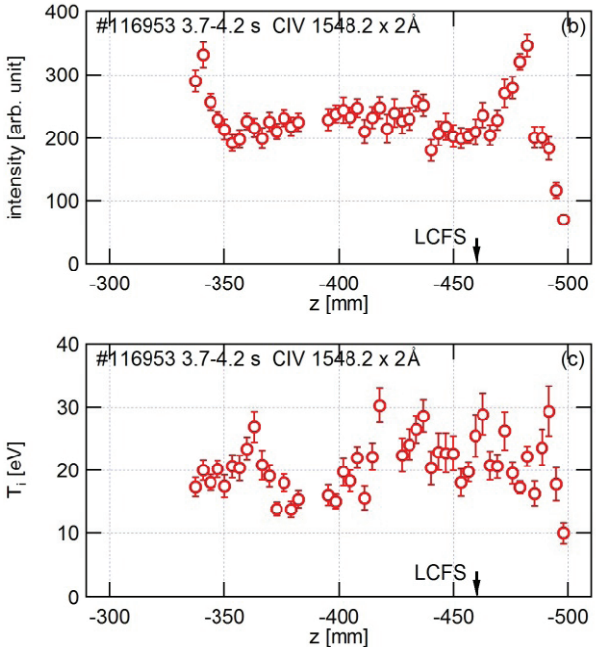

Figure 3: Results of the edge plasma profile measurement for CIV line emission. (a) Wavelength spectrum of CIV 1548.20×2 Å line together with the fitted Gaussian function. Vertical profiles of (b) CIV line intensity and (c) ion temperature derived from the Doppler broadening of CIV spectrum.

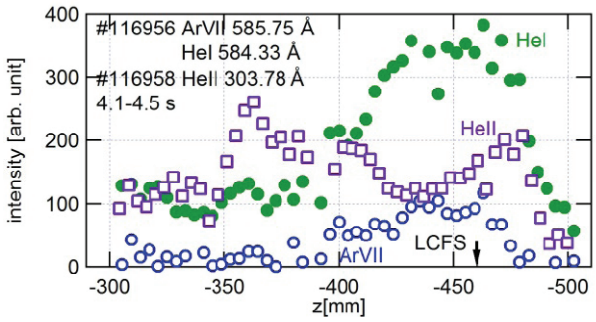

Figure 4: Intensity profiles of ArVII 585.75 Å, HeI 584.33 Å, and HeII 303.8 Å line emissions measured using the edge plasma profile measurement.

In addition, various kinds of line emissions within the wavelength range of 300-3200 Å can be measured using this system. Figure 4 shows intensity profiles of ArVII 585.75 Å, HeI 584.33 Å, and HeII 303.8 Å line emissions measured using the edge plasma profile measurement. The discharge conditions were same as stated above regarding Fig. 3. Helium is the working gas, and Argon is injected externally as impurity gas puffing. In previous studies, it has been observed that HeII line emission has a peak structure outer than LCFS and its position is slightly inner than the peak of CIV emission [17]. Those observations are consistent to the intensity profile shown in Figs. 3 and 4.

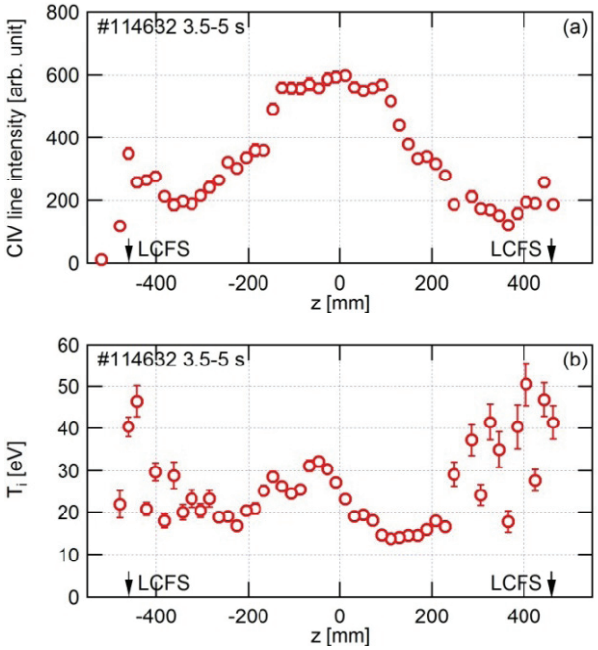

Figure 5: Results of the full plasma profile measurement for CIV line emission. Vertical profiles of (a) CIV line intensity and (b) ion temperature derived from the Doppler broadening of CIV spectrum.

3.2 Wide viewing angle measurement for full plasma profile

In this section, results obtained using sightlines with wide viewing angle measurement for the full plasma

profile are reported. As discharge conditions, hydrogen plasma was initiated by electron cyclotron heating and further heated by hydrogen neutral beams with negative ion sources (NBI #1, 2, 3). The line averaged density is about 5×10^{19} m^{-3}. Figure 5 (a) and (b) shows the vertical profiles of CIV line intensity and T_i, respectively. The intensity profile has peak structures in both top and bottom edge. In addition, the intensity starts to increase again as the position of the sightline moves upwardly from LCFS. It is because the length of the line integral path along the sightline through the ergodic layer becomes longer in the observable region closer to the midplane.

4. Summary

A space-resolved VUV spectroscopy using a 3 m normal incidence spectrometer was developed in LHD to study the plasma transport in the ergodic layer. The spatial profile of VUV lines from impurities was measured in wavelength range of 300-3200 Å. The optical axis of the spectroscopic system was arranged perpendicular to the toroidal magnetic field in the bottom edge at horizontally-elongated plasma cross section to adjust the observable region to the ergodic layer. The sightline can be expanded to measure the full plasma profile with wider viewing angle by using a mirror unit installed between the spectrometer and the torus. Line intensity and ion temperature profiles were obtained simultaneously using the CIV spectra of 1548.20×2 Å in high-density discharges. The intensity profiles of ArVII 585.75 Å, HeI 584.33 Å, and HeII 303.8 Å line emissions were also obtained. This system will be utilized in investigations of the edge plasma physics, especially on the role of the ergodic layer in relation to impurities.

This work was partly supported by the JSPS-NRFNSFC A3 Foresight Program in the field of Plasma Physics (NSFC: No.11261140328).

References

[1] P. C. Stangeby and G. M. McCracken, Nucl. Fusion **30**, 1225 (1990).

[2] R. Burhenn *et al.*, Nucl. Fusion **49**, 065005 (2009).

[3] M. Kobayashi *et al.*, Proc. 22nd Int. Conf. on Fusion Energy, Geneva, Switzerland, 13-18 October 2008 (Vienna: IAEA), EX/9-4 "Study on impurity screening in stochastic magnetic boundary of the Large Helical Device" (2008).

[4] M. B. Chowdhuri *et al.*, Phys. Plasmas **16**, 062502 (2009).

[5] S. Morita *et al.*, Plasma Phys. Control. Fusion **48**, A269 (2006).

[6] S. Morita and M. Goto, Rev. Sci. Instrum. **74**, 2036 (2003).

[7] R. Katai *et al.*, Rev. Sci. Instrum. **77**, 10F307 (2006).

[8] T. Oishi *et al.*, Plasma Fusion Res., "Development of impurity profile diagnostics in the ergodic layer of LHD using 3 m normal incidence VUV spectrometer", *in press*.

[9] R. Katai *et al.*, Plasma Fusion Res. **2**, 014 (2007).

[10] R. Katai *et al.*, J. Plasma Fusion Res. SERIES **7**, 9 (2006).

[11] R. Katai *et al.*, J. Quant. Spectrosc. Radiat. Transfer **107**, 120 (2007).

[12] S. Morita *et al.*, Plasma Sci. Technol. **12**, 341 (2010).

[13] C. F. Dong *et al.*, Rev. Sci. Instrum. **81**, 033107 (2010).

[14] C. F. Dong *et al.*, Phys. Plasmas **18**, 082511 (2011).

[15] C. F. Dong *et al.*, Plasma Fusion Res. **6**, 2402078 (2011).

[16] C. F. Dong *et al.*, Plasma Sci. Technol. **13**, 140 (2011).

[17] E. H. Wang *et al.*, Plasma Fusion Res. **7**, 2402059 (2012).

[18] T. Morisaki *et al.*, J. Nucl. Mater. **313-316**, 548 (2003).

Determination of the Safety Factor Profile by MHD Spectroscopy Using Energetic Particle Driven Modes in Toroidal Plasmas

K. Toi[1], LHD Experiment Team,

J.H. Kim[2], KSTAR Team,

D.A. Spong[3]

[1] National Institute for Fusion Science, Toki, Japan

[2] National Fusion Research Institute, Daejeon, Korea

[3] Oak Ridge National Laboratory, Oak Ridge, U.S.A

Abstract: A new plasma diagnostic method using characteristics of energetic particle driven MHD instabilities, which is called "MHD spectroscopy", is proposed using three Asian super-conducting tori: LHD, KSTAR and EAST. As the first step, potentiality of the MHD spectroscopy based on energetic-ion-driven Alfvén eigenmodes is investigated based on the experimental data of LHD and KSTAR beam heated plasmas. In reversed shear plasmas of LHD, reversed shear Alfvén eigenmodes (RSAEs) are effectively employed for MHD spectroscopy. The minimum of the rotational transform $(\iota/2\pi)_{min}$ (or the maximum of the safety factor q: q_{max}), and the time that the minimum passes the rational value, and the averaged beam beta are derived from the minimum frequency in the temporal sweeping of the RSAE frequency. In KSTAR, recently observed global Alfvén eigenmmodes (GAEs) which is inferred to locate near the plasma center are employed for the purpose. From the frequency sweeping, the time evolution of the q at the magnetic axis q_0 is predicted in sawtoothing plasmas.

1. Introduction

Plasma confinement and MHD stability of tokamak and stellarator/helical plasmas is determined by the characters of magnetic configuration. In particular, the safety factor q or the rotational transform profile $\iota/2\pi$ is a key quantity characterizing the magnetic configuration. Reliable and precise information of the q or $\iota/2\pi$ profile is critically important in order to understand plasma behaviors and to control plasma performance. In most of toroidal devices, it is measured directly by the motional stark effect (MSE) diagnostics and polarimeter. However, the data obtained by the diagnostics often have large experimental error around 20%. Moreover, the installation of some delicate plasma diagnostic systems in a fusion reactor is considerably limited due to high neutron flux. Toward the fusion reactor, a new plasma diagnostic technique called MHD spectroscopy is a promising back up of the direct measurement method such as MSE. It was first proposed by using ELMs and Alfvén eigenmodes (AEs) excited by antennae for tokamak plasmas [1]. Later, energetic-particle

(EP)-driven global modes were included for MHD spectroscopy in 3D plasmas as well as 2D plasmas [2-4]. The EP driven modes should satisfy the following requirements in order to apply to MHD spectroscopy: (1) the dispersion relation depends on plasma equilibrium quantities such as q-profile, (2) the phase velocity is required to be away from electron and ion thermal speeds to avoid strong Landau damping, (3) the frequency range has no large fluctuations due to micro turbulence, and (4) amplitude should be in detectable level but not too large so that EP radial transport would not enhanced noticeably. Alfven eigenmodes satisfy these requirements.

The MHD spectroscopy is an accurate and reliable plasma diagnostic method because it is based on well-developed MHD theory. From a unique relationship between the mode frequencies and locations of Alfvén eigenmodes and various MHD equilibrium, q or $\iota/2\pi$ profile can be predicted accurately. Other important equilibrium information, i.e., effective plasma mass, bulk plasma temperature, specific ratio, the radial gradient of energetic ion density and so on can also be obtained with MHD spectroscopy based on the experimental data of AE frequencies and radial mode location [2-4]. MHD spectroscopy may also contribute to better understanding of MHD events such as sawtooth crash and ELMs. This approach has a similarity to *atomic spectroscopy* and *helioseismology* for the search on the internal structure of the sun.

In the *Category III* of the A3 program, an objective is to develop MHD spectroscopy through collaborations among Asian three super-conducting devices, LHD, KSTAR and EAST. The first research target is to excite candidate modes for MHD spectroscopy by NBI in LHD and KSTAR. This is extended to EAST plasma heated by high power ICRF heating. In parallel to these collaborating experiments, a unique relationship between the mode frequencies and radial locations of EP-driven modes and the $\iota/2\pi$ (=1/q) profiles will be clarified over wide parameter range by using ideal MHD codes such as NOVA-K [5] and AE3D [6] codes. In the next application stage, the $\iota/2\pi$ (=1/q) profile in a certain toroidal plasma will be determined through an iterative fitting procedure so that all observed mode frequencies in the plasma and their radial locations should agree with the calculated results by such MHD numerical codes consistently. Note that in a fusion reactor these global modes should be controlled in acceptable levels without enhancing radial transport of energetic particles and bulk plasma. The MHD spectroscopy is expected to be very powerful for developing attractive operation scenarios for high plasma performance.

In this paper, two main results on development of MHD spectroscopy in LHD and KSTAR are presented. Summary of the results and future prospect will be given in the last section.

2. MHD spectroscopy with RSAEs excited in RS plasmas of LHD

Tokamak and stellarator/helical plasmas have two

types of $\iota/2\pi$ (=1/q) profiles. One is a monotonic profile and the other non-monotonic one which is called "reversed magnetic shear (RS) profile". In the RS-plasmas of tokamaks and LHD, reversed shear Alfvén eigenmodes (RSAEs) are often excited by energetic passing ions and/or ICRF-generated energetic trapped ions. The RSAE frequency is usually swept upward in tokamak RS plasmas as the q-profile evolves in time, keeping the RS profile shape. On the other hand, the RSAE frequency on LHD is swept downward and then upward via the minimum as the minimum of $\iota/2\pi$ decreases in time (which is an opposite time evolution of q for a tokamak RS-plasma), ss mentioned below. In tokamaks, the time evolution of the q_{min} of the RS-plasma was accurately derived using the characteristic time evolution of RSAE frequency [2, 3, 7].

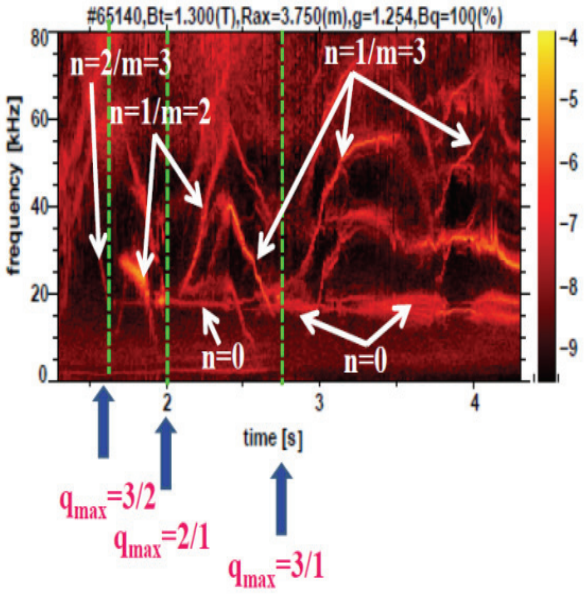

Fig.1 Spectrogram of a magnetic probe signal in a RS hydrogen plasma produced by counter NB current drive, where B_t=1.3T and the line averaged electron density 0.6x10^{19} m^{-3}.

In LHD, RS plasmas are generated by counter neutral beam current drive where beam driven current is induced by counter tangential beams to decrease the external rotational transform generated by external helical coils[8]. Figure 1 shows the spectrogram of a magnetic probe signal in thus produced RS plasma where line averaged electron density is kept constant from t= 1.5 s to ~4.5s. The m=2/n=1 and m=3/n=1 modes indicated with arrows are RSAEs. The m=3/n=2 RSAE is also identified from t~1.5s to t~1.6s. From the minimum of the RSAE frequency, the off-axis minimum value of the $\iota/2\pi$ profile is precisely determined using the character of RSAE on LHD [8]. The general dispersion relation of RSAE is expressed as,

$$\omega^2 = \frac{v_A^2}{R^2}(n - m/q_{\min or \max})^2 + [\omega_{GAM}^2 + \omega_{\nabla P+\nabla F}^2] \quad (1)$$

Here, the minimum frequency of RSAE is determined by two contributions due to the geodesic curvature with the geodesic acoustic mode frequency ω_{GAM} and the contribution due to the radial gradients of thermal plasma pressure and the EP density gradient $\omega_{\nabla P+\nabla F}$. As seen from Fig.1, the minimum frequency of RSAE is nearly equal to the energetic ion driven GAM, for instance at t=2.0s and 2.7s. This fact requires the condition $\omega_{\nabla P+\nabla F}^2 \cong 0$. Since the RSAE shown in Fig.1 propagates in electron diamagnetic drift direction and is a so-called negative frequency mode, the gradient of EPs at the zero-shear layer of the RS configuration can be evaluated with the above condition. Moreover, the EP gradient is constrained by

the condition that both upward and downward frequency-sweeping RSAEs are excited as shown in Fig.1 [8]. From this consideration, the volume averaged EP pressure is estimated to be in the range from 0.15% to 0.25 % [8]. Thus, the temporal sweeping of the RSAE frequency is very useful for MHD spectroscopy.

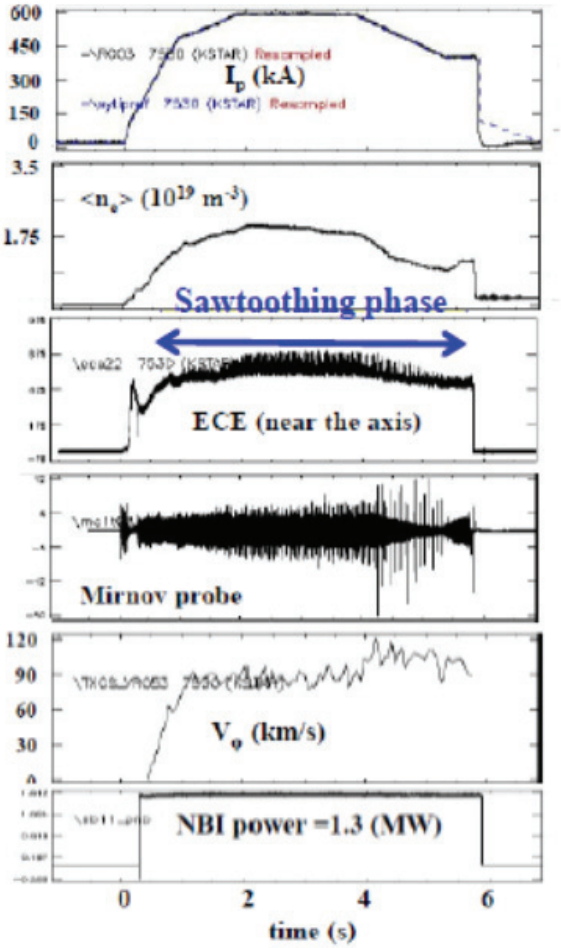

Fig.2 Waveforms of the plasma current, line averaged electron density, ECE signal, magnetic probe signal, toroidal rotation velocity and NBI pulse in the D-shaped diverted plasma heated by 90 keV deuterium beams of 1.3 MW.

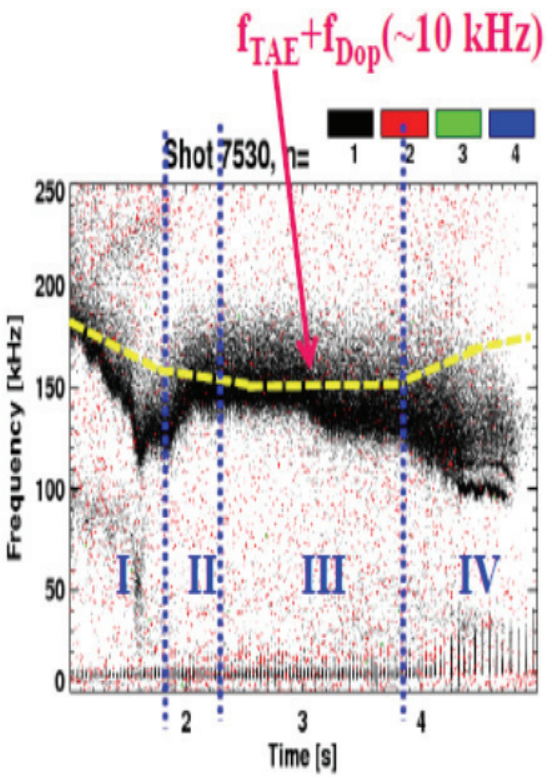

Fig.3 Spectrogram of the toroidal mode number by a toroidal array of magnetic probes. The yellow broken curve indicates the estimated TAE frequency taking account the Doppler shift due to toroidal rotation.

3. MHD Spectroscopy with AEs excited in NBI heated plasmas on KSTAR

On the KSTAR experimental campaign in 2011, an interesting n=2 AEs having upward frequency sweeping in the phase that both the line averaged electron density and plasma current are rising were detected on a circular-cross section plasma with sawtooth oscillations, which suggests the central value of q, q_o below 1. The calculation of shear Alfvén spectra suggests that the mode is a global Alfvén eigenmode (GAE) near the plasma center. The

calculated frequency agrees well with if the value of q_o gradually decreases from ~ 1 at the time of the turn-on of sawteeth down to ~0.85 at the time that the frequency reaches the TAE frequency. The mode frequency seems to stay aroud the saturated value even in sawtoothing phase, although the frequency is slightly modulated by each sawtooth crash. That is, this data suggest that q_o is clamped around ~0.90 - 0.85 less than 1 without considerable oscillation of the mode frequency, associated with each sawtooth crash. This result are similar to those found in some tokamaks TEXTOR, DIII-D and TFTR [9-11].

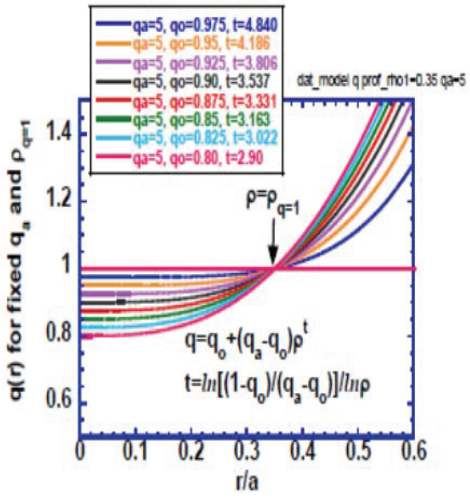

Fig.4 Model *q*-profile for the calculation of shear Alfven spectra and AEs, where q_a=5 and the *q*=1 location is *r/a*=0.35.

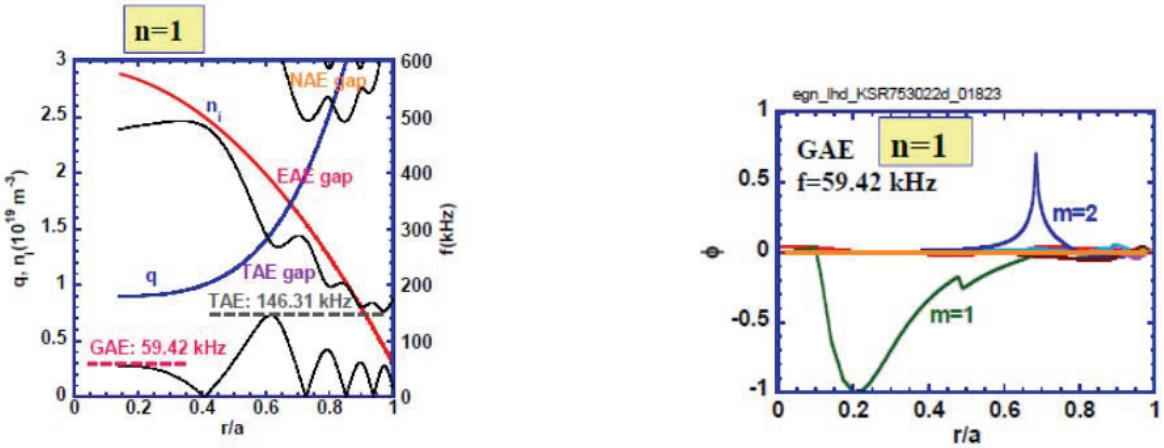

Fig.5 (a) *n*=1 shear Alfven spectra for the monotonic *q*-profile with qo=0.90. Less than 200 kHz, typical TAE and GAE found are indicated. The frequencies of the TAE and GAE are respectively 146 kHz and 59 kHz. (b measure) The calculated eigenfunction of the n=1/m=1 GAE.

In the 2012 experimental campaign, the similar type of AEs was again observed in a D-shaped diverted plasma with sawteeth. The discharge waveform is shown in Fig.2. The plasma was obtained at the toroidal field strength of B_t=2 T at R=1.8m. The line averaged electron density evolves nearly analogous to the waveform of the plasma current. The spectrogram of the magnetic probe signal is shown in Fig.3. The *n*=1 Alfvénic modes are clearly found in the spectrogram. The broken curve indicates the TAE frequency calculated by AE3D code, where the Doppler shift frequency evaluated by the toroidal

rotation velocity measured by soft X-ray crystal spectrometer in the plasma center is taken into account. In four phases, the mode frequency deviates noticeably from the TAE mode frequency in some time windows. In the current ramp-up phase, the AE exhibiting upward frequency-sweeping is observed, although the line averaged density is also rising, as seen from Fig.2. Note that sawteeth already appear in the middle of the current ramp-up because of low ramp-up rate of the plasma current and not high beam heated power. As similar to GAE like mode observed in the 2011 campaign, q_o is inferred to decrease down to ~0.8 before the current flat-top. In order to explain the frequency deviation from the TAE frequency shown in Fig.3, the shear Alfven spectra were calculated for a set of model monotonic q-profile $q=q_o+ (q_a-q_o)(r/a)^t$, changing q_o from 1 down to 0.8 with the other experimental data B_t and $<n_e>$, where q_a=5 and the q=1 radius is fixed at r/a=0.35 with $t=ln[(1-q_o)/(q_a-q_o)]/ln(r/a)$ (Fig.4). As an example, the n=1 shear Alfvén spectra for a q-profile of q_o=0.9 is shown in Fig.5(a), where typical TAE and GAE having the frequency less than 200 kHz are shown. As an example, the eigenfunction of m=1/n=1 GAE exists near the plasma center is shown in Fig.5(b). From the model calculations including other model q-profiles with q_o=0.95 to 0.85 having slightly reversed magnetic shear inside q=1 surface, the dependence of the GAE and TAE frequencies on q_o was obtained as shown in Fig.6. Note that the GAE frequency will be bounded by a certain frequency offset as that in RSAE, as seen from eq.(1). The q_o can be predicted in each phase shown in Fig.3, using the calculation results shown in Fig.6. The q_o is predicted as follows: (1) phase I (t~1.0s =>1.8s): q_o ~ 0.8 => 0.82 (RS profile may be also possible), (2) phase II (t~1.8s => 2.2s): q_o~ 0.82 => 0.80, (3) phase III(t=2.2s => 3.9s): q_o is kept around 0.80 ~ 0.82, and (4) phase IV (t~3.9s => 4.3s): q_o~ 0.82 => 0.90. So far, the detailed excitation condition of the GAE is not clarified yet. Nevertheless, the newly observed low-n GAE locates in the plasma core region is quite useful for development of MHD spectroscopy.

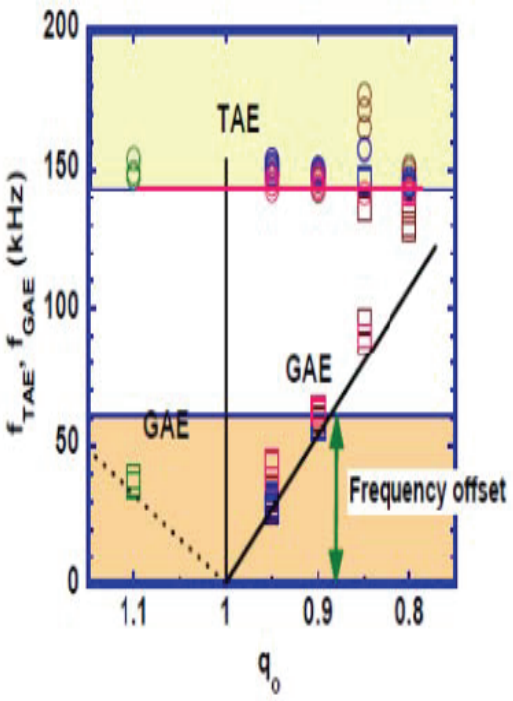

Fig.6 Dependence of GAE (squares) and TAE (circles) frequencies on qo for model q-profiles at the plasma condition of the shot shown in Fig.2.

4. Summary and future prospect

In LHD and KSTAR, it has been shown that the q-profile information such as q_{min} or $(\iota/2\pi)_{min}$ and q_o can be predicted with high precision using the

characteristics of the frequencies of RSAE and newly observed low-*n* GAE in the plasma core. The GAE is added to a potential candidate of AE instabilities for MHD spectroscopy, in addition RSAE which is already recognized as the good candidate. The detailed excitation condition of the GAE in KSTAR should be clarified, and be investigated in plasmas relevant to ITER. In LHD, low-*n* GAEs locate near the plasma center are also observed, and is investigated for a possibility of the MHD spectroscopy. It is important and interesting to search RSAEs and GAEs in the EAST plasmas heated by high power ICRF heating where energetic minority ions near MeV range would be expected. Low frequency AEs such as beta induced Alfven eigenmodes (BAEs) are also potentially useful for MHD spectroscopy [12]. Studies of AEs using these three super conducting toroidal devices will play an important role in establishing MHD spectroscopy that is applicable to wide class of toroidal plasmas. Again, MHD spectroscopy can derive not only *q*-profile information but also temperature ratio, effective mass, specific heat, EP density and so on. MHD spectroscopy including nonlinear frequency chirping phenomena of EP driven modes may extract the information of EP velocity distribution function.

Acknowledgements

We acknowledge the KSTAR team for their support in the collaborative experiments in 2011 and 2012 for studies of energetic particle driven Alfvénic modes. This research is supported in part by the *JSPS A3 Foresight Program on Critical Physics Issues Specific to Steady State Sustainment of High-Performance Plasmas* and by the *Japan-Korean Collaboration Program*. This is also supported partly by This work was supported in part by Grants-in-Aid for Scientific Research from JSPS (No. 24360386).

References

[1] J.P. Goedbloed et al. Plasma Phys. Control. Fusion **35,** B277(1993).

[2] S.E. Sharapov et al., Phys. Lett. A **289**, 127 (2001).

[3] A. Fasoli et al., Plasma Phys. Control. Fusion 44, B159 (2002).

[4] K. Toi et al., Plasma Phys. Control. Fusion **53**, 024008 (2011).

[5] C.Z. Cheng, Physcs Rep. **211**, 1(1992).

[6] D.A. Spong et al., Phys. Plasmas **17**, 022106 (2010).

[7] M. Van Zeeland et al., Nucl. Fusion 46, S880 (2006).

[8] K. Toi et al., Phys. Rev. Lett. **105**, 145003 (2010).

[9] H. Soltwisch et al., in Plasma Physics and Controlled Nuclear Fusion Research, Proceedings of the 11 th International Conference, Kyoto (IAEA, Vienna, 1987), Vol. I, p. 263.

[10] D. Wdblewski and L. L. Lao, Phys. Fluids B3, 2877 (1991).

[11] M. Yamada et al., Phys. Plasmas 1, 3269 (1994).

[12] Ph. Lauber et al., Plasma Phys. Control. Fusion **51**, 124009(2009).

Nonlinear MHD modeling of Resonant Magnetic Perturbation

Yasuhiro SUZUKI[1,2]

[1] National Institute for Fusion Science, Oroshi-cho 322-6, Toki 5095292, Japan

[2] The Graduate University for Advanced Studies, SOKENDAI, Oroshi-cho 322-6, Toki 5095292, Japan

Abstract: Applying 3D nonlinear MHD simulation codes, the magnetic island and its interaction with the MHD activities are studied in the Large Helical Device (LHD) experiment. In an experiment, the collapse in the plasma core was observed in a configuration, which has large magnetic island produced by an intrinsic error field. At the collapse, the temperature profile was flattened. This suggests the magnetic island evolved. The magnetic island was observed by the magnetic diagnostics. The magnetic diagnostics also suggests evolving the magnetic island. 3D MHD equilibria are calculated by the 3D MHD equilibrium code then nonlinear MHD are simulated. Since the comparison of observed and calculated results is comparable, the magnetic island in calculated results is similar to one of the experiment.

1. Introduction

The study of the magnetic island is an important issue because the generation of the magnetic island leads the degradation of the confinement due to flattering of the temperature. In tokamaks, the magnetic island is generated by the resistive MHD instability like the tearing mode [1] at many cases. Especially, the study of the neoclassical tearing mode (NTM) [2] is an important and critical issue. On the other hand, in stellarator and heliotron plasmas, the generation of the magnetic island is observed due to the MHD instability [3-4]. In addition, the evolution and suppression of the magnetic island are also observed without the MHD instability [5]. In such cases, the magnetic island is driven by the equilibrium response [6-8]. Since the magnetic island driven by the equilibrium response is not rotating and appeared in the quasi steady-state, it is good target to measure the magnetic island.

To observe the magnetic island, the profile measurement is widely used. Flattening of the electron temperature and density indicate the existence of the magnetic island. However, if the O-point of magnetic islands does not locate on the line of sight, the profile measurement cannot identify the magnetic island. On the other hand, the magnetic diagnostics directly observe the plasma response and it does not depend on the location of the O-point. The magnetic diagnostics observes total plasma response in the outside of the plasma. Thus, to identify modes of the plasma response, the mode analysis is done. In the LHD experiments, the mode analysis assuming the current filament is used [9] but this analysis cannot model the magnetic field structure. To model the magnetic field more physically, coupling with the numerical

simulation is necessary.

An advantage of the LHD device to study the magnetic island is superposing of the resonant perturbation field (RMP) by external coils. These coils are called to the LID coils, which were prepared for the operation of the Local Island Divertor (LID) [10]. Since these coils can generate the low-*n* magnetic island for the vacuum, we can study only the effect of the plasma response on the magnetic island. Many experiments were done to study the plasma response [10-12]. In those studies, the spontaneous evolution and suppression of the island were observed without the MHD instability. This suggests a possibility the magnetic island changes spontaneously due to the equilibrium response. This also suggests 3D MHD equilibrium analysis can be used to study the magnetic island.

In this study, we study the magnetic island in a low magnetic shear configuration in the LHD. We propose studies of the magnetic island by coupling the magnetic diagnostics and a 3D MHD equilibrium calculation code without assumption of nested flux surfaces. In the next section, we show an experimental result, which is an observation of the perturbation driven by the plasma response. The perturbed field is observed by the magnetic diagnostics. In Sec.3, we show a demonstration of our method by coupling the magnetic diagnostics and the 3D MHD equilibrium code. Finally, we discuss and conclude this study.

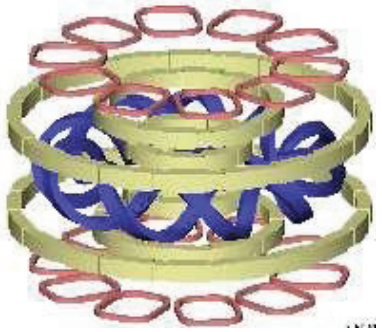

Figure 1: The coils system of the LHD device.

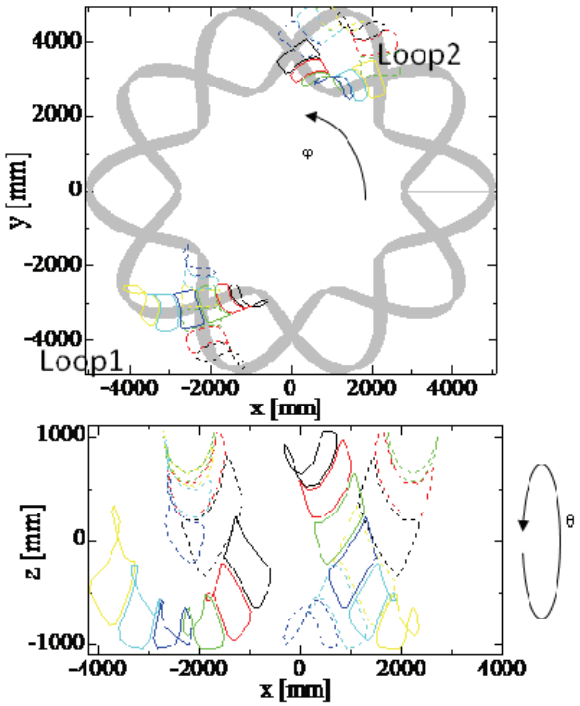

Figure 2: The schematic view of poloidal arrays of flux loops. Two arrays are installed at ϕ=57 and 237 [deg]. One array consists of twelve loops.

2. Experimental results

The LHD is an *L*/*M*=2/10 heliotron. Here *L* and *M* are the pole number of helical coil winding and toroidal field period. In this study, we did an experiment with *n*/*m*=1/1 magnetic island, where *n* and *m* are toroidal and poloidal mode numbers, respectively. As mentioned in the introduction, the LHD device can produce low-*n* magnetic islands by the LID coils.

Figure 1 shows the coils system of the LHD device. The coil system consists of 2 pair of helical coils (blue), 3 pair of poloidal field coils (yellow) and 10 pare of local coils (red). The LID coils produce the dipole field to produce n/m=1/1 field. The plasma response on low-n magnetic islands is observed by the magnetic diagnostics, which are two poloidal arrays of flux loops, "Loop1" and "Loop2". Figure 2 shows a schematic view of poloidal arrays of flux loops. One array consists of twelve flux loops. These arrays measure the perturbed field produce by the parallel current $j_{parallel}$. In the LHD experiments, $j_{parallel}$ is the Pfirsh-Schlueter (P-S) current. If there is no low-n perturbed field smaller than the toroidal field period, two arrays observe same signals. However, appearing low-n perturbation (n < 10), the difference between two arrays appears. From the difference, we can decide the perturbed field Br, mode numbers n/m and phase of the magnetic island ϕ_{island}.

Figure 3 shows discharges in a large plasma aspect ratio configuration (A_p=8.3). In this experiments, the dipole field by LID coils was superposed to a configuration, which is R_{ax}=3.6m and κ~1. The R_{ax} is the vacuum axis position and κ is the averaged elongation of the plasma. The dipole field resonates on ι=1 surface, where ι is the rotational transform. The order of the perturbed field B_{11} is about $O(10^{-4})$. The width of the island is about Δρ ~ 0.4, where ρ is the normalized minor radius. For A_p=8.3 configuration, the rotational transform on the axis ι_0 is larger than n/m=2/3 and the rotational transform at the plasma edge on ι_a is smaller than n/m=3/2. This means only n/m=1/1 island appears in this configuration and it can be considered. The magnetic shear on ι=1 surface is weaker than other configurations with small A_p. Thus, we can expect the equilibrium response will appear strongly. In the figure, the volume averaged beta $<\beta>_{dia}$, the plasma density ne, the plasma current I_p/B_t, the perturbed field b_r/B_t and the phase of the island ϕ_{11} are plotted. The density is almost same and the plasma current is almost zero in all discharge. However, perturbed fields br are different if the LID field is different. For I_{LID}/B_t=-278A/T, the perturbed field is almost zero. For I_{LID}/B_t=0A/T, the perturbed field is not zero. This means the existence of the intrinsic error field. The case of I_{LID}/B_t=-278A/T is a case of compensating the intrinsic error field.

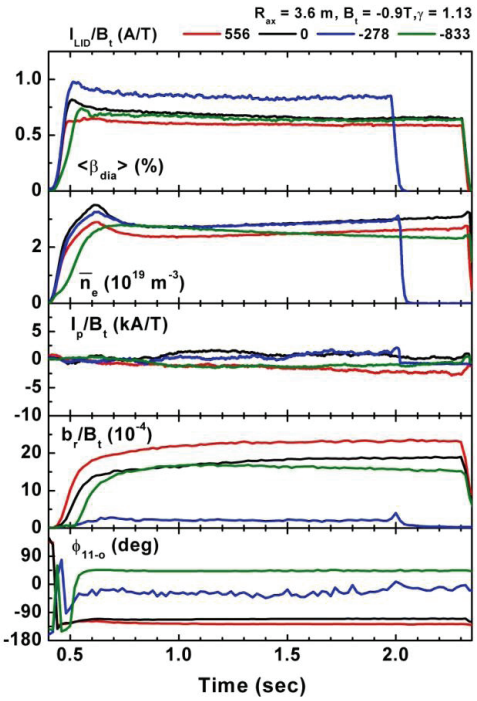

Figure 3: Results of the island experiment. The volume averaged beta $<\beta>_{dia}$, density ne, plasma current I_p/B_t, perturbed field b_r/B_t and phase of the

island ϕ_{11} are shown. Colors indicate the current of the LID coil I_{LID}/B_t.

3. Numerical model

Nonlinear MHD simulation is carried out by using the MIPS code (MHD Infrastructure for Plasma Simulation) which solves the following full MHD equations in the cylindrical coordinates (R, ϕ,Z),

$$\frac{\partial \rho}{\partial t} = -\nabla \cdot (\rho \mathbf{v}) \quad (1)$$

$$\rho \frac{\partial \mathbf{v}}{\partial t} = -\rho \mathbf{v} \cdot \nabla \mathbf{v} - \nabla p + \mathbf{j} \times \mathbf{B} + \frac{4}{3} \nabla [\nu \rho (\nabla \cdot \mathbf{v})] - \nabla \times (\nu \rho \omega) \quad (2)$$

$$\frac{\partial \mathbf{B}}{\partial t} = -\nabla \times \mathbf{E} \quad (3)$$

$$\frac{\partial p}{\partial t} = -\nabla \cdot (\rho \mathbf{v}) - (\gamma - 1) \nabla \cdot \mathbf{v} + (\gamma - 1) \left[\nu \rho \omega^2 + \frac{4}{3} \nu \rho (\nabla \cdot \mathbf{v})^2 + \eta \mathbf{j} \cdot (\mathbf{j} - \mathbf{j}_{eq}) \right] + \chi \nabla \cdot \nabla (p - p_{eq}) \quad (4)$$

$$\mathbf{E} = -\mathbf{v} \times \mathbf{B} + \eta (\mathbf{j} - \mathbf{j}_{eq}) \quad (5)$$

$$\mathbf{j} = -\frac{1}{\mu_0} \nabla \times \mathbf{B} \quad (6)$$

$$\omega = \nabla \times \mathbf{v} \quad (7)$$

where, ρ is the mass density, $\boldsymbol{v}$ is the plasma velocity, p is the pressure, $\boldsymbol{B}$ is the magnetic field, is the resistivity, ν is the viscosity, χ is the thermal diffusion coefficient, μ_0 is the vacuum magnetic permeability and γ is the adiabatic constant. $\mathbf{j}_{eq}$ and p_{eq} are the equilibrium current density and pressure, respectively.

The original MIPS code uses the fourth-order finite difference scheme. The fourth-order Runge-Kutta method is used for the time integration. As the beta value increases, the equilibrium pressure gradient

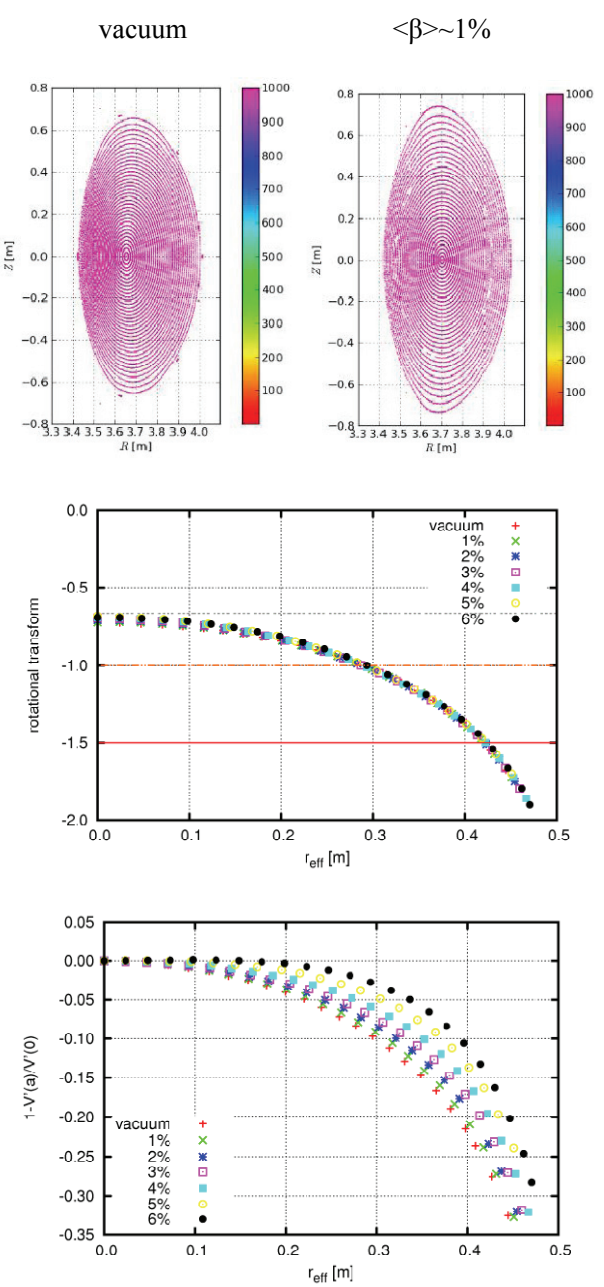

Figure 4: Results of MHD equilibrium analyses. Puncture maps for the vacuum and <β>~1%, profiles of the rotational transform and specific volume are plotted.

becomes steep in the outer torus due to the large Shafranov shift. For the high beta LHD plasmas, the pressure driven modes becomes unstable in the periphery region so that the perturbed plasma flow grows near the plasma boundary. This leads to the

numerical oscillation when the convection terms are treated by the fourth-order finite difference scheme. Thus, in this study, the Kawamura-Kuwabara scheme (3rd order upwind scheme) is used for the convection terms in order to avoid numerical oscillation near the plasma boundary. In the nonlinear simulations, the number of grid points are (256,512,256). The MHD equilibrium is constructed by HINT2 without assuming existence of the nested flux surfaces.

Figure 4 shows the Puncture map of MHD equilibrium analyses. Puncture maps show the vacuum magnetic field and finite-beta equilibrium (<β>~1%). The MHD equilibrium calculation is done without the LID field or intrinsic error field. Clear flux surfaces are kept and the plasma volume is increased a little bit. For references, profiles of the rotational transform and specific volume are plotted. With increased β, profiles of the rotational transform are almost fixed. The specific volume is changed by increased β. However, at ι=1 surface, there is still the magnetic hill.

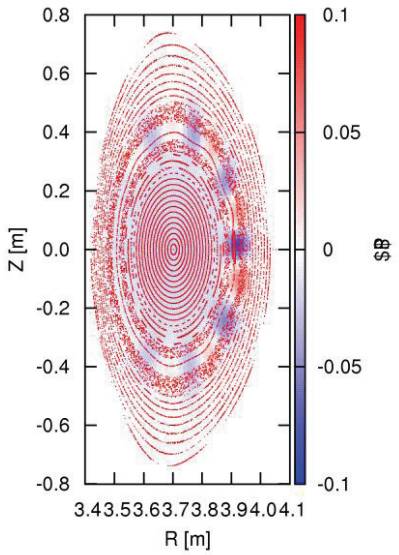

Figure 5: nonlinear MHD simulation without the resonant magnetic perturbation.

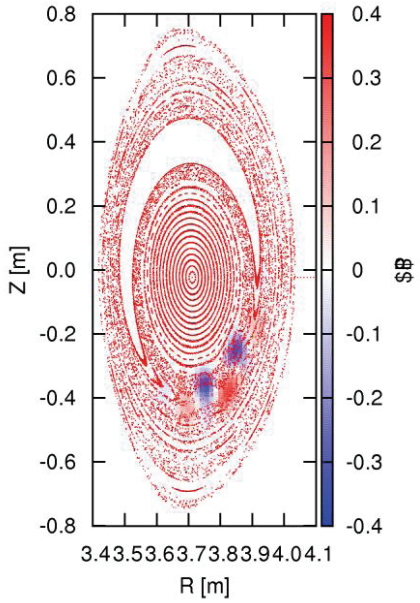

Figure 6: nonlinear MHD simulation with the resonant magnetic perturbation.

Figure 5 shows a result of nonlinear MHD simulation for <β>~1% equilibrium. In the figure, Puncture map of nonlinear MHD and perturbed pressure are shown. At ι=1 surface, n/m=10/10 mode is excited then magnetic field lines become stochastic. Since this simulation is done without the resonant magnetic perturbation, clear island structure is not appeared.

On the other hand, if the intrinsic error field (resonant magnetic perturbation) is considered, clear magnetic island appears then the plasma pressure is flattened. This flattened pressure distribution affects the MHD mode structure. In figure 6, a result of nonlinear MHD simulation including the intrinsic error field is shown. The MHD mode structure is changed and localized at the X-point of the island. The magnetic island is evolved than the vacuum magnetic island. This results

is consistent to the experimental observations.

4. Summary

The nonlinear MHD behavior with the resonant magnetic perturbation is studied. Superposing the perturbed magnetic field, the island growth is changed. Since the intrinsic error field exists, zero perturbed field is unstable. Controlling perturbed field, the island growth is suppressed. To model these experiments, nonlinear MHD simulations are done. With the intrinsic error field, the magnetic island is evolved. This is comparable to the experiment.

This work was partly supported by the JSPS-NRF-NSFC A3 Foresight Program in the field of Plasma Physics (NSFC: No.11261140328).

References

[1] H. P. Furth et al., Phys. Fluids 16 1054 (1973).

[2] Z. Chang et al., Phys. Rev. Lett. 74 4633 (1995).

[3] S. Sakakibara et al., Fusion Sci. Technol. 50 177 (2006).

[4] S. Sakakibara et al., Fusion Sci. Technol. 58 176 (2010).

[5] Y. Narushima, et al., Nucl. Fusion 48 075010 (2008).

[6] A. H. Reiman and A. H. Boozer, Phys. Fluids 27 2446 (1984).

[7] J. R. Cary and M. Kotschenreuther, Phys. Fluids 28 1392 (1985).

[8] C. C. Hegna and A. Bhattacharjee, Phys. Fluids B 1 392 (1989).

[9] S. Sakakibara et al., Fusion Sci. Technol. 58 471 (2010).

[10] N. Ohyabu et al., J. Nucl. Mater. 266-269 302 (1999).

[11] K. Narihara, et al., Phys. Rev Lett. 87, 135002 (2001).

[12] N. Ohyabu, et al., Phys. Rev Lett. 88, 055005 (2002).

Status and plan of fusion plasma simulation research in NFRI

J.Y. Kim

National Fusion Research Institute, Daejeon 305-806, Korea

Abstract: A brief overview is presented on the research status and plan of fusion plasma simulation in NFRI (National Fusion Research Institute), which is mainly being performed for the experimental data analysis and modeling for KSTAR through domestic and international collaborations. A strong effort is first being put on the pedestal area, in relation to the H-mode and ELM control experiments in KSTAR. Particularly, a predictive calculation of KSTAR pedestal structure by the EPED model, a benchmark nonlinear simulation of ELM behavior, and the calculation of RMP (resonant magnetic perturbation) field with plasma response in pedestal are being carried out using ELITE, M3D, NIMROD, XGC0 codes. In addition, a more detailed simulation study of L-H transition trigger and pedestal build-up process is also being made. For the MHD stability area, a simulation study using the NIMROD code is underway to see the effect of energetic electrons and ions on the internal MHD modes. Also, disruption simulation is being performed of KSTAR device model using the TSC code. For the operation scenario area, a predictive simulation using the ASTRA and JINTRAC codes is being made of some target modes for KSTAR and ITER. For the divertor/SOL area, simulation work has started to model the transport of plasma and neutral and also the plasma-wall interaction in KSTAR divertor geometry using the SOLPS and ERO codes. Finally, for the turbulent transport area an extensive simulation study is being done using the gyrokinetic and gyrofluid codes, such as gKPSP, GYSELA, TRB, BOUT++ etc. Also, substantial effort is being made to develop a full-f gyrokinetic code using semi-Lagrangian method and to upgrade the BOUT++ to a global gyrofluid code, which can simulate the whole plasma region from core to edge.

1. Introduction

In NFRI, the simulation research is now being carried out through the two projects. One is the WCI (world-class-Institute) project funded directly from Korean government. The main research subject of this project is the integrated modeling of turbulent transport phenomena and about 15 people, whom are consisted of domestic and foreign research scientists, are now working for the project. The other is an internal project inside NFRI, which supports the theory and simulation research work in the other areas, such as pedestal and ELM control, MHD stability, operation scenario, and divertor/SOL. Here, we present a brief summary of recent research activities being performed in each topical science area through the above two projects in NFRI.

2. Pedestal and ELM control

In relation to the experiments on the pedestal and ELM characteristics in KSTAR a predictive modeling is being performed on the pedestal stability and structure using the EPED model. The two codes of ELITE and HENENA are used to calculate the stability of P-B mode and KBM, respectively and then to estimate the dependence of pedestal width and height on various plasma parameters, such as plasma current I_p, q, magnetic field B_t, collisionality etc. Figure 1(a) shows the initial calculation results where it is found that pedestal height increases almost linearly, while pedestal width is almost constant when I_p increases or q decreases at a fixed B_t. Similar dependence is also observed when I_p increases or B_t increases at a fixed q. Meanwhile, when plasma collisionality increases the pedestal height appears to increase initially and then decrease due to the excitation of medium-n P-B modes

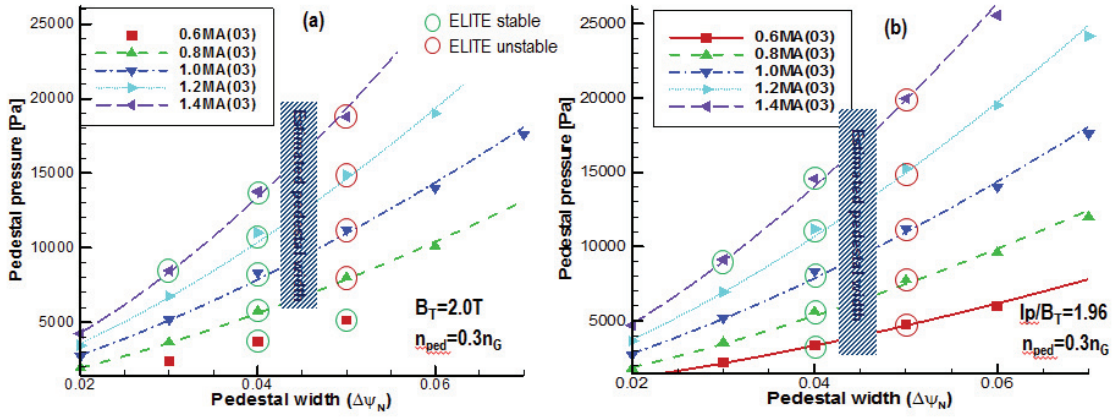

Fig. 1 Dependence of pedestal height and width on Ip with fixed (a) B_T and (b) q (from EPED model)

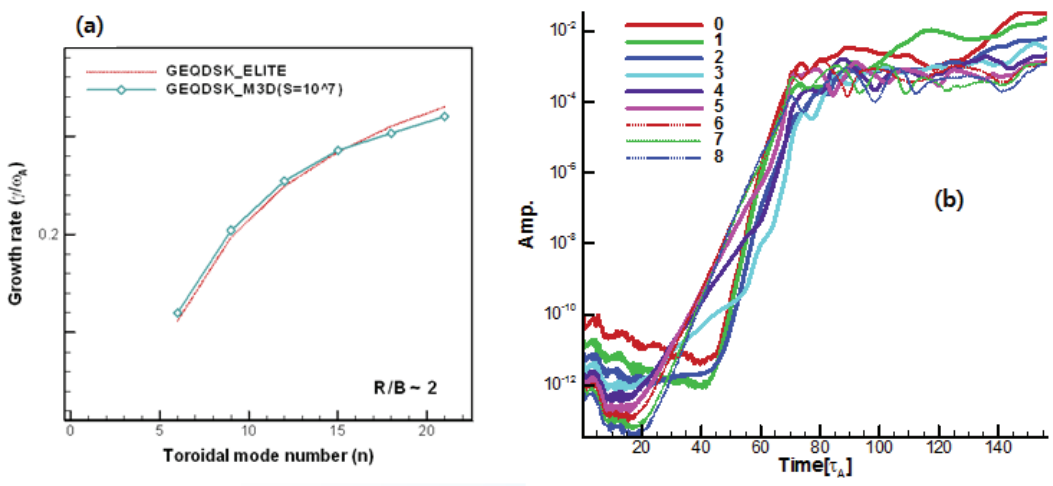

Fig. 2 (a) Linear benchmark between codes and (b) nonlinear simulation result from M3D

A benchmark simulation study of the linear and non-linear ELM behavior is being performed under international collaboration using M3D and NIMROD codes. In the first step, the benchmark simulation of the linear growth rate has been performed and a good agreement between codes has been obtained in the

simple circular plasma equilibrium model, as shown in Fig. 2(a). The benchmark simulation of the nonlinear ELM behavior has been then started in the same circular equilibrium model. Figure 2(b) shows the initial result from the M3D code of the nonlinear evolution of each toroidal harmonic amplitude. It is observed that a substantial nonlinear destabilization occurs with the dominant mode number changing from medium-n to low-n during the evolution. These results are to be compared with those from NIMROD, and the benchmark simulation will be then extended to the KSTAR equilibrium model.

The kinetic simulation study of RMP penetration in pedestal region with a strong ExB flow and pressure gradient has been continued by using XGC0 code combined with M3D code. Main focus in this year work has been put on investigating the effect of plasma density and collisionality on the RMP penetration. As shown in Fig. 3(a), it is found that the RMP penetration becomes weaker, that is, the shielding effect becomes stronger as the collisionality gets higher. As shown in Fig. 3(b), an estimate of the RMP field in the KSTAR model plasma has been also performed for various phases of RMP coil current set, and it appears the magnetic perturbation is strongly peaked near the pedestal top in the 90-degree phase case where n=1 RMP suppression was observed.

Besides, a work has been started to calculate more accurately Er field due to the neoclassical ion orbit loss and/or neoclassical relaxation by using the full-kinetic XGC0 code. Also, a work has been started to model the pedestal profile evolution, such as the inward penetration of pedestal width, by solving the time-dependent transport equations of plasma density, temperature etc.

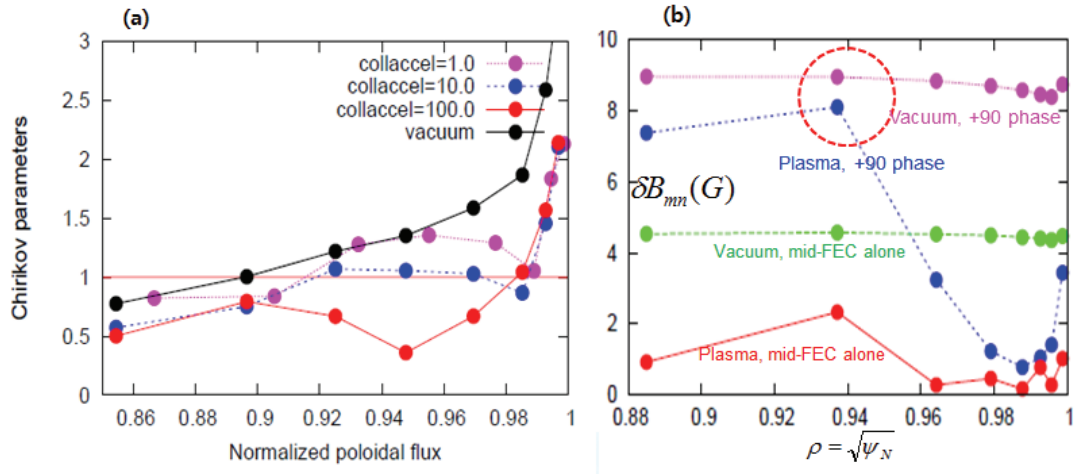

Fig. 3 (a) Collisionality dependence and (b) KSTAR case of RMP penetration with plasma response

3. MHD stability and energetic particles

A work has been started to model the effect of energetic electrons on the internal MHD modes. A main motivation is to understand the KSTAR experimental results of the characteristics change of sawtooth or the excitation of fishbone-like internal

kink mode in ECH heated plasma. A work has been first performed to include the energetic electron part in NIMROD code through international collaboation. Simulation study is then under way and some initial results indicate that energetic electrons can give a destabilizing effect on the internal MHD mode near q~1

During 2011 KSTAR experimental campaign a strong rotation damping was observed in Ohmic and H-mode plasmas when ECH heating is applied, as shown in Fig. 4(left). An interesting feature observed here was that in most cases the rotation damping is accompanied with the excitation of an internal MHD mode. Based on these experimental observations, a theoretical model has been developed where the rotation damping is due to the NTV effect induced by the internal MHD-mode. Figure 4(right) shows the NTV magnitude calculated approximately from the measured internal MHD mode structure and it appears to give a reasonable explanation of the observed rotation damping in both cases of Ohmic and H-mode.

Simulation study of disruption in KSTAR device model has been continued using the TSC code. It is found that with the new passive stabilizer the vertical growth rate of plasma is increased by about 12 times, while the vertical force on the passive stabilizer is reduced by about 4 times during the VDE (Vertical Displacement Event) phase.

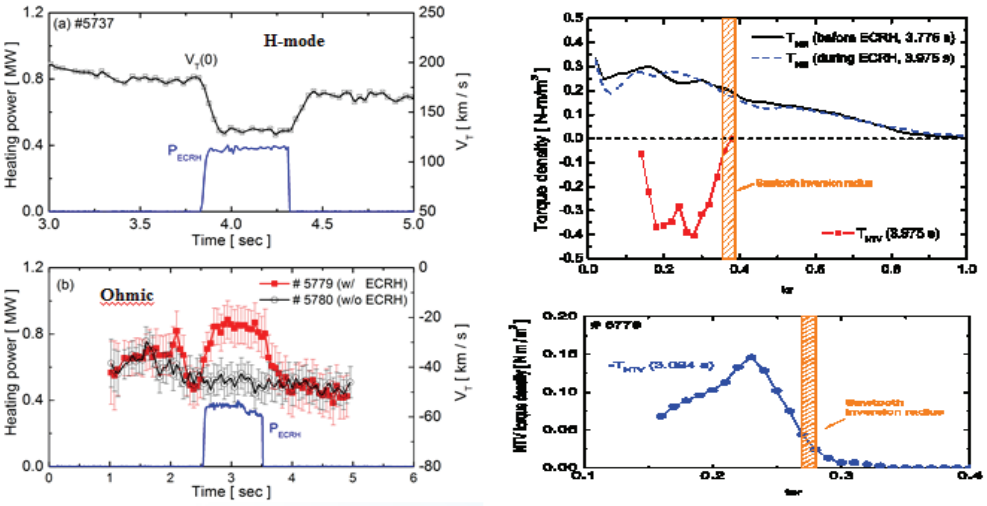

Fig. 4 Rotation damping observed with ECH heating (left) and calculated NTV torque (right).

4. Operation scenario and divertor/SOL

Operation scenario modeling of KSTAR and ITER has been continued. Particularly, for KSTAR some predictive

Hydrogen isotope inventories and structural analysis of co-deposited carbon layer in LHD

N. Ashikawa[1], Suk-Ho Hong[2], Y. Hamaji[3], Y. Torikai[4], Y. Yamauchi[5], Y. Nobuta[5], Y. Ueda[3], T. Hino[5], M. Matsuyama[4], T. Muroga[1] and LHD experimental group[1]

[1] National Institute for Fusion Science, Gifu 509-5292, Japan

[2] National Fusion Research Institute, Daejeon 305-333, Korea

[3] Osaka University, Suita 565-0871, Japan

[4] University of Toyama, Toyama 930-8555, Japan

[5] Hokkaido University, Sapporo 060-8628, Japan

Abstract: Carbonstructures of co-deposition layer on target materials exposed to LHD plasmas have been applied by Raman spectroscopy, X-ray photoelectron spectroscopy (XPS) and ellipsometry. Those deposition layers show characterization of amorphous carbon by Raman spectroscopy and ellipsometry. From these analytical results, characterizations of carbon deposition layer are shown.

1. Introduction

An investigation on hydrogen isotope inventories in deposition layer the plasma facing walls is important issues related to controls of fuel recycling and in-vessel tritium inventories in fusion devices [1-2]. In particular, several allotropes of carbon are known such as graphite, amorphous carbon and diamond, with different characterizations.

Two kinds of different co-deposited carbon layers are produced during one experimental campaign in LHD. One is the sample targets facing graphite divertor and eroded carbons from nearby divertor targets by physical sputtering deposit on these targets. A thickness of deposition layer is about 400 nm. The other is the sample targets non-facing graphite divertor and thin carbon deposition layers of ~50 nm are observed. But a position of eroded carbon sources by physical and chemical sputtering is unknown.

In this study, different co-deposition layers on target samples have been analyzed by Raman spectroscopy, X-ray photoelectron spectroscopy (XPS) and spectroscopic ellipsometry. Retained hydrogen by main plasma and glow-discharge irradiations was measured by thermal desorption spectrometry (TDS). From comparison with these analyzed data, characterizations of hydrogen isotope inventories in deposition layers are discussed.

2. Experimental setup

Targets samples made by SUS316 and Si were installed the section6.5 at inner poloidal cross-section in LHD as shown in Fig.1. These samples were set in the different facing holder [3] and mainly two kinds of group can be separated facing samples, namely S1 and

S2 and not facing samples, namely S3 and S4, to graphite divertor targets. A different point of S1 and S2 is the viewing angles from samples to divertor target.

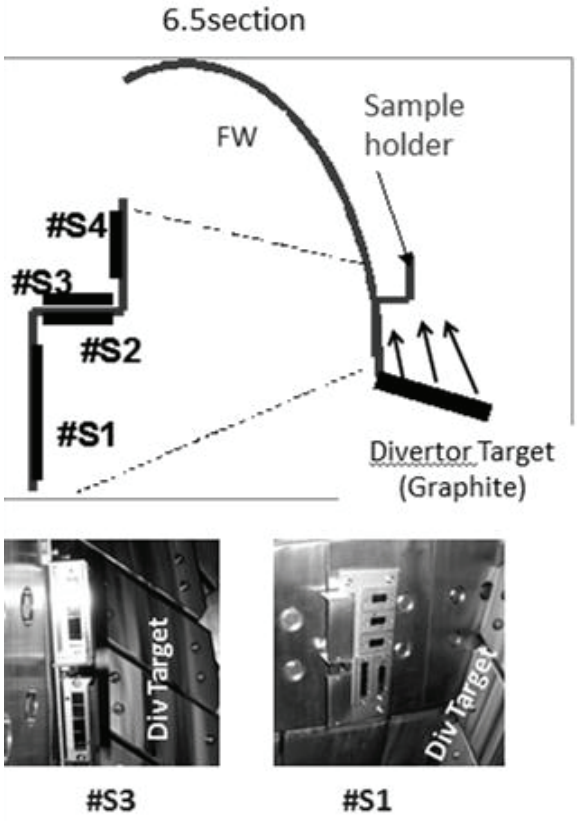

Fig. 1 Location of sample holders in the vacuum vessel. A schematic diagram of positional relation between sample holders and graphite divertor tilein LHD.

In the ellipsometry measurement, a light beam with a known state of polarization is reflected from a sample and the corresponding change in the state of polarization upon reflection is measured. From this change in the state of polarization, the film thickness and the refractive index are calculated. Chemical bindings are analyzed by X-ray photoelectron spectroscopy (XPS) and carbon structures are analyzed by Raman spectroscopy. Retained hydrogen is measured by Thermal desorption spectrometry (TDS).

3. Results

Raman spectroscopy is sensitive to the graphitic structures(phonon distribution) and has been applied in order to study the structural changes of CBMs. Various CBMs, e.g. fine grain graphite, pyrolytic graphite, diamond, CFC, glassy carbon, were characterized.

XPS shows chemical bindings with depth profile using Ar ion etching. Carbon intensity can be separated by fitting analysis and the main carbon peak was calibrated by experimental results using Highly Oriented Pyrolytic Graphite (HOPG). The top surface of HOPG was peeled off to reduce surface contaminations and lower surface layer was used a calibration analysis.

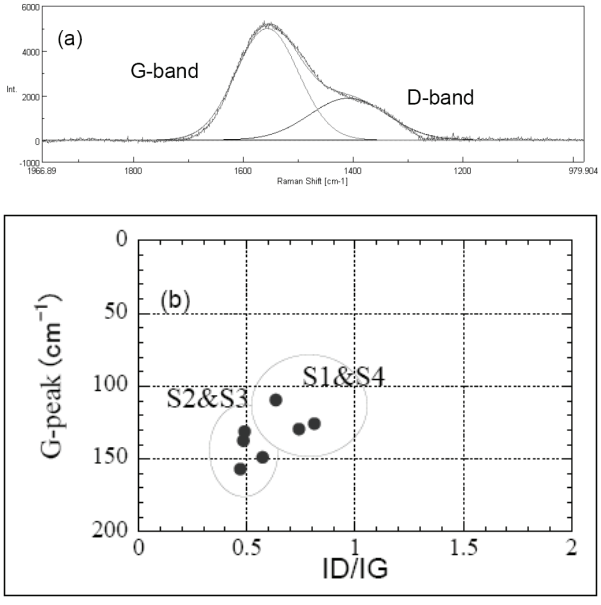

Fig.2 (a) Raman Spectra for deposition layer on LHD sampleS4. (b)Variation of Raman intensity ratios (ID/IG) of target samples vs. shifted G peak position of graphite by Raman spectroscopy.

The Raman spectra [4] from the target samples exhibit two clear peaks, which correspond to the graphite peak (G peak) around 1580 $cm^{-1}$and the disordered peak (D-peak)around 1355 cm^{-1}. Figure 2(a) shows Raman spectra for deposition layer on S4 sample and Fib.2 (b) shows the shifted G-peak position vs Raman intensity ratios (ID/IG). All data show the amorphous like structure. Plotting data are separated two groups, one is the S2 & S3, and the other is the S1 & S4. The situations of samples exposed to diverter plasma and targets are separated S1 & S2 and S3 & S4, but the result in Fig.2 (b) shows different characterization.

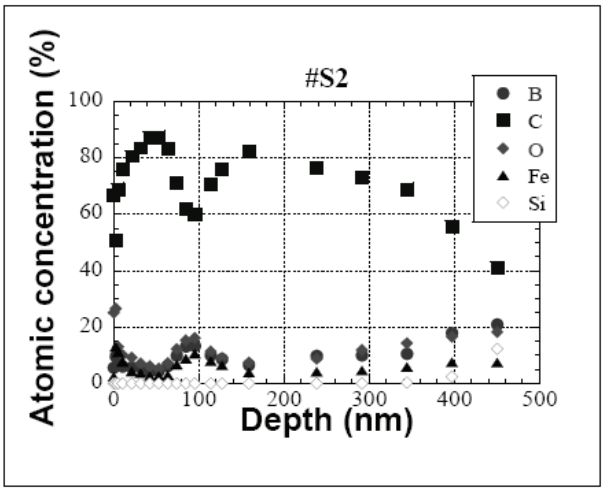

Fig. 3 Depth profile of deposition layer on LHD sample S2measured by XPS.

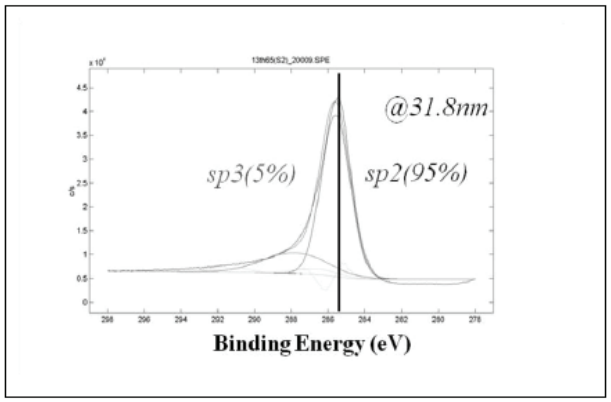

Fig.4 XPS fitting analysis of carbon at the depth of 31.8nm on LHD sample S2.

Figure.3 shows the atomic concentration of deposition layer on LHD sampleS2. Main composition is carbon of 80% and a few amounts of O, Fe and B are observed. As the sample data of carve fitting analysis, a chemical binding energy of carbon is shown in Fig.3. Mainly three kinds of peaks, sp2, sp3 and CO of C1s were set for fitting analysis and the sp2 satellite peak was negligible. From a comparison of Raman spectrum and XPS, the ratio of sp2 to sp3 is different. Because, the depth resolution of XPS is sensitive as shown in Fig.4, but Raman data shows integrated intensities in deposition layer of a few 100nm.

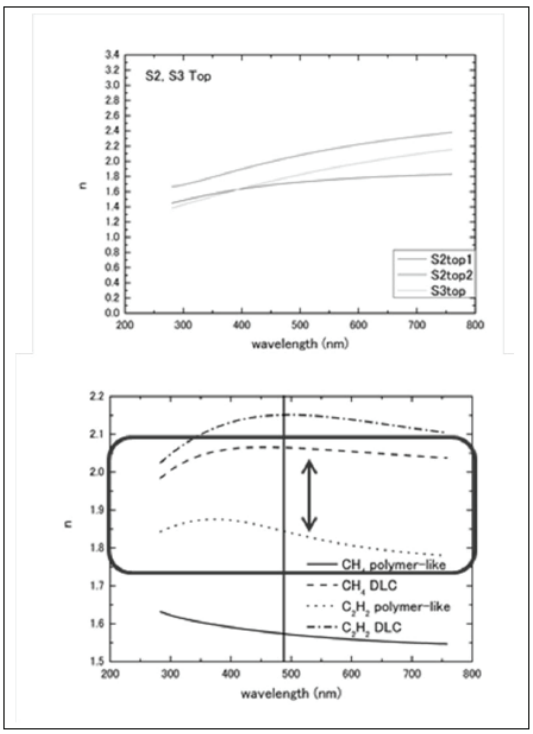

Fig. 5 Refractive index by ellipsometry for LHD samples on S2, S3 and reference samples of CH_4 and C_2H_2.

Quality of fitting analysis for C1s binding energies by XPS is different on S1 and S2samples. Results on S2 at different depth positions by XPS could be done using

the same fitting parameters, but S1 could not be done. The reasons are considered different compositions and hydrogen concentrations, and then carbon structure is also different.

For these deposition layers, TDS, scanning electron microscope (SEM), XPS, Raman spectroscopy were done as previous analyses [3, 4] and then amounts of retained hydrogen and ratios between carbon and hydrogen were shown. Characteristics of carbon bindings seem like amorphous carbon measured by Raman and XPS. From TDS results, methane (CH4) is observed on samples S1 and S2. But more details for carbon bindings by these analyses were not clear. And then, hydrocarbon bindings are measured by ellipsometry [5-6] in NFRI. Two kinds of parameters, refractive index and extinction coefficient, are measured and a comparison with results of reference targets C2H2-DLC, C2H4-polimar like, CH4-DLC and CH4-polimer like, and LHD deposition layers were done as shown in Fig.5. From comparison of these data, results of LHD samples S2 and S3 are located between CH4-DLC and C2H2 polymer-like structures. Two kinds of hydrocarbon on reference samples are composed by C-H bindings. Then hydrocarbons in LHD deposition layer are formed of single C-H bindings.

4. Summary

Carbon bindings and structures for carbon deposition layer in LHD are shown. From XPS and Raman spectroscopy results, carbon deposition layers shows one of amorphous carbon structures and the sp2 structure of carbon is higher than the sp3 structure. From comparison of ID/IG ratio in the other fusion devices measured by Raman, these plotting regions are located on deposition regions of plasma facing areas in fusion devices. More details of carbon –hydrogen bindings are analyzed by ellipsometry in NFRI and carbon –hydrogen bindings are formed of single C-H bindings.

Acknowledgments

This work was supported by the NIFS budgets ULFF004 and KUHR010. The authors would like to thank Mr. Nomura for support of Raman analysis. This work was partly supported by the JSPS-NRF-NSFC A3 Foresight Program in the field of Plasma Physics (NSFC: No.11261140328).

REFERENCES

[1] Roth J, et al. 2008 Plasma Physics and Controlled Fusion 50 : 103001.

[2] Ashikawa N, et al. 2006 Fusion Engineering and Design 81 : 2831.

[3] Nobuta Y, et al. 2013 Journal of Nuclear Materials.

[4] Hamaji Y, et al. 2013 Fusion Science and Technology 63.

[5] Dittmar T, et al. 2009 Nuclear Fusion 49 : 045004.

[6] Hong S.k, et al. 2010 Journal of Physics : 227 : 01204.

Simulation of SOL/Divertor plasmas on EAST tokamak

YiPing Chen[1], F.Q. Wang[1], X.J. Zha[2], L.Q.Hu[1], H.Y.Guo[1]

[1] Institute of Plasma Physics, Chinese Academy of Sciences, Hefei, Anhui, 230031, China

[2] Applied Physics Department, College of Sciences, Donghua University, Shanghai, 201620, China

Abstract: A code site for the simulation of SOL/Divertor plasma and impurity transport has been installed. The code site includes SOLPS, DIVIMP and so on. Dedicated experiments on SOL/divertor with plasma density ramp-up and Ar impurity seeding have been performed on EAST in typical L-mode discharges, the SOL/divertor plasmas in the typical discharges have been modelled. The modelling is carried out by using SOLPS which couples B2 to the neutral Monte-Carlo code Eirene. The modelling results show the cooling processes of divertor plasmas towards detachment and the modelling results are similar to the experiments, but there is still some difference between the experimental measurement and the modelling and further modelling is necessary in order to match the modelling results to the experimental measurement better.

PACS: 52.55 Fa, 52.40.Hf, 52.65.-y, 52.25.Vy

E-mail: ypchen@ipp.ac.cn

1. Introduction

Heat and particle controllability in the divertor has become one of the important issues on EAST tokamak. The total heating and driving power will be increased on EAST in the next years, the plasma temperature and heat fluxes to the target plates of divertor will increase with the heating power. In order to control the divertor power loads in the long pulse discharge the radiative divertor with partial or full detachment will become an important operation regime in EAST. Experiments to address the issue of radiative divertor have been carried out and the divertor detachment has been achieved by gas puffing or impurity seeding in the divertor plasmas on EAST [1]. For understanding the processes of detachment and supporting the experimental measurement in divertor plasmas, the modelling study on radiative divertor in EAST is necessary. The modelling study on radiative divertor in EAST is performed by using SOLPS5.2 code package [2], one of the latest version of SOLPS(B2-Eirene) [3,4]. SOLPS5.2 couples the plasma fluid code B2 [5,3,4] to the neutral Monte-Carlo code Eirene [6,7] and has become an important modelling tool of SOL/divertor plasma in tokamak.

2. Modelling of radiative divertor operation towards detachment

Dedicated experiments on radiative divertor with Ar impurity seeding have been performed on EAST in typical L-mode discharge with single null divertor

configuration. The main parameters in the shot include, ohmic heating power P_{ohm} = 0.519 MW, lower hybrid wave (LH) heating power P_{LH} = 1.0 MW, plasma current I_p = 0.6 MA and toroidal field B_t = 2.0 T. The particle balance is maintained by the gas puffing near the inner midplane and pumping. During the shot time t = 4 − 4.4 s the Ar impurity is seeded near the separatrix strike point at the outer target plate in order to study radiative divertor operation with Ar seeding.

Table 1: Main parameters in the typical L-mode discharge with radiative divertor operation on EAST.

Shot time	t[s]	0-5.0
Major radius	R[m]	1.858
Minor radius	a[m]	0.439
Aspect ratio	A	4.232
Plasma current	I_p[MA]	0.599
Loop voltage	V_{loop}[V]	0.865
Toroidal field	B_0[T]	2.012
Elongation	κ	1.759
Triangularity	δ_u	0.329
Triangularity	δ_l	0.528
Line-averaged density	$\bar{n}_e$ [10^{19} m $^{-3}$]	2.82
Total heating power	P_t[MW]	1.473
LH heating power	P_{LH}[MW]	0.954
Ohmic heating power	P_{ohm}[MW]	0.519
Configuration	–	Single

The main shot parameters in the typical L-mode discharge are shown in the table 1. The plasma current I_p, the loop voltage V_{loop}, the line-averaged electron density $\bar{n}_e$ and LH heating power P_{LH} trace versus time in the shot are shown in the Fig.1. The peak electron temperature T_e and density n_e, peak heat flux q_t and ion saturation flux J_s to the target plates trace versus time in the shot are shown in the Fig.2. The ”peak values” here refer to the maximum values measured by the stationary probes during the discharge, and these values do not necessarily repesent the peak values of the radial profiles, because the full profiles were not measured.

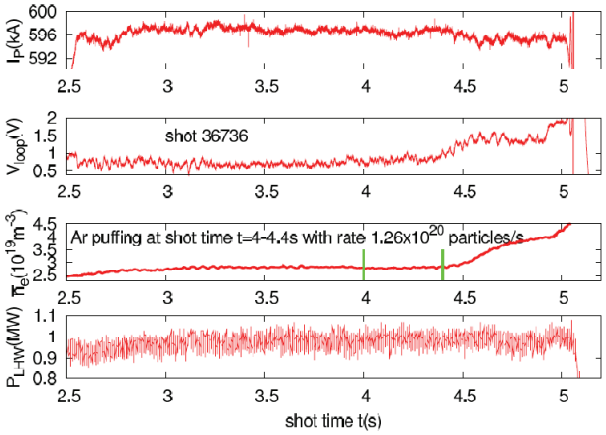

Figure 1: The plasma current I_p, the loop voltage V_{loop}, the line-averaged electron density $\bar{n}_e$ and LH heating power P_{LH} trace versus shot time t in the experimental shot.

From Fig.1, the line-averaged electron density $\bar{n}_e$ and loop voltage V_{loop} increase and plasma current I_p decreases when Ar is seeding, which happens after the shot time t = 4.4 s. $\bar{n}_e$, V_{loop} and I_p begin to response to Ar seeding at the shot time t = 4.4 s which is about 0.4 s later than the starting time of Ar seeding at the shot time t = 4.0 s, which means that before Ar arrives at the core plasma it needs about 0.4 s to travel to the

core plasma from the seeding tube entrance. The seeding tube entrance is the inlet through which the Ar gas is seeded into the plasma and it locates outside the torus. From Fig.2, at the target plates, the peak electron temperature T_e, density n_e, ion saturation current Js and power flux qt have the apparent response to Ar seeding at the shot time t = 4.4 s, which also has about 0.4 s delay than the starting time of Ar seeding at the shot time t = 4.0 s, it means 0.4 s is needed for Ar to pass the seeding tube and arrive at the divertor plasma. After the shot time t = 4.0 s, Te and qt at the target plates begin to respond slowly to Ar seeding, so, it is estimated that a small part of Ar may fastly pass the tube and arrives at divertor plasma earlier during Ar seeding. From Fig.2, the peak electron temperature T_e, electron density n_e, ion saturation current J_s and heat flux q_t to the divertor target plates decrease with the shot time t during the Ar puffing, illustrating the divertor plasma becomes partially detached. The full detachment of divertor plasma at the inner target plate can be estimated at the shot time t = 5 s because at that time $J_s \sim 0$ at the inner target plate.

The SOL/divertor plasma in the typical L-mode discharge is modelled. The modelling is carried out by using SOLPS5.2 which couples B2 to the neutral Monte-Carlo code Eirene. B2 solves the set of fluid transport equations that are similar to the set of Braginski equations. The numerical scheme based on these equations in SOLPS5.0 is quite satisfactory for the simulation of ohmic shots in tokamaks, but, the convergence of the numerical scheme is much worse in some situations. In order to improve the numerical scheme a new equation system is used where strong radial particle and energy convective fluxes are replaced by poloidal fluxes with the same divergence in SOLPS5.2. The new equation system is equivalent to the previous one and has better convergence when implemented into SOLPS5.2 code [2].

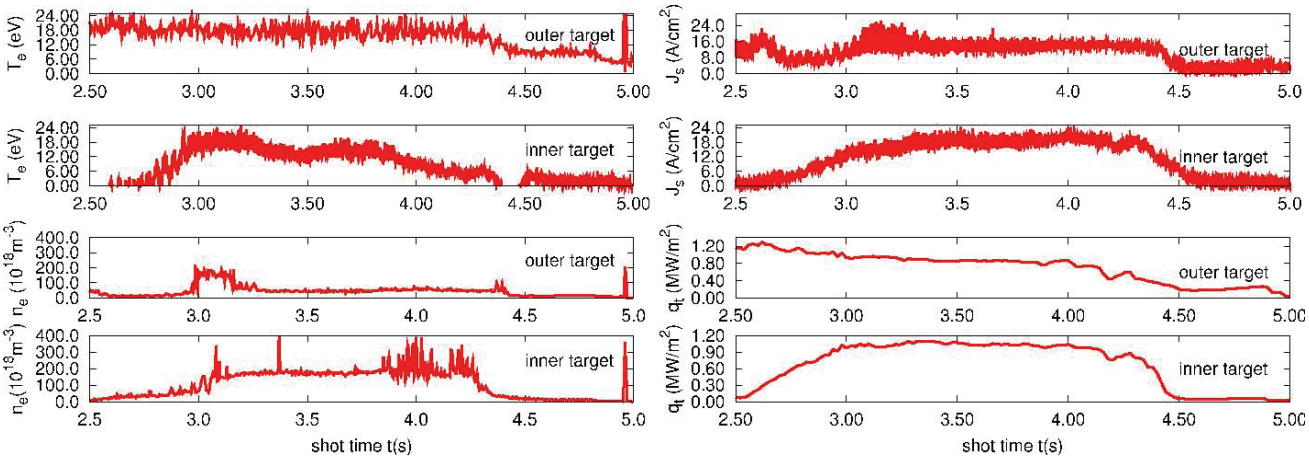

Figure 2: The peak electron temperature T_e and density n_e, peak heat flux q_t and ion saturation flux J_s to the target plates trace versus shot time t in the experimental shot.

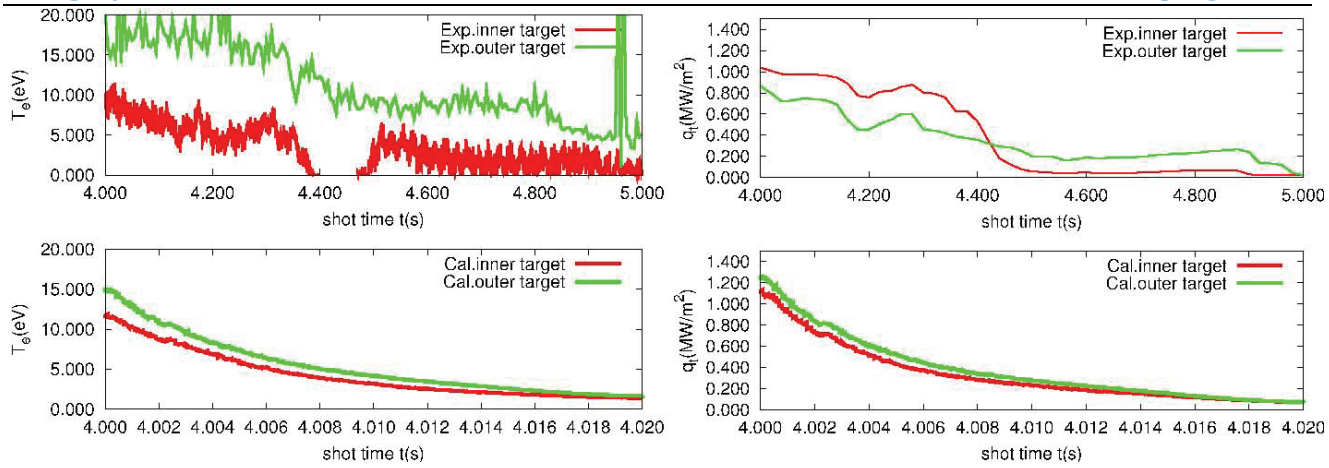

Figure 3: The comparesion between modelled and experimental results on the trace of peak electron temperature T_e and peak heat flux q_t to the target plates versus shot time t.

Fig.3 shows experimental and computational trace of the peak electron temperature T_e and the peak heat fluxes q_t at the inner and outer target plates versus the shot time t when Ar is seeding. From Fig.3 the modelling results show that before Ar seeding the peak electron temperature at the inner and outer targets is respectively T_e = 11.65 eV and T_e = 14.70 eV , the peak heat fluxes to the inner and outer targets are respectively q_t = 1.11 MW/m^2 and q_t = 1.24 MW/m^2. The peak electron temperature at the inner and outer targets T_e > 10.0 eV. With Ar seeding after t = 4.0 s, the peak electron temperature and heat fluxes to the target plates begin to decrease with the increase of the shot time t. At the shot time t = 4.01 s, i.e., the duration of Ar seeding δt = 10 ms, the peak electron temperature and heat flux are respectively T_e = 3.19 eV and q_t = 0.23 MW/m^2 at the inner target plate, T_e = 4.20 eV and q_t = 0.28 MW/m^2 at the outer target plate. The maximum Ar density at the inner core boundary $n_{Ar-core}$ = 4.98 × 10^{17} m^{-3}, $n_{Ar-core}/\bar{n}_e$ = 1.77%. The peak electron temperature at the inner and outer targets 2.0 eV < T_e < 5.0 eV . At the shot time t = 4.02 s, i.e., the duration of Ar seeding δt = 20 ms, the peak electron temperature and heat fluxes are respectively T_e = 1.41 eV and q_t = 0.07 MW/m^2 at the inner target plate, T_e = 1.67 eV and q_t = 0.073 MW/m^2 at the outer target plate, the maximum Ar density at the inner core boundary $n_{Ar-core}$ = 1.01 × 10^{18} m^{-3}, $n_{Ar-core}/\bar{n}_e$ = 3.58%. The peak electron temperature at the inner and outer targets T_e < 2.0 eV . The modelling results show the cooling processes of divertor plasmas due to Ar seeding.

3. Conclusions

The edge plasma code package SOLPS5.2 which couples the plasma fluid code B2 to the neutral Monte-Carlo code Eirene is used for the modelling of SOL/divertor plasma in the typical L-mode discharge with radiative divertor using Ar seeding on EAST tokamak. The real divertor geometry and the MHD

equilibrium from the experimental shot are employed in the modelling. The heat flux $P = 80\% \times P_{in} = 1.18$ MW to the computational region and plasma density at the separatrix $n_{esep} = \frac{1}{3}\bar{n}_e$ are assumed for the modeling with the heating power $P_{in} = 1.475$ MW and the line-averaged electron density $\bar{n}_e = 2.82\times10^{19}$ m^{-3} in the discharge. The modelling results show trace of the peak electron temperature Te and the peak heat fluxes qt at the inner and outer target plates versus the shot time t when Ar is puffing with rate $\Gamma = 1.26\times10^{20}$ s^{-1}.

The modelling results show that before Ar seeding the peak electron temperature at the inner and outer targets $T_e > 10.0$ eV. At the shot time $t = 4.01$ s, i.e., the duration of Ar seeding $\delta t = 10$ ms, the peak electron temperature at the inner and outer targets 2.0 eV < T_e < 5.0 eV. The maximum Ar density at the inner core boundary $n_{Ar-core} = 4.98\times10^{17}$ m^{-3}, $n_{Ar-core}/\bar{n}_e = 1.77\%$. At the shot time $t = 4.02$ s, i.e., the duration of Ar seeding $\delta t = 20$ ms, the peak electron temperature at the inner and outer targets $T_e < 2.0$ eV . The maximum Ar density at the inner core boundary $n_{Ar-core} = 1.01 \times 10^{18}$ m^{-3}, $n_{Ar-core}/\bar{n}_e = 3.58\%$. The modelling results show the cooling processes of divertor plasmas due to Ar seeding and are similar to the experimental measurement, but there is a major difference in time scales when Ar affects the plasma in between experiment and modelling. It should be noted that in the future it will be necessary to monitor the some key data, for example, the peak plasma density and temperature, particle and heat fluxes at the targets, the profiles of plasma density and temperature, particle and heat fluxes at the target plates, the time scales of the measured parameters, more carefully in the experiment in order to benchmark the core solutions better. The operation of the radiative divertor should be further optimized by experiments and modelling on EAST tokamak.

Acknowledgments

The work was supported partially by the JSPS-NRF-NSFC A3 Foresight Program in the field of Plasma Physics (NSFC No.11261140328) and the National Magnetic Confinement Fusion Science Program (No.2013GB109001). The authors would like to thank the EAST team for the experimental data.

References

[1] Dongsheng Wang, Houyang Guo, Huiqian Wang, Guangnan Luo, Zhenwei Wu, Jinhua Wu, Wei Gao, Liang Wang, Qiang Li, and EAST Team, Phys. Plasma 18, 032505(2011).

[2] V. Rozhansky, E. Kaveeva, P. Molchanov, I. Veselova, S. Voskoboynikov, D. Coster, G. Counsell, A. Kirk, S. Lisgo, the ASDEX-Upgrade Team and the MAST Team, Nucl. Fusion 49(2009)025007.

[3] Schneider R., Bonnin X., Borrass K., Coster D.P., Kastelewicz H., Reiter D., Rozhansky V.A. and Braams B.J., Contrib. Plasma Phys. 46, No.1-2, 3-191(2006).

[4] D.P. Coster, X. Bonnin, G Corrigan, G.S. Kirnev,

G. Matthews c, J. Spence, Contributors to the EFDA-JET work programme, J. Nucl. Mater. 337-339(2005)366-370.

[5] B.J.Braams, Contrib. Plasma Phys. 36(1996)276.

[6] D.Reiter, J. Nucl. Mater. 196-198(1992)80.

[7] D. Reiter, C. May, D. Coster, and R. Schneider, J.Nucl.Mater. 220-222(1995)987.

The effects of divertor parameters on the plasma penetration depth of the castellated tile gaps

Chaofeng Sang[1], Shuyu Dai[1], Jizhong Sun[1], Qian Xu[2], Dezhen Wang[1]

[1] Key Laboratory of Materials Modi_cation by Beams of the Ministry of Education, School of Physics and Optoelectronic Technology, Dalian University of Technology, Dalian, China

[2] Institute of Plasma Physics, Chinese Academy of Sciences, Hefei, China

Abstract: Castellation is foreseen as the best construction for the first wall and divertor target in the future fusion device. However, the gaps introduced by this structure may be the ideal hideouts of impurity, causing fuel retention and removal issues. To know how the fuel retained inside the gap, the plasma sheath around the gaps should be understood first. In this work, a kinetic model is applied to study plasma characteristics around the divertor gaps with the focus on the H^+ penetration depth inside the poloidal gaps. By varying the magnetic field strength and plasma temperature, we find the H^+ cyclotron radius has a significant effect on the penetration depth. Besides, the inuences of plasma parameters, gap width and magnetic field angle are also discussed in this work.

Keywords: Divertor, plasma, gap, retention

PACS: *52.40.Hf, 52.55.Fa, 52.65.y, 52.65.Rr*

1. Introduction

Castellated tiles construction is thought to be the best solution to ensure the thermo-mechanical durability and integrity of materials under high heat flux loads, especially for considering the use of metal as plasma facing material (e.g. tungsten and beryllium in ITER) [1, 2]. However, issues such as material migration into gaps and the subsequent fuel retention, are of crucial important for the fusion devices with castellation structure. These issues would bring great challenges for fuel removal [1]. Therefore, concerns over the fuel accumulation and impurity deposition in the gaps calls for dedicated studies.

Experimental studies [3, 4, 5, 6] on the fuel inventory inside the divertor tiles in different fusion devices showed that the divertor gaps can increase the fuel retention amount significantly. Moreover, the experimental results also indicated that fuel retention amount in the gaps depends on the divertor parameters as it is different in different fusion devices [4, 5, 7, 8, 9]. Therefore, understand the impact of gap parameters on the fuel inventory inside the gaps is required [10]. As it is known that the fuel accumulation inside the gaps is influenced directly by the plasma behavior around this region [11]. Thus, it is becoming an important task to study the plasma characteristics around the gap. Calculations of fuel accumulation in gaps and its subsequent release need a model considering the factors such as surface temperature and chemistry, and adequate description of plasma interaction with gap

sidewalls [10, 12]. Due to the complicated geometry and steep gradient of the plasma around gap entrance, fluid models are not suitable for studying the plasma characteristics around the gap, and instead, a kinetic model is needed.

Since Particle-In-Cell (PIC) model possesses the merits of kinetic methods, it has been applied extensively to edge plasma studies. Recently, a number of simulations have been carried out on the divertor gap sheath region using the PIC method [13, 14, 15, 16, 17]. In this work, a two-dimensional PIC model is applied to study the plasma penetration depth (PD) into the gaps of divertor tiles under different simulation parameters. Through this study, the relationship between PD and cyclotron radius (CR) of the ions is obtained, and the effects of gap width, plasma parameters and magnetic field are analyzed and discussed. Finally, based on the simulation results, an optimized gap construction

is proposed.

2 Simulation model

In this work, a two-dimensional in space and three-dimensional in velocity (2d3v) PIC code called EPPIC2D [18] is employed to study the plasma characteristics in the gap region of a castellated divertor. The technique is based on the electrostatic PIC model, similar with models in Refs. [19, 20, 21], and the code has been applied successfully to study the hydrocarbon deposited inside the gap [22, 23] and hydrogen isotope retained inside the gap of tungsten divertor tiles [10]. During simulation, the trajectories of charged particles are traced according to the computed electric field (by solving Poisson's equation) and adscititious magnetic field. The electric potential, plasma density distribution, particles and energy fluxes to the wall, which can be used to simulate plasma surface interactions [10, 24, 25], could all be obtained.

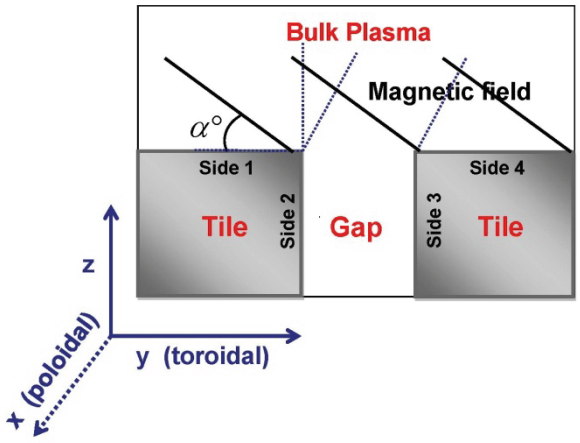

Fig.1 Schematic of the simulation domain. (color online)

Figure 1 shows the schematic of the simulation domain representing a poloidal gap: z represents the gap depth direction, x is aligned along the poloidal direction, and y stands for the toroidal direction. The bulk plasma and the gap bottom plane serve as the upper and bottom boundaries, respectively. Periodic condition is used for left and right boundaries. The charged particles are injected from upper boundary, which is treated as an ideal plasma source, with Bohm velocity along the magnetic field direction and Maxwellian velocity distributions in the perpendicular direction [26]. The electric potential is fixed to zero for upper boundary and $V_0 = -3kT_e$ for the bottom boundary [20], where V_0

is the oat potential, k is the Boltzmann's constant and T_e is the electron plasma temperature. The uniform magnetic field makes an inclination α with the plasma facing surface (PFS). In the simulation, the traced particles are H^+ and electrons with number of 9×10^6 m^{-3}, respectively. The simulation domain is divided into 256×256 grids, and the Poisson's equation is solved by multi-grid method [18]. For convenient presentation, the tile surfaces are labeled in succession as Side 1, Side 2, Side 3 and Side 4, shown in Fig. 1.

In this work, the divertor plasma is taken as fully ionization plasma, and collisions between charged particles and neutrals are neglected. The Coulomb collisions between charged particles (e-e, e-H^+, and H^+-H^+) are included [27] in our model, since it is very important for the high density low pressure plasma [28]. The code runs until the simulated plasma reaches its steady state.

3 Results and discussion

In this work, unless stated otherwise, the simulation parameters are: plasma density $n_e = n_i = 1.0\times10^{19}$ m^{-3}, plasma temperature $T_e = T_i = 20$ eV, simulation domain 2.4 mm×2.4 mm with a gap of 0.6 mm in width (y-direction) and 0.9 mm in depth (z-direction), uniform magnetic field with strength $B = 2$ T and angle $\alpha = 2^o$ with PFS (see Fig. 2). These parameters are taken from EAST tokamak.

In the beginning, the picture of plasma in the gap region is introduced. There is almost no electrons inside gaps, whereas the H^+ can penetrate into the gaps [18]. The electrons are totally confined by the magnetic field due to their small masses (CR of electron is about 7. 5×10^{-3} mm), and the H^+ with much larger masses have their CR (about 0.3 mm) in the same scale with the gap width (0.6 mm), which increases the chance of a H+ penetrating into the gap through its cyclotron motion. The separation of electrons and ions at the entrance of the gaps creates a virtual anode, i.e. a potential hill, which can suppress the H+ penetrating deeper inside the gap [29]. Different fusion devices have similar finding but differ in detail [30, 31, 32], and this influences the fuel inventory amount in the gaps. Therefore, it is quite important to understand the impact of different parameters on the plasma characteristics of divertor gaps, especially the plasma PD inside the gaps [10] to estimate the fuel retention [17, 33, 34] and the erosion of the tiles [35, 36].

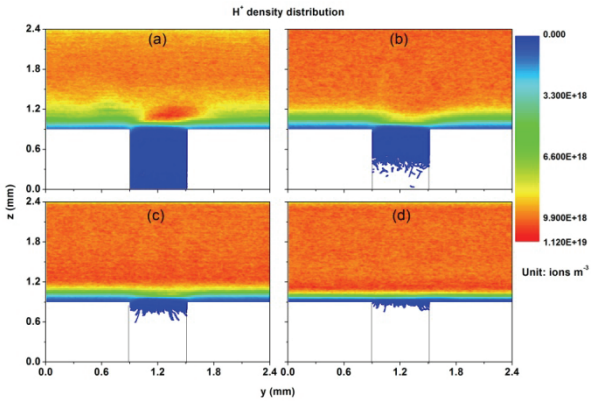

Fig.2 H^+ density distribution under different magnetic field strengths (a) 1 T, (b) 2 T, (c) 3 T, (d) 4 T, at steady state. (color online)

Since different fusion devices has diverse magnetic field strengths (B), to get better understanding of how

H^+ penetrate into the gaps, we first vary B and keep other parameters unchanged. Figure 2 shows the steady-state H^+ density distribution of different B (a) 1 T, (b) 2 T, (c) 3 T, (d) 4 T. It can be seen that, when B = 1 T, H^+ penetrate into the gap deeper than 0.9 *mm* (in our study, the simulate domain of the gap depth is 0.9 *mm*). Increase B to 2 T, the PD decreases to about 0.6 *mm*, and the PD continues to decrease as B increases until that H+ can almost not penetrate into the gaps. One of the requirements for H^+ entering into the gaps is their CR being in the same scale with the gap width. Since the H^+ CR is smaller than the gap width in our case, the PD thus decreases with the increasing B until H^+ being completely confined by the magnetic field. We can see in Fig. 3(d) that the confinement of H^+ is quite well when B = 4 T.

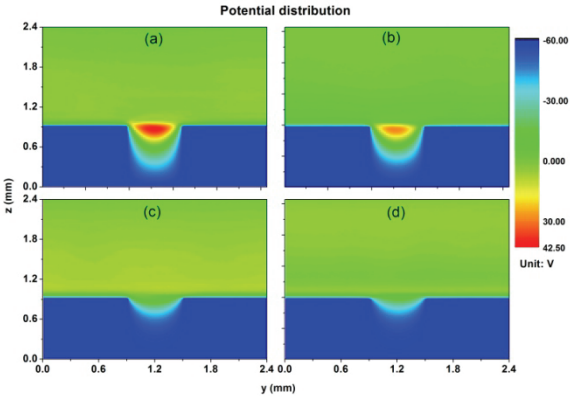

Fig.3 Electric potential distribution of different magnetic field strengths (a) 1 T, (b) 2 T, (c) 3 T, (d) 4 T, at steady state. (color online)

As the PD of H^+ inside the gap varying with B, the plasma characteristics around the gap may also be changed. Figure 3 represents the steady-state spatial distribution of electric potential of different B (a) 1 T, (b) 2 T, (c) 3 T, (d) 4 T. We can see the potential hill exists in all the four different B cases, very like that it appears in different fusion devices [37, 32, 38]. However, it also shows us the potential hill is distinct with each other under different B, and decreases with increasing B. Since it is known that the potential hill is created by the separation of electrons and ions (i.e. net charge) at the entrance of the gap [29] and the electrons can almost not penetrate into the gap, the values of the potential hill is only decided by the amount of H^+ inside the gap (the relationship can be deduced via Poisson's equation). As the amount of H^+ inside the gap decreases with the increasing B, so does the potential hill (see Fig. 3).

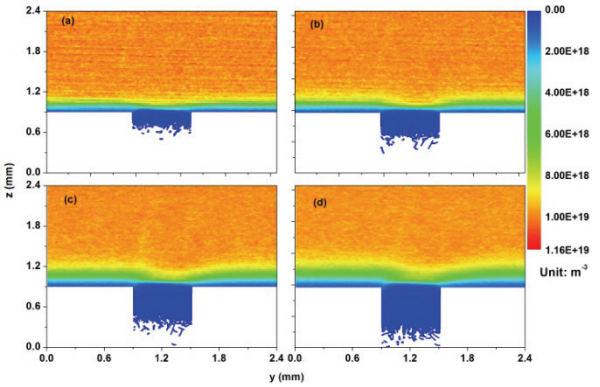

Fig.4 H^+ density distribution for different plasma temperatures (a) 5 eV , (b) 10 eV , (c) 20 eV , (d) 30 eV , at steady state. (color online)

In this study what concerns us mostly is the PD of H^+ inside the gap. In a tokamak, different discharge mode (such as L-mode, H-mode, detachment) or shot has various divertor plasma parameter (plasma temperature

and density). To study the plasma sheath and fuel retention under these conditions, the plasma parameters scanning is necessary. The H^+ density distribution of different plasma temperature (a) 5 eV, (b) 10 eV, (c) 20 eV, (d) 30 eV, at the steady state is shown in Fig. 4. It can be seen in the figure that the PD increases with the plasma temperature. The CR of a charged particle in the magnetic field can be expressed as $r_c = mv_\perp/qB$, where B is the magnetic field, m, $v_\perp$, q are the mass, velocity component perpendicular to B and charge of the charged particle, respectively. Since the value of v is proportional to $\sqrt{T}$ (T is the plasma temperature), we can obtain $r_c \propto \sqrt{T}$, i.e. the CR of a charged particle increases with the plasma temperature. Therefore, we can get that the PD of H^+ also increases with the plasma temperature (shown in Fig. 3).Under very high plasma temperature circumstance (thousands of electron volts during ELMs [39]), this conclusion also satisfied [32]. It can be deduced from this finding that during the divertor detachment operation, in which the divertor plasma temperature is extremely low [40], the H^+ could seldom penetrate into the poloidal gaps.

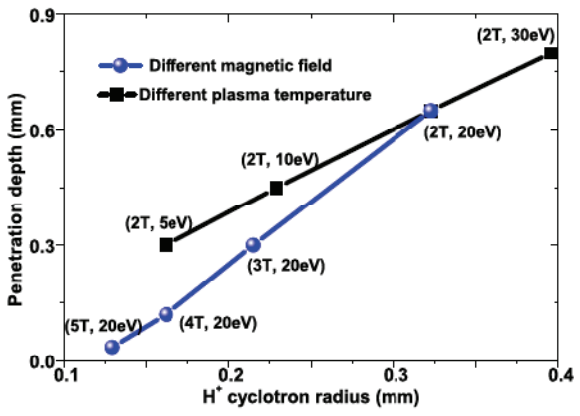

Fig.5 H^+ penetration depth inside the gap of different magnetic field strengths and different plasma temperature. (color online)

The PD of H^+ inside the gaps is influenced by magnetic field strength and plasma temperature, which are both connected to CR of the H^+, as above-mentioned. Figure 5 displays the PD as a function of H^+ CR obtained from different B and T, respectively. The horizontal axis represents H^+ CR calculated by different initial parameters, the vertical axis stands for the simulated PD of H+. We can see PD increases with the H^+ CR for both magnetic field strength and plasma temperature. However, there is a distinction between two lines: the slope of the line of different B is larger than that of T. The CR we used from different T is computed using initial plasma temperature. However, the real plasma temperature will be changed due to the electric potential difference ($V_0 = |3kT_e|$) between the tiles and bulk plasma, which make T higher than we used in Fig. 3. This can explain the existence of difference of the two ratios. It is also found that the potential hill increases with the plasma temperature, and thus restrains the PD of H^+ making the ratio smaller than expected. The plasma density effect is also studied, we find that the variation of plasma density makes minor effect on the PD due to the unchanged CR of H^+.

The effect of the gap width is also studied in this work. It is shown in Fig. 6 the H^+ density distribution of different gap width: (a) 0.6 mm, (b) 1.0 mm, (c) 1.2 mm.

The PD of H^+ into gaps is also almost unchanged with the gap width in our simulation due to that the plasma wetted region in Side 3 is much smaller than the radiation area of H^+ CR. It's worth noting that this is only satisfied in the case the gap width is in the same scale with CR of the H^+ and the magnetic incident angle α is very small. For the very large B case, the H^+ is almost confined by the magnetic field and move along it, causing the CR of H^+ being smaller than plasma wetted region. Therefore, the PD will increase with the gap width. This could also increase the heat flux load on plasma wetted location at the gap entrance of Side 3 causing the tile being eroded. It could be more serious during ELMs [32] when the tiles are made of metal. If the magnetic field angle α is very large (e.g. toroidal gap), the plasma wetted region in Side 3 is much larger than CR radiation area, then the PD would increase with gap width [41] in the condition that the gap depth is large enough; otherwise, it may cause more H^+ reaching the bottom of the gap. The neutral particles, which are not confined by the magnetic field and electric field, would penetrate into the gap increasingly with the gap width; thus, the geometry of the divertor tiles with small gaps is recommended.

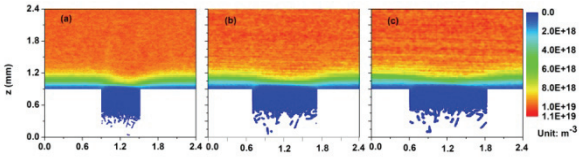

Fig.6 H^+ density distribution of different gap width (a) 0.6 mm, (b) 1.0 mm, (c) 1.2 mm, at steady state. (color online)

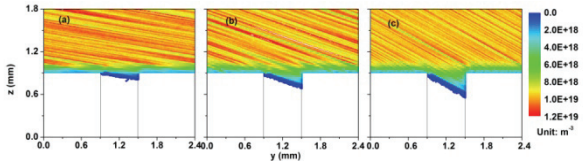

Fig.7 H^+ density distribution of different magnetic field angles (a) 2°, (b) 10°, (c) 20°, (d) 30°, at steady state. The magnetic field strength is 5 T. (color online)

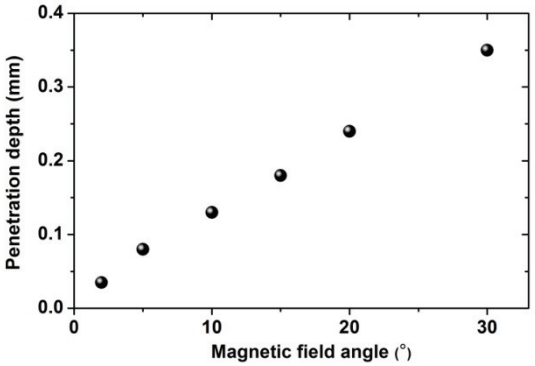

Fig.8 H^+ penetration depth inside the gap as a function of different magnetic field angles at steady state. (color online)

Finally, the influence of the magnetic field angle α is studied. It is shown in Fig. 7 the H^+ density distribution of the different α: (a) 2°, (b) 10°, (c) 20°. Because the CR of H^+ has large effect on the PD, we select a large magnetic field strength (B = 5 T) to eliminate its impact. From this figure, we can see the PD of H^+ inside a gap increases with α and almost all of the H^+ in the gap finally incident into Side 3 as a result of good confinement, which is in agreement with [8, 42]. The plasma wetted region in Side 3 (gap width*$tan(\alpha^o)$) increases with α; therefore, it can be seen that H^+ can get deeper for the larger α. The relation of α with H^+ incident depth is shown in Fig. 8.

Smaller value of α has two effects: decreasing the heat flux load to the PFS of the tile (Side 1 and 4) [43, 44] and reducing the fuel inventory inside the poloidal gaps of divertor. Through above study, we know strong magnetic field with small angle can reduce the H^+ into the gap. The gap width will then be important for both charged particles and neutrals under that condition; therefore, small gap width geometry is recommended. However, this design would lead to high heat flux load to the plasma wetted region in Side 3 (see Fig. 2) and make it more easily to be eroded (melting for metal material) unavoidable, being especially worse during ELMs. Since lower plasma temperature can decrease the heat flux load to the PFS and H^+ amount inside the gap of the divertor tiles, we should manage to reduce the divertor plasma temperature. Divertor plasma detachment operation seems to be the best solution [40], which can cool down the plasma significantly [45].

4. Conclusions

In this work, a kinetic model is applied to study the dependence of the H^+ penetration depth (PD) inside the poloidal gap of the divertor tiles on operation parameters. It is found that both the PD of H^+ and the height of the electric potential hill at the gap entrance decreases with the magnetic field strength, and increases with the plasma temperature, namely, the PD of H^+ increases with its cyclotron radius (CR). In addition, it is also found that the plasma density has limited effect on the PD, and the gap width has effect only under the condition that the gap width is on the same scale as the CR, and the magnetic field angle α is small. The PD also increases with α under the condition that H^+ is well confined. Thus, it is favorable to use the magnetic field with large strength and small angle as well as to construct the divertor gaps with small gap width in fusion devices. However, this design would probably increase the heat flux loads to the plasma-facing side wall of the gap near its entrance and erode (or melt) the tiles. The divertor plasma detachment operation is thus a solution for both fuel retention and heat flux loads.

References

[1] M. J. Rubel, J. Coad, R. A. Pitts, J. Nucl. Mater. 367-370 (2007) 1432.

[2] P. Stangeby, Nucl. Fusion 51 (2011) 033008.

[3] M. J. Rubel, G. Sergienko, A. Kreter, A. Pospieszczyk, M. Psoda, E.Wessel, Fusion Eng. Des. 83 (2008) 1049.

[4] C. H. Skinner, C. A. Gentile, J. C. Hosea, D. Mueller, J. P. Coad, G. Federici, R. Haange, Nucl. Fusion 39 (1999) 271.

[5] K. Sugiyama, T. Tanabe, K. Masaki, N. Miya, J. Nucl. Mater. 367-370 (2007) 1248.

[6] R. A. Pitts, A. Kukushkin, A. Loarte, A. Martin, M. Merola, C. E. Kessel, V. Komarov, M. Shimada, Phys. Scr. T138 (2009) 014001.

[7] W. Daenner, M. Merola, P. Lorenzetto, A. Peacock, I. Bobin-Vastra, L. Briottet, P. Bucci, D. Conchon, A. Erskine, et al., Fusion Eng. Des. 61-62 (2002) 61.

[8] T. Tanabe, K. Sugiyama, C. H. Skinner, N. Bekris,

C. A. Gentile, J. P. Coad, Fusion Sci. Tech. 48 (2005) 577.

[9] A. Litnovsky, P. Wienhold, V. Philipps, K. Krieger, A. Kirschner, D. Matveev, D. Borodin, J. Nucl. Mater. 390-391 (2009) 556.

[10] C. Sang, J. Sun, X. Bonnin, H. Guo, D. Wang, J. Nucl. Mater. Doi: 10.1016/j.jnucmat.2013.01.249.

[11] M. J. Rubel, J. P. Coad, P. Wienhold, G. Matthews, V. Philipps, M. Stamp, T. Tanabe, Phys. Scr. T111 (2004) 112.

[12] V. A. Kurnaev, D. Matveev, N. Trifonov, J. Nucl. Mater. 363-365 (2007) 797.

[13] R. Dejarnac, M. Komm, J. Stockel, R. Panek, J. Nucl. Mater. 382 (2008) 31.

[14] R. Dejarnac, M. Komm, D. Tskhakaya, J. P. Gunn, Z. Pekarek, IEEE Trans. Plasma. Sci. 38 (2010) 1042.

[15] K. Inai, K. Ohya, J. Nucl. Mater. 363-365 (2007) 915.

[16] K. Inai, K. Ohya, Y. Tomita, A. Kirschner, A. Litnovsky, T. Tanabe, J. Nucl. Mater. 390-391 (2009) 119.

[17] D. Matveev, A. Kirschner, A. Litnovsky, M. Komm, D. Borodin, V. Philipps, G. V. Oost, Plasma Phys. Control. Fusion 52 (2010) 075007.

[18] C. Sang, J. Sun, D. Wang, J. Nucl. Mater. 415 (2011) S204.

[19] J. P. Verboncoeur, Plasma Phys. Control. Fusion 47 (2005) A231.

[20] D. Tskhakaya, K. Matyash, R. Schneider, F. Taccogna, Contrib. Plasma Phys. 47 (2007) 563.

[21] C. Sang, J. Sun, D. Wang, Plasma Phys. Control. Fusion 52 (2010) 042001.

[22] S. Dai, C. Sang, J. Sun, D.Wang, Contrib. Plasma Phys. 52 (2012) 309.

[23] S. Dai, C. Sang, S. Liu, J. Sun, D. Wang, Fusion Eng. Des. 87 (2012) 782.

[24] M. Warrier, R. Schneider, X. Bonnin, Comput. Phys. Comm 160 (2004) 46.

[25] G. Kawamura, Y. Tomita, A. Kirschner, J. Nucl. Mater. 415 (2011) S192.

[26] G. Gozadinos, D. Vender, M. M. Turner, J. Comput. Phys. 172 (2001) 348.

[27] K. Nanbu, IEEE Trans. Plasma. Sci. 28 (2001) 971.

[28] E. Kawamura, C. K. Birdsall, Phy. Rev. E 71 (2005) 026403.

[29] M. Komm, R. Dejarnac, J. P. Gunn, A. Kirschner, A. Litnovsky, D. Matveev, Z. Pekarek, Plasma Phys. Control. Fusion 53 (2011) 115004.

[30] K. Inai, K. Ohya, Contrib. Plasma Phys. 48 (2008) 275.

[31] R. Dejarnac, M. Komm, J. P. Gun, R. Panek, J. Nucl. Mater. 390-391 (2009) 1042.

[32] R. Dejarnac, M. Komma, J. P. Gunn, R. Panek, J. Nucl. Mater. 390-391 (2009) 818.

[33] A. Litnovsky, V. Philipps, A. Kirschner, P. Wienhold, G. Sergienko, A. Kreter, U. Samm, O. Schmitz, et.al., J. Nucl. Mater. 367-370 (2007) 1481.

[34] C. Sang, X. Bonnin, M.Warrier, A. Rai, R. Schneider, J. Sun, D. Wang, Nucl. Fusion 52 (2012) 043003.

[35] A. Litnovsky, V. Philipps, P. Wienhold, K.

Krieger, A. Kirschner, D. Borodin, G. Sergienko, J. Nucl. Mater. 386-388 (2009) 809.

[36] K. Wittlich, T. Hirai, J. Compan, N. Klimov, J. Linke, A. Loarte, M. Merolac, et.al., Fus. Eng. Des. 84 (2009) 1982.

[37] R. Dejarnac, J. P. Gun, J. Nucl. Mater. 363-365 (2007) 560.

[38] K. Ohya, J. Nucl. Mater. 415 (2011) S10.

[39] H. Zohm, Plasma Phys. Control. Fusion 38 (1996) 105.

[40] G. Federici, C. H. Skinner, J. N. Brooks, J. P. Coad, C. Grisolia, A. A. Haasz, A. Hassanein, V. Philipps, C. S. Pitcher, J. Roth, W. R. Wampler, D. G. Whyte, Nucl. Fusion 41 (2001) 1967.

[41] K. Ohya, K. Inai, M. Inoue, Y. Tomita, G. Kawamura, T. Tanabe, J. Nucl. Mater. 417 (2011) 602.

[42] K. Inai, Y. Tomita, G. Kawamura, K. Ohya, Fusion Eng. Des. 85 (2010) 1416.

[43] P. C. Stangeby, The Plasma Boundary of Magnetic Fusion Devices, Institute of Physics Publishing, Bristol.

[44] C. Sang, J. Sun, D. Wang, Fusion Eng. Des. 85 (2010) 1941.

[45] C. S. Pitcher, P. C. Stangeby, Plasma Phys. Control. Fusion 39 (1997) 779.

Carbon distribution during plasma detachment triggered by edge magnetic island formation in LHD

C. F. Dong[1], S. Morita[1,2], M. Kobayashi[1,2], T. Oishi[1,2], M. Goto[1,2], E. H. Wang[1] and X. L. Huang[1]

[1] National Institute for Fusion Science, Toki 509-5292, Japan

[2] Department of Fusion Science, Graduate University for Advanced Studies, Toki 509-5292, Japan

Abstract: The detached plasma has been successfully achieved by applying the edge 1/1 magnetic island in Large Helical Device (LHD). Carbon, which is uniquely the dominant intrinsic impurity in general LHD discharges, is considered to be the main radiating species in the island-triggered detached plasma. The vertical profile of CIV measured from general discharges of LHD is characterized by a single edge intensity peak. In detached plasmas triggered by the edge magnetic island formation, however, the vertical profile of CIV shows a significant difference. Double edge peaks of CIV are found during the plasma detachment and the CIV radiation is also remarkably enhanced in the vicinity of X-point, whereas the vertical profile of CVI does not show any significant difference in both the attached and detached plasmas. In this proceeding the carbon distribution during the plasma detachment is presented and the results are discussed with edge magnetic field structure.

1. Introduction

Heat load mitigation on divertor plates is one of the critical issues in the next-generation magnetically confined fusion devices. As a solution to this problem, the so-called 'detached' divertor operation was first proposed as the preferred divertor scenario of the next step device [1]. The detached plasma has been achieved by injection of working gas or gaseous impurities into divertor region of tokamaks. A strong increase in radiation loss near the X-point region is observed, and the radiation is mainly contributed by carbon in deuterium gas injection discharges in JT-60U, DIII-D and JET [2-4] and by neon in neon-seeding discharge in JT-60U.

The divertor detachment in LHD is achieved by impurity gas puffing as well as the tokamaks. Recently, magnetic island-triggered detached plasma is demonstrated in LHD by applying the 1/1 resonant magnetic perturbation (RMP) fields [5]. Since no additional impurity is introduced in the plasma, carbon is considered to be the main radiation species in the island-triggered detached plasma. The vertical profiles of CIII (386.2Å, 3p–2s), CIV (312.4Å, 3p–2s), CV (40.27Å, 2p–1s) and CVI (33.73Å, 2p–1s) are measured by extreme ultraviolet (EUV) spectrometer [6]. The vertical profile of CIV is characterized by an edge intensity peak in general discharges of LHD [7]. In detached plasmas triggered by the edge magnetic island formation, however, the vertical profile of CIV

shows a significant difference. Double edge peaks of CIV are found during the plasma detachment and the CIV radiation is also remarkably enhanced in the vicinity of X-point, whereas the vertical profile of CVI does not show any significant difference in both the attached and detached plasmas.

The paper presents CIV and CVI profiles observed from attached and detached plasma. Due to the weak intensity of CIII and CV, the line emissions of CIV and CVI are mainly analyzed here. The difference in observed profiles is discussed with edge magnetic field structure.

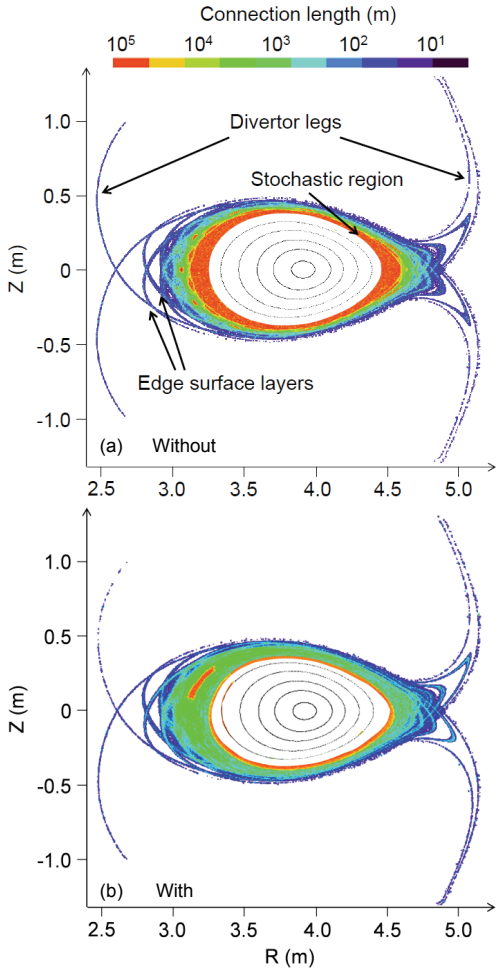

Fig. 1: Connection length structure in ergodic layer of LHD (a) without RMP and (b) with RMP.

2. Magnetic structure in ergodic layer with and without RMP

LHD is a superconducting helical type device with toroidal and poloidal periods number of 2 and 10, respectively. Due to the mode spectrum of magnetic field produced by the helical coils, magnetic island with different mode numbers are created, and they overlap each other. Therefore, a stochastic field line structure appears in the edge region intrinsically. The edge plasma consists of stochastic region characterized by long connection lengths with remnant islands and edge surface layer characterized by a mixture of long and short connection lengths, as shown in Fig. 1(a). Ten pairs of RMP coils installed at the top and bottom of LHD machine are used to form the 1/1 magnetic island. The magnetic island is formed when the RMP resonates at a rational surface fixed by the magnetic configuration. The magnetic field line structure with RMP is shown in Fig. 1(b). The structure is clearly modified when the RMP is applied, and the connection length at island region is dominated by the magnetic field lines with connection length around 1000m. The magnetic island width can be roughly estimated by the electron temperature profile measured by Thomson scattering system [8, 9]. The magnetic surface forms iso-temperature contour very well since the parallel velocity is much faster than the perpendicular diffusion. It has been reported that the island width is dependent on some plasma parameters in LHD. For example, the magnetic island is disappeared at lower collisionality regime due to the healing effect.

3. Experimental results and discussion

The vertical profiles of CIII, CIV, CV and CVI are measured by a space-resolved EUV spectrometer. The EUV spectrometer is installed in LHD perpendicular to the toroidal magnetic field at a horizontally elongated plasma cross section. The emission from the upper half of LHD plasma is recorded for this study. Due to the weak intensity of CIII and CV line emissions in the EUV range, the CIV and CVI line emissions are analyzed here.

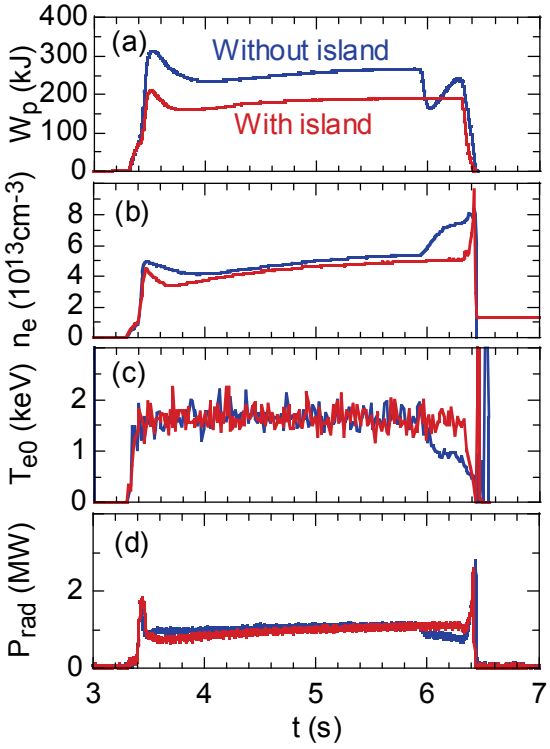

Fig. 2: Time evolution of (a) stored energy, (b) electron density, (c) central electron temperature and (d) total radiation power in discharges without and with magnetic islands.

As the previous result, the vertical profile of CIV is characterized by a single edge intensity peak in general attached discharges of LHD. The effect of magnetic island on the CIV profile is then examined. The time evolution of stored energy, electron density, central electron temperature and total radiation power from attached plasma without and with magnetic islands are shown in Fig. 2. The plasma stored energy in discharge with island is apparently smaller than that in discharge without island. The other parameters in the two discharges are almost identical. The CIV and CVI profiles at t=4.9s are plotted in Fig. 3.

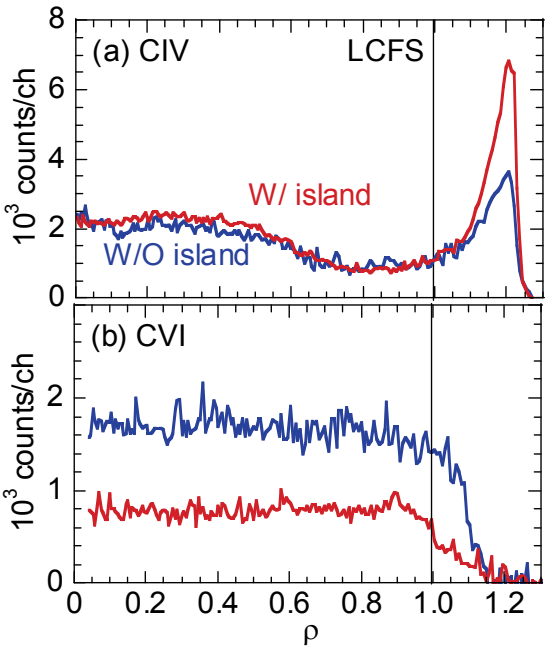

Fig. 3: Profiles of (a) CIV and (b) CVI from discharges without (W/O) and with (W/) magnetic islands.

The intensity of CIV profile, as shown in Fig. 3(a), in range of ρ=0-0.8 and outside the last closed flux surface (LCFS) is mainly emitted from the peripheral regions of X-point and top O-point, respectively. A sharp edge peak is formed in the CIV profile from typical attached plasma, i.e., without island. The CIV emission from X-point region is similar for the two

discharges without and with islands. The intensity at edge peak of CIV profile, however, is enhanced by a factor of 2 when the RMP coils are applied to the LHD plasma. The CVI profiles tend to be flat in two discharges without and with islands, as shown in Fig. 3(b). The intensity of CVI with island is reduced to the half of the CVI intensity without island. The increased CIV intensity at plasma edge and the decreased CVI intensity indicate that the magnetic island has an effect of the impurity screening. On the other hand, the previous study reveals that the position of CIV edge peak corresponds to the edge boundary of ergodic layer at O-point [7]. And the peak position of CIV is mainly determined by the combination of the local temperature and the connection length at plasma edge. Figure 3(a) shows that the CIV has the identical peak position at plasma edge for discharges with island and without island.

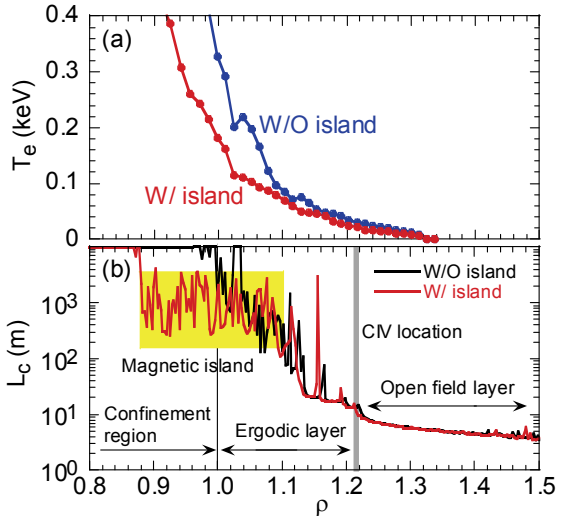

Fig. 4: (a) Temperature profile in discharge without and with islands and (b) connection length distribution at plasma edge without and with islands.

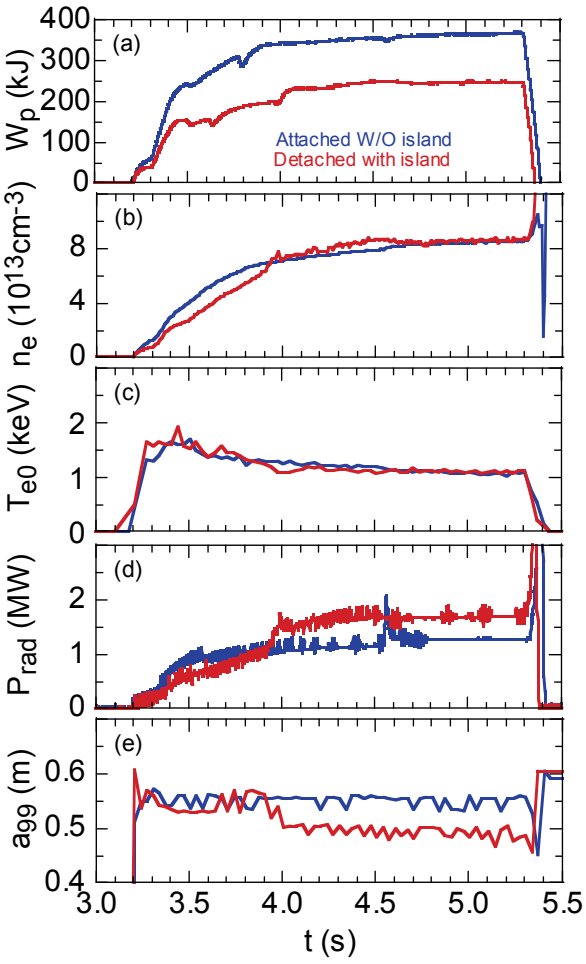

Fig. 5: Time evolution of (a) stored energy, (b) electron density, (c) central electron temperature, (d) total radiation power and (e) minor radius, a99, from attached plasma without magnetic island and detached plasma induced by magnetic islands.

The temperature profile in discharge without and with islands and the connection length distribution at plasma edge without and with islands are plotted in Fig. 4. Although the temperature profiles are apparently different inside ρ=1.1, the T_e at peak position of CIV for two discharges are almost identical, i.e., 27eV: without island and 30eV: with island. As shown in Fig. 4(b), the region with short connection length (<10m) is defined as the open field layer, in which the

plasma cannot be sustained, while plasma confinement region can be defined inside ρ=1.0. The ergodic layer is the region between the confinement region and the open field layer. The connection length structure at island region dominated by the connection length around 1000m is obviously changed, when the magnetic island exists. In contrast, the connection length distribution at the peak position of CIV shows the almost same structure for cases without and with magnetic islands, as seen in Fig. 4(b). From the analysis, it is found that the local temperature and connection length structure at CIV location are almost identical, therefore, the CIV profiles from discharges without and with islands have the same peak position.

The time evolution of stored energy, electron density, central electron temperature, total radiation power and minor radius, a_{99}, from attached plasma without magnetic island and detached plasma induced by magnetic islands are shown in Fig. 5. Here, the minor radius of a_{99} is the radius in which 99% of the total stored energy is confined. The two discharges have the similar electron density and central temperature. However, only the discharge with RMP can enter the detached phase at t=4.0s as shown in Fig. 5. The total radiation power is enhanced and the plasma shrinks after the detachment, although the global plasma confinement is not significantly degraded as seen in Fig. 5(a). The CIV profiles obtained from the attached discharge at t=4.8s and the detached discharge at t=4.8s are presented in Fig. 6. The CIV profile in detached plasma shows a significant difference. That is, the double edge peaks appear and the intensity near X-point region is remarkably enhanced. For comparison, the CIV profile at t=3.8s just before the detachment is also plotted in Fig. 6. The CIV profile at t=3.8s from detached discharge has a similar profile to that obtained from attached discharge, except for the profile near X-point region. It reveals that the double edge peaks only appear at the detached phase.

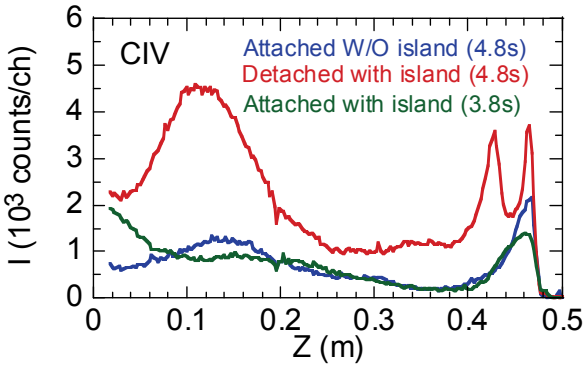

Fig. 6: CIV profiles from attached and detached plasmas.

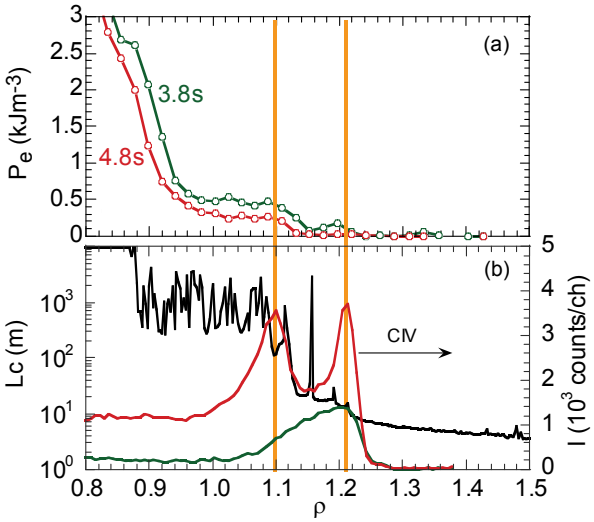

Fig. 7: (a) Electron pressure profile at plasma edge and (b) connection length distribution and CIV profiles.

The electron pressure profile at plasma edge and the connection length distribution are shown with CIV profile in Figs. 7(a) and (b). Both of electron pressure profiles obtained from attached and detached plasmas in region of ρ=0.98-1.1 tend to be flat due to the magnetic island formation, and the electron pressure in detached phase is reduced. The position of CIV at outer edge peak in the detached plasma is the same as that in the attached plasma. The radial position of CIV coincides with the position where the connection length starts to increase, indicating a clear edge boundary of the ergodic layer. On the other hand, the inner peak position of CIV coincides with the outer edge of the magnetic island, at which the connection length rapidly increases. The electron pressure also turns to increase at the inner peak position of CIV. Seeing the electron pressure profile in Fig. 7(a), it is close to zero at plasma edge (ρ=1.21). The Thomson scattering data in Fig. 7(a) are measured along the mid-plane at a horizontally elongated plasma cross section, whereas the magnetic field structure at the plasma edge in Fig. 7(b) is plotted at different poloidal position of the top O-point. The appearance of the inner edge peak of CIV can be explained by the connection length structure with magnetic island formation, and the inner edge peak position of CIV is the practical edge boundary of island-detached plasma at O-point.

The CVI profile is also observed from attached and detached plasmas. The shape of CVI profile from the island-detached plasma is almost kept constant even in the attached plasma, i.e., a flat profile. However, the CVI intensity from detached plasma increases three times compared to the attached plasma, whereas the intensity decreases in the attached plasma with island. It indicates that the impurity screening effect is almost disappeared when the detached plasma is formed by the external island.

4. Summary

The detached plasma is successfully achieved by applying the edge 1/1 magnetic island in LHD. Carbon is demonstrated to be the main radiator in the island-detached plasma. The vertical profile of CIV characterized by en edge intensity peak in the general discharges of LHD shows a significant difference in the detached plasma. In short, double edge peaks appear and the intensity near X-point region is much enhanced. The position of outer edge peak of CIV corresponds to the typical position of CIV in general discharges, and the inner peak position located at the outer edge of magnetic island indicates the practical edge boundary in the detached plasma. The CVI profile does not show such a difference, even in the detached plasma. Although the magnetic island generally enhances the impurity screening, the screening effect seems to be vanished in the present detached plasma triggered by the island formation.

This work was partly supported by the JSPS-NRF-NSFC A3 Foresight Program in the field of Plasma Physics (NSFC: No.11261140328).

References

[1] M. L. Watkins, P. H. Rebut, in 1992 International Conference on Plasma Physics (Proc. Conf. Innsbruck, 1992), Vol. 16C, Part II, European Physical Society, Geneva 731 (1992).

[2] T. Nakano, et al., J. Nucl. Mater. **390-391**, 255, (2009).

[3] M. E. Fenstermacher, et al., Phys. Plasmas **4**, 1761 (1997).

[4] C. F. Maggi, et al., J. Nucl. Mater**. 241–243**, 414 (1997).

[5] M. Kobayashi, et al., Phys. Plasmas **17**, 056111 (2010).

[6] C. F. Dong, et al., Rev. Sci. Instrum. **81**, 033107 (2010).

[7] C. F. Dong, et al., Phys. Plasmas **18**, 082511 (2011).

[8] K. Narihara, et al., Rev. Sci. Instrum. **72**, 1122 (2001).

[9] Y. Narushima, et al., Plasma Fusion Res. **1**, S1094 (2007).

Modelling of local carbon deposition on rough test limiter exposed to the edge plasma of TEXTOR

Shuyu Dai[1,2], A. Kirschner[2], D. Matveev[2,3], D. Borodin[2], C. Björkas[2,4], Jizhong Sun[1], Dezhen Wang[1*]

[1] Key Laboratory of Materials Modification by Laser, Ion and Electron Beams (Ministry of Education), School of Physics and Optoelectronic Technology, Dalian University of Technology, Dalian 116024, China

[2] Institut für Energie- und Klimaforschung – Plasmaphysik, Forschungszentrum Jülich, Association EURATOM-FZJ, Trilateral Euregio Cluster, D-52425 Jülich, Germany.

[3] Department of Applied Physics, Ghent University, Plateaustraat 22, B-9000 Ghent, Belgium

[4] Association EURATOM-Tekes, Department of Physics, P.O.B 64, 00014 University of Helsinki, Finland

[*] Email:wangdez@dlut.edu.cn

Abstract: A Monte-Carlo code called SURO has been developed to study the influence of surface roughness on the impurity deposition characteristic in fusion experiments. SURO uses the test particle approach to describe the impact of background plasma and the deposition of impurity particles on a sinusoidal surface. The local impact angle and dynamic change of surface roughness as well as surface concentrations of different species due to erosion and deposition are taken into account. Coupled with 3D Monte-Carlo code ERO, SURO was used to study the impact of surface roughness on ^{13}C deposition in $^{13}CH_4$ injection experiments in TEXTOR. The simulations showed that the amount of net deposited ^{13}C species increases with surface roughness. Parameter studies with varying ^{12}C and ^{13}C fluxes were performed to gain insight into impurity deposition characteristic on the rough surface. Calculations of the exposure time needed for surface smoothing for TEXTOR and ITER were also carried out for different scenarios.

Keywords: Monte Carlo methods, edge plasma, surface roughness

PACS: 52.65.Pp, 52.40.Hf, 52.55.-s

1. Introduction

Plasma facing components (PFCs) exposed to a severe radiation environment in fusion devices suffer from intense power and particle fluxes [1-5]. The interaction between the edge plasma and PFCs determines the lifetime of PFCs, which is a crucial parameter for the viability of a fusion reactor. Moreover, the eroded impurities can be transported over long distances and be co-deposited together with fuel species. The resulting build-up of tritium-rich layers could become the main limiting factor for reactor availability due to safety restrictions. Therefore, studies of impurity transport, re-deposition and re-erosion are crucial to get a better understanding of underlying mechanisms

involved and to be able to adopt effective measures to minimize the tritium retention and net erosion.

Experimental observations indicated the influence of surface roughness on erosion and deposition. Results in TEXTOR [6], JET [7] and ASDEX Upgrade [8-9] revealed a strongly inhomogeneous erosion-deposition distribution with large erosion on protruding parts of the rough surface and deposition in recessions. Modelling has been performed to investigate this non-uniform erosion-deposition behaviour of impurities [10]. In addition, several simulation works have been carried out to study the development of the surface topography [11-13] and the impact of surface roughness on material sputtering [14-18].

Injection of tracer impurities such as $^{13}CH_4$ is a powerful tool to investigate impurity migration and deposition. The technique of ^{13}C injection through roof-like [19-20] and spherically shaped [21-22] test limiters in TEXTOR was applied to study the influence of various parameters such as substrate material, test limiter geometry, plasma conditions and also surface roughness on the local ^{13}C deposition. The local redeposition efficiency of ^{13}C showed that surface roughness increases the ^{13}C deposition efficiency on rough (~1μm) graphite surface by a factor of 3–5 compared with smooth (~0.1μm) one [22].

A Monte-Carlo code called SURO (abbreviated from SUrface ROughness), which takes into account the (re)erosion, (re)deposition and surface evolution of a rough surface, has been developed to study the effect of surface roughness on the ^{13}C deposition measured in TEXTOR experiments. The code can be combined with the three-dimensional (3D) Monte-Carlo code ERO [23], which simulates the transport of impurity particles in a given background plasma. The necessary input information for SURO (flux, angle and energy of impinging particles) is then provided by ERO. Modelling of the local deposition of ^{13}C has been carried out for various surface roughnesses and varying ^{12}C and ^{13}C fluxes. In addition, dynamic change of surface roughness has been studied.

2. The SURO code

The SURO code (2D in space and 3D in velocity) uses a sinusoidal surface of $z = a \sin(x/b)$ to describe the initial surface topography as shown in Fig.1 (a). The surface roughness (SR) is defined as the difference between the maximum and minimum points of the surface. Hence, the initial SR equals to 2a before the exposure. The initial directions of incoming particles are determined by the nominal angle α_{nom}, which is the angle between the incident direction and z-axis. The incident particles are launched from certain z location close to the surface and move along straight lines until they reach the surface. The effects of electromagnetic forces and resulting nominal angle distributions are treated in ERO code. When the incident particles reach the surface, the local angle α_{loc} is calculated according to the incident direction and the local surface normal at the impact position. The surface is divided into N bins in the x-direction (N is typically around 100). Every segment of the surface

has its own local surface normal vector, which is time dependent due to surface evolution under particle bombardment and resulting erosion/deposition. The time dependency is realized by dividing the SURO simulation into time steps Δt. As a result, the calculated local angles will be changed with dynamic evolution of each segment.

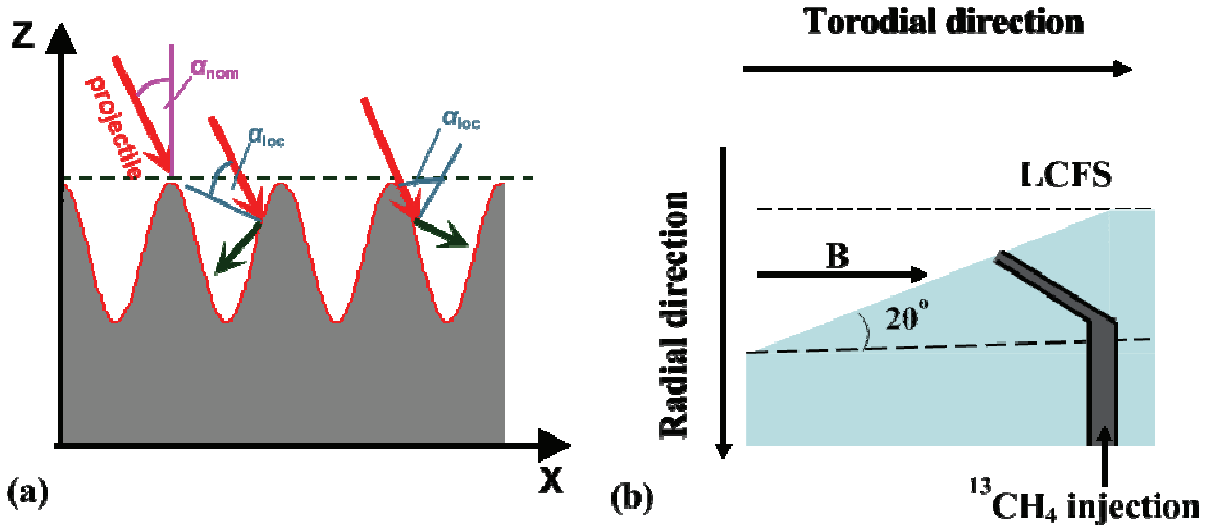

FIG. 1. The schematic of (a) surface topography of the substrate with a sinusoidal surface (b = 1.0 μm) and (b) experimental setup.

The physical sputtering yield due to impinging particles is based on the empirical formulae of Ref. [24]. The chemical erosion yield of graphite substrate by background deuterium ions bombardment is defined by an input parameter. For the simulations presented here, a chemical erosion yield of 1.5% is assumed, which is in general agreement with measured values in TEXTOR [25-26]. It is assumed that CD_4 molecules are generated in the process of chemical erosion [27-29]. A cosine angular distribution is assumed for the eroded particles. The Thompson and Maxwellian energy distributions are used for physically sputtered and chemically eroded particles, respectively [23]. Sticking or reflection of carbon atoms and hydrocarbons is determined by reflection coefficients taken from Ref. [30], which depend on species and incident energies and angles. It is assumed that the reflected particles obey the cosine angular distribution and the azimuthal direction continues in the forward direction of incident direction when reflected according to Refs. [31-32]. The particles are reflected with an energy typically around 32% of the incident energy based on Refs. [31-32].

For the modification of surface topography two correction procedures presented by T. Ishitani *et al* [7] have been taken into account in the model. First, it is necessary to remove the overmuch change of Δz which reverses the slope of the surface at each time step Δt. Second, an averaging technique is introduced for the calculation of Δz, so that $(\Delta z_{n-1} + 2\Delta z_n + \Delta z_{n+1})/4$ is

applied instead of Δz_n at the nth sampling point. These corrections are based on the practical situation that the sputtering process is determined by a collision cascade of finite dimensions. Therefore, the evolution of the apical point is affected by erosion/deposition of the neighboring segments.

The homogeneous mixing model (HMM) [29, 33-36] is used to consider mixing of different materials and to calculate their surface concentrations. For this, the substrate is divided into an interaction layer (the thickness of which is an input parameter) and a bulk volume. At the beginning of the exposure both the interaction layer and the bulk solely consist of substrate atoms. After the impact of impurities different species inside the interaction layer are distributed homogeneously. The total amount of particles in the interaction layer is kept constant, and accordingly, net erosion or deposition results in a shift of particles from the bulk into the interaction layer or from the interaction layer into the bulk, respectively. The concentrations of different species are updated after each time step. With increasing exposure time, the interaction layer reaches steady state and the concentrations of different species do not change anymore. The exposure time for reaching steady state is related to the interaction layer thickness since it is proportional to the total amount of particles in the interaction layer; however, the equilibrium concentrations of different species are independent of this thickness.

3. Simulation results

SURO is combined with ERO to study the deposition characteristic of ^{13}C particles on the smooth and rough test limiter surfaces resulting from $^{13}CH_4$ injection through these limiters. The simulation domain is divided into two regions: Scrape-Off Layer (SOL) plasma region, in which the transport of particles is treated by ERO, and a near surface region where the particles interact with the smooth or rough surfaces addressed by SURO. The current ERO version also can simulate the transport of background plasma particles by means of the test particle approach in order to calculate angular distribution when hitting the (smooth) surface. After reaching the surface, information about flux, angle and energy of deuterium and ^{12}C ions is stored and employed as input for SURO. Also, the transport of injected methane through the edge plasma is simulated by ERO. Part of injected species returns to the surface and again the information (species, angle, energy, charge) of returning ^{13}C species is used as input for SURO. The returning ^{13}C species include hydrocarbon ions and neutrals, and ionized and atomic carbon particles.

The simulation parameters used here for modelling the transport of impurities in ERO are on the basis of tracer injection experiments in TEXTOR [19-20], which had been performed to study the local transport and deposition behaviour of impurities. A defined number of $^{13}CH_4$ molecules is injected through a hole in a roof-like limiter plate with an inclination angle of 20º with respect to the magnetic field as shown in Fig.1 (b).

The magnetic field lies in x-z plane of Fig.1 (a). The tip of the test limiter is positioned at the last closed flux surface (LCFS) with a radial position of 0.46 m. The electron temperature (T_e = 54 eV), ion temperature (T_i = 1.5T_e) and electron density (n_e = 1.9 × 10^{12} cm^{-3}) at the LCFS are used as input in the ERO modeling – these parameters represent typical ohmic discharge conditions. The exponential decay lengths are $\lambda_{T_{e,i}}$ = 40 mm and λ_{n_e} = 22 mm, respectively. The calculated debye length λ_D is around 40 μm and is much larger than surface roughness (~1 μm). In this case, it is assumed that the surface roughness does not significantly affect the E field [10]. The flux densities of background deuterium (carbon) ions are in the range from 8.6 × 10^9 $\mu m^{-2}s^{-1}$ (3.1 × 10^8 $\mu m^{-2}s^{-1}$) to 6.9 × 10^9 $\mu m^{-2}s^{-1}$ (1.8 × 10^8 $\mu m^{-2}s^{-1}$) in the simulations. The ^{12}C concentration at the LCFS is assumed to be 3.5% as reference case according to Refs. [37-38].

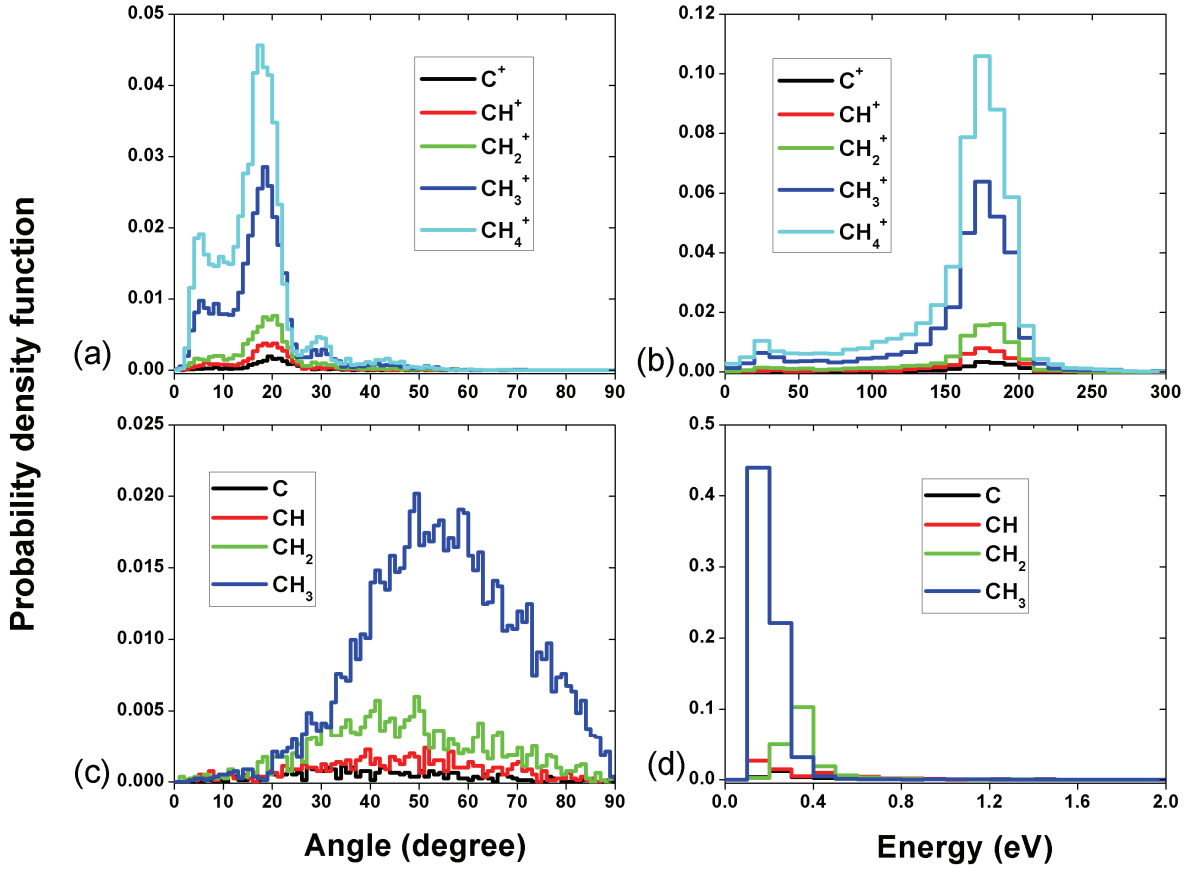

FIG. 2. The nominal angle and impact energy distributions of (a) (b) ionized ^{13}C species and (c) (d) neutral ^{13}C species returning to the surface.

3.1 ERO modelling*: *calculation of nominal angle and impact energy of returning ^{13}C species from $^{13}CH_4$ injection in TEXTOR

The spatial resolution of the limiter surface in ERO is determined by a surface net which divides the surface into predefined cells according to the input parameters.

Since the modelling dimension of ERO (~100 mm, surface cell size at limiter 3×3 mm^2) is much larger than that of SURO (~1μm), it is necessary to check whether different locations of predefined surface cells in ERO have significant difference in the nominal angle and impact energy distributions of returning ^{13}C species. However, the results from ERO reveal similar distributions for all the predefined surface cells as shown exemplarily in Fig.2, presenting the nominal angle and impact energy distributions of ionized and neutral ^{13}C species returning to the surface. Therefore, the location dependence of nominal angle and impact energy distributions of returning ^{13}C species can be neglected and the above results can be used as input data for SURO. As shown in Fig.2 (a) and (c), the ionized ^{13}C species have a much narrower nominal angle distribution compared to the neutral ones. The nominal angles for the ionized ^{13}C species are around 20º whereas the neutral ^{13}C species have a relatively uniform nominal angle distribution. In addition, the energies of the neutral ^{13}C species are mainly below 0.5 eV. The ionized ^{13}C species, which have been accelerated in the sheath potential, carry the kinetic energies in the range from 150 to 200 eV.

Figure3 (a) shows nominal angle distributions of background deuterium and background ^{12}C ions impinging on the smooth surface. The background deuterium and ^{12}C ions with a Maxwellian energy distribution are injected into the SOL far from the limiter surface (typical around 200 mm) and tracked until they reach the limiter surface. It is assumed that the charge state of ^{12}C ions is 3 in the simulation. It can be seen that the ^{12}C ions, whose maximum of angular distribution is located around 40º, have a relatively symmetric angular distribution. For deuterium ions, the maximum is located around 50º. The energies of deuterium and carbon ions impacting the surface are the sum of the thermal energy and energy gained by acceleration in the presheath and sheath: $E = 2T_i + \frac{1}{2}MV_s^2 + 3QT_e$, where M is the charge mass, V_s is the sound speed and Q is the charge state of the ion [39-40].

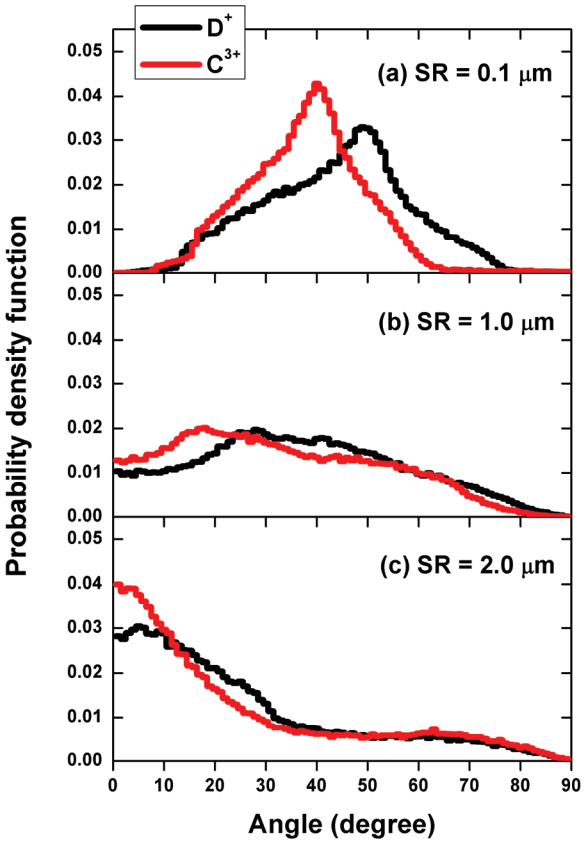

FIG. 3. The angular distributions of background D^+ and C^{3+} particles impinging on the (a) smooth (SR = 0.1 μm) and (b) (c) rough (SR = 1.0 μm, 2.0 μm) surfaces.

3.2 SURO modelling

3.2.1 Calculation of local impact angle

The angular distributions from ERO are used as nominal angles for SURO. The resulting local angle distributions for the background species obtained by SURO for SR = 1.0 and 2.0 μm are indicated in Fig.3 (b) and (c), respectively. It is seen that the local angle distributions of deuterium and ^{12}C ions demonstrate a strong dependence on the surface topography. With increasing SR, the peak values of angular distributions shift to smaller angles gradually. The peak values for SR = 1.0 μm are reduced compared to the smooth surface, and accordingly, the angular distribution becomes more uniform. The azimuthal direction of charged particles is along the forward direction of inclined B-field line (in x-z plane), and the azimuthal direction of neutral ones not constrained by B-field line is uniform. The gross physical sputtering yield (not considering redeposition) is related to the local impact angle according to Ref. [24]. The gross physical sputtering yields calculated with SURO integrated over all segments of the surface are, however, reduced marginally with increasing SR. All the values for smooth and rough surfaces are around 3% and 24% for D^+ and C^{3+}, respectively. Therefore, the influence of gross physical sputtering can be excluded here when comparing net deposited amount of ^{13}C species on the smooth and rough surfaces in the following analysis.

3.2.2 The influence of ^{13}C flux ratio

The effect the ^{13}C flux ratio has been investigated on the deposition of ^{13}C species on the smooth and rough surfaces. The ^{13}C flux ratio is defined as the ratio of ^{13}C flux returning to the surface to the background D^+ flux. Unless otherwise states, the simulations were performed for a total time of 500 s, which is long enough to reach steady state in the interaction layer such that the surface concentrations of different species do not change anymore. As shown in Fig.4, the amount of net deposited ^{13}C species on the rough surface is larger than that on the smooth one. The mechanism of enhanced re-deposition on the rough surface [12-13, 22] is the reason why the amount of net deposited ^{13}C species becomes greater. All reflected and re-eroded ^{13}C species from a smooth surface can "escape" easily while for a rough surface a certain amount will scrape the local wrinkles and thus be re-deposited. Larger SR reduces the probability for ^{13}C species to directly escape from the valley. In addition, it will intensify the trapping ability of rough surface because ^{13}C species experience more reflections through a ping-pong transport between the ridges of rough surface.

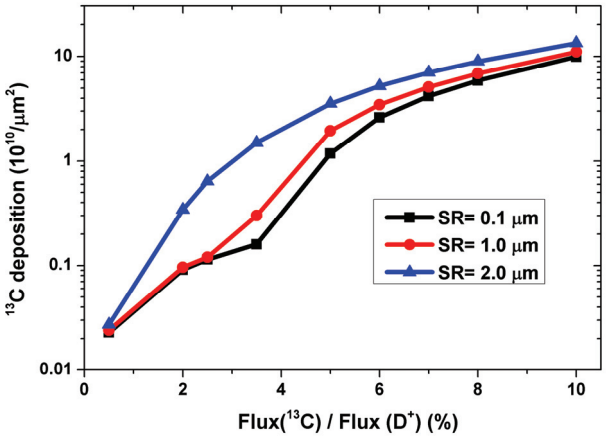

FIG. 4. The ^{13}C deposition as a function of ^{13}C flux ratio for the smooth and rough surfaces. The

concentration of background ^{12}C ions at the LCFS is 3.5%.

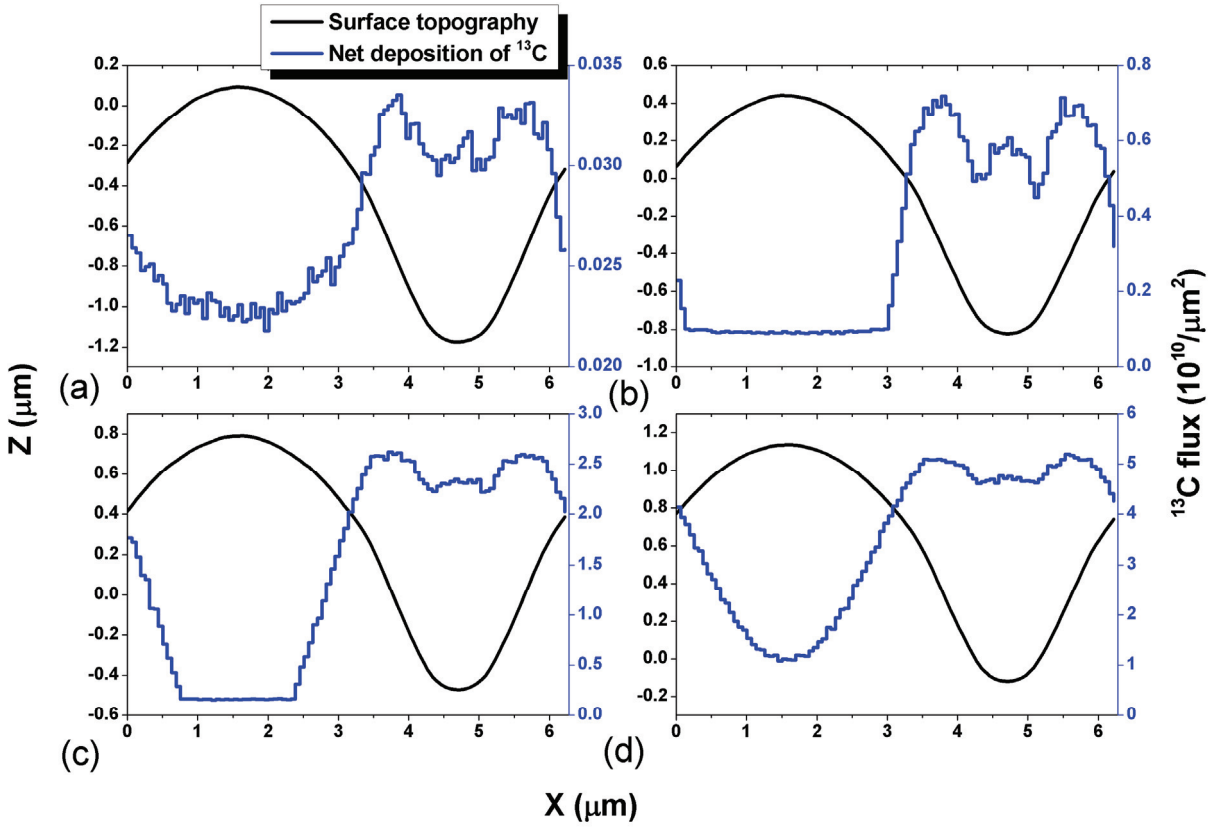

FIG. 5. Profiles of surface topography and net deposited ^{13}C areal density after 500 s exposure for initial SR = 2.0 μm with ^{13}C flux ratios (a) 0.5%, (b) 2.0%, (c) 3.5% and (d) 5.0%. The concentration of background ^{12}C ions at the LCFS is 3.5%.

Figure 5 presents the surface topography and net deposited ^{13}C areal density after 500 s exposure for initial SR = 2.0 μm with different ^{13}C flux ratios. It is obvious that the net deposited ^{13}C fluxes are larger at surface recessions, which is in support of the above-mentioned mechanism of enhanced re-deposition of ^{13}C species on the rough surface. The symmetrical profile of net deposited ^{13}C areal density in Fig.5 is due to the correlation between incident direction (i.e. nominal angle) and topography of rough surface. Since the valley of rough surface is open compared with the nominal angles which are calculated by ERO in Fig.2 and 3, the incident particles can reach both ridges of rough surface as shown schematically in Fig.1 (a). As a result, the symmetrical profile is obtained as shown in Fig.5.

Figure 6 shows the normalized ^{13}C deposition as a function of ^{13}C flux ratios for initial SR = 2.0 μm with different ^{12}C concentrations at the LCFS. The normalized ^{13}C deposition, which is used for a direct comparison of the difference in ^{13}C deposition characteristic between the smooth and rough surfaces, is defined as the ratio of the amount of net deposited ^{13}C species on the rough surface to that on the smooth

one. The normalized ^{13}C deposition first increases and then decreases with ^{13}C flux ratio for all assumptions of ^{12}C concentration. Furthermore, we find that the flux ratios of $(^{13}C+^{12}C)/D^{+}$ at SURO surface, which are calculated by SURO, are kept around 8% for all the maxima of the normalized ^{13}C deposition. This finding indicates that the difference in the amount of net deposited ^{13}C species on the smooth and rough surfaces is dependent on the ratio of $(^{13}C+^{12}C)/D^{+}$.

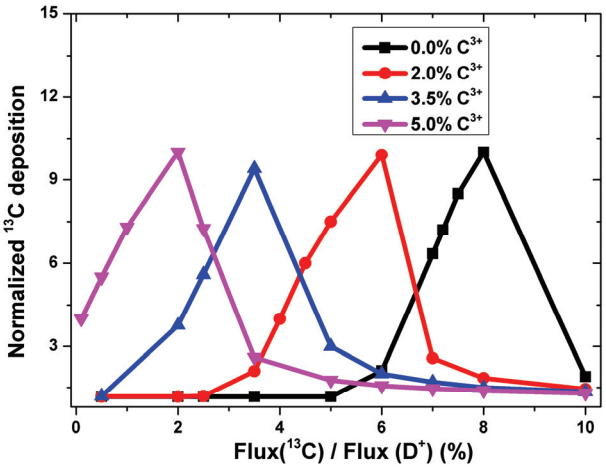

FIG. 6. The normalized ^{13}C deposition as a function of ^{13}C flux ratio for initial SR = 2.0 μm. The concentrations of background ^{12}C ions at the LCFS are 0%, 2.0%, 3.5% and 5.0%.

This phenomenon can be explained with the help of Fig.7 which illustrates the time-evolution of the surface topography for initial SR = 2.0 μm with different ^{13}C flux ratios. At the beginning, there are net deposited ^{13}C species in the surface due to a small ^{13}C surface concentration and with increasing exposure time, the surface concentration of ^{13}C species increases because of subsequent injection, which, in turn, leads to erosion of an increased number of ^{13}C species. After a certain time, the amount of net deposited ^{13}C species does not change anymore and steady state is reached. For a case of small ^{13}C flux ratio in Fig.7 (a), the calculations reveal that both the hills and recessions of rough surface suffer from net erosion. Hence, the amount of net deposited ^{13}C species on the rough surface is similar to that on the smooth surface, which results in small normalized ^{13}C deposition as shown in Fig.6. As the ^{13}C flux ratios increase as shown in Fig.7 (b) and (c), the hills of the rough surface still undergo net erosion while the valley regions are subject to net deposition. The smooth surface still suffers from net erosion (the erosion-dominated case) when the ^{13}C flux ratio is below 8% (data not shown). Therefore, the amount of the deposited ^{13}C species is much larger for the rough surface which leads to a higher normalized ^{13}C deposition. While for an even higher ^{13}C flux ratio of 8%, both the hill and valley regions receive net deposition; meanwhile, the smooth surface also receives net deposition (the deposition-dominated case). As a result, the normalized ^{13}C deposition is reduced correspondingly as shown in Fig.6.

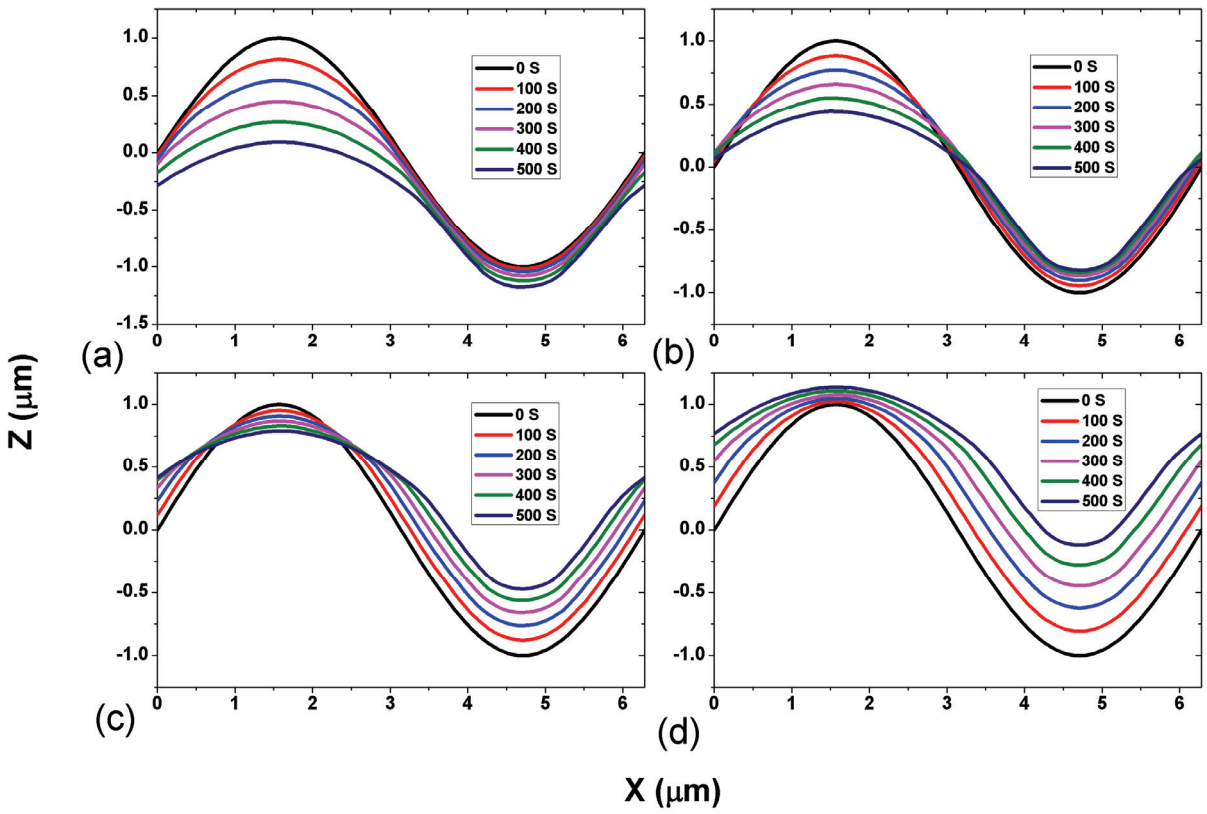

FIG. 7. Profiles of the time-evolution of surface topography for initial SR = 2.0 μm with ^{13}C flux ratios (a) 0.5%, (b) 2.0%, (c) 3.5% and (d) 5.0%. The concentration of background ^{12}C ions at the LCFS is 3.5%.

3.2.3 The influence of background ^{12}C concentration

The ^{12}C concentration in the background plasma is an important input parameter for the modelling. We therefore made a parameter study by varying this concentration and observing the effect on the deposition of ^{13}C species on the smooth and rough surfaces. Three background ^{12}C concentrations of 2.0%, 3.5% and 5.0% at the LCFS were used and these concentrations were assumed to increase exponentially with a decay length of -14cm when going further into the SOL [41]. SURO was applied to an ERO surface cell located at a distance of 18 mm from the LCFS in the radial direction and the corresponding background ^{12}C concentrations at the SURO surface are 2.3%, 4.0% and 5.7%, respectively. Figure 8 illustrates the ^{13}C deposition as a function of ^{12}C concentration at the LCFS for the smooth and rough surfaces. It can be seen that the ^{13}C deposition increases with background ^{12}C concentration. This can be explained by the fact that a larger background ^{12}C concentration results in a higher ^{12}C concentration in the surface. Correspondingly, the resulting reduction of the ^{13}C surface concentration leads to a reduced erosion of ^{13}C species and thus a greater amount of net deposited ^{13}C species. In addition, the above interpretation also can be used to make clear the reason why a larger background ^{12}C concentration along with a reduced ^{13}C flux ratio leads to the maximum of the normalized ^{13}C

deposition in Fig.6.

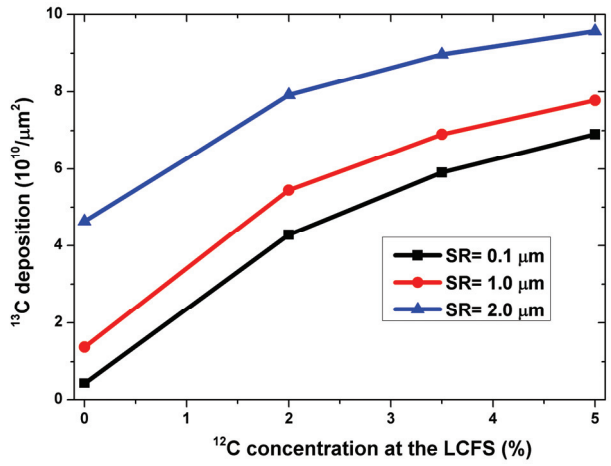

FIG. 8. The ^{13}C deposition as a function of ^{12}C concentration at the LCFS for the smooth and rough surfaces. The ^{13}C flux ratio of 8% is used.

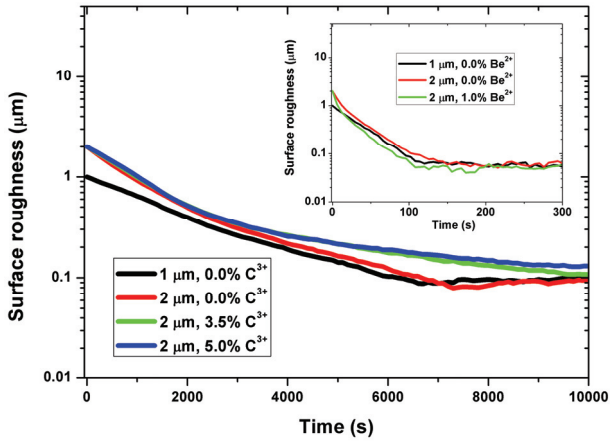

FIG. 9. The profile of the time-evolution of SR for initial SR = 1.0 and 2.0 μm with different ^{12}C concentrations at the LCFS (0%, 3.5% and 5.0%) for TEXTOR case. The inset graph shows the time-evolution of SR for initial SR = 1.0 and 2.0 μm with different Be^{2+} concentrations (0% and 1.0%) in the edge plasma for ITER inner divertor case.

3.2.4 Calculation of the exposure time for surface smoothing for TEXTOR and ITER

The erosion-deposition distribution is inhomogeneous due to surface roughness as shown in Fig.7, with a high erosion or small deposition on protruding parts of rough surface, and a lower erosion or larger deposition at the far side of ridges and at the bottom of recessions. A similar phenomenon is also observed in different tokamak facilities [6-9], which may finally lead to a smoothing of initially rough surface. This effect of long pulse and steady state operation is difficult to study in present tokamak facilities, but predictive modelling can be performed to investigate it.

The time-evolution of SR for initial SR = 1.0 and 2.0 μm with different ^{12}C concentrations at the LCFS in TEXTOR is presented in Fig.9. There are no injected ^{13}C particles for assessing surface smoothing during routine operation of fusion devices. The interaction layer thickness is assumed to be 40 nm in the HMM. Since the exposure time for reaching steady state of surface concentrations is much shorter than that for the smoothing of rough surface, the interaction layer thickness does not have a strong impact on the exposure time for surface smoothing. It is clearly shown that the SR first reduces very sharply before 2000 s, and then its reduction speed becomes slow between 2000-7000 s. Eventually, the steady state of surface topography is reached where the SR does not change anymore. In addition, the inset graph of Fig.9 shows the time-evolution of SR for initial SR = 1.0 and 2.0 μm with different Be^{2+} concentrations in the edge plasma for ITER inner divertor. This modelling was performed using typical plasma edge parameters in ITER based on the Refs. [29, 34]. The modelling location

is chosen to be at the strike point area that receives the maximum particle flux. The Be^{2+} concentration is the ratio of influx of Be^{2+} into the divertor to the deuterium ion flux. As shown in the inset graph, there is also a continuous reduction of the SR with exposure time until an equilibrium value is reached. The exposure time of about 100 s for reaching steady state decreases greatly compared with the TEXTOR case since the particle flux increases by two orders of magnitude.

4. Summary and discussion

The Monte-Carlo code SURO was developed and combined with ERO to investigate the influence of surface roughness on the ^{13}C deposition characteristic in $^{13}CH_4$ injection experiments in TEXTOR. Comprehensive parameter variations, such as different surface roughnesses, ^{13}C flux ratios and background ^{12}C concentrations, were performed to study their effects on the deposition of ^{13}C species. It was seen that the variation of local angle of background deuterium and ^{12}C ions due to surface topography does not have a strong impact on the gross physical sputtering yield, which can therefore be excluded in the analysis of the difference in ^{13}C deposition characteristic between smooth and rough surfaces. The results also showed that the amount of net deposited ^{13}C species increases with surface roughness and that there are more net deposited ^{13}C species at surface recessions due to enhanced re-deposition on rough surfaces. A larger surface roughness can intensify the trapping ability of ^{13}C species which experience more reflections caused by a ping-pong transport between the ridges of rough surface. The variation of the ratio of $(^{13}C+^{12}C)/D^+$ leads to a corresponding change in the normalized ^{13}C deposition (the deposition on the rough surface compared to the smooth one). With increasing $(^{13}C+^{12}C)/D^+$, the rough surface experiences an erosion-dominated case, intermediate state (half erosion and half deposition case) and deposition-dominated case, which is determined by the balance of incoming and outgoing particle fluxes. Furthermore, the amount of net deposited ^{13}C species showed a clear dependence on background ^{12}C concentration, which plays a protective role in the erosion of deposited ^{13}C species. An increased background ^{12}C concentration results in a reduced ^{13}C flux ratio for the maximum of the normalized ^{13}C deposition. For TEXTOR conditions, the exposure time for smoothening of the rough surface was around 7000 s, which is two orders of magnitude larger than that for an ITER case.

Experimental results in TEXTOR have shown that surface roughness leads to increased ^{13}C deposition efficiency [22]. The surface roughness is on the micron scale, which makes it difficult to reproduce the experimental result in a much larger scale. However, the experimental result can be explained qualitatively on the basis of the current modelling. Since the area around the injection hole is in the deposition-dominated case due to great ^{13}C incident flux, almost the same deposited ^{13}C amounts are obtained in the same area for the smooth and rough

surfaces according to the above modelling results (Fig.6). This is also supported by the experimental result which showed that the difference in the ^{13}C deposition efficiency is mainly due to a wider deposition pattern on the rough surface compared with the smooth one, which indicates that the deposited ^{13}C amounts in the same area around the injection hole are similar for the smooth and rough surfaces. The areal expansion of ^{13}C deposition is caused by a step-wise transport through a repetitive process of erosion of ^{13}C species from the layer and its subsequent re-deposition nearby. During this step-wise transport, the gradual reduction of ^{13}C incident flux leads to the rough surface far from the injection hole turning into the intermediate state, whereas the smooth surface is in the erosion-dominated case. Therefore, some deposited ^{13}C species on the rough surface can survive re-erosion of background plasma due to the trapping effect of rough surface. The wider deposition pattern of ^{13}C deposition on the rough surface supports this interpretation experimentally.

Acknowledgements

This work was supported by National Magnetic Confinement Fusion Science Program No. 2013GB109001, National Natural Science Foundation of China under Grant No.11275042 and Chinese Scholarship Council. This work was partly supported by the JSPS-NRF-NSFC A3 Foresight Program in the field of Plasma Physics (NSFC: No.11261140328). Authors would like to express their appreciation to F. Wang, Z.F. Yao and A. Kreter for their assistance in computation and helpful discussions.

Reference

[1] Federici G, Skinner C H, Brooks J N *et al* 2001 *Nucl.Fusion* **41** 1967

[2] Shimada M, Campbell D J, Mukhovatov V *et al* 2007 *Nucl.Fusion* **47** S1

[3] Roth J, Tsitrone E, Loarer T *et al* 2008 *Plasma Phys. Control. Fusion* **50** 103001

[4] Roth J, Tsitrone E, Loarte A *et al* 2009 *J. Nucl. Mater.* **390-391** 1

[5] Merola M, Loesser D, Martin A *et al* 2010 *Fusion Eng. Des*. **85** 2312-2322

[6] Wienhold P, Weschenfelder F, Karduck P *et al* 1999 *J. Nucl. Mater.* **266–269** 986

[7] Mayer M, Likonen J, Coad J P *et al* 2007 *J. Nucl. Mater.* **363–365** 101

[8] Mayer M, Rohde V, Ramos G *et al* 2007 *Phys. Scr.* **T 128** 106

[9] Mayer M, Andrzejczuk M, Dux R *et al* 2009 *Phys. Scr.* **T 138** 014039

[10] Schmid K, Mayer M, Adelhelm C *et al* 2010 *Nucl.Fusion* **50** 105004

[11] Nobes M J, Colligon J S, Carter G 1969 *J. Mater.Sci.* **4** 730-733

[12] Ishitani T, Kato M, Shimizu R 1974 *J. Mater.Sci.* **9** 505

[13] Ohya K, Kawakami R, Aizawa H, 2000 *J. Plasma Fusion Res. SERIES* **3** 288

[14] Ruzic D N and Chiu H K 1989 *J. Nucl. Mater.*

162-164 904

[15] Brooks J N and Ruzic D N 1990 *J. Nucl. Mater.* **176-177** 278

[16] Ruzic D N 1990 *Nucl. Instrum. Methods B* **47** 118

[17] Küstner M, Eckstein W, Dose V and Roth J 1998 *Nucl. Instrum. Methods B* **145** 320

[18] Küstner M, Eckstein W, Hechtl E and Roth J 1999 *J. Nucl. Mater.* **265** 22

[19] Wienhold P, Esser H G, Hildebrandt D *et al* 2001 *J. Nucl. Mater.* **290-293** 362

[20] Kreter A, Wienhold P, Borodin D *et al* 2007 *J. Nucl. Mater.* **363–365** 179

[21] Kreter A, Borodin D, Brezinsek S *et al* 2006 *Plasma Phys. Control. Fusion* **48** 1401

[22] Kreter A, Brezinsek S, Hirai T *et al* 2008 *Plasma Phys. Control. Fusion* **50** 095008

[23] Kirschner A, Philipps V, Winter J *et al* 2000 *Nucl.Fusion* **40** 989

[24] García-Rosales C, Eckstein W and Roth J 1994 *J. Nucl. Mater.* **218** 8-17

[25] Pospieszczyk A, Philipps V, Casarotto E *et al* 1997 *J. Nucl. Mater.* **241–243** 833

[26] Brezinsek S, Posieszczyk A, Borodin D *et al* 2007 *J. Nucl. Mater.* **363–365** 1119

[27] Ohya K, Inai K, Inoue M *et al* 2011 *J. Nucl. Mater.* **417** 602

[28] Inai K, Ohya K, Tomita Y *et al* 2009 *J. Nucl. Mater.* **390-391** 119

[29] Kirschner A, Borodin D, Droste S *et al* 2007 *J. Nucl. Mater.* **363–365** 91

[30] Ohya K, Kikuhara Y, Inai K *et al* 2009 *J. Nucl. Mater.* **390–391** 72

[31] Alman D A, Ruzic D N, 2003 *J. Nucl. Mater.* **313-316** 182

[32] Alman D A, Ruzic D N, 2004 *Phys. Scr.* **T111** 145

[33] Droste S, Borodin D, Kirschner A *et al* 2006 *Contrib. Plasma Phys.* **46** 628

[34] Kirschner A, Borodin D, Philipps V *et al* 2009 *J. Nucl. Mater.* **390–391** 152

[35] Kirschner A, Ohya K, Borodin D *et al* 2009 *Phys. Scr.* **T138** 014011

[36] Matveev D, Kirschner A, Litnovsky A *et al* 2010 *Plasma Phys. Control. Fusion* **52** 075007

[37] Ding R *et al* 2010 *Plasma Phys. Control. Fusion* **52** 045005

[38] Droste S *et al* 2008 *Plasma Phys. Control. Fusion* **50** 015006

[39] Stangeby P C, 2000 *The Plasma Boundary of Magnetic Fusion Devices* (Bristol: Institute of physics Publishing)

[40] Warrier M, Schneider R, Bonnin X, 2004 *COMPUT. PHYS. COMMUN* **160** 46

[41] Wienhold P 1989 *J. Nucl. Mater.* **162-164** 369

DIVIMP modeling of impurity transport in EAST

WANG Fuqiong，CHEN Yiping，HU Liqun

Institute of plasma physics, Chinese academy of sciences, Hefei 230031, China

Abstract: Simulations of carbon impurity transport in SOL/divertor plasma with ohmic heating on EAST tokamak were performed using two-dimensional Monte Carlo impurity transport code DIVIMP. The background plasmas for DIVIMP simulations were externally taken from B2.5/Eirene calculations. Besides the basic outputs of DIVIMP, the two-dimensional density distributions of carbon impurity with different ionization states and neutral carbon atoms were obtained. The two-dimensional distributions of CII and CIII emissivities from C^{+1} and C^{+2} radiation respectively were also calculated. The comparison between the measured and calculated CIII emissivities showed favorable agreement, which verified the reliability of the carbon impurity transport models used in the simulation process and the validity of the modeling results.

Keywords：Impurity transport, Simulation, DIVIMP, EAST

PACS: 52.55 Fa, 52.40.Hf, 52.65.-y

1. Introduction

The Experimental Advanced Superconducting Tokamak (EAST), the fully superconducting tokamak is an advanced experimental device with long pulse operation capable of studying on some key scientific issues of plasma physics and fusion technology in the steady state operation in support of ITER and use of fusion energy. The production and accumulation of impurities become a serious problem with the long pulse operation in EAST. In order to control the impurity behavior in the long pulse operation and to fulfill the scientific missions of EAST, the study of impurity behavior in EAST is an indispensable approach [1]. The impurities ranging from low Z(C, Be, O) to high Z (W, Mo) in a tokamak are produced because of the interactions between plasma and first wall. The beneficial aspects of impurities are power exhaust by the impurity radiation in front of divertor plates or first wall and the reduction of power fluxes to the targets and wall. To the contrary, the impurities transporting to the main plasma could reduce the fusion power due to fuel dilution and deteriorate the energy confinement due to radiation loss. Therefore, the performances of divertor and SOL plasmas depend to a large degree on the behavior of impurities. The investigation of properties of impurity transport in tokamaks like EAST could give us hints for improvement of plasma performances in this region as well as that in the core.

Experiment diagnostics and code simulations are two main methods to help understand the underlying physical mechanism of impurity production and

distribution in tokamaks. It is disappointed that some important information related to impurities such as the impurity density cannot be directly diagnosed, and that the range of diagnostics in the region of divertor is limited. For this reason, some of the unknown parameters for impurity property describing must be inferred from the limited experimental measurements, which will result in great uncertainties sometimes. In turn, these uncertainties and the diagnostics themselves may miss useful information on impurity transport. Fortunately, we can use simulation code to supplement the missing information of both the background plasma parameters and the impurity distribution. The simulation is essential to interpret the impurity behavior in the divertor, since it makes more information about impurity transport available and it can clarify the complicated interaction between the background plasma and the impurity. Moreover, comparing the modeling results to the experimental measurement could validate models in the code and help interpret the experiments. As for the EAST divertor, spectroscopic methods for acquiring the information of impurity profiles and influxes have been successfully used. However, it is the first time that we have made comparison between the impurity transport properties from modeling results and that from the experimental diagnostics in this device.

Impurity transport simulation codes are classified into fluid code and Monte Carlo code [3]. Since the Monte Carlo code has many merits, such as the possibility of carrying out the simulations in realistic tokamak geometry and the consideration of parallel motion and various collisional effects [4]; it is more suitable to be used for better understanding of impurity behavior. DIVIMP [2] (DIVertor IMPurity), one of the most widely used 2D Monte Carlo codes, is used to simulate carbon impurity transport in EAST plasma with ohmic heating. The detail parameters of this shot are described in section 3.

2. EAST divertor and experiment diagnostics

EAST can operate with single and double null plasma configuration. The divertor of EAST composed of inner-targets, outer-targets and domes, which are symmetrical to equator plane [6]. The divertor has 16 separate modules along toroidal direction. Inner, outer target plates and dome form two deep V shape valleys, which can congregate impurities and other particles. Figure 1 shows in-vessel components in the cross-section of EAST. It clearly shows that [7] the inner-target is connected to the inside toroidal limiter and the outer-target is connected to the passive feedback stabilizer. Since the inner-target and outer-target intersect with separatrix, most energy from the core plasma is deposited on the targets. As a consequence, impurities caused by particle impacts and heat load on the plasma facing components mainly come from inner-target and outer-target of the EAST divertor. At present, the divertor targets are covered by carbon materials called multi-element doped graphite, thus the following discussion will be focused on carbon impurity.

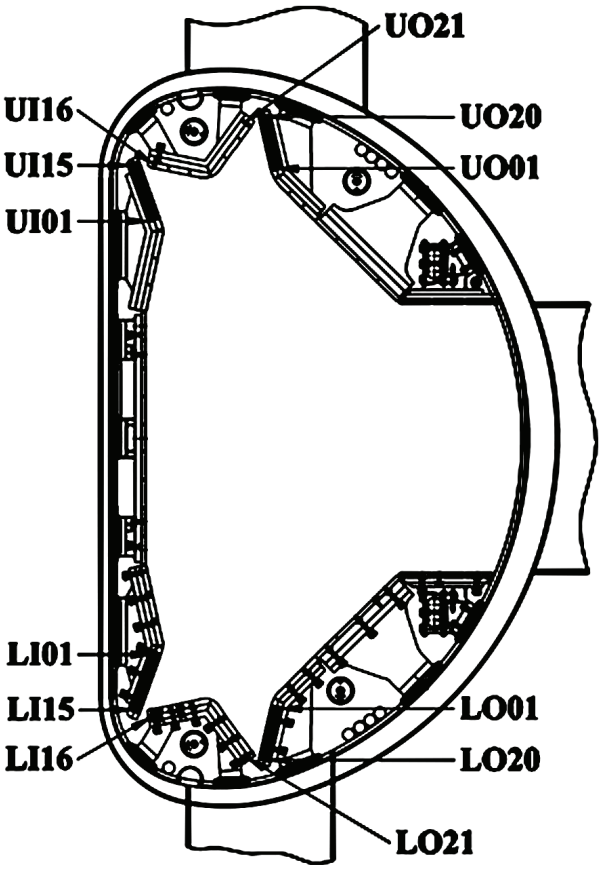

Figure 1: The in-vessel components in EAST

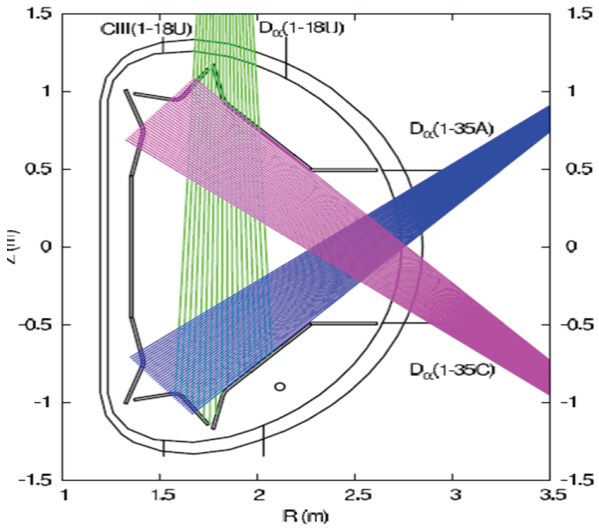

Figure 2: Chords for D_α and CIII measurement

In terms of the present EAST device, three-pin probe systems to identify the plasma parameters, as well as the plasma particle flux and heat flux at the target plate are set up, meanwhile, the experimental measurement with respect to impurity and background plasma emissivities in the SOL/divertor plasmas of EAST is now available for the study of impurity and plasma particle transport. Chords for the measurement of these two kinds of emissivities are shown on figure 2. Figure 2 shows the measurement system with 18 chords, named CIII (1-18U), which covers the upper and the lower SOL/divertor regions for the measurement of CIII and CII emissivities. The intersection angles made by every two of adjacent chords in this system are equal to one another, which indicate that the angular width of each independent LOS (Line Of Sight) is a constant.

3. DIVIMP simulation of carbon impurity transport in EAST

DIVIMP is a two dimensional Monte Carlo code widely used for modeling transport of impurity particles in a divertor equipped tokamak fusion device by means of following the trajectories of the neutrals and ions[5]. An OUT run is needed to present the results of the DIVIMP run directly and vividly. To perform the modeling, one should provide the following input files for the DIVIMP or OUT run:

1) The tokamak geometry and MHD equilibrium to generate DIVIMP computational grids. MHD equilibrium is usually obtained from the magnetic measurement in an experiment by using an equilibrium fitting code, such as EFIT. DIVIMP can simulate the production of impurity and

interaction between impurities and the plasma facing components in a realistic geometry without any simplification or approximation. Figure 3 shows the calculation grids for the carbon impurity transport modeling in EAST.

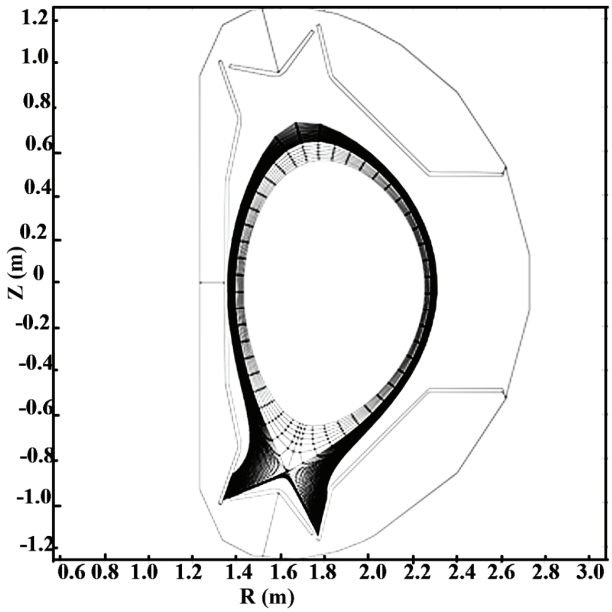

Figure 3: The DIVIMP calculation grids for EAST

2) Impurities and SOL plasma coexist and strongly couple with each other through force acting on impurity ions and radiation loss, which determines the impurity profile in the plasmas. For this reason, the modeling of the impurity transport in the SOL/divertor of tokamak devices should be performed in background plasmas correspond to the realistic discharge. The background plasma for the modeling presented here was externally obtained from the calculation of B2.5/Eirene, using the boundary conditions in the computational region including the boundary conditions at the inner core boundary, the wall, the inner boundary of private flux regions and the divertor target plates.

Alternatively, quantities describing the background plasma can also be specified by onion skin model (OSM), one-dimensional plasma model along magnetic field B, using radial measurement as boundary conditions [6,7], which could produce the profile of plasma parameters. The background plasma related to simulations mentioned in this paper is described as follows in detail.

3) The input file containing the listing of options and their settings for a DIVIMP run must be provided. A value for each quantity, including the ones to describe the cross field diffusion coefficient and impurity source, must be specified in this file. Though, maintaining this file may entail significant work, it is necessary for the user to be familiar with the range of every option available in DIVIMP to prevent this code being run with an invalid set of default options.

4) Lastly, the input file for an OUT run, which contains specification for the plots to be produced just after the DIVIMP run, should be provided.

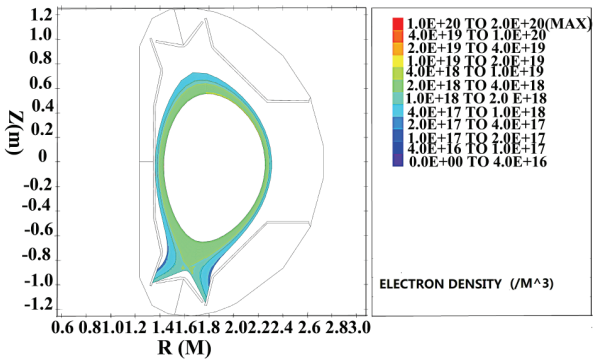

Figure 4: Distribution of electron density in the boundary of EAST for shot 12303

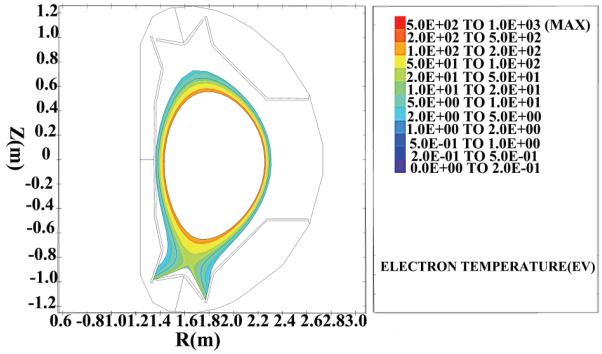

Figure 5: Distribution of electron temperature in the boundary of EAST for shot 12303

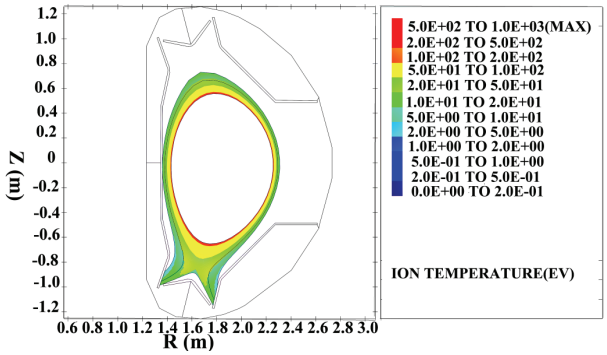

Figure 6: Distribution of ion temperature in the boundary of EAST for shot 12303

Simulations mentioned here refer to the shot 12303 in EAST, a deuterium discharge with single null configuration subject to ohmic heating of 161kW at the shot time t=5s. Table 1 shows the main parameters in the shot. The background plasma characteristics provided by B2.5/Eirene calculations for the DIVIMP simulation can be passed through DIVIMP to the OUT program for plotting. Figures 4, 5, 6 illustrate the two-dimensional distributions of background electron density and temperature as well as the ion temperature respectively. Figure 4 shows that the electron density in the inner boundary ranges from $1 \times 10^{18} m^{-3}$ to $6 \times 10^{18} m^{-3}$, while in the outer boundary it ranges from $4 \times 10^{17} m^{-3}$ to $1 \times 10^{13} m^{-3}$. In terms of the distribution of plasma temperature in the edge of EAST for this shot, the temperature decreases from hundreds of electron volts (eV) in the inner boundary to only a few electron volts (eV) in the outer boundary. Physical sputtering, chemical sputtering, thermal evaporation, radiation enhanced sublimation are all the possible mechanisms to produce impurities in a tokamak. For different plasma facing materials and different background plasmas, the dominant impurity production mechanisms are different. For example, chemical sputtering mainly occurs in tokamaks with carbon materials covered first wall. The radiation enhanced sublimation cannot be brought about when the plasma temperature is lower than several thousand electron volts. In the light of background plasma in ohmic shot 12303 before mentioned, the electron temperature and ion temperature are both much less than 1KeV. Moreover, in consideration of the fact that plasma facing components in EAST is covered by carbon materials called multi-element doped graphite, the C impurity species in simulations presented here are supposed to be generated by the physical sputtering and chemical sputtering. Data related to physical sputtering is based on Eckstein (1993) with small change to H, D, T taken from Garcia-Rosales and Roth (1996). The dependence of physical sputtering yield on the projectile energy and the incident angle of bombarding particles are described in reference [8] [12]

[13] in detail. It also assumed that all of the impurity particles are only sputtered by the background ions, and that the self-sputtering cascade does not occur. The impact energy of the background plasma ion is given by

$$E_{imp} = T_b(2 + 3Z_b) \quad (1)$$

Where Z_b=1, T_b is the local background plasma ion temperature. The chemical sputtering yield is supposed to be a constant. Physical processes such as ionization, recombination and charge exchange of C impurities are taken into consideration simultaneously in the modeling. Ionization and radiation data are taken from the ADAS.

DIVIMP calculated the carbon impurity transport in the test particle limit taking the classical parallel-to-B transport and anomalous perpendicular-to-B diffusion with diffusion coefficient $\mathbb{D}_\perp$ of $1m^2s^{-1}$ into consideration the initial velocity, v and the angle normal of the target, θ of the sputtered particles are given by [9]

$$\vartheta = arcsin\$, \quad \$ \text{ in } (0,1) \quad (2)$$

$$v = \sqrt{\frac{2E_{bd}}{m_i\sqrt{\frac{1}{\$}-1}}} \quad \$ \text{ In } (0, 1) \quad (3)$$

Where E_{bd} is the binding energy of the target material, and m_i is the atomic number of the target material.

Table 1 Main parameters in EAST tokamak for shot 12303

Parameters	Unit	
Shot time	t (s)	5.0
Major radius	R (m)	1.84
Minor radius	a (m)	0.449
Aspect ratio	A	4.10
Plasma current	I_p(MA)	0.251
Toroidal field	B_ϕ(T)	2.0
Elongation	κ	1.674
Upper triangularity	δ_u	0.182
Lower triangularity	δ_l	0.467
Edge safety factor	q_{95}	9.291
Toroidal β	β_T(%)	4.4
Poloidal β	β_p	0.324
Line–averaged density	$\bar{n}_e(10^{19}m^{-2})$	1.088
Plasma volume	$V_p(m^3)$	11.069
Plasma surface	$S_p(m^2)$	0.971
Heating power	P_{in} (MW)	161.0
Heating method	_	Ohmic
Configuration	_	SN

(a): Density of neutral carbon C^0 **(b):**Density of carbon with ionization states C^{+1}

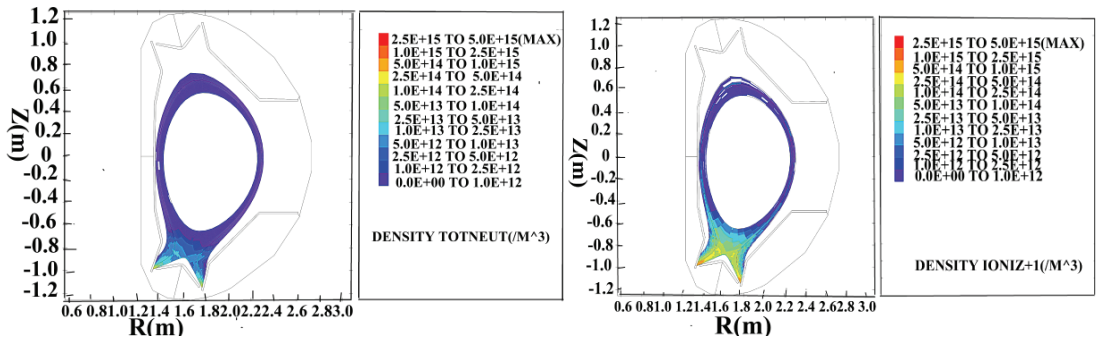

(c): Density of carbon with ionization states C^{+2} **(d):** Density of carbon with ionization states C^{+3}

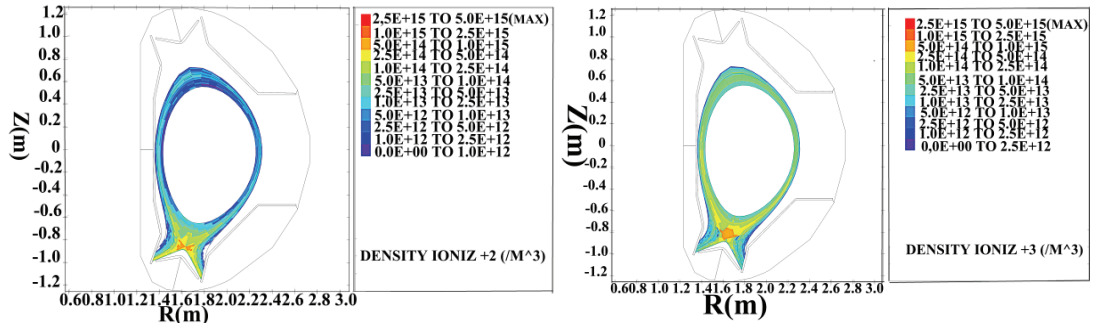

(e): Density of carbon with ionization states C^{+4} **(f):** Density of carbon with ionization states C^{+5}

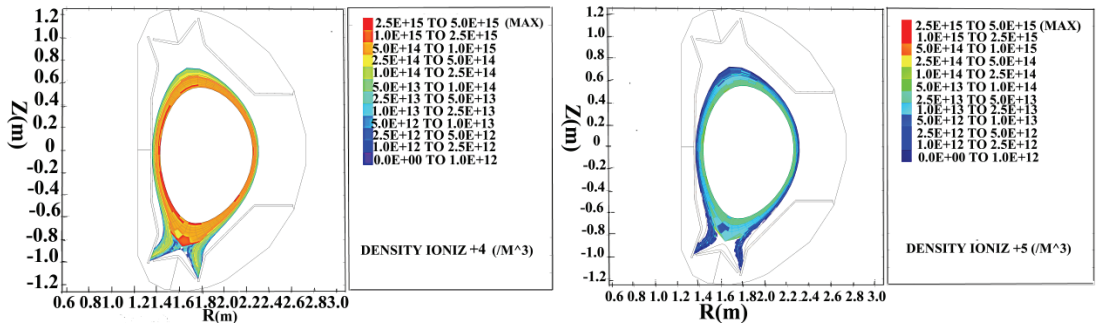

(g): Density of carbon with ionization states C^{+6} **(h):** Density of carbon with all the ionization states

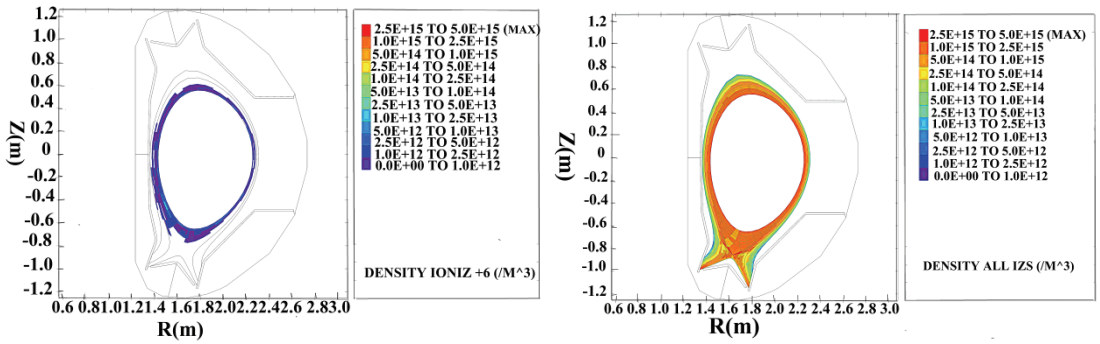

Figure 7((a)-(h)): Distribution of carbon impurity density in the SOL/divertor of EAST for shot 12303. (a): Density of carbon neutral C^0 , (b)-(g):Density of carbon with ionization states C^{+1}-C^{+6} , (h): Density of carbon impurity with all the ionization states

4. Results and discussions

Figure 7 ((a)-(h)) shows the density distribution of carbon impurity with different ionization states and neutral carbon atoms in the SOL/divertor plasma of EAST from DIVIMP modeling for shot 12303. From Fig.7, the maximum density of C^0 and C^{+1} appears near the target plates of divertor, the maximum density n_{max} of C^0, $n_{max} < 5 \times 10^{14} m^{-3}$ and the maximum density of C^{+1}, $n_{max} < 1 \times 10^{15} m^{-3}$. The minimum density of C^0 and C^{-1} appears near the core plasma, the minimum density n_{min} of C^0 $n_{min} < 1 \times 10^{12} m^{-3}$ and the minimum density of C^{+1}, $n_{1min} < \times 10^{13} m^{-3}$, For C^{+2}, the maximum density appears near the target plates and X-point and the minimum density appears near the core plasma with $n_{max} < 1 \times 10^{15} m^{-3}$ and $n_{min} < 5 \times 10^{12}$. For C^{+3}, C^{+4} and C^{+5}, the maximum density appears near X-point and the minmum density appears near the core plasma, the maximum density n_{max} is less than $1 \times 10^{15} m^{-3}$, $2.5 \times 10^{15} m^{-3}$ and $2.5 \times 10^{13} m^{-3}$ respectively, the minimum density n_{min} is less than $5 \times 10^{12} m^{-3}$, $2.5 \times 10^{15} m^{-3}$ and $2.5 \times 10^{13} m^{-3}$ respectively. The C^{+6} impurity mainly exists in the region near to the inner core boundary and the maximum density of C^{+6}, $n_{max} < 1 \times 10^{12} m^{-3}$.

The density distributions of carbon impurity show that neutral C atoms concentrate on the regions near the target plates. They are produced by physical and chemical yields due to the interactions between the plasma and target plates, after emitting from the target plates they travel in straight line until thee collide with the background plasma and become ionized. The plasma temperature is very low near the target plates and it is not easy for the neutral C atoms to ionize in such a low plasma temperature. So, C atoms abound in this region. For the lower ionization states of C impurity, C^{+1} and C^{+2} mainly concentrated near the target plates, they exist mainly in the regions with lower plasma temperature because C^{+1} and C^{+2} can be easier ionized by particles (electrons or ions) with not too high energy. In the regions near the target plates the plasma temperature is lower and particles in the plasma have lower energy. Most of the ions with higher ionization states, C^{+2} and C^{+4}, are in regions near the X-point where there are higher plasma temperature and the stronger particle fluxes. With the increase of ionization states, from C^{+2} to C^{+4}, the impurity concentration zone extend from the X-point to the core plasma. Near the X-point and the core plasma the plasma temperature is higher and C impurity can be ionized to ions with higher charge states, so, the densities of ions with higher charge states become higher. It is very difficult to ionize helium like C^{+4} particles to much more higher

charge states, C^{+5} and C^{+6}, so, the density of C^{+5} is much lower in the region with lower plasma temperature, even in the region with higher plasma temperature near the core plasma. The density distribution of C^{+6} is empty in some the computation region, which means the density of C^{+6} is too low to be shown. The figure about DENSITY ALL IZS show the total density of the carbon with all the ionization states C^{0} to C^{+6}, this figure shows that the level of C impurity is much high near the core plasma in EAST even in the condition with low ohmic heating power of 0.161MW, the content of C impurity in the inner boundary is much higher than that in the outer boundary, which is also the consequence of the higher plasma temperature and density in the inner boundary. So, the impurity control has become an important task for long pulse operation on EAST tokamak.

Based on the two-dimensional distributions of the C impurity density, the two-dimensional distributions of CII and CIII emissivities from C^{+1} and C^{+2} radiation respectively were also calculated and shown in figure 8. Figure 8 illustrates that the contours of CII (b) and CIII (a)emissivity intensities from C^{+1} and C^{+2} radiation respectively are similar to the density contours of C^{+1} and C^{+2} particles shown in the figure 7.

The two-dimensional radiation distribution of CIII spectral lines can be integrated along given lines of sight for direct comparison with measurements [10]. Simulations of CIII signals observed by the divertor spectrometer were performed under the assumptions illustrated in section 3. In order to assess the reliability of the modeling results shown in figure 7 and figure 8, chord-integrated CIII emissivity from the modeling results has been compared to the experimental observations by using the chords CIII(1-18U) which is shown in the Fig.2. Fig.9 (a) shows the chord-integrated CIII emissivities from the DIVIMP and B2.5/Eirene-SOLPS5.0 modeling results and experimental measurement. It is known from some other experiments [11] that usually the uncertainty of the separatrix position δr_{sep} is several centimeters. This magnitude is comparable to typical decay lengths of plasma parameters in SOL plasma. On the other hand, MHD equilibrium which is used for the present modeling for shot 12303 do not match the experimental measurement exactly at the time, so, the experimental profiles of the chord-integrated CIII emissivity has 3 channel number shift to the left along the X-axis in figure 9 in order to match the modeling results from SOLPS and DIVIMP well. From Fig.9（a）, the modeling results from DIVIMP are better than SOLPS, the model in Monte-Carlo code DIVIMP is more suitable for impurity transport simulation than the fluid model in SOLPS.

(a): CIII(4650nm) (b): CII (6582nm)

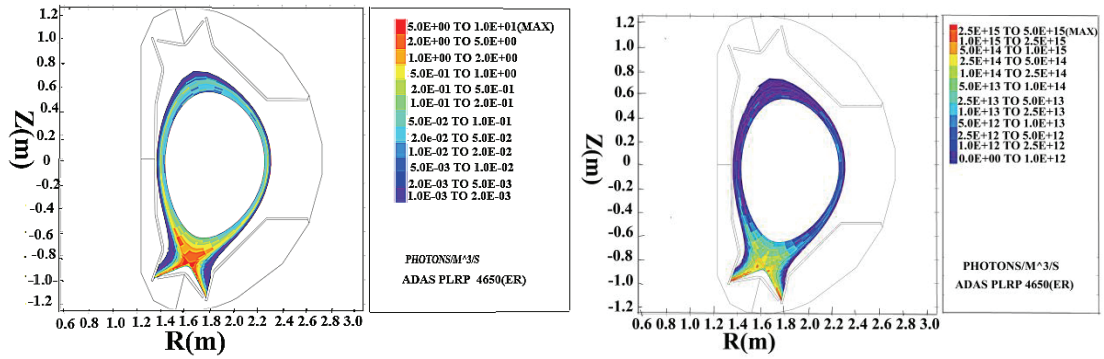

Figure 8: Two-dimensional distribution of CIII (4650nm)(a) and CII(6582nm)(b) radiation intensity

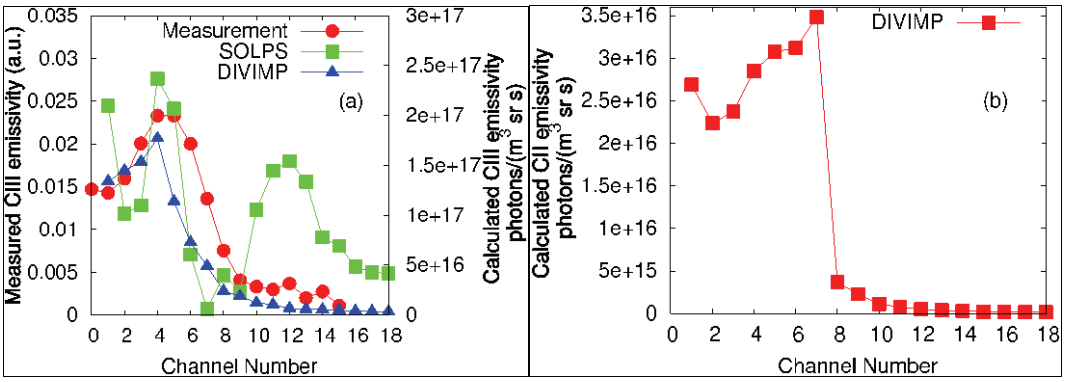

Figure 9: Chords integrated CIII (a) and CII (b) emissivities

Chord-integrated CII emissivity is also obtained and shown in figure 9 (b). Unfortunately, there are no experiment measurements of chord-integrated CII emissivity available to be compared and the comparison may be done in future.

In figure 9 the measured signals of CIII emissivity are dimensionless and relative values, while the modeling results of CIII emissivity are real values. Comparison in figure 9 demonstrates a favorable agreement between the modeling signals and experimental measurement of CIII emissivity. Differences between modeling CIII signals and the measured ones may lie in the points as follows. First the divertor experiment in EAST tokamak is at the beginning stage, so the measured parameters have inevitable errors. Second, model used in this simulation work may have some inappropriate simplification. Figure 9 also shows that the intensity of CIII radiation in this region is much higher than that of the CII radiation, which means that the density of $C^{+1}$is higher than that of. C^{+2}. It is not difficult to find that those regions of high impurity (C^{+1},C^{+2}) density will also have high impurity radiation intensity.

5. Conclusion

By one of the most commonly used Monte Carlo codes DIVIMP, the carbon impurity transport properties in

EAST ohmic shot 12303 was simulated in real divertor geometry. Background plasma in this shot was externally taken from the calculation of B2.5/Eirene. In the simulation the two-dimensional distributions of temperature and impurity density for different ionization states and for the neutral atoms are calculated. From these calculations, the two-dimensional distributions of CII and CIII line emission were calculated further. The two-dimensional of CIII line emission was integrated along given lines of sight and directly compared with the measurements. The profile of CIII emission signals from simulation is similar to the measured profile of CIII emission signals. This favorable agreement demonstrated that the simulations presented in this paper are reliable. Moreover, for better understanding of the impurity production and transport properties in EAST tokamak, greater efforts should be made in both the divertor experiments and the related simulations in the future.

Acknowledgments

This work was supported by the National Natural Science Foundation of China (No.10975158), the National Magnetic Confinement Program (No.2010GB104005). The authors would like to thank the EAST team for the experimental data.

REFERENCES

[1] Chen YiPing, Wang D.S., Guo H. Y. 2011, Nuclear Fusion, 51:3042.

[2] Krieger K., Bosch H. S., Eckstein W., et al. 1995, Journal of Nuclear Materials, 221: 548

[3] Shimizu K., Takizuka Sakasai T., A. 1997, Journal of Nuclear Materials, 241: 167

[4] Stangeby P.C., Farrell C., Hoskins S., et al. 1988, Nuclear. Fusion 28:1945.

[5] Stangeby P.C., Elder J.D. 1992, Journal of Nuclear Materials, 196:258

[6] Wu Songtao, EAST team. 2007, Fusion Engineering and Design, 8:463

[7] Liu Xufeng, Du Shijun, Yao Damao, et al. 2009, Fusion Engineering and Design 84:78

[8] Garcia-Rosales C., Eckstein W., Roth J. 1994, Journal of Nuclear Materials, 218:8

[9] Jarvinen A., Giroud C., Groth M., et al. 2011, Physica Scripta, 145:4013

[10] Haddad E., Meo F., Marchand R., et al. 2000, Journal of Nuclear Material, 278:111

[11] Neuhauser J., Bessenrodt-Weberpals M., Braams B.J., et al. 1989, Plasma Physics and Controlled Fusion, 31:1551

[12] Eckstein W., Preuss R., 2003, Journal of Nuclear Materials, 320:209

[13] Eckstein Wolfgang. 2007, Topics Appl. Physics, 110,:33

Preliminary research onflat-type W/Cuplasma-facing materials and components for EAST

Y Xu[1], C Y Xie[1], S G Qin[2], J P Song[3], Q Li[1], S X Zhao[1], DH Zhu[1], G H Liu[2], T J Wang[2], Y Yu[3] and G-N Luo[1*]

[1] Institute of Plasma Physics, Chinese Academy of Sciences, 230031 Hefei, China

[2] Advanced Technology & Materials Co. Ltd., 100081 Beijing, China

[3] Xiamen Honglu Tungsten Molybdenum Industry Co. Ltd., 361021 Xiamen, China

E-mail: gnluo@ipp.ac.cn

Abstract: To upgrade the Experimental Advanced Superconducting Tokamak (EAST) dome and first-wall, flat-type W/Cu plasma-facing components (PFCs) will be applied in coming years to exhaust the increasing heat flux. Mock-ups with an interlayer of oxygen-free Cu (OFC) made by vacuum hot pressing (VHP) have been developed and the bonding strength was over 100 MPa. Behaviors of the mock-ups under steady-state high heat flux (HHF) loads have been studied. No crack or exfoliation occurred on the W surface and W/OFC/CuCrZr interfaces after screening tests with heat fluxes of 2.24~7.73 MW/m^2. The mock-up survived up to 1000 cycles heat load of 3.24 MW/m^2 with cooling water of 4 m/s, 20 ^{o}C. However, cracks appeared in W around the gaps at 300th cycle under heat load of 5.37 MW/m^2. Chemical vapor deposition (CVD) W coated CuCrZr with an OFC interlayer has also been studied. It has been found that (1) the OFC interlayer plays a significant role in achieving coatings without any crack; (2) deposition rate was about 0.3~0.5 mm/h at 490~580 ^{o}C; and (3) CVD-W has a better thermal conductivity than that of powder metallurgy W (PM-W).

Keywords: EAST, Flat-type W/Cu PFCs, Vacuum hot pressing, CVD, High heat flux tests.

PACS numbers: 81.05.Bx, 52.55.Rk, 81.15.Gh

1. Introduction

In 2012 campaign, the Experimental Advanced Superconducting Tokamak (EAST) plasma-facing components (PFCs) were Mo tiles bolted to Cu alloy heat sink in the first wall area and SiC coated graphite tiles for the divertor with the maximum heat flux tolerance of 2 MW/m^2 in steady state [1, 2]. With a gradual increase in heating and driving power, the EAST dome and first-wall areas have to handle the expected heat fluxes of 3~5 MW/m^2 in steady state [3, 4]. Tungsten (W) has been considered as the leading candidate for the plasma-facing material (PFM) for current and future fusion devices because of its beneficial properties, e.g., high melting point, low vapor pressure, good thermal conductivity, good high-temperature strength, low sputtering yield, and low hydrogen retention, etc. [5-8]. As a PFM, it has to be bonded onto CuCrZr heat sink to withstand the cyclic heat loads. However, the main technological difficulty is to join W with CuCrZr due to their big

differences of the thermal expansion coefficients and elastic modulus. These differences lead to high thermal stresses during manufacturing and operation which could damage the joint [9, 10]. To reduce high thermal stresses, various joining techniques have been proposed, e.g., vacuum plasma spraying W coating, brazed W coating, cladding and diffusion bonding [11-15]. Recently, the Institute of Plasma Physics, Chinese Academy of Sciences (ASIPP) has extensively developed W/Cu flat-type mock-ups by means of vacuum hot pressing (VHP) and chemical vapor deposition (CVD) techniques, respectively, in collaboration with Advanced Technology & Materials Co. Ltd. (AT&M) and Xiamen Honglu Tungsten Molybdenum Industry Co. Ltd. An oxygen-free Cu (OFC) interlayer has been used between W coating and CuCrZr heat sink to reduce thermal stresses. Since the evaluation of thermal performance of the bonding interface is critical for the PFCs design, thermal screening and fatigue tests of VHP-W/Cu mock-ups were carried out using the 60 kW electron beam material testing scenario (EMS-60) at Southwestern Institute of Physics (SWIP). Crack observation of scanning electronic microscopy (SEM) and ultrasonic non-destructive tests (NDT) after HHF tests were performed. Temperature and thermal stress distribution in the mock-ups were simulated by ANSYS code. For CVD technique, in order to enhance the bonding strength, laser surfi-sculpt was applied to rough the surface. The effects of temperature and OFC interlayer on the morphology of W coatings were discussed.

2. Flat-type VHP-W/Cu mock-ups

Flat-type VHP-W/Cu mock-ups have been developed in collaboration with AT&M. Two phases were involved in the manufacturing process [3]. The first was to join W flat tile to the OFC interlayer by casting at 1200 ^{o}C. The pre-treatments of W tile including degreasing and grit blasting were employed to improve adhesion. The second was to join the W flat tile with an OFC interlayer to CuCrZr heat sink by means of VHP technique. In this phase, mock-ups were heated up to 600 ^{o}C with duration of 120 minutes at the pressure of 20 MPa. Up to 100 MPa of bonding strength was achieved after operation.

2.1 Screening tests

Figure 1a shows the mock-ups for HHF tests. The samples' size is 45 mm x 30 mm x 33 mm with a 12 mm diameter cooling channel inside. The thickness and density of W tile are 5 mm, 19.2 g/cm^3, respectively. Several 0.5 mm width gaps were machined in the W tile using wire cutting machine. The location of the thermocouple measuring bulk temperature is shown in figure1b. The thermocouple groove is 1.8 mm in diameter and 25 mm in depth, close to the OFC interlayer. Figure 1c shows schematically the EMS-60 with various diagnostics. The EMS-60 can produce a maximum beam power of 60 kW from 1 ms to continuous operation with a maximum acceleration voltage of 150 kV and a maximum scanning frequency of 30 kHz, which is similar to JUDITH-1, Germany [15-17]. Mock-up was

monitored by CCD and IR camera during HHF tests and the detachment of the W tile from heat sink can be detected as the appearance of continuous hot spots on the monitor screens [9]. Figure 1d shows the photograph of the mock-up fixed in vacuum chamber.

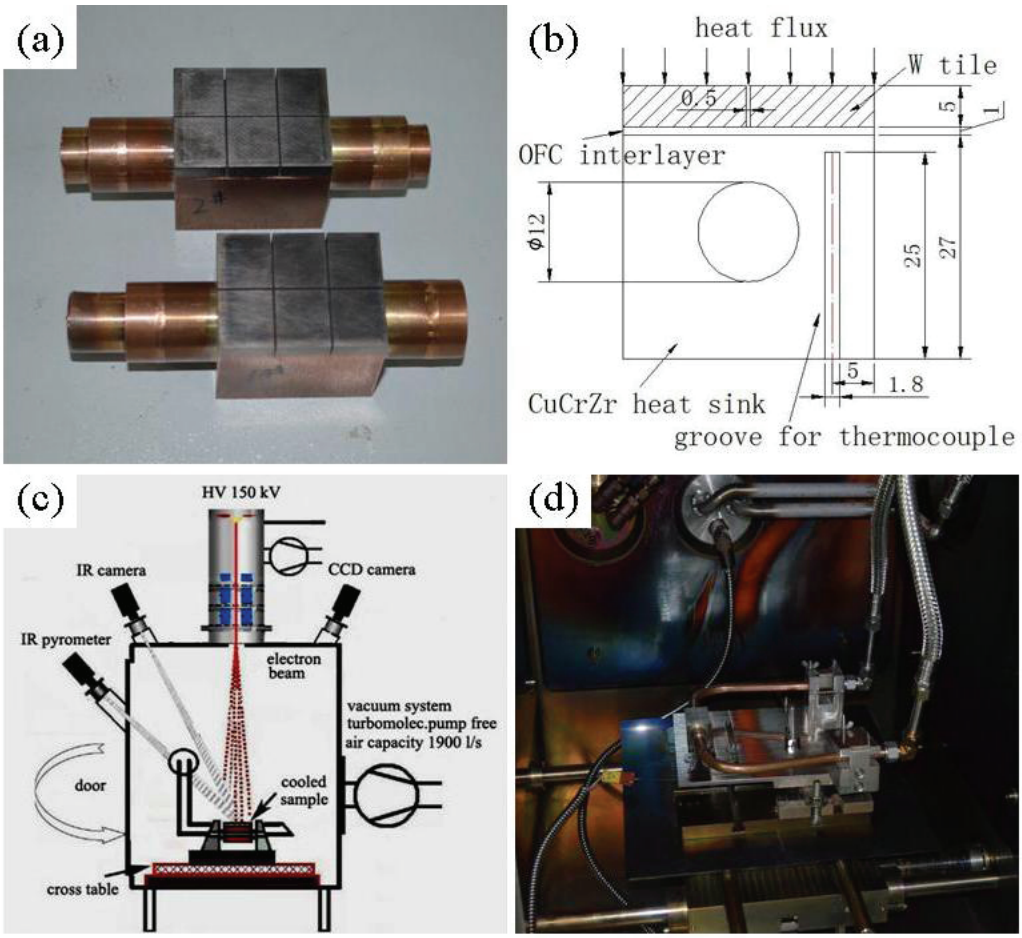

Figure 1. (a) A picture of VHP-W/Cu mock-ups, (b) groove for thermocouple in the mock-up, (c) sketch of the EMS-60, (d) a picture of the mock-up fixed in vacuum chamber.

The purpose of screening tests is to reach critical performance of the mock-up under HHF. During screening tests, electron beam scanned in a fast scanning mode on the sample's surface with a frequency of 10 kHz to get a homogeneous loaded area. The mock-up which was actively cooled by water of 4 m/s, 20 ^{o}C was loaded with 15 s on and 15 s off and the beam current increased from 41 to 143 mA with an acceleration voltage of 120 kV. The absorbed power density (P_{abs}) can be calculated by the formula (1):

$$P_{abs} = \frac{\rho c Q \Delta T}{S} \quad (1)$$

Where ρ is the density of water (kg/m^3), c is the specific heat of water (J.kg^{-1}.K^{-1}), Q is the flow rate (m^3/s), ΔT is the temperature difference between the inlet and outlet water (^{o}C), and S is the sample's surface area (m^2). P_{abs} can be obtained once ΔT is measured. The coefficient of absorption (η) can be defined as formula (2):

$$\eta = \frac{S \cdot P_{abs}}{UI} \quad (2)$$

Where U is the acceleration voltage (kV), and I is the incident current (mA).

Figure 2 shows that ΔT and P_{abs} increased linearly with the evolution of I. ΔT and P_{abs} increased 1.59~5.49 □ and 2.24~7.73 MW/m^2 respectively. It was calculated that the η kept stable at the value of ~60% with the increase of the electron beam power. In figure 3, temperatures measured by thermocouples are compared with those calculated by ANSYS code. The surface and bulk temperatures increased linearly with heat loads, which shows a good agreement with calculations. But all the experimental values were lower than those simulated by ANSYS code because of the poor thermal contact and the problem of surface emissivity calibration. No hot spot was observed on the monitor screen of IR camera during tests. No crack or exfoliation occurred on the W surface and W/OFC/CuCrZr interfaces.

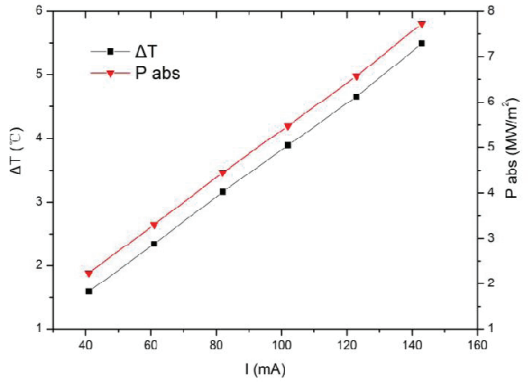

Figure 2. ΔT and P_{abs} changed with the evolution of I.

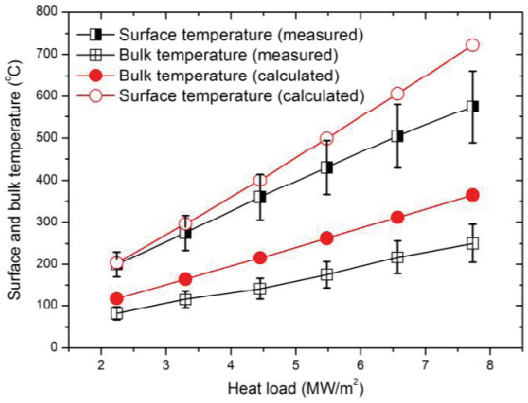

Figure 3. Surface and bulk temperatures changed with the evolution of heat loads.

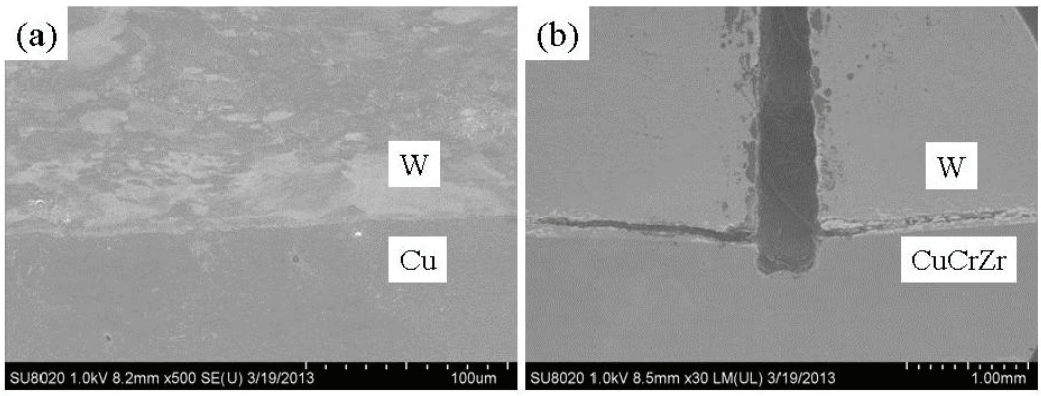

Figure 4. SEM images of W/Cu/CuCrZr interfaces at heat load of (a) 3.24 MW/m^2, (b) 5.37 MW/m^2.

2.2 Thermal fatigue

2.2.1 Experiments and results.

Cyclic heat load tests were performed at flow rate of 4 m/s. The mock-up survived up to 1000 cycles at heat load of 3.24 MW/m2 without damages, as shown in figure 4a. However, cracks appeared in W around the gaps at 300th cycle under heat load of 5.37 MW/m^2, as figure 4b describes. CCD images of the mock-up at

5.37 MW/m2 are shown in figures 5a~c. IR camera showed a first continuous hot point at 300th cycle during fatigue tests and the defect area was getting lager obviously. Figure 5d shows that surface temperature increased significantly when cracks appeared and propagated in the mock-up due to the weakened ability of exhausting heat flux.

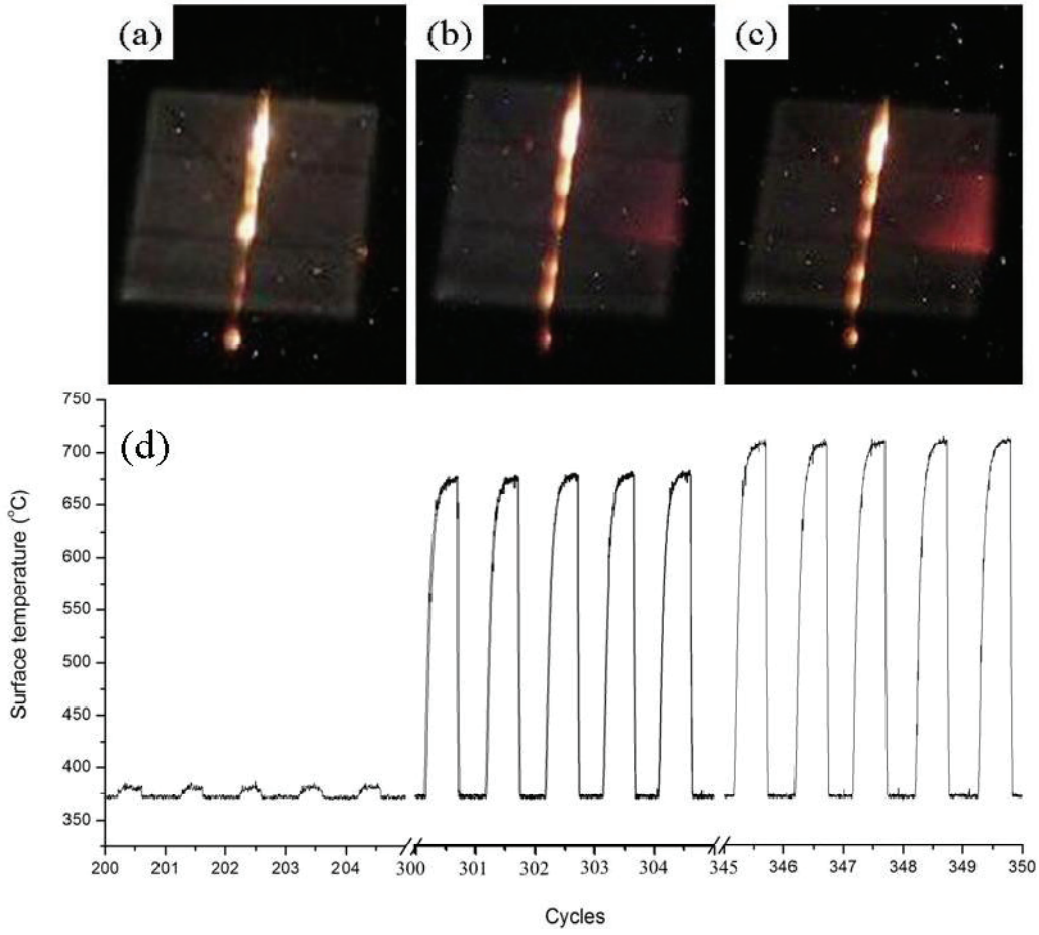

Figure 5. CCD images of the mock-up under cyclic heat load of 5.37 MW/m^2 at (a) the 200th cycle, (b) the 300th cycle, (c) the 350th cycle and (d) surface temperature changed with the evolution of heat load cycles.

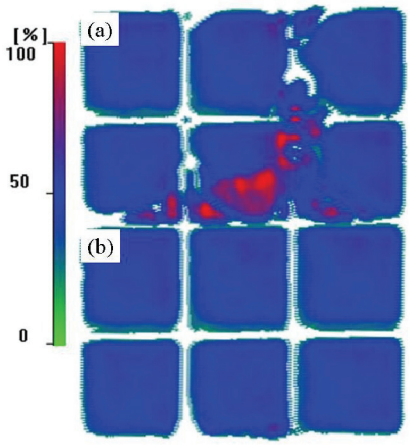

Figure 6. Ultrasonic NDT results of the mock-ups after cyclic heat loads of (a) 5.37 MW/m^2, (b) 3.24 MW/m^2.

The development of NDT techniques is very important to evaluate the connection quality between the PFM and heat sink. Ultrasonic inspection has been developed for testing interface quality of EAST PFCs at ASIPP. Figure 6 shows the ultrasonic NDT results

of the mock-ups after fatigue tests. It shows that defects only appeared at heat load of 5.37 MW/m^2, which is in accord with the experimental results.

2.2.2 Modeling and discussions.

A 1/4 model was used for finite element analysis. Figure 7 shows the calculated results from ANSYS code. The maximum surface temperature reaches ~480 ^{o}C, a little higher than the measured value due to the poor thermal contact and the problem of surface emissivity calibration. The maximum stress occurred around the gaps where cracks appeared. Since the W tile was rolled before connecting to the heat sink, tensile strength along the vertical direction was much lower than that of equiaxed pure-W. This preferred orientation of rolled-W grains which was perpendicular to the heat flux makes it easier to be destroyed under cyclic heat loads.

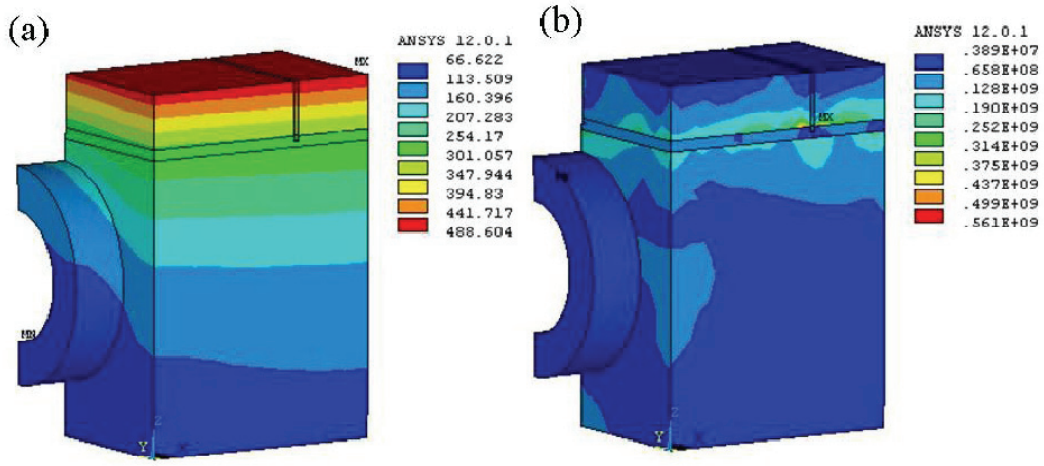

Figure 7. 3D temperature (a) and stress (b) distributions of the mock-up at heat load of 5.37 MW/m^2 simulated by ANSYS code.

3. CVD-W coatings

Blocks of CuCrZr alloy were coated with W by the CVD technique in collaboration with Xiamen Honglu Tungsten Molybdenum Industry Co. Ltd., with an interlayer of OFC hot pressed onto the CuCrZr blocks before coating. The deposition rate was about 0.3~0.5 mm/h at 490~580 ^{o}C. The final thickness, density and purity of W coating were ~2 mm, 19.2 g/cm^3 and 99.9999%, respectively.

3.1 Microstructure observation.

Surface morphology of CVD-W coatings deposited at 490 ^{o}C, 520 ^{o}C, 550 ^{o}C and 580 ^{o}C were observed. Figure 8 shows the SEM images of W coatings deposited at 490 ^{o}C and 550 ^{o}C. With increasing temperature, deposition rate got faster and W grains became smaller significantly because the nucleation rate increased much faster than the crystal nucleus growth. W surface was coarse at 580 ^{o}C and W coatings would exfoliate when temperature was relatively low (490 ^{o}C) due to the weak bonding, as figure 8b describes.

Cracks only appeared on W coatings without an OFC interlayer at temperatures of 490 °C, 520 °C, 550 °C, and 580 °C. As shown in figure 9, CVD-W coating deposited at 550 °C with an OFC interlayer was intact, while visible cracks occurred on that without an interlayer. This can be explained that the plasticity of OFC is much better than that of CuCrZr, thus releasing more stresses and keeping W coatings from cracking [18].

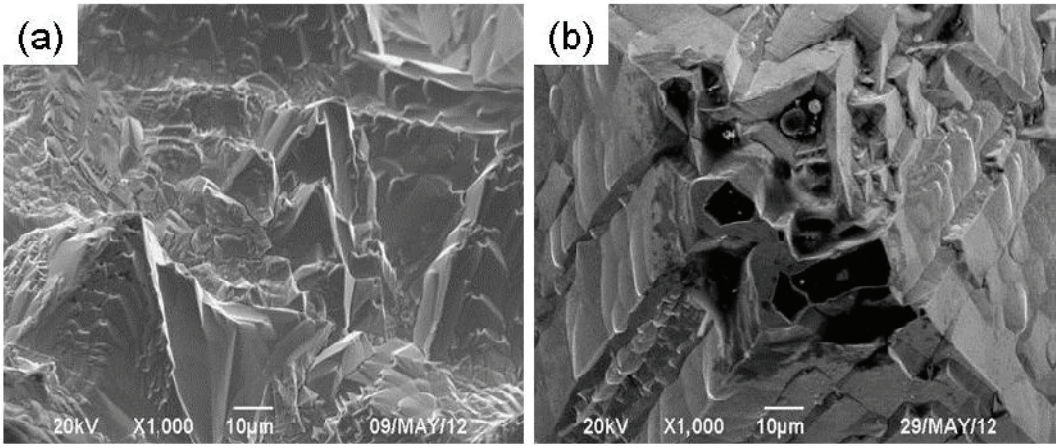

Figure 8. SEM images of CVD-W coatings deposited at (a) 550 °C, (b) 490 °C.

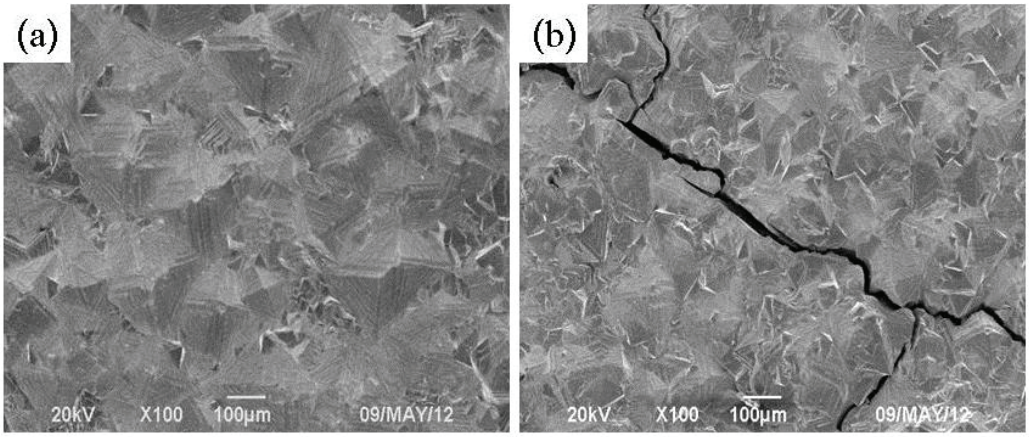

Figure 9. SEM images of CVD-W coatings deposited at 550 °C with (a) and without (b) an OFC interlayer.

The cross-sectional view of W coating is shown in figure 10a. Clearly, CVD-W coating consists of three different crystal zones, i.e. equiaxed grain zone, mixed crystal zone and columnar crystal zone. The columnar crystal zone with regular shape is dominated. Figure 10b shows the XRD pattern of CVD-W coating. A significant reflection peak appeared at 2θ of 58 degree, which was produced by the crystal plane (211). The preferred orientation helps to improve thermal conductivity along the W grains growth direction.

3.2 Thermal properties.

Figure 11 shows that CVD-W has a better thermal conductivity than that of powder metallurgy W (PM-W)

[19]. This is because PM-W has the equiaxed crystals with a lot of grain boundaries, which will weaken the capacity of heat conducting, while CVD-W can conduct heat flux directly to the heat sink due to the regular columnar crystals.

3.3 Bonding strength.

The main issue of W coated CuCrZr is the high residual stresses due to the mismatch of thermal expansion coefficients and Young's modulus. The coefficients of thermal expansion differ by a factor of 3.7 and 4.7 Cu to W at room temperature and 1000 ^{o}C respectively [10]. Besides, W and Cu are not soluble at all. Thus, enhancing the mechanical connection of W/Cu can be an effective approach to strengthen adhesion. The pre-treatments of Cu include degreasing and surface roughening. Figure 12 shows the SEM images of CVD-W/Cu interface with and without laser surfi-sculpt. As shown in figure 12b, slots of 40 um width and 200 um spacing were sculpted on Cu surface before coating. The contact area increased significantly and W grains in the slots grew up in a disorderly direction. A relatively high bonding strength of 53.7 MPa was obtained due to this mechanism.

4. Summary

The ASIPP has developed mock-ups of VHP-W/Cu PFCs for EAST. HHF tests were carried out using the EMS-60 to evaluate thermal performances. Screening tests showed that the mock-up can withstand heat loads from 2.24 to 7.73 MW/m^2 without visible damages. Thermal fatigue tests indicated that the W/OFC/CuCrZr joint survived up to 1000 cycles at heat load of 3.24 MW/m^2 without failure. However, cracks appeared in W around the gaps at 300th cycle under heat load of 5.37 MW/m^2, because the preferred orientation of rolled-W grains perpendicular to the heat flux makes it easier to be destroyed under cyclic heat loads. The optimization of VHP technique is still underway.

Preliminary results of CVD-W coatings for EAST have been presented in detail in this paper. A well performed W coating was acquired at 520~550 ^{o}C and the OFC interlayer plays a significant role in achieving coatings without any crack. Bonding strength of 53.7 MPa was achieved. CVD-W has a better thermal conductivity than that of PM-W. HHF tests of CVD-W/Cu mock-ups will be carried on soon.

Acknowledgements

This work was partially supported by National Magnetic Confinement Fusion Science Program Nos. 2010GB109004, 2010GB104005, 2011GB110003 and 2013GB105001, National Nature Science Foundation of China Nos. 11075186, 11005125, 11105180, 11205198. Authors from ASIPP would like to thank Dr. X Liu and his team of SWIP for their contribution to the HHF tests.

References

[1] Wan B 2009 *Nucl. Fusion* **49** 104011

[2] Li Q, Qi P, Zhou H S, Zhang Y Y, Yang Z S, Wu J,

Luo G N and Li J G 2010 *Fusion Eng. Des.* **85** 1106-12

[3] Luo G-N, Li Q, Chen J M, Liu X, Liu W, Zhou Z J and Yao D M 2012 *Fusion Science and Technology* **62** 9-15

[4] Luo G-N, Zhang X D, Yao D M, Gong X Z, Chen J L, Yang Z S, Li Q, Shi B and Li J G 2007 *Phys. Scr.* **T128** 1-5

[5] Rieth M, Boutard J, Dudarev S, Ahlgren T, Antusch S, Baluc N, Barthe M F, Becquart C, Ciupinski L and Correia J 2011 *J. Nucl. Mater* **417** 463-7

[6] Hino T and Akiba M 2000 *Fusion Eng. Des.* **49** 97-105

[7] Davis J, Slattery K, Driemeyer D and Ulrickson M 1996 *J. Nucl. Mater* **233** 604-8

[8] Bolt H, Barabash V, Krauss W, Linke J, Neu R, Suzuki S, Yoshida N and Team A U 2004 *J. Nucl. Mater* **329** 66-73

[9] Boscary J, Suzuki S, Nakamura K, Suzuki T and Akiba M 1998 *Fusion Eng. Des.* **39-40** 537-42

[10] Hirai T, Kreter A, Linke J, Malzbender J, Ohgo T, Philipps V, Pintsuk G, Pospieszczyk A, Sakawa Y and Sergienko G 2006 *Fusion Eng. Des.* **81** 175-80

[11] Li J, Yang J F and Chen J L 2011 *J. Nucl. Mater* **418** 110-4

[12] Wang T, Chen J, Chen Y and Wu Y 2007 *J. Nucl. Mater* **363** 1294-8

[13] Shen W, Li Q, Chang K, Zhou Z and Ge C 2007 *J. Nucl. Mater* **367** 1449-52

[14] Akiba M and Suzuki S 1998 *Fusion Eng. Des.* **39** 219-25

[15] Wirtz M, Linke J, Pintsuk G, Singheiser L and Uytdenhouwen I 2011 *Phys. Scr.* **2011** 014058

[16] Roedig M, Kupriyanov I, Linke J, Liu X and Wang Z 2011 *J. Nucl. Mater* **417** 761-4

[17] Ogorodnikova O, Pestchanyi S, Koza Y and Linke J 2005 *J. Nucl. Mater* **337** 791-4

[18] Zhu D H, Wang K, Wang X P, Chen J L and Fang Q F 2012 *Plasma Sci. Technol.* **14** 656-60

[19] Bergman T L, Incropera F P, Lavine A S and DeWitt D P 2011 *Fundamentals of Heat and Mass Transfer* John Wiley & Sons

Initial study of divertor particle and heat flux width scaling in lower-single-null configuration on EAST

WANG Liang[1,2,*], XU Guosheng[1], GUO Houyang[1,3], GAN Kaifu[1], GONG Xianzu[1], HU Liqun[1], and EAST Probe Team

[1] Institute of Plasma Physics, Chinese Academy of Sciences, Hefei 230031, China

[2] School of Physics and Optoelectronic Technology, Dalian University of Technology, Dalian 116024, China

[3] Tri Alpha Energy, P. O. Box 7010, Rancho Santa Margarita, CA 92688, USA

*Email: wliang@ipp.ac.cn

Abstract: The dependence of divertor particle and power deposition widths on plasma current (I_p) for lower hybrid current driven (LHCD) L- and H-mode plasmas was initially studied in the Experimental Advanced Superconducting Tokamak (EAST) under a lower single null (LSN) divertor configuration. And the profile widths were obtained from the divertor triple Langmuir probe array and an infra-red (IR) camera. It is shown that the deposition widths of divertor particle and heat flux profiles both display a strong negative dependence on increasing plasma current, in L-mode, ELM-free H-mode and ELMy H-mode scenarios. The experimental results show good agreement with the heuristic SOL width model proposed by Goldston [R. J. Goldston 2012 Nucl. Fusion 52, 013009].

Keywords: particle and heat flux widths, lower single null, EAST

PACS: 52.55. Fa, 52.55.Rk

1. Introduction

The widths of particle and power deposition on divertor targets are critical parameters for operation of many present tokamaks and ITER. Characteristic widths affect many issues related to divertor targets such as particle and power exhaust, recycling, and the upper limit of peak heat flux to avoid material damage. Definitions on the width of divertor heat flux profiles, include the FWHM, the simple e-folding decay length in the near SOL, and the integral decay length of Loarte [1]. Scaling of the SOL width as a function of various operational parameters has been studied for many years on JET, ASDEX-U, DIII-D and others. In 2010, coordinated experiments were performed in H-mode scenarios on NSTX [2], Alcator C-Mod [3], and DIII-D [4] aiming at improving the prediction of divertor heat flux profile for next step devices including ITER and beyond. Analysis of the combined dataset reveals that the primary dependence of the parallel heat flux width is strongly inverse with I_p. All three tokamaks independently demonstrate this

dependence, pointing to a common transport dynamic and projects a much narrower SOL for ITER than relations currently in use. The exportation to ITER needs to be revised with more data on other tokamaks, though much progress has already been achieved [3-6].

Also in 2010, stationary H-mode plasmas were achieved successfully on EAST in both lower single null (LSN) and double null (DN) configurations either by using lower hybrid current drive (LHCD) alone or combined with ion cyclotron resonance heating (ICRH) with lithium wall conditioning. Detailed divertor particle and power behavior during various H-mode scenarios on EAST were reported in [7-8]. The divertor particle and power deposition widths were also studied in the campaign, mainly using divertor triple Langmuir probe (LP) arrays embedded in the target plates, along with an infra-red (IR) camera viewed the lower divertor region. In this work, the dependence of divertor particle and power deposition widths on I_p in LHCD LSN L- and H-modes on EAST was investigated. Initial experimental results show that like recent results in Refs. [2-5] the divertor particle and power deposition widths in EAST also have strong negative dependence on I_p, both in L-mode and H-mode scenarios. The divertor conditions of this study were all in attached regimes. In this paper experimental results for the lower outboard (LO) divertor only are presented, since the behavior at the inboard strike point is greatly affected by the secondary separatrix in the present LSN configuration [7]. To reduce the uncertainty inherent in LP evaluation, e.g., the effect of a non-Maxwellian fast electron population leading to over-estimation of electron temperatures, coherent averaging of a number of similar ELMs was employed in the ELMy H-mode phases. This averaging method was also conducted in both L-mode and ELM-free H-mode intervals in each discharge to minimize the scatter of data arising from fluctuations.

2. Divertor heat flux diagnostics and experiments

EAST is the first fully superconducting tokamak with a modern divertor configuration, starting operation in 2006. At present, two diagnostics on the machine can evaluate the heat flux on the divertor targets in EAST, i.e., the divertor triple LP arrays [7, 9] and the IR camera which is tilted downward toroidally to view the lower divertor region. The divertor LPs can also provide valuable information on the plasma density, electron temperature and particle fluxes in the divertor region. Parallel heat fluxes measured by LPs are calculated using the standard sheath model. The IR camera can directly measure the surface temperature of divertor target plates, and a 2D finite element code called DFLUX is used to calculate target heat flux from the surface temperature. Figure 1 shows the poloidal layout of the two diagnostics, as well as a typical LSN configuration with $dR_{sep} < 0$. The spatial resolution of triple LPs along the target plates is 10-15mm poloidally, while the temporal resolution is 0.2ms. The

power supplies for each group of divertor triple LPs are all 200V DC. The IR camera system has a target poloidal resolution of 6 mm and a framing rate of 50Hz.

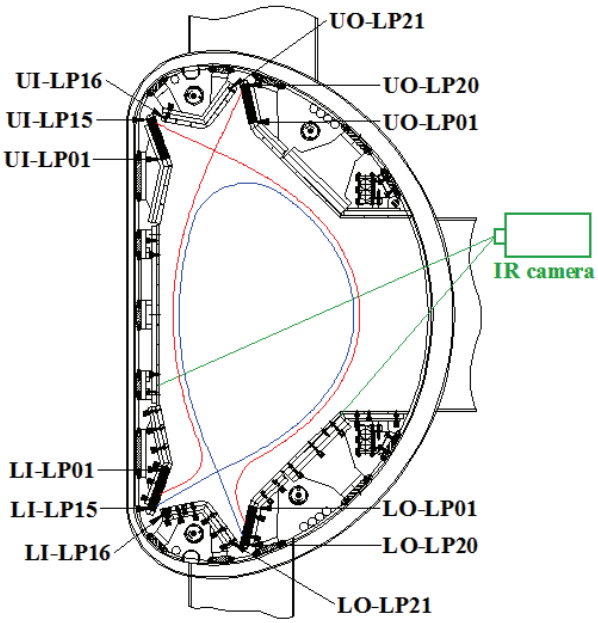

Fig. 1 The poloidal layout of divertor triple LPs and the field of view of the IR camera in EAST. UO(I)-Upper Outboard (Inboard) divertor; LO(I)-Lower Outboard (Inboard) divertor; LP-Langmuir Probe. Also shown is a typical LSN configuration with $dR_{sep} < 0$.

In this study, experiments were carried out in LHCD driven LSN H-mode discharges by varying the plasma current. The temporal evolutions of some key parameters in three representative type-III H-mode discharges at different I_p levels are shown in Figure 2. The shaded time windows which cover both L-mode and H-mode regimes are selected for later profile analysis, with the green window for shot #34407 (0.5MA), and the cyan window for shots #34388 (0.8MA) and #34397 (0.6MA), respectively. In the shaded windows, the values of dR_{sep} for the three shots are about -1.3cm. Line-averaged densities during the selected time windows of the three shots are similar, in both L-mode and H-mode phases, i.e., $\sim 2.7\times10^{19} m^{-3}$ in L-mode and $\sim 3.5\times10^{19} m^{-3}$ in H-mode regime. Auxiliary LHCD heating power plotted is the injected power minus the reflected power, which is about 1MW for all the three shots except the H-mode regime of shot #34388, due to the auto-protection of the LHCD system. Note that the toroidal field of shot #34397 is about 1.8T, a little less than that of shot#34388 and shot #34407 (2T).

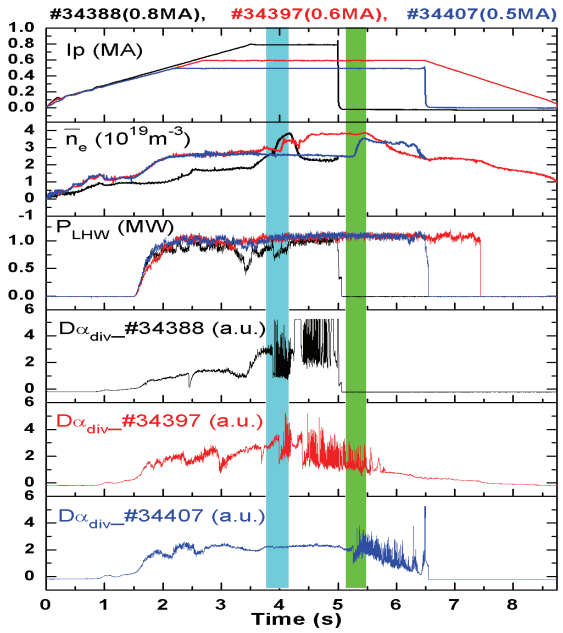

Fig. 2 Time traces of plasma current, line-averaged density, LHCD power, and divertor D_α emission in three representative discharges at different I_p levels. Shaded time windows are used for profile characterization in the text.

3. Results and discussion

In each discharge, the particle and power deposition profiles of three different regimes were investigated, that of an L-mode phase, an ELM-free H-mode phase, and an ELMy H-mode phase. To better contrast the difference between L-mode plasmas, the L-mode phases were all taken just prior to the L-H transition, i.e., 20ms before the L-H transition in each discharge, with consistent line-averaged densities. As aforementioned in Section 1, the data selected to generate each single profile were averaged over a time interval, i.e., 20 ms for both L-mode and H-mode regimes. For the LPs, each representative profile is the average on the data of 100 time points during the 20 ms interval (sampling rate: 5kHz).

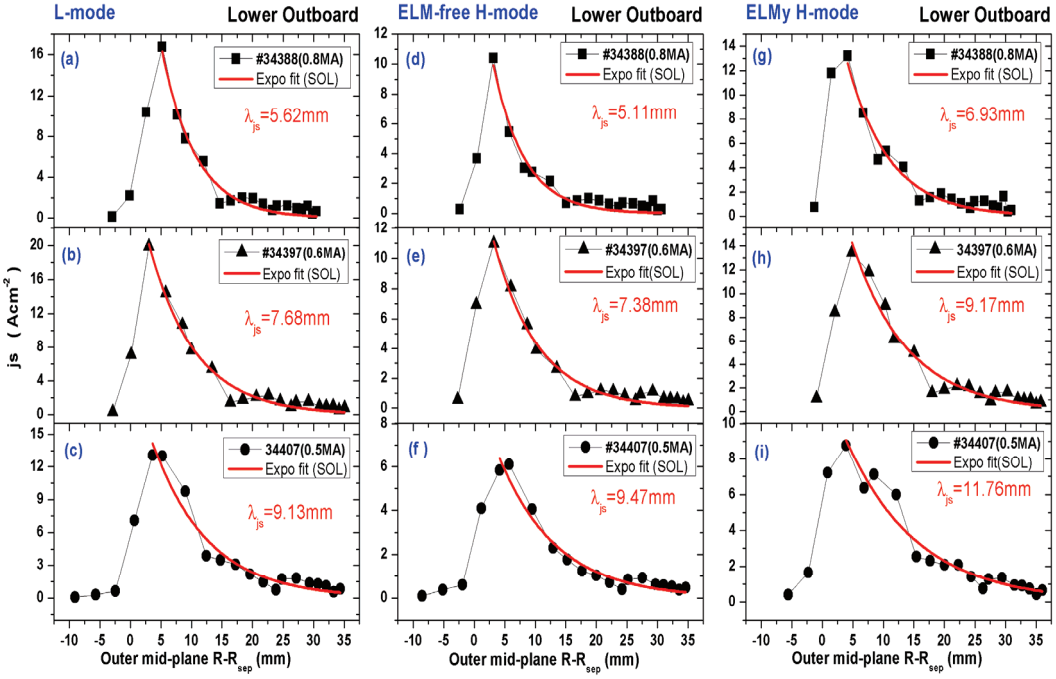

Fig. 3 Profiles of j_s at the LO divertor target, mapped to the LFS mid-plane with the EFIT code in L-mode (a, b and c), ELM-free H-mode (d, e and f), ELMy H-mode (g, h and i) phases. The solid symbols are experimental data, and the bold curves are exponential fittings in the SOL.

3.1 Dependence of λ_{js} on I_p

Figure 3 shows the ion saturation current densities (j_s) at the LO divertor targets for L-mode, ELM-free H-mode and ELMy H-mode phases in three discharges of different I_p. All profiles are mapped to the outer mid-plane using the EFIT magnetic equilibrium reconstruction code. Data points are from the experiments, with the instrument error of about ±10% [7]. Bold lines represent the simple exponential fitting to the profile outboard of the separatrix, which is expressed in the form of $A_{js}\exp[-(R-R_{\max})/\lambda_{js}]$ using the least square fitting method, where $R_{\max}$ is

the major radius of the maximum j_s mapped to the outer mid-plane and A_{js} is a fitting constant for the amplitude. The ion flux to the divertor plates in terms of j_s is $\Gamma_{ion} = n_t C_{st} = j_s / e$, where n_t and C_{st} are the electron density and ion sound speed at the target respectively, i.e., $\Gamma_{ion}[m^{-2}s^{-1}] = 6.24\times10^{22} j_s[Acm^{-2}]$. Note that on the SOL side, the j_s profiles decay smoothly in the region measured by the divertor LPs, which is the reason that simple e-folding length to describe the particle deposition width on the divertor targets is employed, and also in the parallel heat flux profiles to be presented in Section 3.2. This profile pattern is different from profiles measured in Alcator C-Mod [3] and NSTX [10], both of which observe a sharp decay in the near-SOL region and a long flatter tail in the far-SOL region.

As can be seen, the outer mid-plane decay length of ion saturation current density (λ_{js}) decreases inversely with I_p in both L-mode and H-mode regimes. In the same discharge, the L-mode data has a maximum peak j_s value, while the ELM-free H-mode has the minimum peak j_s value. The peak j_s in the ELMy phase is only slightly more than that in the ELM-free phase, which arises because each ELMy H-mode profile is generated by averaging the inter-ELM and during-ELM profiles in a given time window (20ms). Also in the same discharge, the j_s profile during the ELM-free H-mode phase is steeper than that during ELMy H-mode phase.

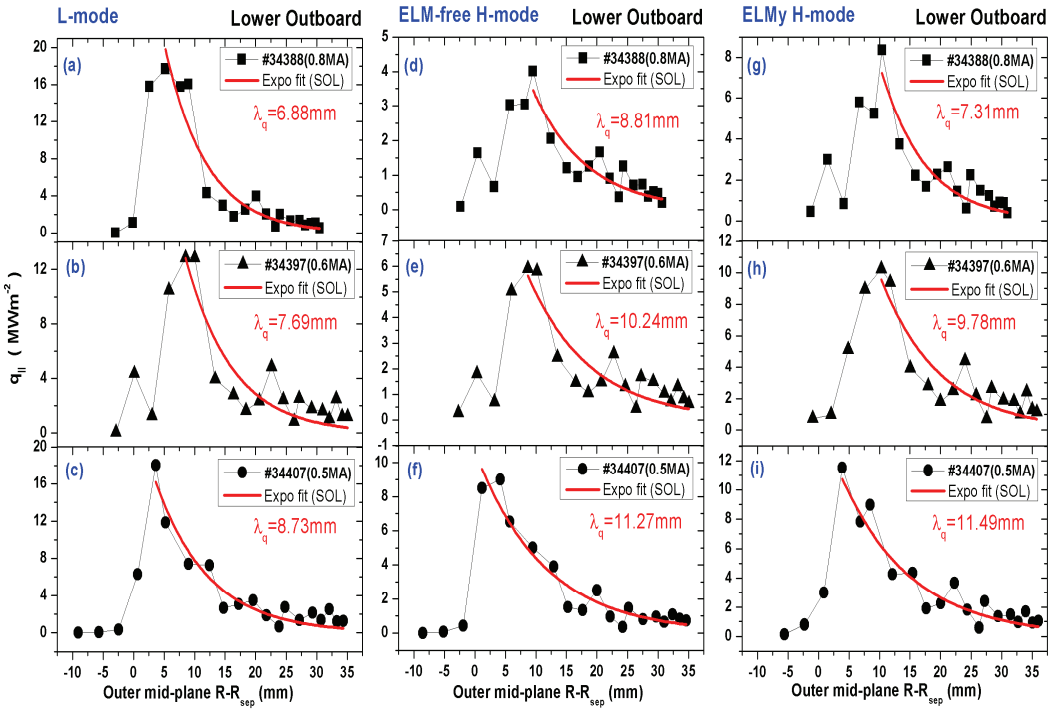

Fig. 4 Same as Fig. 3 for profiles of parallel heat flux at the LO divertor target.

3.2 Dependence of λ_q on I_p

Figure 4 illustrates the parallel heat flux ($q_{//}$) at the LO divertor targets for L-mode, ELM-free H-mode and ELMy H-mode phases as in Fig. 3. The parallel heat fluxes are obtained from divertor LPs, and are calculated using the standard sheath model ($q_{//} = \gamma j_s T_t / e$) by assuming $\gamma = 7$, which is discussed in detail in Ref. [7]. The exponential fitting on the SOL side is $A_q \exp[-(R - R_{\max})/\lambda_q]$ using the least square fitting method, where $R_{\max}$ is the major radius of the maximum $q_{//}$ mapped to the outer mid-plane. These experimental results suggest the power deposition widths on divertor target also display strong negative dependence on I_p, in both L-mode and H-mode regimes, showing good agreement with the heuristic SOL width model proposed by Goldston [6]. In the 20ms-averaged time widows of each discharge, the divertor targets in L-mode and ELM-free H-mode phases exhibit the maximum and the minimum peak heat flux, respectively. The discrepancy of peak heat flux in different discharge phases is consistent with the measurements of the IR camera, which will be shown later. In the profiles of #34388 (0.8MA) and #34397 (0.6MA), the LO heat fluxes on the SOL side display a secondary peak. However, in the LO j_s profiles shown in Fig. 3, no such secondary peaks were observed. The secondary peaks in the heat flux profiles may result from the secondary separatrix of the upper X-point, as illustrated in Fig. 1. And the influence of the secondary separatrix on the cross-field transport between particle and power may be different at high I_p.

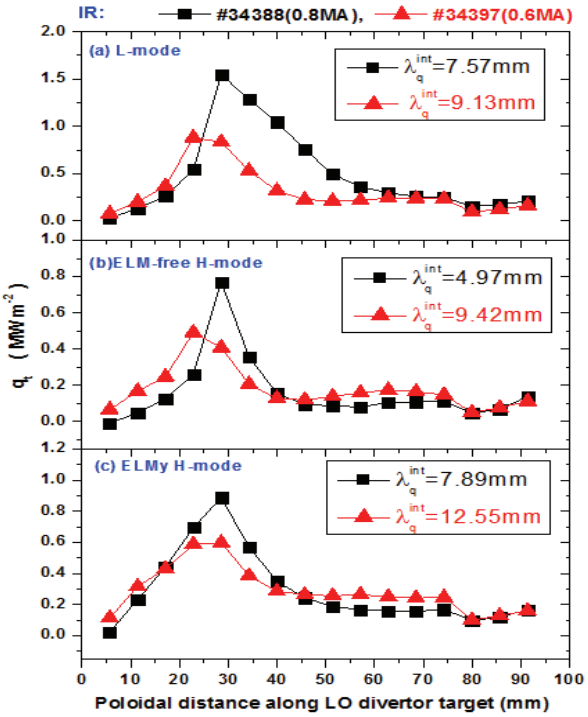

Fig. 5 Profiles of target heat flux along the LO divertor target in L-mode (a), ELM-free H-mode (b), and ELMy H-mode (c) phases as measured by an IR camera.

To verify the power deposition widths between cross-diagnostics, Figure 5 shows the target heat flux profiles measured by IR camera in shot #34388 and shot #34397. Unfortunately, results from the IR camera in shot #34407 are unavailable. The profiles obtained from the IR camera exhibit a significant departure from an exponential. For these IR heat-flux width studies, we employ the integral power width defined by Loarte [1],

$$\lambda_q^{\text{int}} = \frac{\int_{div} q_{div} 2\pi R_{div} ds}{2\pi R_{div}^{peak} q_{div}^{peak} f_m} \quad (1)$$

where λ_q^{int} refers to the outer mid-plane, q_{div} is the measured power flux onto the divertor, s is the poloidal distance along the LO target plates, and $f_m = (R_{mid} B_{\theta,mid})(R_{div} B_{\theta,div})^{-1}$ is the poloidal magnetic flux expansion factor. As shown in the legend of Fig. 5, the integral power deposition widths obtained from IR camera also depend strong inversely on the plasma current, again both in L-mode and H-mode regimes. The comparison of peak heat fluxes between different phases in one shot is similar to the results of divertor LPs, i.e., the L-mode imposes the maximum and the ELM-free H-mode imposes the minimum heat flux on divertor target plates. Furthermore, the IR results also suggest that the peak heat fluxes of $I_p = 0.8MA$ are higher than that of $I_p = 0.6MA$ during the same corresponding phases.

4. Summary

In summary, the initial measurements of the dependence of divertor particle and power deposition widths on the plasma current in EAST have been shown. Experiments were carried out in LHCD LSN L- and H-mode plasmas with lithium wall conditioning, with results presented from divertor LPs and an IR camera. Experimental results from the lower outboard divertor suggest that both the particle and power deposition profiles display a strongly negative dependence on I_p in L-mode, ELM-free H-mode and ELMy H-mode regimes. Particle and power deposition widths measured by divertor LPs were estimated using a simple e-folding decay length on the SOL side, while the power deposition width measured by IR camera was calculated using the Loarter integral width. The experimental results show good agreement with the heuristic SOL width model.

Acknowledgements

This work was supported by the JSPS-NRF-NSFC A3 Foresight Program in the field of Plasma Physics (NSFC No.11261140328) and NSFC No. 11105177. It was also partly supported by ITER-CN No. 2013GB107003.

References

[1]A. Loarte et al., J. Nucl. Mater. 266-269 (1999) 587.

[2]T. K. Gray et al., J. Nucl. Mater. 415 (2011) S360.

[3]B. LaBombard et al., Phys. Plasmas 18 (2011) 056104.

[4]M. A. Makowski et al., Phys. Plasmas 19 (2012) 056122

[5]T. Eich et al., Phys. Rev. Lett. 107 (2011) 210501.

[6]R. J. Goldston et al., Nucl. Fusion 52 (2012) 013009

[7]L. Wang et al., Nucl. Fusion 52 (2012) 063024.

[8]L. Wang et al., "Characterizations of power loads on divertor targets for Type I, compound and small ELMs in EAST superconducting tokamak", submitted to Nucl. Fusion (December 2012)

[9]T. F. Ming et al., Fusion Eng. Des. 84 (2009) 57.

[10]J -W. Ahn et al., J. Nucl. Mater. 390-391 (2009)

421

Molecular dynamics simulation of hydrogen defect interaction and bubble growth in tungsten

Xiao-Chun Li[1,2], Xiaolin Shu[2], Yi-Nan Liu[2], Yi Yu[2], F. Gao[3], Guang-Nan Luo[1], Guang-Hong Lu[2,*]

[1] Institute of Plasma Physics, Chinese Academy of Sciences, Hefei, Anhui 230031, China

[2] Department of Physics, Beihang University, Beijing 100191, China

[3] Pacific Northwest National Laboratory, Richland, WA 99352, USA

[*] E-mail address: lgh@buaa.edu.cn (G.-H. Lu), xcli@ipp.ac.cn (X.-C. Li).

Abstract: Molecular dynamics (MD) simulations were performed to investigate the H-defect interaction in W using an analytical bond-order potential for W-H system. We first investigated the H-H interaction in W. The binding energies between H and H cluster are shown to be very small. As a result, H bubbles can not form spontaneously by self-trapping. Then we investigated the interaction between H and W self-interstitial atoms (SIAs). Although the binding energies between H atoms and small H-SIA clusters are positive, these interactions are still not strong enough for the formation of large H-SIA clusters. Finally, we analysed the binding energies of a H, a vacancy and a self-interstitial W to a H-vacancy cluster in W, respectively. The binding energies depend on the ratio of H to vacancy. The binding energies of a H atom and a self-interstitial W atom to a H-vacancy cluster both decrease as the ratio increases, while the binding energy of vacancy to H-vacancy cluster increases as the ratio increases. On the basis of these results, we conclude that H bubble formation needs a high concentration of H atoms in W, and propose a initial H bubble formation and growth process.

PACS numbers: 71.20.Be, 67.63.Gh, 61.72.J-, 02.70.Ns

Keywords: tungsten; hydrogen; defect; molecular dynamics

1. Introduction

Tungsten (W) is considered to be a promising candidate for the divertor and first wall of fusion reactor because of not only its high melting point and high thermal conductivity, but also its low sputtering yield of light elements [1]. However, as the plasma facing materials (PFMs), W is subjected to high flux irradiation of hydrogen (H) isotope ions, which leads to microstructural changes and significant effects on its intrinsic mechanical properties. Such high flux H can induce the formation of H bubbles, which produces surface roughening and blistering. This remains a key obstacle in the development of W as a PFM. The physical mechanism of H trapping and blistering in W is still not well understood, thus require further investigation.

The first detailed description of H trapping and bubble formation in metals by first principles is given by Liu *et al*. [2], who suggest that H tends to bind at the isosurface of an optimal charge density inside the

monovacancy in W and proposes a vacancy trapping mechanism for H bubble formation which is expected to be generally applicable for metals [2, 3]. Two H atoms will occupy the two neighboring tetrahedral interstitial sites in W along the <110> direction, with the distance of 2.22 Å [4]. More accurate energetics and configurations of multi-H at the monovacancy were given in both W [3, 5] and Mo [3], which shows one monovacancy can trap as many as 12 and 8 H with different trapping energies in W and Mo, irrespective of the zero point energy correction. On the other hand, the number of trapped H at the vacancy in W decreases with the increasing temperature according to the molecular dynamics simulation [3] using a newly developed W-H potential [6], suggesting that temperature weakens the H trapping capacity of vacancy. At temperature of 300 K, only ~6.5 H atoms can be trapped by a monovacancy, while it decreases to ~5 H at 900 K. This confirms that the thermodynamic estimation on the number of trapped H atoms at the vacancy in W is basically correct, which gave 5 H at the room temperature [7]. The difference in formation of H and He clusters in W was investigated by Henriksson et al. by the molecular dynamics (MD) and Monte Carlo methods [8, 9], which shows that H atoms do not form bound states with other H atoms in the bcc metal W, while He atoms do. As a result, He atoms form bubbles close to the surface in W, while H atoms do not.

Atomic scale simulation is one of the most attractive methods to understand interacting processes between materials (atoms), which contain detailed structure information. In addition to the experiment [10-13], atomic scale simulation has been severed as an essential tool to understand the H [14-16], helium (He) behaviours [16-18] in W, the H-He interaction in W [19, 20], as well as in other fusion materials [21-25]. Molecular dynamics has become a key tool for modelling material processes based on an atomic level description. We have developed new interatomic potentials for W-H system [6], in order to obtain further knowledge about the initial stage of H-vacancy cluster and H bubble nucleation. MD simulations are performed to investigate the H-defect interactions in W, including the H-H interaction, H-SIA interaction and H-vacancy interaction in W. The high energy neutron radiation will cause high concentration of vacancies and SIAs, which may be the trapping centres of H atoms. The small H-vacancy clusters may also play an important role in the nucleation of H bubble. As a result, we have investigated the binding energies of a H, a vacancy and a self-interstitial W to a H-vacancy cluster in W.

2. Computational method

We investigate the H behavior in W with MD simulation, using a self-developed interatomic potential based on an analytical bond-order scheme for W-H system [6]. The potential is fitted based on the defect energetics and structural properties of W and W-H systems from the experimental values and the first-principles calculations, with the defect properties such as vacancy and H interstitial formation energies

especially considered in order to make the potential suitable for simulating the W-H system with defects. The potential can reproduce the energies of the W surfaces, the defect properties of both W and W-H systems, the energies of W-H molecules, the W melting point and H diffusion barriers in W. Thus, it can be applid to investigate the H behaviors in W which contains defects such as vacancies and SIAs.

All works are performed using the MD code LAMMPS [26]. The simulation box size is $10a \times 10a \times 10a$, where a is the lattice constant of bcc W. For all the MD simulations, the Polak-Ribiere version of the conjugate gradient (CG) algorithm is used, and the stopping tolerance for energy and force are 10^{-9} eV and 10^{-9} eV/Å, respectively.

In order to find the lowest energy configuration of H_nV_m cluster, for each case with a fixed number of n and m, we generate 10*n different H_nV_m cluster configurations by putting n H atoms to the vacancy cluster (V_m) randomly, and then perform MD simulations for each configuration. In this way, we could obtain the lowest energy configuration of each H_nV_m cluster, and it is considered as the most stable configuration of the H_nV_m cluster. Then we can obtain the formation energies of these H_nV_m clusters, which are defined as

$$E_f(H_nV_m) = E_{tot}(H_nV_m) - [nE_H^C + (N-m)E_W^C] \quad (1)$$

where N is the total number of W atoms in the perfect crystal, and E_H^C, E_W^C refer to half of the chemical potential of H_2, cohesive energy of the single W atom in perfect bcc crystal, respectively.

3. Results

3.1. H self-binding

We first investigate the interaction between two H atoms in bulk W. We put one H atom at a tetrahedral interstitial site (TIS), while the other H atom occupies another TIS. The binding energy between the two H atoms, $E_b(H+H)$, can be calculated by

$$E_b(H+H) = 2E_f(H) - E_f(H+H) \quad (2)$$

where $E_f(H)$ is the formation energy of one H atom at the TIS, which is 0.86 eV. And $E_f(H+H)$ is the formation energy of two H atoms at different TISs. We have determined the H-H binding energy as a function of H-H distance, in comparison with the first-principles calculations [4], as shown in Fig. 1. According to present MD simulation, the binding energies between two H atoms are all negative. As a result, two H atoms will be repulsive in bulk W. Although the first-principles calculation gives a maximum binding energy of 0.01 eV with the H-H distance of 2.22 Å, but such a small binding energy maybe negligible. Generally speaking, the present MD simulation gives lower binding energies in comparison with the first-principles calculation. When the H-H distance is less than 1.7 Å, both calculations lead to negative binding energies lower than -0.1 eV. As two H atoms are repulsive in bcc W, it is reasonable to assume that H atoms are unable to form large H cluster

by self-trapping.

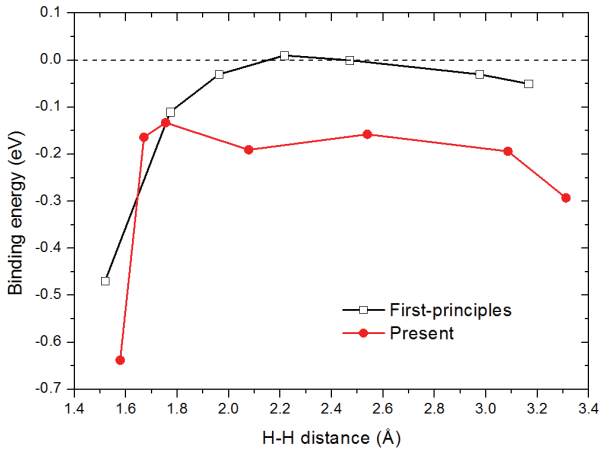

Fig. 1. H-H binding energy as a function of the H-H distance obtained from present MD simulation, in compared with the first-principles calculations.

We next investigate the binding energy between H atom and small H cluster (H_n), and the average binding energy of the H clusters, where the number of H atom (n) ranges from 1 to 10. The H binding energy can be calculated by

$$E_b(H+H_{n-1}) = E_f(H) + E_f(H_{n-1}) - E_f(H_n) \quad (3)$$

where $E_f(H_n)$ is the formation energy of H_n cluster. The average binding energy of H cluster can be calculated by

$$E_b^{avg}(H_n) = [nE_f(H) - E_f(H_n)]/n \quad (4)$$

We have determined the H binding energy and the average H binding energy in H_n cluster as a function of the H number in the cluster, as shown in Fig. 2. Most of the H binding energies are negative as we predicted, except two positive binding energies in the curve. The binding energy between H and H_3 cluster is 0.20 eV, while the average binding energy of H_4 cluster is only 0.007 eV, which is almost negligible. Moreover, there is a positive binding energy between H and H_8 cluster, while the average binding energy of H_9 cluster is -0.09 eV, which means 9 H atoms will consume energy to bind together. Generally speaking, the average binding energy is negative, and H atoms are unable to form cluster by self-trapping. At the same time, the structures of these H_n cluster were plotted in Fig. 3 which shows that it is easy for H atoms to occupy the tetrahedral interstitial positions. The H atoms tend to be distributed dispersively instead of forming a cluster.

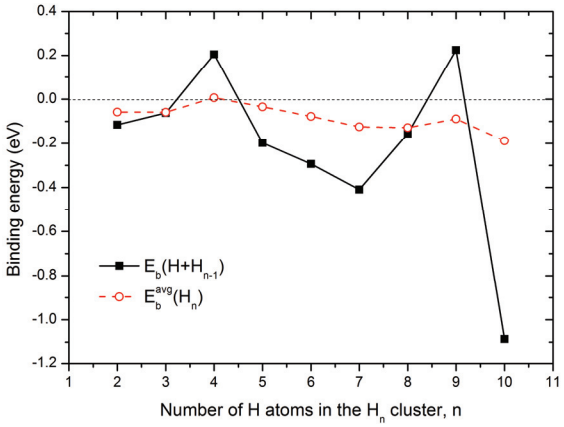

Fig. 2. The H binding energy and the average binding energy of H cluster as a function of the number of H atoms in the H cluster.

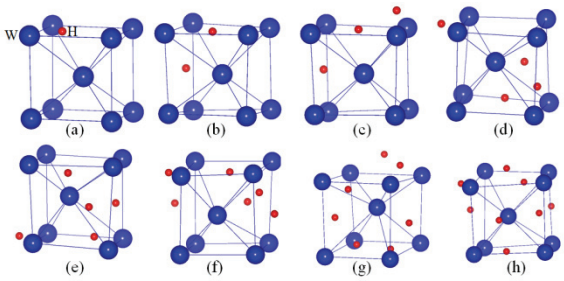

Fig. 3. Configuration of H_n clusters. The larger blue spheres represent W atoms, while the smaller red spheres represent H atoms.

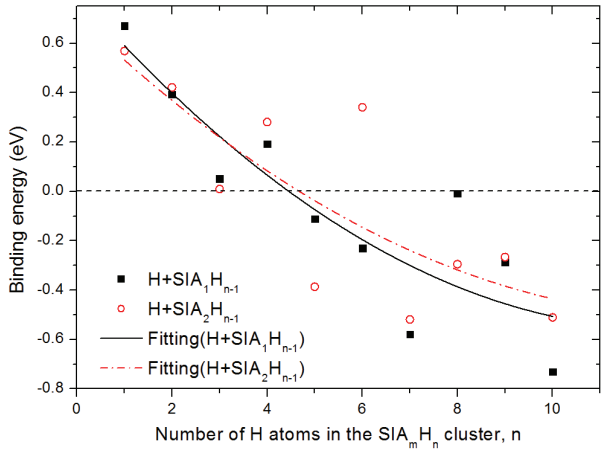

Fig. 4. The H binding energy as a function of the number of H atoms in the clusters. The lines are the quadratic polynomial fitting results of the binding energy.

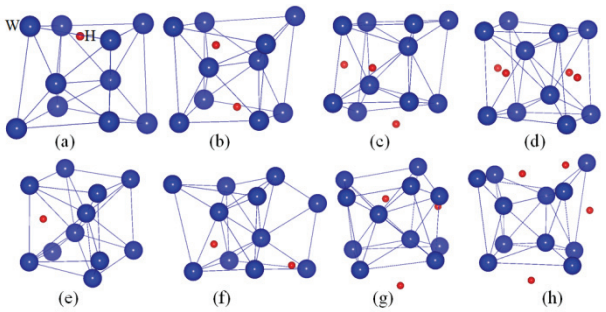

Fig. 5. Configuration of SIA_mH_n clusters. The larger blue spheres represent W atoms, while the smaller red spheres represent H atoms.

3.2. Binding energy of H with W SIA

SIA is a common defect in W under the fusion environment. In order to understand the H bubble formation mechanism, it is important to understand the interaction between H and SIA. Here we use MD simulations to investigate the binding energy of H to SIA_mH_{n-1}, where the SIA number (m) is 1, 2, and the H atoms number (n) ranges from 1 to 10. The H binding energy can be calculated by

$$E_b(H+SIA_mH_{n-1}) = E_f(H)+E_f(SIA_mH_{n-1})-E_f(SIA_mH_n) \quad (5)$$

where $E_f(SIA_mH_n)$ is the formation energy of SIA_mH_n cluster. We have determined the H binding energy as a function of H number (n) in SIA_mH_n cluster and the results are shown in Fig. 4. The H binding energy decreases with the increasing of H number although there is certain fluctuation. According to the fitting results, when H atoms number is larger than five, the binding energy comes negative which indicates that H atoms and those SIA_mH_n cluster are repulsive. And when H number is less than four, the binding energies of H to SIA_1H_{n-1} and H to SIA_2H_{n-1} are almost the same positive values. The highest binding energy for H to SIA_1 and H to SIA_2 are 0.67 eV and 0.57 eV, respectively. Thus, although H atoms have positive binding energies with small SIA_mH_n clusters, they are still not enough to form big SIA_mH_n clusters. As a proof, the structures of some SIA_mH_n clusters are plotted in Fig. 5 which show that H atoms do not tend to form a cluster, same as the trend of H_n .

3.3. Self binding of SIA and vacancy

Since H_2 molecule could not be formed in mono-vacancy with the temperature effect considered [3], the vacancy-type defects such as vacancy cluster could be a likely place for H atoms to fill in and it is important to understand the interaction between vacancy and vacancy cluster. We first calculate the formation energy of a vacancy clusters (V_m), where m is the number of vacancies in the cluster. The binding energy of the m*th* vacancy to the vacancy cluster can be calculated by

$$E_b(V+V_{m-1}) = E_f(V)+E_f(V_{m-1})-E_f(V_m) \quad (6)$$

We obtain the binding energy of the m*th* vacancy to the vacancy cluster (V_{m-1}) as a function of the vacancy number in the cluster (V_m, m from 1 to 10), and the results are show in Fig. 6. The binding energy ranges from 0.62 eV to 1.93 eV, and generally increases with the vacancy number. The binding energy of the nearest neighbored di-vacancy is 0.62 eV, which is very close to the result of first-principles calculations 0.40 eV [27] and the experimental value of 0.70 eV [28].

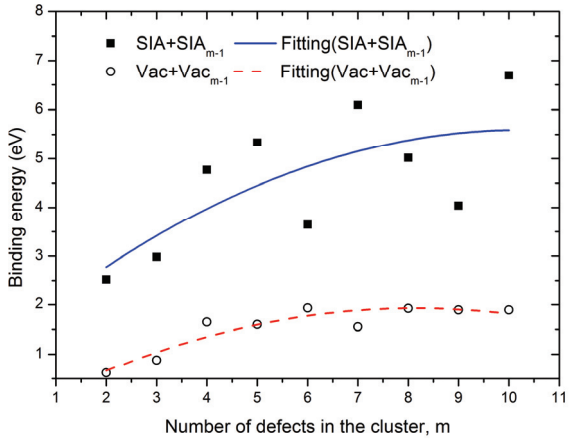

Fig. 6. Vacancy binding energy and SIA binding energy as a function of the number of defects in the cluster. The lines are the quadratic polynomial fitting results of these binding energies.

In contrast, we also investigate the binding energy of the m*th* SIA to the SIA cluster versus the number of SIA in SIA cluster. The structures of the SIA clusters are determined by repeatedly adding an interstitial W atom to the SIA cluster. The binding energy of the m*th* SIA to the SIA cluster can be calculated by

$$E_b(SIA + SIA_{m-1}) = E_f(SIA) + E_f(SIA_{m-1}) - E_f(SIA_m) \quad (7)$$

The SIA binding energy generally increases with the SIA number as shown in Fig. 6, leaving out the slight oscillation. When the SIA number in the cluster increases from 1 to 10, the SIA binding energy is increased from 2.5 eV to 6.7 eV. The SIA binding energy is much higher compared with the vacancy binding energy in vacancy cluster.

3.4. Binding energies of H, W and vacancy with H_nV_m clusters

In the next session we will introduce H atoms to the vacancy clusters to study the thermal stability of H-vacancy clusters (H_nV_m), where n and m are the numbers of H atoms and vacancies in the cluster. Here the vacancy number (m) is from 1 to 10, and the H density is defined as the atomic ratio of H to vacancy in the H_nV_m cluster, which is provided by n/m. The H-to-vacancy ratio ranges from 1 to 10. The formation energy of a H_nV_m cluster is obtained by MD simulations, and the thermal stability of H_nV_m cluster could be described by the binding energies of a vacancy ($E_B(V)$), a H atom ($E_B(H)$) and a self-interstitial W atom ($E_B(W)$) to the H_nV_m cluster, which are calculated from the following equations,

$$E_B(V) = E_f(H_nV_{m-1}) + E_f(V) - E_f(H_nV_m) \quad (8)$$

$$E_B(H) = E_f(H_{n-1}V_m) + E_f(H) - E_f(H_nV_m) \quad (9)$$

$$E_B(W) = E_f(H_nV_{m+1}) + E_f(SIA) - E_f(H_nV_m) \quad (10)$$

where $E_f(H_nV_m)$ is the formation energy of a H_nV_m cluster with n H atoms in a vacancy cluster of m vacancies, and $E_f(V)$, $E_f(H)$ and $E_f(SIA)$ are the formation energies of an isolated vacancy, interstitial H atom and SIA, respectively. The average binding energy of H atoms to the vacancy cluster can be calculated by

$$E_B^{avg}(H) = [E_f(V_m) + nE_f(H) - E_f(H_nV_m)]/n \quad (11)$$

where $E_f(V_m)$ is the formation energy of the V_m cluster. Then we make statistical analysis of the binding energy as a function of H-to-vacancy ratio. As shown in Fig. 7 and Fig. 8, the binding energies show a strong dependence on the H-to-vacancy ratio, not the number of vacancies in the H_nV_m cluster.

The binding energy of a vacancy to the H_nV_m cluster ($E_B(V)$) increases dramatically with the rising H-to-vacancy ratio. In comparison with the vacancy binding energy to pure vacancy cluster, the vacancy binding energy is dramatically changed when H atoms are introduced into the vacancy clusters. When the H-to-vacancy ratio is small, the binding energy of vacancy to H_nV_m cluster is about 1.0 eV, which is similar with that to the pure vacancy cluster. When the H-to-vacancy ratio increases from 0 to 9, the vacancy binding energy increases from 1.0 eV to 13.0 eV. This indicates that it is energetically difficult to remove a vacancy from the H_nV_m clusters even at high temperature. On the other hand, with such a high vacancy binding energy, H-vacancy clusters can be easily combined with another vacancy. The vacancy binding energy is much higher than the H binding energy, indicating that it is easier for the H-vacancy cluster to combine with a vacancy with respect to a H atom.

The binding energy of a self-interstitial W to the H_nV_m cluster ($E_B(W)$) is with the opposite trend to the vacancy binding energy. The W binding energy greatly decreases with the increasing H-to-vacancy ratio. When the H-to-vacancy ratio is small, the W binding energy is about 11.0 eV, which is much higher than the H binding energy and vacancy binding energy. When the H-to-vacancy ratio is increased from 0 to 10, the W binding energy decreases from 11.0 eV to 1.0 eV accordingly.

Generally speaking, if the concentration of H atoms in W is low, H atoms would diffuse to the vacancy sequentially (the sequential way). The binding energy of a H atom to the H_nV_m cluster ($E_B(H)$) represents the energy required to separate the n*th* H atom from the H_nV_m cluster. Higher binding energy means stronger combination of the H atom to the vacancy clusters. The H binding energy shows a strong dependence on the H-to-vacancy ratio despite of the larger deviation at the higher H-to-vacancy ratio. The H binding energy gradually decreases with the increasing H-to-vacancy ratio. When the H-to-vacancy ratio increases is larger than 5, the H binding energy has fallen negative, which indicates that in this regime, energy will be needed in order to combine more H atoms. And when the ratio is

from 0 to 5, the H binding energy has decreased from 2.0 eV to 0.0 eV but remains positive which suggests that this H_nV_m cluster with a low H-to-vacancy ratio could absorb H atom spontaneously and a vacancy can trap about 5 H atoms on average.

As a comparison of the vacancy binding energies and W binding energies, the W binding energy is much higher than the vacancy binding energy, which indicates that it is very easy for the H-vacancy cluster to combine with a self-interstitial W atom. This will cause the combination of a vacancy in the H-vacancy cluster and a self-interstitial W atom, leading to a smaller H-vacancy cluster.

As contrast, if the concentration of H atoms in W is high enough, multiple H atoms can diffuse to the vacancy at the same time (the simultaneous way). Fig. 8 shows the average binding energies of H atoms to vacancy cluster (V_m) in W as a function of H-to-vacancy ratio. The average binding energies of H atoms represents the average binding energy of n H atoms to the vacancy cluster. Higher binding energy means stronger combination of the n H atoms to the vacancy clusters. When H-to-vacancy ratio increases from 0 to 10, the average binding energies of H atoms decrease from 2.4 eV to 0.2 eV. The average binding energy is still positive, even if the H-to-vacancy ratio is largeer than 10, which suggests that one vacancy could trap more than 10 H atoms on average.

When the concentration of H atoms in W is high enough, a vacancy can trap more than 10 H atoms in a H_nV_m cluster on average. As long as the H-to-vacancy ratio is greater than 6, the vacancy binding energy is much higher than the W binding energy, as shown in Fig. 8, which indicates that it is easier for the H-vacancy cluster to combine with another vacancy. This will increase the size of H-vacancy cluster and reduce the H-to-vacancy ratio. As long as the ratio is lower than 5, the cluster would absorb H atoms again to increase the ratio, and then more vacancies will be captured. In this way, the H-vacancy cluster will capture more H atoms and vacancies, causing the H-vacancy cluster grow bigger and bigger. This might be the initial stage of the bubble formation in fusion environment. According to these discussion, the H bubble formation needs a high concentration of H atoms in W. And in fusion environment, it is possible to accumulate such high concentration of H atoms in some local area of W PFM, such as the area near surface.

Based on these results, we give a H-vacancy cluster formation and growth process: the vacancy first capture H atoms ($V_m+H_n=V_mH_n$), and with the increase of H number in vacancy, it is more and more difficult for the vacancy to capture more H atoms. However, at this time, it is easy for H-vacancy cluster to combine with a neighboring vacancy ($V_mH_n+V=V_{m+1}H_n$). Once the H-vacancy cluster absorbs new vacancies, it will lower the H-vacancy ratio and the cluster can capture more H atoms, which leads to the emergence of a larger H-vacancy cluster ($V_{m+1}H_n+H_x=V_{m+1}H_{n+x}$). Since the H-vacancy clusters can be considered as the initial nucleation of H bubbles, this is actually a initial H bubble formation and growth process.

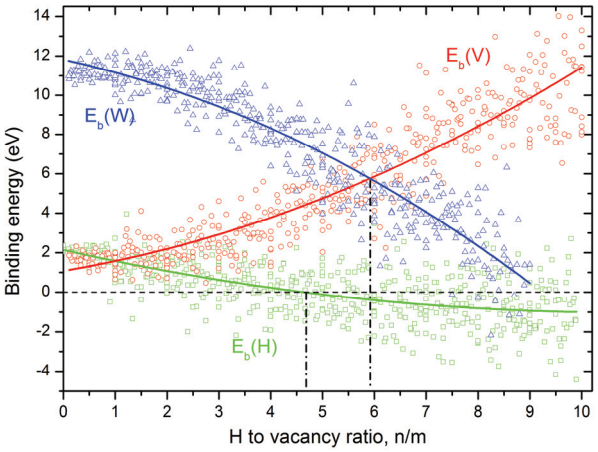

Fig. 7. The binding energies of a H atom, a vacancy and a self-interstitial W atom to a H-vacancy cluster in W as a function of H-to-vacancy ratio. The solid lines are the quadratic polynomial fitting results of these binding energies.

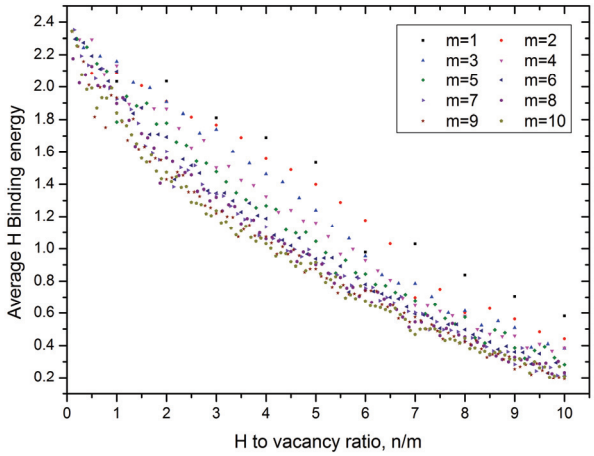

Fig. 8. The average binding energies of H atoms to vacancy cluster in W as a function of H-to-vacancy ratio.

4. Conclusions

The interaction of H with defects in W was investigated using the molecular dynamics simulations. H atoms cannot form H cluster by self-trapping. Although H has positive binding energy with small SIA clusters, it is still not strong enough to form big H-SIA cluster. The binding energies of a vacancy, a H atom and a self-interstitial W atom to a H_nV_m cluster depend on the H-to-vacancy ratio (n/m). The H binding energy and SIA W binding energy decrease with the increasing H-to-vacancy ratio, while the vacancy binding energy increases. When the H concentration in W is low, the H-vacancy cluster is very easy to capture a SIA W atom, and makes the size of H-vacancy cluster smaller. When the H concentration in W is high enough, it is easy for the H-vacancy cluster to gradually bind another vacancy and more H atoms, thus causing the size of H-vacancy cluster grow bigger and bigger. In summary, the formation and growth of the H bubble nuclei experiences a process of H-vacancy clusters formation, H capture, vacancy capture, and again H capture, vacancy capture. The high concentration of H is an essential condition for the H bubble formation.

Acknowledgments

This work has been supported by Natural Science Foundation of China (NSFC) Grant No. 51171008 and National Magnetic Confinement Fusion Program with Grant No. 2013GB109002. F. Gao is grateful for the support by the US Department of Energy, Office of Fusion Energy Science, under Contract DE-AC06-76RLO1830.

References

[1] H. T. Lee, A. A. Haasz, J. W. Davis, and R. G. Macaulay-Newcombe, J. Nucl. Mater. **360**, 196 (2007).

[2] Y. L. Liu, Y. Zhang, H. B. Zhou, G. H. Lu, F. Liu, and G. N. Luo, Phys. Rev. B **79**, 172103 (2009).

[3] L. Sun, S. Jin, X. C. Li, Y. Zhang, and G. H. Lu, J. Nucl. Mater. **434**, 395 (2013).

[4] Y. L. Liu, Y. Zhang, G. N. Luo, and G. H. Lu, J. Nucl. Mater. **390-91**, 1032 (2009).

[5] K. Ohsawa, J. Goto, M. Yamakami, M. Yamaguchi, and M. Yagi, Phys. Rev. B **82**, 184117 (2010).

[6] X.-C. Li, X. Shu, Y.-N. Liu, F. Gao, and G.-H. Lu, J. Nucl. Mater. **408**, 12 (2011).

[7] K. Heinola, T. Ahlgren, K. Nordlund, and J. Keinonen, Phys. Rev. B **82**, 094102 (2010).

[8] K. O. E. Henriksson, K. Nordlund, A. Krasheninnikov, and J. Keinonen, Appl. Phys. Lett. **87**, 163113 (2005).

[9] K. O. E. Henriksson, K. Nordlund, A. Krasheninnikov, and J. Keinonen, Fusion Eng. Des. **50**, 43 (2006).

[10] G. N. Luo, W. M. Shu, and M. Nishi, J. Nucl. Mater. **347**, 111 (2005).

[11] G.-N. Luo, W. M. Shu, and M. Nishi, Fusion Eng. Des. **81**, 957 (2006).

[12] M. Fukumoto, Y. Ohtsuka, Y. Ueda, M. Taniguchi, M. Kashiwagi, T. Inoue, and K. Sakamoto, J. Nucl. Mater. **375**, 224 (2008).

[13] G. N. Luo, M. Liu, Z. Q. Kuang, X. D. Zhang, Z. S. Yang, C. G. Deng, Z. C. Zhang, J. G. Li, and K. S. Zhou, J. Nucl. Mater. **363**, 1241 (2007).

[14] H. B. Zhou, S. Jin, Y. Zhang, G. H. Lu, and F. Liu, Phys. Rev. Lett. **109**, 135502 (2012).

[15] S. Jin, Y.-L. Liu, H.-B. Zhou, Y. Zhang, and G.-H. Lu, J. Nucl. Mater. **415**, S709 (2011).

[16] H. B. Zhou, S. Jin, X. L. Shu, Y. Zhang, G. H. Lu, and F. Liu, Europhys. Lett. **96**, 66001 (2011).

[17] Y. L. Liu, H. B. Zhou, Y. Zhang, S. Jin, and G. H. Lu, Nucl. Instr. and Meth. B **267**, 3193 (2009).

[18] H. B. Zhou, Y. L. Liu, Y. Zhang, S. Jin, and G. H. Lu, Nucl. Instr. and Meth. B **267**, 3189 (2009).

[19] B. Jiang, F. R. Wan, and W. T. Geng, Phys. Rev. B **81**, 134112 (2010).

[20] H. B. Zhou, Y. L. Liu, S. Jin, Y. Zhang, G. N. Luo, and G. H. Lu, Nucl. Fusion **50**, 115010 (2010).

[21] L. Zhang, Y. Zhang, and G. H. Lu, Nucl. Instr. and Meth. B **267**, 3087 (2009).

[22] Y. Zhang, W. Q. Feng, Y. L. Liu, G. H. Lu, and T. M. Wang, Nucl. Instr. and Meth. B **267**, 3200 (2009).

[23] L. Zhang, C. C. Fu, and G. H. Lu, Phys. Rev. B **87**, 134107 (2013).

[24] L. Zhang, X. L. Shu, S. O. Jin, Y. Zhang, and G. H. Lu, J. Phys.: Condens. Matter **22**, 375401 (2010).

[25] L. Zhang, Y. Zhang, and G. H. Lu, J. Phys.: Condens. Matter **25**, 095001 (2013).

[26] S. Plimpton, J Comput Phys **117**, 1 (1995).

[27]P. M. Derlet, D. Nguyen-Manh, and S. L. Dudarev, Phys. Rev. B **76**, 054107 (2007).

[28] Y. Park, H.-C. W. Huang, R. W. Siegel, and R. W. Balluffi, Philos. Mag. A **48**, 397 (1983).

Extended MHD simulation of 2.5D Rayleigh-Taylor instability

R. Goto[1], H. Miura[1,2], A. Ito[1,2], M. Sato[2] and T. Hatori[1]

[1] The Graduate University for Advanced Studies, Toki, Gifu 509-5292, Japan

[2] National Institute for Fusion Science, Toki, Gifu 509-5292, Japan

Abstract: The gyro-viscous effect to the Rayleigh-Taylor instability in a 2D rectangular slab is studied numerically. Growth rate of the Rayleigh-Taylor instability obtained in nonlinear simulations shows a good coincidence with linear stability analysis. Analysis on the nonlinear stage suggests a possible change of dominant structures due to the gyro-viscosity.

1. Introduction

Dynamical behaviors of the ballooning instability attract a large attention because of its significance in torus plasma events such as the Edge Localized Modes (ELMs) in tokamak devices and high beta achievement in the Large Helical Device (LHD) [1]. Though the dynamical growth of the ballooning modes have been studied extensively by means of a numerical simulation of magnetohydrodynamic (MHD) equations, the understanding on the subject is still limited partially because the single-fluid MHD model ignores effects of small length scales such as the ion skindepth and the ion Larmor radius while the ballooning modes have larger growth rates for larger wave numbers. Thus, for the sake of improving this shortcoming, studying this subject by means of numerical simulations of an extended MHD model which includes small-scale effects appears reasonable.

Some nonlinear extended MHD simulation codes such as the M3D [2] and the NIMROD code [3] are equipped with the Hall term, the gyro-viscosity and other two-fluid effects. We have also studied a Hall term effect in the full-toroidal MHD simulation of LHD by our simulation code, MINOS [4]. However, fundamental characteristics of growth of the ballooning modes especially in the nonlinear stage are not fully clarified yet. Since a large computer resource is required in a full 3D computation to clarify these small-scale effects, it can be effective to study a 2D problem before studying a full-3D subject. For simplicity, we study the Rayleigh-Taylor (RT) instability in the two dimensional (2D) slab, instead of studying the ballooning instability.

A few aspects of the RT instability in a 2D slab with some small-scale effects have already been studied numerically [5-7]. Roberts and Taylor [4] have introduced the Finite Larmor Radius (FLR) effect as the anisotropic pressure which is call as the gyro-viscous tensor [8] and shown the dispersion relation for the RT mode. Their dispersion relation implies that the growth of the higher modes is stabilized by the gyro-viscosity. Huba [6] has carried

out 2D particle/fluid hybrid simulations, and shown that the growth of the high wave number modes is suppressed by the gyro-viscosity relatively compared with the MHD simulations. Winske [6] has also carried out 2D hybrid simulations and shown that the gyro-viscosity reduces the growth rates of the higher modes while the Hall term increases them. Although these studies have clarified some characteristics of the Hall term and the gyro-viscosity, typical parameters such as beta value and the density gradient are more suitable for space plasma than for torus plasma. Thus, extended MHD simulations with low beta and low density ratio can be helpful for clarifying some important characteristics of the RT instability in fusion plasma. Here, we concentrate on the system with only gyro-viscosity and neglect the Hall term for simplicity.

This paper is organized as follows. In sec. 2, the outline of our simulations is shown. In sec. 3, numerical results and analysis in the linear stage are shown. Summary is shown in sec. 4.

2. Extended MHD equations and initial equilibrium

Extended MHD equations that include the Hall term and the gyro-viscosity in a 2D slab are expressed in conservative form except pertaining to the Hall term.

$$\frac{\partial \rho}{\partial t} = -\nabla \cdot (\rho \mathbf{v}) \tag{1}$$

$$\frac{\partial}{\partial t}(\rho \mathbf{v}) = -\nabla \cdot \left[\rho \mathbf{v}\mathbf{v} + \mathbf{I}\left(p + \frac{B^2}{2}\right) - \mathbf{B}\mathbf{B} + \delta \prod_i\right] + \rho \mathbf{g} \tag{2}$$

$$\frac{\partial e}{\partial t} = -\nabla \cdot [(e + p)\mathbf{v} - \mathbf{v} \cdot \delta \prod_i] \tag{3}$$

$$\frac{\partial \mathbf{B}}{\partial t} = -\nabla \cdot (\mathbf{v}\mathbf{B} - \mathbf{B}\mathbf{v}) - \nabla \times \left[\frac{\epsilon}{\rho}(\mathbf{J} \times \mathbf{B} - \nabla p_e)\right] \tag{4}$$

Here, the total energy e is defined as $e \equiv p/(\gamma-1) + \rho \mathbf{v}^2/2$. Here, we consider the system being uniform in the z direction, $w = 0$ and $\partial/\partial z = 0$ in eqs.(1)-(4), while keeping the z component of the magnetic field $\mathbf{B} = (B_x, B_y, B_z)$. The gyro-viscosity is given by

$$(\prod_i)_{xx} = -(\prod_i)_{yy} = -p_i\left(\frac{\partial v}{\partial x} + \frac{\partial u}{\partial y}\right) \tag{5}$$

$$(\prod_i)_{xy} = -(\prod_i)_{yx} = -p_i\left(\frac{\partial u}{\partial x} + \frac{\partial v}{\partial y}\right) \tag{6}$$

The total pressure is defined as the sum of the ion pressure and the electron pressure $p = p_i + p_e = (\alpha+1)p_e$, $\alpha = p_i/p_e$. All variables in eqs. (1)-(4) have been already normalized by the representative quantities such as the length scale L, the density ρ_0, the characteristic value of the background magnetic field B_0 which is in z direction, the Alfven velocity $V_A = \sqrt{B_0^2/(\mu_0 \rho_0)}$ where μ_0 is the vacuum permeability, Alfven time scale L/V_A. The symbol $\mathbf{g}$ is the gravitational acceleration where $\mathbf{g} = (0,-g,0)$. The symbols δ and γ are the gyro-viscosity and the ratio of the specific heats, respectively. To consider the Rayleigh-Taylor problem, the initial equilibrium is given to satisfy

$$\frac{\partial}{\partial y}\left(p + \frac{B_z^2}{2}\right) = -\rho g \tag{7}$$

The initial equilibrium is perturbed by a random perturbation so that various unstable modes can grow simultaneously for a wide range of wave numbers. We consider a 2D region $-\pi \le x \le \pi$ and $-3\pi \le y \le 3\pi$. Periodic boundary condition is imposed at $x = \pm\pi$ and the simple outflow condition $\partial/\partial y = 0$ is used at $y = \pm 3\pi$. The initial density profile is given by connecting

the upper density ρ_2 and the lower density ρ_1 linearly:

$$\rho = \begin{cases} \rho_2 & (y \geq d) \\ \rho_1 + \frac{\rho_2 - \rho_1}{2d} & (-d < y < d) \\ \rho_1 & (y \leq d) \end{cases} \quad (8)$$

$$p(y=0) + \frac{B_Z^2(y=0)}{2} = \frac{B_{Z0}^2}{2} \quad (9)$$

A schematic view of the initial equilibrium profiles is shown in Fig. 1.

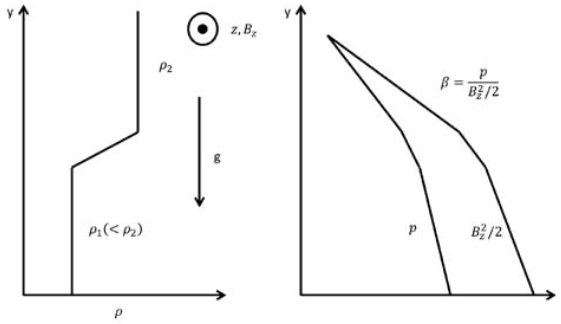

Figure 1: A schematic view of the initial equilibrium profiles used in the simulations.

Some parameters such as the density ratio ρ_2/ρ_1, the jump width of the density Λ = 2d and the β value $\beta = 2p/B_z^2$ control the initial equilibrium. Equations (1)-(4) are solved by the use of the 4th order central finite difference scheme and the 4th order Runge-Kutta-Gill method. To suppress numerical noise, the 4th order hyperviscosity term is added to the system. We have verified that the hyperviscosity influence is sufficiently little in the numerical results shown below.

3. Numerical results

To clarify the gyro-viscous effect to the RT instability, Hall term is ignored in our simulations (ϵ = 0.00). In tab. 1, sets of the parameters in our numerical simulations are shown. The ratio between ion and electron pressure p_i/p_e = 1.0, g = 0.1, B_{z0} = 10.0, β = 10% are assumed in all simulations.

Table 1: Sets of the parameters

	N_x	N_y	β	δ	ρ_2/ρ_1	Λ
Run.1	1024	4096	10%	0.00	2.0	1.0
Run.2	1024	4096	10%	0.07	2.0	1.0
Run.3	1024	4096	10%	0.10	2.0	1.0

3.1 Linear analysis of the RT instability

Firstly, the linear stage of the RT instability is studied. The linear growth rate in a nonlinear simulation is evaluated by fitting an exponential function to the time evolution of the Fourier amplitudes. The power spectrum of the variable A is defined by the integration of the Fourier components in the y direction, $P_A(k_x, t) = \int |\tilde{A}(k_x, y, t)|^2 \, dy$. Here, $\tilde{A}(k_x, y, t)$ is the Fourier transformation of a variable A(x,y,t) in the x direction. Fig. 2 shows the time evolution of the integrated kinetic energy $E(k_x, t) = \frac{1}{2}(P_u(k_x, t) + P_v(k_x, t))$ in Run. 1 (MHD case). Here we plot the integrated kinetic energy only for 1 ≤ k ≤ 10. Growth rates of Fourier modes in Fig. 3 are comparable to each other. Their linear growth is saturated at t ~ 50.0.

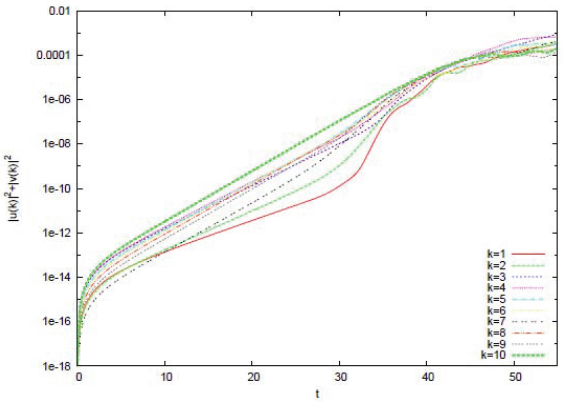

Figure 2: Time evolution of the integrated kinetic energy in MHD case (Run. 1).

Fig. 3 shows the growth rate obtained by runs 1–3. In the MHD case (Run. 1), the growth rate increases as the function of the wave number as it is often expected from the linear stability analysis. It is also found that the wave-number-dependency of the growth rate is small in high wave numbers. We have verified that this behavior is consistent with the linear analysis.

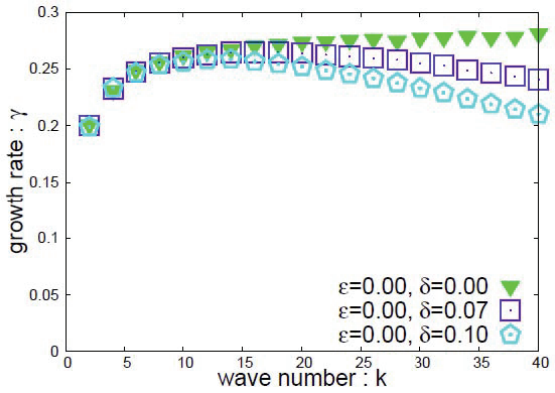

Figure 3: Linear growth rate evaluated by the simulations

In Run. 2 ($\delta = 0.07$), the growth rate at the low wave numbers ($k < 10$) are not affected by the gyro-viscosity very much. However, growth rates of relatively high wave number modes ($k > 10$) show some dependency on the gyro-viscosity. The growth rate becomes maximum at $k = 15$ and start decreasing as the function of the wave number. In Run. 3, a similar behavior as Run 2 is observed. Since a larger gyro-viscous coefficient is used in run. 3, the growth rate of high wave number modes are reduced much larger than those in Run. 2. These tendency suggests that the high wave number modes can be suppressed and only low wave number modes play major roles in the dynamical evolution of the RT instability in the limit of a very large gyro-viscosity.

In Fig. 4, the contour plot of the mass density in the nonlinear stage (at $t = 50.0$) is shown. Fig. 4 (a) is for the single-fluid MHD case (Run. 1) and Fig. 4 (b) is for a finite gyro-viscous coefficient (Run. 3). We can easily see that the growth of the high wave number modes is suppressed and only low modes grow in Fig. 4 (b) while there are fine structures in the contours in Fig. 4(a). Obviously, the change of the growth rates of the RT instability affects to the spatial structures. The most dominant structures associated with the introduction of the gyro-viscosity may play a significant role in a strong nonlinear coupling process in the time evolution.

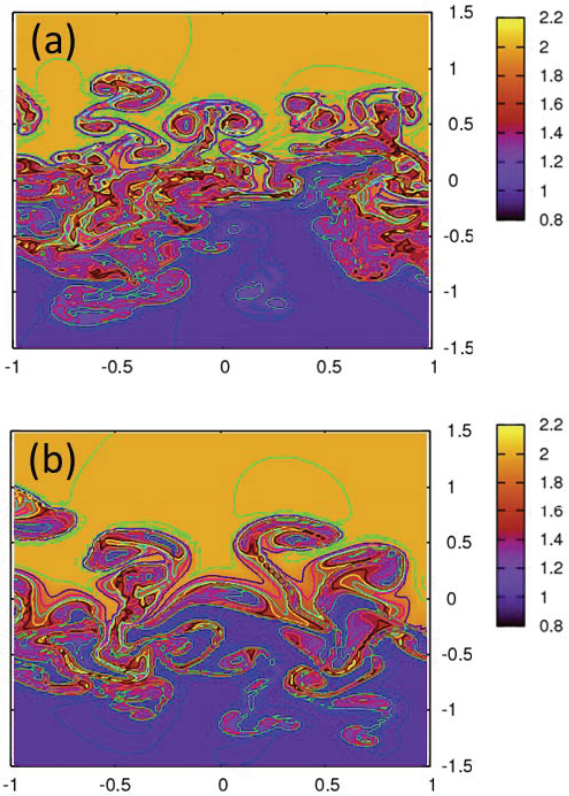

Figure 4: Contour plot of the mass density at $t = 50.0$ (nonlinear stage) in (a) Run. 1 ($\delta = 0.00$) and (b) Run. 3 ($\delta = 0.10$).

4. Summary

The effect of the gyro-viscosity is studied by means of numerical simulations of extended MHD equations. In absence of the gyro-viscosity, the growth rate is larger for a higher wave numbers and its wave number dependence becomes smaller for higher wave numbers. On the other hand, the growth rate is reduced by the introduction of the gyro-viscosity, especially at relatively high wave numbers. Due to the reduction of the growth rate at high wave numbers associated with the introduction of the gyro-viscosity, plasma behaviors from a late stage of the linear growth to the nonlinear stage is governed by the RT modes with moderate wave numbers. The change may play a significant role in the nonlinear saturation process of a pressure-driven instability. Detailed analysis of the nonlinear process is one of our next subjects.

Acknowledgement

This work was partly supported by the JSPS-NRF-NSFC A3 Foresight Program in the field of Plasma Physics (NSFC: No.11261140328) and KAKENHI 23540583.

Reference

[1] A. Komori et al., Fusion Sci. Technol. **58**, 1, (2010).

[2] W. Park et al., Phys. Plasmas **6**, 1796, (1999).

[3] C. R. Sovinec et al., J. Comput. Phys. **195**, 355, (2004).

[4] H. Miura and N. Nakajima, 23rd IAEA-FEC (Oct. 11-16, 2010, Daejeon, Korea) TH/P5-12.

[5] K. V. Robrts and J. B. Taylor, Phys. Rev. Lett. **8**, 197, (1962).

[6] J. D. Huba, Phys. Plasmas **3**, 2523, (1996).

[7] D. Winske, Phys. Plasmas **3**, 11, (1996).

[8] S. I. Braginskii, Transport processes in a plasma, Reviews of plasma physics **1**, 205, (1965).

Deuterium retention under different plasma parameters on EAST with full graphite wall

B. Cao, J.G. Li, J.S. Hu, H.Y. Wang, Y.W. Yu and EAST Vacuum Group

Institute of Plasma Physics, Chinese Academy of Sciences, PO Box 1126, Hefei, Anhui 230031, People's Republic of China

Abstract: In 2010 fall EAST campaign, the deuterium retention is investigated via particle balance method. The influence of plasma parameters for the retention situation is investigated. And the difference of L-mode and H-mode discharges is also investigated.

Keywords: retention, particle balance, L-mode and H-mode

1. Introduction

The tritium retention is a crucial issue for next-step fusion device, such as ITER [1-3], mostly due to safety limitation. In addition, the retained particles would influence the recycling, plasma density control and the neutral density particles in the boundary of plasma, which in turn affects the plasma confinement. Retention is the process of interaction between plasma and first wall. However, there is no systematic study on the corrections between plasma parameters and retention. An investigation of retention on EAST 2010 fall campaign with full graphite wall is used to find out the correction between plasma parameters and retention.

There are 3 main fuel retention mechanisms in tokamaks: absorption, implantation and co-deposition [3]. Normally the absorbed particles will release after the discharges. The implantation depth is limited by incident SOL plasma temperature and the first wall material and temperature. Both of them can reach saturation. But there is no saturation for co-deposition.

Table 1 Pumping speed of EAST pumping system

Pumping system	Kind of pumps	Pumping speed (m^3/s)	Number	Total pumping speed (m^3/s)
Main pumping system	Turbo molecular pumps 1#	3.13	3	48.85
	Turbo molecular pumps 2#	1.74	1	
	Cryo-pumps	9.43	4	
Up divertor pumping system	Cryo-pumps	5.29	2	10.58
Low divertor pumping system	Cryo-pumps	5.29	4	21.16

2. Gas balance

Gas balance used the difference between the puffed particles and the pumped particles to calculate the retained particles in the wall. Normally we used equation as below:

$$Q_{retention} = Q_{puff} - Q_{pump} - Q_{plasma} - Q_{vessel} \quad (1)$$

In equation (1), the $Q_{retention}$ is the retained particles in the wall. The Q_{puff} is the inject particles by gas puff, it can be calculated by $\Delta P_{tank} \times V_{tank}$, where the ΔP_{tank} is the pressure difference of the puffing tank between before and after discharge, and the V_{tank} is the volume of this puffing tank. The Q_{pump} is the particles pumped by the pumping system, it can obtained from the pressure at the pumping system port by equation as $\int P_{pump} \times Sdt$, here the P_{pump} is the pressure at the pumping system and the S is the pumping speed for this pumping system which was listed in Table 1. And the total integral time in this paper is about pulse duration with an additional 160s after discharge. Q_{plasma} is the particles in plasma and it can be calculated by $\frac{\langle n_e \rangle V_{plasma}}{2}$, here $\langle n_e \rangle$ is the averaged electron density of plasma and the V_{plasma} is the volume of plasma. Q_{vessel} is the neutral particles in this vessel and it can be calculated by $P_{vessel} \cdot (V_{vessel} - V_{plasma})$, here the P_{vessel} is the pressure of vacuum vessel and V_{vessel} is the volume of vacuum vessel . Flowing this discuss, $Q_{retention}$ can be obtained as below:

$$Q_{retention} = \Delta P_{tank} \times V_{tank} - \int P_{pump} \times Sdt - \frac{\langle n_e \rangle V_{plasma}}{2} - P_{vessel} \cdot (V_{vessel} - V_{plasma}) \quad (2)$$

Equation (2) can give the retention inventory at any time during a pulse or between pulses. Thus, the retention fraction f_{fre} is defined as $f_{fre} = \frac{Q_{retention}}{\Delta P_{tank} \times V_{tank}}$. We calculated the derivation of both sides of equation (2) to get the retention rate, shown as below:

$$q_{retention} = V_{tank} \frac{dP_{tank}}{dt} - P_{pump} \times S - \frac{d\langle n_e \rangle V_{plasma}}{2dt} - \frac{dP_{vessel} \cdot (V_{vessel} - V_{plasma})}{dt} \quad (3)$$

Here the $q_{retention}$ is the retention. Normally during discharge, the change of $\langle n_e \rangle$ is small, and the compared with the others the neutral particles in the vessel is very small. So we can ignore them, and equation (3) can be written as:

$$q_{retention} = V_{tank} \frac{dP_{tank}}{dt} - P_{pump} \times S \quad (4)$$

3. Experiment Setup

EAST is a non-circular advanced steady-state experimental device and the first entirely superconducting tokamak in the world. The major radius is 1.75 m and the minor radius is 0.4 m. For divertor operation, an elongation of 1.2–2 and with single null or double null will be used [4]. In EAST the divertors are used graphite with SiC coating as the facing plasma components (PFCs), and the first wall is also used carbon as the material. The volume of plasma vacuum vessel is about 40 m^3 and the plasma facing surface is about 60 m^2.The material of first wall on EAST is graphite with SiC coating.

The pumping system of EAST is organized with three subsystems: main pumping system, up and low

divertor pumping systems [5]. The main pumping system is a pumping duct with 0.8 m of diameter and 6 m in length, connecting with one horizontal port of plasma vacuum vessel including 4 sets of turbo molecular pumps (TMP) and 4 sets of cryo-pumps. The total effective pumping speed is about 48.85 m^3/s. The detail of the pumping speed is listed on Table 1. The two cryo-pumps were installed at the bottom ports and four were installed at the top ports, connecting with the divertor region through tubes (2.5 m in length and cross-section area of 0.07 m^2). The pumping speed is list on the Table 1, too.

We used five gauges to measure the pressure of the vacuum chamber and the pumping tubes and used these data to calculate the total pumped particles and the particles in vacuum chamber. All the locations of the five gauges are shown on figure 1. Gauge G1.5 was installed at D window and mid-plane to measure the pressure of vacuum chamber. Gauge G1.6 was installed at the ports of up divertor pumping tube, and G1.9 was installed at the ports of low divertor pumping tube. The two gauges were used to measure the up and low divertor pumping systems. There are two gauge (G1.7 and G1.1), which are respectively installed at the head and back of the main pumping tube, to measure the pressure of the main pumping tube. There are two mass spectrometers at the same locations to measure the components of the pumping gas.

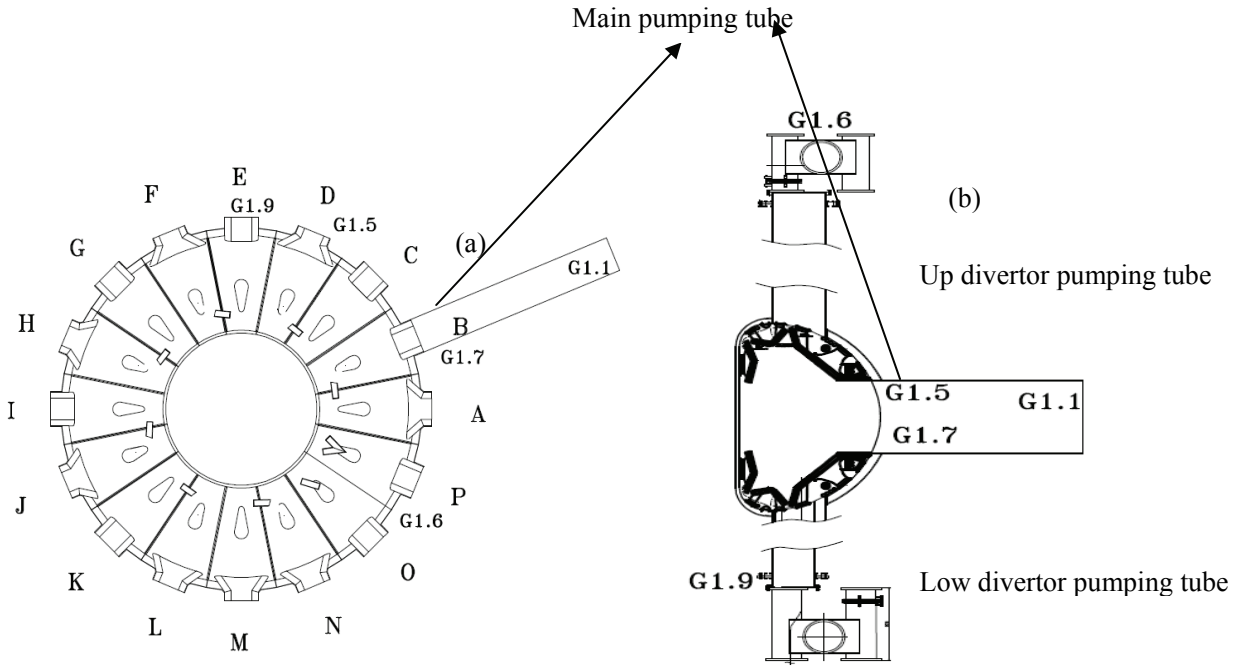

Fig. 1 Top view (a) and horizontal view (b) of EAST

4. Experiment results

4.1 Effect of plasma current on retention

Plasma current is a main parameter for plasma confinement [6]. In figure 2 we show the relation between plasma current and retention, (a) for retention rate and (b) for retention fraction. All shots in this

figure are non-disruptive shots. From this figure, the retention rate is not related to plasma current, but the retention fractions have a bigger range in low plasma current than in high plasma current.

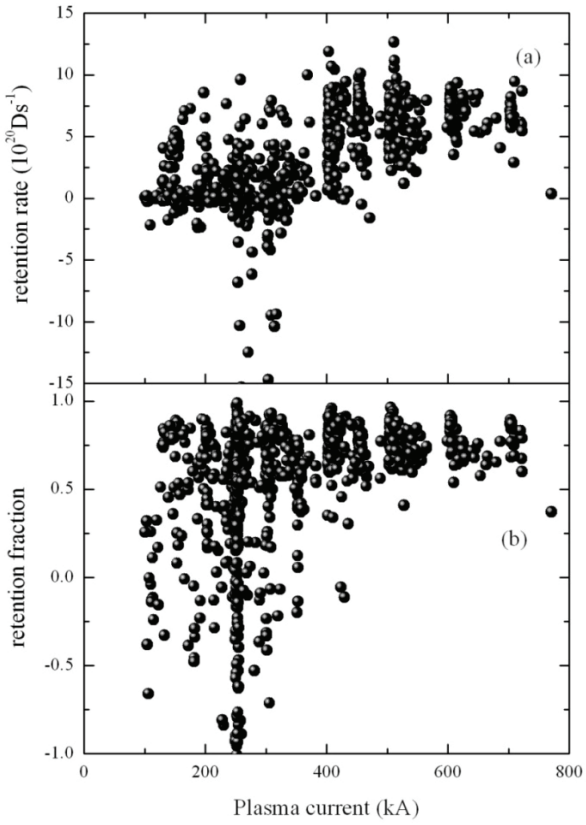

Fig. 2 Effect of plasma current on retention

4.2 Effect of plasma density on retention

Figure 3 shows the relation between plasma electron averaged density and retention, (a) for retention rate and (b) for retention fraction. All shots in this figure are non-disruptive shots. It looks like there is no connecting between retention rate and electron averaged density.

4.3 Influence of injected LHCD power on retention

In EAST analysis of the retention during discharges heated with lower hybrid current drive (LHCD) still indicated a strong dependence of the retention rate on the LHCD power as shown in figure 4. A possible explanation could be the change of SOL introduced by LHCD. The same phenomenon was found on Tore Supra [7].

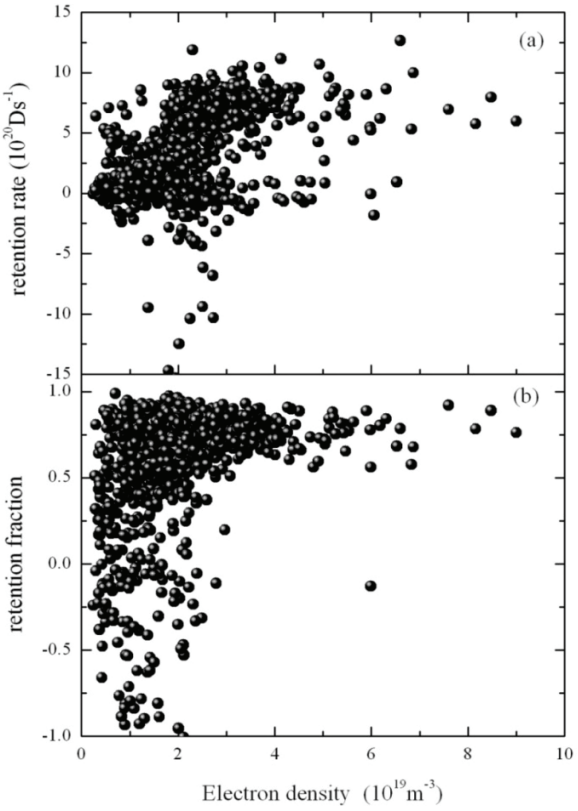

Fig. 3 Effect of plasma density on retention

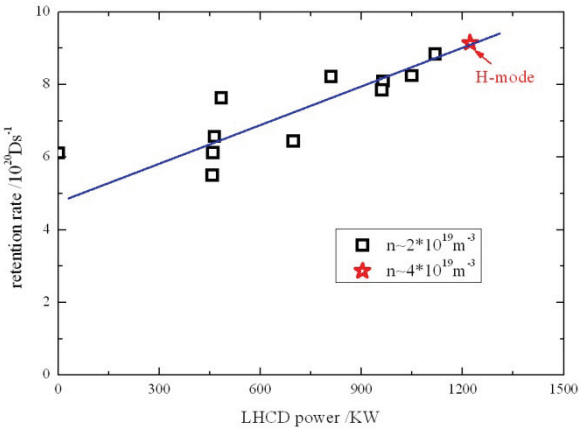

Fig. 4 Influence of LHCD power

4.4 Retention for long and short discharges

The difference of retention for long and short discharges is shown in figure 5. In this figure, all these shots have the similar plasma current (250 ~ 300 kA) and electron density (1.5 ~ 2×10^{19} m^{-3}), and all the shots are non-disruptive shots. The pulse length for long discharges is about 8s, and for short discharges is about 60~100s.

From this figure, long pulses have a bigger averaged retention rate than short pulses. And long pulses have much larger averaged retention fraction than short pulses.

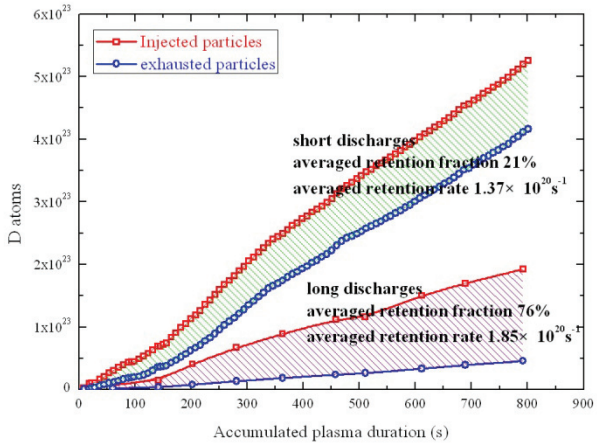

Fig. 5 Retention for long and short discharges

4.5 Retention for L-mode and H-mode discharges

The high-confinement mode (H-mode) with type-III edge localized modes (ELMs) has been obtained on 2010 EAST fall experiments campaign. The H-mode is the projected baseline operational scenario for the International Tokamak Experimental Reactor (ITER) [9]. We tried to find out is there different between H-mode and L-mode discharges in retention. Figure 6 shows the retained particles versus injected particles for 123 H-mode shots and 320 L-mode shots.

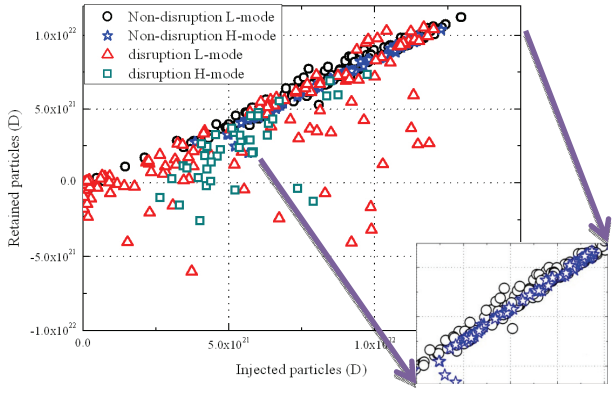

Fig. 6 Retention for L-mode and H-mode discharges

As shown in this figure, H-mode discharges have slightly smaller retention than L-mode discharges. Since the disruption would lead to a lot of outgassing from wall, the disruptive shots have lower retention than normal shots.

4.6 Influence of different shape configuration

Figure 7 shows the difference of retention under limiter and divertor configuration. As shown in this figure, retained particles under divertor configuration are much more than under limiter configuration. Inner vessel cryo-pump is on during all the shots, but under limiter configuration the inner vessel cryo-pump is useless. So divertor configuration need more injected particles than limiter configuration.

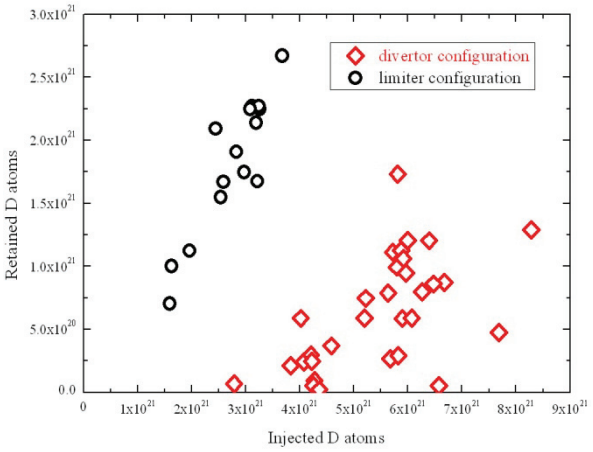

Fig. 7 Influence of different shape configurations

5. Summary

The results show no effect of plasma current or density on fuel retention. LHCD is an important auxiliary heating method on EAST. The retention would increase with increase of injected LHCD power. The averaged retention rate and fraction is higher in long pulses than short pulses. In this campaign, EAST achieved the first H-mode discharges after a lot of

lithium coating. By comparing the retention of H-mode shots and L-mode shots, H-mode discharges have slightly lower retention than L-mode. The disruptions lead to more outgassing from wall. And retained particles under divertor configuration are much more than under limiter configuration.

Acknowledgments

This research was funded by National Magnetic confinement Fusion Science Program under Contract No.2013GB114004, and National Nature Science Foundation of China under Contract No.11075185 and No.11021565.

References

[1] G. Federici et al., *Nucl. Fusion*, 41 (2001) 1197-2137

[2] J. Roth et al., *Plasma Phys. Control*. Fusion 50 (2008) 103001

[3] T. Loarer et al., *J. Nucl. Mater.* 390-391, (2009) 20-28

[4] J. S. Hu et al, *Fusion Eng. Des.*, 84 (2009) 2167-2173

[5] J. H. Li et al, *Vacuum*, 47 (2010)

[6] ITER Physics Basis, *Nucl. Fusion,* 39 (1999) 1295

[7] J. Bucalossi et al., *32nd EPS Conf. on Plasma Physics (Taragona, 27 June-1 July 2005)*, 29C (ECA) O-4.005

[8] C. Gormezano et al., 2007 Progress in the ITER Physics Basis Chapter 6: Steady State Operation, *Nucl. Fusio*n, 47, S285

[9] C. H. Skinner et al., J. Nucl. Master., 266-269 (1999) 940-946

A Fast-Response Extreme Ultraviolet Spectrometer for Measurement of Impurity Line Emissions in EAST

Ling ZHANG[1], Shigeru MORITA[2], Zhenwei WU[1], Liqun HU[1], Chunfeng DONG[2], Baonian WAN[1], and Jiangang LI[1]

[1] Institute of Plasma Physics, Chinese Academy of Sciences, Hefei 230031, China

[2] National Institute for Fusion Science, Toki 509-5292, Gifu, Japan

Abstract: In the next EAST campaign, the auxiliary heating power increases up to 24MW in total, including lower hybrid heating of 10MW, electron cyclotron resonance heating of 2MW, ion cyclotron range of frequency heating of 8MW and neutral beam heating of 4MW. Various materials are planned to use for plasma facing components in EAST, e.g., molybdenum for main vacuum chamber, W/Cu monoblocks for upper divertor and SiC-coated graphite tiles for lower divertor. The high heat load on divertor plates enhances the impurity production through physical and chemical sputterings during the steady state operation. The lithium coating is also scheduled for wall conditioning to suppress the hydrogen and deuterium recycling. Therefore, the impurity diagnostics are very important to improve the plasma performance of EAST discharges in the next experimental campaign. In particular, the measurement of intrinsically existing high-Z impurities of Mo and W is crucially important in addition to light impurities of Li, C and O because radiation loss from such high-Z impurities is really big. For the purpose an extreme ultraviolet (EUV) spectrometer working in 50-500Å wavelength range has been newly developed in EAST to measure line emissions from such impurities. A flat-field focal plane for spectral image detection is made by a laminar-type varied line spacing concave holographic grating with an angle of incidence of 87°. A back-illuminated charge-coupled device (CCD: Andor DO920P-BN) with 1024 x 255 pixels is used for measuring the focal image of spectral lines. The high readout rate and the pixel binning of the CCD can improve the temporal resolution of time-resolved spectrum, at least a few milliseconds per frame. It makes possible a variety of studies, e.g., impurity behavior during edge-localized mode (ELM) activity and ELM mitigation in long pulse discharges. In the seminar the progress on the EUV spectrometer newly developed for the impurity diagnostics in EAST is presented.

1. Introduction

The passive spectroscopy in vacuum ultraviolet (VUV:500-2000Å) and extreme ultraviolet (EUV/XUV: 10-500Å) wavelength range are conventionally used on the magnetic confinement fusion (MCF) devices to study the physics of impurity transport and provide the information on impurity levels to assist the experimental operations. VUV and EUV spectrometers

are the primary tools to observe the impurities line emission, which consist of three optical elements:entrance slit, diffraction grating and the detector.

Over the past 2-3 decades, significant progress has been achieved in the instrument benefiting from the development of both grating and detector technology. For spectroscopic instruments with the wavelengths below 200-300 Å, a grazing incidence mount is used to increase the reflectance of the grating surface. The typical EUV spectrometer constructed in the 1980s based on entrance slit and a spherical concave grating positioned on the same Rowland circle, and the grating diffracting and focusing the light to the microchannel plate (MCP) which was mounted tangential to the Rowland circle [1-4]. However the concave grating causes curved image and strong astigmatism perpendicular to the plane of the circle, which does not allow to mount the multichannel flat detector to do the simultaneous spatially resolved measurements of the plasma. The mechanically ruled aberration-corrected concave [5,6] or aberration-corrected toriodal holographic gratings [7-10] were used to construct the flat focal field spectrometers in the following 10-20 years. Before 2000, the typical detector unit was very complicated. The head of the detector was composed of a flat rectangle MCP, which was coupled to a phosphor screen image intensifier. The EUV photons produce the photoelectrons at the MCP surface then those photoelectrons are multiplied inside the microchannel. The exiting electrons are then accelerated and focused onto the phospher screen which converts the electron signal to visible photons. The visible photons are optically coupled and transferred to a photodiode array (PDA) [1,3,4,7-9] or a charge-coupled device (CCD) [2,6,10] by fiber optic bundle. Recently, the laminar-type concave holographic gratings with varied line spacing (VLS) grooves were widely used [11,12-18] to construct the flat focal field EUV spectrometer. And at the meanwhile the development of the manufacture of high energy CCD camera make the spectrometer system more compact and easier control, and most important to take the spectral-, time- ande space- resolved measurement simultaneously. For instance, the 1D [15,17,18] and 2D [16] space-resolved EUV spectrometer have been developed in LHD, HL-2A and EAST succesively. The newly developed EUV spectrometer in EAST tokamak described in this paper has the same optical design as in LHD [13,15].

This paper is organized as follows, the detailed setup of the EUV spectrometer is described in Sec. II, the emission lines which may be detected by the EUV spectrometer is overviewed in the Sec. III, the available method applied to the absolute calibration is introduced in the Sec. IV, and finally the main research topics is summarized in Sec. V.

2. Details of the EUV spectrometer

This spectrometer will view EAST plasma center from a rectangle flange on the D port. Fig. 1 shows the EAST poloidal cross section and the viewing range

from the spectrometer. As shown in Fig. 2, a cuboid extension tube with the length of 2m and inclination of 8° extends from the port flange. Another end of the extension tube is assembled with a CF63 (ICF114) flange and then a CF63 high vacuum manual control gate valve which separates the vacuum of spectrometer from the EAST device. The pump unit is employed to keep the vacuum of the spectrometer which is connected to a CF63 flange at the right side on the spectrometer. There are supports for the extension tube and the spectrometer.

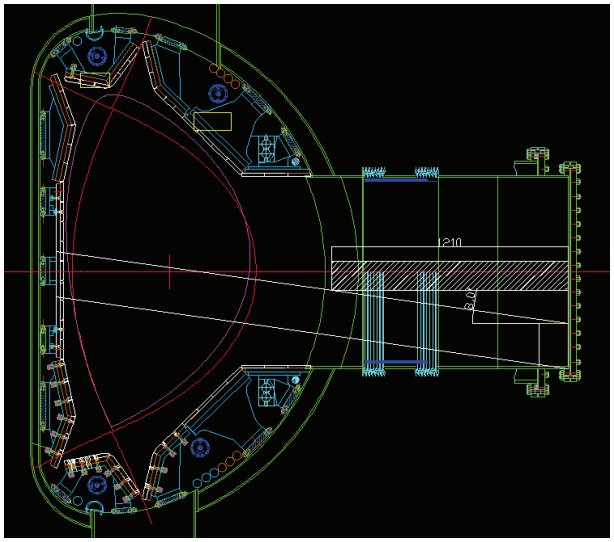

Fig. 1 EAST cross section and viewing range from EUV spectrometer

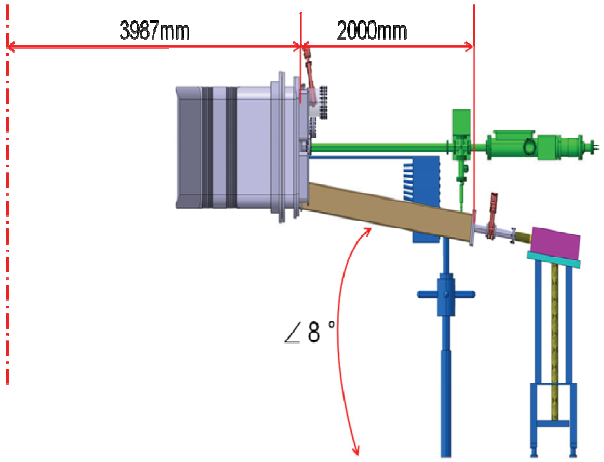

Fig. 2 Initial mechanical design

The pump unit consist of a dry scroll pump (Varian now Agilent TriScroll 300) as the primary pump with the pumping speed of 250L/min, a turbo molecular pump (Agilent Turbo-V301) with the maximum pumping speed of 280L/s and the ultimate vacuum of 5×10^{-7}Pa, and a full range gauge. A height adjustable mobile system as shown in Fig. 3 makes the pump unit compact and portable.

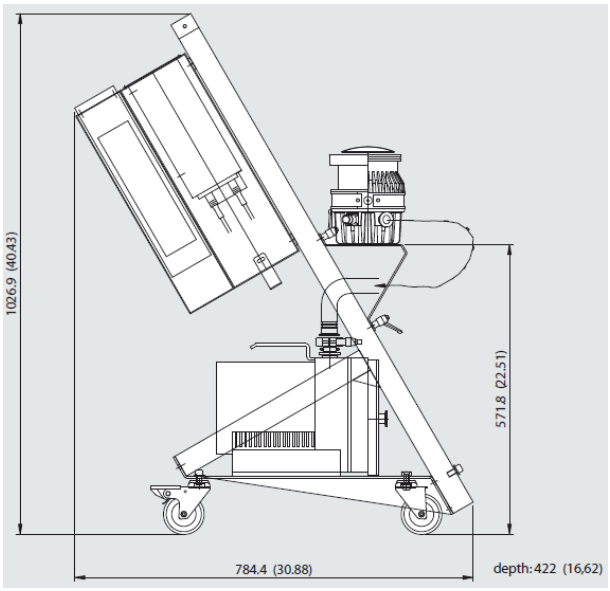

Fig. 3 The mobile turbo-pump system for the EUV spectrometer

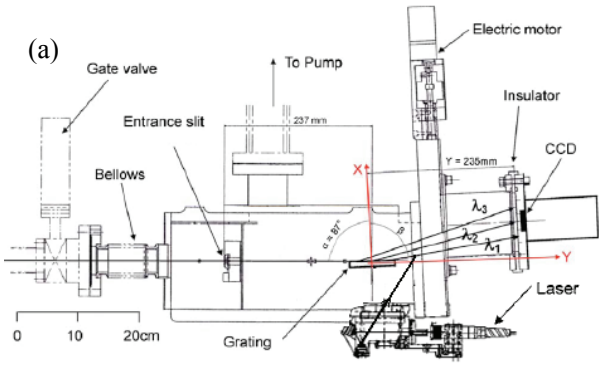

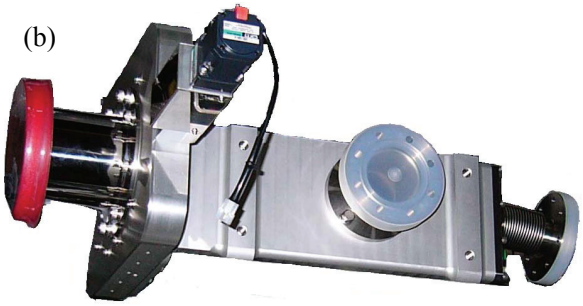

Fig. 4 The spectrometer system (a)Mechanical and optical design [13,15] (b) Picture

The Fig. 4 shows the detailed mechanical and optical design, and appearance of the spectrometer system. The Fig. 5 illustrates the schematic diagram of the optical design. The entrance slits with width of 30 and 100 μm are available. The 1200 grooves/mm (at grating center) laminar-type VLS concave grating (Shimadzu 30-002, as shown in Fig. 6) covers a wavelength range of 50–500 Å at an angle of incidence of α =87°, which is used to make a flat-field focal plane for spectral image detection. A laser light is attached for the spatial calibration.

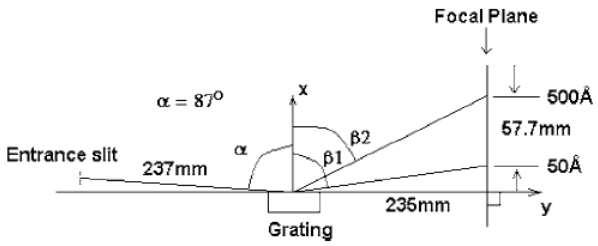

Fig. 5 The schematic diagram of optical design [13]

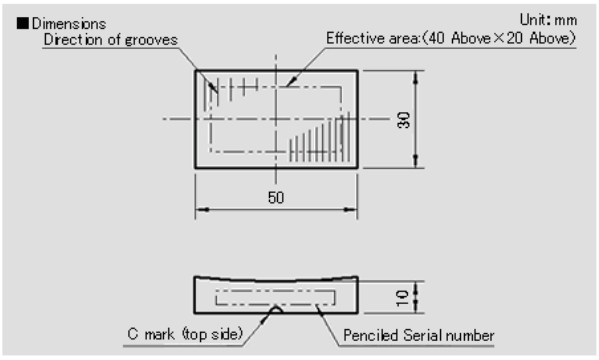

Fig. 6 A laminar-type VLS concave holographic grating

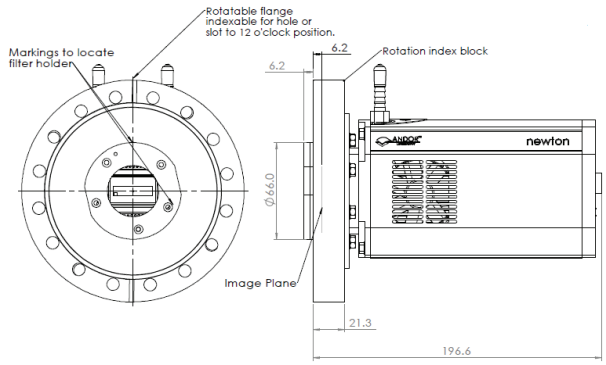

Fig. 7 Mechanical design of the flange at the front of CCD

A back-illuminated charge-coupled device (CCD: Andor DO920P-BN) with 1024 × 255 pixels is used for measuring the focal image of spectral lines. The full image area is 26.7 × 6.7mm with the pix size of 26μm. Without spatial resolution at the initial design phase, the CCD could binning all the pixels in 6.7mm side. With the high readout rate up to 3MHz and the pixel binning, the CCD can improve the temporal resolution of time-resolved spectrum, at least a few miliseconds per frame. Fig. 7 illustrates the mechanical design of the flange at the front of CCD.

3. Emission Lines

Sputtering from plasma facing components and

antenna of auxiliary heating system, the plasma surface conditioning and gas puffing for diagnostics and radiation cooling in the divertor combine to provide the abundant emission lines from low-Z to high-Z charge states.

In the next EAST campaign, various materials are planned to use for plasma facing components in EAST, e.g., molybdenum for main vacuum chamber, W/Cu monoblocks for upper divertor and SiC-coated graphite tiles for lower divertor. The auxiliary heating power increases up to 24MW in total, including lower hybrid heating of 10MW, electron cyclotron resonance heating of 2MW, ion cyclotron range of frequency heating of 8MW and neutral beam heating of 4MW. For ICRF antenna, the components nearest to the plasma are current strap, faraday shield and baffle. The strap is made of copper-plated SS316L, faraday shield is made of SS316L itself and with Cu based and B_4C coated tubes, and baffle is composed of graphite tiles [19].The boronization, siliconization and lithium coating are the available wall conditioning, which use $C_2B_{10}H_{12}$, SiH_4/He or SiD_4/He and pure Li as working materials respectively [20].

Thus, the species which are/will be shown in EAST plasma include H, D, He, Li, B, C, O, Si, Cr, Mn, Fe, Ni, Cu, Mo, W. Diagnostic such as x-ray crystal spectrometer and divertor radiation cooling may employ the gases puffing in the edge, e.g. Ne, Ar. The measurement results from pulse height analysis system shows there is Ti Kα peak sometimes. The emission lines in the range 50-500Å from the different charge states of those species and corresponding energy level and transition coefficients could be searched in the online NIST Atomic Spectra Database [21]. The emission lines shown in some MCF devices in the VUV and EUV range are overviewed in table 1.

Table 1. Emission lines from MCF devices in VUV and EUV range

Impurities	Wavelength range (Å)	Device	Ref.
H I, He I II, C III, O IV V VI, Fe XV XVI, Ti XI XII XIV XIX XX	100-1100 155-1700	PDX	[7]
O V VI VII VIII,Ti XIX, Se XXII XXIII XXIV	15-360	PLT	[1]
CXR excited C VI, O IV V VI VIII	100-320 100-1100	TFTR SPRED PBX	[8]
C IV V, O VI VII VIII, Al XII XIII, Ti XIV XV XVI XVII XVIII, Cr XXI, Fe XVII XVIII XX XXII XXIII,	5-340 5-85	PLT TFTR	[3]

Ni XI XXV, Zr XXVIII XXIX XXX, Mo			
C VI V, O VII VIII, Ti XVIII XIX XX, Mo XXXI XXXII	5-50, 5-500, 20-200, 50-1220	JT-60	[9]
C II III IV, O II III IV V VI	150-1050	GAMMA10	[6]
Mo XXXI XXXII, Sc, Ar	50-1000	Alctor C-mod	[4]
C, B, O, Fe, Cr, Ni, Cu, W, F, Al, Si, Zr, Mo, Wo, Ta	25-105, 90-240, 200-660, 600-1600	W7-X	[10]
He II, C IV V, Ar XV XVI, Fe XIV XV	50-500	LHD	[13]
K-shell emission of O, N, C, B, O VII VIII, N VI VIII, C VI, Ti XIII, Fe XVIII XIX XXI, Mo XXV XXVI,	10-65	NSTX	[12]
C VI V, N VI VII, O VIII, Ne IX X, Ti X-XX (15-27 Å), Fe XVII-XXIV(10-17 Å)	10-130	LHD	[14]
H-, He-like B,C,O, H-like Li, Ne IX X, Ar IX-XV, Ti XIII, Ni X-XIII, Fe VIII-XIII XVII XVIII XX, Mo XXV	5-135 60-400	XEUS LoWEUS in NSTX	[22]
He II, C IV V	60-400	LHD	[15]
H-, He- like B N, Ar XIV-XVI, F VIII IX, Ca XVI-XVIII, Mo XXXI XXXII, W 40-60Å	80-1050 10-70	Alcator C-Mod	[11]
He I, C II-V, N IV V, O V-VII, F VI VII, Ne VII IX, Si XI XII, Ar VII-XVI, Ti XI XII, Cr XIV, Fe XVI, C V VI, O II, O VIII	300-3200 50-500	HL-2A	[26]
C IV VI, O VI V, Fe VII VIII X, Cr VI VII XIV, Ni XV XVI XVIII	50-500	EAST	[18]

4. Absolute calibration

The primary absolute calibration for EUV spectrometers were using synchrotron radiation [1,8,9,6,23] and other calibration sources [10] in their wavelength range. The later developed EUV spectrometer could simply calibated by comparing some emission lines which are simultaneously recorded by other absolutely calibrated spectrometers in the same device [7,3,14]. An in-situ absolute calibration technique using branch ratio to an absolutely calibrated visible spectrometer

was applied to several EUV and VUV spetrometers [4,13,24]. However, this technique requires the same viewing chords between the EUV/VUV and visible spectrometer, and the absent doublet make the calibration hardly covering the full wavelength working range of EUV/VUV spectrometer.

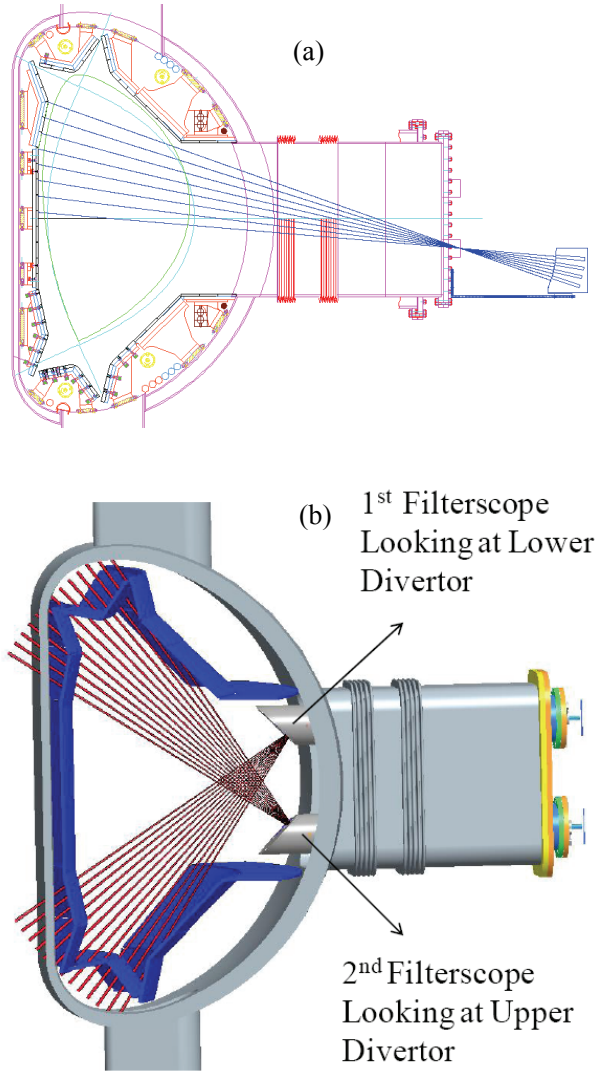

Fig. 8 The viewing chords of (a) VB PMT array (b) Filterscope

Recently, another in-situ technique using EUV bremsstrahlung continuum profile in comparison with absolute values of visible bremsstrahlung (VB) continuum profile is more and more popular [13,15,25,26]. There are three steps applying this technique. Firstly, the VB continuum is measured using an absolutely calibrated spectrometer or photomultiplier tube (PMT) array. Normally, the EUV and visible measurement don't share the same viewing chords, then secondly, the Zeff profile is essential by doing the Abel reversion to the measurement combining the EFIT equilibrium reconstruction, Te and ne profile. Finally, the relative calibration could be determined by comparing the calculated bremsstrahlung emission in EUV range varying with ne and the measurement results from EUV spectrometer at several wavelengths.

In EAST, there will be three visible spectroscopy system available to assist the absolute calibration of the EUV spectrometer, e. g. the conventional PMT array with the optical filter at the undisturbed wavelength of 523±2 nm and with the viewing chords covering the upper half cross section of EAST as shown in Fig. 8(a), the newly installed Filterscope system with the viewing chords covering the upper and lower divertor as shown in Fig. 8(b), a UV/visible spectrometer sharing the same viewing chords with Filterscopy system. All the three systems could be absolutely calibrated by the integral sphere standard source (Labsphere USS-600C).

5. Research topics

As we know, studies of impurity behavior from the measurement of impurity line emission in tokamak plasmas are of fundamental interest because of the increased radiated power and ion dilution. The EUV

spectrometer is an efficient tool to determine the distribution of mid- and high- Z impurities and their contribution to the average Zeff and plasma density, to monitor the impurity release from the screen of RF antenna, to check the impurity screen effect of divertor during the gas of Ar, Ne is puffed locally in divertor to make the plasma in divertor detachment, to assist to determine the impurity transport coefficient in simulation.

Particularly, this newly developed fast-response EUV spectrometer in EAST will be additionally applied to study the high-z intrinsic impurity (Mo and W) transport in the edge plasma in the near future, especially the impurity behavior during ELM activity and ELM mitigation in long pulse discharges. However, for the high-z impurity study such as Mo and W, the great effort still needs to make on their emission lines determination, ion distribution calculation from C-R model etc. The powerful simulation is also essential. Recently the OEDGE code package coupling the OSM, Eirene and DIVIMP code is applying to EAST, which could be combined to do the transport simulation of background plasma, background neutral particle and impurity in the edge region successively.

Acknowledgements

This work was partly supported by the JSPS-NRF-NSFC A3 Foresight Program in the field of Plasma Physics (NSFC No.11261140328)

References

[1] W. L. Hodge, B. C. Stratton, and H. W. Moos, Rev. Sci. Instrum. **55**, 16 (1984)

[2] D.Content, D.Wroblewski, M.Perry, and H.W.Moos, Rev.Sci.Instrum. 57, 2041(1986)

[3] J. L. Schwob, A. W. Wouters, S. Suckewer, and M. Finkenthal, Rev. Sci. Instrum. **58**, 1601 (1987).

[4] M. A. Graf, J. E. Rice, J. L. Terry, E. S. Marmar, J. A. Goetz, G. M. McCracken, F. Bombarda, and M. J. May, Rev. Sci. Instrum. **66**, 636(1995)

[5] T. Kita, T. Harada, N. Nakano, and H. Kuroda, Appl. Opt. 22, 512(1983).

[6] Naohiro Yamaguchi, Jungo Katoh, Yukiko Sato, Tatsuya Aota, Atsusi Mase, and Teruo Tamano, Rev. Sci. Instrum. **65**, 3408 (1994)

[7] R.J. Fonck, A.T. Ramsey and R.V. Yelle, Appl. Opt. 21 (1982) 2115

[8] B. C. Stratton, R. J. Fonck, K. Ida, K. P. Jaehnig, and A. T. Ramsey, Rev. Sci. Instrum. **57**,2043(1986).

[9] H. Kubo, T. Sugie, A. Sakasai, N. Nishino, H. Yokomizo, H. Takeuchi, ST-60 Team, K. Tanaka, H. Maezawa, and N. Yamaguchi, Rev. Sci. Instrum.59, 1515 (1988).

[10] W. Biel, G. Bertschinger, R. Burhenn, R. König, and E. Jourdain, Rev. Sci. Instrum. **75**, 3268 (2004)

[11] M. L. Reinke, P. Beiersdorfer, N. T. Howard, E. W. Magee, Y. Podpaly, J. E. Rice, and J. L. Terry, Rev. Sci. Instrum. 81, 10D736 (2010)

[12] P. Beiersdorfer, J. K. Lepson, M. Bitter, K. W. Hill, and L. Roquemore, Rev. Sci. Instrum. 79, 10E318 (2008)

[13] M. B. Chowdhuri, S. Morita, M. Goto, H.

Nishimura, K. Nagai, and S. Fujioka, Rev. Sci. Instrum. 78,023501(2007).

[14] M. B. Chowdhuri, S. Morita, and M. Goto, Appl. Opt. 47, 135 (2008).

[15] C.Dong, S. Morita, M. Goto, H. Zhou, Rev. Sci. Instrum. **81**, 033107(2010)

[16] E. Wang, S. Morita, M. Goto, C. Dong, Rev. Sci. Instrum. **83**, 043503(2012)

[17] CUI Zhengying, ZHOU Hangyu, S. MORITA,FU Bingzhong, XU Yuan, DONG Chunfeng, YANG Qingwei. Plasma Sci. Technol., 2013, 15(2): 110-114.

[18] Y.Shen, X.Du, W.Zhang, et al., Nuclear Instruments and Methods in Physics Research A 700(2013) 86-90

[19] Q. X. Yang, Y. T. Song, S.T.Wu, et al., Fusion Engineering and Design 87(2012)1249-1252

[20] G Z Zuo, J S Hu, S Zhen, et al., Plasma Phys.Control. Fusion 54(2012)015014

[21] http://physics.nist.gov/PhysRefData/ASD/lines_form.html

[22] J. K. Lepson, P. Beiersdorfer, J. Clementson, M. F. Gu, M. Bitter, L. Roquemore, R. Kaita, P. G. Cox, and A. S. Safronova, At. Mol. Opt. Phys. 43(2010)144018

[23] R.D.Wood and S.L.Allen, Rev. Sci. Instrum. **59**, 1537(1988)

[24] K. D. Lawson, I. H. Coffey, J. Zacks, M. F. Stamp and JET-EFDA contributors, 2009 JINST 4 P04013

[26] Z. Cui, S. Morita, B. Fu, Y. Huang, P. Sun, et al., Rev. Sci. Instrum. **81**, 043503 (2010)

[25] C.Dong, S. Morita, M. Goto, and E. Wang, Rev. Sci. Instrum. **82**, 113102(2011)

Trapped electron hole equilibria for Alfven wave

Minhao WOO[1], ChengRim Choi[2], and ChangMo Ryu[3]

[1] National Fusion Research Institute, Daejeon 305-333, Korea

[2] Department of Physics, Korean Advanced Institude of Science and Technology, Deajeon 305-701, South Korea

[3] Department of Physics, Pohang University of Science and Technology, Pohang 790-784, South Korea

Abstract: New Alfven wave structure with trapped electrons are found. It is found that Alfven wave can also have BGK-like structure with trapped electrons due to the transverse electric field.

1. INTRODUCTION

Large amplitude Alfvenic structure found in space plasma plays important rule in plasma heating and electron acceleration. Especially heating of the solar corona is closely related to Alfvenic turbulence. As noted by Wu, et al. that for intrinsic Alfven waves with broad spectrum changing slowly in time can heat plasma in perpendicular direction through random scattering of such Alfven wave by non-resonant wave particle interaction [1, 2]. Another candidate is through the stochastic particle motion in large amplitude Alfven wave [3, 4].

Guo et al. has found that heating can be archived directly through linear or nonlinear cyclotron resonance of Alfven wave [5]. In solar wind plasma, Mevdev et al. has found dissipative quasi-stationary structure when plasma beta is ~1 [6]. For such case, large amplitude Alfven wave nonlinearly drives ion acoustic wave and then ion acoustic wave damps through linear/nonlinear landau damping [7–9]. Lastly by Hasegawa and Chen, it has been found that plasma heating can be archieved by mode conversion of Alfven wave through resonant surface in inhomogeneous plasma [10, 11].

In this paper, we will present new large amplitude solitary Alfven wave with effect of the trapped electrons. In other words, solitary type BGK structure for the case of the Alfven wave. It is important to understand analytical structure of Alfvenic BGK because stability of the wave with trapped particle can drastically change dissipation mechanism of the large amplitude Alfven wave. Heating of the plasma and acceleration of the electrons due to the Alfven wave can be explained in the context of BGK equilibrium. Especially for the wave perturbation that has similar scale compared to the Alfvenic BGK mode, Lewis and et al. has developed eigenvalue analysis method for the inhomogeneous plasma equilibrium that is directly applicable to our case [12, 13]. From this view point, our paper can provide another starting point to understand

damping of the large amplitude Alfvenic structure.

2. BASIC EQUATIONS

As noted by [15], in low beta plasma with $\beta << Q$ where $Q = m_e/m_i$ and the wave is propagating obliquely in x−z plane and external magnetic field is in z direction. Then equation satisfied by density is given as

$$\frac{d^2}{d\xi^2}\frac{1}{n^2} = \frac{2l_z^2}{Ql_x^2M^2}(n-1)(\frac{1}{n} - \frac{M^2}{l_z^2}) \quad (1)$$

Here l_x, l_z is directional cosine and M is wave phase velocity and $\xi = l_x x + l_z x - Mt$. Now we will slightly modify this equation with full electron dynamics along the magnetic field. As we are assuming strongly magnetized plasma, it is consistent to neglect electron gyro-radius and up to zeroth order, electron vlasov equation is given as

$$\frac{\partial f}{\partial t} + v_z\frac{\partial f}{\partial z} + \frac{1}{Q}\frac{\partial \psi}{\partial z}\frac{\partial f}{\partial v_z} = 0 \quad (2)$$

Here ψ and ϕ is two potential for the transverse electric field. Instead of normal BGK mode derivation, we use Ampere's law and Far aday's law to close equation.

$$\frac{\partial^4}{\partial x^2 \partial z^2}(\phi - \psi) = \frac{\partial^2 J_z}{\partial z \partial t} \quad (3)$$

For the electron distribution we divide it into trapped and passing particle. For the passing electrons, we assume beam-distribution, that is

$$f_u(H) = \frac{M}{l_z}\delta[H - \frac{M^2}{2l_z^2}] \quad (4)$$

Here H is total electron energy along the magnetic field in the moving frame. H is given as

$$H = \frac{1}{2}(v_z - \frac{M}{l_z})^2 - \frac{\psi}{Q} \quad (5)$$

With this distribution, passing particle density contribution is given as

$$n_u(\xi) = \int_{H_s}^{\infty}\frac{f_u(H)}{\sqrt{2H+\frac{2\psi}{Q}}}dH = \frac{M}{l_z\sqrt{\frac{2\psi}{Q}+\frac{M^2}{l_z^2}}} \quad (6)$$

For the passing particle distribution, we use abel's inversion technique to express the solution in terms of the density as

$$f_t(H) = \frac{1}{\pi}\int_{-H_s}^{-H}\frac{n_t'(H')}{\sqrt{H-H'}}dH' \quad (7)$$

As noted by F.Chen, our main idea is that with appropriate ratio of trapped particle and un-trapped particle density, we can construct BGK solution.[14] That is, we first assume some relation between trapped particle and un-trapped particle with appropriate boundary condition. Then we can get potential by Sagdev's method while trapped electron distribution is found by solving Abel's integral equation.So, we assume that

$$n_t = A(1-n_u)(B+n_u) \quad (8)$$

Then total density contribution is given as

$$n = n_t + n_u \quad (9)$$

Re-deriving Sagdeev's equation for the trapped and passing particle density, we have

$$\frac{d^2}{d\xi^2}\frac{1}{n_u^2} = \frac{2l_z^2}{Ql_x^2M^2}(n-1)(\frac{1}{n} - \frac{M^2}{l_z^2}) \quad (10)$$

With relation between trapped particle and passing particle given in eq.(8), Trapped particle distribution can be written as

$$f_t(H) = \frac{Al_z\sqrt{2r}}{\pi}[Br_c + r_s^2 Arctanh(r_c)] \quad (11)$$

Here r_c, r_s and r is defined as

$$r_c = \sqrt{\frac{-2Hl_z^2}{-2Hl_z^2+M^2Q}} \quad (12)$$

$$r_s = \sqrt{\frac{M^2Q}{-2Hl_z^2+M^2Q}} \quad (13)$$

$$r_s = \frac{1}{\sqrt{-2Hl_z^2+M^2Q}} \quad (14)$$

Also, sagdeev potential is given as

$$\frac{1}{2}(\frac{d^2}{d\xi^2}\frac{1}{n_u^2})^2 + V(n_u) = 0 \quad (15)$$

Here $V(n_u) \equiv \tilde{V}(n_u) - \tilde{V}(n_u = 1)$ where $\tilde{V}(n_u)$ is given as

$$\tilde{V}(n_u) = C_1[aArctanh\frac{2An_u-b}{\sqrt{I}} + \frac{c}{n_u} + \frac{d}{n_u^2} + e\ln n_u + f\ln n] \quad (16)$$

Coefficients C_1, a, b, c, d, e,f is given as

$$C_1 = 2l_z^2/A^3B^3l_x^2M^2Q$$

$$a = 2(1+A-AB)[(1+A)^2 + AB(AB+A-2)]$$

$$b = 1+A-AB$$

$$c = \frac{2bAB}{l_z^2}(l_z^2 - A^2B^2M^2)$$

$$d = \frac{A^2B^2(AB-1)(-l_z^2+ABM^2)}{l_z^2}$$

$$e = \frac{[(A+1)^2 + AB(-2+A+AB)]l_z^2 - A^4B^3M^2}{l_z^2}$$

$$f = 1 + A[2 + A - (2+A)B + AB^2]$$

$$I = 1 + A[2 - 2B + A(1+B)^2]$$

In order that solitary wave exist, second derivative of Sagdev's potential should be smaller than zero at equilibrium which is expressed as $V''(n_u = 1) < 0$. This gives

$$\frac{4(AB+A-1)(M^2-l_z^2)}{l_z^2M^2Q} < 0 \quad (17)$$

Now it is clear that SKAWs can propagate either in super-Alfvenic speed with $M > l_z$ when

$$A < \frac{1}{B+1} \quad (18)$$

or in sub-Alfvenic speed with $M < l_z$ when

$$A > \frac{1}{B+1} \quad (19)$$

If A is small, trapped particle fraction is small and this corresponds to "weakly" trapped particle limit. For large A, trapped particle effect will become important and we denote it as "strongly" trapped limit.

3. CONCLUSION

In this paper, we have found that BGK-type structure can be formed for obliquely propagating Alfven wave in magnetized plasma. It has been found that instead of using conventional BGK approach, assuming some relation between trapped electron density and passing electron density gives exact analytical structure for the trapped electron distribution and solitary wave solution for density. It has been found that is density distribution is electron hole where density is localized near separatix in configuration space. Also, the density is dip at center and hump at edge.

In Alfvenic BGK, charge-neutrality is strictly satisfied and spatial scale of such electron hole is much larger than ion-acoustic solitary wave case. Such large scale electron hole can be sustained because parallel electric field is provided through transverse component of Alfven wave rather than electron-ion separation like form ion acoustic type BGK. The crucial point that why such Alfvenic scale electron hole can be formed is due to the different dynamics along the field due to electrons and across the field due to the ions and their connection through the parallel current and electric field along the external magnetic field.

Acknowledgements

This work was partly supported by Creative Research program in KSTAR project from Korean government

MSIP (GN1308) and partly supported by the JSPSNRF-NSFC A3 Foresight Program in the field of Plasma Physics (NSFC No.11261140328).

References

[1] C. S. Wu and P. H. Yoon, Phys. Rev. Letters, 99(2007), 075001.

[2] C. B. Wang, C. S. Wu, and P. H. Yoon, Phys. Rev. Lett. 96(2006), 125001.

[3] R.White, L. Chen, and Z. H. Lin, Phys. Plasmas 9(2002), 1890.

[4] L. Chen, Z. H. Lin, and R.White, Phys. Plasmas 8(2001), 4713.

[5] Z. Guo, C. Crabtree and L. Chen, Phys. Plasmas, 15(2008),032311.

[6] J. H. Hollweg, Phys. Rev. Lett. 27(1971), 1349-1352.

[7] M. V. Medvedev and P. H. Diamond, Phys. Plasmas, 3(1996), 863-873.

[8] M. V. Medvedev, V. I. Shevchenko, P. H. Diamond and V. L. Galinsky, Phys. Plasmas, 4(1997), 1257-1285.

[9] M. Prakash and P. H. Diamond, Nonlinear Processes in Geophysics, 6(1999), 161-167.

[10] A. Hasegawa and L. Chen, Phys. Fluids 19(1976), 1924-1934.

[11] A. Hasegawa and L. Chen, Phys. Rev. Letters 32(1974), 9.

[12] H. R. Lewis and K. R. Symon, J. Math. Phys. 20(1979), 413-436.

[13] J. L. Schwarzmeier, H. R. Lewis, B. Abraham-Shrauner and K. R. Symon, Phys. Fluids, 22(1979), 1747-1760.

[14] Chen, F. F. Introduction to Plasma Physics. 2nd ed. New York, NY, Springer, 1984.

[15] M.K. Kalita and B.C. Kalita, J. Plasma Phys. 35(1986), 267

Recent progress of fast-ion loss detector project in Asian fusion experiments

Mitsutaka Isobe[1,2], Yipo Zhang[3], Jun-Young Kim[4], Kunihiro Ogawa[1], Xiaobing Luo[5], Yiqin Liu[5], Yi Liu[3], Junghee Kim[6], Jiafeng Chang[7], and Liqun Hu[7]

[1] National Institute for Fusion Science (NIFS), Toki, Japan

[2] The Graduate University for Advanced Studies (SOKENDAI), Toki, Japan

[3] Southwestern Institute of Physics (SWIP), Chengdu, China

[4] University of Science and Technology (UST), Daejeon, Korea

[5] Institute for Nuclear Science and Technology, Sichuan University, Chengdu, China

[6] National Fusion Research Institute (NFRI), Daejeon, Korea

[7] Institute for Plasma Physics, Chinese Academy of Sciences (ASIPP), Hefei, China

Abstract: The A3 foresight program is accelerating close collaboration for fast-ion diagnostics development between Asian three countries. A recent big step in our activities is that the operation of fast-ion loss detector (FILD) on HL-2A has begun lately. The localized bright spot appeared on the scintillator screen while a high-energy neutral beam was tangentially co-injected. The design of FILD system on EAST is steadily ongoing. The diagnostics port available for our purpose was decided in March, 2013. For KSTAR, the FILD is working successfully. In order to understand observed beam-ion loss signals while the RMP coils are turned on, the LORBIT code has been improved recently to treat non-axisymmetric perturbed field due to RMP coils and discreteness of TF coils.

Keywords: Fast ions, NBI, scintillator, RMP, TF ripple

1. Introduction

Issues related to fast particles are of great concern in nuclear fusion research. For example, in ITER, D-T produced 3.5 MeV alpha particles are super-Alfvénic and can potentially destabilize fast-ion-driven MHD instabilities, e.g. fishbone mode and Alfvén eigenmode. As a result of excitation of those modes, the anomalous loss of alphas may occur, leading to a reduction of fusion power output and damage to the first wall. The A3 foresight program on critical physics issues specific to steady state sustainment of high-performance plasmas was lunched in 2012. For the reason mention above, a physics study on fast ions is one of main subjects in this program. Our immediate goal in the early stage of the A3 program is to set up scintillator-based fast-ion loss detectors onto four major fusion devices in Asia, i.e., KSTAR, EAST, HL-2A, and LHD. In the latter stage of this program, joint experiments will be proposed to reveal physics issues associated with fast ions in toroidal fusion plasmas. In this paper, recent progress on fast-ion detector project in Asia in the first half of 2013 is

overviewed.

2. Scintillator-based fast-ion loss detectors in fusion

Scintillator-based fast-ion loss detectors (FILDs) have been widely employed to investigate orbit issues and/or anomalous loss of fast ions due to fast-ion-driven MHD instabilities in toroidal fusion plasmas, e.g. TFTR [1], JFT-2M [2], NSTX [3], JET [4], ASDEX-U [5], DIII-D [6], KSTAR [7], Alcator C-Mod [8], and HL-2A [9] in tokamaks, and CHS [10], W7-AS [11], LHD [12], and TJ-II [13] in helical/stellarator devices. The typical head section of FILD is schematically depicted in Fig. 1. The detector is classified into a magnetic spectrometer, providing gyroradius centroid and pitch angle of escaping fast ion simultaneously as a function of time. Further detailed information for FILD is available in Ref. 1-13.

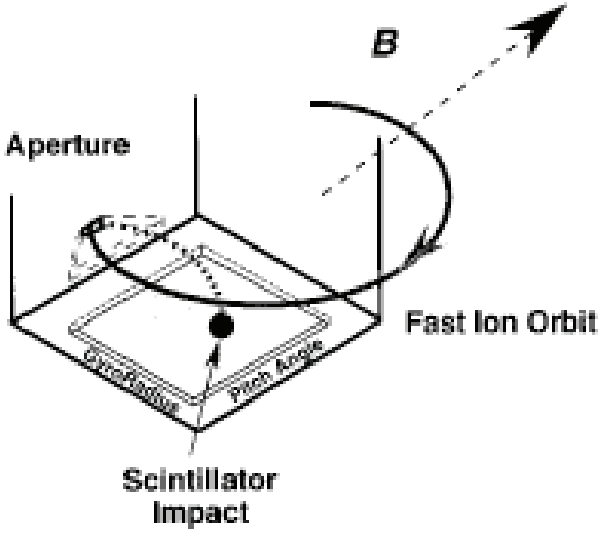

Fig. 1 Schematic drawing of the head section of FILD. [10]

3. Results from collaborative works

3.1. Progress of HL-2A FILD

Institute of Nuclear Science and Technology, Sichuan University, SWIP and NIFS have formed a trinity to design and develop the FILD for HL-2A. The detector was fabricated in Sichuan University and was installed onto HL-2A in March, 2013 [14]. The detector was designed so as to realize wide coverage in gyroradius centroid and pitch angle, detecting escaping fast ions having co-going transit and/or banana orbits. The ZnS:Ag (25 mm x 25 mm) was chosen as a phosphor because of high luminosity and fast decay time which is less than 10 □s. The detector is placed at the equatorial plane and is horizontally movable. The detector tip is typically ~3 cm away from LCFS.

Fast-ion loss signals were successfully obtained by the FILD in beam-heated discharges. Localized bright spot appeared on the scintillator screen when NB was tangentially co-injected. Fig. 2 shows time evolutions of scintillation light patterns on the screen. Main discharge parameters in this shot were as follows, i.e., B_t=1.3 T, I_p=160 kA, n_e=1.2x10^{19} m^{-3}, and P_{NBI}=0.8 MW. The frame rate of camera was set to be ~3 fps with exposure time of 1/30 s. As can be seen in Fig. 2, the localized scintillation light spot appears on the screen right after NB turn-on. The light spot becomes brighter during beam injection. After NB turn-off, the scintillation light disappears as expected. It can be therefore reasonably concluded that measured scintillation light spot is due to impact of escaping

beam ions.

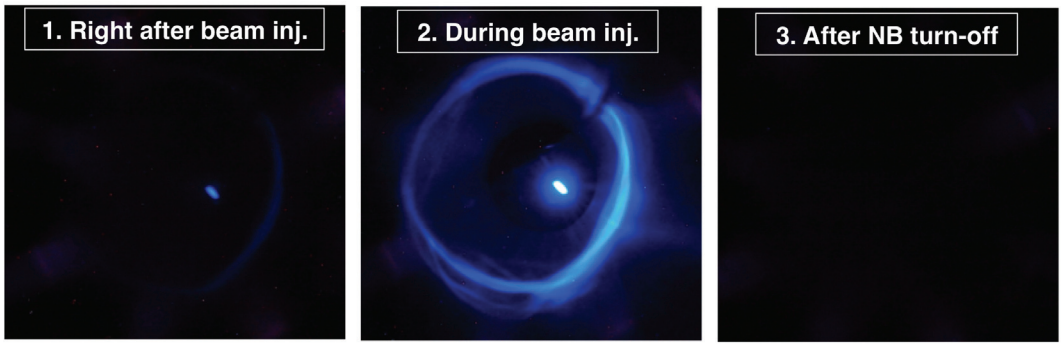

Fig. 2. Time evolutions of scintillation light distribution on the screen in a beam-heated discharge of HL-2A. B_t and I_p were 1.3 T and 160 kA, respectively.

Analysis considering the scintillator size and aperture structure indicated that the measured scintillation light spot center is consistent with the beam injection energy (E_b~40 keV). It also indicated that the measured pitch angle ranges from 65 degrees to 70 degrees. To understand orbit of escaping beam ions reaching the FILD of HL-2A, beam ions were launched from the FILD head position, i.e., (R, Z)=(2.13 m, 0 m) with energy/pitch angle of ~35 keV (D+)/68 degrees and calculated orbits backward in time by using the LORBIT code [15]. Fig. 3 shows a typical example of escaping fast-ion orbit reaching the FILD. Because B_t and I_p are relatively low in this particular shot, the orbit becomes fairly fat banana.

Measurement section of HL-2A FILD is going to be upgraded. In next campaign, PMT array (8x8) having fast-time response will be available. In HL-2A, fast-ion driven fishbone mode [16] and high-frequency mode, most likely toroidal-Alfvén eigenmode have been observed while NB is injected. Effect of those instabilities on fast-ion transport and/or loss is going to be investigated in next campaign.

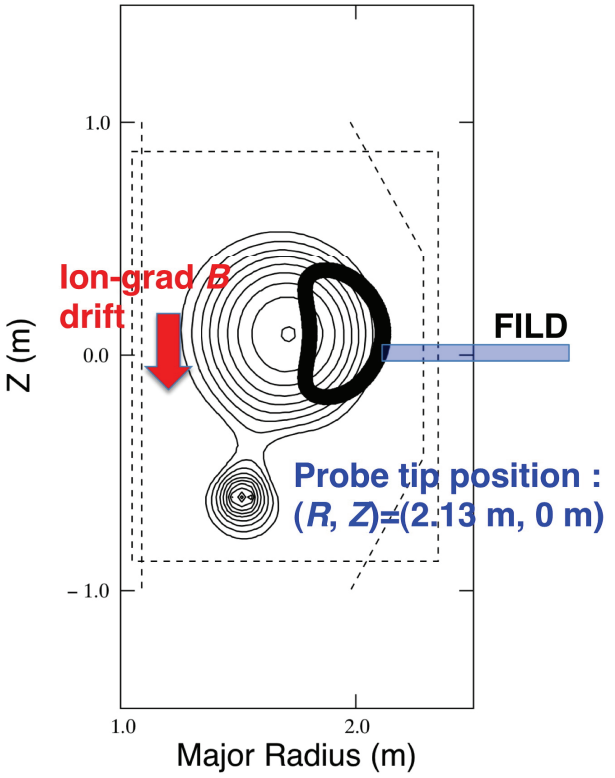

Fig. 3. Typical orbit of escaping beam ions reaching the FILD.

3.2. EAST

The design of FILD for EAST is steadily ongoing in the collaboration between ASIPP and NIFS. The diagnostics port available for our purpose was decided

in March, 2013 with the help of the LORBIT code. The structure of the detector head section is being designed carefully by using the NLSDETSIM3 code to realize wide coverage in detectable energy and pitch angle. In EAST, the FILD will be installed on the upper half plane of the J port because ion-grad *B* drift direction is upward in the standard operation of EAST. The detector is designed to be horizontally movable. The diagnostics port for FILD and preliminary drawing of the FILD on EAST are shown in Fig. 4.

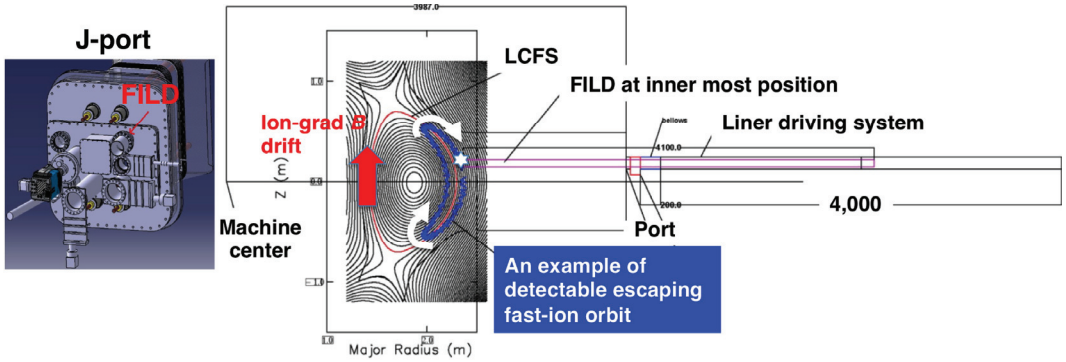

Fig. 4. External appearance of J-port of EAST (left figure) and preliminary design of bellows driving system for the probe shaft (right figure).

3.3. KSTAR

For KSTAR, the FILD is working successfully. LORBIT code of 2-D version has been used to check a class of escaping fast-ion orbit reaching FILD on KSTAR. In 2012 KSTAR campaign, effect of perturbed field produced by RMP coil on fast-ion loss detector signal was observed. In this case, existing 2-D LORBIT is no longer available for understanding of fast-ion transport caused by 3D effect. In order to understand observed beam-ion loss signals while the resonant magnetic perturbation (RMP) coils are turned on, the LORBIT code has been improved lately in the collaboration between NFRI and NIFS to treat non-axisymmetric perturbed field due to RMP coils. Toroidal field (TF) ripple caused by discreteness of TF coils can be also considered in the revised code. At first, we made a comparison of flux surfaces between contours of poloidal flux □□calculated by EFIT and field line reconstructed by □□without RMP field. Fig. 5 shows the comparison between the two. Black solid lines and red fine dots represent contours of □ and flux surfaces calculated by the field line, respectively. As can be seen, we got good agreement between the two. Next, we calculated magnetic flux surfaces for two patterns of RMP coil currents, i.e. n=1, +90 phase with 4 kAt and n=2, even parity with 4 kAt. Magnetic islands appear when RMP coils are turned on. In addition, magnetic flux surfaces become stochastic due to perturbed field due to RMP coil. Magnetic islands and stochasticity of field line can potentially

cause a visible effect on fast-ion orbit and transport. Effect of non-axisymmetric RMP coil field on fast-ion behavior is being intensively carried out [17].

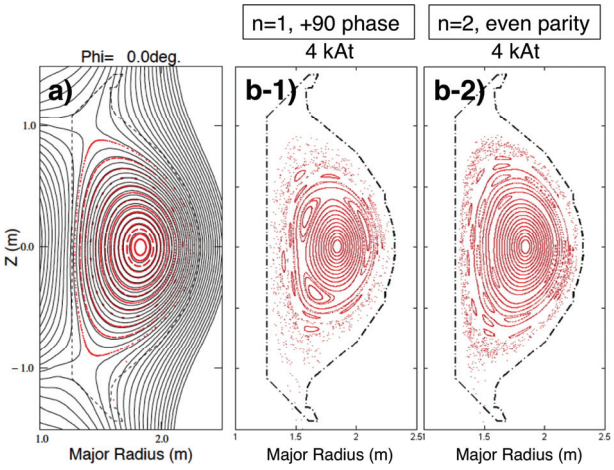

Fig. 5. a) Comparison of flux surfaces between contours of poloidal flux calculated by EFIT and field line reconstructed by without RMP field. b) Flux surfaces for two patterns of RMP coil currents, i.e. n=1, +90 phase with 4 kAt and n=2, even parity with 4 kAt.

4. Conclusion

Scintillator-based FILDs have been steadily enhanced in Asian fusion experiments to investigate physics associated with fast ions. A recent big step is that the operation of FILD on HL-2A has begun lately. The localized bright spot appeared on the screen while NB was tangentially co-injected. It disappeared after NB was turned off as expected. The analysis indicated that the measured energy of escaping beam ions matches the beam injection energy. The measured scintillation light in HL-2A is therefore due to impact of escaping beam ions. The design of FILD system on EAST is steadily ongoing. The diagnostics port available for our purpose was decided in March, 2013 with the help of the LORBIT code. The structure of the detector head section is being designed carefully to realize wide coverage in detectable energy and pitch angle. For KSTAR, the FILD is working successfully. In order to understand observed beam-ion loss signals while the RMP coils are turned on, the LORBIT code has been improved recently to treat non-axisymmetric perturbed field due to RMP coils. TF ripple caused by discreteness of TF coils can be also considered in the modified code. The preliminary orbit calculation suggested that the effect of non-axisymmetric RMP field on collisionless beam-ion orbit is visible.

Acknowledgments

This work was partly supported by the JSPS-NRF-NSFC A3 Foresight Program in the field of Plasma Physics (NSFC: No.11261140328). This work was also partly supported by Japan-Korea Fusion Collaboration Program and Japan-China JWG collaboration.

REFERENCES

[1] S.J Zweben, Nucl. Fusion, **29** (1989) 825.

[2] K. Shinohara *et al*., Plasma Phys. Control. Fusion **49** (2004) S31.

[3] D.S. Darrow, Rev. Sci. Instrum. **79** (2008) 023502.

[4] S. Baeumel *et al*., Fus. Eng. Des. **74** (2005) 853.

[5] M. García-Muñoz *et al*., Rev. Sci. Instrum. **80** (2009) 053503.

[6] R.K. Fisher *et al*., Rev. Sci. Instrum. **81** (2010)

10D307.

[7] Junghee Kim *et al*., Rev. Sci. Instrum. **83** (2012) 10D305.

[8] D.C. Pace *et al*., Rev. Sci. Instrum. **83** (2012) 073501.

[9] Xiaobing Luo, in 21st Meeting of the ITPA Topical Group on Diagnostics, Hefei, China, 17-20, Oct. 2011.

[10] M. Isobe *et al*., Rev. Sci. Instrum. **70** (1999) 827.

[11] A. Werner *et al*., Rev. Sci. Instrum. **72** (2001) 780.

[12] K. Ogawa *et al*., J. Plasma Fusion Res. **8** (2009) 655.

[13] D. Jiménez-Rey *et al*., Rev. Sci. Instrum. **79** (2008) 093511.

[14] Yiqin Liu *et al*., this seminar.

[15] M. Isobe *et al*., J. Plasma Fusion Res. SERIES **8** (2009) 330.

[16] W. Chen *et al*., Nucl. Fusion **50** (2010) 084008.

[17] Jun-Young Kim *et al*., this seminar.

Investigation of the slowing down of neutral beam-injected energetic ions in the HL-2A plasma with various environments

ZHANG Yipo[1], M. Isobe[2], LIU Yi[1], YUAN Guoliang[1], SONG Xianying[1], SONG Xianming[1], CAO Jianyong[1], WEI Huiling[1], YAN Longwen[1], YANG Qingwei[1], DUAN Xuru[1] and HL-2A team

[1] Southwestern Institute of Physics, P.O. Box 432, Chengdu 610041, China

[2] National Institute for Fusion Science, 322-6 Oroshi-cho, Toki 509-5292, Japan

Abstract: In the present paper, it is reported that the slowing down of the neutral beam-injected energetic ions in the HL-2A plasma with various environments has been investigated. For the set of discharges carried out in this experiment, very short pulses of a deuterium neutral beam, so-called "blip" with duration of 5 ms were tangentially co-injected into deuterium plasmas with different density and temperature. 2.45 MeV D-D fusion neutrons will be produced by beam-plasma reactions following neutral beam injection (NBI). Since the decay time of the neutron emission is related to the slowing-down of the energetic ions, the deceleration of energetic ions can be quantitatively researched from studies of the neutron emission decay rate. Experimental results show that the energetic ions have a longer slowing-down time in high-temperature or low-density plasmas as expected. Moreover, the energetic ions are well confined with a peaked profile and the ions are slowed down classically without significant loss in the HL-2A tokamak.

Keywords: Energetic ions, Fusion neutrons, Neutral beam injection (NBI), Tokamaks

PACS: 52.20.Dq, 52.55.Pi, 52.50.Gj

1. Introduction

Energetic ion physics is an active area of interest for magnetically confined fusion research with particular relevance to ITER [1]. Fusion produced alpha particles can excite some magnetohydrodynamic (MHD) instabilities, in turn, the instabilities cause a degradation of alpha confinement. The resulting increase in alpha transport may reduce the self-heating ability of fusion reactors, which would also reduce net energy again. Moreover, the localized heat load on the plasma facing components (PFCs) due to the escaping alphas can result in a significant melting and vaporization of the PFC surfaces, which constitute a serious threat to the safe operation of f reactors. For this reason, numerous efforts have been made in existing devices to reveal issues related to energetic ions.

Neutral beam injection (NBI)-injected energetic ions have velocities v_b that are much larger than the thermal velocity of the background plasma ions v_i, but much less than the thermal velocity of the background plasma electron v_e, i.e., $v_i << v_b << v_e$. When the

duration of NBI is much shorter than the slowing-down time of the beam ions, the affect of the NBI blip on the bulk plasma is very slight and can be neglected. Moreover, the energetic ion density n_b is much less than the background plasma density n_e, i.e., $n_b << n_e$. Thus, the NBI blip ions can act as a test energetic particle with a monoenergetic distribution in the initial velocity space. Beam ions is slowed down and deflected due to multiple Coulomb collisions with the background ions and electrons. This process is described by classical transport theory [2,3]. This method is often called "beam blip" and has been widely carried out in magnetically confined plasma experiments, such as DIII-D [4], TFTR [5], JT-60U [6], and CHS [7]. Note that beam blip injection does not have any significant effect on the background plasma.

In this paper, the slowing down of the neutral beam-injected energetic ions in the HL-2A plasma with various environments has been investigated. We have measured the decay time of neutron emission following the injection of a 5 ms pulse of deuterium NBI into MHD-quiescent deuterium plasma. It was found that the slowing-down times of the beam ions in plasma with various environments are consistent with the analytical classical slowing-down model.

2. Experimental setup

2.1 HL-2A tokamak

The HL-2A device is a medium-size tokamak with closed divertor chambers [8]. The main parameters of HL-2A are major radius R = 1.65 m, minor radius a = 0.4 m, and plasma current (I_p) up to 0.5 MA. Sixteen toroidal field coils can create and maintain a toroidal magnetic field (B_t) up to 2.8 T. The magnetic field is directed to be clockwise, whereas the plasma current is oriented to be counter-clockwise in the standard operation as seen from the top. The divertor of the device is characterized with two closed divertor chambers and at present it is operated with a lower single null configuration.

2.2 Beam ions in HL-2A

An NBI equipped with four-positive-ion sources is installed on the HL-2A [9]. Each ion source consists of a multi-pole plasma generator and an accel-decel extraction system. The beam injection energy E_b is typically 30 keV and a total beam power of up to 2.0 MW is delivered. The neutral beam is tangentially co-injected with a tangency radius, R_{tan} of 1.4 m. The deuterium neutrals are injected into the target plasma at an angle of 32° with respect to the plasma current at the magnetic axis. The arrangement of the NBI system on the HL-2A is schematically depicted in Fig. 1.The initial beam ion velocities are therefore not perfectly parallel to the magnetic axis. In a series of experiments, a short pulse neutral deuterium beam with the duration of 5 ms was tangentially injected into target deuterium plasma with various T_e and n_e parameters. The Lorentz orbit code has been developed to check the class of initial beam-ion orbit right after ionization in the HL-2A tokamak. Currently, the toroidal field ripple due to the finite number of toroidal coils is not

considered. Fig.1 shows three typical orbits of beam ions ionized at different location on the NBI line. The calculation indicates that the intial orbits of beam ions are classified as passing orbits in the HL-2A plasma.

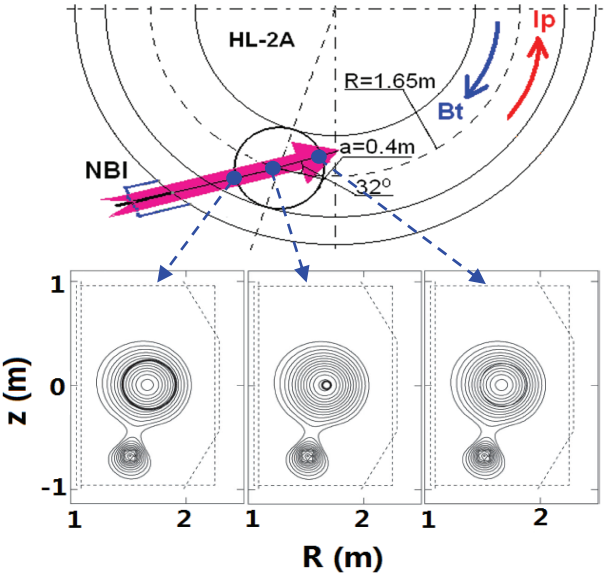

Fig.1 Arrangement of the NBI system and the calculation results of the beam ions obtained by the Lorentz orbit code.

2.3 Neutron type and neutron emission rate measurement

In NBI plasma, 2.5 MeV neutrons will be produced through *d(d,n)* ^{3}He fusion reaction. There are three ways to produce fusion neutrons: beam-induced fusion reactions occurring either when the injected fast deuterons collide with thermal deuterons (beam-target reactions, BT) or when the injected deuterons collide with other injected deuterons (beam-beam reactions, BB), and thermonuclear reactions from the background plasma (plasma-plasma reactions, PP). The fraction of each neutron type can be elucidated by using the TRANSP transport code. The calculation results for HL-2A plasma is shown in Fig. 2, it can be seen that > 70% of the neutrons during NBI in the HL-2A tokamak are BT type neutrons. Thus, the BT type neutrons dominate the overall neutron rate. Furthermore, due to the fact that the *d*(*d*,*n*) ^{3}He fusion cross section falls rapidly as beam ion energy decrease, the neutron emission decay as the beam fast ions decelerate. The decay time of the neutron emission is therefore simply related to the slowing-down time of the beam fast ions. So, the deceleration of beam fast ions has been quantitatively checked from neutron emission rate measurement following NBI blip [10].

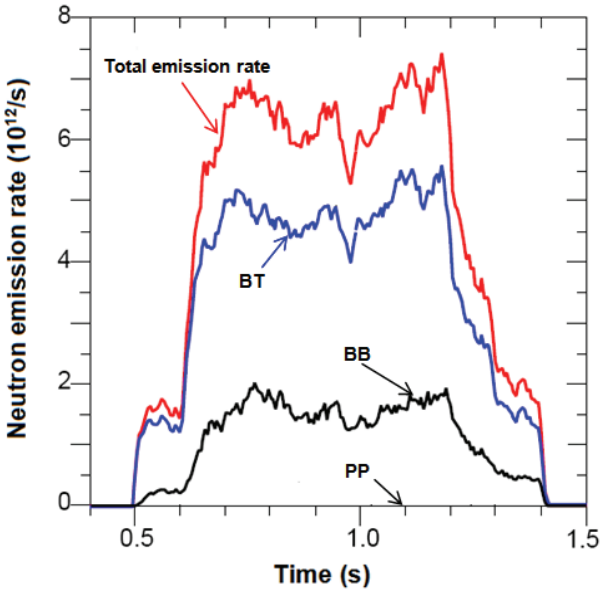

Fig.2 The fraction of the three neutron type during NBI discharge in the HL-2A tokamak obtained by using the TRANSP transport code.

The detection of the total neutron emission rate in the HL-2A tokamak is performed by means of a ^{235}U fission chamber (FC) with uranium oxide of 3 g [11]. The FC is surrounded by the polyethylene-moderator of ~5 cm thick to decelerate D-D neutrons to thermal

energy range in order to enhance neutron counts. The FC is positioned about 1.5 m away from the diagnostic port at the equatorial plane of the outboard side of the HL-2A tokamak. The width of the output pulses from the preamplifier does not exceed 100 ns, so that the count rates capability can reach 10^6 cps within the linearity. Currently, the FC system is operated in pulse counting mode and the sampling time is set at 1 ms.

3. Experimental results and theoretical analyses

A typical NBI blip discharge is illustrated in Fig.3. The plasma current is about 150 kA and the safety factor at the plasma edge is about 4. The toroidal magnetic field was 1.35 T. The central line-averaged electron density and the central T_e were about 1.0×10^{19} m^{-3} and 0.9 keV, respectively. A NB blip of 0.8 MW was injected into the ohmic plasma during the current flat-top phase and the NB pulse duration was 5 ms. Fig. 4 shows the typical time evolution of the neutron emission rate during this NBI blip discharge. It can be found that fusion neutrons suddenly appear right after the NBI turn-on and the neutron emission rate starts to decay exponentially following the NBI termination. Note that the decay time of the neutron emission rate is much longer than the pulse width of the NBI blip. Since the injected beam ions of 30 keV will be slowed down due to Coulomb collisions with the background plasma, the $<\sigma v>_b$ becomes lower as time goes by. Here, $<\sigma v>_b$ represents the D-D fusion reactivity of the neutron branch (D(d,n)^{3}He) for a high-energy deuterium beam injection into a deuterium Maxwellian plasma at finite-ion temperature. The e-folding neutron emission decay time τ_{n-ex} is evaluated to be about 13.1 ms in this ohmic discharge.

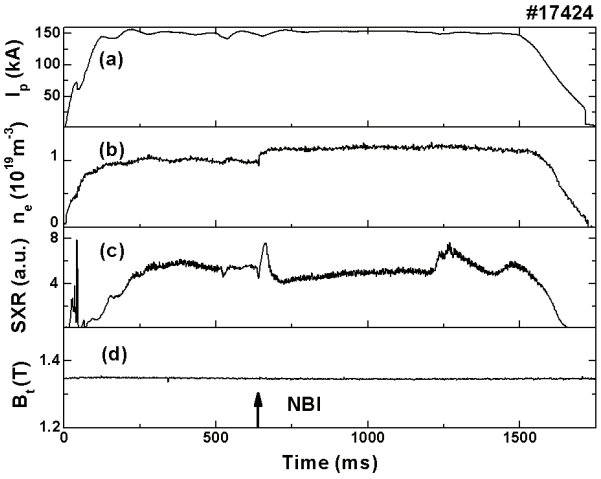

Fig.3 Time evolutions of the main parameters in a typical NBI blip discharge. From top to bottom: (a) plasma current I_p; central line-averaged electron density n_e; (c) soft x-ray emission intensity SXR; (d) toroidal magnetic field. The arrow in (d) indicates the time interval in which NBI blip is applied.

In order to investigate the slowing down of beam ions in plasma with various environments, NB blips were injected into the higher T_e and n_e plasmas while keeping the values of I_p, B_t and plasma edge safety factor. ECRH system and gas puffing system were employed to increase the background T_e and n_e, respectively. Fig. 5(a) shows a typical time evolution of the neutron emission rate when a deuterium beam blip was injected into the plasma heated by ECRH. The electron density in this shot is the same as for shot 17424 shown in Fig. 4 (about 1.0×10^{19} m^{-3}). ECRH with the power of 1.0 MW was launched into the

plasma from 500 to 900 ms and the T_e was about 1.6 keV during ECRH. A 0.8 MW NBI blip with 5 ms pulse duration was injected into the plasma at 635 ms, that is, the NBI blip injection occurred during ECRH. As can be seen in Fig. 5(a), the e-folding neutron emission decay time is evaluated to be about 16.7 ms and the decay time is longer than that seen in Fig. 4. Keeping the value of T_e (~1.6 keV), the electron density was increased to investigate experimentally the trend of the slowing down of the beam ions in high-n_e plasma. The comparison of the slowing down of the beam ions in low-n_e (1.0×10^{19} m^{-3}) and high-n_e (1.5×10^{19} m^{-3}) plasma is shown in Fig.5. It can be seen that the e-folding neutron emission decay time in the high-n_e plasma is significantly shorter than that in the low-n_e plasma.

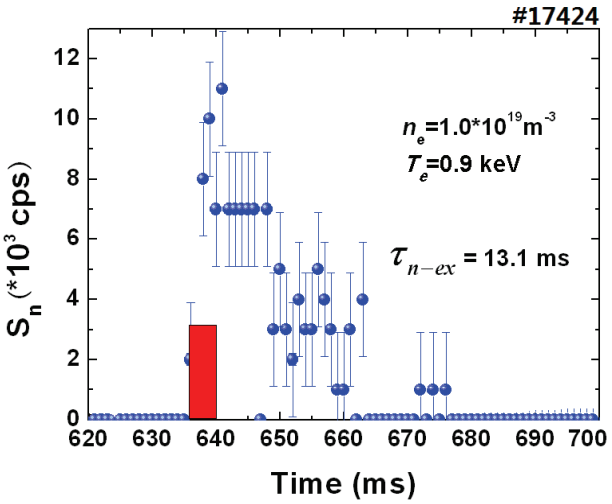

Fig4. Time evolutions of the neutron emission rate S_n when a deuterium beam blip is injected into the MHD-quiescent plasma with and without ECRH. The red shaded area indicates the time interval in which NB blip is applied.

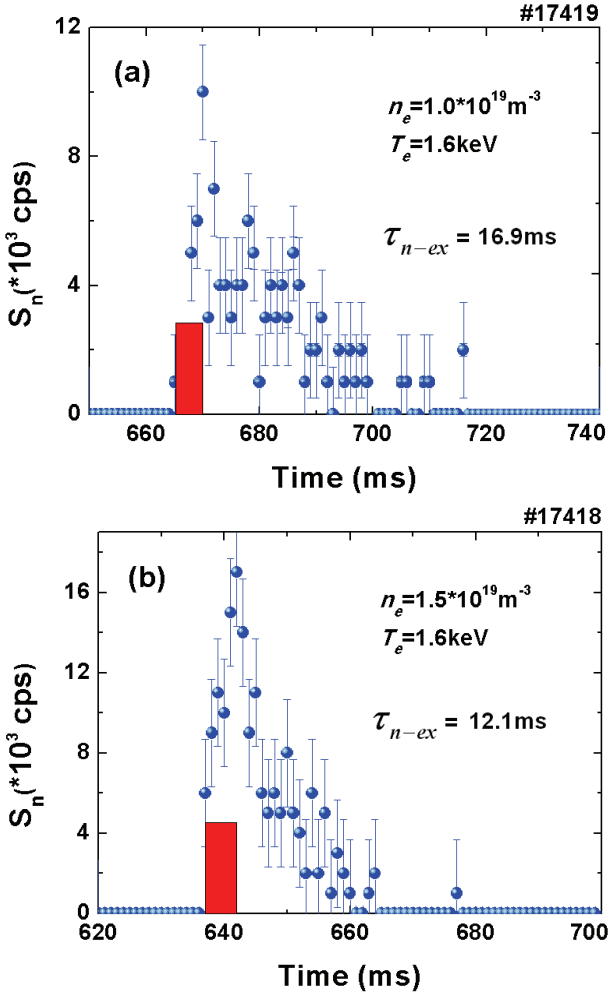

Fig.5 Time evolutions of the neutron emission rate S_n when the deuterium beam blip is injected into ECRH plasma with different electron density. The red shaded area indicates the time interval in which NB blip is applied.

The neutron emission rate S_n due to the beam-plasma reactions is scaled as follows [10],

$$S_n \propto n_i n_b < \sigma\upsilon >_b \qquad (1)$$

where n_i and n_b are the background plasma ion density and beam ion density, respectively. $<\sigma v>_b$ is the beam-plasma D-D reactivity for a deuterium NB injection into a deuterium Maxwellian plasma. $<\sigma v>_b$ will descend after the NBI termination because the

injected beam fast ions will be slowed down through Coulomb collisions with the background plasma. Assuming that $<\sigma v>_b$ decreases exponentially as beam fast ions slow down classically without loss and n_i is constant after the NBI termination, then S_n is predicted as

$$S_n(t) \propto <\sigma(\upsilon(t))\upsilon(t)>_b \propto \exp(-t/\tau_{n-th}) \qquad (2)$$

where $\tau_{n\text{-}th}$ is the e-folding decay time of the neutron rate predicted by the above-mentioned model. $\tau_{n\text{-}th}$ based on the classical slowing-down model can be expressed as follows,

$$\tau_{n-th} = -\int_{E_n}^{E_b} \frac{dE}{(dE/dt)_{th}} \approx \frac{\tau_{se}}{3} \ln \frac{E_b^{3/2} + E_c^{3/2}}{E_n^{3/2} + E_c^{3/2}} \propto \tau_{se} \qquad (3)$$

$$\tau_{se} = \frac{1.3 \times 10^9 T_e^{3/2}}{n_e \ln \Lambda} \propto T_e^{3/2} n_e^{-1} \qquad (4)$$

where E_n is the energy at which $<\sigma v>_b$ is reduced by 1/e from the value at E_b, E_c is the critical energy of beam ions at which the background electron Coulomb friction equals the background ion Coulomb friction and $\ln\Lambda$ is the Coulomb logarithm.

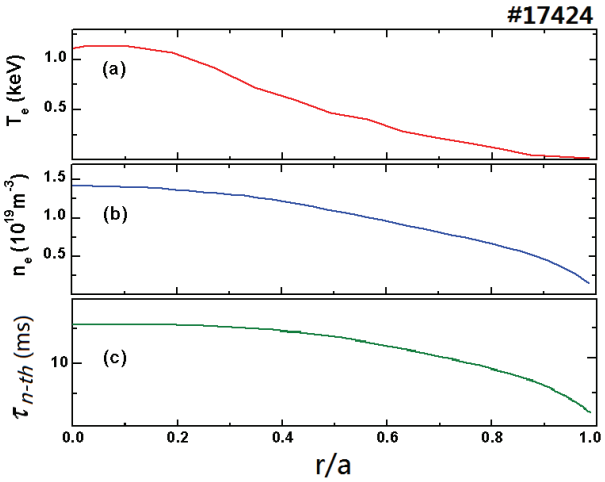

Fig.6 Radial profiles of the Te, n_e and $\tau_{n\text{-}th}$ as a function of the normalized minor radius r/a for discharge No. 17424. From top to bottom: (a) electron temperature; (b) electron density; (c) the e-folding decay time of the neutron rate predicted by the classical slowing-down model.

The radial profiles of T_e and n_e for shot No. 17424 are shown in Fig. 6 (a) and (b). Assuming that the T_i profile is equal to the T_e profile, we can obtain the $\tau_{n\text{-}th}$ profile according to the classical slowing-down model, as shown in Fig. 6(c). The value of the experimentally measured neutron decay time $\tau_{n\text{-}ex}$ is also drawn in Fig. 6 (c). From Fig. 6, it can be seen that the value of the $\tau_{n\text{-}th}$ decreases, when the normalized minor radius increase, i.e., $\tau_{n\text{-}th}$ becomes shorter toward the plasma peripheral region, which is due to τ_{se}. τ_{se} is a key parameter in determining $\tau_{n\text{-}th}$. From Equation (4), we know that $\tau_{se} \propto T_e^{3/2}$. Moreover, from Fig. 6(a), it can be seen that T_e becomes lower toward the plasma peripheral region. Therefore, τ_{se} becomes shorter toward the peripheral region, resulting in the changes of $\tau_{n\text{-}th}$. E_c becomes smaller as T_e becomes smaller, and E_n becomes slightly larger toward the plasma edge. E_n is a function of $<\sigma v>_b$ through the value of T_i. From Fig. 6(c), it can be found that $\tau_{n\text{-}ex}$ is approximately consistent with $\tau_{n\text{-}th}$ in the plasma core region (r/a < 0.4), which means that the tangentially co-injected beam fast ions have a peaked profile and decelerating classically without significant loss in HL-2A plasma. In addition, the experimental and calculated results suggest that the measured fusion neutrons were

primarily produced from beam-plasma reactions in the plasma core region.

4. Summary

The slowing down of tangentially co-injected fast ions in plasma with various environments has been investigated in the HL-2A tokamak by injecting a very short pulse high-energy deuterium beam with pulse duration of 5 ms. The slowing-down time of the fast ions in the higher T_e and lower n_e plasma is longer than that in lower T_e and higher n_e plasma. According to the classical slowing-down model, we can obtain the $\tau_{n\text{-}th}$ profile. Analyses show that the tangentially injected fast ions have a peaked profile and decelerating classically without significant loss in HL-2A plasma, and the measured fusion neutrons were primarily produced from beam-plasma reactions in the plasma core region.

Acknowledgments

The authors deeply appreciate the cooperation and assistance of the discharge operation group and the NBI group of the HL-2A tokamak. This work was partially supported by the JSPS-NRF-NSFC A3 Foresight Program in the field of Plasma Physics (NSFC No. 11261140328).

REFERENCES

[1] Fasoli A, Gormenzano G, Berk H L, et al. 2007, Nucl. Fusion, 47: S264

[2] Rostoker N, 1961, Nucl. Fusion, 1:101

[3] Li D, 2001, Nucl. Fusion, 41: 631

[4] Heidbrink W W, 1990, Phys. Fluids B, 2: 4

[5] Heidbrink W W, 1991, Phys. Fluids B, 3: 3167

[6] Tobita K, Tani K, Kusama Y, Nishitani T, et al. 1995, Nucl. Fusion, 35: 1585

[7] Isobe M, Sasao M, Okamura S, et al. 1998, J. Plasma Fusion Res. SERIES, 1: 366

[8] Yan L W, Duan X R, Ding X T, Dong J Q, et al. 2011, Nucl. Fusion, 51 : 094016

[9] Liu H, Cao J Y, Jiang S F, Luo C W, et al. 2009, Plasma Sci. Technol. 11: 613

[10] Strachan J D, Colestock P L, Davis S L, et al. 1981, Nucl. Fusion, 21: 67

[11] Yang J W, Song X Y, Zhang W, Li X, et al. 2005, Plasma Sci. Technol., **7**: 2860

Study progress on the ECE bursts in tokamak plasma

Erzhong Li, for all Collaborators

Institute of Plasma Physics Chinese Academy of Science, Hefei Anhui, China

E-mail: rzhonglee@ipp.ac.cn

Abstract: Understanding electron cyclotron emission (ECE) is essential not only for the diagnostic purpose but also for the heating in tokamak. This work mainly cares for the ECE bursts in high-beta plasma with ELMs, and will introduce several other cases that are physically in contrary to the high-beta case in future.

1. Introduction

The electron cyclotron emission (ECE), of which the optically thick second harmonic extraordinary mode (X-mode) is used as a diagnostic for electron temperature profiles in most tokamaks, has been widely studied in thermodynamic equilibrium plasma [1-2]. However, kinds of magneto-hydrodynamics (MHD) instabilities indeed make ECE signals complex, sometimes even elusive. One of cases related to the later is the ECE burst in synchronization with ELMs [3-4]. This problem is not understood presently. Nevertheless, we have a good sense that the superthermal population is not the necessary factor [5]. We are also sure that this burst must come from electron cyclotron emission [6]. This paper will firstly give the general experimental impression from the Ref [4]. Then, we suggest a model to explain this.

2. Observation

The main properties are that the ECE bursts appear on the low-field-side with an intensity of several times the thermal emission level and a bandwidth as narrow as the instrumental bandwidth of 400 MHz. Moreover, they are in synchronization with the D-alpha radiation in time. For detailed experimental observations, one can refer to the Ref.4 where a plenary expression of ECE bursts was presented.

3. Explanation

We use an ELMy model to explain this phenomenon, during which we must define a quantity called radiation temperature T_{rad}. It may be conceptually equal to the electron temperature T_e but only when the re-absorption was adequate over the emitting (resonant) layer. In other word, it must be satisfied that the plasma could be deemed as black-body. We suggest that this condition would be violated in an ELM event. With this consideration, we can calculate the radiation temperature $T_{rad}(\omega)$ at a changing resonant frequency with the given electron distribution function $f(u_\perp, u_\parallel)$. Here, we only show the Maxwellian distribution case.

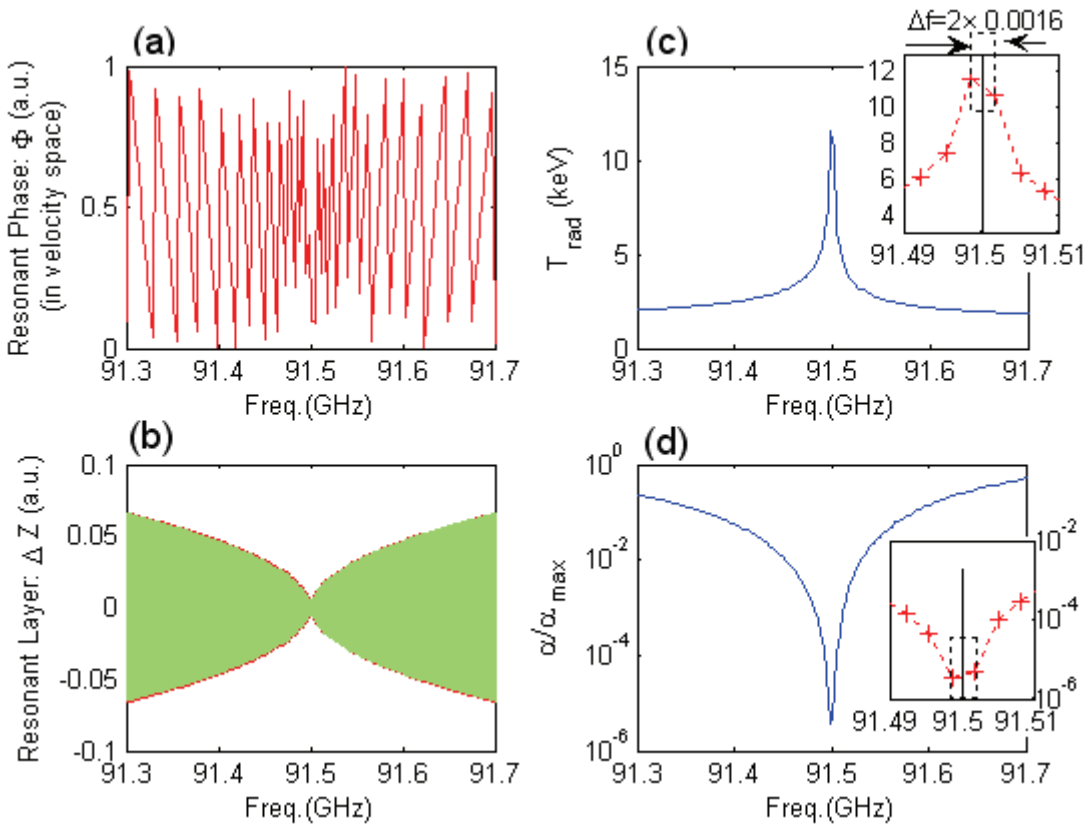

Figure 1. Simulation for the radiation temperature (c) and absorption coefficient (d), as well as showing the resonant phase (a) and resonant layer width (b).

It was obvious that the radiation temperature promptly increased away from the thermal value of $T_e = 2keV$ in figure 1(c), as the absorption coefficient decreased sharply in figure 1(d). This was due to the resonant layer width reducing in figure 1(b) as the cold plasma resonant frequency moved near to the singular point 91.5(GHz). This was also exposed by the increasing phase oscillations in figure 1(a).

4. Conclusion

It was found that the usual observed bursts on ECE signals in high-beta-plasma could indeed originate from ECE radiations when a varying cyclotron frequency was considered due to an ELMy evolution.

Acknowledgements

E. Li thanks Dr. Max E. Austin, and Prof. K. W. Gentle, Dr. W. L. Rowan, Dr. H. Huang (University of Texas at Austin, USA), as well as GA (San Diego, USA) for their hospitality during this study. This work was partly supported by the JSPS-NRF-NSFC A3 Foresight Program in the field of Plasma Physics (NSFC: No.11261140328)

Reference

[1] M. Bornatici et al, Nucl. Fusion 23 1153 (1983)

[2] M. E. Austin et al, Rev. Sci. Instrum. 74 1457

(2003)

[3] G. Taylor et al, Nucl. Fusion 32, 1867 (1992)

[4] Ch. Fuchs et al, Phys. Plasmas 8, 1549 (2001)

[5] Discussions with staffs working on DIII-D (2011-2012)

[6] Collaboration study with Dr. Max E. Austin (2011-2012)

Experimental studies on the interaction of drift-wave turbulence and intermittent zonal flow in a cylinder plasma

Chen Ran[1,2], Xie Jin-lin[1], Yu Chang-Xuan[1], Liu A-Di[1], Lan Tao[1], Xu Guo-Sheng[2], Kong De-Feng[1], Zhang Shou-Biao[1,2], Hu Guang-Hai[1,2], Li Hong[1], and Liu Wan-Dong[1]

[1] CAS Key Laboratory of Geospace Environment, Department of Modern Physics, University of Science and Technology of China, Hefei 230026, PRC

[2] CAS Institute of Plasma Physics, Hefei 230031, PRC

Abstract: The interaction of the low-frequency potential fluctuation which was previously identified as zonal flow (ZF) and broadband drift-wave turbulence is systematically explored in a linear magnetic plasma device, showing some different properties about the drift wave turbulence-zonal flow system in contrast with the previously published experimental results performed on several analogous devices. Besides, utilizing ZF's intermittent property observed in experiment, the radial propagation characteristics of both ZF wavephase and average burst of ZF energy are initiatively studied via conditional analysis. At last, ZF's damping mechanism is also explored qualitatively and quantitatively, suggesting that rather than ion-ion collision, the ion-neutral collision should be the crucial damping mechanism of ZF.

Keywords: zonal flow, drift wave, turbulence, cylinder plasma, nonlinear coupling.

PACS: 52.35.Ra, 52.25.Fi, 52.35.Mw, 52.35.Kt

1. Introduction

Zonal flows (ZFs) are found ubiquitous not only in fluid turbulence such as the planetary atmospheres etc., but also in the laboratory magnetically confined plasmas. In the last decade, spontaneous ZFs [1] generated via the nonlinear energy transfer from drift wave (DW) turbulence are universally observed in variety of magnectically confined plasmas (see [2] for a review). At present, ZFs are paid more and more attention especially in fusion devices such as tokamaks and stellarators, for the reason that they were predicted to be the potential trigger during the transition from low-to high-confinement regimes (L-H transition) by bifurcation theory model [3]. This prediction was supported by some experimental evidences [4-9] where the interactions of turbulence, time-dependent zonal flows and equilibrium E × B shear flow result in the so called "I phase" (or "dithering phase") regime normally between L- and H-mode regimes, that is consistent with the "predator-prey" model with two competing predators (ZF and mean flow) and one prey (turbulence) included [3]. In this model, the evolution of the self-regulated energy conservation system known as DW-ZF turbulence [10] constituted by the

ambient DW turbulence and turbulence-driven ZFs via nonlinear energy transform should take responsibility for the dithering period and eventually trigger L-H transition. Then, instead of ZFs which decrease the amplitude to very small level accompanying with DW turbulence after the formation of H mode regime, strong mean shear flow driven by steep edge pressure gradient should sustain H-mode regime operation via the shearing effect of this mean flow.

Due to the crucial role played by ZFs in suppressing and regulating DW turbulence and related transport of particle and energy, as well as potentially in triggering L-H transition, they have been an important and active topic in magnetically confined fusion research area. Comprehensive understanding of the interaction in the DW-ZF turbulence and its evolution should help us to resolve some key problems of magnetically confined fusion research, especially L-H transition related physics. Abundant experimental investigations have been performed in both toroidal and cylinder plasmas, while the latter [11-18], focusing on the topics including ZF identification, characterization, generation mechanism, as well as the interaction in the DW-ZF turbulence [10], are still rather limited. Anyway, investigations on these topics performed in cylinder plasmas with much less complexities in contrast with toroidal fusion plasmas, should provide some deeper insight on the underlying common and fundamental physics.

In this paper, to shed light on the DW-ZF turbulence, the authors present some detailed experimental studies in a cylinder plasma focusing on the DW-ZF interactions in a weak DW turbulence environment. In addition, ZF's radial propagation properties and its probable damping mechanism are also novelly explored, providing instructive and overall understandings of ZF's fundamental characteristics. The article is organized as the following: experiment set-up and some backgrounds are given in Sec.2. In Sec.3, experimental results about above topics are successively presented. And in the last section, the results are summarized.

2. Experimental set-up and backgrounds

The experiments are performed on the Linear Magnetized Plasma Device (LMPD) which has a cylindrical experimental chamber with the length of 2 m and the diameter of 0.25 m. Helium plasma is created by a hot cathode inside the source chamber connected at one end of this experimental chamber, and then diffuses into the experimental chamber in which the magnetic field (1000G at maximum) in the axial direction is generated by field coil group for plasma confinement. Langmuir probes are used in experiment for the measurement of plasma equilibrium parameters including electron temperature, density and potentials, as well as fluctuating signals of both potential and density. More detailed introduction to LMPD could be found in previous paper [19].

By the previous work [19], the low-frequency ($f < 2$ kHz) structure, generated in potential fluctuation approximately at B≈480 G and rising the amplitude as

B is increased, has been explicitly identified as ZF by the direct measurement of its complete 3D spectral characteristics. And on that basis, some deeper explorations about the interactions of ZF and DW turbulence together with some other ZF fundamental properties including its radial propagation behavior and damping mechanism were performed, and related experimental results are presented in the next section.

3. Experimental results

3.1 Spectrum evolution with B

Figure 1 (a)-(d) exhibit the comparisons of auto-power spectra of both relative ion saturation current fluctuation $\tilde{I}_s / \overline{I}_s$ and relative floating potential fluctuation $\tilde{\varphi}_f / \overline{T}_e$ at the same radial position of r = 4 cm where electron density steepens most but four typical incremental axial magnetic fields respectively. By assuming negligible electron temperature fluctuation, $\tilde{I}_s / \overline{I}_s$ and $\tilde{\varphi}_f / \overline{T}_e$ are treated as relative density fluctuation $\tilde{n}_e / \overline{n}_e$ and plasma potential fluctuation $\tilde{\varphi}_p / \overline{T}_e$ respectively.

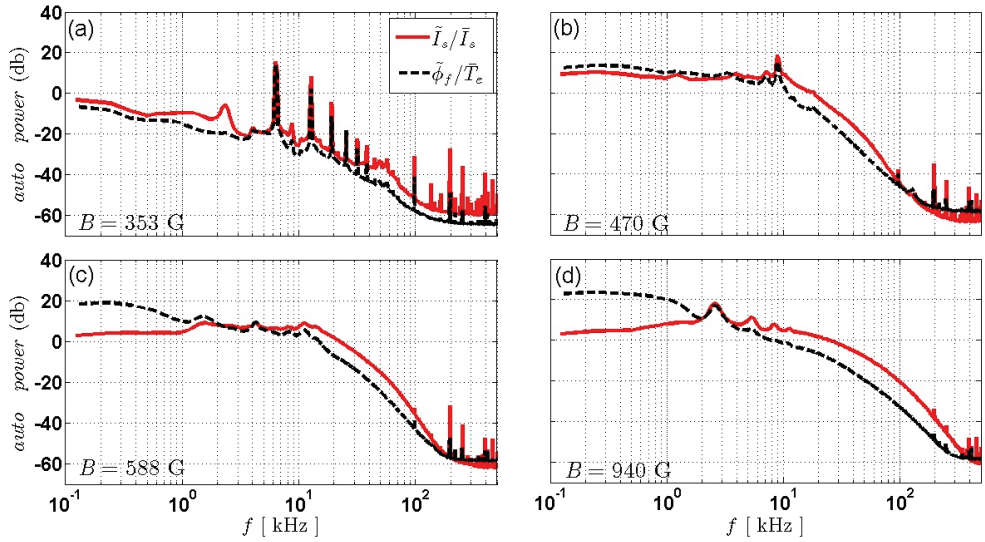

Figure 1. Auto-power spectrum evolutions of both relative ion saturation current (red solid line) and floating potential (black dash line) fluctuations with B.

From these figures, one should find that at the minimal magnetic field B = 353 G which is below the experimental-observed magnetic threshold 420 ~ 480 G for ZF onset, auto-power spectra of both density and potential fluctuations displayed in figure1(a) similarly show relative narrowband property dominated by discrete coherent harmonics with relative high (compared to another coherent mode normally observed at higher magnetic field, and this mode will be introduced in the following) characteristic

frequency of f ≈6−7 kHz and azimuthal mode number of m≈4 for the fundamental mode. In figure1(b), as B is increased marginally beyond the above-mentioned magnetic threshold for ZF onset, one should notice that both the two fluctuations undergo a transition from coherent mode(CM) just like the case at B = 353 G shown in figure 1(a) to the weak turbulence regime, representing the enhancement of total turbulence energy, as well as the spectrum broadening with two major appearances as: CM (the frequency of fundamental mode slightly increase to f ≈9 kHz, and higher harmonics show almost unobservable) energy fraction significantly decrease while high-frequency turbulence energy fraction increase. As B is continued increasing to 588 G, from figure 1(c) one could find that in both of the auto-power spectra of density and potential fluctuations the above-mentioned relative high-frequency (here the fundamental mode's frequency continue increasing to f ≈10～11kHz) CM further reduce in amplitude and shows nearly unidentifiable, while a new CM with relative low frequency at f ≈1.5kHz and azimuthal mode number of m = 1 generates. And from the exhibited spectra of the two fluctuations at the maximum magnetic field of B = 940 G in figure 1(d), the high-frequency coherent modes show completely unobservable even for the fundamental one, while the newborn one with relative low frequency and azimuthal mode number shows a further enhancement of fundamental mode in amplitude as well as the higher harmonics. Similar to the high-frequency coherent harmonics observed at lower magnetic field, a tiny up-shift of fundamental mode frequency as B is increased is also observed, i.e., from f ≈1.5 kHz at B = 588 G displayed in figure 1 (c) to f ≈2.6 kHz at B = 940 G displayed in figure 1 (d). In addition, the amplitude of high-frequency broadband turbulence especially in the frequency range of tens to hundreds kHz also grows to maximum at B =940 G in contrast to the situations at lower magnetic fields, exhibiting a prominently broader auto-power spectrum.

In experiment we conclude that both the CMs mentioned above respectively with relative high or low frequency and azimuthal mode number show some theoretically predicted DW characteristics, including:

(1), driven by density gradient, and thus the mode in density fluctuation prior to that in potential fluctuation,

(2), mode's amplitude reaches maximum at maximum in radial density gradient,

(3), the wave travels along the the electron diamagnetic drift direction,

(4),the amplitudes of relative density and potential fluctuations are approximately equal.

Therefore, both of the two kinds of CM should be consistently identified as DW modes driven by density gradient in the radial direction.

In a cylinder plasma, it is not novel that the magnetic field in axial direction plays the key role for the growth of DW which gains free energy from the gradient in equilibrium density, via controlling the density profile [20]. Also, the transition of plasma fluctuations from the regime dominated by DW harmonics to the more turbulent one as DW growth rate continues increasing

accompanying with B, originated from the nonlinear energy transform from the linearly unstable DW modes to perturbations at other wavenumbers which are linear stable [21], was studied in detail by previous work performed in cylinder hot-cathode [22, 23] and helicon [24] plasmas. Therefore, the magnetic threshold for ZF onset observed in our experiment should represent the theoretically predicted threshold in growth rate of DW in nature by common-accepted "predator-prey" model [10]. Beyond this threshold generation of ZF should be observed due to its growth overcoming the damping, while the DW growth rate keeps on enlarging as B is continuously increased, leading to the continuous enhancement of ZF in amplitude. Furthermore, it should be noted that some critical value of B ≈800 kHz beyond which both DW and ZF show saturation trends is also observed in experiment, probably attributed to saturation of linear growth rate as B exceeds some value. Detailed studies on scalings of saturation level of both turbulence and ZF with B, and on the basis of which clear elucidation of self-regulating dynamics in the DW-ZF turbulence, will be specifically given in another work in preparation.

In addition, it should be paid special attention to that in figure1(b) at B = 470 G just beyond the magnetic threshold of ZF onset the relative potential fluctuation slightly exceeds density fluctuation in low-frequency (f<2 kHz) region of auto-power spectra, while an opposite comparison result between these two relative fluctuations is displayed as we focus on the high-frequency (f > 10 kHz) region where broadband turbulence is dominant. Dramatically, from figure 1(c) and (d) the differences between the auto power spectra of these two relative fluctuations in both low- and high-frequency regions respectively are consistently amplified as B is increased.

To interpret this phenomenon, firstly, as known that low-frequency zonal flow is the potential-fluctuation structure with negligible density fluctuation intensity [2], the continual amplification of the difference between the two auto-power spectra of two different fluctuating quantities in the low-frequency region with B should thus be the representation of ZF growth in amplitude. Secondly, the observed amplification of the difference between these two spectra in the high-frequency region with B should imply that ZF interacts with high-frequency fluctuations in potential or density by two different ways. In particular, the interaction between ZF and high-frequency potential fluctuation follows the "predator-prey" model, and to be more specific, on the one hand the former gains energy from the latter nonlocally via nonlinear energy coupling, leading to a reduction in amplitude of the latter, and on the other hand the shearing effect [25, 26] of ZF on turbulence gives rise to an energy transform from the low-frequency fluctuation normally with larger spatial size to the high-frequency one normally with smaller spatial size, thus resulting in an increase in amplitude of high-frequency broadband turbulence. However, as to discuss the interaction between ZF and high-frequency density fluctuation, it should be a different case since only the shearing effect of the

former on the latter works.

Therefore, we infer that the observed difference between the auto-power spectrum of relative potential fluctuation and that of relative density fluctuation, as well as its amplification with B, should represent a joint effect caused by ZF generation and its reaction, i.e., shearing effect of ZF on ambient DW turbulence, by assuming that ZF is generated predominantly via nonlinear energy transfer from the high-frequency broadband potential fluctuation. Specifically, during ZF generation the energy transfer process from high-frequency fluctuation to low-frequency ZF fluctuation only exists in potential fluctuating quantity, thus resulting the above-described amplification of spectral difference accompanying with continual enhancement of ZF energy and also energy transfer from high-frequency potential fluctuation, as B is kept increasing. Meanwhile, it should also be noted that by integrating the spectra of this two fluctuating quantities over frequency, we still have the relationship $\tilde{n}_e / \overline{n}_e \approx \tilde{\varphi}_p / \overline{T}_e$ satisfied. In addition, it is also found that in the mid-frequency (normally 2 ~ 10 kHz) region where DW harmonics are dominant, auto-power spectra of these two fluctuations keep roughly equal to each other with B, especially at the very characteristic frequency of DW fundamental mode. This result should suggest that DW harmonics do not significantly contribute to ZF generation via nonlinear coupling according to the same reasoning process.

Taken together, the authors conclude that the continual steepening of radial density gradient as B is increased results in an increase of DW growth rate, which is the crucial controlling parameter not only in the transition of plasma fluctuations from CM regime to broadband turbulence regime but also in determining the magnetic threshold of ZF onset and subsequent continual enhancement of ZF intensity with B, all shown in figure 1. Besides, on the basis of common-accepted DW-ZF turbulence dynamics [10, 27], by comparing the spectral evolutions of relative potential and density fluctuations respectively as B is increased, the interaction between ZF and high-frequency broadband turbulence, as well as that between ZF and DW harmonics, is indirectly inferred. In the next subsection, the interactions between ZF and DW fluctuations in different frequency bands are directly studied in more detail via different methods of analysis, showing consistent and instructive results.

3.2 Interactions between ZF and DW turbulence

Bispectral analysis, a method to estimate degree of the phase coherence among three fluctuating quantities at frequencies satisfying the frequency matching condition $f_3 = f_1 + f_2$ by calculating the spectrum of the third order correlation function, is widely used in dealing with nonlinear coupling issues in plasma, especially the topic of ZF-DW interactions.

Figure 2(a) shows the contour plot of squared auto-bicoherence of $\tilde{\varphi}_f$ at B =940G with maximum ZF amplitude, estimated via

$$\hat{b}^2(f_1,f_2)=\frac{\left|\left\langle\Phi(f_1)\Phi(f_2)\Phi^*(f_3=f_1\pm f_2)\right\rangle\right|^2}{\left\langle\left|\Phi(f_1)\Phi(f_2)\right|^2\right\rangle\left\langle\left|\Phi(f_3=f_1\pm f_2)\right|^2\right\rangle}$$ [27],

where Φ(fn) is the Fourier component of $\tilde{\varphi}_f$ at fn. Apparently, around the lines of $f_3 = f_1+f_2 \simeq 0$ and $f_2 \simeq 0$ the estimated values of auto-bicoherence $\hat{b}^2(f_1,f_2)$ far exceed the noise value, indicating a significant level of nonlinear coupling among ZF with its characteristic frequency very close to zero that was proven by previous work [19] and two turbulent fluctuation signals with their frequencies in a broadband (up to 300 kHz) and satisfying the frequency matching condition. Moreover, it is found from figure 2(a) that nonlinear interaction also generally occurs among the broadband turbulent modes.

The summed squared auto-bicoherence $\sum\hat{b}^2(f_3)$, defined as a sum of squared auto-bicoherence $\hat{b}^2(f_1,f_2)$ over all f_1 and f_2 satisfying the matching condition and then normalized by the number $N(f_3)$ of Fourier components for each f_3 in the summation, i.e., $\sum\hat{b}^2(f_3)=\frac{1}{N(f_3)}\sum_{f_3=f_1+f_2}\hat{b}^2(f_1,f_2)$, quantifies the power fraction at the frequency $f_3=f_1+f_2$ due to three-wave coupling. Figure 2(b) exhibits the estimated $\sum\hat{b}^2(f_3)$, demonstrating that at B = 940 G the power fraction of potential fluctuation due to three-wave coupling keeps remarkablely exceeding the level of noise (given by dash-dot line in amaranth) at arbitrary frequency f_3 in the whole broadband up to the Nyquist frequency (f_N = 500 kHz determined by the sampling rate of 1 MHz) , and this power fraction reaches the maximum value with f_3 in the low-frequency region of f < 2 kHz where ZF is dominant, more than a factor of two larger than the value of $\sum\hat{b}^2(f_3)$ with f_3 in other frequency regions. This figure should manifests that the coupling strength of nonlinear interactions with ZF as the participant is the most prominent.

To further investigate the nonlinear coupling between ZF and DW turbulence, the squared auto-bicoherence and auto-biphase (estimated by $\hat{\theta}(f_1,f_2)=\arctan\frac{\mathrm{Im}\left(\left\langle\Phi(f_1)\Phi(f_2)\Phi^*(f_3=f_1\pm f_2)\right\rangle\right)}{\mathrm{Re}\left(\left\langle\Phi(f_1)\Phi(f_2)\Phi^*(f_3=f_1\pm f_2)\right\rangle\right)}$) spectra of some representative resonant wave triads satisfying $f_3 = f_{ZF}\equiv f_1 - f_2 = 0.366$ kHz, are illustrated in figure 2(c) by black solid line and (d) by black markers of cross, respectively, using f_1 as the variable. It should be stressed here in above estimation f_{ZF} = f3 =0.366 kHz is optionally chosen in the low-frequency range of f< 2 kHz dominated by ZF, and relative estimated results change very little as $f_3 = f_{ZF}$ is varied arbitrarily in this region of frequency. According to the details in the slices of squared auto-bicoherence and auto-biphase with $f_3 = f_{ZF}$ =0.366 kHz which should represent some characteristics of three-wave coupling with ZF concerned, we have every reason to separate the spectra into three distinguishable parts with the variable f_1 located in different frequency regions, i.e., f_1 < 2 kHz, 2 kHz < f_1 < 20 kHz, and f_1 > 20 kHz,

marked by ”Case I, II, and III” and also shaded in the different colors respectively in figure 2(c) and (d). One should notice that in both “Case I” and “Case III”, significant level of auto-bicoherence with the value much larger than noise level (given by dash-dot line in amaranth in figure 2(c)), as well as the almost convergent auto-biphase with its value close to π, is illustrated. However, for “Case II” with f1 in the mid-frequency range, it exhibits quite distinct results with the value of auto-bicoherence much smaller than that of above two cases and only slight larger than noise level, together with some hops in auto-biphase spectrum from $\hat{\theta} \approx \pi$ to $\hat{\theta} \approx 0$ as f_1 locates at some special frequencies which are confirmed equal to the characteristic frequencies of DW harmonics from the fundamental mode to the third harmonic respectively. These results should strongly suggest that three-wave coupling among ZF and two other fluctuating quantities at frequencies located in the low-frequency range of $f_1 < 2$ kHz for “Case I” is the same kind of nonlinear interaction as “Case III” with two other high-frequency fluctuating quantities in the region $f_1 > 20$ kHz, but quite different from “case II” with two other mid-frequency fluctuating quantities in the region 2 kHz < f_1 < 20 kHz where DW harmonics are dominant shown in figure1(d). Previous results in theory [29] predicted that the weak dependence of biphase on the frequencies of ambient turbulence, just like the above-described results of “Case I ” and “Case III”, and in sharp contrast to the situation for “Case II”, was a particular feature of the nonlinear coupling between DW and ZFs(including low-frequency zonal flow or GAM) for the “DW-ZF system”.

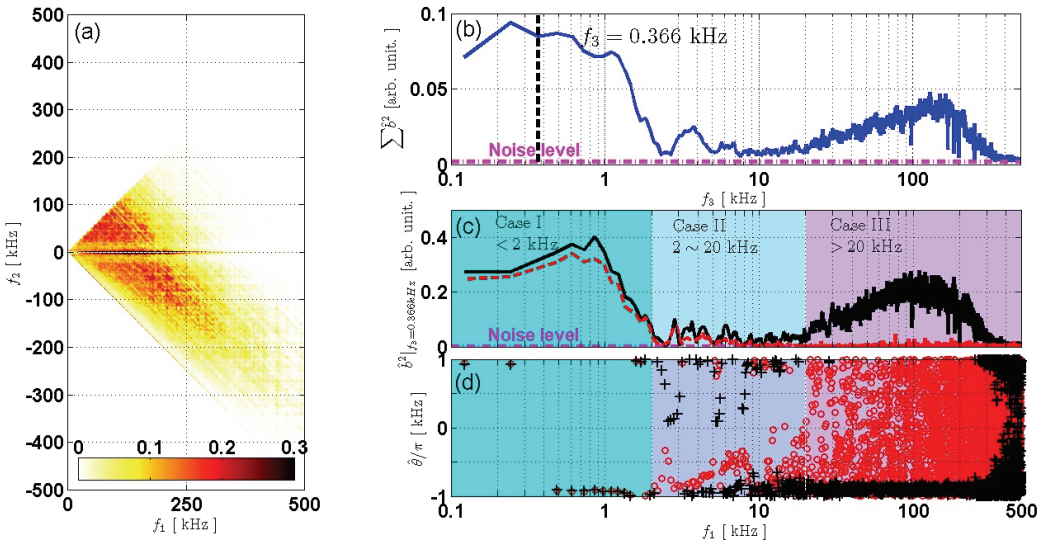

Figure 2. (a), contour plot of squared auto-bicoherence of floating potential fluctuation, (b), the summed squared auto-bicoherence, (c), typical slices of auto-(black solid curve) and cross-bicoherence(red dash curve) with f_3 =0.366 kHz, and (d), related auto-(black crosses) and cross-biphase (red cycles) slices(divided by π)also with f_3 =0.366 kHz, here r =4 cm, B =940 G.

To ascertain the features of nonlinear interactions between ZF and DW in above three cases with the frequencies of other two fluctuating quantities located in different regions, in the following we specifically present some deeper explorations focusing on the potential interactions in these three cases one by one.

Firstly, in previous work [19] by estimating the squared coherence of two potential fluctuations azimuthally separated by π,i.e., $\tilde{\varphi}_f^{\theta=0}$ and $\tilde{\varphi}_f^{\theta=\pi}$ both measured at r =4 cm, the authors concluded that in the low-frequency range of f < 2 kHz ZF was definitely dominant with the proportion of its energy to the total up to 80%, while the remaining 20% of total energy should be contributed by low-frequency DW turbulence. Therefore, in "Case I" the significant level of three-wave coupling exhibited in figure 2(c) should likely represent the nonlinear interactions either between ZF and other two fluctuating quantities of DW turbulence in this region or among the resonant wave triads of ZF fluctuations at different frequencies.

On the basis of ZF symmetrical property in azimuthal direction, we can clearly distinguish between these two kinds of nonlinear interactions by comparing the spectra of squared cross-bicoherence and related cross-biphase estimated by

$$\hat{b}^2(f_1,f_2)=\frac{\left|\left\langle \Phi^{\theta=0}(f_1)\Phi^{\theta=\pi}(f_2)\Phi^{\theta=0,*}(f_3=f_1\pm f_2)\right\rangle\right|^2}{\left\langle\left|\Phi^{\theta=0}(f_1)\Phi^{\theta=\pi}(f_2)\right|^2\right\rangle\left\langle\left|\Phi^{\theta=0}(f_3=f_1\pm f_2)\right|^2\right\rangle}$$ and

$$\hat{\theta}(f_1,f_2)=\arctan\frac{\mathrm{Im}\left(\left\langle \Phi^{\theta=0}(f_1)\Phi^{\theta=\pi}(f_2)\Phi^{\theta=0,*}(f_3=f_1\pm f_2)\right\rangle\right)}{\mathrm{Re}\left(\left\langle \Phi^{\theta=0}(f_1)\Phi^{\theta=\pi}(f_2)\Phi^{\theta=0,*}(f_3=f_1\pm f_2)\right\rangle\right)}$$

(here $\Phi^{\theta=0}$ and $\Phi^{\theta=\pi}$ denote the Fourier representations of the potential fluctuating quantities of $\tilde{\varphi}_f^{\theta=0}$ and $\tilde{\varphi}_f^{\theta=\pi}$,respectively) respectively to above-mentioned estimations of squared auto-bicoherence and auto-biphase. Related results of squared cross-bicoherence and cross-biphase spectra using the same resonant wave triads satisfying the frequency matching condition of $f_3 = f_{ZF} \equiv f_1 - f_2 = 0.366$ kHz are estimated and also illustrated in figure 2(c) by red dash line and (d) by markers of red cycle respectively for the clear comparison. From these figures, one should notice that the squared cross-bicoherence in "Case I" shows a comparable value to the squared auto-bicoherence with only a tiny decrease, while the estimated auto-and cross-biphase spectra are quite similar. These findings should suggest that, in "Case I" the three-wave coupling exhibited by bispectral analysis should predominantly be the representation of nonlinear interaction among three ZF fluctuating quantities satisfying the frequency matching condition rather than ZF-DW interaction, for the reason that only ZF with special azimuthal symmetry should be capable of resulting in such estimated results of cross-bispectral analysis which are almost the same to that of auto-bispectral analysis.

Moreover, one should also find that as f_1 is located in the mid-frequency range dominated by DW harmonics in "Case II", the estimated cross-bicoherence shows comparable value to the auto-bicoherence, that is similar to the comparison results mentioned above in "Case I". However, the comparison result between

cross-and auto-biphase spectra is found in sharp contrast to the situation in "Case I". As to "Case III" with f_1 located in the high-frequency range, the estimated value of cross bicoherence decreases rapidly to noise level, and accordingly the cross-biphase spectrum shows complete randomness. These facts demonstrate no observable three-wave coupling in this case.

By combining the previous work [19] about the characteristic structures of DW harmonics and high-frequency turbulence, there is no difficult to interpret the comparison results in these two cases. At first, the previous-estimated squared coherence of the two potential fluctuations separated by π in azimuthal direction showed significant coherency of DW harmonics especially for fundamental mode, that should result in a comparable value of cross-bichoherence in contrast to that of auto-bicoherence in "Case II", while the variation between related cross-and auto-biphase spectra should be the response of the azimuthal phase propagation of DW harmonics. And second, for "Case III" where two turbulent fluctuations in this high-frequency range are completely not correlated with each other as the de-coherent length is much shorter than the azimuthal separation between them, resulting in the noise-level cross-bicoherence and random cross-biphase. Therefore, the authors emphasis that these bispectral analyses should be in good self-consistence.

Secondly, we continue to focus on exploring the interactions between ZF and fluctuating quantities in "Case II" with their frequencies located in the mid-frequency range where DW harmonics are dominant. In figure 3 (a) we present the temporal evolutions of two floating potential fluctuations $\tilde{\varphi}_f^{\theta=0}$ and $\tilde{\varphi}_f^{\theta=\pi}$, measured respectively by two Langmuir probes both located at the same radial position of r =4 cm but separated by π in azimuthal direction. From this figure, one should notice that some occasional negative spikes arise in both of the two fluctuating series simultaneously, marked by the shadows in nattier blue, representing the temporal behavior of ZF structure which is azimuthally symmetric. In addition, fundamental mode of DW is also exhibited in these two potential fluctuating series as the regular quasi-sinusoidal oscillation with relative smaller intensity. In sharp contrast to the azimuthal-symmetric ZF, the DW fluctuations measured respectively from the two probes show definitely antiphase, that should be interpreted by its azimuthal mode number of m = 1 identified by previous work [19].

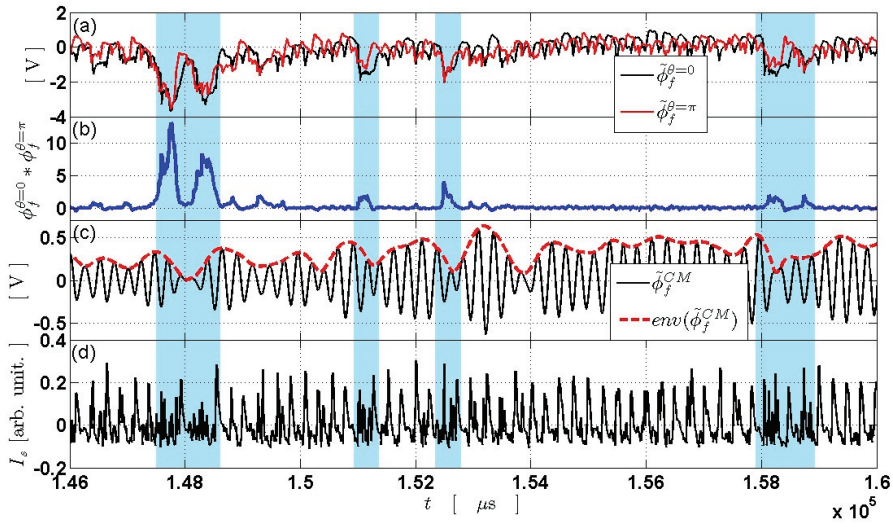

Figure 3. (a), time series of two floating potential fluctuations separated azimuthally by π, (b) temporal evolution of ZF energy estimated by multiplying these two potential fluctuations, (c), filtered signal of floating potential fluctuation in the frequency band 3kHz < f < 5kHz(black solid curve) and its envelope(red dash curve) in the same time period, and(d), raw signal of ion saturation current, here r =4 cm, B =940 G.

Utilizing ZF symmetric property in azimuthal direction, we thus calculate the temporal evolution of ZF energy roughly by multiplying the two potential fluctuating series, and related result is shown in figure 3(b). According to ZF temporal evolution shown in figure 3(a) , one should take an intermittent temporal feature of ZF energy for granted, that is in good agreement with the result exhibited in figure 3(b), where ZF energy bursts in those very periods of time marked by the shadows in nattier blue. Then the fluctuation series of DW fundamental mode $\tilde{\varphi}_f^{CM}$ is extracted from the potential fluctuation by filtering the raw potential fluctuation $\tilde{\varphi}_f$ using a digital filter with its passband of 3 kHz < f < 5 kHz (in this discharge we have $f^{CM} \approx$ 4 kHz with Δf^{CM} < 1 kHz as the bandwidth). Figure3(c) exhibits the temporal evolution of $\tilde{\varphi}_f^{CM}$ in solid black line, as well as its envelope which represents DW intensity in dash red line. One should conclude an approximate antiphase modulation between temporal evolutions of ZF energy and DW intensity by comparing figure 3(b) and(c), suggesting that DW mode should be pronouncedly suppressed by ZF structure.

As we continue studying the temporal evolution of $\tilde{I}_s$ which is shown in figure 3(d), it is displayed that in the quiet periods between ZF bursts, density fluctuation represented approximately by $\tilde{I}_s$ assuming negligible electron temperature fluctuation, shows quite regular qusi-triangular waves. Since DW fundamental mode together with higher harmonics is significantly dominant in density fluctuation, that is

ascertained from the auto-power spectrum of relative ion saturation current exhibited in figure 1 (d) at B = 940 G, these qusi-triangular waves is explicitly identified as the time series of DW coherent modes. Dramatically, as time series of ZF energy displayed in figure3(b) shows bursting behavior, in the density fluctuation series above-mentioned regular qusi--triangular signals are pronouncedly suppressed, and replaced by high-frequency irregular oscillations with relative smaller intensity. This phenomenon should be interpreted by shearing effect of ZF on density fluctuation, i.e., density fluctuation undergos an energy transition from DW coherent modes in the mid-frequency region to turbulent structures with relative smaller spatial size in the high-frequency region.

Lastly, we turn on to explore the interaction between ZF and high-frequency fluctuations in "Case III". Utilizing the bursting characteristic of ZF intensity shown from figure 3 (a) and (b), we adopt the conditional statistical analyses [30], which is frequently used to extract intermittent signals contributed by coherent structures such as blobs, etc., from a turbulent background with broadband spectrum and then evaluate the coherency between different bursting quantities or propagation information of coherent eddies between some two spatial positions, for this study. Given ZF intensity larger than a certain threshold $\left|\tilde{\varphi}_{f|f<2kHz}\right| > 2\sigma$ as the condition, where time series of ZF is estimated roughly as the low-frequency (f < 2 kHz) oscillation of potential fluctuation $\tilde{\varphi}_f$ since ZF was previously demonstrated dominant in potential fluctuation in this very frequency region [19], and σ is the root-mean-square value of such a low-frequency potential fluctuating quantity, we thus estimate the conditional averages of three different fluctuating quantities including ZF intensity, high-frequency potential and density intensities respectively using the formula $S_C = \left\langle S \,|\, \tilde{\varphi}_{f|f<2kHz} > 2\sigma \right\rangle$ (here $\langle \cdots \rangle$ denotes ensemble averaging over the chosen realizations).

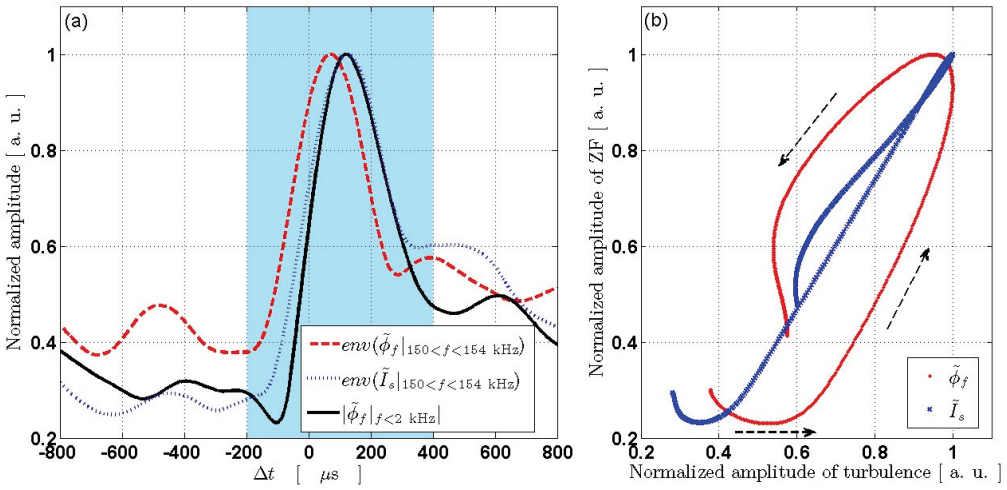

Figure4. (a),average bursts of high-frequency potential fluctuation intensity (red dash curve),

high-frequency density fluctuation intensity (blue dotted curve) and low-frequency ZF intensity (black solid curve), respectively, estimated via conditional analysis, and all normalized by respective maximum value for better comparison, and (b), the hodograph of ZF and high-frequency potential turbulence intensities(red), and that of ZF and high-frequency density turbulence intensities(blue), here r =4cm, B =940 G.

The estimated results (normalized by relative maximum value for clearer comparisons) are given in figure 4 (a) by black solid line (ZF intensity), red dash line (envelope of high-frequency floating potential fluctuation) and blue dotted line (envelope of high-frequency ion saturation current fluctuation) respective, while the latter two should represent the conditional average of intensities of potential and density fluctuations respectively. Note that to the benefit of better comparison between temporal evolutions of related structures with different temporal scales, here the chosen high-frequency turbulent quantities of potential and density fluctuations both locate in a narrow frequency band of 150 kHz < f < 154 kHz in which auto-bicoherence reaches almost the maximum value, seen from figure 2 (c), indicating the most pronounced level of ZF-DW coupling. From this figure, we find that the envelope of high-frequency potential fluctuation (red dash line) obviously precedes the low-frequency ZF amplitude (black solid line) by approximate 50 μs which is about one third of the full width at half maximum of ZF intensity burst (≈ 150 μs), in sharp contrast with that of density case (blue dotted line) which seems to be definitely coincide with ZF.

On the basis of conditional average results, we thus draw the hodographs of turbulence and ZF intensities, displayed in figure 4(b) which reconfirms the results exhibited in figure 4(a). The hodograph (red) of ZF and high-frequency potential turbulence intensities shows the typical limit-cycle oscillation where temporal evolution of ZF intensity lags behind that of potential turbulence by some delay time which is about 50 μs, while the hodograph in blue exhibits an almost coincidence between ZF intensity and that of high-frequency turbulence of plasma density. It is important to note that as above-mentioned narrow frequency band is altered optionally in the frequency range of 20 kHz～300 kHz, related results show remarkably consistent with only some slight change of lag time of ZF intensity to the envelope of high-frequency potential fluctuation.

Such a limit-cycle oscillation should indicate that, ZF gains energy from potential turbulence in this frequency band, in the meanwhile, ZF has a reaction on this turbulent quantity via its shearing effect. Therefore an adaptive DW-ZF system regulated by theoretically predicted “predator-prey” model [10] should be constituted by ZF in the low-frequency band and potential turbulence in the high-frequency band. Limit-cycle oscillation has been experimentally observed in various devices, and all the previous

experimental observations show consistent time lags of ZF intensity comparing with fluctuation of turbulence with each other, as well as related theoretical predictions according to which DW energy (or its growth rate) variation should be the key control parameter in this system, and only when the growth rate of DW reaches some threshold can ZF generate via overcoming its damping. However, the observed temporal coincidence of ZF and density turbulent quantity in the same high-frequency band should predict only the shearing effect of ZF on ambient turbulence. Combining the results displayed in figure 3, one should thus definitely conclude that this shearing effect results in both of the reduction in amplitude of density fluctuation in the middle band where DW modes are dominant and the enhancement in amplitude of that in the high band, while the latter mechanism leads to the observed in-phase evolutions of ZF intensity and the envelope of high-frequency density fluctuation shown in figure 4.

Taken together, in this part the interaction between ZF and DW turbulence are explored in detail. According to the analysis results of auto-bispectrum, the ZF-DW turbulence interaction is artificially divided into three cases based on the three frequency bands where DW turbulent fluctuation locates. In “Case I” with $f < 2$ kHz where ZF occupies the most of the total energy, the bispectral analysis implies nonlinear coupling among three ZF fluctuating quantities with matching frequencies. Since the amplitude of DW turbulence in this frequency band is much smaller than that of ZF fluctuation, we are not able to tell exactly the interaction between ZF and ambient DW turbulence in this case. In “Case II” with $2\ \text{kHz} < f < 20\text{kHz}$ where DW harmonics are dominant, simply by comparing the temporal evolutions of intensities of different fluctuating quantities, an approximate anti-phase modulation of ZF intensity on DW coherent modes especially for the fundamental one, strongly suggesting the suppression of DW modes due to the shearing effect of ZF. This fact should well interpret the finding about the approximate consistent spectral evolutions of DW harmonics in density and potential fluctuations with the magnetic field, displayed in figure 1, but be in sharp contrast to the results performed in some other linear devices where DW modes were identified to be responsible for ZF generation [14-18]. Such a suppression of DW modes subsequently leads to a significant reduction of radial flux, the largest fraction of which is found to be driven by these coherent modes. Detailed analysis of ZF shearing on radial transport of particle will be introduced systematically in some other paper which will be published in the near future. Moreover, temporal evolution of ZF, with its characteristic frequency identified very close to zero by previous work [19], definitely exhibits intermittent property in intensity. Utilizing this intermittent characteristics of ZF, interactions between ZF and high-frequency DW turbulence in “Case III” are studied via conditional analysis. Temporal evolution of the envelope of high-frequency potential fluctuation is found lag behind that of ZF intensity by some delay

time (≈50 μs), exhibiting the typical limit-cycle oscillation, that is in sharp contrast to the observed coincident evolutions of ZF intensity and high-frequency density fluctuation. These experimental findings should demonstrate distinct types of nonlinear interaction between ZF and high-frequency DW turbulence in potential fluctuation comparing with the case concerning high-frequency density fluctuation. To be more specific, ZF and potential fluctuation in this high-frequency band together constitute the common-accepted DW-ZF system in which "predator-prey" model regulates both the evolutions of the two fluctuating quantities, while as to the case of ZF and density fluctuation in the same band only the shearing effect of ZF on ambient turbulence exists. This finding is also self-consistent with the experimental results described in **3.2** where the auto-spectrum of potential fluctuation exhibits a significant shift of energy nonlocally from DW turbulence in the high-frequency band to ZF in the low-frequency band comparing with that of density fluctuation, with the relationship $\tilde{\varphi}_f / \overline{T}_e \square \tilde{I}_s / \overline{I}_s$ keeping satisfied.

3.3 Radial propagation of ZF

In sharp contrast with the common-view ZF symmetries in both toroidal and poloidal directions for toroidal devices or in both azimuthal and axial directions for cylinder plasmas through a large number of theoretic works and experimental observations, the radial propagation of ZF structures, which is also one of the fundamental characteristics of ZF, however, has still been rarely explored up to now especially in linear devices. In the following contents of this subsection, detailed observations focusing on this important topic will be presented.

A rake probe with six radial-aligned tips is adopted for analyzing ZF propagation in radial direction via simultaneous measurement of the floating potential fluctuations at different radial positions. In addition, It should be stressed that another single-tip probe also used for measuring the floating potential fluctuation separated by π in azimuthal direction is arranged for the purpose of filtering the interference from the background turbulent structures and thus exacting substantial information of azimuthal-symmetric ZF. More detailed description about the arrangement of these probe arrays could be found in published paper [19], where the radial wavenumber as well as its width should have been estimated more accurately using this kind of probe arrangement, comparing with only local measurement of potential fluctuations by which unignored interference from ambient turbulence should always exist. Firstly, distribution of ZF's radial wavenumber could be estimated as following. Set α_1(f)and α_2(f)are the estimations of cross-phase spectrum respectively using two potential fluctuating pairs ($\tilde{\varphi}_{f1}^{\theta=0}$,$\tilde{\varphi}_{f}^{\theta=\pi}$) and($\tilde{\varphi}_{f2}^{\theta=0}$,$\tilde{\varphi}_{f}^{\theta=\pi}$), where $\tilde{\varphi}_{f1}^{\theta=0}$ and $\tilde{\varphi}_{f2}^{\theta=0}$ are the potential fluctuations measured respectively by two adjacent tips of the rake probe,

and $\tilde{\varphi}_f^{\theta=\pi}$ is measured by the single-tip probe which is azimuthally separated away with the rake probe by π. Then the difference between this two cross-phase spectra, i.e., $\alpha_1(f)$ and $\alpha_2(f)$, can thus be written as $\Delta\alpha = \alpha_1(f)-\alpha_2(f)= k_r(f)\delta r+k_\theta(f)\delta l_\theta$. Here $k_r(f)$ and $k_\theta(f)$ denote the radial and azimuthal wavenumber spectra of fluctuating structures respectively, δr is the radial separation between this two adjacent tips of the rake probe, and δl_θ is the separation between the rake and the single-tip probes in azimuthal direction. In the specific frequency band where ZF is dominant, Δα could be simplified as $\Delta\alpha \approx \Delta\alpha^{ZF} = k_r^{ZF}(f)\delta r + k_\theta^{ZF}\delta l_\theta$, since ambient turbulence, with its decorrelation length much less than the azimuthal separation between the two potential fluctuations, is thus ignored. Considering ZF symmetric characteristic in azimuthal direction we have $k_\theta^{ZF} \equiv 0$ always satisfied, one should finally calculate the average radial wavenumber of ZF as $\bar{k}_r^{ZF} \approx \frac{1}{\delta r}\int_{f=f_{ZF}} \Delta\alpha(f)\,df$, where $\int_{f=f_{ZF}} \cdots df$ denotes integration over the frequency band of ZF.

By synchronously sweeping both the rake and single-tip probes along the radial direction, we estimate the radial distribution of ZF average radial wavenumber $\bar{k}_r^{ZF}(r)$, which is displayed in figure 5 (a). Note that the errorbars in this figure as well as the following case in figure 5 (b) are estimated from the dispersion of the results among several reproducible discharges. From this figure, we find it that in the radial area where ZF is experimentally observed, the average radial wavenumber of ZF keeps almost constant as +0.1 cm^{-1} (Here a positive radial wavenumber denotes an outward propagation of wavephase), except the several outmost positions at which $\bar{k}_r^{ZF}$ increases roughly by a factor of two.

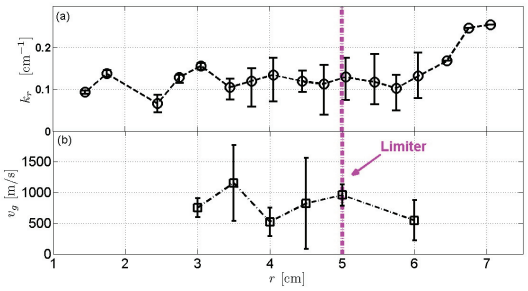

Figure 5. (a), radial distribution of average radial wavenumber of ZF, and (b), that of average propagation velocity of ZF bursts in radial direction, here B =940 G.

This result is quite different from that was performed in another linear device and published in Ref [13], where a turnover position around r = 3 cm of ZF radial wavenumber was observed, and to be specific, ZF showed radially outward propagation in phase inside the turnover position, while outside this position the propagation of ZF wave phase changed it's direction to be inward. It should be noted that this turn over position of ZF radial wavenumber propagation observed in Ref [13] was coincide approximately with that at which density gradient increased to maximum. However, in our case the distribution of ZF's radial wavenumber seems to be definitely unaffected by the

local gradient of density.

Let's continue to focus on the radial propagation of ZF wave packet by estimating the distribution of ZF average group velocity as following.

Firstly, temporal evolution of ZF is extracted from the floating potential fluctuation approximately by filtering the latter using a digital low-pass filter with its passband f < 2 kHz where ZF was identified to occupy around 80% of the total energy at B = 940 G. Then, we thus estimate the temporal evolutions of ZF energy at locations of different tips of the rake probe as $E_i^{ZF} \propto \left|\tilde{\varphi}_{fi|f<2kHz}\right|^2$, where the subscript i =1... 6 denotes the serial number of the tips radially from inside to outside.

No wondering that this calculated E_i^{ZF} show consistent intermittent behavior, then conditional analysis is also utilized here for one to get the average bursts of ZF energy at different radial locations as $CA_i^{ZF} = \left\langle E_i^{ZF} \mid E_1^{ZF} \geq 2\sigma \right\rangle$ (i =1... 6), where the E_1^{ZF}, calculated by potential fluctuation which is measured from the innermost tip of rake probe, is used here as the reference. And the bursts in time series of ZF energy larger than the given condition 2σ (here σ denotes the root-mean-square value of E_1^{ZF}) are selected out for averaging.

Next, utilizing above-calculated CA_i^{ZF} (i =1... 6) which should represent the average bursts of ZF energy measured from the six radially-aligned tips of the rake probe respectively, one should be able to estimate the propagation velocity of average ZF bursts in the radial direction by studying the times which are taken as ZF bursts propagate along the six probe tips. The average delay times which should be taken as the average ZF bursts propagate radially from the innermost tip of the rake probe to another outer one could be estimated respectively as $\overline{\tau}_i = \frac{\sum_{-\Delta T \propto \Delta T} t \cdot C_{1i}}{\sum_{-\Delta T \propto \Delta T} C_{1i}}$ (i =1... 6), where C_{1i} represents the correlation function of CA_1^{ZF} (reference) and CA_i^{ZF}, and ΔT denotes the period time of the average ZF burst.

Finally, simply by fitting the sequence of calculated $\overline{\tau}_i$ and the radial separation δr between related two tips of the rake probe using a linear function, the average propagation velocity vg of ZF bursts could thus be estimated from the slope of the fitted curve, while the radial distribution of vg is exhibited in figure 5(b). From this figure, we conclude that in the radial area of r =3 ~ 6 cm ZF bursts keep propagating outward at the average group velocity approximately as 0.5 ~ 1 km/s, which is about one order of magnitude smaller than the ion-sound speed $C_s = \sqrt{T_e / M_i} \approx 8.5\text{km/s}$ (Using T_e =1.5 eV at r =4 cm).

This work should be the first time for a comprehensive study on the radial distributions of ZF's radial propagations, including not only ZF phase but also the average bursts of ZF energy, to be performed

experimentally, providing a deeper understanding of ZF radial propagation as well as its radial structure. In addition, the authors need to state that, although the results in this work show universal radial-outward propagation of ZF wave phase at any radial location where ZF is observed, from the estimated conditional radial wavenumber-frequency spectrum of ZF displayed by previous work [19], one should realize that standing wave components also exist in ZF.

Furthermore, it should be also emphasized that, given the estimation of ZF radial wavenumber as small as $\bar{k}_r^{ZF} \sim 0.1 \sim 0.25 cm^{-1}$ from above analysis together with previous work [19], one should not decidedly conclude that the radial extending of ZF structure is comparable to or even larger than the machine size (R = 12.5 cm) via evaluating ZF wavelength in the radial direction as $\lambda_{ZF} = \frac{2\pi}{\bar{k}_r^{ZF}} \sim 25 \sim 63 cm$. Instead, the decorrelation length of ZF, which should actually represent the radial extending of ZF structure, could be estimated as $L_c^{ZF} = \sqrt{2} / \Delta k_r^{ZF} \sim 1.3 cm$ (here Δk_r^{ZF} denotes the width of ZF wavenumber and from previous work [19] we have $\Delta k_r^{ZF} \approx 1.1 \mathrm{cm}^{-1}$ at B = 940 G, r =4cm). Therefore, although radial wavelength of ZF is estimated to be even much larger than the scale of device, a significant attenuation of ZF intensity should exist in radial direction, resulting that ZF amplitude reduces to about 1/e as it propagates radially only by a relative tiny distance $L_c^{ZF} \approx 1.3 \mathrm{cm}$, which is just several percent of the average radial wavelength of ZF.

3.4 ZF damping mechanism

In the last part of this section, some analysis on ZF damping mechanism is presented as following.

Figure 6 (a), (b), and (c) exhibit the cross-power spectra of $\tilde{\varphi}_f^{\theta=0}$ and $\tilde{\varphi}_f^{\theta=\pi}$ in the low band of f < 1 kHz by markers of cross in black at three typical magnetic field respectively. At the lowest magnetic field of the three, i.e., B =470G which is just beyond the threshold of ZF onset described in 3.1, in figure 6(a) we should pay close attention to the red dash line which displays the fitting curve of related cross-power spectrum using the Lorentzian distribution function $S(f) = \frac{E\lambda}{f^2 + \lambda^2}$. In this case, with almost negligible ZF intensity, one should find it that the spectrum is only approximately fitted by this function with relative high dispersion, in sharp contrast to the cases with pronounced ZF intensity at the other two incremental magnetic field, i.e., B =588G and B = 824 G, at both of which the dispersion of the fitting shows much lower, displayed in figure 6(b) and(c). These facts should imply that the spectral broadening of ZF is probably caused by the collision damping effect, and ZF damping rate can be deduced approximately via the relation of $\beta_{ZF} \approx 2\pi\lambda$, where the fitting factor λ specifies the half-width at half-maximum of the spectrum.

Figure 6(d) and(e) show the calculated λ along with the axial magnetic field B keeping r = 4 cm fixed and

along with the radial position r at the fixed magnetic field B =940G respectively, where the errorbars are given from the 95% confidence intervals in the fitting processes. One should notice from figure 6(d) that λ is evaluated to be almost constant in the magnetic field ranging 588 ~ 940G. At lower two magnetic field 470 G and 530 G, the parameter λ shows significant larger values by approximately a factor of two. However, considering the fact that ZF has very weak intensity at these two magnetic fields which are just beyond the threshold of experimentally observed ZF onset, the reliability of λ evaluated in these two cases at marginal B should thus be quite low. Therefore, we conclude that the damping rate of ZF has a weak dependence on the axial magnetic field B from figure6 (d). In addition, from figure6 (e), the fact that λ is also evaluated to be near constant at almost all the radial locations is also observed, except for the case at the outmost radial position r =6.5 cm where ZF similarly shows negligible intensity. This result exhibited in figure6 (e) implies that the damping rate of ZF also has a weak dependence on the radial position r at the fixed magnetic field B = 940 G. These observations about the qualitative evolution of ZF damping rate with B as well as r should greatly help one to further explore the underlying mechanism of ZF damping in detail.

Generally, linear damping mechanism of low-frequency zonal flow includes the ion-ion collision and ion-neutral collision, while the damping rate of ZF caused by the former could be estimated by $\beta_{ii} \approx \left(\overline{k}_r^2 + \Delta k_r^2\right)\rho_i^2 \nu_{ii}$, and that caused by the latter could be estimated by $\beta_{in} \approx n_n V_{in} \sigma_{in}$ [31]. Here $\overline{k}_r$ and Δk_r denote the average and the width of ZF radial wavenumber respectively, ρ_i is the ion gyroradius which is inversely proportional to B, ν_{ii} is the ion-ion collision rate which changes as a function of plasma density n and ion temperature T_i, n_n is the density of neutral gas, V_{in} is the relative velocity between ion and neutral, and in our case assuming a fixed neutral background V_{in} could be estimated approximately equal to T_i, $\sigma_{in} \approx \sigma_L + \sigma_{CX}$ is the cross section of ion-neutral collision and could be simplified as a sum of just two parts related to elastic scattering (σ_L) and charge-exchange (σ_{CX}) processes respectively, with other collision processes ignored in such a low-energy environment [32].

In our experiments, both ion and neutral temperatures are estimated approximately to be room temperature and independent of B as well as r, subsequently resulting an almost constant cross section of ion-neutral collision. Moreover, density of neutral gas n_n also keeps constant with B and r, since the gas pressure is fixed and the ionization rate is even less than 0.01% in our discharges. Therefore, ion-neutral damping rate of ZF should be inferred approximately independent on both B and r, in sharp contrast to ion-ion damping rate of ZF, since not only that ρ_i is

dependent on B but also that ν_{ii} is dependent on ion density which varies with B as well as r. Therefore, according to above analysis, the experimentally observed weak dependence of ZF damping rate on both B and r implies that the predominant ZF damping mechanism should be the ion-neutral collision rather than the ion-ion collision. This conclusion should be reasonable, since our experiments are performed in such a particular background where plasma density is much smaller than neutral density by more than four orders of magnitude, resulting that ion-ion collision should probably be too weak to significantly effect ZF damping comparing with ion-neutral collision.

To ascertain this conclusion, values of β_{ii} and β_{in} are estimated via above-mentioned relations respectively using related plasma parameters as well as those of neutral gas at B = 940 G and r = 4 cm, then a quantitative comparison between these two ZF damping mechanism is thus made. Taking ion density $n_i = n_e \approx 1\times10^9 \mathrm{cm}^{-3}$, ion temperature $T_i \approx 0.03\mathrm{eV}$, A = 4 and Z = 1 for helium plasma, $\overline{k}_r \approx 0.15\mathrm{cm}^{-1}$ and $\Delta k_r \approx 1.1\mathrm{cm}^{-1}$ given by previous work[19], we thus estimate ion-ion collision damping rate of ZF as $\beta_{ii} \approx 0.07\mathrm{kHz}$. Considering density of neutral gas $n_n \approx 1.2\times10^{14} cm^{-3}$, then the estimated value of ZF ion-neutral collision damping rate is calculated roughly as $\beta_{in} \approx 36.2\mathrm{kHz}$ by referring to related researches in [32]. Therefore, we should definitely get the conclusion that ion-neutral collision should be identified as the predominant ZF damping mechanism, rather than ion-ion collision whose effect on ZF damping seems to be negligible in our case via the quantitative relation $\beta_{ii} / \beta_{in} < 0.002$. This conclusion is consistent with the above-described implication that ZF damping rate estimated via the scale parameterλhas the weak dependences on both axial magnetic field B and radial position r. This observation should also be in marked contrast to the cases performed in plasmas created by helicon source, where the typical ionization rate is generally dozens of percent and ion density is thus more than three orders of magnitude larger than that in our case, resulting in a much larger and probably predominant ion-ion damping rate of ZF.

However, in particular, there is also some discrepancy that ZF damping rate estimated via the relation of $\beta_{ZF} \approx 2\pi\lambda$ should be approximate 1 ~ 2 kHz, which is at least one order of magnitude smaller than the estimated ZF ion-neutral damping rate β_{in}. The reason for this disagreement is still unclear, and the authors speculate that here vin might be overestimated, resulted from the uncertainties of related parameters such as temperatures of ion and neutral gas as well as the value of ion-neutral cross section used in the estimation. Further studies concerning the topic of ZF damping via ion-neutral collision is planned to be performed in more detail via varying ion-neutral collision rate actively by means of changing the

pressure or type of the discharged gas.

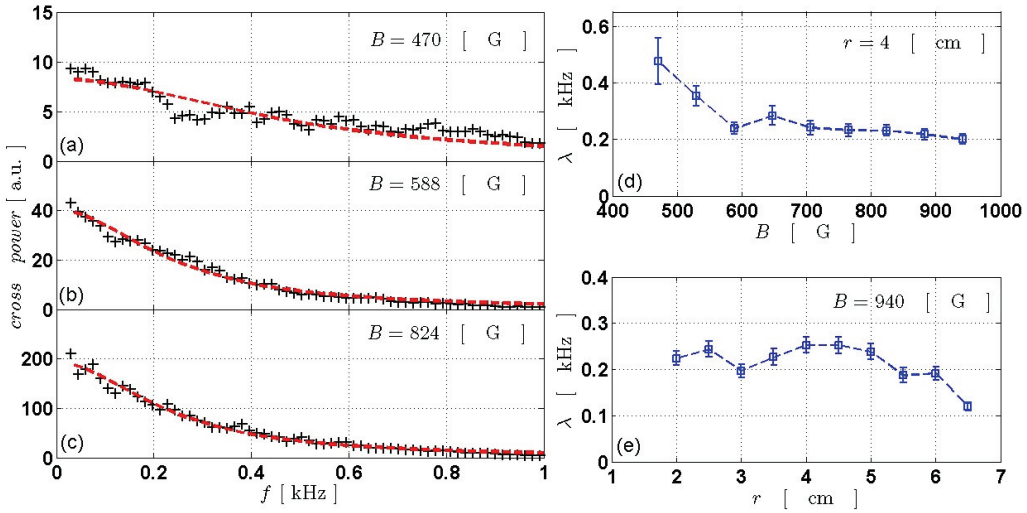

Figure 6. (a), (b), and (c) exhibit the cross-power spectra of $\tilde{\varphi}_f^{\theta=0}$ and $\tilde{\varphi}_f^{\theta=\pi}$ at different magnetic fields by black crosses, respectively, at r = 4 cm, and respective fitting curves of these spectra using Lorenzian distribution function are also displayed by red dash lines, (d), evolution of fitting parameter λ with B at fixed radial location r =4 cm, and (e), radial distribution of λ at fixed magnetic field B =940 G.

4. Summary and Discussion

In conclusion, in this article we focus on presenting some experimental studies on DWZF interactions, radial propagation and probable damping mechanism of ZF. And the highlights are summarized as follow:

(1), In the low-frequency region f<2kHz of the bispectra of potential fluctuations, prominent ZF-ZF nonlinear interaction is identified, suggesting the generation of second harmonics of ZF. Similar phenomenon was found in edge plasma of HT-7 tokamak [33], where nonlinear coupling between two kinetic geodesic acoustic modes(KGAMs) with different characteristic frequencies was observed in experiment, resulting in a second harmonic of GAM with its characteristic frequency equal to the difference frequency between those of the two fundamental GAMs. This process should be considered as a nonlinear mechanism of ZF saturation.

(2),The experimentally observed limit-cycle oscillation constituted by ZF and high-frequency potential fluctuation implies a ZF-DW turbulence interaction regulated by “predator-prey” model, in sharp contrast with the interaction between ZF and density fluctuation in this very frequency band where only the shearing effect of ZF works, leading to the approximately in-phase evolutions of both ZF and high-frequency density fluctuation in amplitude. These facts should well interpret the observed distinguishing evolutions of auto-power spectra of potential and density fluctuations with B.

(3), Radial propagations of both ZF phase and average burst of ZF energy are studied, both showing outward direction at any observing location of ZF.

(4), Ion-neutral collision is definitely identified as the primary ZF damping mechanism via not only qualitative analysis but also quantitative comparison, although there is still some inconsistency remained and potential physics is desired to be further revealed.

These systematic studies on ZF properties should provide deeper understanding of fundamental features of ZF as well as the underlying physics about common-accepted DW-ZF turbulence.

Acknowledgments

This work was partly supported by the JSPS-NRF-NSFC A3 Foresight Program in the field of Plasma Physics (NSFC No.11261140328).

REFERENCES

[1] Hasegawa A, Maclennan C G, and Kodama Y 1979 Phys. Fluids 22 2122

[2] Fujisawa A 2009 Nucl. Fusion 49 013001

[3] Kim Eun-jin, and Diamond P H 2003 Phys. Rev. Lett. 91 075001

[4] Manz P, Ramisch M, and Stroth U 2010 EPL 92 35001

[5] Estrada T, Happel T, Hidalgo C, E. Ascasibar and Blanco E 2010 Phys. Rev. E 82 056403

[6]Zweben S J, Maqueda R J, Hager R, Hallatschek K, KayeS M, Munsat T, Poli F M, Roquemore A L, Sechrest Y, and Stotler D P 2010 Phys. Plasma 17 102502

[7] Conway G D, Angioni C, Ryter F, Sauter P, Vicente J, and ASDEX Upgrade Team 2011 Phys. Rev. Lett. 106 065001

[8] Xu G S et al. 2011 Phys. Rev. Lett. 107 125001

[9] Schmitz L, Zeng L, Rhodes T L, Hillesheim J C, Doyle E J, Groebner R J, Peebles W A, Burrell K H, and Wang G 2012 Phys. Rev. Lett. 108 155002

[10] Diamond P H, Itoh S -I, Itoh K, and Hahm T S 2005 Plasma Phys. Control. Fusion 47 R35.

[11] Sokolov V, Wei X, and Sen A K 2007 Phys. Plasmas 14 055906.

[12] Sokolov V, and Sen A K 2010 Phys. Rev. Lett. 104 025002.

[13] Nagashima Y et al. 2008 Journal of the Physical Society of Japan 77 114501.

[14] Nagashima Y et al. 2009 Phys. Plasmas 16 020706.

[15] Xu M, Tynan G R, Holland C, Yan Z, Muller S H, and Yu J H 2009 Phys. Plasmas 16 042312.

[16] Yan Z, Tynan G R, Holland C, Xu M, M¨uller S H, and Yu J H 2010 Phys. Plasmas 17 012302.

[17] Yan Z, Tynan G R, Holland C, Xu M, M¨uller S H, and Yu J H 2010 Phys. Plasmas 17 032302.

[18] Xu M, Tynan G R,1, Diamond P H, Holland C, Yu J H, and Yan Z 2011 Phys. Rev. Lett. 107 055003.

[19] Chen R, Xie J L, Yu C X, Liu A D, Lan T, Zhang S B, Hu G H, Li H, and Liu W D 2011 Chin. Phys. Lett. 28 025202.

[20] Hendel H W, Chu T K, and Politzer P A 1968 Phys. Fluids 11 2426.

[21] Hasegawa A, Maclennan C G, and Kodama Y 1979 Phys. Fluids 22 2122.

[22] Kauschke U, and Schl¨uter H 1990 Plasma Phys. Control. Fusion 32 1149.

[23] Kauschke U 1993 Plasma Phys. Control. Fusion 35 93.

[24] Burin M J, Tynan G R, Antar G Y, Crocker N A, and Holland C 2005 Phys. Plasmas 12 052320.

[25] Lin Z, Hahm T S, Lee W W, Tang W M, and Diamond P H 1999 Phys. Rev. Lett. 83 3645.

[26] Hahm T S 2002 Plasma Phys. Control. Fusion 44 A87.

[27] Itoh K, Hallatschek K, Itoh S -I, Diamond P H, and Toda S 2005 Phys. Plasmas 12 062303.

[28] Kim Y C, and Powers E J 1979 IEEE Transactions on Plasma Science PS-7 No.2.

[29] Itoh K, Nagashima Y, Itoh S -I, Diamond P H, Fujisawa A, Yagi M and Fukuyama A 2005 Phys. Plasmas 12 102301.

[30] Townsend A A 1949 Aust. J. Sci. Res. 2 451.

[31] Holland C, Yu J H, James A, Nishijima D, Shimada M, Taheri N, and Tynan G N 2006 Phys. Rev. Lett. 96 195002.

[32]Lieberman M A et al., Principles of Plasma Discharge and Materials Processing, (New York, Wiley, 2005).

[33] D.F. Kong et al., 2013 submitted to Nucl. Fusion.

Effect of magnetic fluctuations on the confinement and dynamics of runaway electrons in the HT-7 Tokamak

R.J.Zhou, L.Q.Hu, E.Z.Li, M.Xu, G.Q.Zhong, L.Q.Xu, and S.Y.Lin

Institute of Plasma Physics, Chinese Academy of Sciences, Hefei 230031, China

Abstract: Experimental results in the HT-7 tokamak indicated significant losses of runaway electrons due to magnetic fluctuations, but the loss processes did not only rely on the fluctuation amplitude. Efficient radial runaway transport required that there were no more than small regions of the plasma volume in which there was very low transport of runaways. A radial runaway diffusion coefficient of $D_r \approx 10\ m^2 s^{-1}$ was derived for the loss processes, and diffusion coefficient near the resonant magnetic surfaces and shielding factor $\Upsilon = 0.8$ were deduced. Test particle equations were used to analyze the effect of magnetic fluctuations on runaway dynamics. It was found that the maximum energy that runaways can gain is very sensitive to the value of α_s. α_s = (0.28 – 0.33) was found for the loss processes in the experiment, and maximum runaway energy could be controlled in the range of E = (4 MeV – 6 MeV) in this case. Additionally, to control the maximum runaway energy below 5 MeV, the normalized electric field needed to be under a critical value D_α = 6.8, and the amplitude normalized magnetic fluctuations $\tilde{b}$ needed to be at least of the order of $\tilde{b} \approx 3 \times 10^{-5}$.

I. INTRODUCTION

This paper investigates the effect of magnetic fluctuations on runaway electrons in the HT-7 Tokamak. It is demonstrated that, under proper conditions, magnetic fluctuations result in significant radial runaway transport, which reduces the runaway population effectively. Moreover, the dynamics of runaway electrons can be affected in this process, and the maximum runaway energy will be restrained. The paper is organized as follows. Section II presents experimental results and analysis, Section III uses test particle equations to analyze the effect of magnetic fluctuations on runaway dynamics, and Section IV presents conclusions.

II. EXPERIMENTAL RESULTS AND ANALYSIS

A. The Effect on Runaway Confinement

A typical discharge that we are concerned with in the HT-7 tokamak is shown in Figure 1. Magnetic fluctuations emerged at about 0.487 s and their amplitude increased gradually as seen from the Mirnov signal. The RA signal was obtained from one of the BGO scintillators, which measured the thick-target Bremsstrahlung emission resulting from lost runaway electrons. At the onset of the emergence of the magnetic fluctuations, the RA signal began to increase, which indicated the loss of runaway electrons. These runaway electrons were generated by the loop voltage

and were confined well in the plasma before they were lost. The ECE signal also increased, resulting in a small ”spike” in the ECE signal. The RA signal then decreased to almost zero, and the ECE and FEB signals began to decrease also. Until about 0.492 s, the increase in the RA signal indicated that runaway electrons experienced another loss process. Both ECE and FEB signals slightly increased. The loss process then disappeared. This clearly demonstrated that the magnetic fluctuations were responsible for the loss processes of runaway electrons, but the loss processes did not only rely on the amplitude of the magnetic fluctuations.

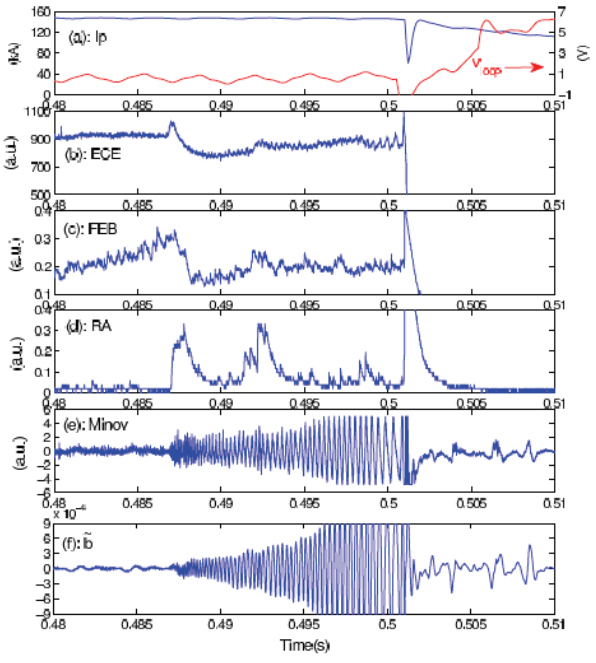

FIG. 1. Typical discharge in HT-7 tokamak. From the top to bottom the waveforms are: plasma current and loop voltage, ECE signal, FEB signal from fast electron bremsstrahlung, RA signal from thick-target bremsstrahlung emission caused by lost runaway electrons, Mirnov signal and the normalized amplitude of magnetic fluctuations $\tilde{b} = \tilde{B}_r/B_0$ deduced from Mirnov signal.

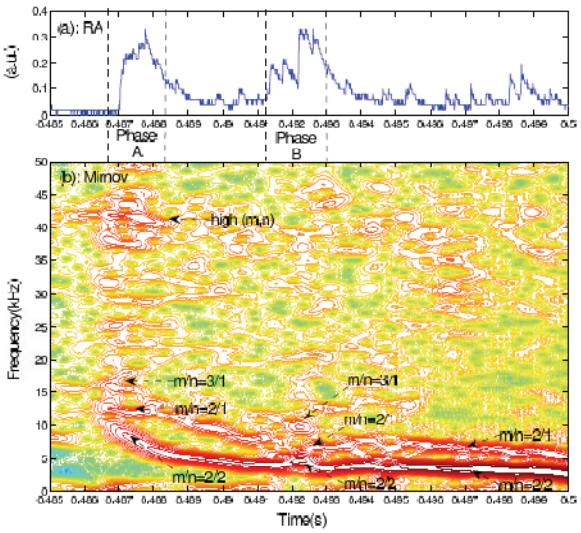

FIG. 2. RA signal from thick-target bremsstrahlung emission caused by lost runaway electrons (a), and the timefrequency spectrum of magnetic fluctuations from Mirnov signal with marked mode numbers (b). The two loss runaway processes are marked as phase A and phase B.

Figure 2 shows the time–frequency spectrum of the magnetic fluctuations combined with the RA signal on the same time scale. The two loss processes are marked as phases A and B in the figure. The MHD modes with low frequency ($f < 20$ kHz) were identified from Mirnov signals and are marked also. However, we cannot be sure about the MHD modes at high frequency ($f > 30$ kHz), which demoted as ”high (m,n)”. It is seen that the main MHD modes of the magnetic fluctuations were m/n = 2/2 and m/n = 2/1. These two modes exist throughout the whole period. Additionally, it is clear that other modes were

destabilized in phases A and B. In phase A, the mode with m/n = 3/1 and high (m,n) modes emerged. In phase B, only the mode with m/n = 3/1 emerged, and no clear high (m,n) modes are seen. The fact that runaway loss occurred in both and in only phases A and B indicates the important role of the m/n = 3/1 mode in the loss processes, and clearly high (m,n) modes did not play a key role. According to the analysis of this region [1], it is possible that stochastic magnetic fields resulted from modes overlapping in phases A and B. This indicates that, although the amplitude of the magnetic fluctuations was increasing, runaway electron losses only occurred when modes m/n = 2/2, m/n = 2/1 and m/n = 3/1 all existed, and perhaps stochastic magnetic fields existed because of the overlapping of modes.

This gives the general picture that efficient radial runaway transport requires there to be only small regions of low transport of runaways in the plasma volume. Therefore, mixed magnetic topology must be considered in experiments to analyze the effect of magnetic fluctuations on the runaway transport [2–4]. In the following, the fraction of the plasma volume with reduced transport is denoted α_s. It is seen that even small α_s may reduce the effect of magnetic fluctuations on runaway transport greatly. The total width of magnetic islands associated with modes m/n = 2/2, m/n = 2/1 and m/n = 3/1 can be deduced from the parameters of the magnetic fluctuations, and was no more than 3 cm in this experiment. However, the fraction of plasma volume of stochastic regions must be large in our experiment to result in significant losses of runaways. Additionally, in the simulation of G. Papp [5], the reason why RMPs are ineffective in expelling runaway electrons from the core so that they are lost at the edge of large devices such as the JET was explained as the minor radius being too large for RMPs to create a stochastic magnetic region in the core of the plasma. This also supports the experimental conclusion that efficient radial runaway transport requires that α_s is small. Considering the delay time of about 1ms from the emergence of the MHD modes to the peak of runaway losses in the RA signal, the runaway loss process requires a radial diffusion coefficient of approximately $D_r \approx 10\ \mathrm{m^2 s^{-1}}$. This is the average runaway diffusion coefficient over the plasma radius.

B. Deduce the diffusion coefficient near the resonant magnetic surfaces

In theory, the diffusion coefficient of runaway electrons, D_r, is thought to be governed by magnetic turbulence in the plasma. The runaway diffusion coefficient can be roughly written as [6–10]:

$$D_r = \Upsilon \pi q v_{\parallel} R \sum_{mn} \left|\tilde{b}_{mn}\right|^2 \delta\left(n - \frac{m}{q}\right) \qquad (1)$$

where $\delta(x)$ is the Dirac's delta function. The factor Υ, known as a shielding factor, describes the deviation of the runaway electron diffusion from the thermal electron diffusion due to the displacement of the runaway electron orbits from the magnetic surfaces (orbitaveraging) and their large gyro-radii

(gyro-averaging). The latter means that the runaway electrons do not experience the full strength of the magnetic turbulence present at the resonant surfaces [7–12]. The shielding effect depends on a few parameters of the particle orbit and its gyro-radius, and strongly depends on the width of the poloidal spectrum of magnetic turbulence [7, 12]. Additionally, it has been pointed out that the radial profiles of the diffusion coefficients of the chaotic transport have fractal-like structures with reduced diffusivity near the low-order rational drift surfaces thus forming transport barriers for the radial transport, and isolated MHD modes may even form effective local barriers to the turbulent transport of runaway electrons [11]. The diffusion coefficients are reduced by this correction [11, 13–15].

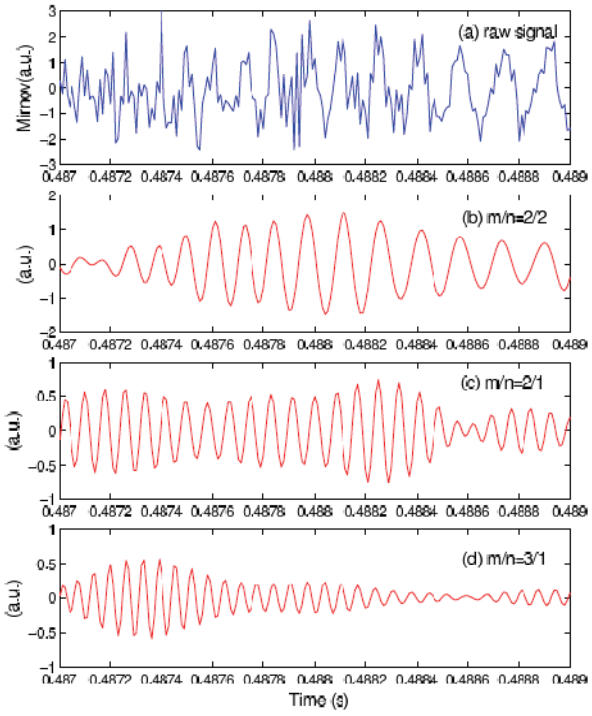

FIG. 3. The raw Mirnov signals (a) and the three extracted main modes by the FFT filtering method, with m/n=2/2 (b), m/n=2/1 (c) and m/n=3/1 (d).

According to Eq.1, to obtain the radial profile of the runaway diffusion coefficient, the radial profile of the normalized amplitude of magnetic fluctuations must be deduced. Here we only attempt to obtain this profile during phase A. First, the characteristics of the three main modes in the Mirnov signal were extracted by FFT filtering owing to their different frequencies. The results are shown in figure 3.

Then, according to the normalized amplitude of the magnetic fluctuations of the raw signal, which is $\tilde{b} = 1 \times 10^{-4}$ as seen in figure 1, the normalized amplitude of magnetic fluctuations of the extracted modes can be deduced as $\tilde{b}_{m/n=2/2} = 4 \times 10^{-5}$, $\tilde{b}_{m/n=2/1} = 2 \times 10^{-5}$ and $\tilde{b}_{m/n=3/1} = 1.2 \times 10^{-5}$.

Just considering the diffusion coefficient near the resonant magnetic surfaces r_{mn}, Eq.1 can be reduced to:

$$D_r(r = r_{mn}) = \Upsilon \pi q(r_{mn}) v_{\parallel} R \left|\tilde{b}_{mn}(r_{mn})\right|^2 \qquad (2)$$

Then, runaway diffusion coefficient near the resonant magnetic surfaces can be deduced if the shielding factor Υ is assumed to be constant. To estimate the value of the shielding factor Υ, the radial profile of diffusion coefficient was derived by fitting through the three coefficient value near the resonant magnetic surfaces, and assuming the coefficient value at the core and edge of plasma were zero. Then comparing with the experimental value of the average radial diffusion coefficient, $D_r \approx 10\ m^2 s^{-1}$, it gave the shielding factor $\Upsilon \approx 0.8$. The result is shown in figure 4. Although this estimation of the runaway diffusion coefficient and shielding factor is rough, it presents a reasonable

picture of the runaway diffusion. However, it have to be mentioned that if the detailed profile of the shielding factor ϒ is considered, the profile of the diffusion coefficient may be corrected significantly [11].

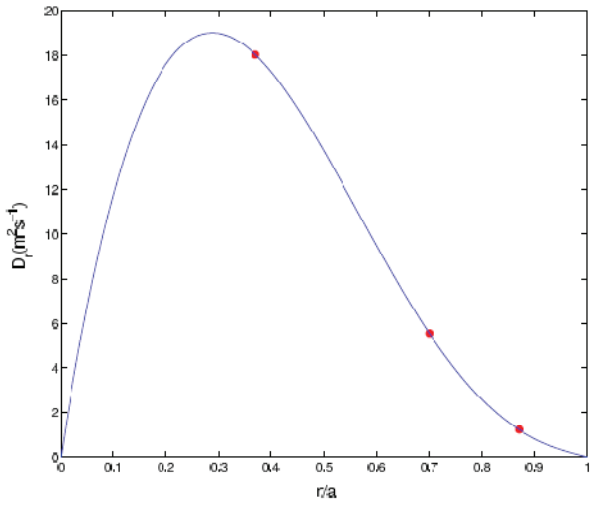

FIG. 4. Runaway diffusion coefficient near the resonant magnetic surfaces with q=1, q=2, q=3 (three red dots), and deduced radial profile of runaway diffusion coefficient by fitting through the coefficient value near the three resonant magnetic surfaces, and assuming the coefficient value at the core and edge of plasma were zero, with shielding factor ϒ = 0.8 (blue line).

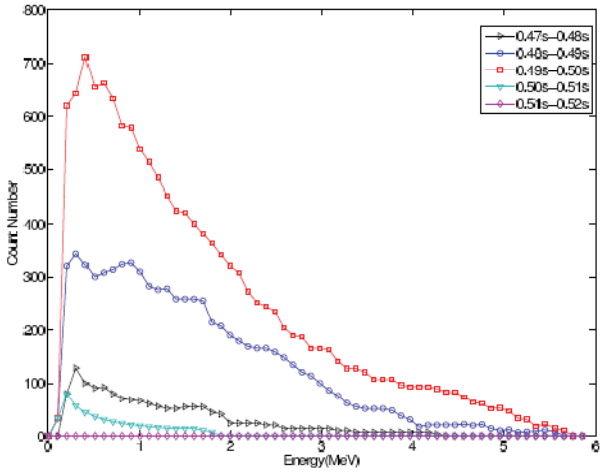

FIG. 5. Energy evolution of lost runaway electrons from one BOG scintillator detector. The time resolution of the energy spectrum is 10ms, and five spectrums is given from 0.47s to 0.52s. Phase A and phase B were in (0.48s-0.49s) and (0.49s-0.50s), respectively.

C. The Effect on Runaway Dynamics

To obtain the energy evolution of the lost runaway electrons, the energy spectrum of one BOG scintillator detector is shown in figure 5. The time resolution of the spectrum is 10 ms, and five spectrums are presented from 0.47 to 0.52 s. Phases A and B correspond to the periods 0.48C0.49 s and 0.49C0.50 s, respectively. It is seen that almost no runaway electrons were lost from plasma before phases A and B. Magnetic fluctuation in phase A resulted in great losses of runaway electrons. The energy of these lost runaway electrons was less than 6 MeV, and most of the energy was concentrated under 4 MeV. In phase B, many runaway electrons were also lost from the plasma; again the electrons had energy less than 6 MeV, but there was a much larger fraction in the energy range of 4 MeV < E < 6 MeV. The time interval between the two loss processes in phases A and B was less than 10 ms, and the acceleration of electrons was comparatively slow. If only considering the acceleration of runaway electrons due to the toroidal electric field, collision with plasma particles and synchrotron radiation losses, it takes at least 400 ms for fast electrons to become runaway electrons with

energy of 6 MeV. It is thus obvious that not all runaway electrons were from the plasma in phase A. The surviving runaway electrons were accelerated to higher energy, and lost in phase B. The fact that runaway electrons can survive in phase A with very poor magnetic surfaces indicates the good confinement of runaway electrons in the plasma. This coincides with the experimental results of TEXTOR [16]. In their experiment, a stochastic field formed after pellet injection through the plasma. Runaway electrons were then lost with an effective diffusion coefficient of $D_r \approx 300\ \mathrm{m^2 s^{-1}}$, and a beam of runaway electrons survived the turbulent phase.

III. RUNAWAY DYNAMICS VIA TEST PARTICLE EQUATIONS

To further analyze the effect of magnetic fluctuations on the dynamics of runaway electrons in phases A and B, test particle equations are presented in this section. Although kinetic theory should be used in a detailed description of runaway dynamics [17–20], as we have mentioned, the collision of runaway electrons with other plasma particles is very weak owing to the high velocities. Moreover, since the runaway population is a very small fraction of the electrons in the plasma, runaway electrons can be regarded as test particles.

The test particle equations describing the motion of a runaway electron in momentum space were derived from the kinetic Fokker–Planck equation, taking into account the effect of acceleration due to the toroidal electric field, collision with plasma particles, synchrotron radiation losses, and diffusion associated with fluctuations [4, 21].

The essential feature of this set of test-particle equations is that two singular points in momentum space can be obtained by solving the equations: a saddle point (γ_c) that gives the critical energy for runaway generation and a stable focus (γ_l) that gives the energy limit for the generated runaway electrons. An analytical relation between the two points and the normalized electric field can be obtained from the test-particle equations [4]:

$$D = \frac{\gamma_s^2}{\cos\theta_s(\gamma_s^2-1)} \times \left\{1 + F_{gy}\frac{(\gamma_s^2-1)^{\frac{3}{2}}}{\gamma_s}\sin^2\theta_s + F_{gc}\frac{(\gamma_s^2-1)^{\frac{5}{2}}}{\gamma_s}\right\} + \frac{(\gamma_s^2-1)^{1/2}}{\cos\theta_s \tau_{dr}} \quad (3)$$

Here $\tau = v_r t$ is the time multiplied by the collision frequency, where $v_r = n_e e^4 \ln\Lambda / 4\pi\varepsilon_0^2 m_e^2 c^3$; $D = E_\parallel / E_R$ is the normalized electric field, where $E_\parallel$ is the toroidal electric field and $E_R = (kT_e/m_e c^2)\, E_D$, and $E_D = n_e e^3 \ln\Lambda / 4\pi\varepsilon_0^2 kT_e$ is the Dreicer field; γ is the relativistic gamma factor; F_{gc} and F_{gy} are parameters describing the two contributions to the synchrotron radiation losses (the guiding center motion and the electron gyromotion, respectively), where $F_{gc} = F_{gy}(m_e c / eB_0 R_0)^2$ and $F_{gy} = 2\epsilon_0 B_0^2 / 3 n_e \ln\Lambda m_e$; $\tau_{dr} = v_r \tau_d$ is the normalized diffusion time, where $\tau_d = a^2/(j_0^2 D_r)$ is the characteristic radial diffusion time; a is the minor radius; j_0 is the first zero of the Bessel function J_0; and D_r is the effective radial diffusion coefficient that describes the diffusion losses of runaway electrons resulting from the fluctuations. cos θ_s is the cosine of the pitch angle

at a singular point, which can be determined from the solution to the algebraic equation:

$$a_{dr}\cos^7\theta_s + b_{dr}\cos^6\theta_s + c_{dr}\cos^5\theta_s + d_{dr}\cos^4\theta_s + e_{dr}\cos^3\theta_s + f_{dr}\cos^2\theta_s + g_{dr}\cos\theta_s + h_{dr} = 0 \quad (4)$$

The coefficients a_{dr} to h_{dr} can be found in the Appendix of Ref. (41).

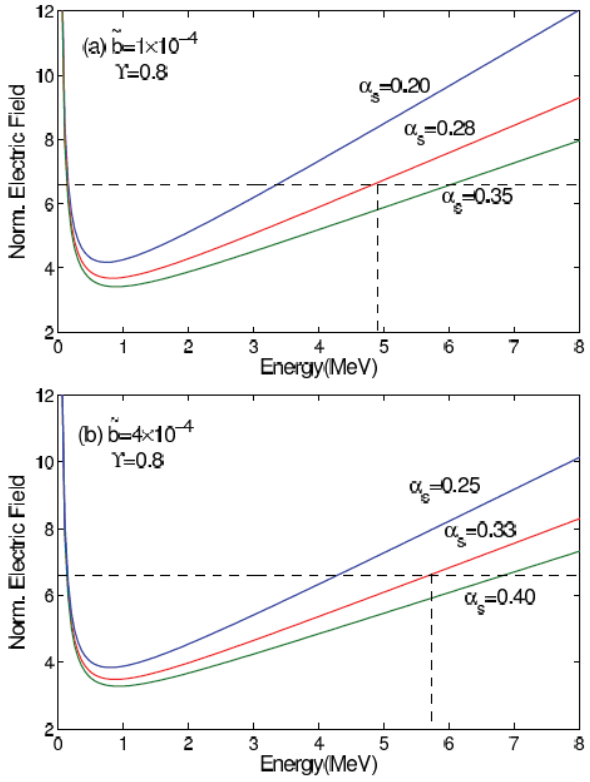

FIG. 6. The relation between normalized electric field and the runaway energy at the singular points. Experimental condition in phase A is considered in figure 10(a), with normalized magnetic fluctuations amplitude $\tilde{b} = 1 \times 10^{-4}$ and three potential value of α_s are calculated for comparing. Condition in phase B is considered in figure 10(b), with $\tilde{b} = 1 \times 10^{-4}$.

Considering both corrections for the runaway diffusion coefficient, orbit-averaging and gyro-averaging effects and the mixed magnetic topology, the effective radial diffusion coefficient D_r is constructed as [3, 4]:

$$D_r = \Upsilon \frac{D_e}{\upsilon_\parallel} \frac{D_e + 2(D_m D_e)^{1/2}\cos\delta\upsilon_\parallel + D_m\upsilon_\parallel^2}{D_e + \alpha_s[2(D_m D_e)^{\frac{1}{2}}\cos\delta\upsilon_\parallel + D_m\upsilon_\parallel^2]} \quad (5)$$

where D_m and D_e are the magnetic field line diffusion coefficient and electrostatic diffusion coefficient respectively; $D_m = \pi q R \tilde{b}^2$, $D_e = \pi q R \upsilon_E^2$ and $\upsilon_E = \tilde{E}/B_0$ is the drift electron velocity induced by the fluctuating poloidal electric field $\tilde{E}$. This is the average effective radial runaway diffusion coefficient. The normalized diffusion time $\tau_{dr} = \upsilon_r \tau_d = \upsilon_r a^2/(j_0^2 D_r)$ can then be derived.

In this experiment, the normalized electric field was D = 6.6 without great change in the whole period. The two contributions of synchrotron radiation losses are estimated as $F_{gc} \approx 5.75 \times 10^{-8}$ and $F_{gy} \approx 0.11$. The normalized amplitude of magnetic fluctuations is $\tilde{b} = 1 \times 10^{-4}$ in phase A and $\tilde{b} = 4 \times 10^{-4}$ in phase B. The drift electron velocity is taken as $\upsilon_E = 10^3\, m/s$, and the shielding factor ϒ= 0.8. The two singular point energies can then be obtained as the two roots when solving Eq. 3. The results are shown in figure 6.

Figure 6(a) considers the experimental conditions for phase A, in which $\tilde{b} = 1 \times 10^{-4}$, and three potential values of α_s were calculated for comparison. The crossing-points between the fixed D = 6.6 and the curves in the low-energy region give the critical energy for runaway generation (γ_c). In all three situations, the critical energy was approximately 150 keV. In the high-energy region, the crossing-point gave the energy

limit for the generated runaway electrons (γ_l), which changed greatly in the three situations. For the lower value of α_s, which corresponds to a large fraction of plasma volume in the stochastic magnetic region, the maximum runaway energy can be controlled to a lower level. $\gamma_l \rightarrow$ 6 MeV for α_s = 0.35 and $\gamma_l \rightarrow$ 3.5 MeV for α_s = 0.2. Therefore, the maximum runaway energy is very sensitive to α_s. In phase A, the energy of most runaway electrons was concentrated under 5 MeV, which coincides mostly with the situations of α_s = 0.28. The conditions for phase B are considered in figure 6(b). In the figure, the critical energy for runaway generation (γ_c) is about 150 keV, which is almost the same as the value in phase A. In terms of the maximum energy that a runaway electron can gain, α_s = 0.33, $\gamma_l \rightarrow$ 5.8MeV fits best in this phase. Comparing the results in figure 6(a) and figure 6(b), it is seen that for the same value of α_s, almost the same maximum runaway energy is obtained for different amplitudes of the normalized magnetic fluctuation $\tilde{b}$. This indicates that the maximum runaway energy is much more sensitive to α_s than the amplitude of normalized magnetic fluctuations $\tilde{b}$. This coincides with the experimental results presented above.

Although the maximum runaway energy is much more sensitive to the fixed value of α_s, the amplitude of the normalized magnetic fluctuations $\tilde{b}$ plays an important role also. Given α_s, the minimum level of magnetic fluctuations $\tilde{b}_{min}$ needed to keep the runaway energy below a value γ_l can be derived from Eq.3 [4]:

$$\tilde{b}_{min}^2 = \frac{a^2 \upsilon_r \gamma_l^2}{\Upsilon j_0^2 L_{\parallel} c \tau_{de} (\gamma_l^2 - 1) \cos^2\theta_l} \frac{\tau_{de} \cos\theta_l B_{min} - \gamma_l}{\gamma_l - \alpha_s \tau_{de} \cos\theta_l B_{min}} \quad (6)$$

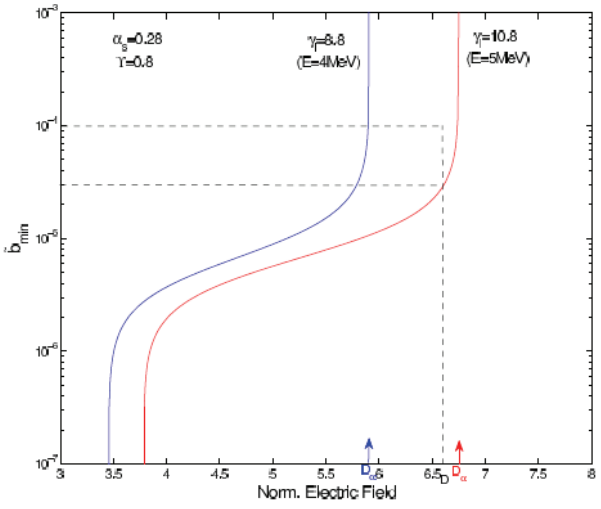

FIG. 7. The relation between minimum level of magnetic fluctuations and normalized electric field. α_s = 0.28 is taken as the situation in phase A, and two energy limits, γ_l = 8.8($E \approx$ 4MeV) and γ_l = 10.8($E \approx$ 5MeV) are considered. D_α denotes the critical normalized electric field beyond which runaway energy can't be controlled below the value γ_l even with the largest levels of $\tilde{b}$.

Taking into account the parameter α_s = 0.28 in phase A in the experiment and considering the two energy limits, γ_l = 8.8($E \approx$ 4 MeV) and γ_l = 10.8($E \approx$ 5 MeV), the relation between the minimum level of magnetic fluctuations and normalized electric field is obtained as shown in figure 7. First, it is seen that for given α_s, there is a critical normalized electric field D_α beyond which runaway energy cannot be controlled below the value γ_l even with the largest level of $\tilde{b}$. To control the runaway energy below 4 MeV, the normalized electric field should be under 5.9. Additionally, to control the runaway energy below 5 MeV, the normalized electric

field should be below approximately 6.8. For the conditions in phase A, D = 6.6 and $\tilde{b} = 1 \times 10^{-4}$, the maximum runaway energy can be controlled in the range of 4 MeV < E < 5 MeV. Additionally, to control the runaway energy below 5 MeV, the normalized amplitude of magnetic fluctuations $\tilde{b}$ should be at least on the order of $\tilde{b} \approx 3 \times 10^{-5}$.

Therefore, in general, the electric field D, the normalized amplitude of magnetic fluctuations $\tilde{b}$ and the fraction of plasma volume of good magnetic surfaces α_s can all affect the dynamics of runaway electrons. D is the main energy source of runaways. In many runaway mitigation experiments, the key idea is decreasing the electric field. The fluctuation level $\tilde{b}$ strongly affects both the dynamics and transport of runaways. However, unless $\alpha_s \rightarrow 0$, the effect of magnetic fluctuations on runaway transport will decrease greatly. Both the transport and dynamics of runaways are highly sensitivity to α_s.

IV. CONCLUSIONS

The nature of runaway electrons is such that the transport and dynamics of the electrons are strongly affected by magnetic fluctuations in the plasma. The operational region of the HT-7 tokamak in which plasma has large magnetic fluctuations has been investigated in former experiments, and it was found that large stochastic magnetic field regions were formed by the overlapping of modes. In this paper, we further investigated the effect of the magnetic fluctuations on runaway electrons in this operational region.

Experiment results indicated significant losses of runaway electrons due to magnetic fluctuations, but the loss processes did not only rely on the amplitude of the magnetic fluctuations. Although the amplitude of magnetic fluctuations increased, runaway electrons losses only occurred when modes m/n = 2/2, m/n = 2/1 and m/n =3/1 all existed in plasma, which made it easier for runaway electrons to be transported from the plasma center to the outside region and then lost. When only modes m/n = 2/2 and m/n = 2/1 existed, there were no significant losses. This indicates that efficient radial runaway transport requires there to be no more than small regions of the whole plasma volume in which there is very low transport of runaways. The diffusion coefficient of radial runaways $D_r \approx 10\ m^2 s^{-1}$ was derived for the loss processes, and the radial profile of the diffusion coefficient was deduced with the shielding factor Υ = 0.8. Additionally, it was found that only some of the runaway electrons were lost in the loss processes, and those that survived runaways were accelerated to higher energy. This indicates the good confinement of runaway electrons in plasma.

Test-particle equations were used to analyze the effect of magnetic fluctuations on runaway dynamics. It was found that the maximum energy that runaways can gain is very sensitive to the value of α_s. For a lower value of α_s, the maximum runaway energy can be controlled at a lower level. α_s = (0.28 – 0.33) was found for the loss processes in the experiment, and the

maximum energy of runaways could be controlled in the range of E = (4 MeV – 6 MeV) in this case. Additionally, to control the maximum runaway energy, the electric field must below a critical value D_α. In the experiment, to control the runaway energy below 5 MeV, the normalized electric field needed to be under 6.8, and the normalized amplitude of magnetic fluctuations $\tilde{b}$ needed to be at least of the order of $\tilde{b} \approx 3 \times 10^{-5}$.

ACKNOWLEDGMENTS

This work was supported partially by the JSPS-NRFNSFC A3 Foresight Program in the field of Plasma Physics (NSFC No.11261140328), by the National Nature Science Foundation of China through grant number 10935004, 11205197 and was partially supported by the CAS Key International S&T Cooperation Project collaboration with grant number GJHZ1123.

[1] E. Li, L. Hu, V. Igochine, O. Dumbrajs, and K. Chen, Plasma Phys. Control. Fusion **53**, 085019 (2011).

[2] C. C. Hegna and J. D. Callen, Phys. Fluids B **4**, 1855 (1992).

[3] C. C. Hegna and J. D. Callen, Physics of Fluids B **5**, 1804 (1993).

[4] J. R. Martin-Solis, R. Sanchez, and B. Esposito, Phys. Plasmas **6**, 3925 (1999).

[5] G. Papp, M. Drevlak, T. Fulop, and P. Helander, Nucl. Fusion **51**, 043004 (2011).

[6] A. B. Rechester and M. N. Rosenbluth, Phys. Rev. Lett. **40**, 38 (1978).

[7] T. Hauff and F. Jenko, Phys. Plasmas **16**, 102308 (2009).

[8] J. R. Myra and P. J. Catto, Phys. Fluids B **4**, 176 (1992).

[9] J. R. Myra, P. J. Catto, H. E. Mynick, and R. E. Duvall, Phys. Fluids B **5**, 1160 (1993).

[10] J. R. Myra, P. J. Catto, A. J. Wootton, R. D. Bengtson, and P. W. Wang, Phys. Fluids B **4**, 2092 (1992).

[11] S. S. Abdullaev, K. H. Finken, and M. Forster, Phys. Plasmas **19**, 072502 (2012).

[12] S. S. Abdullaev, K. H. Finken, T. Kudyakov, and M. Lehnen, Contrib. Plasma Phys. **50**, 929 (2010).

[13] M. Forster, S. S. Abdullaev, K. H. Finken, T. Kudyakov, M. Lehnen, G. Sewell, O. Willi, and Y. Xu, Nucl. Fusion **52**, 083016 (2012).

[14] A. Wingen, S. S. Abdullaev, K. H. Finken, M. Jakubowski, and K. H. Spatschek, Nucl. Fusion **46**, 941 (2006).

[15] K. H. Finken, S. S. Abdullaev, M. W. Jakubowski, R. Jaspers, M. Lehnen, R. Schlickeiser, K. H. Spatschek, A. Wingen, and R. Wolf, Nucl. Fusion **47**, 91 (2007).

[16] R. Jaspers, N. J. L. Cardozo, K. H. Finken, B. C. Schokker, G. Mank, G. Fuchs, and F. C. Schuller, Phys. Rev. Lett. **72**, 4093 (1994).

[17] A. V. Gurevich, K. P. Zybin, and Y. N. Istomin, Nucl. Fusion **27**, 453 (1987).

[18] M. N. Rosenbluth and S. V. Putvinski, Nucl.

Fusion **37**, 1355 (1997).

[19] P. Helander, L. G. Eriksson, and F. Andersson, Phys. Plasmas **7**, 4106 (2000).

[20] P. Helander, L. G. Eriksson, and F. Andersson, Plasma Phys. Control. Fusion **44**, B247 (2002).

[21] J. R. Martin-Solis, J. D. Alvarez, R. Sanchez, and B. Esposito, Phys. Plasmas **5**, 2370 (1998).

Experimental Study of Long-lived Saturated Mode in EAST ELM-free H mode Sawtoothing Plasma

Liqing Xu, Liqun Hu, Kaiyun Chen, Erzhong Li, Youcai Shen, Jizong Zhang, Ruijie Zhou, Ming Xu and EAST team

Institute of Plasma Physics, Chinese Academy of Sciences, Hefei 230031, China

Abstract: Two types of long-lived saturated impurity ions induced modes (LLMs) including ideal-like kink mode which damp before large sawtooth crash, termed sawtooth-free LLMs (SF-LLMs) and complex LLMs (C-LLMs, similar with LLMs reported in C-Mod) which coexistence with compound sawtooth and final damping by sawtooth crash were observed in EAST ELM-free H mode sawtoothing plasma. The strong coupling of C-LLMs and 2/1 tearing mode (TM) can trigger neo-classic tearing mode (NTM) after sawtooth crash. The frequencies of LLMs are related to the plasma toroidal rotation. Finally, discussion about the role of lower hybrid current drive (LHCD) driven current to large compound sawtooth and the role of fast particles produced by LHCD to the excitation of LLMs were also given in this paper.

1. Intoduction

Tokamak plasmas are observed to be highly sensitive to a variety of large-scale instabilities which can degrade the plasma confinement. The LLM is a long debt large-scale instability found at Joint European Tours [1] in 1987. A second type, the accumulation of impurities induced LLMs is also observed in C-Mod [2, 3] and EAST [4]. In this paper, we report the formation of impurity LLMs and dynamic of LLMs in EAST sawtoothing plasma.

2. Experiment results

As shown in figure1, the impurity LLMs can persists for a surprisingly long time, shown by surviving tens to hundreds of sawtooth cycles. And the LLMs located inside q=1 region.

As the typical features of impurity LLMs, it is commonly found that on-axis peaking of radiation profile before the formation of LLMs, as shown in Fig.2 (b). And good agreement between LLMs and impurity emissions are also observed in EAST, shown in Fig.2 (a, c). Moreover, it is also found the intensity of impurity profile become flat in the core region during LLMs process, as shown in Fig.2 (d). In addition, the electron density oscillation produced by impurity LLMs is also detected by HCN interferometer (Fig.2 a).

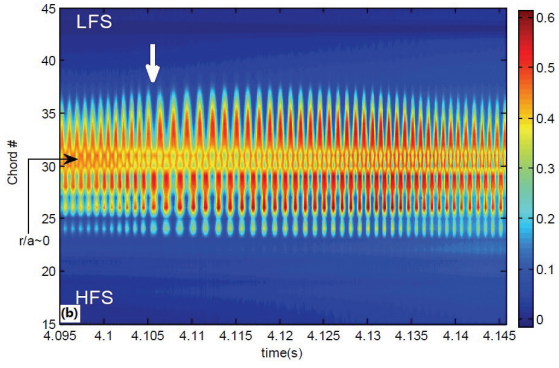

Fig.1 SXR brightness time history profiles of the impurity LLMs in EAST. The white arrow indicate the timepoint of sawtooth crash. LFS –Lower Feld Side, HFS-Higher Field Side.

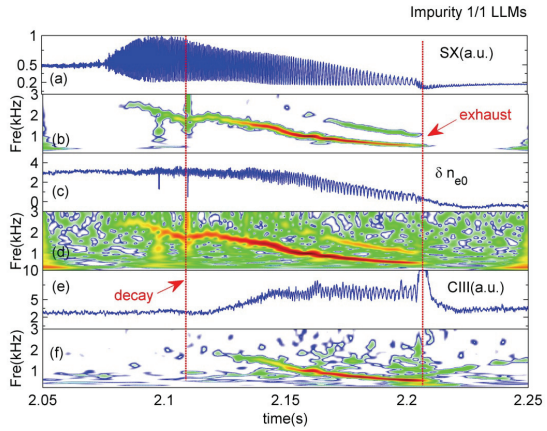

(a)

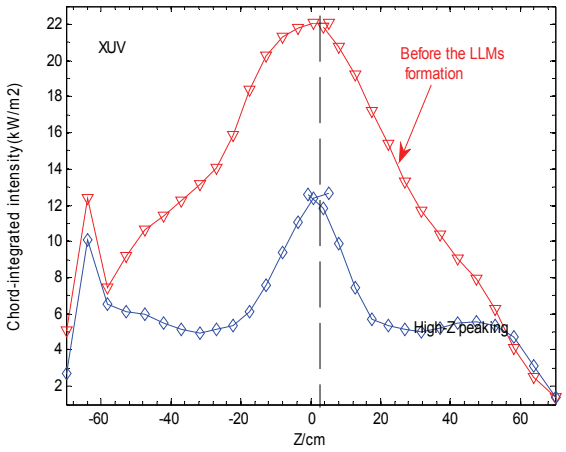

(b)

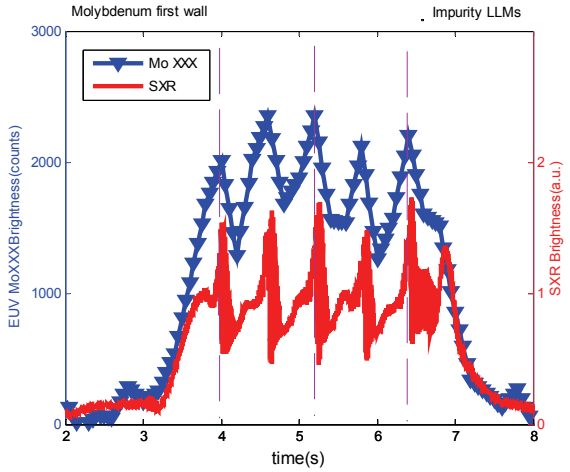

(c)

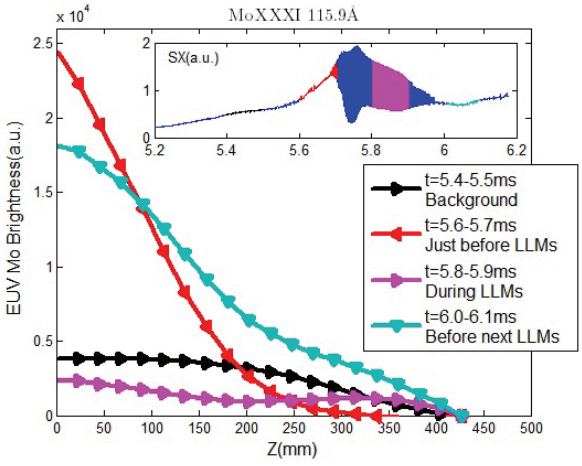

(d)

Fig.2 Features of LLMs. (a) Typical Carbon induced LLMs in EAST. (b) on-axis peaking of radiation profile before the formation of LLMs. (c). Good agreement between LLMs and MO emissions. MOXXX emissions from EUV spectrometer. (d) Time evolution of MO emission profile.

The LLMs always coexist with compound sawtooth instability in EAST ELM-free H mode plasma. Based on the difference of compound sawtooth behavior, two types of LLMs are classified in EAST. One is SF-LLMs, ideal-like kink mode like which damp before larger sawtooth crash, as shown in Fig.3 (a). The other one is C-LLMs which coexistence with compound sawtooth and final damping by sawtooth crash, as shown in Fig.3 (b). An interesting result shown in Fig.3 (b) is that the strong coupling of C-LLMs and 2/1 TMs can lead a forced magnetic reconnection process during ST crash [5], hence, give a seed island for 2/1 NTMs.

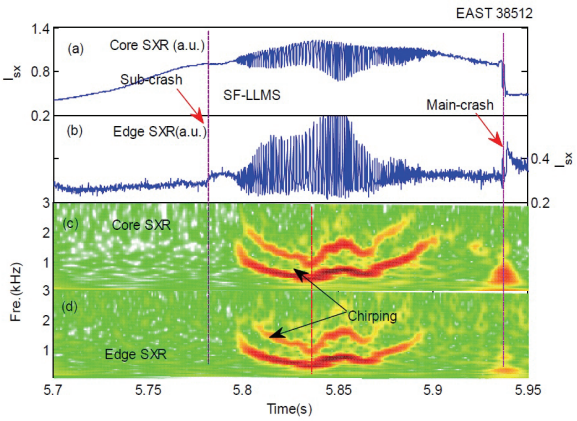

(a)

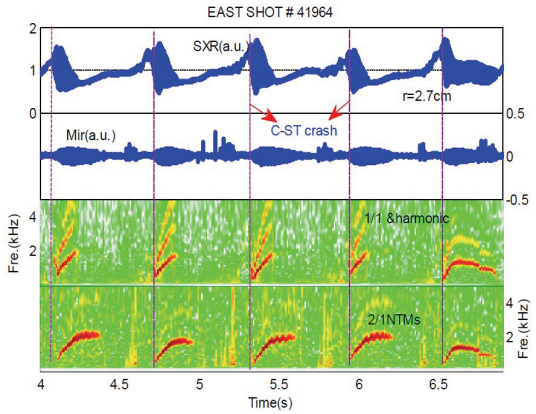

(b)

Fig.3 Two kinds of LLMs in EAST. (a) SF-LLMs, frequency chirping is clear in SF-LLMs. (b) C-LLMs, 2/1 NTMs triggered by strong mode coupling under sawtooth crash.

In EAST, we also find the frequencies of LLMs are related to the toroidal rotation, as shown in Fig.4. And same phenomenon is reported in TCV, the rotation of sawtooth precursor is corresponding to plasma toroidal rotation [6].

Finally, the loss of supra-thermal electrons due to LLMs is also visible in EAST, as shown in Fig.5. The discussion of the interplay between supra-thermal electrons and LLMs is beyond this paper.

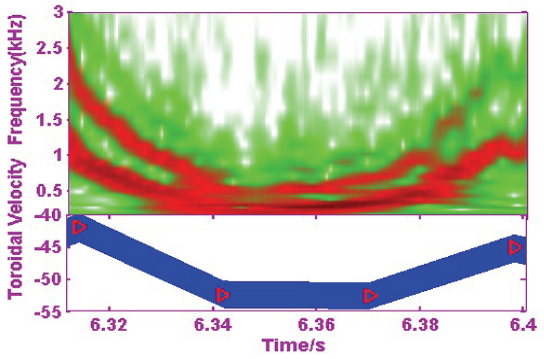

Fig.4 The rotation of LLMs related to the plasma toroidal rotation. The plasma rotation data from XCS.

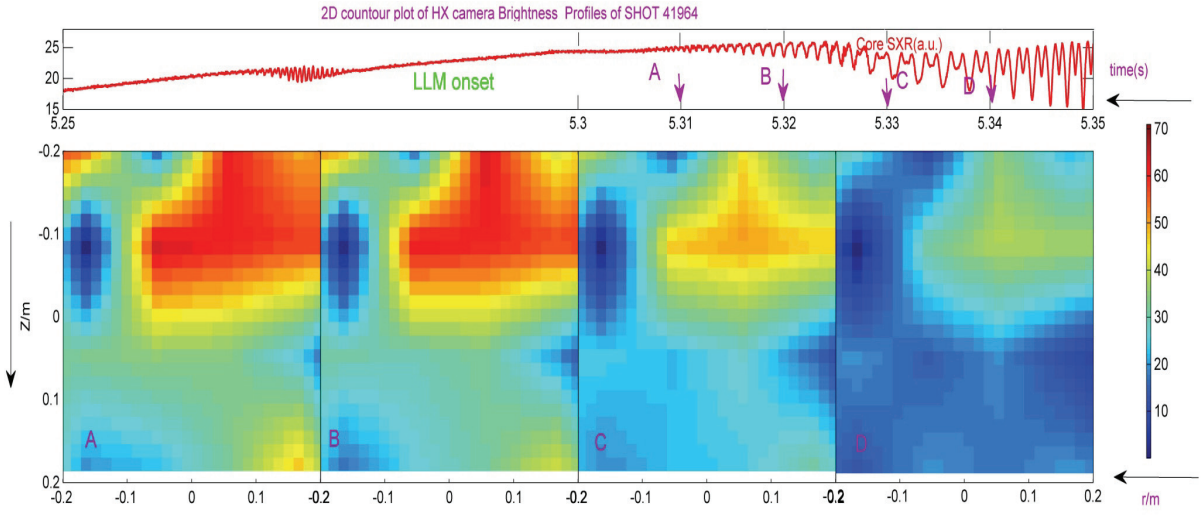

Fig.5 Large supra-thermal electrons loss during LLMs process.

3. Conclusions

In summary, transient bursts of LLMs are frequently observed in EAST ELM-free intermittent H mode plasma. In consideration of the complex relationship between compound sawtooth and LLMs, two types of LLMs are classified. Many questions regarding LLMs formation, long-term survival, interaction with other instabilities (with EHOs, electron fishbone) remain.

The role of strong $E \times B$ flow to the excitation of LLMs, and the q profile (magnetic shear) to the stability of LLMs is still need to further study.

Acknowledgments

This work was partially supported by the JSPS-NRF-NSFCA3 Foresight Program in the field of Plasma Physics (NSFC No 11261140328). This work was partially supported by the National Nature Science Foundation of China through grant numbers 10935004, 11205007 and was partially supported by the CAS Key International S&T Cooperation Project collaboration with grant number GJHZ1123.

References

[1] Weller A.et al Phys.Rev.Lett. 59(1987) 2303

[2] L.Delgado-Aparicio et al. Nucl. Fusion 53(2013) 043019

[3] L.Delgado-Aparicio et al. Phys.Rev.Lett. 110 (2013)065006

[4] Liqing Xu et al Plasma Phys.Control.Fusion 55 (2013)032001

[5] Q.Yu et al Nucl. Fusion 52 (2012)063020

[6] A.Bortolon et al Phys.Rev.Lett. 97(2006)235003

[7] L. J. Zheng et al. Phys. Plasmas 20, 012501 (2013)

Upgrade of ICRF heating system on EAST

CHEN Gen, ZHAO Yanpin, MAO Yuzhou, ICRF team

Institute of Plasma Physics, Chinese Academy of Sciences, Hefei 230031, China

Abstract: ICRF (Ion Cyclotron Range of Frequency) heating is an essential heating and current drive tool on EAST (Experimental Advanced Superconducting Tokomak). The high-power steady-state transmitters were designed as a part of research and development of ICRF heating system which aimed at output power of 1.5 MW for 1000 s in a frequency range of 25 to 70 MHz. There are 3 stage power amplifiers for each transmitter. Tube TH525A and TH535 were chosen for drive power amplifier (DPA) and final power amplifier (FPA), respectively. The power supply system of DPA and FPA were upgraded by using reliable PSM high voltage sources, whose response time is less than 5 μs. The ICRF system, which consists of 8 transmitters, will give out more than 10 MW total output power in the future. Four of them have been already fabricated, and another four are under construction. Three liquid stub tuners are used for impedance matching between antennas and transmitters, which can be only tuned shot to shot. There are two fast wave heating antennas which are assembled at I port and B port on EAST. Several projects are in progress including fast response impedance matching, distributed data acquisition and control system and so on for EAST ICRF heating system.

Keywords: EAST; ICRF; transmitter;

PACS: 52.50.Qt

1. Introduction

Ion Cyclotron Range of Frequency (ICRF) heating is one of the most successful heating and current drive tools, especially for Tokomak plasmas, by using radio frequency (RF) wave with tens of MHz. A RF source for ICRF heating has a long development history and great advancements have been made so far, such as JT-60U [1], Tore Supra [2], and C-Mod [3], KSTAR [4].

Ion heating experiments have been carried out in IPP for many years, and good results were observed [5] [6] [7] [8]. Though, many efforts have been made [9] since 1996 for these research works, it is not fit for the requirements of ICRF heating for EAST. The high-power steady-state transmitters were designed as a part of research and development of ICRF heating system which aimed at output power of 1.5 MW for 1000 s in a frequency range of 25 to 70 MHz in a CW (Continuous Wave) mode of operation. Recently the ICRF system has been upgraded for several aspects, and it will be illustrated from three important parts: transmitter, antenna and matching network.

2. Transmitter

In order to attain 1.5MW of output power, the ICRF

transmitter consists of three stage amplifiers [10]. An amplitude-modulated signal generator is used as a master oscillator to drive a 5kW solid state amplifier, which in turn drives two tuned tetrode stages. The tubes for the DPA (Driver Power Amplifier) and FPA (Final Power Amplifier) are Thales TH525 and TH535, respectively. The RF signal from 5 kW solid-state amplifier is fed to DPA, which has a 100kW output power and nearly the same input and output cavity structure as FPA, as shown in Fig. 1.

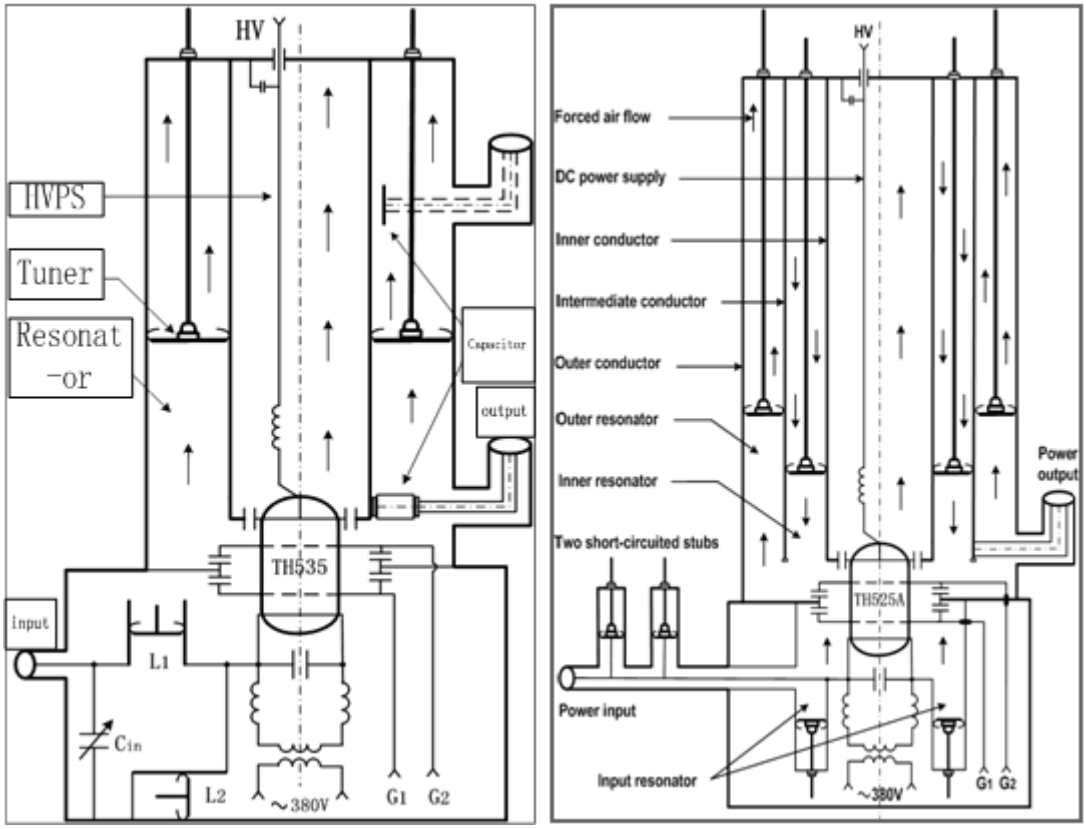

Fig. 1 Schematic diagram of DPA and FPA.

To ensure stable and reliable operation, a grounded grid configuration was chosen to provide the essential electrostatic shielding between input and output. The screen grid, which is connected to RF ground, prevents capacitive feedback from anode to the control grid, thus minimizes self oscillation of the amplifier. The whole impedance matching circuit is divided into two important parts, i.e. input circuit and output circuit.

For DPA, to realize a continuous change in parameter value and a compact structure, each component of the input circuit of the DPA was designed to consist of strip line except the input vacuum capacitance. The input stage is a pi-type matching circuit, which consists of a variable coupling capacitance, a variable-length strip line inductance, and a section of variable-length strip line with a characteristic impedance of 45Ω. The model TH535 tetrode operating in class B was chosen for the DPA, which is capable of delivery of a rf output power of 100 kW to drive the FPA. The output circuit of the DPA consists of a coupling capacitance and an

output cavity. A square single coaxial cavity in cross section was adopted as the output cavity for tuning, variable from 30 to 280 cm in length. A vacuum variable capacitance was selected for coupling rf power to the FPA, changing from 10 to 250 pF. This kind of structure is often employed in broadcasting amplifiers.

For FPA, because of the grounded-grid configuration, the input impedance of the FPA is seriously dependent on operation conditions, in particular, anode current. Different output power levels will result in big changes in input impedance, so that matching status between the DPA and the FPA should be adjusted carefully during testing of the amplifiers. The high reflected power fraction may cause damage of amplifier components because of over-current and/or high VSWR or arcing inside the tube. Because of the DPA output impedance of 50Ω, a 6-in. coaxial transmission line with characteristic impedance of 50Ωwas employed as the DPA output power delivery to drive the FPA. To achieve a perfect matching state between FPA and DPA, the input circuit, which is composed of an input resonator, a double-stub tuner, and a U-link, is used as an impedance matching network between the DPA and the FPA to match the input impedance of the FPA to 50Ω. The stub tuner is a section of transmission line short-circuited at one end, i.e., a choke-type tuner, and is movable from 0 to 200 cm in length. The U-link is a section of transmission line variable in length that is shaped like a letter U. As usual, the input resonator used as the preparing matching tuner is fixed during the tests. As is known, there is a forbidden range of load impedances that cannot be matched with a double-stub tuner matching system. To eliminate the forbidden range, the changeable U-link is used to change the length between the stub tuners to cover the whole working frequency range, as shown in Fig. 2.

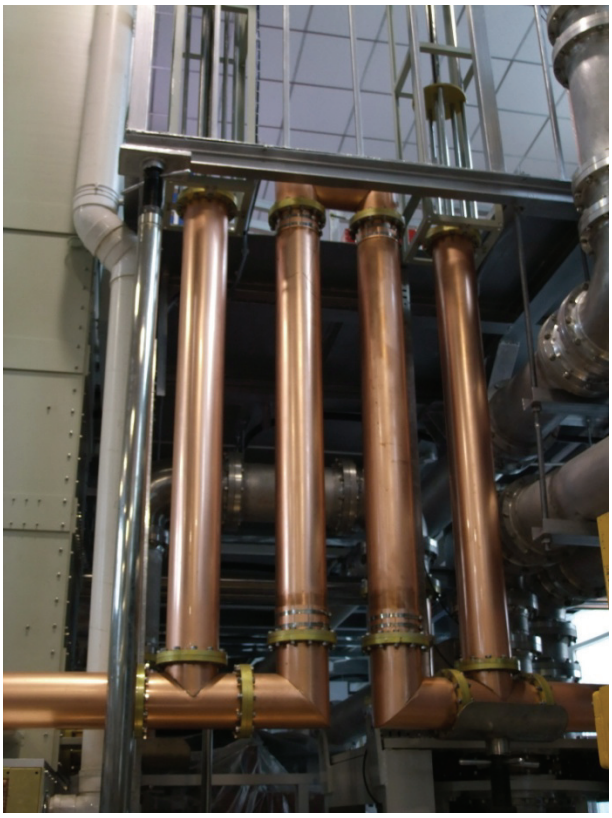

Fig. 2 Assembling and dimentions of waveguide absorbing structures

The output circuit of FPA is a double coaxial wave resonator, and two tuning stubs motivated by motors are installed among the inner, intermediate and outer conductors, which can change the length of resonator for impedance matching. The cross sections of the outer, intermediate, and inner conductor are a square, a 12-sided polygon, and a circle, respectively, for convenient assembly. As is known, spurious frequency

will appear when the tube works at rated power condiction. For TH525, the frequency of stray signal is about 1.2 to 1.3 GHz. To suppress the spurious frequency, a kind of rectangle waveguide structure terminated by wedge-shape absorbing materials was used. In this research and development, waveguide dimensions were chosen so that only the modes of which the cutoff frequency is in a range of 0.75 to 1.5 GHz will propagate, and then be absorbed, such as TE_{10}, TE_{01}. There are 17 waveguide absorbing structures assembled around the tetrode.

It is definitely necessary to effectively cool the components of the amplifier for long-pulse operation at high power level. Water cooling was mainly used for the tetrode and anode blocking capacitor and the power transmission line, and forced-air cooling was mainly used for the cavity and the tetrode socket terminals. the dissipated rf power on the surface of the intermediate conductor is higher than those of the inner and outer conductors because the double surfaces of the intermediate conductor are in effect. A gas blower was employed to drive air with an airflow rate of ~20 m^3/min and a pressure of 1500 Pa at the air tube inlet to remove the heat loss inside the output cavity, which is generated by the dissipated rf power.Another blower, which can provide a flow rate of 10 m^3/min with an air pressure of 1000 Pa, was used to cool the tetrode and socket terminals. Such a forced-cooling airflow can maintain high thermal efficiency to avoid overheating of the cavity

The DPA and the FPA were tested at each integer frequency over the whole designed frequency range. The averaged output power of 1.5 MW for each was achieved in a frequency range of 25 to 65MHz, and energy conversion efficiency from dc to rf was 60% to 70%, as shown in Fig. 3. However, it was found that rf output power and energy conversion efficiency decreased sharply when the amplifiers operated at frequencies higher than 65 MHz. The decreases in output power and in efficiency at the higher frequencies were caused by a limitation of the tetrode operating frequency, which is probably induced by the lead inductance of the electrodes, the geometry, and the electrode material of the tetrode. It was also found that output power was slightly low at 35 and 36 MHz. The reason is not clear. It needs to be further analyzed what caused this drop in rf power.

The crowbarless HVPSs based on PSM technology, as shown in Fig. 3, were developed for the THALES TH535 and TH525A tetrodes because of its great advantages compared with a conventional power supply with a crowbar, such as fast response, low short-circuited energy, safety, etc. The response time of such PSM power supply is about 2 μs for a specified overcurrent value of 200 A. Furthermore, another feature of PSM HVPS is that the response time is inversely proportional to the loop current of power supply. That is mainly because the energy in the circuit can be discharged faster with large currents. In addition, it takes a shorter time for a large current to reach to the specified threshold values. This character of PSM power supply will cause faster response under

the situation of over current to avoid severe damage of RF transmitter components. Therefore employment of the PSM HVPS ensures that the transmitters operate stably and reliably at high RF power levels.

Fig. 3 PSM power supply for TH535 and TH525A tetrodes

There will be eight sets of rf power amplifiers for rf heating in EAST in the future. Four of them have been already fabricated, and another four are under construction which will be finished at the end of this year.

3. Antenna and Matching network

Two fast wave antennas will be assembled in EAST and the performance of them will be tested in the next experiment campaign, as shown in Fig. 4. One is a 4-strap antenna which will be fabricated at I-port and each strap will be connected to a 1.5MW transmitter. Another one is a 2×2 loop antenna at B-port and each loop will be also connected to a 1.5MW transmitter, respectively, which inform that the total injected power will be more than 10 MW.

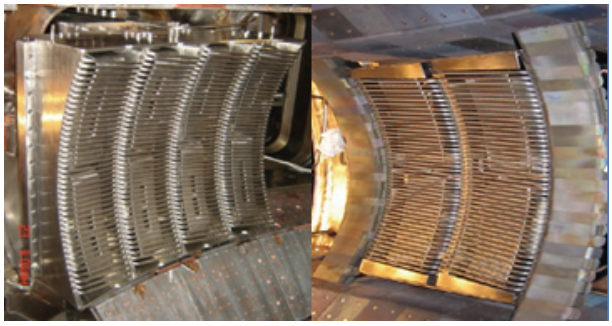

Fig. 4 4-strap antenna at I-port and 2×2 loop antenna at B-port

Liquid stub tuners were used for impedance matching network, which match the transmitter to antenna. However according to theoretical and experimental studies, some events such as L-H mode transition, ICRF operation during edge localized modes (ELMs) will induce time-varying loading impedance of ICRF antenna during a shot. The traditional choke-type and liquid stub matching networks are non-ideal any more due to their low tuning speed.

A Fast Ferrite Tuner consists of iron yoke, biasing magnets and ferrite loaded strip line which is biased by a pair of external magnetic coils. By changing the biasing magnetic field, variable permeability of the ferrite material which affects the propagation velocity, and hence equivalent electrical length of the device can be obtained.

The design of fast ferrite tuner and built of first prototype have already been finished. The test results

of first prototype have demonstrated that the FFT with the tuning speed of 340 ms is obviously faster than the traditional methods. As for future work, due to the saturation magnetization of ferrite materials which is a strong function of temperature, decreasing as temperature increases, the high power performance of the FFT should be tested in 2013 EAST winter campaign.

4. Conclusion

The design of FPA aimed at output power of 1.5 MW for 1000 s. The maximum output power of 1.5MW was achieved within the frequency range of 25 to 65MHz. The power supply system of DPA and FPA were upgraded by using reliable PSM high voltage sources, whose response time is less than 5 μs. The ICRF system, which consists of 8 transmitters, will give out more than 10 MW total output power in the future. Four of them have been already fabricated, and another four are under construction. Three liquid stub tuners are used for impedance matching between antennas and transmitters, which can be only tuned shot to shot, and new ferrite tuner is under developing. There are two fast wave heating antennas, which are assembled at I-port and B-port and will be tested in next experiment campaign, on EAST.

Although it was a very encouraging result for the research and development of ICRF system, several projects are in progress including fast response impedance matching, distributed data acquisition and control system and so on for EAST ICRF heating system.

Acknowledgments

The authors would like to thank the technical staff from Changfeng Broadcasting and Communications Equipment Company of Beijing for their helpful support. This work was partly supported by the JSPS-NRF-NSFC A3 Foresight Program in the field of Plasma Physics (NSFC No. 11261140328)".

REFERENCES

[1] Ogawa M, Tsuji-Iio S, Komori A, et al. 2007, Nuclear Instruments and Methods in Physics Research Section A, 577: 30-36

[2] Brémond S, Agarici G, Beaumont B, et al. 2003, Fusion Engineering and Design, 66-68: 453-460

[3] Greenwald M, Andelin D, Basse N, et al. 2005, Nuclear Fusion, 45: S109–S117

[4] Kwak J, Wang S J, Yoon J S, et al. 2009, Fusion Science and Design, 84: 1140

[5] Zhao Y P, Li J, Luo J R, et al. 2001, Plasma Physics and Controlled Fusion, 43: 343–353

[6] Zhao Y P, Hu J S, Zhang X J, et al. 2009, AIP Conference Proceedings, 1187: 181-188

[7] Qin C M, Zhao Y P, Li D C, et al. 2010, Plasma Physics and Controlled Fusion, 52: 085012

[8] Zhang X J, Zhao Y P, Wan B N, et al. 2010, Physics and Engineering Aspects of the ICRF Heating System on EAST. 23rd IAEA Fusion Energy Conference, Daejeon Convention Center, Korea

[9] Yang X K, Wang Z S, Zhao Y P, et al. 1998, Fusion Engineering and Design, 39-40: 129-133

[10] Mao Y Z, Yuan S, Zhao Y P, et al. 2012, Fusion Science and Technology, 61(3):216-226

[11] Chen G, Zhao Y P, Mao Y Z, et al. 2012, Fusion Science and Technology, 61(4):301-308

Program of A3 Workshop in Beijing

(19-24 May 2013)

19 May 2013 (Sunday) Registration & preparation of seminar: 15:00-21:00			

20 May 2013 (Monday)			
Session 1 (Opening) Chair: Prof. L.Q. HU	08:30	**J.G. LI** (ASIPP)	**Welcome speech** (10 min)
	08:40	**Officer** (CAS, NSFC, JSPS, NRF)	**Opening address** (20 min)
	Group photo and Tea & Coffee Break 09:10-09:40		
Session 2 (Category I) Chair: Prof. S. MORITA	09:40	**Akihiko ISAYAMA** (JAEA)	*Progress in the Development of JT-60SA toward Steady-State High-Beta Plasma Research* (17+3 min)
	10:00	**Jinhyun JEONG** (NFRI)	*Plan for the sawtooth control study by the ECH in KSTAR* (17+3 min)
	10:20	**Satoru SAKAKIBARA** (NIFS)	*Threshold of Mode Penetration in Helical Plasmas* (17+3 min)
	Tea & Coffee Break 10:40-11:00		
Session 3 (Category II-a)	11:00	**Shigeru MORITA** (NIFS)	*A problem to be solved for tungsten diagnostics through EUV spectroscopy in fusion devices* (17+3 min)

Chair: Prof. Y.K. OH	11:20	**Zhengying CUI** (SWIP)	*First measurement of radial profile of high-ionization impurity emission using grazing-incidence flat-field EUV spectrometer in HL-2A* (17+3 min)
	11:40	**Daiji KATO** (NIFS)	*Measurements of visible forbidden lines and ion distributions of tungsten highly charged ions at the LHD* (17+3 min)
	12:00	**Tetsutarou OISHI** (NIFS)	*Development of impurity profile diagnostics in the ergodic layer of LHD using space-resolved 3 m normal incidence VUV spectrometer* (17+3 min)
	12:20	**Seung Hun LEE** (KAIST)	*Overview of transport study based on X-ray imaging and VUV diagnostics on KSTAR* (17+3 min)
Lunch	12:40-14:00		
Session 4 (Category II-b) Chair: Prof. B.J. XIAO	14:00	**Yeong-Kook OH** (NFRI)	*Research Highlights in 2012 KSTAR Experimental Campaigns* (17+3 min)
	14:20	**Kazuo TOI** (NIFS)	*Determination of the Safety Factor Profile by MHD Spectroscopy Using Energetic Particle Driven Modes in Toroidal Plasmas* (17+3 min)
	14:40	**Satoshi OHDACHI** (NIFS)	*MHD activities in the stochastic region of the Large Helical Device* (17+3 min)
	15:00	**Yasuhiro SUZUKI** (NIFS)	*Nonlinear MHD modeling of Resonant Magnetic Perturbation* (17+3 min)
	15:20	**Shoubiao ZHANG** (ASIPP)	*Edge fluctuations during ELM-free phase in EAST* (17+3 min)
	Tea & Coffee Break 15:40-16:00		
Session 5 (Category III) Chair: Prof. K. TOI	16:00	**MinHo WOO** (NFRI)	*Alfven BGK mode in space plasma environment* (17+3 min)
	16:20	**Mitsutaka ISOBE** (NIFS)	*Recent progress of fast-ion loss detector project in Asian fusion experiments* (17+3 min)
	16:40	**Tieshuan FAN** (Peking U.)	*Development of Digital Neutron Diagnostic Systems for Fusion Plasmas Diagnostics* (17+3 min)
	17:00	**Biao SHEN** (ASIPP)	*The magnetic diagnostics in EAST steady state operation* (17+3 min)
	17:20	**Yipo ZHANG** (SWIP)	*Investigation of the slowing down of neutral beam-injected energetic ions in the HL-2A tokamak* (17+3 min)
	17:40	**Yi TAN** (Tsinghua U.)	*Recent Progress in the SUNIST Spherical Tokamak* (17+3 min)

21 May 2013 (Tuesday)			
Session 6 (Category I) Chair: Prof. B.J. DING	08:30	**Jianhua YANG** (ASIPP)	*The high-speed and wide-angle visible observation diagnostic on EAST using catadioptric optics* (12+3 min)
	08:45	**Guangmin CAO** (ASIPP)	*The simultaneous measurements of core and outer core fluctuations using CO2 laser collective scattering diagnostic in the EAST superconducting tokamak* (12+3 min)
	09:00	**Zhen SUN** (ASIPP)	*The newest progress of lithium experiments in ASIPP* (12+3 min)
	09:15	**Xiaofeng HAN** (ASIPP)	*Imaging Thomson Scattering diagnostic system on HT-7 tokamak* (12+3 min)
	09:30	**Guoqiang ZHONG** (ASIPP)	*Study the ICRF heating performance by neutron signal on EAST* (12+3 min)
	09:45	**Changzheng LI** (ASIPP)	*First results of SMBI and pellet injection experiment on EAST* (12+3 min)
	Tea & Coffee Break 10:00– 10:20		
Session 7 (Category II-a) Chair: Prof. Z.Y CUI	10:20	**Joohwan HONG** (KAIST)	*Investigation of Ar impurity transport with UTC-SANCO in 2012 KSTAR experiments* (12+3 min)
	10:35	**June-Eok LEEM** (POSTECH)	*Measurement of electron density fluctuations through microwave imaging reflectometry (MIR)* (12+3 min)
	10:50	**Shuyu DAI** (Dalian U. of Tech.)	*Modelling of local carbon deposition on rough test limiter exposed to the edge plasma of TEXTOR* (12+3 min)
	11:05	**Fuqiong WANG** (ASIPP)	*DIVIMP modeling of impurity transport in EAST* (12+3 min)
	11:20	**Yue XU** (ASIPP)	*Preliminary research on flat-type W/Cu plasma-facing materials and components for EAST* (12+3 min)
	11:35	**Feng LIU** (ASIPP)	*GAS-DRIVEN DEUTERIUM PERMEATION AND RETENTION IN 3D-QUASI-HOMOGENEOUSLY IRRADIATED TUNGSTEN* (12+3 min)
	11:50	**Guojian NIU** (ASIPP)	*Molecular Dynamics Simulation on Deposition and Damage of Tungsten Plasma-Facing Materials by Tungsten Dusts* (12+3 min)
	12:05	**Liang WANG** (ASIPP)	*Scaling of Divertor Particle and Heat Flux widths in EAST* (12+3 min)
Lunch	12:20-14:00		

Session 8 (Category II-a and II-b) Chair: Prof. J.Y. KIM	14:00	**Min Keun BAE** (Hanyang U.)	*Recent Development of Poloidal Fixed Probes in KSTAR Device* (12+3 min)
	14:15	**Hyung Jin KIM** (Hanyang U.)	*Current Status of a Divertor Inner Scanning Probe for KSTAR device* (12+3 min)
	14:30	**Aihui ZHAO** (Tsinghua U.)	*Spatial Amplification of Parametric Instabilities and Pump Depletion during Lower Hybrid Waves Injection into Tokamaks* (12+3 min)
	14:45	**Jing WU** (ASIPP)	*Erosion on marked PFMs exposed to EAST discharges* (12+3 min)
	15:00	**Xiaochun LI** (ASIPP)	*Molecular Dynamics Investigation of H/He Behaviors in W* (12+3 min)
	15:15	**Ryousuke GOTO** (NIFS)	*Extended MHD simulation of 2.5D Rayleigh-Taylor instability* (12+3 min)
	15:30	**Minjun CHOI** (POSTECH)	*Advanced 2-D measurement and analysis of tearing modes with the ECEI diagnostics on KSTAR* (12+3 min)
	15:45	**Jae-Hyun LEE** (POSTECH)	*2/3-D imaging of the edge-localized modes (ELMs) using ECEI systems in KSTAR* (12+3 min)
	16:00	**Houyin WANG** (ASIPP)	*Neutral Particles Diagnostic Systems for the EAST Divertor* (12+3 min)
	Tea & Coffee Break 16:15– 16:35		
Session 9 (Category III) Chair: Prof. K. HANADA	16:35	**Jun Young KIM** (UST)	*Fast ion loss induced by MHD instability and resonant magnetic perturbation in KSTAR* (12+3 min)
	16:50	**Chansoo KANG** (UST)	*Design of a hard x-ray spectrometer for fast electron bremsstrahlung studies in KSTAR* (12+3 min)
	17:05	**Huiqiao XIE** (Tsinghua U.)	*Electron Temperature and Density Diagnostics for Helium Plasmas in SUNIST by Line Ratio Method Based on Collisional Radiative Model* (12+3 min)
	17:20	**Yiqin LIU** (Sichuan U.)	*Study of Scintillator-based Fast Ion Loss Detector for HL-2A* (12+3 min)
	17:35	**Ran CHEN** (ASIPP)	*Experimental studies on the interaction of drift-wave turbulence and intermittent zonal flow in a cylinder plasma* (12+3 min)
	17:50	**Ruijie ZHOU** (ASIPP)	*Effect of magnetic fluctuations on the confinement and dynamics of runaway electrons* (12+3 min)
	18:05	**Liqing XU** (ASIPP)	*Experimental Study of Long-lived Saturated Mode in EAST ELM-free H mode Sawtoothing Plasma* (12+3 min)

22 May 2013 (Wednesday)			
Session 10 (Category I) Chair: Prof. M.H. YU	08:30	**Kazuaki HANADA** (Kyushu U.)	*Power balance estimation in long duration discharges on QUEST* (17+3 min)
	08:50	**Heung-Su KIM** (NFRI)	*Improvements in magnetic measurements for plasma control* (17+3 min)
	09:10	**Yaowei YU** (ASIPP)	*Fuelling efficiency studies by particle balance in KSTAR* (17+3 min)
	09:30	**Fangchuan ZHONG** (Donghua U.)	*Development of fast visible and Soft X-ray CCD imagining system for EAST tokamak* (17+3 min)
	09:50	**Yang ZHANG** (ASIPP)	*Design of a real-time control system for NTMs suppression with ECRH/ECCD on EAST* (17+3 min)
	Tea & Coffee Break 10:10– 10:30		
Session 11 (Category II-a) Chair: Prof. B. SHEN	10:30	**Jin-Yong KIM** (NFRI)	*Status and plan of fusion plasma simulation research in NFRI* (17+3 min)
	10:50	**Naoko ASHIKAWA** (NIFS)	*Hydrogen isotope inventories and structural analysis of co-deposited carbon layer in LHD* (17+3 min)
	11:10	**Yiping CHEN** (ASIPP)	*Simulation of SOL/Divertor plasmas on EAST tokamak* (17+3 min)
	11:30	**Chaofeng SANG** (Dalian U. of Tech.)	*The effects of divertor parameters on the plasma penetration depth of the castellated tile gaps: a kinetic simulation* (17+3 min)
	11:50	**Chunfeng DONG** (NIFS)	*Carbon distribution during plasma detachment triggered by edge magnetic island formation in LHD* (17+3 min)
	12:10	**Bin CAO** (ASIPP)	*The deuterium retention under different plasma parameters on EAST with full graphite wall* (17+3 min)
Lunch	12:30-14:00		
Session 12 (Category I) Chair: Prof. S. SAKAKIBARA	14:00	**Ryo YASUHARA** (NIFS)	*Short interval measurement of the Thomson scattering system at the pellet injection by using the event triggering system in LHD* (17+3 min)
	14:20	**Kazuo NAKAMURA** (Kyushu U.)	*Shape Reconstruction of Steady State Divertor Plasma on QUEST* (17+3 min)
	14:40	**Binjia XIAO** (ASIPP)	*Plasma control activities on EAST* (17+3 min)
	15:00	**Bojiang DING** (ASIPP)	*Recent LHCD experiments in EAST* (17+3 min)

	15:20	**Haiqing LIU** (ASIPP)	*Development of Far-infrared Polarimeter/ Interferometer System for EAST tokamak* (17+3 min)
	15:40	**Yanmin DUAN** (ASIPP)	*Radiated power measurement with AXUV photodiodes in EAST tokamak* (17+3 min)
	Tea & Coffee Break 16:00–16:20		
Session 13 (Category III) Chair: Prof. K. NAKAMURA	16:20	**Hyung Ho LEE** (NFRI)	*Tearing Modes induced by Perpendicular Electron Cyclotron Resonance Heating in the KSTAR tokamak* (17+3 min)
	16:40	**Sunho KIM** (KAERI)	*Status of fast neutral spectrum analyzer in KSTAR* (17+3 min)
	17:00	**Erzhong LI** (ASIPP)	*Study process on the ECE bursts in tokamak plasma* (17+3 min)
	17:20	**Ming XU** (ASIPP)	*Discussion for the Excitation Mechanism of Beta-induced Alfven Eigenmodes during Strong Tearing Modes on EAST tokamak* (17+3 min)

23 May 2013 (Thursday)	
Session 14 Chair: Prof. L.Q. HU Prof. S. MORITA Prof. Y.K. OH	09:00-12:00 Discussion with young scientists on further studies related to this A3 Foresight Program. Summarize this workshop, and prepare the electronic version of the seminar proceeding.
Session 15 Chair: Prof. Y.K. OH Prof. S. MORITA Prof. L.Q. HU	14:00-17:00 Discussions on future collaboration. Individual discussions on plans for personnel exchange. Summary of the meeting. Discussions on the next A3 meeting in Korea.
Closing Prof. L.Q. HU	Adjourn

(END)

List of Participants

Name	Affiliation
ASHIKAWA Naoko	NIFS
BAE Min Keun	Hanyang U.
CAO Bin	ASIP
CAO Guangmin	ASIPP
CHEN Ran	ASIPP
CHEN Gen	ASIPP
CHEN Yiping	ASIPP
CHOI Minjun	POSTECH
CUI Zhengying	SWIP
DAI Fuqiong	ASIPP
DAI Shuyu	Dalian U. of Tech.
DING Bojiang	ASIPP
DONG Chunfeng	NIFS
DUAN Yanmin	ASIPP
FAN Tieshuan	Peking U.
GOTO Ryousuke	NIFS
HAN Xiaofeng	ASIPP
HANADA Kazuaki	Kyushu U.
HONG Joohwan	KAIST
ISAYAMA Akihiko	JAEA
ISOBE Mitsutaka	NIFS
JEONG Jinhyun	NFRI
KANG Chansoo	UST
KATO Daiji	NIFS
KIM Heung-Su	NFRI

KIM Hyung Jin	Hanyang U.
KIM Jin-Yong	NFRI
KIM Jun Young	UST
KIM Sunho	KAERI
LEE Hyung Ho	NFRI
LEE Jae-Hyun	POSTECH
LEE Seung Hun	KAIST
LEEM June-Eok	POSTECH
LI Changzheng	ASIPP
LI Erzhong	ASIPP
LI Xiaochun	ASIPP
LIU Feng	ASIPP
LIU Haiquing	ASIPP
LIU Yiqin	Sichuan U.
MORITA Shigeru	NIFS
NAKAMURA Kazuo	Kyusyu U.
NIU Guojian	ASIPP
NIU Liang	ASIPP
OH Yeong-Kook	NFRI
OHDACHI Satoshi	NIFS
OISHI Tetsutarou	NIFS
SAKAKIBARA Satoru	NIFS
SANG Chaofeng	Dalian U. of Tech.
SHEN Biao	ASIPP
SUZUKI Yasuhiro	NIFS
SUN Zhen	ASIPP
TAN Yi	Tsinghua U.
TOI Kazuo	NIFS

WANG Fuquiong	ASIPP
WANG Houyin	ASIPP
WANG Liang	ASIPP
WOO Mi Ho	NFRI
WU Jing	ASIPP
WU Jing	SIPP
XIAO Binjia	ASIPP
XIE Huiqiao	Tsinghua U.
XU Liqing	ASIPP
XU Ming	ASIPP
XU Yue	ASIPP
YANG Jianhua	ASIPP
YASUHARA Kazuo	Kyushu U.
YASUHARA Ryo	NIFS
YU Yaowei	ASIPP
ZHANG Ling	ASIPP
ZHANG Shoubiao	ASIPP
ZHANG Yang	ASIPP
ZHANG Yipo	SWIP
ZHAO Aihui	Tsinghua U.
ZHOU Ruijie	ASIPP
ZHONG Fangchuan	Donghua U.
ZHONG Guoqiang	ASIPP